Twenty–five Years Progress

of the

Comprehensive Nuclear-Test-Ban Treaty Verification System

Contents

Contents

INTRODUCTION

Martin B. Kalinowski, Georgios Haralabus, Peter Labak, Pierrick Mialle, Eli Sarid, Mario Zampolli

Most nuclear testing monitoring technologies have been developed and used over decades; ever since nuclear testing began in 1945. The functioning of data communication and analysis methodologies were demonstrated by the Group of Scientific Experts Technical Tests. This experience helped to pave the way for the technical feasibility of the Comprehensive Nuclear-Test-Ban Treaty (CTBT). During formal negotiations at the Conference on Disarmament started in 1994 in Geneva, Switzerland, many countries offered to host stations and laboratories of the International Monitoring System (IMS). Efforts intensified to further develop technologies that, at the time when the effort was started, were not mature enough for use in an operational field environment. This undertaking was further advanced at the Prototype International Data Centre (pIDC) established in Arlington, USA in the 1990s.

On 19 November 1996, the United Nations General Assembly adopted resolution CTBT/MSS/RES/1 which established the Preparatory Commission for the Comprehensive Nuclear-Test-Ban Treaty Organization (CTBTO) with the mandate to build up the IMS, the International Data Centre (IDC) and to prepare the capabilities for on-site inspections (OSI). The goal was to have the completed verification system in place under provisional operation so that it would be ready for entry into force of the Treaty. When the Provisional Technical Secretariat (PTS) of the Preparatory Commission for the CTBTO started its work in Vienna, Austria, in March 1997, a lot of the available science and technology was inherited from the pIDC and States Signatories.

Since 1996, the PTS has grown dramatically. At the beginning of 2024, there are 187 States Signatories and 177 Ratifying States. The PTS has installed a global network monitoring the world for signs of nuclear explosions that include: a sustainable IMS, a provisionally operating IDC, and developing OSI capabilities. In the following 27 years since its inception, tremendous improvements in all domains of science and technology have been achieved by international experts and implemented by the CTBTO and the States Signatories. All stakeholders are committed to a credible and trustworthy verification regime as the cornerstone for entry into force of the Treaty.

According to Article IV, paragraph 11 of the CTBT *"Each State Party undertakes to cooperate with the Organization and with other States Parties in the improvement of the verification regime, and in the examination of the verification potential of additional monitoring technologies such as electromagnetic pulse monitoring or satellite monitoring, with a view to developing, when appropriate, specific measures to enhance the efficient and cost-effective verification of this Treaty."*

Improving the quality and sustainability of the verification regime is vital to sustaining and further building the confidence of States Signatories in the data and products of the CTBTO. The verification regime of the CTBTO is a remarkable union of ingenuity, engineering and international cooperation.

The IMS is almost complete with 90.8% of its 337 facilities certified at the end of 2023, providing a continuous flow of real time data that feed into IDC analysis products. While the IMS technologies are supported via maintenance and recapitalization, the scientific methods driving the detection, association and characterization of events of interest are being continually improved. This unique verification system is already delivering on its promise to ensure that no nuclear explosion goes undetected – anywhere and anytime – providing States Signatories with essential confidence building.

In 2014, OSI capabilities of the CTBT were showcased with the Integrated Field Exercise 2014 in Jordan. Since then, OSI technologies and data analysis methodologies have been further developed and tested to ensure readiness for entry into force of the Treaty. Progressive testing, training and validation in field conditions is carried out through regular exercises, with the next IFE to be conducted in Sri Lanka in 2025.

Technological improvements since the inception of the PTS and the IMS network are notable. For example, noble gas monitoring had never been operated in the field before, infrasound data processing and sensor design started from a very rudimentary stage, fusion of seismic with hydroacoustic and infrasound data posed a tremendous challenge, advanced methods for event screening and expert technical analysis to identify the source of specific events had to be invented and developed, and many OSI techniques had to be adapted to match the specific needs of the CTBT or had to be developed from scratch. The IMS system and OSI techniques are unique in many respects.

Monitoring data are suitable not only for CTBT verification purposes but also for a broad range of civil and scientific applications that are progressively being explored and demonstrated by pioneering work. Some of which include tsunami early warning and climate change studies. These data provide invaluable benefits to all States Signatories and many more new applications remain to be discovered. This treasure trove of data for civil and scientific applications remains an almost untapped resource with a huge potential to be still discovered. With the technological and scientific advancement in other fields, in particular monitoring techniques and data analysis with machine learning and artificial intelligence, new possibilities emerge for integrating new methods into the CTBT sensors and analysis.

The 25th anniversary of the opening for signature of the CTBT was marked at the CTBT: Science and Technology 2021 Conference (SnT2021) with a series of invited talks presenting the evolution over the past quarter century, and the technical challenges and prospects for the future of the verification system. This present collection of papers is based on 13 SnT2021 presentations augmented by three additional papers to cover more broadly the verification regime and its related scientific and technological achievements. A full summary and description of the scientific and technological advancements presented at the SnT2021 is publicly available.

The 25th anniversary of the Treaty was commemorated during SnT2021 with opening day discussions and a series of panels and invited talks. These talks constitute a very valuable resource for the CTBT community, bringing together wide perspectives on the development of the monitoring network over the past 25 years, discussions of current challenges and recommendations for the future.

All presenting authors were invited to write a full paper on their topic together with co-authors of their choice. In addition, two more papers were solicited to supplement the invited talks with information about sensor technologies. This booklet is comprised of these papers.

This collection of papers is not the first that summarizes the status of science and technologies for nuclear explosion monitoring and on-site inspection to verify compliance with the CTBT, but it is the first ever released by the PTS.

Most publications released since 2002 have focused on incremental advancements (please refer to the bibliography section at the end of this booklet for more detailed information). This was the case in several peer-reviewed publications compiled in dedicated journal volumes providing an overview of science and technology in the IMS, IDC and OSI published in 2001 and 2002.

A decade later, a monograph was published on the verification of the nuclear test ban from the perspective of States Signatories. It draws heavily on the presentations made by experts at the [International Scientific Studies conference](#) organized by the PTS in June 2009. This was complemented in 2010 and 2014 by several publications in journals on topical issues on recent advances in nuclear explosion monitoring.

In 2017, national initiatives by States Signatories also emerged. Several scientists from National Laboratories in the United States provided their views on the trends in nuclear explosion monitoring research and development, while the German National Data Centre compiled their introductions to the technologies for CTBT monitoring and enriched it with examples of event analysis.

Over the last decade, the PTS organised the SnT Conference Series in Vienna, Austria, where researchers, scientists, technologists, academics, civil society and States Signatories representatives, as well as CTBTO Youth Group members from around the world gathered to build and strengthen the PTS relationship with the broader science community in support of the CTBT. Proceedings of the SnT Conferences from 2011 to 2023 are summarized in specific reports.

In 2019, the tradition of topical issues of a peer-reviewed journal was revitalized. These contain publications of papers based on selected presentations made at SnT conferences in [2019](#), [2021](#) and [2023](#).

The collection of papers presented in this booklet constitutes a unique review of the achievements made in the last 25 years and provides a comprehensive description of the state of the art science and technologies for CTBT verification. They demonstrate that the CTBTO is at the forefront of scientific and technological advancements thanks to a strong and growing community of international experts and highly skilled technical staff members of the PTS, past and present, who contribute their expertise.

These papers, reviewing more than 25 years of progress in the development of the robust and reliable CTBT verification system, should aid in supporting global peace and security, now and in the future.

Challenges and Achievements of Seismological Monitoring for Nuclear Test Explosions in the Context of the Comprehensive Nuclear-Test-Ban Treaty

P. G. Richards, D. P. Schaff, W.-Y. Kim

Lamont-Doherty Earth Observatory of Columbia University,
New York, United States of America

Abstract

This paper addresses seismological methods of monitoring for earthquakes and explosions and the challenges of dealing with many seismic events — most of them small — which sometimes need to be thoroughly understood. Examples of procedures now being applied to continuous waveform archives are described, that show significant improvements over traditional methods of monitoring.

1. INTRODUCTION

The main *challenge* in monitoring for compliance with the Comprehensive Nuclear-Test-Ban Treaty (CTBT) is that many different activities — both natural and human-made — generate signals which are detected many times a day by networks contributing to CTBT monitoring. Such signals can have at least some resemblance to the signals generated by a nuclear test explosion. The main *achievement* of monitoring for CTBT compliance is that decades of practical experience have led to monitoring capabilities that have become reliable in detecting and identifying even very small nuclear tests. Support for this claim is documented at length, for example by the National Research Council of the United States of America (USA) (2012) and the US National Academy of Sciences (2002); and by extensive technical literature supported by research institutions and national and international agencies.

The purpose of this paper is to convey a sense of what monitoring methods entail, with an emphasis on seismology since it is the key technology relevant to monitoring for underground nuclear test explosions (UNEs). The underground environment is generally understood to be the hardest to address from a monitoring perspective. Seismology was deemed inadequate for monitoring UNEs in the final stages of negotiating the Limited Test Ban Treaty of 1963 — which banned nuclear testing in all other environments (space, atmosphere, and underwater).

Monitoring methods have changed over the years in ways related to changes in the quality and quantity of seismic signals recorded since nuclear testing began in the 1940s. Figure 1 shows that beginning in the 1990s there has been a huge reduction in testing rates towards a norm of no nuclear testing. The numbers in red indicate that there were more than 850 nuclear tests conducted by the USA and more than 540 by the former Soviet Union, in the era dominated by analogue recording. The numbers in green indicate nuclear tests conducted in the era of digital recording, which grew rapidly in the early 1980s. Digital data enables the application of sophisticated computational methods to assist in the extraction of pertinent information from seismic signals. All nuclear test explosions in space and underwater took place only in the pre-digital era — as well as almost all the atmospheric nuclear explosions and the majority of UNEs. For purposes of establishing basic characteristics of signals from nuclear test explosions in all environments, technical and scientific information contained in earlier forms of recording can be saved (by scanning), and made useful (by digitizing and combining with metadata that describes the seismometer) to help analysts engaged in monitoring become familiar with the wide range of features of actual signals of nuclear tests (Richards and Hellweg 2020).

This paper has two goals: to lay out some of the basic procedures and steps in the monitoring process, and to convey a sense of what can be achieved with more sophisticated procedures. This paper will convey basic procedures and terminology (concerning monitoring methods) for non-specialists, and characterize results at the research frontier for those interested in learning what specialists can achieve (now and in the future).

The following sections describe basic methods of seismic monitoring; some specific details on the capability to monitor for nuclear tests conducted by the Democratic People's Republic of Korea; examples of high-precision/low-magnitude monitoring capability; and a summary.

2. BASIC METHODS OF SEISMIC MONITORING

In the decades following World War II, with its development of nuclear weapons and their eventual use in 1945, more than two thousand nuclear test explosions were conducted in various environments and monitored at first by detection and analysis of radionuclides. As the Limited Test Ban Treaty of 1963 gathered adherents and nuclear testing moved from the atmosphere to

Nuclear Tests per Decade, for different countries

Country	1940 to 1949	1950 to 1959	1960 to 1969	1970 to 1979	1980 to 1989	1990 to 1999	2000 to 2009	2010 to 2019	2020 to 2029	∑ NTs per country
USA	6	188	426	234	155	21	0	0	0	1030
Former USSR (Russia)	1	82	232	227	172	1	0	0	0	715
UK		21	5	5	11	3	0	0	0	45
France			31	69	92	18	0	0	0	210
China			10	16	8	11	0	0	0	45
India				1	0	2	0	0	0	3
Pakistan						2	0	0	0	2
Democratic People's Republic of Korea							2	4	0	6

to October 28, 2022

Numbers in red: these explosions took place in the era of analog recording

Almost all nuclear testing in the atmosphere took place in the analog era

Numbers in green: explosions after the era of digital recording had begun.

FIGURE 1.

Numbers (principally from Yang et al. 2002) showing a great reduction in the rate of nuclear testing, per decade, by the five permanent members of the United Nations Security Council. The rate for three additional countries with announced test programmes are also shown. Numbers in red include all the multimegaton explosions, all those underwater or in space, and almost all nuclear test explosions in the atmosphere. Tables by Mikhailov et al. (2014) indicate agreement on the number of tests by the USA, former USSR and UK in this Figure; but some slight differences for France and China. (USSR denotes the Union of Soviet Socialist Republics, whose treaty obligations are now assumed by the Russian Federation.)

the underground environment, monitoring relied more and more on seismological methods. They entail a sequence of six steps:

- Detection;
- Association of all the signals from separate stations that are due to a particular event;
- Locating that event;
- Characterizing it (natural earthquake, chemical explosion, nuclear test, or something else);
- Estimating its size; and (if nuclear)
- Attributing it to a particular country.

For decades since 1963 the work of monitoring large countries for nuclear tests relied on teleseismic signals (see Figure 2).

Regional signals can be of several different types. They can be favourable for use in seismic monitoring of small seismic events to the extent that, if available, they usually provide the largest signals. But for reliability there is usually the need to document their performance in detail since they exhibit significantly different characteristics in different regions.

In the 1970s and 1980s teleseismic monitoring alone could achieve a capability for detection and characterization of seismic events in the range around magnitude 4 to 4.5 and larger, depending on the level of effort put into signal gathering and data analysis. This indicated that explosions of around 1 kiloton could be monitored. It is relevant to be aware of basic issues that need to
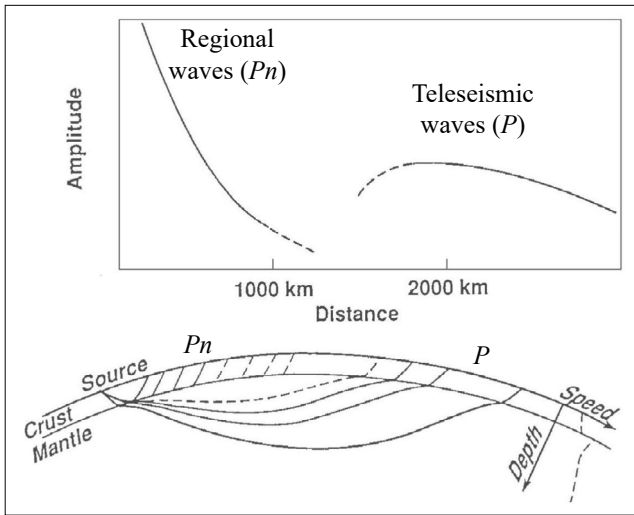
FIGURE 2.

Illustration (credit: Carl Romney 1960) showing basic differences between the amplitudes of teleseismic signals (recorded at distances beyond about 1500 km) and those of regional seismic signals (which travel within the Earth's crust or at shallow levels within the mantle). Adapted from Richards and Zavales (1996).

be addressed in the attempt to reach consensus on exactly what the capability of a particular monitoring network might be — whether evaluating an actual network or a hypothetical one. They include:

(1) Whether there is a need for speed in reaching conclusions on the nature of a seismic source that has apparently generated a specific set of signals;

(2) Whether an effort is needed to ensure, for problematic events (i.e. those hard to characterize), that a thorough search has been made for relevant signals obtained fortuitously from stations emplaced for non-monitoring purposes (e.g. for scientific research) and that happened to be in the right place at the right time;

(3) Whether there might be the possibility of a nuclear test conducted with specific efforts to reduce its seismic signals for purposes of making the test hard to detect and/or to identify.

The possibilities associated with item (3) above are limited because (as noted in the US National Academy of Sciences 2002) there are several practical layers of difficulty in executing a

nuclear test programme that could evade detection or assessment by a well-run monitoring system. Furthermore (as noted in US National Research Council 2012) the prospect of failing to hide an attempt at evasion may be deemed sufficiently serious by an organization planning to carry out such attempt, that it would drive down the yield of any attempted test to a very low level, and thus be of limited significance. It is appreciated that considerations of what is militarily and/or politically significant are separate from technical evaluations of monitoring capability.

Of the six practical steps in monitoring listed previously, one of the most important is that of locating a seismic event. Basic features of this step are shown Figure 3, which builds on the fact that an earthquake or an underground explosion generates both primary (P) and secondary (S) waves, so named because P-waves arrive first. The time separation between arrivals of these two waves increases with distance, and measurement of the 'S minus P time' from a seismogram can be translated via standard tables to a distance — which is simple to interpret as the radius of a circle centred on the station where the seismogram was recorded. Figure 3 shows the seismograms at three stations, three circles derived from the measured S minus P times, and the point of circle intersection giving an estimate for the source location (in California for this example).

Information on the quality of the location estimate can be gleaned from the degree to which the three circles intersect at a common point. There can be more than three circles if data are available from more stations. Alternative approaches can be based on using the absolute times of P- and S-arrivals at each station, noting that the locus of points for which the difference in distances to a pair of stations is constant, is a hyperbola. The source is then where a mix of hyperbolas and circles intersect. Such methods, based on measured arrival times at different stations to locate seismic events, have been in use for more than a hundred years. They can be good for getting an approximate location, but typically there are three inherent weaknesses of this traditional method:

(1) They use only a small fraction of the information in seismograms;

(2) They are based on measurements made where the signal is often very small;

(3) They require a method to convert the measurement of *time* differences made on seismograms to a *distance* (for example the radius of a circle) — and the conversion factor is known to be different for different regions. It can even vary significantly within a region.

Nevertheless, the most widely used lists of seismic event locations are based on the interpretation of measured seismic wave arrival times. Such lists include: the main Bulletin of the International Seismological Centre; the Reviewed Event Bulletin and the Late Event Bulletin of the International Data Centre (IDC) based on the International Monitoring System (IMS) data; the Preliminary Determination of Epicenters of the US Geological Survey; and numerous national/regional/local bulletins of seismicity around the world.

Fortunately, considerable attention has been directed toward the third weakness (3). For example, regional variation in the relation between time and distance was the subject of technical workshops held from 1999 to 2003 in Oslo, Norway, under the auspices of the CTBTO's Provisional Technical Secretariat. They developed extensive information on the variation in speed of the principal regional seismic waves *Pn*, *Pg*, *Sn*, and *Lg*. So-called Source Specific Station Corrections (SSSCs) were developed for IMS primary and auxiliary stations. SSSCs correct the simplifying assumption in Figure 3a that a time
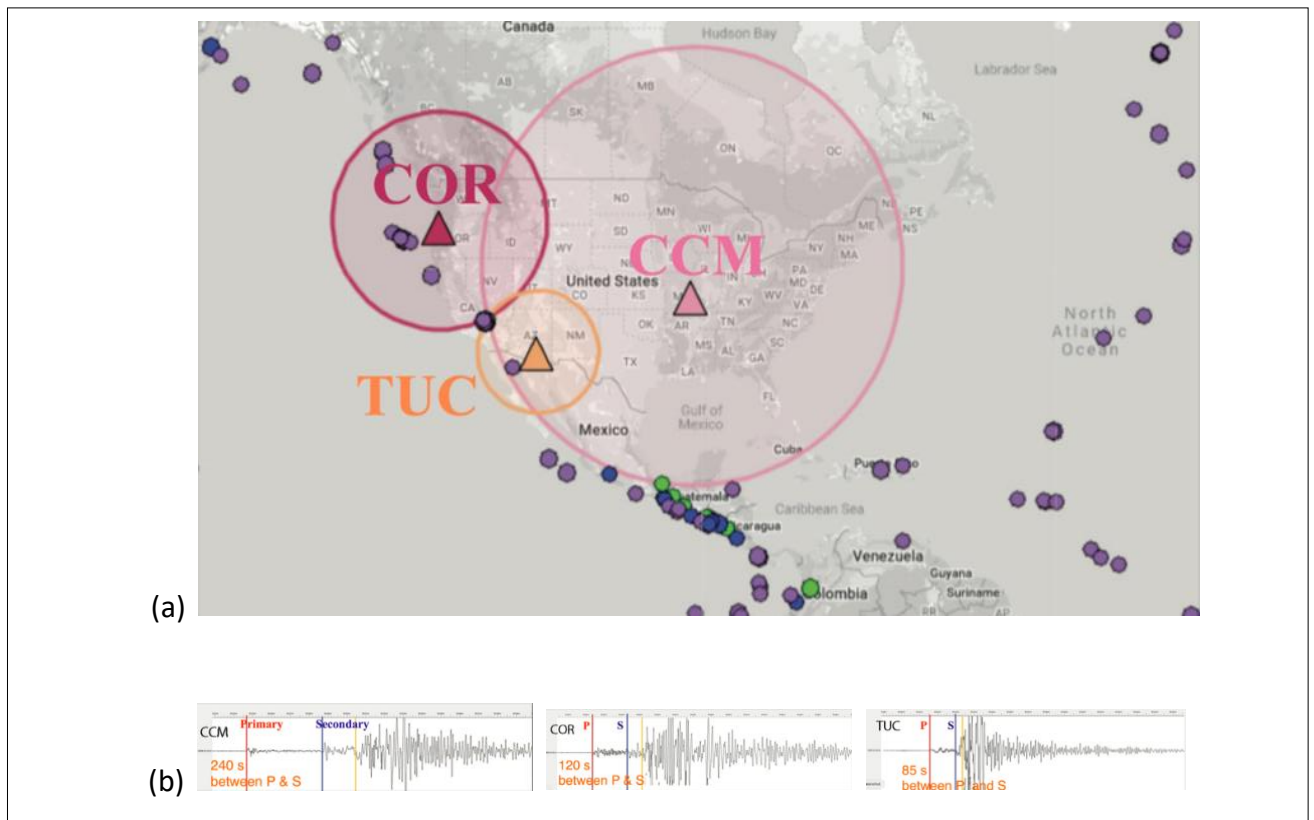
FIGURE 3.

Traditional method for locating a shallow earthquake in western USA on the basis of P-wave and S-wave arrival times, measured at three stations indicated by triangles: Cathedral Cave, Missouri (CCM); Corvallis, Oregon (COR); and Tucson, Arizona (TUC). (a) shows the three stations, each at the centre of a circle whose radius is proportional to the time between the arrivals of S-waves and P-waves at that station. The earthquake must lie on each circle, and hence at the place where they all intersect. Green and purple dots indicate the location of different earthquakes. (b) shows a seismogram at each station, indicating the time separation between S and P arrivals. (Based on Locating an Earthquake with Seismic Data*)*

measurement (S minus P) could be translated into a circle centred on each station. That work led to the development of a Regional Seismic Travel Time (RSTT) Model, as described by Begnaud et al. (2020, 2021) that enables an improvement on SSSCs, by providing a quick method to estimate the time for a regional seismic wave of interest to travel from any candidate source location to a station reporting a regional-wave arrival time. The key source parameters (latitude, longitude, depth, origin time) of the source are then obtained by iterating until values are found that best fit the set of observed arrival times of various regional seismic waves as reported via the set of stations used for monitoring the region.

The outcome has been a significant improvement in the accuracy of seismic event locations based on regional data, using a method that retains a virtue of the traditional approach to event location, namely that it can be applied to the study of individual events of interest since events are located one at a time. But the RSTT approach can give good results only to the extent that it is based on a regional model of the Earth's structure that can generate accurate travel times from any candidate source location to any station from which an arrival is measurable. The RSTT approach still suffers from using minimal information from recorded seismograms, and from extracting that information from parts of the seismogram where the signal is small and thus prone to measurement error.

The use of modern methods of event location, which extract information from waveforms recorded over (typically) a few tens of seconds, shows that these more sophisticated methods can provide more precise locations. But they entail the need to study groups of events in a particular region, with the goal of estimating their relative locations.

3. EXAMPLES OF CAPABILITY TO MONITOR FOR NUCLEAR TEST EXPLOSIONS IN THE DEMOCRATIC PEOPLE'S REPUBLIC OF KOREA

Since the nuclear test explosions of May 1998 in India and Pakistan, the only country (as of October 2022) to have engaged in nuclear testing is the Democratic People's Republic of Korea. At the time of writing the Democratic People's Republic of Korea has conducted six tests, the first on 9 October 2006; the last on 3 September 2017.

There are many seismographic stations at regional distance from the Democratic People's Republic of Korea test site, including some dedicated to monitoring in the context of the CTBT (stations of the IMS), some operated globally for general purposes of research (the Global Seismographic Network as described by Ringler et al. 2022), plus stations of regional agencies based in China, Japan, the Republic of Korea and elsewhere. It has been useful to have access to recordings from temporary stations operated in the region. Some of these assets are shown in Figure 4, which also indicates the location of seismic events of interest that have enabled practical experience to be acquired for purposes of developing and applying seismological methods of discrimination between different types of seismic events. Figure 4 indicates the location of underground nuclear test explosions in the Democratic People's Republic of Korea.

By studying signals from the six Democratic People's Republic of Korea nuclear tests and from numerous small seismic events in the region, including aftershocks of some of the nuclear tests, it has been shown that underground explosions, down to a few tonnes of TNT equivalent, can be detected. This section highlights a five-year effort to seek, find, and evaluate, seismographic data from a very small seismic event in 2010. It occurred on 12 May that year, with a magnitude reported at less than 1.5. This section also addresses small seismic events detected in the
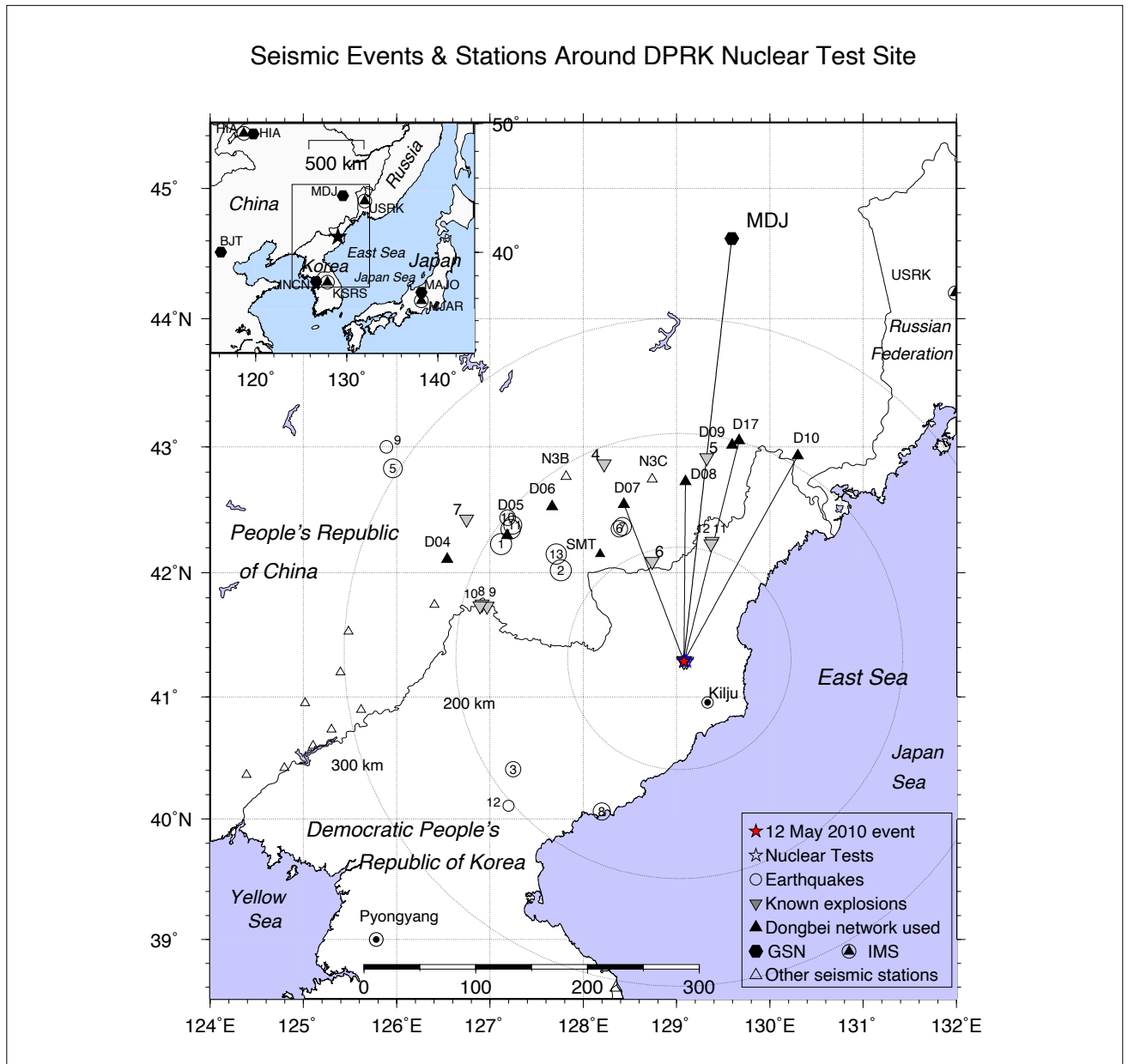
FIGURE 4.

A map of northern parts of the Korean peninsula and nearby regions, with locations of nuclear tests conducted by the Democratic People's Republic of Korea (stars); a small seismic event on 12 May 2010 (red star); an IMS array at Ussuriysk in the Russian Federation (labelled USRK); a Global Seismographic Network (GSN) station in Mudanjiang, China (labelled MDJ); several temporary stations (of the Dongbei network and others); and several earthquakes and known explosions. (Adapted from Kim et al. 2017.)

vicinity of the previous Democratic People's Republic of Korea nuclear test explosions. They appear to be small earthquakes triggered by stress changes due to the explosions.

3.1. 12 May 2010 Seismic Event

A paper by De Geer (2012) reported unusual detections in Spring 2010 of radioxenons and radioxenon progeny nuclides at four sampling stations located outside the borders of the Democratic People's Republic of Korea. De Geer and several subsequent papers proposed that a previously unknown nuclear test explosion was the underlying cause. Schaff et al. (2012) searched for seismic signals from small explosions in North Korea on specific days in 2010 proposed by De Geer, which included 11 May but not 12 May.

Principally efforts went into examining records from the nearest open station of the GSN (the Mudanjiang station in north-eastern China – see Figure 4) but those efforts failed to find seismic signals that would be expected if the scenarios proposed by De Geer were valid. Therefore, it was concluded that any explosion would have had to be very small (local magnitude less than about 2) to escape detection. An important issue emerging from this analysis was the practical difference between two types of detection threshold: (a) estimating the present or future detection capability of a monitoring network, absent any templates similar to the signal one is attempting to detect, and (b) estimating the detection capability for a specific time period in the past when it is known what data are available and for which a station (such as Mudanjiang) has templates (that is, recordings of actual explosions, with basic features similar to the signals being sought). Detection capability is much better in the latter situation.

In view of these previous studies and several additional papers interpreting the radionuclide data of 2010 in terms of a low-yield nuclear test, it was of considerable interest that Zhang and Wen (2015) reported data from a small seismic event in the Democratic People's Republic of Korea, occurring early on 12 May 2010 at about 00:08:45 UTC, which was characterized unambiguously as a small nuclear explosion. Data from seismographic stations in Jilin Province, China, in the distance range of about 80–200 km from the Democratic People's Republic of Korea test site were used, including the high-quality borehole station SMT indicated in Figure 4.

Results from Zhang and Wen led to additional searches for regional seismic signals, and Kim et al. (2017) reported on two different temporary deployments of seismometers that had recorded useful signals of the event on 12 May 2010. The first deployment had been led by Kin-Yip Chun of the University of Toronto who installed stations of a network (Dongbei) at locations indicated in Figure 4. The stations operated for several years and had recorded signals from the Democratic People's Republic of Korea nuclear tests of 2006 and 2009 (Chun et al. 2011). The second was a

shorter-term deployment of a research array in north-east China, from which one station (NE3C, see Figure 4) had good signals. Of interest also were the measurements reported by Zhang and Wen (2015) as derived from seismograms at borehole station SMT.

Kim et al. (2017) measured the spectral ratio of P-waves and S-waves at different frequencies, at first using data from the open station Mudanjiang in north-east China, for training sets of earthquakes and explosions. Decades of research has shown that measurements of P/S spectral ratios can provide an effective discriminant between earthquakes and underground explosions, and Pan et al. (2007) and others have affirmed that this method can discriminate between seismic events that are very small. Kim et al. (2017) went on to apply standard statistical methods that provided the combination of P/S spectral measurements from Mudanjiang recordings (at different frequencies) which are most effective in separating the earthquake and explosion populations in the training sets. Mudanjiang lacked usable data for the event of interest, and as noted above the seismograms used by Zhang and Wen were not openly available. But their paper does provide values of the spectral ratios measured at different frequencies from borehole station SMT.

When the combination of P/S spectral ratios for events in the region, as derived from the station with the most extensive set of spectral measurements (Mudanjiang), is applied to the events of interest, using P/S spectral ratios derived from the additional regional stations, Kim et al. (2017) reported that the combination from known explosions (in 2006 and 2009) was explosion-like; but for the 12 May 2010 event, the combination was earthquake-like. In physical terms, this result can be summarized as indicating that the seismic data from Dongbei stations, from NE3C and from the borehole station SMT, all indicate that the event on 12 May 2010 had S-waves which were significantly stronger than would be expected from an explosion of the size indicated by its P-waves. In this respect, the S-wave strengths recorded at these stations were those to be expected from an earthquake.

The seismic event of 12 May 2010 was about two and a half units lower in magnitude than that of the first Democratic People's Republic of Korea nuclear test of 2006, and thus had signals about 300 times smaller. It was both a challenge and an achievement to obtain relevant seismic signals and interpret them. The full archive of seismic recordings made over about six years by the Dongbei Seismographic Network was delivered in 2022 to the Incorporated Research Institutions for Seismology (IRIS) Data Management Center, and preliminary studies indicate that a background of small natural seismic events exists for the northeastern part of the Democratic People's Republic of Korea — which includes the region of nuclear testing.

It remains a challenge to find a consistent explanation for the unusual radionuclide signals of 2010.

3.2. Brief Comments on the Additional Democratic People's Republic of Korea Nuclear Tests, and Related Seismic Activity

The sixth nuclear test explosion conducted by the Democratic People's Republic of Korea on 3 September 2017, was far larger than previous tests. It created an underground cavity that collapsed about 8.5 minutes after the explosion. It has also resulted, at the time of writing, in hundreds of small aftershocks that have themselves provided opportunities for developing ever-improving methods of seismic monitoring for the region. Adushkin et al. (2017) pointed out the potential for remote identification of aftershock activity as a method of explosion monitoring.

In December 2017, a few months after the large nuclear test explosion, the American Geophysical Union hosted a special session on the event and its aftershocks. In late 2018, 17 papers were published on these events in a Focus section of the journal *Seismological Research Letters* (October 2018). As noted in the introduction to the Focus section by Walter and Wen (2018), these papers covered "a full range of topics from surface observations, acoustic observations through detailed seismological investigations
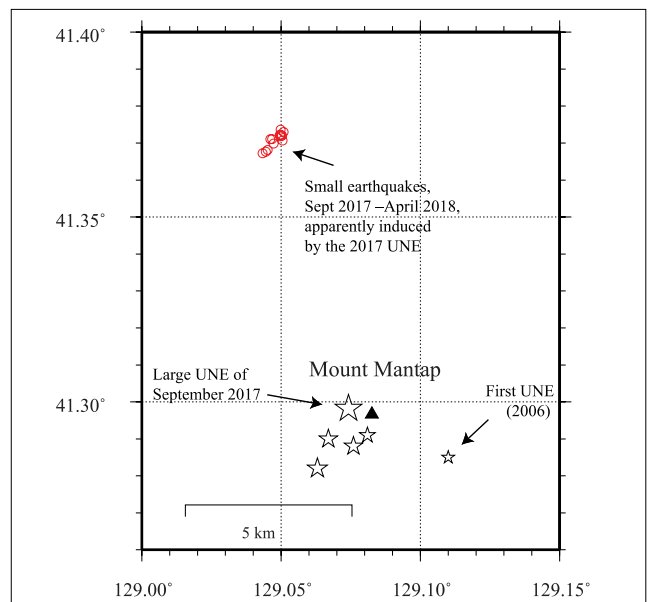
FIGURE 5.

Location of six Democratic People's Republic of Korea nuclear tests from 2006 to 2017 (open stars), obtained by combining information on the relative location of all pairs of events. Precise relocations of 13 aftershocks of the large-yield test of 3 September 2017, as reported by Schaff and Kim et al. (2018), are plotted as red circles whose centroid lies on the absolute location given by Tian et al. (2018) for an aftershock on 23 September 2017. (Adapted from Kim et al. 2018.)

of the nuclear test, the post-test collapse, and the additional seismic events, including event detection, location, depth and yield estimation, and source-type discrimination." The aftershocks of the sixth test explosion have continued in subsequent years, and aftershocks have also been found for earlier nuclear tests conducted by the Democratic People's Republic of Korea (Kitov and Rozhkov 2019).

In practice the relative location of seismic events in the same neighbourhood can often be estimated precisely by using, as input data, the relative arrival times of signals from pairs of events that are near each other, as measured from data recorded at each station obtaining signals from both events. This approach avoids all three of the inherent weaknesses associated with the traditional method of event location described in section 2. Thus, the better approach:

- Uses cross-correlation methods applied to waveforms, and hence a larger fraction of

the information in recorded waveforms, than merely an estimated arrival time;

- Is based typically on parts of the signal where amplitudes are largest;
- Avoids problems arising from ignorance of the velocity of seismic waves in the crust and upper mantle structures between the source region and each observing station.

The method of relative locations was first applied to signals from the Democratic People's Republic of Korea nuclear testing by Won-Young Kim days after the second test occurred on 25 May 2009. He obtained regional seismograms from more than 20 stations that had recorded both tests and that had a good azimuthal distribution around the test site. He showed that the second nuclear test was about 2.6 km in the west-north-west direction from the first nuclear test on 9 October 2006. His result was reported at the International Seismic Studies meeting on 11 June 2009 in Vienna. The second test was the first to be conducted beneath Mt. Mantap (which also became the site of tests three to six as indicated in Figure 5).

Extensive information and analysis of activities at the Democratic People's Republic of Korea nuclear test site as well as descriptions of regional geology and the system of tunnels can be found on the website 38north.org.

Extensive uses have been made of the method of relative locations in application to broad areas. Some examples are described in the next section of this paper. Figure 5 shows locations of the subset of 13 aftershocks after the Democratic People's Republic of Korea sixth nuclear test that were studied in detail by Schaff and Kim et al. (2018) and which lie several kilometres to the north of this presumably causative explosion. They display the earthquake-like characteristic of being aligned as if on a fault. It is about 700 m long and strikes to the north-east.

4. EXAMPLES OF HIGH-PRECISION EMPIRICAL METHODS OF SEISMIC EVENT LOCATION

4.1. Background

Section 2 outlined the traditional method of locating events one at a time based on matching the times of arrival measured for specific waves detected at a set of seismographic stations. A logical way to avoid inherent weaknesses of that approach and achieve the goal of reducing errors associated with traditional methods would be to improve:

- Models of Earth structure (i.e. the details of the way its seismic waves, P and S travel at different speeds in different places, and density variations);
- Models of earthquake and explosion seismic sources, characterized for small events by their moment tensor;
- Methods of computing 'synthetic' seismic waves in such Earth models for seismic sources of interest.

These improvements could make it possible to carry out an iterative process of adjusting the four parameters of latitude, longitude, depth, and origin time, until the synthetics obtained are a good fit to the waveforms observed at high-quality broadband stations.

Such an approach works to the extent that (1) waveform data are selected (by filtering or choice of instrumentation) to avoid use of frequency content that is too high to be successfully computed; and (2) the fine detail of actual Earth structures is adequately known. But in practice for purposes of matching the details of observed regional seismograms, there are serious practical difficulties with items (1) and (2). Specifically, signals are observed at frequencies higher than the waveforms can be computed; and their features (the wiggles of observed seismograms) are influenced by structure at scales too fine to be known in detail. Thus, regional waves from the Democratic People's Republic of Korea explosions,

for example at the GSN stations Mudanjiang and Incheon, Republic of Korea, and at the IMS arrays Ussuriysk in Russia and KSRS in the Republic of Korea, are recorded (to about 10 Hz and above) after propagating hundreds of wavelengths; and the duration of substantial high-frequency amplitudes (called coda) in such seismograms can be tens of seconds. The community of expert analysts cannot yet generate synthetics for Earth models with variability in all three spatial dimensions that are a good fit to such observations, although progress is being made.

For example, Olsen et al. (2018) simulated wave propagation in state of the art models of the Korean peninsula using smooth three-dimensional varying seismic velocities and density, having 24 billion points at uniform spacing (100 m). They noted that modern capabilities enable synthetics up to 4 Hz to be computed out to distances of several hundred kilometres. By including anelastic attention parameterized by a variety of Q models, they achieved some success with synthetics that matched the timing of observed regional wave arrivals; but at first they grossly overpredicted Rayleigh-wave amplitudes and underpredicted the coda. It has been a puzzle for decades that observed short-period coda can last so long in regional seismograms. Olsen et al found that the key to achieving better fits between synthetics and recordings of the Democratic People's Republic of Korea 25 May 2009 nuclear test recorded at Incheon — of Pn, Pg, Sn, Lg, including the long lasting coda of these waves — was to add small scale perturbations of the P- and S-velocities according to statistical rules that are summarized by the strength and length scale of inhomogeneities. This still does not achieve wiggle-for-wiggle agreement between computational results and observations (i.e. synthetics and waveform data) at short period. The actual Earth structure at this level of detail is unknown and in practice is probably unknowable. But it is good to get these indications that broad features of strong scattering of high frequency seismic waves within the heterogenous Earth are being simulated, such as long coda.

It is well worth the effort to fit details of synthetics to observations at frequencies as high as possible. Success would come with the associated benefits of improving our knowledge of Earth structure, of the statistical features of stochastic scattering, and of source properties such as stress drop and details of the distribution of slip over a finite fault region. But the observed band of seismic waves in practice extends to high frequencies that cannot be fully modelled today.

Fortunately, empirical methods have been developed that work quite well to access waveform information pertinent to event location and discrimination. Such empirical methods improve event detection and location in regions where many events take place. Each event can be compared with its neighbours to obtain relative locations and sizes of seismic events in active regions. It is preferable to work with absolute locations rather than relative ones, but for studies in earthquake physics and patterns of stress, relative locations can be adequate. And relative locations may be converted to absolute ones based on special information on some of the events — for example, by associating one or more of the events with changes in a feature of the surface of the Earth obtained via satellite observations.

4.2. Some Success

Many different groups have contributed practical methods of monitoring regions of active seismicity, where the emphasis is on comparative analysis of two waveforms at each station that recorded both the signals from a neighbouring pair of events. In particular, the relative time of arrival, ΔT, of a whole waveform compared to another can be measured from waveform pairs recorded at a common station. Precision that had been on the order of a few tenths of a second (in measurement of the arrival time of weak P-waves) can be improved—even to within a few milliseconds—in measuring the relative time of waveforms from two events near each other. Obtaining the relative location for each event within an event cluster can then be done using double-difference methods, as described by Waldhauser and Ellsworth (2000), again with significant improvement in precision. What is sought is the relative location of event pairs, and ignorance of the velocity of seismic waves in

the region between a group of events and each recording station does not matter when the input measurement from each station is ΔT for each event pair. Only the horizontal velocity in the source region, of the phase of interest, enters the relationship between ΔT measurements made at different stations, and the relative vector location of the two events.

Waveform correlation was applied to digital seismic data for the first time on a significant scale in the 1980s in Iceland (Slunga et al., 1995). Empirical methods were used rather than synthetics to detect, locate, and characterize many small seismic events in that tectonically active region. Many authors, often working independently, have developed versions of these methods for application to diverse regions. In the next section, a sequence of papers is summarized that explores techniques for limited regions, and reports preliminary results when the new techniques are applied on a much larger scale for part of East Asia (Mongolia and surrounding regions). For practical results in broad regions with data from a sparse network of stations, the focus is on estimating epicentral locations only — that is, for shallow sources with no indication of significant depth. Thus, Schaff and Richards (2004a) used data from five GSN stations in China and the Republic of Korea to study in detail the relative location of 28 events in Liaoning Province, China that occurred in 1999. Cross correlation of Lg-wave windows provided highly accurate differential travel times — they could be measured with sub-sample precision. Remarkably, the error estimated from internal consistency was only about 7 ms, and associated location precision was about 150 m even though stations were typically at distances 500 to 1000 km from the source region. Epicentre estimates were not substantially affected by the paucity of stations nor by large azimuthal gaps. Much larger studies of the seismicity of China and nearby regions for the period 1985 to 2005 were shown by Schaff and Richards (2004b, 2011) to have a significant fraction of repeating events. These were defined phenomenologically. That is, event pairs had seismograms, at each station recording the repeating events, which looked highly similar – indeed so similar that the events would have

to have been within 1 km of each other. The repeat events comprised more than 10% of the seismicity of China, and more than 2000 pairs of them, broadly distributed, were used by Jiang et al. (2014) to assess the quality of locations published in seismicity bulletins based on arrival times picked from data of the China National Seismograph Network and the Beijing Capital Region Seismograph Network. Each event had been separately located using traditional methods, and the issue was: how far apart had they been placed in this way, when clearly they had to be within 1 km (from their waveform similarity at common stations). Jiang et al. reported that such event pairs located by traditional methods were reported as being on the order of a few km apart even in the best monitored regions with high station density; and were typically reported as being a few tens of km apart in remote regions such as the Tibetan plateau.

Success with repeats among known events suggests the possibility of finding additional repeats using seismograms from known events as templates, and then searching continuous recorded ground motion for new events with similar but smaller signals. Slinkard et al (2016) evaluated methods for searching continuous data for a large region of central Asia from 2006 to 2008. They used data from three high-quality stations in Kazakhstan: Borovoye and Makanchi (small arrays), and the GSN station Kurchatov (a three-component station). Underlying issues were: what quality of template is needed for effective detection; and how could newly detected events be validated? Slinkard et al evaluated three methods of confirming detections: bulletin confirmation (using local information provided by Kazakhstan's Institute of Geophysical Research); multi-station validation; and high correlation with a template. They confirmed over 6500 unique detections that were not in event bulletins for the region, most of them by multi-station validation (i.e. the same event was detected at different stations).

Slinkard et al. (2014) obtained practical experience with detection methods by exploring three different types of seismic signal to use as templates. Best was just the main part of the Lg-

wave, using a 25 s window. Presumably this was because the *Lg*-wave for the region being studied had the highest signal-to-noise ratio. They used the passband from 0.5 Hz to 5 Hz. Slinkard et al. (2014) also introduced a method for choosing correlation-detection thresholds tailored for each template applied to each station channel to achieve a pre-determined false alarm rate. To obtain template thresholds at which a detection would be declared, each template was time-reversed and run on three years of continuous data to generate a histogram of all correlation values. Credible detections are those based on the forward template, at cross-correlation values where the detection distribution has diverged from those of the (false) detections from the reversed template. A correlation detection threshold can then be selected based on the desired false alarm rate. In this manner, all templates can be assigned a correlation threshold that is consistent in false alarm rate, allowing consistency across templates of different window lengths or filtering parameters. Supplementing these results on event detection for a large region, case studies reported by Richards et al. (2015) explored the capability of locating seismic events precisely using GSN *Lg* waveforms recorded at far-regional distances from a small source region. An underlying issue is how well can the work be done when the events are close enough to each other.

Figure 6 shows the seismicity of a part of China for a period of more than seven years. Cross-correlation methods were applied to measure *ΔT* values of pairs of events within sub-clusters, within the smaller boxed region of dense seismicity shown west of station Baijiatuan; and these values were then used to obtain relative epicentres. The first relocated cluster (shown in Figure 7(a)), consisted of ten events spread out over about ten km. It was relocated with precision at the level of about 1 km. Contributing to each of the measurements *ΔT* of the relative arrival times of signals from each pair of events, as recorded at a common station, is a small uncertainty presumably due to the waveforms being slightly different. The second cluster (shown in Figure 7(b)) consisted of nine events spread out over only about 1.4 km, and in this case their signals are so similar at each of the stations recording

them, that sub-sample measurements of *ΔT* are essentially due only to the slight differences in event location. The resulting confidence ellipses in Figure 7b are then only a few tens of meters across, a remarkably precise result for such a sparse far-regional network.

Aftershocks can be a challenge to monitoring agencies since they may occur at the rate of hundreds per day in the hours and days after a major earthquake. Characterizing them well is a part of understanding the process by which stress release occurs throughout the overall source volume of the main event. A case study by Slinkard et al. (2016) used a set of template waveforms from known aftershocks from the Wenchuan earthquake (12 May 2008, Ms7.9), as listed in a seismicity bulletin from the IDC. They searched for these same waveforms in continuous data recorded by three GSN stations at regional distance (Xi'an, EMH, Kunming), plus five temporary stations deployed as part of the
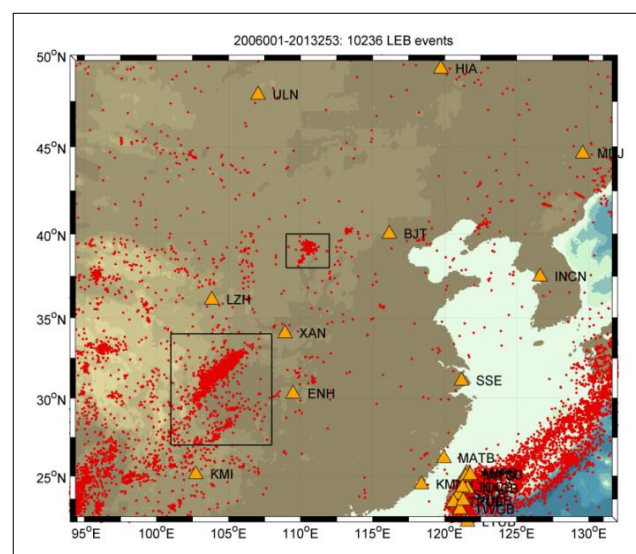
FIGURE 6.

The seismicity of part of East Asia is shown for slightly more than seven and a half years beginning in 2006, as reported in the Late Event Bulletin of the IDC. Richards et al. (2015) relocated two sub-clusters of seismic events in the smaller box (see Figure 7), on the basis of their Lg-wave signals as recorded on just three GSN stations, Ulaanbaatar (ULN), Baijiatuan (BJT) and Xi'an (XAN), operated jointly by the China Earthquake Administration and the US Geological Survey. The larger box includes many aftershocks of the damaging Wenchuan earthquake of 12 May 2008.

Array Seismology Collaborative Experiments in north-eastern Tibet (ASCENT). Slinkard et al. (2016) detected more than 6000 additional events in the mainshock source region from 1 May 2008 to 12 August 2008. These new detections extend the magnitude of completeness downward by 1.1 magnitude units. They lead to a more than fivefold increase in number of known aftershocks compared with the global bulletins published by the IDC and the International Seismological Centre in the United Kingdom. Moreover, more M > 2 events were detected than were reported by the nearby Sichuan Seismograph Network. Several clusters of these detections were then relocated by Slinkard et al. (2016) using the double-difference method, yielding locations that reduced travel time residuals by a factor of 32 compared with the initial bulletin locations. These results suggest that using waveform correlation on a few regional stations can find aftershock events very effectively and can locate them with high precision.

Experience acquired from the case studies of Richards et al. (2015) and Slinkard et al. (2016) was then applied by Schaff and Richards et al. (2018) to see how well relocation could be done for a broad area. Epicentral relocations for all of mainland China and surrounding areas using cross-correlation measurements (about 111 million of them) were made on *Lg* waves recorded at regional distances on a sparse station network. They obtained final locations for 5623 events—3689 for all of China from 1985 to 2005 and 1934 for the Wenchuan area from May 2008 to August 2008. These high-quality locations comprise 20% of a starting catalogue for all of China and 25% of a catalogue for Wenchuan. The final locations explain the residuals about 90 times better than the catalogue locations for all of China (3.730–0.042 s) and 32 times better than the traditionally-obtained locations for Wenchuan (0.841–0.027 s). The average semi-major axes of the 95% confidence ellipses are only 420 m for all of China and 370 m for Wenchuan, even though the average azimuthal gaps are quite large - 205° for all of China and 266° for Wenchuan. It is remarkable that such good relocations were obtained in view of the large azimuthal gaps and station distances:
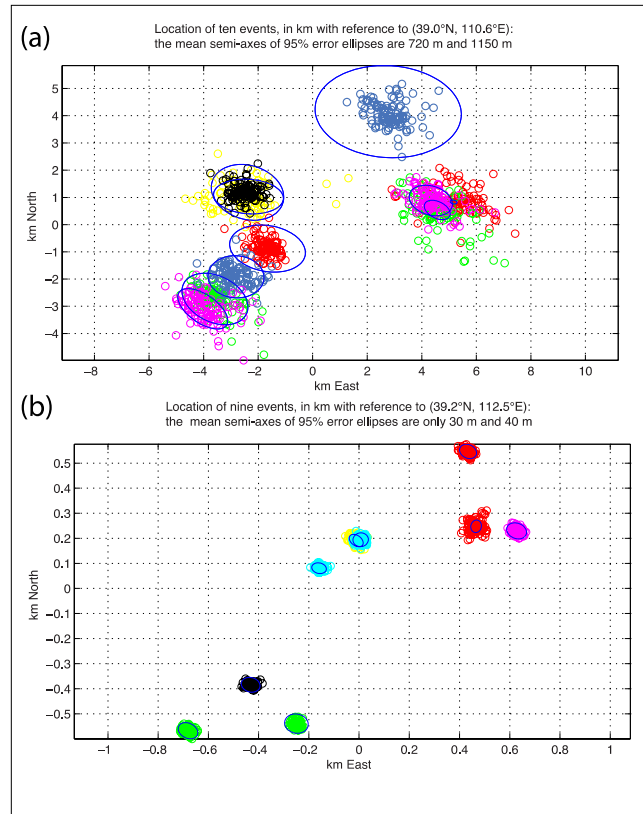
FIGURE 7.

Estimates of the relative location of two clusters of seismic events, and the precision of these estimates. (a) Ten events clustered in the time period from December 2009 to August 2012 at about 39.0°N, 110.6°E and spread up to about 14 km apart. These locations, lying within the smaller box shown in Figure 6, are more than 300 km from Baijiatuan (BJT), 1000 km from Ulaanbaatar (ULN), and 600 km from Xi'an (XAN) (the three stations at which Lg signals from these events were cross-correlated to obtain precise relative arrival times). The mean sigma of the residuals is 0.26 s. The bootstrap errors (distribution of small circles) agree well with the error ellipses. (b) Similar to (a), but now for the relative location of nine events clustered in the time period from April 2006 to August 2006 at about 39.2°N, 112.5°E and spread only up to about 1.8 km apart. These locations are about 500 km, 1000 km, and 550 km, from stations Baijiatuan, Ulaanbaatar, Xi'an, respectively. The mean sigma of the residuals is only 0.012 s.

98% of the station distances for all of China were over 200 km, and the mean and maximum station distances were 898 km and 2174 km. Yet these results provide order-of-magnitude improvements in locations for event clusters, using waveforms from a very sparse far-regional

network for which data are openly available. It was found that the percentage of events which can be relocated with high precision is about double the number of repeating events reported earlier (i.e. Schaff and Richards, 2011), enabling better insight into the underlying tectonic structures associated with seismic events whose relative locations can now be well-estimated.
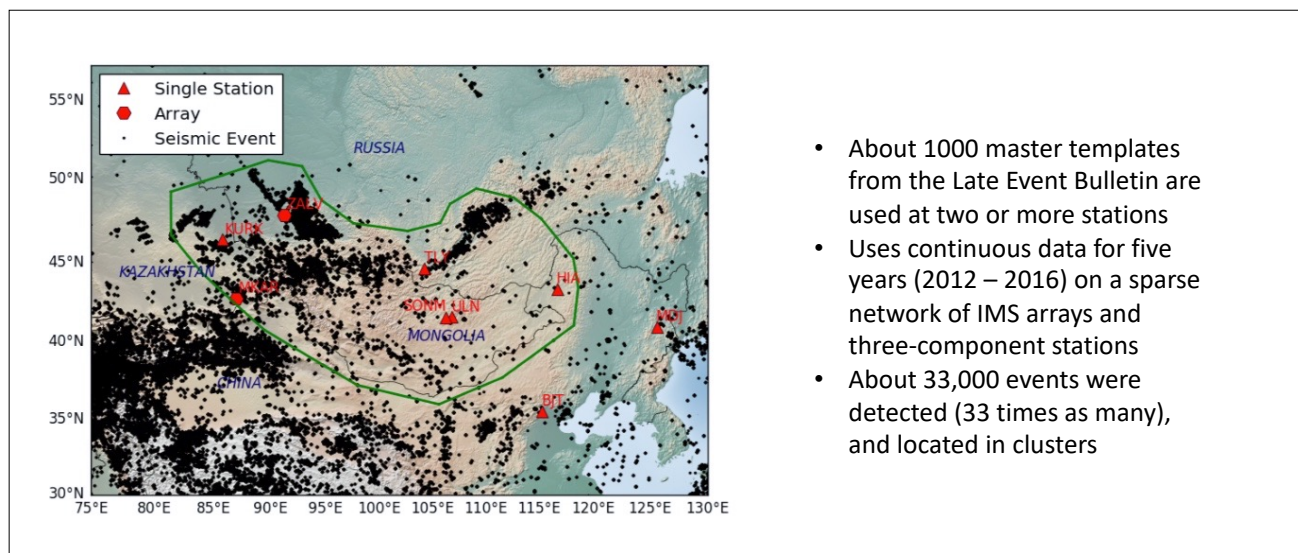
Schaff & Richards et al. (2018) used waveforms only from events reported from 1985 to 2005 in the Annual Bulletin of Chinese Earthquakes (and located therein from phase picks). With the prospect of being able to detect (and then relocate) many more events if modern methods of template searching were applied over a broad region, they proposed a six-step scheme to apply modern methods of event location within a particular region of space and time:

(1) Identify seismic events likely to be well recorded, using, for example, a regional bulletin or detailed global bulletin;

(2) Pull out waveforms to serve as templates (a few tens of seconds of the Lg wave had been identified as suitable);

(3) Cross-correlate the template for each channel against the continuous archive for that channel, and note detections (e.g. via cross-correlation values greater than a value identified via a predetermined false alarm rate, as discussed in Slinkard et al. 2014);

(4) Validate such detections (via an association approach or against a local bulletin) after a review of the quality of the detections;

(5) Measure the relative arrival times (via cross correlation) of pairs of events that were not far apart from each other and were recorded at common stations;

(6) Relocate as many events as possible using double-difference methods.

Preliminary results are now emerging of such an approach applied for five years (2012 to 2016) to seismicity in the polygonal region shown in Figure 8. It is almost 4.5 million sq km in size and includes all of Mongolia, plus large regions of China, Kazakhstan and the Russian Federation — in particular the Kuzbass region of southern Siberia where extensive blasting is conducted to remove sediments in strip mining operations for coal and iron ore. Using thousands of templates from a longer time period (a different number for each station, on average about one

- About 1000 master templates from the Late Event Bulletin are used at two or more stations
- Uses continuous data for five years (2012 – 2016) on a sparse network of IMS arrays and three-component stations
- About 33,000 events were detected (33 times as many), and located in clusters

FIGURE 8.

A map of Mongolia and neighbouring regions, used for a study of seismicity from 2012 to 2016, that combines template-matching of continuous data to detect new events, and relocation of events using regional Lg waveforms recorded at common stations for event pairs. Black dots show events reported in the IDC's Late Event Bulletin for this region. The region a few degrees to the east of station ZAL (Zalesovo, in southern Siberia) includes the Kuzbass basin, where numerous blasting events are associated with strip mining for coal.

thousand), cross-correlation detections were made from searches of continuous data for the sparse network shown in Figure 8 consisting of three IMS array stations, plus six long-running three-component open stations. About 33 000 candidate new events were detected, but for most of them there were too few stations in the detection network to perform locations.

Fortunately, a temporary Portable Array Seismic Studies of the Continental Lithosphere network with many stations had been deployed in Mongolia by scientists of Lehigh University, USA, at locations shown in Figure 9 during the five-year time period of our study. Adding windowed data from that network, derived from a major data request to the IRIS Data Management Center based on expected arrival times derived from *Lg*-waves based on the sparse network, shown in Figure 8, allowed measured differential travel times at enough stations to make location estimates.

Preliminary results of this 'Mongolia' study (the region is about twice the size of Mongolia alone) were reported by Schaff at the CTBT: Science and Technology 2021 conference. They included location results for event clusters, some of which are shown in Figure 9. The quality of these locations is similar to those obtained in a previous study for all of China (Schaff & Richards et al. 2018), in which the existence of the events was previously known from a traditional bulletin.

For the whole Mongolia region average residuals were remarkably small — 0.0164 s — and 95% confidence ellipses had on average 157 m semi-major axes. Ninety-three per cent of the pairs were less than 1 km apart.

It is informative to look at the time-of-day and day-of-week bar charts for clustered events, as a primitive way to get indications of which events are anthropogenic (the mine blasts), and which are natural earthquakes. As shown in Figure 10, it is obvious by their time-of-occurrence that many of these events are mine blasts in the Kuzbass region. The upper pair of charts in Figure 11 show that the events in the cluster almost all occurred between the hours of 9 am and 5 pm local time, and almost all Monday to Friday. The lower pair, in contrast, indicate most of the events were on a Sunday (as was the main event), with declining numbers on later days in the week. This was a cluster of aftershocks from a significant earthquake.

This subsection shows that the uncertainties of traditional locations of seismic events can be at the level of a few tens of km (unless the event occurred within a network of stations significantly denser than the combined IMS primary and auxiliary networks). Traditional methods, based on locating events one-at-a-time with phase picks, are a good preliminary basis for publication of seismicity bulletins, and the need

FIGURE 9.

Stations operated in the region (40 – 57°N, 80 – 13°E) from 2012 to 2016, with data available from the IRIS Consortium.

for them continues for areas where seismicity is low. Modern methods of event location, applied to groups of neighbouring seismic events, can attain order-of-magnitude improvements in location precision in situations where the seismic events have been recorded by high quality broadband stations. Today's methods enable detailed analysis of events far smaller than could be characterized previously.

Traditional methods cannot compete with the results of modern cross-correlation processing of continuous recordings.

- Blue circles: clusters with 4 or more events in cluster and 75% or more from 9 am thru 5 pm
- Cyan circles: clusters with 3 or less events in cluster or less than 75% from 9 am thru 5 pm
- Red stars: clusters with 30 or more events in cluster and 75% or more from 9 am thru 5 pm
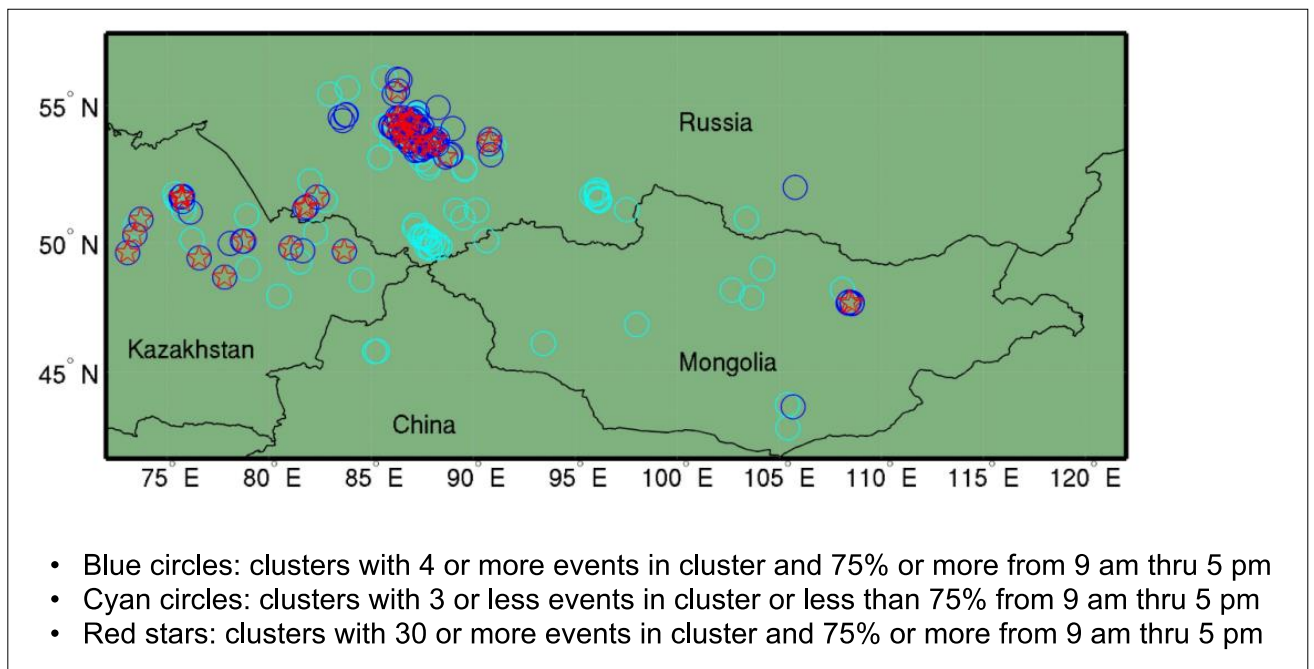
FIGURE 10.

Map of clusters of seismic events found within the region outlined in Figure 8 from 2012 to 2016. A region of intense activity (53–56°N, 85–88°E), is principally associated with blasting/strip mining in the Kuzbass region of southern Siberia.
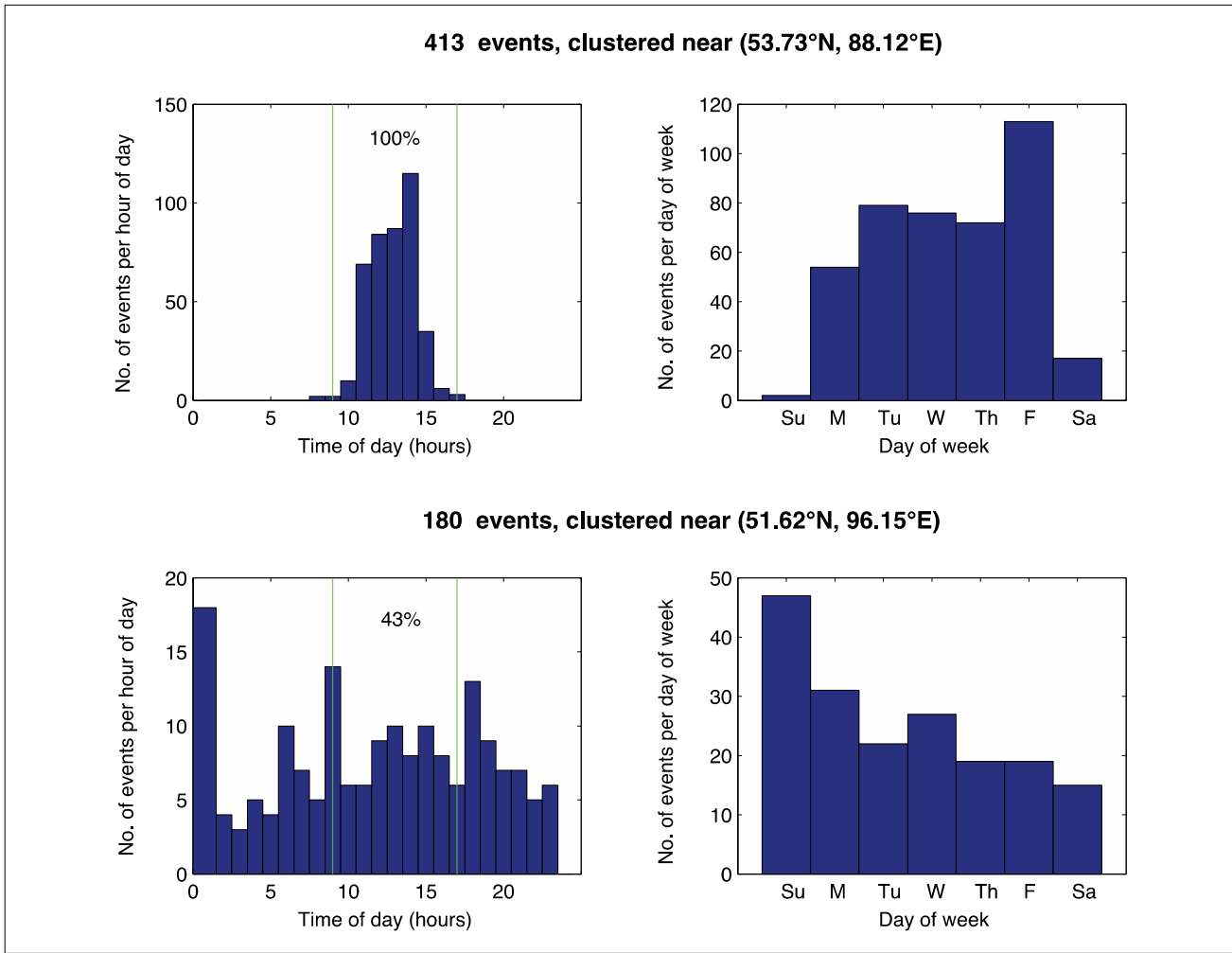
FIGURE 11.

Bar charts for two clusters (see Figure 8) indicating the distribution of local time-of-day and day-of-week for the events in each cluster. The upper pair of more than 400 events exhibit the timing of blasts in a mining operation. The lower pair includes the cluster of aftershocks of a significant earthquake that occurred on Sunday, 26 February 2012.

3. CONCLUSION

Recent decades of research on seismic event detection and location have produced results offering far more detailed information on spatial and temporal patterns of seismicity than can be derived from the traditional approach using phase picks (seismic-wave arrival times) — which dominates today's bulletins of seismicity. Bulletins in which events are located one at a time continue to be a good starting guide and they will continue to be important for prompt reporting and reporting events in areas where few events occur. But monitoring communities today are beginning to appreciate that much better products are possible, which avoid the three inherent difficulties of the traditional approach mentioned previously.

A major asset in the study of patterns of seismicity is the existence of continuous high-quality waveforms archives. Seismogram archives have always been important as they allow seismicity to be studied over time. Benefits are to be expected from the fact that the percentage of events amenable to analysis via modern methods gets larger as archives grow; and being able to study seismicity that is denser allows relative locations to be assigned with higher precision. There is always pressure to increase the number of stations deployed in regions of seismic hazard, but if the purposes of network operation is to lower detection thresholds and to improve event characterization (e.g. locations), then these goals must be taken into account especially when considering replacement of old stations with new ones. There also needs to be consideration of whether the development and application of modern methods of event detection and location should be done as a community service by a centrally organized unit or should be left to scientists who apply the new methods on a small scale to enable high-quality analysis of particular regions of interest.

REFERENCES

Adushkin, V.V., Bobrov, D.I., Kitov I.O., Rozhkov, M.V., Sanina, I.A. (2017). Remote detection of aftershock activity as a new method of seismic monitoring, *Doklady Earth Sciences* **473** 303–307.

Begnaud, M.L., Myers, S.C., Young, B., Hipp, J.R., Dodge, D., Phillips, W.S. (2020). Updates to the Regional Seismic Travel Time (RSTT) Model: 1. Tomography. *Pure Appl. Geophys* **178** 2475–2498.

Begnaud, M.L., Anderson, D.N., Myers, S.C., Young, B., Hipp, J.R., Phillips, W.S. (2021). Updates to the Regional Seismic Travel Time (RSTT) Model: 2. Path-dependent Travel-time Uncertainty, *Pure Appl. Geophys* **178** 313–339.

Chun, K.-Y., Wu, Y., Henderson, G.A. (2011). Magnitude estimation and source discrimination: A close look at the 2006 and 2009 North Korean underground nuclear explosions, *Bull. Seismol. Soc. Am.* **101** (3) 1315–1329.

De Geer, L.-E. (2012). Radionuclide evidence for low-yield nuclear testing in North Korea in April/May 2010, *Science & Global Security* **20** (1) 29.

Jiang, C., Wu, Z., Li, Y., Ma, T. (2014). Repeating events as estimator of location precision: The China National Seismograph Network. *Pure and Applied Geophysics* **171** (3) 413–423.

Kim, W.-Y., Richards, P.G., Schaff, D.P., Koch, K. (2017). Evaluation of a seismic event, 12 May 2010, in North Korea, *Bulletin of the Seismological Society of America* **107** (1) 1–21.

Kim, W.-Y., Richards, P.G., Schaff, D.P., Jo, E., Ryoo, Y. (2018). Identification of seismic events on and near the North Korean test site after the underground test explosion of 3 September 2017, *Seismological Research Letter*s **89** (6) 2120–2130.

Kitov, I., Rozhkov, M. (2019). "Comparison of the DPRK aftershocks observed in 2019 with the aftershocks between September 2016 and April 2018." Poster presented at CTBTO Science and Technology 2019 Conference, Vienna, Austria, 2019.

Mikhailov, V.N. and many others (2014). Catalog of Worldwide Nuclear Testing, https://web.archive.org/web/20140716032420/http://www.iss-atom.ru/ksenia/catal_nt/4.htm#Table5.

Olsen, K.B., Begnaud, M., Phillips, S., Jacobsen, B.H. (2018). Constraints of crustal heterogeneity and *Q(f)* from regional (<4Hz) wave propagation for the 2009 North Korea Nuclear Test. *Bulletin of the Seismological Society of America* **108** (3A) 1369–1383.

Pan, C.-Z, Jin, P., Wang, H.-C. (2007). Applicability of P/S amplitude ratios for the discrimination of low magnitude seismic events, *Acta Seismologica Sinica*, **20**, 553–561, doi: 10.1007/s11589-007-0553-6.

Richards, P.G., Heck, S., Schaff, D.P., Slinkard, M. Young, C. (2015). Preliminary results for a data-intensive study of China seismicity to detect small events and improve location estimates for event clusters, *Research and Technology Review, Bulletin of the National Nuclear Centre, Kazakhstan,* **64** (4).

Richards, P.G., Hellweg, M. (2020). Challenges and opportunities in turning large U.S. archives of analog seismograms into a modern usable resource, *Seismological Research Letters* **91** (3) 1531–1541.

Richards, P.G., Zavales, J. (1996). "Seismological methods for monitoring a CTBT: The technical issues arising in early negotiations." *Monitoring a Comprehensive Test Ban Treaty* (Husebye, E.S., Dainty, A.M., Eds). Kluwer, Dordrecht, pp 53–81.

Ringler, A.T., et al. (2022). Achievements and prospects of global broadband seismographic networks after 30 years of continuous geophysical observations, *Reviews of Geophysics* **60** (3).

Schaff, D.P., Richards, P.G. (2004a). *Lg*-wave cross correlation and double- difference location: Application to the 1999 Xiuyan, China, sequence. *Bulletin of the Seismological Society of America* **94** (3) 867-879.

Schaff, D.P., Richards, P.G. (2004b). Repeating seismic events in China. *Science* **303** (5661)1176–1178.

Schaff, D.P., Richards, P. G. (2011). On finding and using repeating seismic events in and near China. *Journal of Geophysical Research: Solid Earth* **116** (B3).

Schaff, D.P., Kim, W.-Y., Richards, P.G. (2012). Seismological constraints on proposed low-yield nuclear testing in particular regions and time periods in the past, with comments on "Radionuclide evidence for low-yield nuclear testing in North Korea in April/May 2010" by Lars-Erik De Geer, *Science and Global Security* **20** (2) 155–171.

Schaff, D.P., Richards, P.G., Slinkard, M., Heck, S., Young, C. (2018). *Lg*-wave cross correlation and epicentral double-difference location in and near China. *Bulletin of the Seismological Society of America* **108** (3A) 1326-1345.

Schaff, D.P., Kim, W.-Y., Richards, P.G., Jo, E., Ryoo, Y. (2018). Using Waveform Cross Correlation for Detection, Location, and Identification of Aftershocks of the 2017 Nuclear Explosion at the North Korea Test Site, *Seismological Research Letters* **89** (6) 2113–2119.

Slinkard, M., Schaff, D., Mikhailova, N., Heck, S., Young, C., Richards, P.G. (2014). Multistation validation of waveform correlation techniques as applied to broad regional monitoring. *Bulletin of the Seismological Society of America* **104** (6) 2768-2781.

Slinkard, M., Heck, S., Schaff, D., Bonal, N., Daily, D., Young, C., Richards, P. (2016). Detection of the Wenchuan aftershock sequence using waveform correlation with a composite regional network. *Bulletin of the Seismological Society of America* **106** (4) 1371-1379.

Slunga, R., Rögnvaldsson, S.Th., Bödvarsson, R. (1995). Absolute and relative locations of similar events with application to microearthquakes in southern Iceland. *Geophysical Journal International* **123** (2) 409-419.

Tian, D., Yao, J., Wen, L. (2018). Collapse and earthquake swarm after North Korea's 3 September 2017 nuclear test, *Geophysical Research Letters* **45** (9) 3976–3983.

US National Academy of Sciences (2002). *Technical Issues Related to the Comprehensive Nuclear Test Ban Treaty*. National Academy of Sciences, Washington, DC.

US National Research Council (2012). The Comprehensive Nuclear Test Ban Treaty: Technical Issues for the United States. National Academy of Sciences, Washington, DC.

Waldhauser, F., Ellsworth, W.L (2000). A double-difference earthquake location algorithm: method and application to the northern Hayward fault, California, *Bulletin of the Seismological Society of America* **90** (6), 1353-1368.

Walter, W.R., Wen, L. (2018). Preface to the focus section on North Korea's September 2017 nuclear test and its aftermath. *Seismological Research Letters* **89** (6) 2013–2016.

Yang, X., North, R., Romney, C., Richards, P.G. (2002). "Worldwide nuclear explosions", International Handbook of Earthquake & Engineering Seismology, Part A, (W.H.K. Lee, H. Kanamori, P. Jennings, and C. Kisslinger, Eds) **84**. *International Association of Seismology and Physics of the Earth's Interior*, Academic Press, New York.

Zhang, M., Wen, L. (2015). Seismological evidence for a low-yield nuclear test on 12 May 2010 in North Korea, *Seismological Research Letters* **86** (1) 138–145.

International Monitoring System Seismic Equipment and the Value of Ambient Noise Tomography Methods for Arrays

Y. Starovoyt

Comprehensive Nuclear-Test-Ban Treaty Organization, Vienna, Austria

Abstract

This paper describes different equipment solutions installed in the International Monitoring System (IMS) seismic array and three component stations of the primary and auxiliary networks. Special attention was paid to the sensors and digitizers compliance with technical requirements of the draft IMS Operational Manual. The IMS utilizes different models of modern active and passive short period and broadband sensors manufactured by recognized suppliers. They have demonstrated a time proven reliable operation for not only the IMS but for other seismological projects. Sensor orientation and calibration aspects are supported by ongoing annual programmes. To ensure better performance with high dynamic range requirements, hybrid frequency response sensors were proposed and installed at several array stations. In the digitizer area the IMS uses known models available in the production lines of the different equipment suppliers but with improved characteristics like self-noise, timing accuracy, state of health parameters, remote command&control and temperature range specifications. The prospects of utilizing ambient noise technology methods have shown to be a useful and promising aspect of further developments for the enhancement of the event location accuracy both for the routine data processing in the International Data Centre and possibly for temporary operational local deployments for aftershock monitoring system in on-site inspection.

Future progress in the development of a sustainable verification regime should be abreast with modern technologies in the seismic hardware and software markets, adjusted for IMS specific needs and requirements.

1. INTRODUCTION

In the framework of the Comprehensive Nuclear-Test-Ban-Treaty (Treaty) the International Monitoring System (IMS) is a unique technical tool for the collection of waveform technologies and radionuclide data for verification purposes. It is being established and near to completion to ensure that any attempted Treaty violation will be detected in a timely manner worldwide and the information provided to the International Data Center (IDC) for processing purposes. For seismic waveform technology two primary and auxiliary networks send their data to the IDC where they are used in the Reviewed Event Bulletin.

Weak signal detection is the design goal underlying IMS verification technology (Bowers and Selby 2009) in the solid Earth. Since building up the programme for IMS seismic networks, attention has been paid to the assurance that an individual seismic station is compliant with the minimum technical requirements and therefore capable to implement its verification mission. Seismic networks of the IMS are equipped with modern types of instrumentation that are also used for other seismological projects. However during implementation of the installation programme, certain IMS specific requirements were met to ensure that the best quality of seismic data would be delivered to the IDC.

Different types of key seismic instrumentation installed at primary and auxiliary stations of the IMS will be described in this paper.

2. IMS SEISMIC NETWORK: PRIMARY AND AUXILIARY STATIONS

IMS seismic networks are comprised of primary and auxiliary stations. Fifty stations of the primary network send continuous data to the IDC where they are used for signal detections, event association and preliminary location. The primary network is the backbone of the solid Earth verification technology. It consists of 30 array, 19 three component (3-C) stations and one station to be determined in type and location. It is a unique network of sensors deployed worldwide with the highest number of simultaneously working array stations sending data to the central processing point in IDC where they are jointly processed.

The location coordinates for all stations are defined in the Treaty and the installation activities have strived to follow their installations as close as possible to the Treaty locations. However due to non-technical issues, it was not always feasible. For instance, infrastructure development and construction work in host countries have often led to unfavorable installation conditions with elevated levels of human-made background noise.

Sustainability aspects of IMS networks have always been considered so that station location has to provide the station operator with optimal maintenance capability with the aim of minimizing the whole station or equipment components downtime. When the preferable station location is outside of the Treaty coordinates, the justification of the station move was prepared and approval was sought from the Comprehensive Nuclear-Test-Ban Treaty Organization Policy Making Organs. A tenths of a degree deviation in latitude or longitude from the Treaty location was the accuracy threshold when initiation of the station relocation process was required.

Unlike primary stations, auxiliary stations are designed to arrange availability of their data to IDC upon request. The IMS auxiliary network has 120 facilities located worldwide and are mainly comprised of 3-C stations. Only seven array stations are operational in the IMS auxiliary network and the status of one station in the auxiliary network is yet to be determined. The segmented strategy of data consumption from the auxiliary network

is needed for better event locations when the azimuthal coverage of the preliminary epicenter location, defined by the primary network, is necessary to narrow down the error ellipse.

The key operational aspect of the auxiliary network is that it includes many stations which are working and sharing the same infrastructure and equipment under different projects, so not exclusively serving the purpose of the CTBTO. As one examples the international IRIS Consortium shares 47 stations with the IMS which work mainly under the affiliation with IU (IRIS USGS) and II (IRIS IDA) sub-networks. The cooperation with different station operators and parent network organizations is technically important

and beneficial for the IMS. Such cooperation enables the IMS to follow modern trends in equipment upgrades therefore being abreast of market innovations and ready to adapt them to the specific IMS requirements. It is important to note that besides the different strategy of data delivery from the primary (continuous flow) and auxiliary station (segmented mode) there were no differences in technical requirements applied for the installation of these two station types. This point will be addressed in greater detail further in this paper.

Both networks are designed to send data to Vienna via approved topology of the Global Communication Infrastructure (GCI).

3.   ARRAY VERSUS 3-C STATIONS

3.1.   Seismic Array Stations

Seismic array stations could be divided into two main categories, regional and teleseismic (Schweitzer et al. 2009). The primary difference between them is the aperture of the deployment or the distance between the most remote elements. The distribution of intersensory distances is also important. Teleseismic arrays like PS3, PS9, PS27, PS45, AS104 etc. are mainly so called legacy IMS stations where elements configuration and the station itself has a long operational history in the corresponding host countries for the period of time before the establishment of the CTBTO. Their aperture is more than 10-15 km but could be as big as 60 km, such as for NOA (Bungum et al. 1971). The overall number of elements varies but is usually more than 20.

Regional arrays of the IMS (Mykkeltveit et al. 1990, Mykkeltveit et al. 1983) such as PS12, PS13 (see Figure 1a), PS23, PS37, AS57, etc. are mainly newly built facilities with the average aperture of about 3-5 km and the overall number of elements equal to ten, but not always. Some of the regional arrays continue their successful operation in the IMS as being a legacy station, for example PS28, PS19, PS45, etc. For all legacy stations the IMS has undertaken significant

efforts ensure they are technically compliant with the minimum technical requirements.

The assignment of the array of either teleseismic or regional is often conditional as both array categories record signals from a variety of epicentral distances. Very often the geometry of the array element is arranged in a way that it has the capability of both teleseismic and regional events characterization. It is difficult to strictly say to which category a station belongs. At such stations (for example PS31 shown in Figure 1b) there is the dense population of the array single component vertical elements (19 sites shown as the black dots) with the aperture of about 8-10 km. This configuration is supplemented with six broadband seismometers (sampled with 4 Hz sampling rate) with intersensory distances of about 10 km (red circles) which have been deployed to boost the quality of lower frequency surface wave detections.

The array geometry is important to consider when different signal detection recipes in IDC data processing pipelines are built for different array stations.

Regional arrays are tuned for enhanced detection capability at higher frequencies f>3-5

Hz and for higher values of slowness or wave vectors $k = \frac{2\pi}{\lambda}$ where **l** is the apparent wavelength for the detected signal. The teleseismic array works better at lower frequency (f< 2 Hz) and slowness domains. One of the array characteristics reflecting the quality of the spatial distribution of array elements on the surface of the Earth is its response function (Ingate et al. 1985). This function defines two main characteristics of the array: (i) signal spatial resolution in 2-D plane of the wave vector $k=(k_x,k_y)$ and (ii) undesirable appearance of the harmful side lobes of the response function that may often complicate the interpretation of the f-k diagram. To a certain extent the array response function could be roughly compared with tapering of the time series in the time domain to avoid negative appearance of the side lobes from the rectangular time window, diminishing the spectral leakage outside the main lobe. One of the examples of the smoothed and well adjusted response function for PS28 is shown in Figure 2. Almost no side lobes are seen in the response function.

During the construction phase for IMS arrays it was often the case when a relocation of the initially planned element location to the new sites was necessary. It was a usual practice when deployment at a certain place was difficult because of topography, security, land permits or other issues arose. Verification of the response function was always the IMS practice. The response function was sometimes purposely designed with an asymmetrical shape (PS2, PS9, AS59, AS104) aiming the directivity of the response diagram towards certain areas with intrinsic monitoring purposes. This type of situation does not mean the inability of the array station to monitor other regions of the world, but it allows simplifying and characterizing the waveforms upon their arrival from certain and expected azimuths.

One of the valuable accomplishments in the IMS buildup is presented by the commissioning of the newly built array in Niger (PS26). Since the time of the site survey and after commencing its operation, it has become clear that this station is a good candidate for superior detection capability. It was shown that the seismic background power
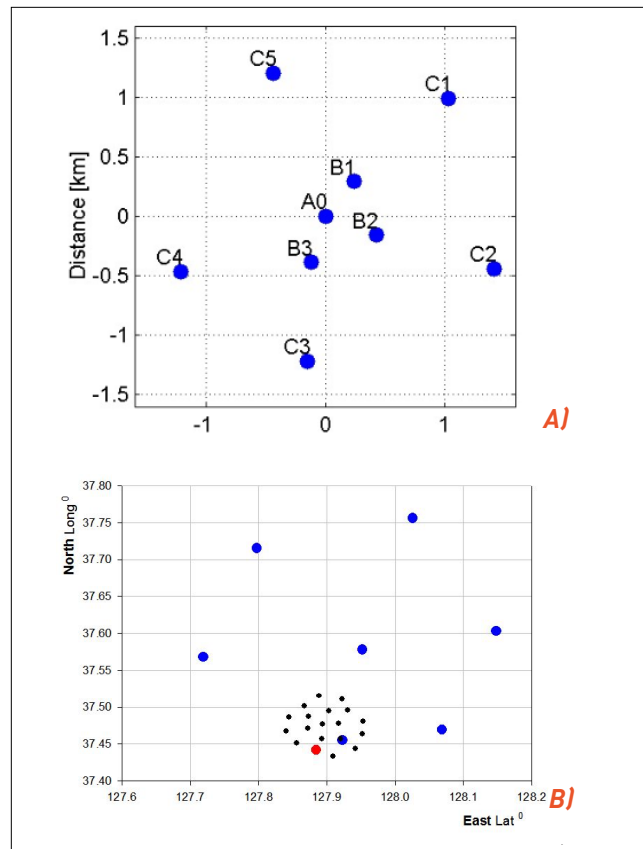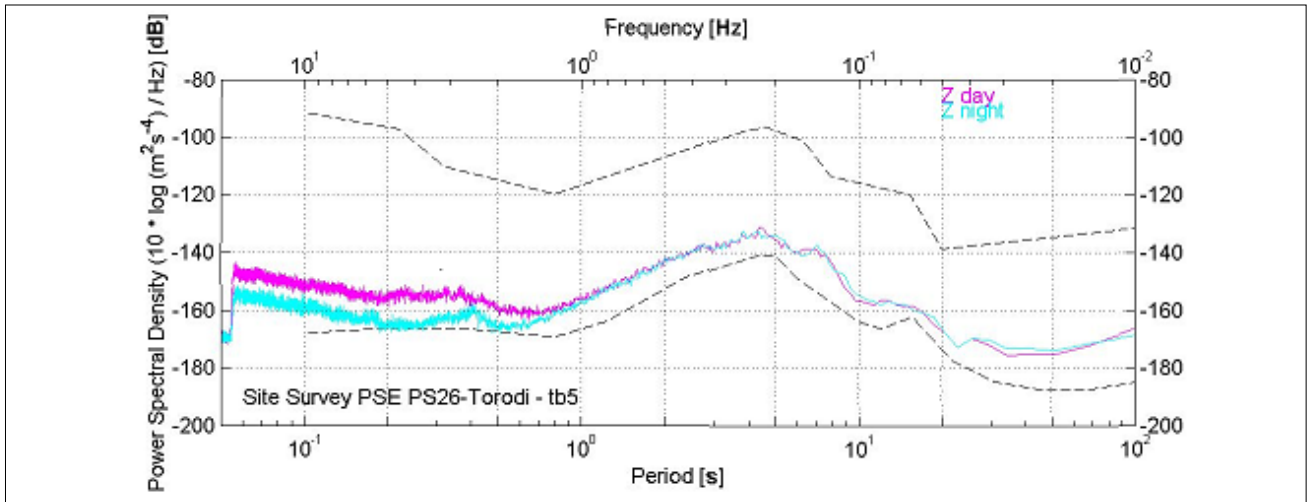

FIGURE 1.

Array elements deployment for: (a) regional array PS13 and (b) bigger aperture array PS31 that combines short period (black dots) and medium period channels (blue circles). The broadband channel for this array equipped with KS54000 sensor is shown with the red circle. Array elements depicted in (b) panel have a different channel naming in comparison to (a).
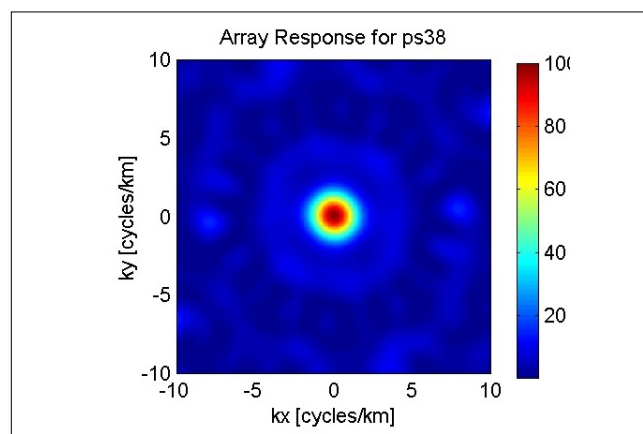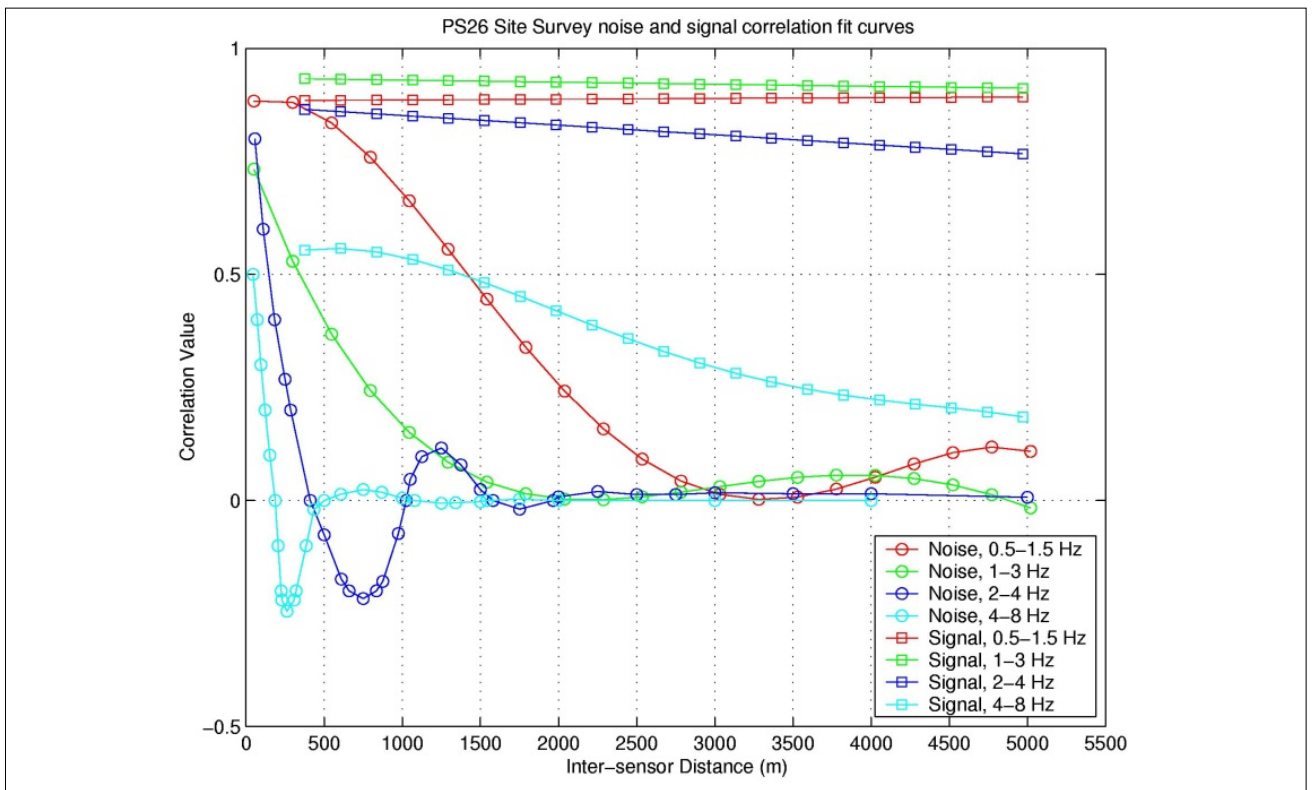

FIGURE 2.

Array response function for PS28 (ARCES) in Norway.

spectral density estimates were nested close to the new low noise model (NLNM) (Peterson 1993) at higher frequencies f>2 Hz (Ebeling et al. 2002).
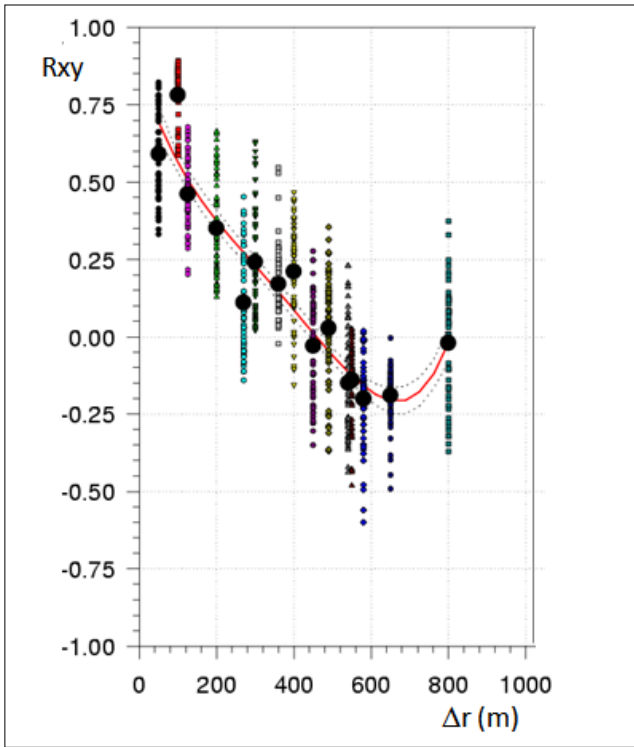
FIGURE 3.

An example of the mean power spectral density estimated at PS26 during the site survey. The indication of day and night variance of the mean noise level is shown using pink and cyan colors.

FIGURE 4.

Summary of signal and background noise correlations for site survey at PS26, Niger.

The testing and evaluation phase after array installation confirmed the expectation. The verification capability with this array will be even more enhanced if the extra seven 3-C broadband seismometers would be added to the third concentric ring around the array center. The configuration of this array comprises 16 seismometers (Estabrook et al. 2008). The final deployment at this station has the aperture of about 6 km with favorable median noise power spectral density at around 166 dB rel. $(1(m/s^2)^2/Hz$ at 5 Hz (see Figure 3) and it provides a valuable contribution to the IDC Reviewed Event Bulletin. The data from this station has become an important contributor to the monitoring tasks of many authorized IDC users.

In addition to the measurement of the noise power spectral density as a marker of the detection capability, spatial correlation of seismic noise was another key indicator of favorable array geometry. The seismic background decorrelation properties in several frequency bands of expected regional arrivals were the key expectation for array deployment as the way for detection capability improvements. The IMS regional array configuration was usually built in the double ring configuration as it was earlier defined as a promising geometry (Mykkeltveit et al. 1983). The favorable ring diameters were preliminary defined during site survey based on the noise decorrelation for certain intersesnor distances. As array processing techniques are based on superposition (summation) of individual elements the SNR improvement for uncorrelated noise is expected to be proportional to $\sqrt{N}$, where N is the number of elements (Schweitzer et al. 2009). Negative noise correlation can sometimes provide even better expectations (Mykkeltveit et al. 1990). Decorrelation of the noise has to be supported by event signals correlation. Only in such condition of still correlated event signals could the detection capability

improvements be expected when applying signal summation methods.

For regional signal detection, the frequency range around 2-8 Hz was carefully investigated at site candidates during surveys. The examples of seismic correlations are shown in Figure 4 where the compilation of signal and noise correlations is shown for different passbands for PS26. In Figure 5 the similar drop of the noise spatial correlation versus intersensory distances is shown for the frequency band from 2.5-5 Hz for PS38 (not yet certified station). Interestingly the minimum of the noise correlation is revealed at both sites for similar distances around 600-700 m. It justifies selection of the inner ring radius around 500-700 m for these arrays.

3.2. Seismic Three Component Stations

Three component IMS seismic stations have a conventional configuration of broadband seismometers recording the ground motion in cross perpendicular directions. There is no difference in these deployments with common practice of the other seismic projects. The difference is in a self-noise consideration. It has to be mentioned that installation of at least one 3-C sensor, in addition to a single component vertical element, is the mandatory requirement for IMS arrays. As the 3-C site of the array has to have the extended passband the data from this element are mainly used to characterize surface wave detections. For 3-C stations the detection of body and surface waves is done by the single seismometer. However, in those rare cases when all array elements are working with the same broadband response (PS23 for example) the 3-C channels are all involved in the f-k and beamforming process.

There are several cases in the IMS seismic network when 3-C stations are running as a combination of 3-C broadband seismometer (usually KS54000) and single component vertical short period sensor like 23900A, GS21 (for example PS1, PS7, PS30, etc.). Such a configuration is aimed for the augmentation of the detection capability of the broadband instrument at high frequencies of more than 5 Hz by a very low self-noise short period sensor. This is the way to compensate

the elevating trend of the sensor self-noise behavior, for example for KS54000 (Geotech USA) seismometer, which is crossing the NLNM at about 5 Hz. Even though the short period seismometer is used in a single component configuration, such a combination was used at several IMS 3-C stations.

The augmentation method for the enhancement of a high frequency operation was also used for the 3-C broadband elements of the array. In such a case the KS54000 was supplemented by vault installations with 3-C GS13 seismometer from Geotech USA. Such deployment could be mentioned for PS23 and PS48. Very low self-noise instruments like GS13, S13 (either 3-C or 1-C versions) remain popular as the augmentation element or the single component seismometer at several IMS arrays, such as at PS9, PS46, AS83 and AS101.

IMS technical requirements allow covering the required 3-C passband not only by a single broadband instrument but also by the combination of short (ZM-500, HM-500) and long or medium period (LPZA-12s, LPHA-12s) vertical and horizontal sensors. Such a solution is not used often but is in use at several stations (PS25, PS18, AS008, AS32 and AS61) (Larsonnier et al. 2019 and all references CEA/DASE, 1999).

3.3. International Monitoring System Technical Requirements

Installation of all stations of the IMS seismic networks has to be carried out in compliance with the technical requirements specified in the draft IMS Operational Manual (Preparatory Commission for the CTBTO 2009). Compliance is mandatory for IMS station certification. If the station undergoes an upgrade or change of the sensor or/and the digitizer the compliance with requirements has to be granted through the whole station operational cycle.

Technical requirements are equally applied for both primary and auxiliary stations. The T phase hydroacoustic station is very similar in configuration to a 3-C station of seismic networks and has very similar installation requirements. The key technical requirements relevant for sensors and digitizers are those which define the detection capability of the station and therefore have to be carefully addressed during the station design phase (see Table 1). They could be conditionally divided into two categories as sensor and digitizer related. There are several station specifications that are relevant for data transmission, format, and IMS data surety aspects. They are not considered in this paper and not shown in Table 1.

Table 1. Minimum Requirements for Station Specifications

CHARACTERISTICS	MINIMUM REQUIREMENTS
Sensor related	
Position (with respect to ground level)	Borehole or vault
Three component passband	Short Period: 0.5 to 16 Hz plus Long Period: 0.02 to 1 Hz or Broadband: 0.02 to 16 Hz
Sensor response	Flat to velocity or acceleration over the passband
Array passband	(Short Period: 0.5 to 16 Hz Long Period: 0.02 to 1 Hz)
Number of sensors for new array	9 Short Period (one component) plus (1 Short Period (3-C) plus 1 Long Period (3-C)) or single Broadband
Seismometer noise	at least 10 dB below minimum-earth noise at the site over the passband
Seismometer orientation	$\leq$ 3 degrees
Calibration	Within 5% in amplitude and 5 degrees in phase over the passband

Table 1. Minimum Requirements for Station Specifications (cont.)

CHARACTERISTICS	MINIMUM REQUIREMENTS
Digitizer related	
Sampling rate	$\geq$ 40 samples per second Long Period: $\geq$ 4 samples per second
System (digitizer)noise	at least 10 dB below the noise of the seismometer over the passband
Resolution	at least 18 dB below the minimum local seismic noise
Dynamic range	$\geq$120 dB
Absolute timing accuracy	$\leq$10 ms
Relative timing accuracy	$\leq$1 ms between array elements
Both sensor and digitizer	
Operation temperature	-10°C to + 45°C (both for sensor and digitizer)
Mission-capable arrays	$\geq$80% of the elements should be operational

3.4. Frequency Response Considerations

As shown in Table 1 seismic installations accept both flat to velocity and acceleration types of seismic sensors. Newly built IMS stations have been mainly using velocity type of the response by utilizing, for example for single components array elements the short period passive sensors as in GS13 (PS46), S13 (PS9), GS21 (AS58, PS37), 23900 (PS27 before the major upgrade) manufactured by Geotech USA. Brick or embedded pre-amplifiers were used for signal conditioning with passive sensors (Rodgers 1994). However, as it is known from specifications for these sensors their left corner frequency does not reach the required 0.5 Hz edge of the passband but is located at around 0.8Hz-1 Hz. These passive sensors are also known to be very quiet instruments with low level of the self-noise in average of about 20 dB below the NLNM up to the required 16 Hz as the high frequency end of the IMS passband (Kromer et al. 2007b, Slad and Merchant 2020). Historically these seismometers have demonstrated the time proven reliable operation as being used in many other verification related projects. Therefore many station operators expressed the wish to continue using these sensors. The superior detection capability of these sensors (especially for the sites with very low level of the seismic background) was considered a sufficient argument to mitigate the slight incompliance with the required passband and qualified these installations as substantially meeting the 1-C passband requirement.

On the contrary the broadband installations at array elements and at 3-C stations were usually utilizing the known models of the velocity type broadband sensor like STS-2, STS-2.5 Streckeisen, Switzerland (PS13, PS24, AS062) CMG3T/B Guralp UK, (PS21, PS32, PS33, PS36, PS37) Trillium 120, Nanometrics Canada (AS3). The frequency response of these seismometers exceeds IMS specifications and is at the lower end of the passband at 0.00833 Hz instead of the required 0.02 Hz.

Several IMS stations are equipped with the combination of STS-1 (Streckeisen, Switzerland) with superior behavior at lower frequencies and GS13 short period instruments (for example: PS9, AS050, AS092). Since the establishment of the Global Seismic Network (GSN) the STS-1 seismometers became the primary seismometer of this network and they continue to be in operation at some sites (Ringler et al. 2020). However obsolescence issues have triggered the GSN modernization campaign where STS-6A and Trillium 360 (GSN version) broadband seismometers have been selected as successors and have already shown promising functionality (Ringler et al. 2020, Ringler and Anthony 2021).

Flat to acceleration solution was not forgotten in IMS practice. KS54000 broad borehole seismometer with flat to acceleration response from 0.01 to 16 Hz was installed in many IMS stations as 3-C component site of the IMS array

(for example PS3, PS23, PS43, PS41) (Kromer 2003), and as the key sensor at 3-C stations (for example PS1, AS9) (Kromer 2003).

With advancement in the market of seismic instrumentation, single component elements of IMS arrays have started to utilize the active (feedback) sensor installation option. These sensors have either flat to velocity response from 0.033 Hz to 16 Hz (for example PS2) or in a similar passband but with flat to acceleration response (PS13, PS40, PS45, AS049). These stations were using different models of CMG3ESP or CMG3V sensors manufactured by Guralp UK. Even though the acceleration type of the response allows better utilization of the dynamic range, it often leads to undesirable human-made noise bursts at high frequencies triggering an excessive amount of false detections. It is especially true for stations located in populated areas where high frequencies cultural noise dominates, for example PS40. At this station retrofitting of the response from initially installed flat to acceleration back to the flat to velocity was requested by the station operator and implemented by the IMS.

Verification methods often require installation of high sensitivity in V/m/s seismic sensors to reduce the equivalent digitizer self-noise over the IMS passband (Kromer et al. 2007a, Slad and Merchant 2018, Slad and Merchant 2020). Such stations were often using higher sampling rates, more than the minimum required 40s/s, to advance new processing techniques for explosion type source characterization. It has been revealed however that keeping the big channel sensitivity factor for flat to velocity sensors at high frequencies with a high gain factor at the digitizer front end may lead to undesirable clipping of the instrument by high amplitude crust surface waves in the frequency range 0.02-0.05 Hz. Such cases were observed at PS28 in Norway. When the time came for the major upgrade of the array hybrid frequency response sensors were installed, which combine over the passband the fraction of the bands with flat to velocity and flat to acceleration shapes (Schweitzer et al. 2014, Pirli 2013). The normalized frequency response of the hybrid seismometer is shown in Figure 6. The response is scaled in units of sensitivity to
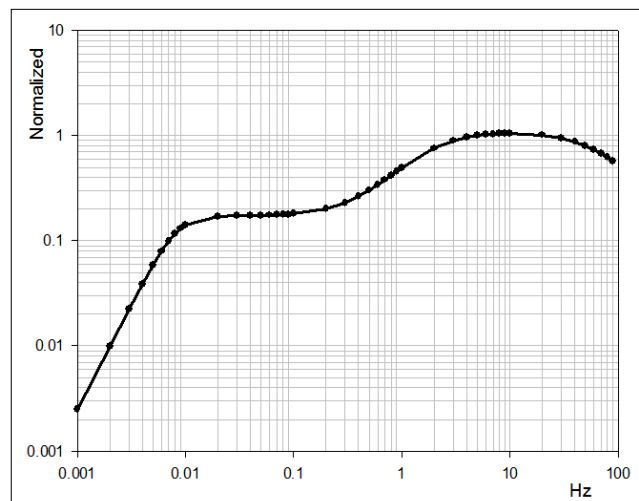
FIGURE 6.
Normalized hybrid frequency response of the CMG3T seismometer utilized at PS27 and PS28.

the ground velocity. It combines therefore flat in velocity portions (2-20Hz) and first order decay toward lower frequencies for flat to acceleration part (0.3-2Hz). It returns back to the flat to velocity in the frequency range 0.2-0.00833Hz. This response is utilized at each element of two IMS arrays PS27 and PS28 in Norway. In addition to the optimization and enhancement of the dynamic range issues previously mentioned, the installation of 3-C sensors at each element has allowed for better characterization of events within local and regional epicentral distances.

The 'light' version of the hybrid response could be also implemented for a single component array element by using active sensor when the flat in velocity response up to the required 0.5 Hz is extended by the first order decay toward to the lower frequencies and up to 0.03 Hz. Below the frequency f=0.03 Hz the second order decay continues. Unlike earlier mentioned passive sensors with 1 Hz corner frequency such a solution is fully compliant with frequency passband requirement for 1-C element to be flat in velocity up to 0.5 Hz (see Table1). Moreover the first order decay of the sensitivity in velocity means flat in acceleration as mentioned. It makes possible and more probable the detection of the weak surface waves by such channels. This solution was implemented at PS44 and at the auxiliary teleseismic array station AS59 and continues to be tested in the IDC processing pipeline.

Sensor Orientation

Three component IMS sensors have to be installed with orientation accuracy of at least three degrees relative to the geographical north (Table 1). For borehole installation such accuracy is often difficult to implement as some sensors go down to the borehole bottom in arbitrary orientation, for example CM3TB instrument. In such cases the actual orientation of the horizontal components is being measured by the sensor installed on the surface and close to the well-head termination unit. Digital rotation technique is applied to reach the maximum coherency between horizontal component on the surface and the one down in the hole. Usually the coherency is sought in the frequency range of the secondary microseisms around 0.02 Hz. Measured rotation is propagated to the channel header as orientation angles and thus requiring the name changing as BH1 and BH2 (for broadband sensors) instead of conventional BHN, BHE. Such method ensures the good quality of the relative alignment between two (borehole and surface) sensors but the quality of the absolute orientation remains to be opened. The emergence in the market of the new orientation devices like gyrocompass IXEA Octan and Teledyne CDL's TOGS-S fiber optic gyro allowed building significantly better than three degree accuracy of fiducial lines in the vaults and therefore the reassessing the installation quality of the surface instruments at IMS stations. The IMS Division of the CTBTO was tasked in 2010 to launch an orientation quality check programme at IMS seismic stations as one of quality control initiatives. As there are many auxiliary stations of the IMS which share sensors with GSN operators Albuquerque Seismological Lab (ASL) and International Deployment of Accelerometers (IDA) group from the University of California in San Diego, this work was closely coordinated with them and results were shared. Orientation issues at GSN stations were also mentioned in their operational practice and being rectified (Ringler and Anthony 2021, Ringler et al. 2013). Achieved improvements for both orientation accuracy and precision has led to horizontal channel naming at all GSN sites as BH1, BH2 indicating the feasibility of the high orientation accuracy relative to the true North up to the fraction of degree.

## Mission Capability (Additional Broadband Seismometer)

Mission capability requirement shown in Table 1 specifies that a minimum 80% number of single component elements of the array must be operational at any time. In addition the draft IMS Operational Manual requires fully operational broadband 3-C element to sustain the mission capability of the array and 3-C station. The mission capability status contributes to the array data availability metrics in a way that non-mission capable array status shall lead to a zero data availability indicator. Such a situation defines precedent of the undesirable situation when the failure of even a single component at the 3-C site (while all others 1-C elements continue reliable data transmission) may drop to zero the official data availability number because of the non-mission capable status of the whole array station.

To mitigate the impact of such cases at those stations where the only one broadband element was planned at the time of array certification the IMS Division of the CTBTO has initiated the installation of the extra broadband instrument to secure and support the mission capability status at the array station. This work was carried out, for example at PS40 and PS22. An additional broadband element is installed of the same type as the main one. Other parameters as sensitivity, poles and zeroes presentation, channel sampling rate were also selected the same thus allowing the smoothness of the data processing aspects in case of the urgent transition from the main one to the 'hot spare'.

As previously mentioned several arrays (PS26, PS27 and PS28) are running the broadband sensor at each element thus having the very low probable scenario to fall in the category of no-mission capable station because of the malfunction of a single broadband element.
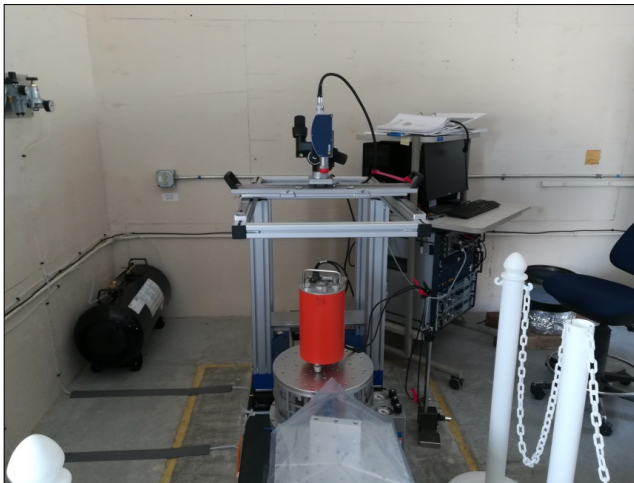
Sensor Calibration

Since commissioning of the first seismic station, calibration has been an important procedure to ensure reliable operation as the
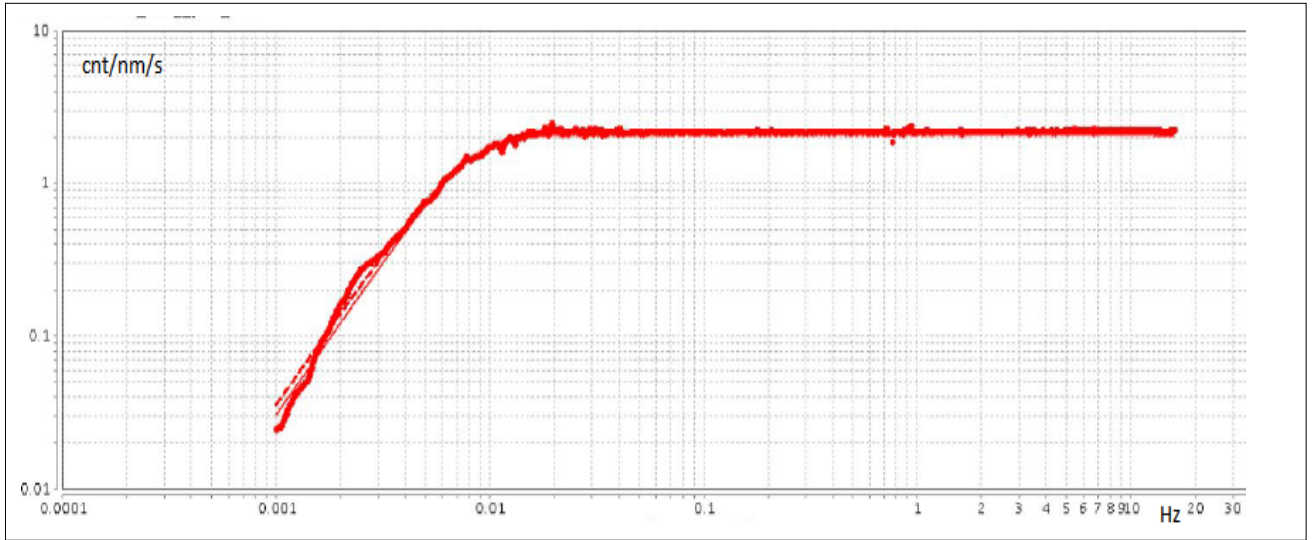
FIGURE 7.
Random binary calibration of the broadband seismometer CMG3T for three hours where the three red lines are depicted. The thick line is the result of smoothed spectral computations of the sensor response, thin solid line is the nominal poles and zeroes response and the dashed thin red line is the best fit of the measured curve with the new set of low frequency complex conjugate poles.

FIGURE 8.
Frequency response check of GS13 sensor on the SNL shake table prior to its use as the reference sensor in the field calibration campaign at PS19 (courtesy of SNL testing reports).

ground measurement tool. IMS requirements in this regard are not unique. IMS ensures an accuracy within 5% in amplitude and five degrees in phase for the channel frequency response. However the implementation of the IMS calibration process with such variety of different instrumentation in the IMS networks is a complicate task. The annual calibration programme is being run in the IMS for each station and each array element. Assistance from the station operator here is essential for the success of this key project.

The IMS is using both the full frequency and single frequency (1/CALPER where CALPER is a nominal calibration period) calibrations. The full frequency calibration utilizes random binary signals (Berger et al. 1979) of a long duration of up to four hours to restore the shape of the response and provide the best fit with poles and zeros (Scherbaum 2007) of the observed curve.

An interesting example of broadband sensors calibration verification using Earth tides signal as stimulus is presented for IDA segment of GSN stations in (Davis and Berger 2007) that allowed carrying out the re-check of the calibration factors at several II stations including the joint ones with the IMS.

The full frequency calibration utilizes the remote method of sending computer command via secure GCI link to the station digitizers requesting initiation of the calibration process of pre-selected duration and shape. The system completes the acquisition of both stimulus and channel output data and performs restoration of the response function using output to input smoothed spectral ratio. After it the process automatically adjusts (if necessary) poles and zeroes using the nominal values as the first guess. The procedure similar to the one mentioned above (Ringler et al. 2012) is used for the best fitting. In the initial stage the fit

was implemented in the low frequency edge of the response where two complex conjugate roots are mainly responsible for shaping the response function. At higher frequency end toward to the Nyquist frequency, the process requires most probably reacquiring of the data with higher sampling rates to provide reliable fitting. This solution is not yet implemented. That should be important for the broadband sensor's calibration with a known 'humps' at high frequency, such as STS2, 2.5 and Trillium 120. The example of the random – binary two hours calibration of CMG3T seismometer during quiet nighttime conditions is shown in Figure 7.

The single frequency calibration at the second stage of the remote calibration uses sinusoidal stimulus at CALPER sent to the calibration coil with known force constant. A similar approach is applied at ASL for to monitor changes of the calibration coil constant in time (Ringler et al. 2014a). Estimation of the CALIB constant in NM/CNT allows to scale the measured full frequency response function and to carry out the comparison with nominal NCALIB parameter. After the completion of the calibration process the measured CALIB is populated into the CD1.1 data sub-frames headers that are being transmitted to the IDC.

At some seismic stations a certain and significant mismatch of more than 5% between the nominal and observed calibration factors (or channel sensitivities) were revealed during their operation and confirmed by the remote calibration. The reference sensor in situ calibration was implemented for rectification. Such a case was noted at auxiliary station AS079 and successfully applied. The reference sensor periodic check is a reliable and viable method of periodic check and rectification of those issues where the remote calibration is incapable to resolve observed discrepancies.

There is an IMS requirement, established by the CTBTO, to have the capability of the calibration process to run under command&control mode (Preparatory Commission for the CTBTO Vienna, 2002, CTBT/WGB/TL-1/33/Rev.2 18). It basically means that the process must obey the requirement to be securely implemented via the data transmission layer or via the GCI. The first prototype of such software developed by the IMS Contractor Instrumental Software Technologies Inc. (ISTI, USA) incorporates this functionality. The module is also capable to support a fully automated process with AutoDRM formatted replies (to the initiator) of the obtained calibration results. This module is installed at several IMS stations and undergoes a permanent and thorough testing. It should be noted that there is difficulty related to the development of the permanent updates to interface with newly appeared models of digitizers and seismometers. The reliable operation of such software with wide variety of passive and active sensors is a challenging technical task.

After a long operational time, several IMS stations have undergone a major upgrade or even recapitalization phase in their life cycle. If the utilization of the previously used sensors (that have demonstrated the reliable operation) was requested by the station operator, the reinstallation plan included recalibration of at least several old referenced instruments to use them during the field installation campaign in a huddle recalibration test with other sensors. Figure 8 shows a shake table verification process of the frequency response of the previously used GS13 short period seismometer before re-installation for the major upgrade at PS19.

As many other calibration processes, the one described above represents a slightly modified version to satisfy IMS specific requirements described in (Preparatory Commission for the CTBTO Vienna, 2009, CTBT/WGB/TL-11,17/15/Rev.5).

4. TYPE OF SEISMIC SENSOR INSTALLATION

Borehole Installation

The majority of IMS arrays use the borehole method of sensor installation. It is known in seismological practice that sensor installation below the ground surface has diminished seismic noise level especially in the high frequency domain (Carter et al. 1991). It is a site dependent result but in general the deployment in the borehole is one of the methods used to reach better detection capability of the weak ground motion at higher frequencies f>3-5 Hz.

At lower frequencies (f<0.05 Hz) the effect of the noise attenuation is often not very obvious despite known ground displacement decrease versus depth and caused by air pressure fluctuations (Sorrells 1971, Ziolkowski 1973). To diminish the influence of air pressure fluctuations on low frequency seismic noise the installation in sand at the bottom of the borehole has been proposed and utilized at some sites (Holcomb et

FIGURE 9.
Drilling rig at one of the array elements at PS29.

al. 1998). This method was used at PS45 array-station. CMG 3ESP seismometers (by Guralp, UK) were used at single components elements of the array. Guralp manufacture has offered the special baffles to be applied in borehole installation to prevent air convection influence on the broadband seismometer (Guralp 3TB, UK, 2019). This method was attempted for installation of the broadband seismometer CMG3TB at PS40. However its efficacy has not been quantitatively proven and requires further investigation.

For regional newly built IMS arrays, ten boreholes (nine for vertical-component sensors and one for a 3-C broadband sensor) have been drilled and cemented to provide the best coupling to house seismometers with surrounding rocks. The target depths were 30 m for the vertical-element boreholes, and 60 m for the 3-C element borehole. Deviation from target depths was possible if appropriate geological justifications were discovered during drilling. It was a requirement for vertical-element boreholes to be cased with steel casing having an inner diameter between 102 mm and 128 mm. The 3-C borehole was usually cased with steel casing sections (not less than 5 m long and 6.5 mm thick) either welded or threaded and having an inner diameter between 153 mm and 177 mm. IMS contractors were responsible for ensuring that the finished boreholes met requirements of verticality, diameter size, water tightness and quality of cementation. The latter was applied to make sure there were no voids or shrinkage over the entire depth of the borehole and up to the wellhead termination entry. Mobilization of the drilling rig at PS26 is shown in Figure 9.

There were several cases in IMS practice when severe problems encountered during the drilling process had changed the planned location of an array element (for example PS31, PS44, PS36). Such situations have been handled by the array response checking to approve the element relocation.

Installation of seismometers in the IMS boreholes was done using three-jaw or single-jaw

hole-locks (Guralp 3TB, UK, 2019). Direct burial of the instruments in shallow postholes (Greig et al. 2014) was also applied at several sites, for example at AS03.

The following acceptance tests for the boreholes were required as a minimum:

- Each finished borehole was tested inside the casing for its final verticality to be less than $2.5^{0.}$
- Each finished borehole was tested against obstruction inside the casing using a cylindrical test dummy the length and outer diameter of the largest piece of borehole instrumentation to be installed.
- Each finished borehole was tested inside the casing against leaks, by filling and monitoring the pressurized water level for at least 24 hours.

Even though the IMS preferred dry installation, waterproof connectors and submersible operation (up to 100 m) were required from the supplier to sustain the underwater operation in case of undesirable flooding in the borehole. Prior to installation works the borehole was monitored over a period of at least one week against the entry of the groundwater.

In the initial stage of the IMS build-up programme seismic boreholes were filled mainly with CMG3TB (Guralp, UK) and KS54000 (Geotech, USA) broadband seismometers at 3-C site of the array and at 3-C stations. For the single component (vertical) borehole installations CMG3ESP, CMG3V from (Guralp, UK) and GS21, 23900, GS13BH (Geotech, USA) (Slad 2020) were mainly utilized. In the early 2000s Trillium120BH family of the broadband instruments from Nanometrics, Canada and STS-5A from Kinemetrics, USA joined the IMS fleet of the borehole instrumentation. These sensors were approved to support future borehole installations in the IMS seismic networks.

Vault Installation

The vault installation was also a very popular and well known method of sensor installation widely used in the IMS work programme. It was utilized for both single component vertical array elements and the 3-C element of the array as well as for conventional 3-C stations. For legacy 3-C stations, especially in the auxiliary network, IMS surface installation had benefited a lot from earlier installations in shallow and short horizontal tunnels with stable temperature and well-designed decoupled seismic pillars or chambers like at PS22 (array 3-C site), PS24, AS30, AS62, AS84, AS81 and some others.

For the newly built stations the surface vaults were constructed to provide a protected environment for a set of three (one vertical and two horizontal [CEA/DASE, France, 1999]) or single cased (STS-2, 2.5, CMG3T, CMG3V) seismometers sheltered from wind, animals, snow, water, abrupt temperature changes, and other ambient environmental effects. A single component element of the array often used reliable installation of the vault models of the low self-noise GS13, S13 (Geotech), for example at PS46, AS101 and PS9 respectively.

A level surface or pier was constructed using poured-in-place concrete well coupled to the host rock by metal reinforcement bars drilled and cemented into bedrock at depth. The pier was de-coupled from the adjacent enclosure as much as possible by a flexible material so as to minimize the transmission of motion from the enclosure to the sensors.

It was often requested that the surface 3-C vault enclosure had to be finished with easy access swing-up doors in a manner similar to other enclosures located at the single component array element sites.

5. INSTRUMENTATION TESTING

During the installation phase of the IMS seismic networks significant attention was paid to equipment component testing to ensure compliance of the components with IMS requirements for station specifications. Table1 shows that there are several specific requirements for sensors and digitizers to be carefully assessed prior to installation at IMS stations. The testing process was applied for seismometers and digitizers along with appearance of the particular unit as the candidate for installation or proposed by the hosting country for IMS applications. The IMS Division of the CTBTO usually requests, in the framework of its contractual activity with equipment, suppliers to provide the evidence of component testing by recognized technical laboratories.

System Self-Noise Testing

Testing sessions of the IMS equipment mainly took place at Sandia National Laboratory (SNL) in Albuquerque NM, USA as the recognized and independent state agency. SNL is widely known for using a qualified methodology (Kromer at al. 2007a, 2007b) to carry out such tests. It is important to note at SNL there is a large database of testing results for different types of equipment available that ensures easy reference and comparison. An example of testing experiments for seismometers and digitizers at SNL is shown in Figures 10 and 11.

The IMS was aware of the long term ongoing sensor testing programme at the Albuquerque Seismological Laboratory (ASL) of the United States Geological Survey (USGS). Almost all known broadband sensors, installed under b different projects and affiliated with different sponsorship programmes, have been tested at ASL. Results of these tests and the testing methodology used were published (Holcomb 1989, Ringler et al. 2014b). Cooperation with ASL in this regard was always beneficial as it has allowed coordination of equipment installation and upgrade plans at joint IMS – GSN facilities.
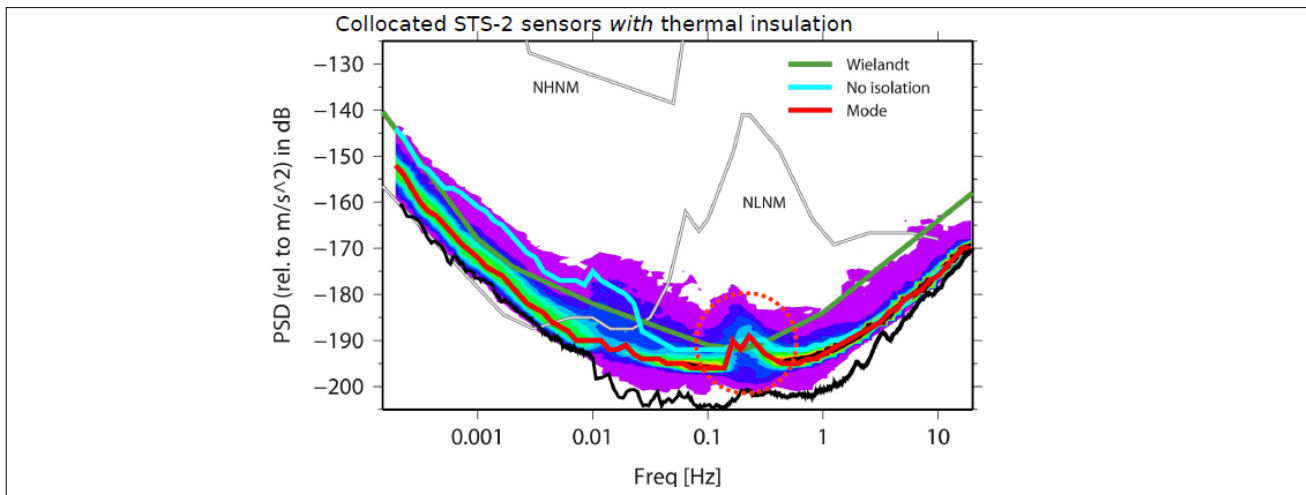

FIGURE 10.
Testing of the borehole version of CMG 3 type of instruments clamped to the concrete wall with special fixtures (courtesy of SNL testing reports, for example: Hart and Merchant 2014).

Until the early 2000s, the two sensor coherence test was usually used for self-noise evaluation. Appearance of the new testing approach with three sensors installation for self-noise evaluation (Sleeman et al. 2006) has triggered the re-assessment of the self-noise for some seismometers (Ringler and Hutt 2010). The importance of the seismometer casing temperature insolation was emphasized (Sleeman and Melichar 2012).

FIGURE 11.
Self-noise testing of Q330M+ (Kinemetrics, USA) and Centaur (Nanometrics, Canada) digitizers inside the temperature chamber at SNL (left panel) and side-by-side testing of two CMG3V vault seismometers at the right panel (courtesy of SNL testing reports).
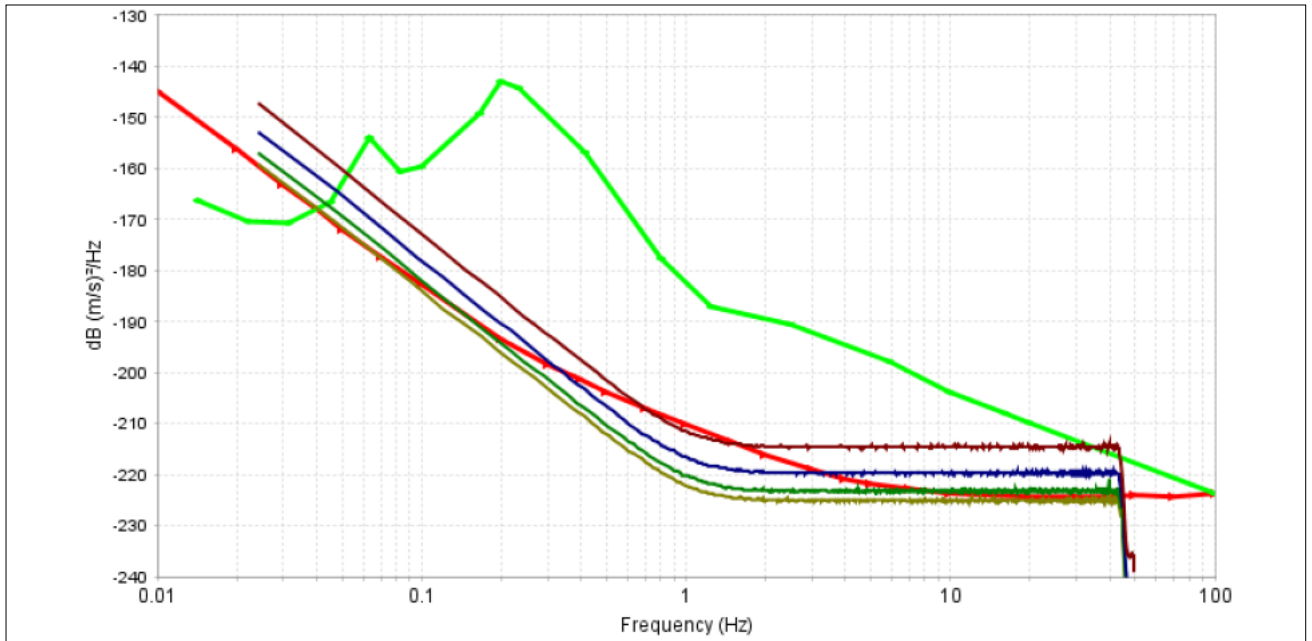

FIGURE 12.
Long term (one year) measurement of STS-2 self-noise at the Conrad Observatory, Austria. The picture shows the importance of thermal insulation in carrying out long term observation of the instrumental noise (Sleeman and Melichar, 2012).

Figure 12 shows the result of almost a year-long testing experiment. Even though the details of STS-2 self-noise test are mainly outside the IMS passband, it has been demonstrated that accurate estimation of this important sensor characteristic is not an easy experimental task.

The way to account for the sensor misalignment during the testing experiment and how to enhance the self-noise estimation in the frequency range of the ocean mircroseisms is well demonstrated (Gerner and Bokelmann 2013).

The importance of self-noise investigation is driven by the requirement to have it at least 10 dB below the minimum background noise at the station (shown in Table 1). Spectral characteristics of the minimum background noise at IMS stations were preliminary taken from the site survey for the new stations. For the legacy stations historical data were utilized from the parent network assessment reports. The fifth quantile of the power spectral density or the low boundary of the 95% confidential interval was considered as the benchmark for the minimal site noise characterization.
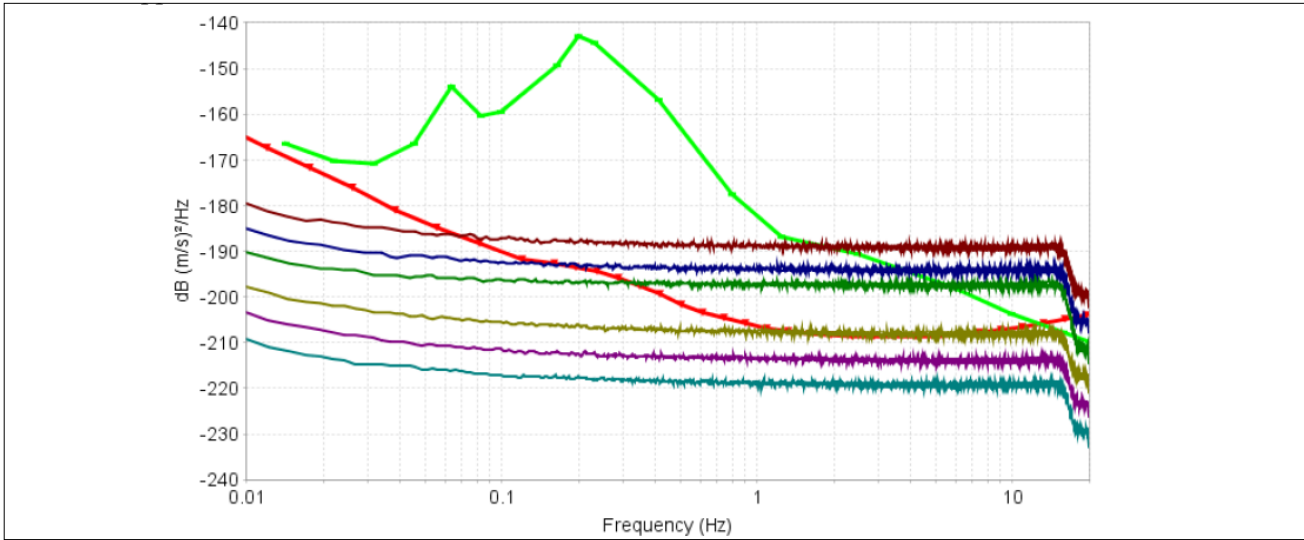
FIGURE 13.

Self-noise of the Affinity digitizer (Guralp, UK) connected to the GS21 passive short period seismometer through the gain factor 61.39 preamplifier. Different digitizer front end gain settings of the digitizer: g=1- brown line the uppermost, g=8 - dark olive is the lowest one. The two colored lines in between are self-noise measurements for step 2 gain factor changes (Merchant 2018). The solid red line depicts the sensor self-noise (Townsend and Kromer 2004) model and the light green line is the NLNM (Peterson 1993).

An interesting and important case of instrumental noise testing is presented when the preamplifier circuit is involved in arranging the compliance with IMS requirements for the sensor self-noise. Such case is known from the earlier days of seismic observations as an efficient method to achieve a good resolution of the ground motion at seismic high frequencies (Rodgers 1994). As previously mentioned passive short period instruments are still widely used in many IMS arrays and 3-C stations. The combination of different front end gain settings for the Affinity (Guralp, UK) digitizer and the preamplifier connected to the GS21 output has been tested at SNL (Merchant 2018). Figure 13 shows the result in comparison with the NLNM and the sensor self-noise model. It demonstrates that for potentially low seismic background sites, approaching the NLNM, the compliance with IMS specifications to be at least 10 dB below the minimum background at high frequency is not always easy to achieve as the preamplifier starts to contribute to the instrumental noise. It thus requires a high gain setting and testing of such sensor and preamplifier combination on a case by case basis.

Digitizer Self-Noise Testing

The digitizer at a seismic station is another equipment component contributing to the resolution capability of the seismic station. As per the requirements listed in Table 1 the self-noise of the digitizer has to be in its turn at least 10 dB below the seismometer noise over the IMS passband. However it is not always practical to establish such conditions especially at those stations where very low self-noise sensors are installed. In such case the actual seismometer self-noise is considered as exceeding the minimum IMS requirement for the sensor self-noise. The digitizer self-noise is therefore adjusted relative to the sensor self-noise requirement, or at least 20 dB below the minimum station background over the passband. The example of Q330M+ (Kinemetrics, USA) digitizer self-noise evaluation is shown in Figure 14. The plot shows the self-noise power spectral density (PSDs) for different settings of the front end gain assuming the application with STS-5A seismometer.

Digitizer self-noise characteristics were usually tested not only for room temperature

FIGURE 14.

Self-noise of the Q330M+ digitizer (Kinemetrics, USA) connected to the high-gain STS-5A broadband seismometer for different front end gain settings of the digitizer: g=1- brown line the uppermost, g=32 - dark blue, the lowest one. The four colored lines in between are self-noise measurements for step 2 gain factor changes (Slad and Merchant 2020). The solid red line depicts the sensor self-noise model and the light green line is the NLNM (Peterson 1993).
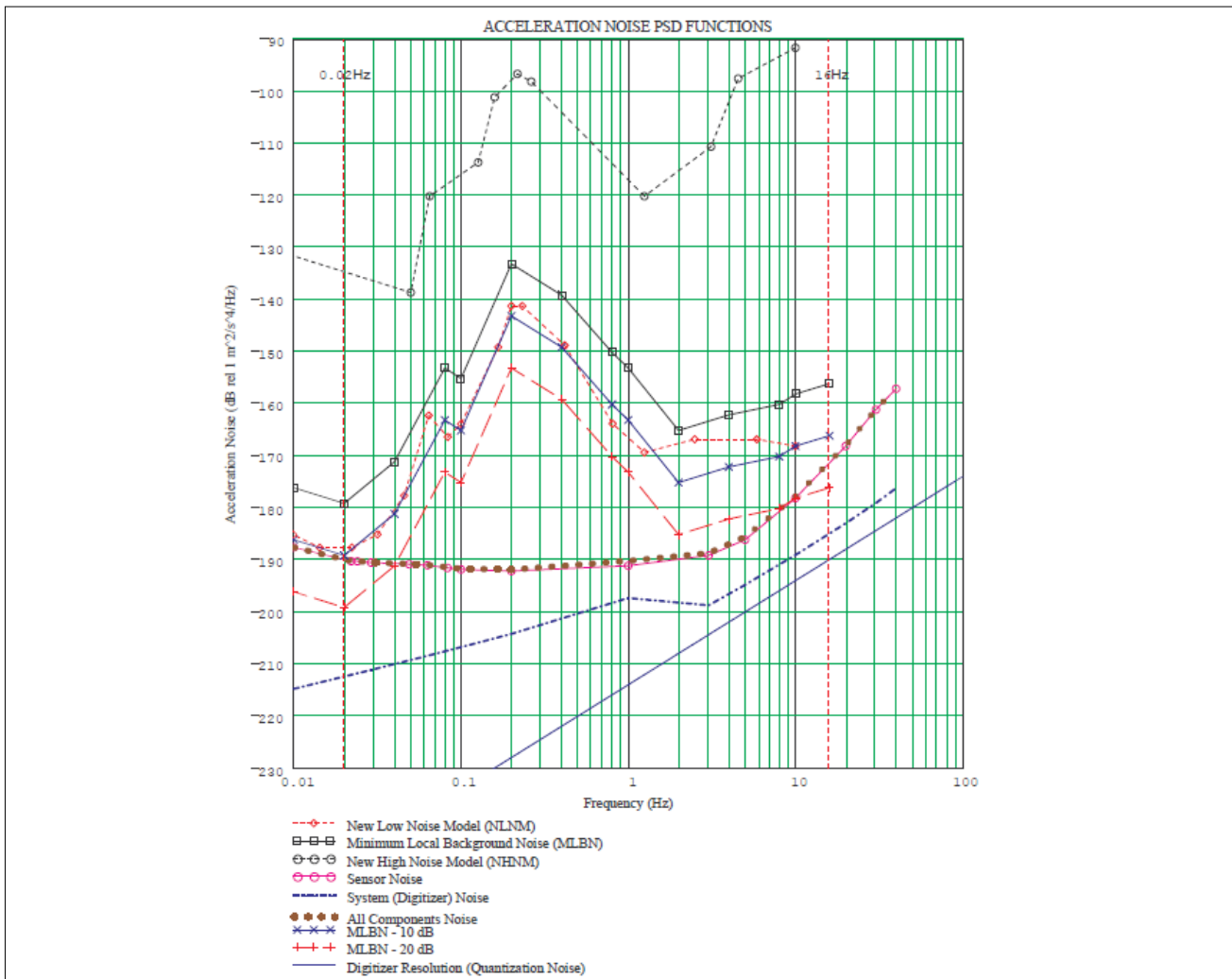
FIGURE 15.

The example of the noise study carried out by the IMS equipment contractor (Nanometrics, Canada) for PS26.

conditions but also for extreme ends of the temperature limits -10°C and +45°C respectively. Two models of digitizers undergoing the temperature testing in the special SNL chamber are shown in the left panel of Figure 11.

IMS equipment suppliers are requested to carry out a preliminary integration noise study of the signal recording conditions at any IMS station before installation. The example of such integration noise study is shown in Figure 15 for the broadband elements of the array-station PS26. Different curves in the plot show the averaged noise characteristic for the particular type of seismometer and digitizer that was planned to be installed at the station. The benchmark graph for the station minimum noise was provided by the IMS and the corresponding self-noise of the sensor and digitizer (with particular front end gain settings) were plotted based on the testing results and explained in the caption of Figure 15.

System Timing Testing

The timing accuracy requirement for synchronization of data samples with UTC has been always important for any seismic installation (Agnew 2020, Ringler et al. 2021). Accuracy was tested for key models of GSN digitizers like Q330HR where individual GPS/GNSS receivers provide high absolute timing accuracy within several microseconds (Slad and Merchant 2018). As mentioned in comparison with the GSN, the IMS seismic network has many array stations. Besides the absolute timing accuracy there is an important relative timing requirement for an array station to have — desynchronization accuracy between array elements not more than one (see Table 1).

While the absolute timing accuracy to be 10 ms is not difficult to achieve by the majority of modern digitization equipment the relative timing accuracy needs to be assessed by adding several extra timing tests to the procedure.

The compliance with relative timing between array elements to be 1 ms basically means that any digitizer at IMS array should be within 500 ms accuracy at any particular time moment. In case of the GPS synchronization loss, the timing system starts drifting. Therefore the information about measured drift rate is important characteristic of the digitizer model to get conservative estimate of how long it would take for the internal clock to be out of 500 ms critical threshold. Testing of the timing accuracy drift for several models of IMS digitizers synchronized with individual GPS/GNSS receivers was carried out at SNL (Merchant 2018, Slad and Merchant 2020). For example, for Affinity (Guralp, UK) and Q330M+ (Kinemetrics, USA) units the measured drift rate was found to be around 5-8 ms/h. Both digitizers are known to support the Precise Time Protocol (PTP) option for UTC time synchronization. This PTP method is based on network synchronization
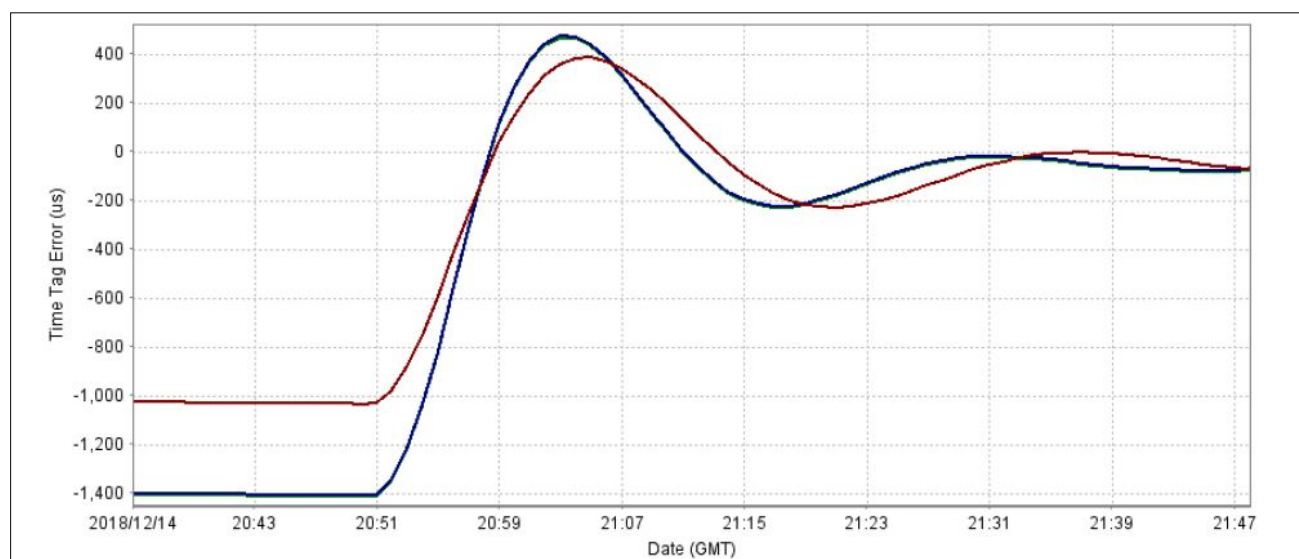
FIGURE 16.
Recovery of the timing accuracy after the GPS receiver resumed its operation (Slad and Merchant 2020).

by sending formatted time stamps from a central recording facility. This method is convenient and a promising alternative to the individual GPS/GNSS option. It provides the possibility of synchronizing all digitizer clocks using a single central time PTP master clock which operation is supported with the 'hot' spare in case of a main failure.

PTP synchronization was also tested at SNL. It was found acceptable with absolute timing accuracy to be much less than 10 ms and thus even exceeding IMS requirements. But the higher than individual GPS drift rate was measured as about 25-40 ms/h in case of GPS PTP master clock synchronization loss (Slad and Merchant 2020). By knowing the drift rate it was possible to implement the corresponding State of Health (SoH) CD1.1 status bits settings. It is helpful for the IDC recipients to flag those absolute time segments in the data stream where the timing accuracy from the particular digitizer could be out of specification.

When GPS antenna resumes its operation after the long outage or the signal coverage loss, it was found that restoration of the normal operation of the timing system takes some time to show the good synchronization. Figure 16 shows the transient response of Q330M+ digitizer after the GPS resumed. After being of about -1.5 ms out of timing accuracy (left hand side of the graph) it took about one hour after the digitizer came back to the normal synchronization accuracy of 50 ms.

The particular importance for the IMS stations to obey timing accuracy requirements is defined by the fact that almost all automatic data processing methods used in the IDC for arrays (like f-k and beamforming) are utilizing aggregation of data segments from array element and summation methodology of simultaneous data. Their efficiency for the improvement of SNR therefore requires extra care to be taken for monitoring of the raw data timing quality. The above is important for 3-C stations also but seismic arrays with closely collocated elements and special requirement for the relative timing accuracy have a more challenging technical task in this regard.

6.   IMS ARRAYS AND THE AMBIENT NOISE TOMOGRAPHY.

Over the last decades seismic noise has been converted by semiologists into informative wave fields that could be used in tomography tasks for imaging of the uppermost structures of the Earth. This approach is known as the Aki method (Aki 1957). The basic idea is that the seismic noise spectrum of the Earth (McNamara et al. 2009) over the specific range f>0.02 Hz is combined of body and surface waves of spatially incoherent but uniformly distributed sources. Therefore its spatial correlation properties could be converted into the interior structure velocities under the station deployment (Campillo and Roux 2015). The Aki method of spatial cross-correlation has been modified (Bettig et al. 2001, Köhler et al. 2007) during the last decades and the vast number of publications have led to the development of a new investigation tool of the Earth interior known as ambient noise tomography (ANT) (Shapiro et al. 2005).

The noise sources could be of different external or internal origin including atmospheric perturbations, ocean, groundwater or rivers, possible micro cracking in the upper crust and human-made activity (Bonnefoy-Claudet et al. 2006). For application of cross-correlation techniques, spatially deployed N stations are converted into configuration of N(N-1)/2 source-receiver pairs (Wapenaar et al. 2010). Revealed cross-correlation maximums at certain time lags for each pair reflect the velocity structure of the underlying layers (Bensen et al. 2007). The lower the frequency of revealed cross-correlation maximum, the deeper penetration into the Earth interior is possible. Restoration of the regional Green functions has become possible using seismic noise correlation method (Sabra et al. 2005, Tsai 2010).

Working with the surface wave branch in the noise data has shown the possibility of building

phase velocity dispersion curves for Rayleigh and Love waves after applying inversion methods to restore the underlying velocity models at different scales and regions (Ekstr**ö**m et al. 2009, Lin et al. 2008, Villasenor et al. 2007).

Seismic array as a group of spatially installed sensors on the surface of the Earth represents an obvious temptation to apply noise correlation techniques for reconstruction of the 3-D Earth structure underneath the installation area. Knowledge of the structure details around sensor deployment is beneficial for a better modeling of seismic waves travel times from the regional events and therefore improves the observed arrival time residuals pattern enhancing events location accuracy. The amount of noise data in continuous data streams from IMS primary array stations is almost infinite in comparison with data associated with recorded events. Noise analysis could be carried out with special care and results could be not only revised but their stability in time verified.

For trial purposes the noise spatial correlation technique was applied to data fragment collection at PS28. Figure 17 shows that this array was conditionally divided into four sectoral areas roughly corresponding to East and North locations. Data fragments of only seismic noise

data from each of 25 elements about 10 h in duration were used for spatial noise correlation analysis in the frequency band 0.2-10 Hz.

Noise correlation calculations and construction of phase velocities dispersion curves were carried out using the open source Geopsy software package (Wathelet et al. 2020). Further restoration of the compressional (V_p) and shear (V_s) waves velocity models were done using the neighborhood algorithm (Wathelet 2008) as implemented in the *dinver* module, which is available in the Geopsy.

Positive experience about the exploitation of ANT correlation technique for ARCES data has come after trial analysis of the noise spatial correlation versus frequency for different intersensory distances. The example of such correlation is shown in Figure 18. As expected the bigger intersensory distances depicted by red and brown curves show the faster drop of the noise cross-correlation coefficients (see figure caption for more details). The theory predicts for vertical components cross-correlation the oscillating pattern described by Bessel function of zero order (Aki 1957, Asten 2006). It is interesting to note that the visual resemblance of the curves in Figure 4 and in Figure 18. The first one depicts spatial correlation versus intersensory distances but in the
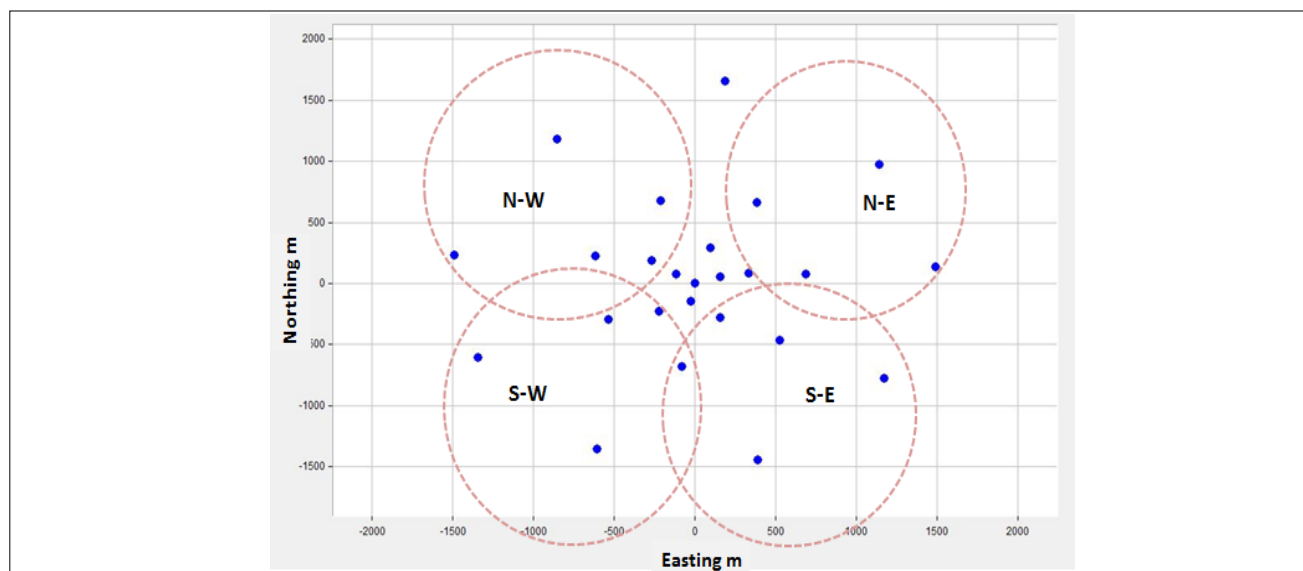
FIGURE 17.

Sectoral arrangement for velocity models retrieval at PS28 array. Four circle areas rounded by brown dash lines conditionally show several array elements used in spatial cross-correlation analysis of seismic noise. Notation S-E, S-W, N-W and N-E indicate south-east, south-west, north-west and north-east sectors respectively. The blue dots are array element locations.

narrow frequency bands Df0 whereas the second one depicts the similar oscillating behavior versus frequency for several intersensory distances Dr0. This could be explained by the symmetry of the spatial cross-correlation $C(k,r)$ described by Bessel function (Asten 2006, Tsai 2010):

$$C(k,r) = J_0(k,r) = J_0\left(\frac{2\pi f}{V(f)} r\right),$$ where k is the wave vector, r is the intersensory distance and $V(f)$ is the propagation wave of the seismic wave mode under consideration. It is frequency dependent in case of surface waves.

The example of the phase velocity dispersion curve restored from the noise cross-correlation for array elements located in the N-W sector is shown in Figure 19. The grey area in the plot indicates the region of the best misfit (0.1) between the observed (solid line) and restored dispersion using intersensory noise cross-correlation.

Further on, the inversion of the dispersion curves into the velocity models at two N-W and S-W sectors are shown in Figure 20 a, b. The restored velocity models for two sectors are shown for comparison. The difference between the two models that may indicate a promising way to continue investigating such findings. Preliminary ANT results for IMS array in Norway demonstrates the feasibility study that may further be applied for other IMS array stations.

The above described preliminary results convey the suggestion about the application of this technique for IMS arrays in general. The expediency of ANT methods for verification related data processing methods has been also mentioned (Harris et al. 2012). The IDC database has a unique collection of seismic noise data obtained at different geographical locations. This allows for consideration of the application of the ANT techniques at IMS arrays as a prospective project not only as the way to enhance the SNR for signal detections (see Section 3) but also for restoration of the underlying velocity models as the way for enhancement of especially regional events location algorithms and thus to sustain SHI expert technical analysis initiatives (Kitov et al. 2021).
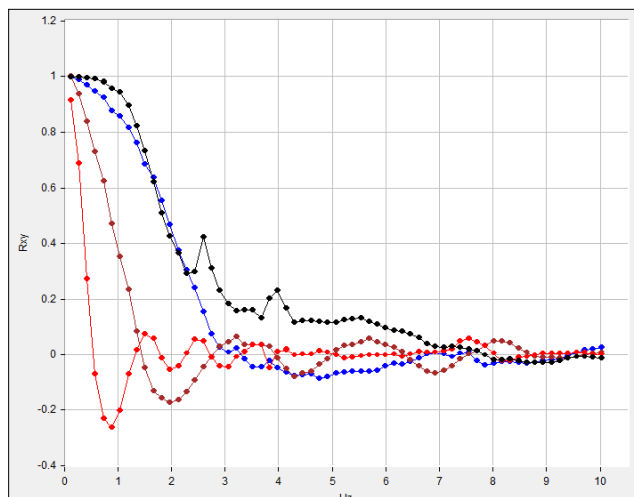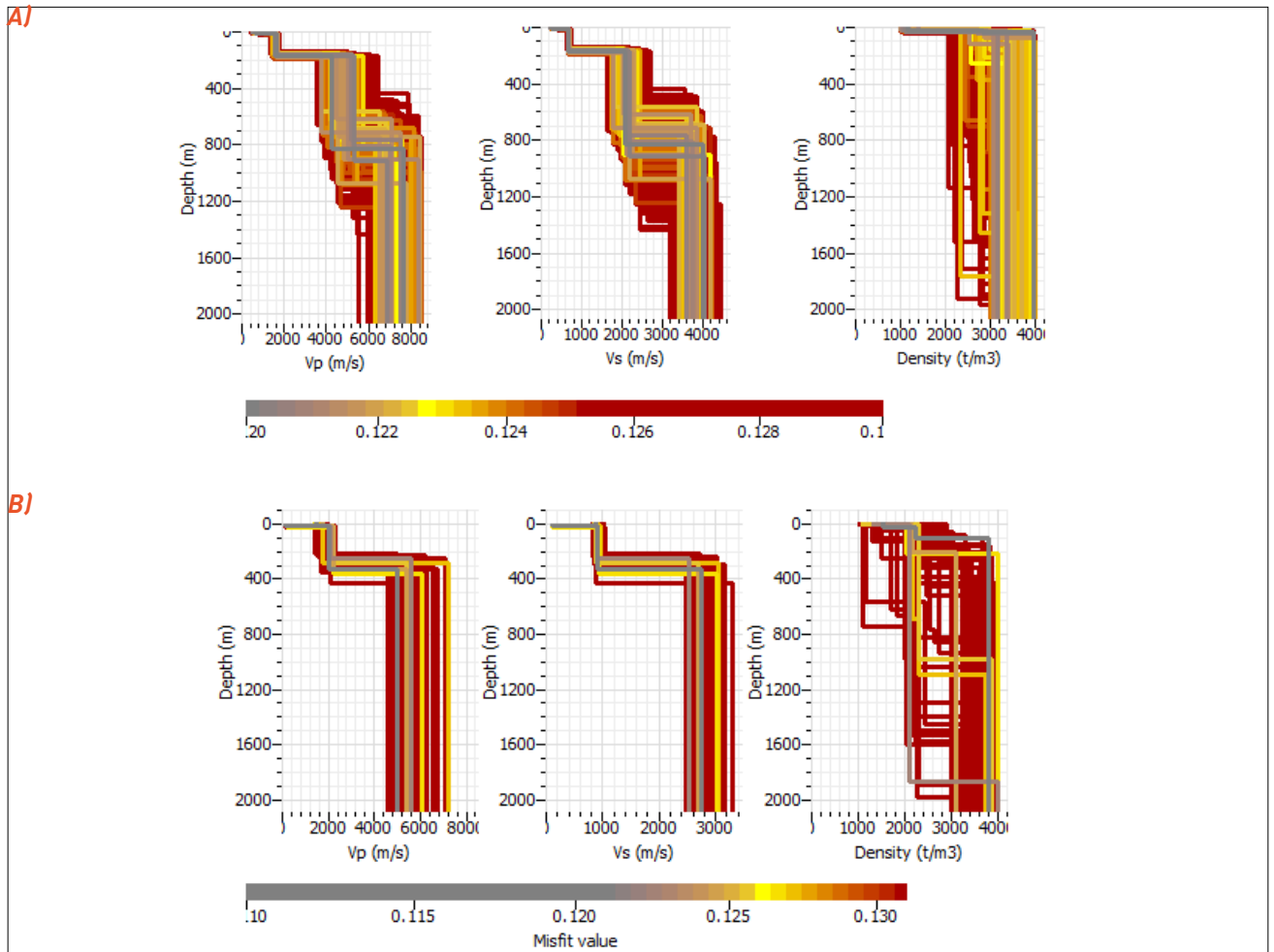

FIGURE 18.
The spatial noise cross-correlation coefficients versus frequency for PS28. The red curve is for intersensory distances 2.5 km, the brown one is for 1.1 km, the blue one is for 0.4 km and the black line is for 0.15 km.

Restoration of surface waves dispersion curves as presented in the above examples for PS28 requires a good quality of timing system throughout all sites involved in the observation. IMS instrumentation testing accounted timing system verification under the different angles and special SoH timing status bits are foreseen in the CD1.1 sending format. This means that IMS noise data are supposed to be ready to contribute
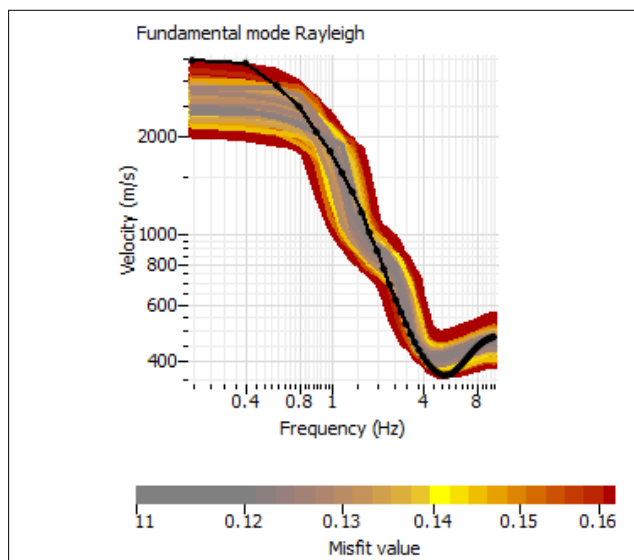
FIGURE 19.
Phase velocity dispersion curve for the fundamental mode of Rayleigh waves obtained from spatial correlation of background noise recorded at PS28 array elements in the N-W sector of the array shown in Figure 17. The legend under each plot shows the color range of the obtained misfit values.

FIGURE 20.

Restored Vp, Vs velocity models and density model (right panel in both plots) of the underlying layers for S-W (a) and N-W (b) sectors of PS28 array. The legend under each plot shows the color range of the obtained misfit values.

to the development of ANT initiatives. It should be noted that the interelement noise correlation method had been proposed earlier to monitor possible QC issues of the time synchronization system at PS19 array (Koch and Stammler 2003). Perhaps the combination of these efforts for timing QC and utilization of seismic noise for ambient noise tomography purposes may constitute an interesting and useful development branch for both the IMS and the IDC.

Within the CTBTO environment this method may find its application also for enhancement of the aftershock monitoring system as one of the approved technologies in the on-site inspection field activities. By knowing the velocity models under the temporarily deployed station network significant improvement of aftershock location accuracy could be achieved.

7. CONCLUSION

Different equipment solutions installed in the IMS seismic networks have been described in this paper. Special attention was paid to the sensors and digitizers compliance with technical requirements of the draft IMS Operational Manual. The IMS seismic network comprises the largest amount of array stations in the world which provide the weak signal detection capability with the highest number of seismometers emplaced into boreholes up to 100 m depth. Site preparation works for the IMS borehole and 3-C vault installations have been carried out with special care to ensure the necessary standards. The IMS utilizes different models of modern active and passive short period and broadband instruments manufactured by recognized suppliers (in alphabetical order: CEA/DASE, Geotech, Guralp, Kinemetrics, Nanometrics). They have demonstrated a time proven concept during operation for not only the IMS but for other seismological projects. Sensor orientation and calibration aspects are supported by ongoing annual programmes. To ensure better performance with high dynamic range requirements, hybrid frequency response sensors were proposed and installed at several array stations.

In the digitizer area the IMS uses known models in the production lines of the key equipment suppliers like (in alphabetical order: Geotech, Guralp, Kinemetrics, Nanometrics, Science Horizons, Tekelec) but with improved and tested characteristics like self-noise, timing accuracy, SoH parameters, remote command&control and temperature range specifications. Special attention was always given to the IMS equipment testing. The verification and acceptance process was driven by innovations in the equipment market and by the needs of the host countries.

Implementation of the data acquisition process based on the central timing solutions for IMS array stations may represent the future path for improvement of data processing algorithms which rely on simultaneously sampled raw data with high accuracy.

The prospects of utilizing ambient noise technology methods may appear to be a useful aspect of interdivisional cooperation with the CTBTO for the enhancement of the event location accuracy both for permanent data processing in IDC and for temporary operational local deployments for aftershock monitoring system in on-site inspection.

Future progress in the development of a sustainable verification regime should be abreast with modern technologies in the seismic hardware and software markets, adjusted for IMS specific needs and requirements.

REFERENCES

Agnew, D.C. (2020). Time marks and clock corrections: A century of seismological timekeeping. *Seismological Research Letters* **91** (3) 1417-1429.

Aki, K. (1957). Space and time spectra of stationary stochastic waves, with special reference to microtremors. *Bulletin of the Earthquake Research Institute* **35** 415-457.

Asten, M. (2006). On bias and noise in passive seismic data from finite circular array data processed using SPAC methods. *Geophysics* **71** (6) 153-162.

Bensen, G.D., Ritzwoller, M., Barmin, M.P., Levshin, A., Lin, F., Moschetti, M.P., Shapiro, N., Yang, Y. (2007). Processing seismic ambient noise data to obtain reliable broad-band surface wave dispersion measurements, *Geophysical Journal International* **169** (3) 1239-1260.

Bettig, B., Bard, P.Y., Scherbaum, F., Riepl, J., Cotton, F., Cornou, C., Hatzfeld, D. (2001). Analysis of dense array noise measurements using the modified spatial auto-correlation method (SPAC): application to the Grenoble area. *Bollettino di Geofisica Teorica ed Applicata* **42** (3) 281-304.

Berger J., Agnew, D.C., Parker, R.L., Farrell, W.E. (1979). Seismic system calibration: 2. Cross-spectral calibration using random binary signals. *Bulletin of the Seismological Society of America* **69** (1) 271-288.

Bonnefoy-Claudet, S., Cotton, F., Bard, P-Y. (2006). The nature of noise wavefield and its applications for site effects studies: A literature review. *Earth-Science Reviews* **79** (3–4) 205-227.

Bowers, D., Selby, N.D. (2009). Forensic seismology and the Comprehensive Nuclear-Test-Ban Treaty. *Annual Review of Earth and Planetary Sciences* **37** (1) 209-236.

Bungum, H., Husebye, E.S., Ringdal, F. (1971). The NORSAR Array and preliminary results of data analysis. Geophysical Journal International **25** (1-3) 115-126.

Carter J.A., Barstow, N., Pomeroy, P.W., Chael, E.P., Leahy, P.J. (1991). High-frequency seismic noise as a function of depth. *Bulletin of the Seismological Society of America* **81** (4) 1101-1114.

CEA/DASE, Long-Period vertical seismometer LPZA 12S, technical manual, Bruyères-Le-Châtel, FR (1999).

CEA/DASE, Long-Period horizontal seismometer LPHA 12S, technical manual, Bruyères-Le-Châtel, FR, (1999).

CEA/DASE, Short-Period seismometer, vertical model ZM500 for digital networks, Maintenance and instruction operating manual, Bruyères-Le-Châtel, FR (1999).

CEA/DASE, Short-Period seismometer, horizontal model HM500 for digital networks, Maintenance and instruction operating manual, Bruyères-Le-Châtel, FR (1999).

Campillo M., Roux, Ph. (2015). "Crust and lithospheric structure - seismic imaging and monitoring with ambient noise correlations". Treatise on Geophysics, 2nd edition, Vol. 1. (G. Schubert, Ed.).Elsevier, Oxford, pp. 391-417.

Davis, P., Berger, J. (2007). Calibration of the global seismographic network using tides. *Seismological Research Letters* **78** (4) 454-459.

Ebeling, C., Astiz, L., Starovoyt, Y., Barrientos, S., Tavener, N., Perez, G., Yamamoto, M., Hfaiedh, M., Given, H., Stewart, R., Estabrook, C. (2002). Low noise results from IMS site surveys: A preliminary new high-frequency low noise model. *American Geophysical Union* abstract id S71A-1057.

Gerner, A., Bokelmann, G. (2013). Instrument self-noise and sensor misalignment. *Advances in Geoscience* **36** 17-20.

Ekstr**ö**m, G., Abers, G.A., Webb, S.C. (2009). Determination of surface-wave phase velocities across USArray from noise and Aki's spectral formulation. *Geophysical Research Letters* **36** (18) L18301.

Estabrook, C.H., Bergsson, B.H., Soumana, S., Boureima, O., Moumouni, M. (2008). Results from IMS seismic array in Niger. *American Geophysical Union* Abstract ID S43D-1905.

Greig, W., Spriggs, N., Bainbridges, G. (2014). "Comparison study between vault seismometers and a posthole seismometer". *Geophysical Research Abstracts* (Proceedings Second European Conference on Earthquake Engineering and Seismology, Istanbul, 2014).

G**ü**ralp 3TB (2019). *Operator's Guide*. Document No. MAN-BHO-0001, Güralp Systems Limited, Aldermaston.

Harris, D.B., Gibbons, S.J., Rodgers, A.J., Pasyanos, M.E. (2012). Nuclear test ban treaty verification: Improving test ban monitoring with empirical and model-based signal processing. *Institute of Electrical and Electronics Engineers Signal Processing Magazine* **29** (3) 57-70.

Hart, D.M., Merchant, B.J. (2014). *Evaluation of Three Refurbished Guralp CMG-3TB Seismometers*. Sandia National Lab (SNL-NM), Albuquerque, New Mexico.

Holcomb, L.G., Sandoval, L., Hutt, B. (1998). *Experimental Investigations Regarding the use of Sand as an Inhibitor of air Convection in Deep Seismic Boreholes*. USGS Open-File Report 98-362, Albuquerque Seismological Laboratory, Albuquerque, New Mexico.

Holcomb, G.L. (1989). A Direct Method for Calculating Instrument Noise Levels in Side-by-Side Seismometer Evaluations. USGS Open File Report 89-214. U.S. Geological Survey, Albuquerque Seismological Laboratory, Albuquerque, New Mexico.

Ingate, S.F., Husebye, E.S., Christoffersson, A. (1985). Regional arrays and optimum data processing schemes. *Bulletin of the Seismological Society of America* **75** (4) 1155-1177.

Kitov, I., Rozhkov, M., Starovoyt, Y., Le Bras, R. (2021). *New applications at the IDC for SHI Expert Technical Analysis*. (Proceedings of the CTBTO Science and Technology Conference, Vienna, 2021) Abstract ID Is1-353.

Koch, K., Stammler, K. (2003). Detection and elimination of time synchronization problems for the GERESS array by correlating microseismic noise. *Seismological Research Letters* **74** (6) 803-816.

K**ö**hler, A., Ohrnberger, M., Scherbaum, F., Wathelet, M., Cornou, C. (2007). Assessing the reliability of the modified three-component spatial autocorrelation technique. *Geophysical Journal International* **168** (2) 779–796.

Kromer, R.P., Hart, D.M., Harris, J.M. (2007a). *Test definitions for the evaluation of digital waveform recorders: Version 1.0*. SAND2007-5037, Sandia National Lab (SNL-NM), Albuquerque, New Mexico.

Kromer, R.P., Hart, D.M., Harris, J.M. (2007b). *Test Definition for the Evaluation of Seismic Sensors*. SAND2007-5025, Sandia National Lab (SNL-NM), Albuquerque, New Mexico.

Kromer, R.P. (2003) Ground-based Monitoring R&E Technology Report, 2003. Evaluation of the Science Horizons AIM24S Borehole Digitizer for BRTR/Turkey IMS Application, 30 December 2003.

Larsonnier, F., Rouillé, G., Bartoli, C., Klaus, L., Begoff P. (2019). Comparison on seismometer sensitivity following ISO 16063-11 standard. Proceedings 19th International Congress of Metrology, 27003. Paris, France, September 24-26.

Lin, F-C., Moschetti, M.P., Ritzwoller, M.H. (2008). Surface wave tomography of the western United States from ambient seismic noise: Rayleigh and Love wave phase velocity maps. *Geophysical Journal International* **173** (1) 281-298.

Merchant, J.B. (2018). *2017 Guralp Affinity Digitizer Evaluation*. SAND2018-2136, Sandia National Lab. (SNL-NM), Albuquerque, New Mexico.

McNamara, D., Hutt, C.R., Gee, L.S., Benz, H.M., Buland, R.P. (2009). A method to establish seismic noise baselines for automated station assessment. *Seismological Research Letters* **80** (4) 628-637.

Mykkeltveit, S., Ringdal, F., Kvaerna, T., Alewine, R.W. (1990). Application of regional arrays in seismic verification research. *Bulletin of the Seismological Society of America* **80** (6) 1777-1800.

Mykkeltveit, S., Åstebøl, K., Doornbos, D.J., Husebye, E.S. (1983). Seismic array configuration optimization. *Bulletin of the Seismological Society of America* **73** (1) 173-186.

Peterson, J. (1993). *Observations and Modeling of Seismic Background Noise*, Open-File Report 93-322, U.S. Geological Survey, Albuquerque, New Mexico.

Pirli, M. (2013). *NORSAR System Responses Manual*, 3rd Edn, NORSAR, Kjeller, Norway.

Preparatory Commission for the Comprehensive Nuclear-Test-Ban Treaty Organization (2002). *Command and Control of IMS Stations: Procedures for Issuing Commands.* Doc. No. CTBT/WGB/TL-1/33/Rev.2 18 Preparatory Commission for the CTBTO, Vienna.

Preparatory Commission for the Comprehensive Nuclear-Test-Ban Treaty Organizations (2009). *Draft Operational Manual for Seismological Monitoring and the International Exchange of Seismological Data*, Doc. No. CTBT/WGB/TL-11,17/15/Rev.5. Preparatory Commission for the CTBTO, Vienna.

Ringler, A.T., Hutt, C.R. (2010). Self-noise models of seismic instruments. *Seismological Research Letters*, **81** (6) 972 983.

Ringler, A.T., Hutt, C.R., Aster, R., Bolton, H., Gee, L.S., Storm, T. (2012). Estimating pole/zero errors in GSN-IRIS/USGS network calibration metadata. *Bulletin of the Seismological Society of America* **102** (2) 836-841.

Ringler, A.T., Hutt, C.R., Persefield, K., Gee, L.S. (2013). Seismic station installation orientation errors at ANSS and IRIS/USGS stations. *Seismological Research Letters* **84** (6) 926-931.

Ringler, A.T., Hutt, C.R., Gee, L.S., Sandoval, L.D., Wilson, D. (2014a). Obtaining changes in calibration-coil to seismometer output constants using sine waves. *Bulletin of the Seismological Society of America* **104** (1) 582-586.

Ringler, A.T., Sleeman, R., Hutt, C.R., Gee, L.S. (2014b). "Seismometer self-noise and measuring methods". *Encyclopaedia of Earthquake Engineering*. Springer, Berlin and Heidelberg, pp. 1-13.

Ringler, A.T., Steim, J., Wilson, D.C., Widmer-Schnidrig, R., Anthony, R.E. (2020). Improvements in seismic resolution and current limitations in the Global Seismographic Network. *Geophysical Journal International*, **220** (1) 508–521.

Ringler, A.T., Anthony, R.E., Wilson, D.C., Auerbach, D., Bargabus, S., Davis, P.W., Gunnels, M., Hafner, K., Holland, J.F., Kearns, A., Klimczak, E. (2021). A review of timing accuracy across the Global Seismographic Network. *Seismological Research Letters* **92** (4) 2270-2281.

Ringler, A.T., Anthony, R.E. (2021). Local variations in broadband sensor installations: Orientations, sensitivities, and noise levels. *Pure and Applied Geophysics* **179** 217–231.

Rodgers, P.W. (1994). Self-noise for 34 common electromagnetic seismometer/preamplifier pairs. *Bulletin of the Seismological Society of America* **84** (1) 222-228.

Sabra, K.G., Gerstoft, P., Roux, Ph., Kuperman, W.A. (2005). Extracting time-domain Green's function estimates from ambient seismic noise. *Geophysical Research Letters* **32** (3).

Scherbaum, F., (2007). "Of poles and zeros: Fundamentals of digital seismometry". 3rd rev edn, Springer, Berlin and Heidelberg.

Schweitzer, J., J. Fyen, J., M. Roth, M. (2014). *The Modernized Large-Aperture Broadband Array NOA*, NORSAR Scientific Report, Kjeller, Norway.

Schweitzer, J., Fyen, J., Mykkeltveit, S., Kværna, T. (2009). "Seismic arrays". *New Manual of Seismological Observatory Practice (NMSOP)* (P. Bormann, Ed.) Potsdam: Deutsches GeoForschungsZentrum GFZ, pp. 1-52.

Shapiro, N.M., Campillo, M., Stehly, L., Ritzwoller, M.H. (2005). High-resolution surface-wave tomography from ambient seismic noise. *Science* **307** (5715) 1615-1618.

Slad, G.W., Merchant, B.J. (2018). *Next Generation Qualification: Quanterra Q330HR Digitizer Evaluation*. SAND2018-9105 667165. Sandia National Lab. (SNL-NM), Albuquerque, New Mexico.

Slad, G.W., Merchant, B.J. (2020). *Kinemetrics Q330M+ Digitizer Evaluation*. SAND-2020-3030 684849. Sandia National Lab. (SNL-NM), Albuquerque, New Mexico.

Slad, G.W. (2020). *Evaluation the Geotech GS-13BH Borehole Seismic Sensor*, SAND2020-9776 690918. Sandia National Lab. (SNL-NM), Albuquerque, New Mexico.

Sleeman, R., van Wettum, A., Trampert, J. (2006). Three-channel correlation analysis: A new technique to measure instrumental noise of digitizers and seismic sensors. *Bulletin of the Seismological Society of America* **96** (1) 258-271.

Sleeman, R., Melichar, P. (2012). A PDF representation of the STS-2 self-noise obtained from one year of data recorded in the Conrad Observatory, Austria. *Bulletin of the Seismological Society of America* **102** (2) 587-597.

Sorrells, G.G. (1971). A preliminary investigation into the relationship between long-period seismic noise and local fluctuations in the atmospheric pressure field. *Geophysical Journal International* **26** (1–4) 71-82.

Townsend, T.O., Kromer, R.P. (2004). Ground-based Monitoring R&E Technology Report, Evaluation of the Geotech GS21A Seismometer for AFTAC EL090 Application, 24 February 2004.

Tsai, V.C. (2010). The relationship between noise correlation and the Green's function in the presence of degeneracy and the absence of equipartition. *Geophysical Journal International* **182** (3) 1509-1514.

Villasenor, A., Yang, Y., Ritzwoller, M.H., Gallart, J. (2007). Ambient noise surface wave tomography of the Iberian Peninsula: Implications for shallow seismic structure, *Geophysical Research Letters* **34** (11).

Wapenaar, K., Draganov, D., Snieder, R., Campman, X., Verdel, A. (2010). Tutorial on seismic interferometry: Part 1 — Basic principles and applications. *Geophysics* **75** (5) 75A195-75A209.

Wathelet, M., et al. (2020). Geopsy: A user-friendly open-source tool set for ambient vibration processing. *Seismological Research Letters* **91** (3) 1878–1889.

Wathelet, M. (2008). An improved neighborhood algorithm: Parameter conditions and dynamic scaling. *Geophysical Research Letters* **35** (9).

Ziolkowski, A. (1973). Prediction and suppression of long-period nonpropagating seismic noise. *Bulletin of the Seismological Society of America* **63** (3) 937-958.

The Comprehensive Nuclear-Test-Ban Treaty Hydroacoustic Network

M. Lawrence
Sydney Institute of Marine Science, Australia

G. Haralabus, M. Zampolli, D. Metz
Comprehensive Nuclear-Test-Ban Treaty Organization, Vienna, Austria

Abstract

An overview is provided of the hydroacoustic component of the International Monitoring System of the Comprehensive Nuclear-Test-Ban Treaty Organization. This overview addresses the history of Treaty negotiations leading to the rationale for and overarching design of the hydroacoustic network of stations. Hydroacoustic propagation is so efficient that the great majority of the ocean can be monitored with just 11 stations, providing a unique global observatory. There are two types of hydroacoustic station used in this network: hydrophone stations and T phase stations. The basis of the design and operation of each type is described together with their configuration and deployment location. Also addressed is a history of substantial changes to each station, together with significant incidents, and ongoing work to keep these stations mission capable. Existing problems and sustainment actions are described as well. While the hydroacoustic network's primary purpose is to detect, locate, and identify underwater explosions, secondary benefits come from the civil and scientific applications of the data. Such applications addressed here include: ocean acoustic tomography and thermometry; ocean soundscape; marine mammal ecology; undersea volcanoes, earthquakes, and tsunamis; detection of marine disasters (such as the loss of a submarine) and detection of at sea explosions.

1. INTRODUCTION

The Comprehensive Nuclear-Test-Ban Treaty (CTBT) was opened for signature in 1996. It bans nuclear explosions by everyone, everywhere on the planet. As sound propagates efficiently through deep water, relatively few hydroacoustic stations are sufficient to cover the world's oceans and ensure that no nuclear explosion goes undetected. Of the 337 International Monitoring System (IMS) Treaty verification facilities worldwide — some located in the most remote places on the planet — 11 are hydroacoustic stations which 'listen' for sound waves in the oceans (Figure 1). With this relatively modest number of IMS stations, compared to 50 primary seismic, 120 auxiliary seismic, 60 infrasound and 80 radionuclide stations, plus 16 radionuclide laboratories, the hydroacoustic network can monitor the world's oceans; which cover 70% of the surface of the globe.

As of June 2017, the last of the 11 hydroacoustic stations foreseen by the Treaty, HA4 was certified. This event marked the completion of the IMS hydroacoustic network, the first IMS component to be fully installed and certified. Five of the hydroacoustic stations are T phase stations which use near-shore seismometers to pick up waterborne signals from acoustic events coupled in the crust of coastal areas. These seismometers are required to have a passband of at least 0.5 Hz to 20 Hz, and a noise floor of at least 10 decibels below the minimum earth noise at the site.

The other six hydroacoustic stations are cabled stations that utilize underwater hydrophones. Each hydrophone station consists of two triplets of hydrophones, located to the north and south of the island where the central recording facility is located (except for HA1 which has only one triplet to the west). The triplets are connected to the shore by tens of kilometres of electro-optical trunk cable laid on the seafloor. The data is transmitted from the triplet via a fibre-optic link provided by the trunk cable and received at the shore. From there it is transmitted to the International Data Centre (IDC) in Vienna in real time via a satellite link. The longest cable is at the north triplet of HA8 with a total length of more than 210 km. Each hydrophone is suspended in the
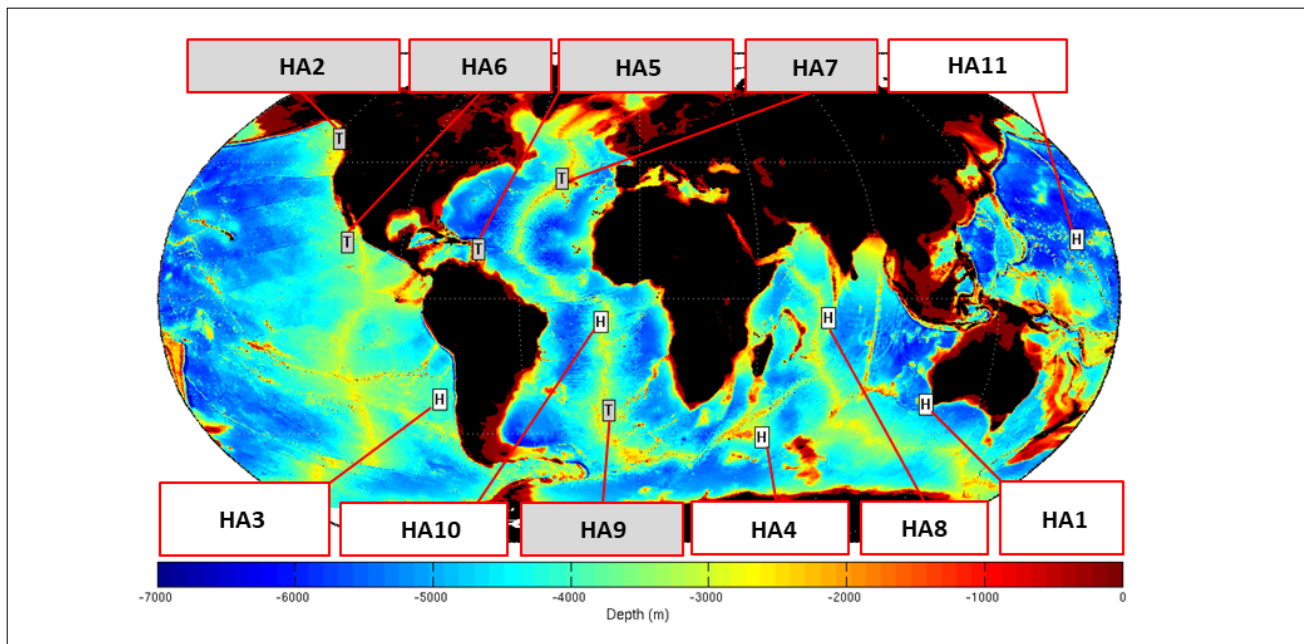
FIGURE 1.
IMS hydroacoustic stations.
The colour scale indicates ocean water depth in metres.
White boxes: IMS hydroacoustic hydrophone stations.
Grey boxes: IMS hydroacoustic T phase stations.

water column by a submerged float, which is moored to a seafloor anchor by a vertical riser cable. To enable maximum range of acoustic coverage from each site, the hydrophones are placed in the sound fixing and ranging (SOFAR) channel, a layer of minimum sound speed in the oceanic water column that effectively serves as a long range, low frequency waveguide (for an extensive treatment of underwater propagation, the interested reader is referred to Jensen et al. 2011). Each triplet forms an equilateral triangle with 2 km sides. The hydrophone sensors record signals in the 1-100 Hz frequency range. The self-noise of the system is required to be 10 decibels below the ocean noise for a typically quiet ocean to maximize the detection range of the hydroacoustic network. The hydrophone stations are by design very sensitive. Figure 2 shows acoustic transmission loss (in decibels)
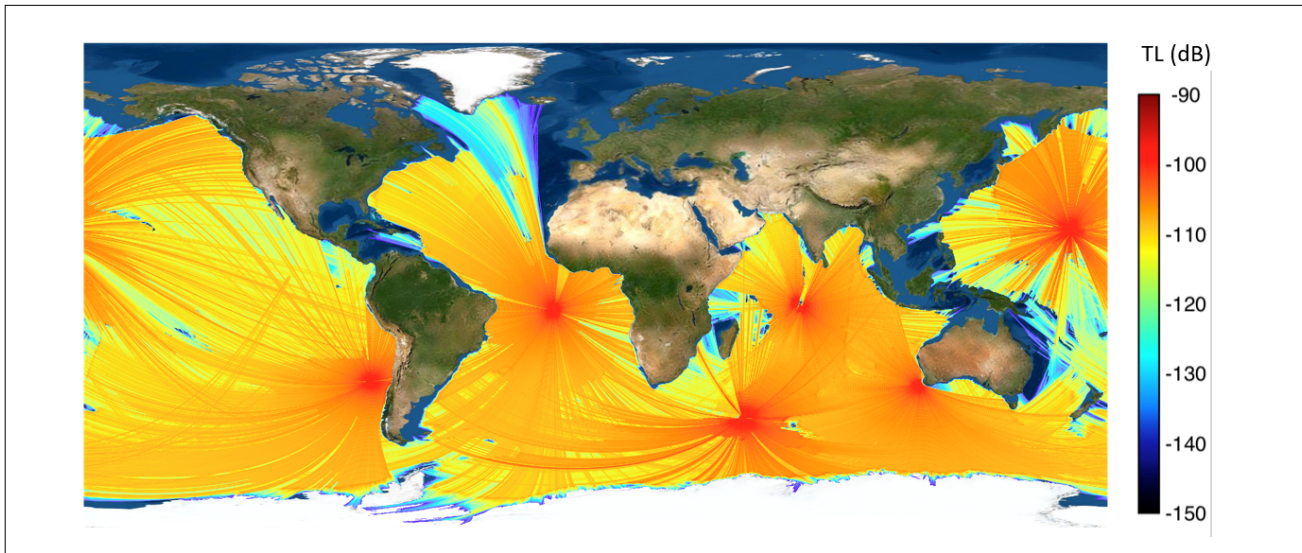
as a proxy for 'acoustic coverage' for all six IMS hydroacoustic hydrophone stations. The establishment of the hydroacoustic component of the IMS has posed ocean engineering challenges unprecedented in the history of arms control (Haralabus et al. 2017).

The names and locations of the IMS T phase stations and those of the triplets of the cabled hydrophone hydroacoustic stations are shown in Table 1.

For the H Stations (cabled hydrophone stations), the latitudes and longitudes are given for the triplet centroids, and the depths are the averages for the triplet. For the T stations, the coordinates of the seismometer location are given, and the negative depth denotes the elevation above sea level at the location of the seismometer.

Table 1. Names and Locations of IMS Hydroacoustic Stations as of 2022

Station Name	Type	Station Code	Latitude (deg. N)	Longitude (deg. E)	Sensor Depth (m)	Water Depth (m)	Certification Date
Cape Leeuwin	H	H1W	-34.892	114.141	1077	1558	10 Dec 2001
Haida Gwaii	T	H2S1	53.202	-132.477	-82	-	20 Dec 2006 (Revalidated in Q4 2022)
		H2S2	53.202	-132.477	-82	-	
Juan Fernández Islands	H	H3N	-33.449	-78.938	824	1866	14 Nov 2003 (Revalidated 23 Dec 2015)
		H3S	-33.823	-78.846	830	2071	
Crozet Islands	H	H4N	-46.180	51.590	555	1310	19 Jun 2017
		H4S	-46.885	51.794	551	1309	
Guadeloupe	T	H5N	16.316	-61.057	-268	-	30 Jan 2002
		H5S	14.425	-60.837	-6	-	
Socorro Island	T	H6E	18.781	-110.925	-316	-	22 Dec 2002
		H6N	18.862	-110.986	-16	-	
		H6S	18.735	-110.958	-35	-	
Flores	T	H7N	39.691	-31.120	-479	-	21 Nov 2005 (Revalidated in Q1 2022)
		H7S	39.379	-31.206	-478	-	
Diego Garcia	H	H8N	-6.338	71.002	1224	2342	18 Dec 2000
		H8S	-7.639	72.484	1376	1861	
Tristan da Cunha	T	H9N	-37.068	-12.315	0	-	22 Dec 2004
		H9W	-38.097	-12.335	0	-	
Ascension Island	H	H10N	-7.838	-14.490	842	2005	15 Dec 2004
		H10S	-8.951	-14.652	855	1733	
Wake Island	H	H11N	19.721	166.899	733	1426	08 Jun 2007
		H11S	18.498	166.698	739	1174	

FIGURE 2.

Acoustic transmission loss in decibels for the six IMS hydroacoustic hydrophone stations as a proxy for 'acoustic coverage'. Three-dimensional parabolic equation propagation modelling computations courtesy of K.D. Heaney et al. at Applied Ocean Sciences, Inc. (USA).

2. TREATY NEGOTIATIONS AND THE HYDROACOUSTIC NETWORK

Less than a decade after the first nuclear weapon test in 1945, discussions began on banning nuclear test explosions. The Partial Test Ban Treaty of 1963 banned nuclear weapon tests in all environments except underground. This treaty was partial in terms of environment and in that only a limited number of countries signed it.

This was followed by a lengthy process of developing a comprehensive test ban. From the start, there was recognition of the need for a technical monitoring regime. Initial discussions on monitoring, in the 1960s and early 1970s, were wide ranging and included hydroacoustic monitoring stations. Seismic monitoring for detection and identification of underground explosions was considered the most problematic so there was a focus on developing this technology. The Group of Scientific Experts was established in 1976 to progress and validate seismic technology. By the mid-1990s, seismic technology had improved significantly. Additionally, there was political will to move ahead with a comprehensive test ban treaty.

Preliminary negotiations during 1993 concluded that CTBT negotiations should formally begin within the Conference on Disarmament in Geneva, Switzerland. Four monitoring technologies were flagged for greater consideration: Three were based on wave propagation (seismic, hydroacoustic, infrasound) and the fourth was radionuclide technology. In 1994, formal CTBT negotiations commenced. These negotiations occurred during two-week periods, separated by a few months. General agreement was quickly established that the above four technologies should be used to perform real time monitoring. After two years of dedicated effort, the CTBT treaty text was finalized, leading to it being opened for signature in 1996. While the real time monitoring regime is only part of the CTBT, it is the part relevant to this paper.

Questions during discussions arose as to why hydroacoustic monitoring should be used for the CTBT. There are several reasons. Historically, nuclear weapon testing had taken place in the ocean. Further a comprehensive monitoring regime needs monitoring of all environments. Each of the chosen technologies has some capability in each terrestrial environment. Synergy of the technologies ensures that there is increased difficulty for a test to go unnoticed. For example,

hydroacoustic technology, as well as covering the oceans, can detect explosions underground and in the atmosphere (provided the distance to the ocean is not great) and hydroacoustic signals are of the highest quality. Hydrophone detectors are extremely sensitive and provide a very clean signal, that is with high signal to noise ratio. Therefore, they are capable in terms of discriminating between signals from explosions and those from other sources. Another advantage is that they can provide excellent directional information.

During the initial plenary session of CTBT negotiations interested States presented their individual visions of a suitable hydroacoustic network. Working teams were then established to provide a technical model for consideration, in which all States would then agree on concepts and draft treaty text. Each of these working teams consisted of experts from many countries.

An early decision from this process was that the purpose of the hydroacoustic network was for discrimination of events and for use in location of events. Discrimination recognizes explosions from various other events that cause signals.

Initially, two alternative types of hydroacoustic station were considered. One type used fixed hydrophones (floated up from the seafloor) cabled back to shore, which have the prime advantage that they send excellent real time waveform data. The prime disadvantage is that they are very expensive to install. The alternative discussed was to use moored buoys, with hydrophones in mid-water depth between an anchor and a floating buoy. The prime advantage of this type of station is that they would be cheaper to install. However, a crucial disadvantage is that waveform data would *not* be sent, but only characteristics of events, following on-board processing. Another problem with these stations is the limited lifetime of deep-water moorings. Therefore, there would be a requirement to periodically (perhaps annually) replace them. The recommendation for the hydroacoustic network was that stations should be based on hydrophones cabled back to shore to send real time data.

The hydroacoustic network of stations first proposed by the pertinent working team involved 20 cabled stations. However, this was rejected by session participants due to the anticipated high cost. To reduce cost the hydroacoustic station network was reduced from 20 to 11 stations, all using cabled hydrophones. There was less redundancy in this sparser network of stations and some regions were not covered as well as previously. Also, at this stage hydroacoustic monitoring of the Arctic Ocean was discarded. The rationale included that seismic station coverage of the relatively small Arctic Ocean was sufficient. Also, it was anticipated that an Arctic hydrophone station would have been particularly difficult (and expensive) to build, due to ice cover.

The 11-station network was agreed by session participants but with the requirement that the cost had to be reduced further. The next proposal, which was accepted, was for a hydroacoustic network comprised of six cabled hydrophone stations, and five seismic stations using T phase signals. T phase signals utilize the ocean for most of the propagation path, but inherently have conversion of the hydroacoustic signal to seismic energy and subsequent transmission seismically to the seismometer. These T phase stations have the advantage that they are much cheaper, but the disadvantage is that the signals are quite distorted and noisy compared to the signals on the hydrophone stations. At this stage of the negotiations, there were several extra seismic stations added to the auxiliary seismic network to reduce the loss of coverage in the above compromise.

This network of five T phase plus six hydrophone stations became the hydroacoustic part of the IMS of the CTBT. The basic specifications and locations of these stations were also agreed. Station locations were chosen based on modelling studies of acoustic propagation, together with considerations of practicality of installation and operation.

In order to enable early experience in receiving and processing data from hydrophone stations, two sites were chosen where there were

existing hydrophone stations that could be made available for this purpose. These stations had been constructed as missile impact locating stations by the United States. They played a very useful role in providing the IDC with hydroacoustic data in the very early years before any of the CTBT stations were built. However, these missile impact locating stations were old (near the end of their useful life) and (being designed for a different purpose) did not meet CTBT specifications.

Some basic specifications were agreed for the two types of hydroacoustic stations. Regarding sampling rate of the signal, for hydrophone stations, there is more high frequency information usefully available than for any other IMS station. The ocean also transmits these higher frequencies much better than does the earth or the atmosphere. For T phase stations (or T stations), the frequency range is chosen to be higher than for other seismic stations (although not as high as for the hydrophone stations) again, to utilize the higher frequencies in ocean signals. An explosion in the ocean generates a pulsing bubble of gas, which can be used to discriminate from other types of events.

In general, the hydrophone stations are located on islands. It was agreed that each hydrophone station could have up to two cables, avoiding a potential problem with acoustic shadowing from the island. It was also agreed that there would be three sensors per cable.

Following the establishment of the Comprehensive Nuclear-Test-Ban Treaty Organization (CTBTO) the basic specifications of the stations had to become more detailed. Working Group B, a subsidiary body of the Preparatory Commission of the CTBTO, had responsibility for this effort and several hydroacoustic workshops played a role in developing technical advice for it to consider. (Workshops were held in Kiel (FWG), Tahiti (DASE), San Diego (Scripps) etc. to gather technical advice to further this work. Some agreed outcomes from this process were that there would be three horizontally separated hydrophones; achieving directionality from only one hydrophone station and suitable rates for sampling the signals were finalized at 250 samples/s for hydrophone stations and 100 samples/s for T stations.

The ocean provides signals that have excellent signal to noise ratio as a result of a combination of two effects. First, as illustrated in Figure 3, due to the profile of sound speed with depth, refraction limits interactions with either the sea surface or the sea floor. The sound speed minimum, occurring at depths of order 1 km, continually refracts acoustic energy back to travel near the sound speed minimum. That is, the acoustic energy is trapped in a waveguide.
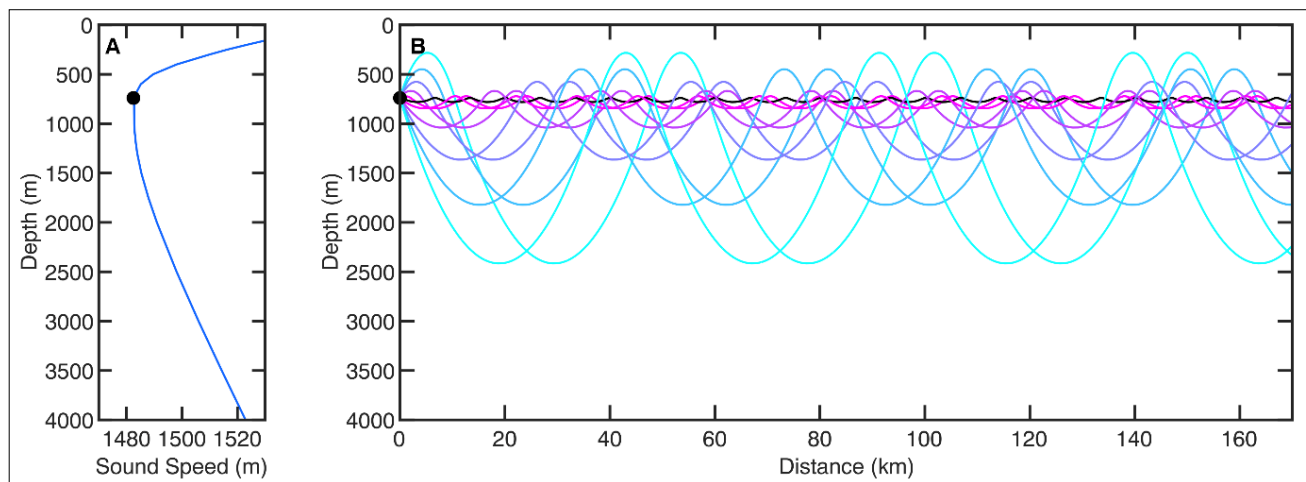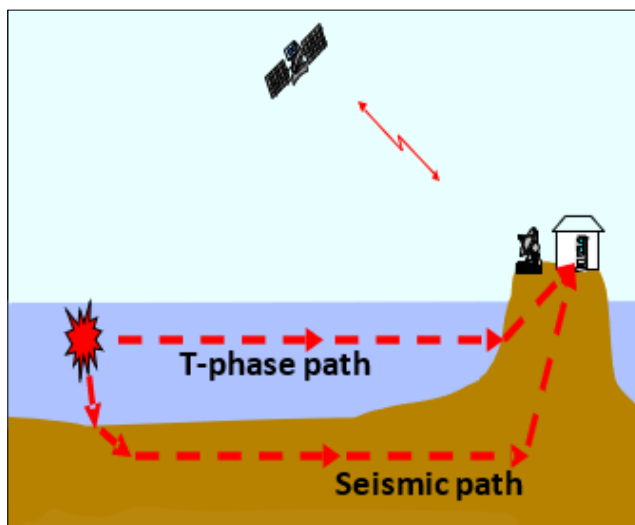

FIGURE 3.
Long range hydroacoustic propagation and the SOFAR channel.
The graph in (a) shows a typical deep-water profile of compressional sound speed at mid latitude. In (b), results from ray tracing, using the profile in (a), illustrate range independent propagation in a deep-water waveguide. The point source (black circle) is located at 740 m depth, i.e. within a few meters of the sound speed minimum that is typically referred to as the 'axis' of the SOFAR channel.
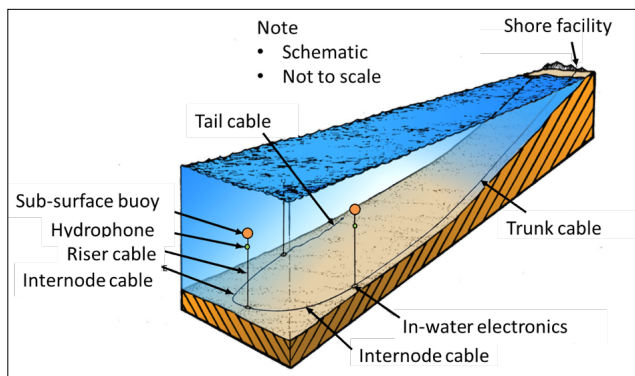
FIGURE 4.
Conceptual diagram of a hydrophone station (Image courtesy of L3Harris MariPro, USA).

FIGURE 5.
Conceptual diagram of a T phase station.

The second effect that makes propagation so effective is that absorption of acoustic energy is extremely low (at the frequencies of interest).

Acoustic propagation is so good that explosions as small as a few kilograms can be clearly recorded across an ocean. It is this excellent acoustic propagation throughout the ocean that allows the relatively small number of stations to monitor the oceans of the world.

As illustrated in Figure 4, a CTBT hydrophone station has three sensing elements, i.e. hydrophones, each located at a depth near the sound speed minimum. The hydrophones are supported by flotation buoys, which remain subsurface. Cables take the signal down from the hydrophones to the trunk cable lying on the sea floor, and from there back to the shore facility. Satellites then take the signal back to the IDC. Typically, hydrophones are at approximately 1 km depth (or as close as possible to the minimum sound speed) and trunk cables are tens to hundreds of kilometres long, depending on the location of the station. Hydrophones are placed with a horizontal separation of approximately 2 km.

The T phase station (or T station) is located on land, near the ocean, with a steep decline from the land to deep water. Figure 5 shows two paths from an underwater explosion. The T phase path travels mostly as hydroacoustic energy through the ocean, and only has a short path through the ground. The seismic path shown is fully through the ground, except for a short path near the explosion through which the energy traverses the water.

In the following sections T phase stations and hydrophone stations are briefly presented in chronological order by installation date.

3. THE T PHASE COMPONENT OF THE HYDROACOUSTIC NETWORK

Contrary to hydrophone stations that employ water column hydrophones for detecting underwater sound waves, T phase stations use near-shore seismometers to detect waterborne acoustic energy when it hits land. Upon impact with a steep island slope, underwater acoustic (hydroacoustic) waves are coupled into seismic waves. These converted seismic waves (T phases) travel upslope into the earth's crust and are detected by the seismometers at T phase stations. The T phase stations are mostly three-component stations (measuring ground motion in the horizontal plane and in the vertical) with one or more seismometers. A typical layout is shown
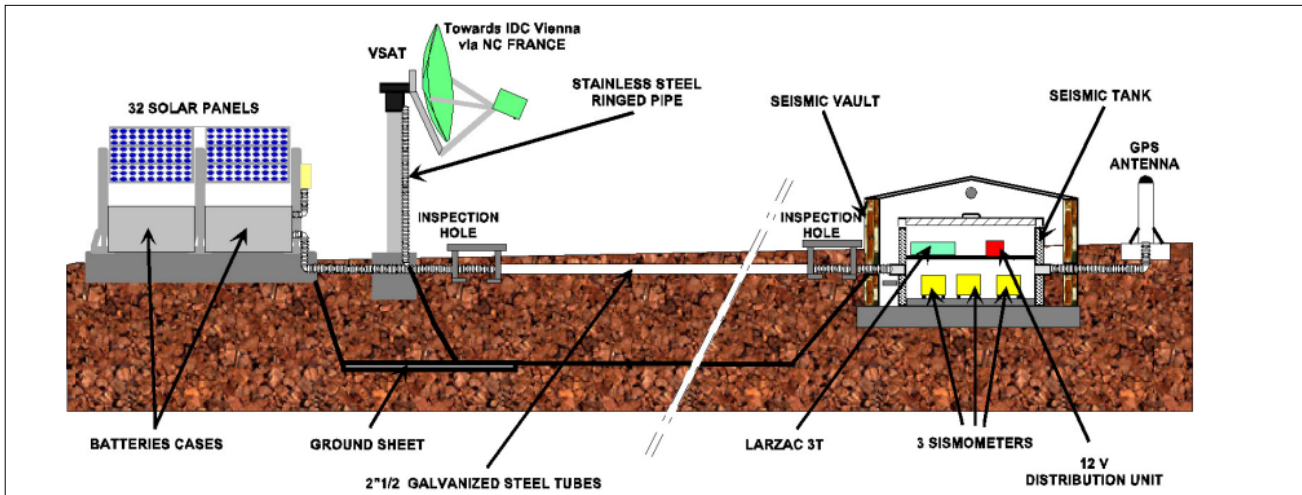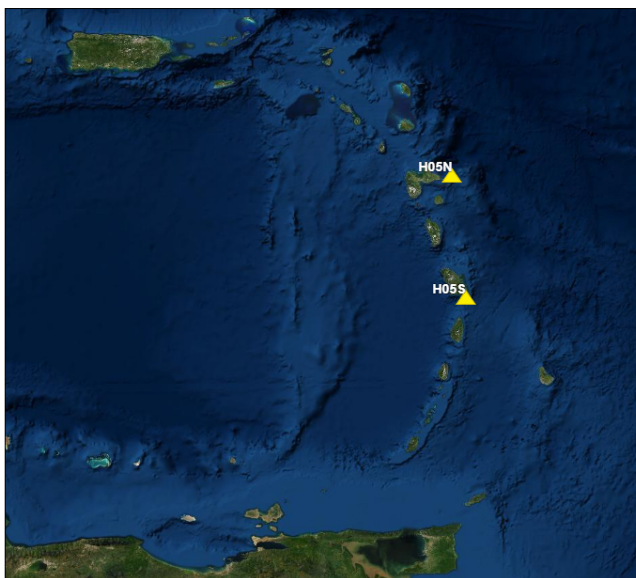
FIGURE 6.
A typical layout of a T phase hydroacoustic station.

in Figure 6 although variations are possible from one station to another. Like hydrophone stations, T phase stations transmit continuous data in real time via satellite to the IDC.

3.1. HA5

In 2002, IMS station HA5 became the first T phase station of the hydroacoustic network to enter active service. The two three-component seismometers provide seismoacoustic coverage in the Atlantic Ocean and the eastern Caribbean Sea (see Figure 7).

FIGURE 7.
HA5 seismometers.

3.2. HA6

Construction of HA6 began in 2004 and concluded with the successful certification of the station in 2005. Station HA6 covers the South-East Asia, Pacific and the Far East region and comprises three T phase receiver sites, the northern one of which is in a remote part of the island that is accessible only by boat (Figure 8).
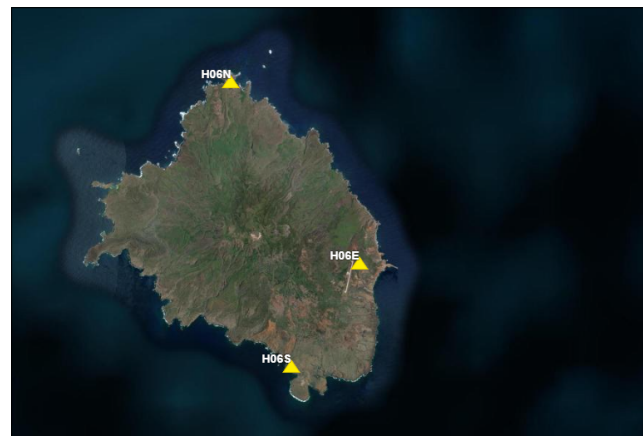
FIGURE 8.
HA6 seismometers.

3.3. HA9

T phase station HA9 was certified in December 2004. It consists of two seismometers (Figure 9). Data gathered by the station shortly after its installation in the first quarter of 2004 played an important role in the analysis of seismic activity associated with a nearby submarine volcanic
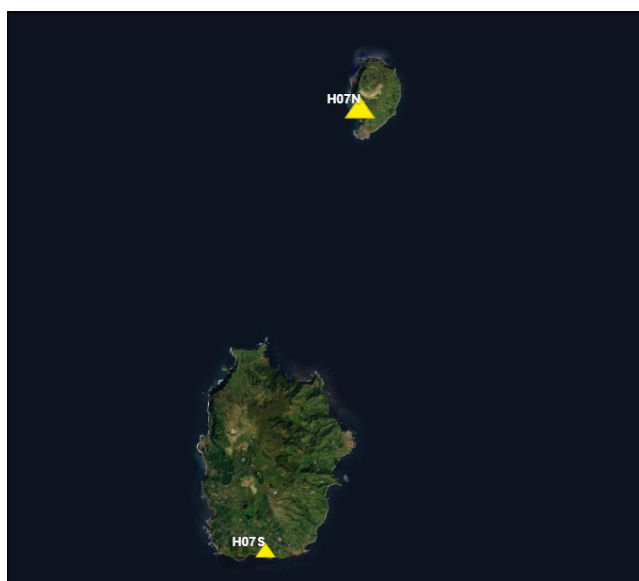
eruption (O'Mongain et al. 2007). Contributing to the development of Tristan da Cunha, generators installed as part of the IMS infrastructure help to provide around-the-clock electricity to the few homes of Edinburgh-of-the-Seven-Seas, the only settlement on the island.

FIGURE 9.
HA9 seismometers.

3.4.   HA7

IMS station HA7 was certified in 2005 and comprises a pair of three-component seismometers located in the north Atlantic Ocean. As is the case for all T phase stations, instruments are positioned in proximity of the coastline to maximize sensitivity for seismoacoustic energy converted at the ocean–island interface; T phase stations are typically situated at a certain distance from roads, airports, and larger settlements to keep noise contamination at a minimum. Figure 10 shows the layout of the two seismometers. The southern site of station HA7 is in direct proximity of a shoreline.

3.5.   HA2

T phase station HA2 was certified in late 2006 and entered IDC operations in early 2007. This installation marked the completion of the T phase component of the hydroacoustic network. HA2 (Figure 11) provides seismoacoustic coverage in the northern Pacific Ocean. The original installation comprised two independent/ redundant sites (H2N) and (H2S). H2N at ~1000 m above sea level has been challenging to sustain for several years without an on-site operator. Its data availability has been very low, probably due to natural electrical surges and lightning strikes. As access to the station elements is via helicopter only, the sustainment of this component has been associated with high costs and delayed interventions. Because of this, in 2018 it was decided to construct a redundant station at the same location as H2S, changing the nomenclature of the original south station to H2S1, while naming the second station constructed in its vicinity H2S2.

FIGURE 10.
HA7 seismometers (07N) and (H07S).
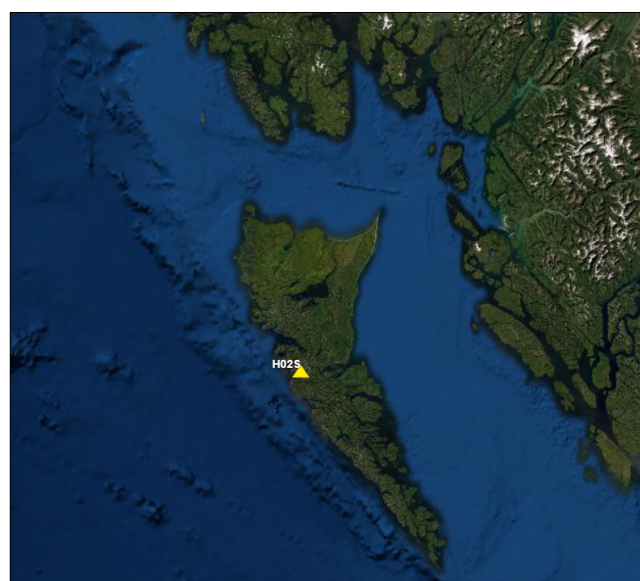
FIGURE 11.
Location of HA2 seismometers.

4. THE HYDROPHONE HYDROACOUSTIC STATIONS OF THE INTERNATIONAL MONITORING SYSTEM NETWORK

Hydrophone hydroacoustic stations detect acoustic signals using underwater microphones. They convert in-water pressure fluctuations from sound waves into electric signals with measurable amplitude and frequency content. The hydrophones are deployed in two triplet formations on opposite sides of an island to avoid acoustic shadowing by the island in either direction. HA1 is the only IMS hydrophone station with one triplet covering part of the Indian Ocean. This means that the six hydrophone stations include eleven triplets that are connected to shore with underwater cables that may be a couple of hundreds of kilometres long. Every triplet is suspended in the water column at SOFAR channel depth for each deployment location. Figure 12 shows a typical deployment of a hydrophone node at a hydroacoustic station.

The installation of hydrophone stations is very challenging from the logistical and ocean engineering point of view. It involves manufacturing using state of the art technology and highly demanding equipment qualification to satisfy CTBTO operational requirements,
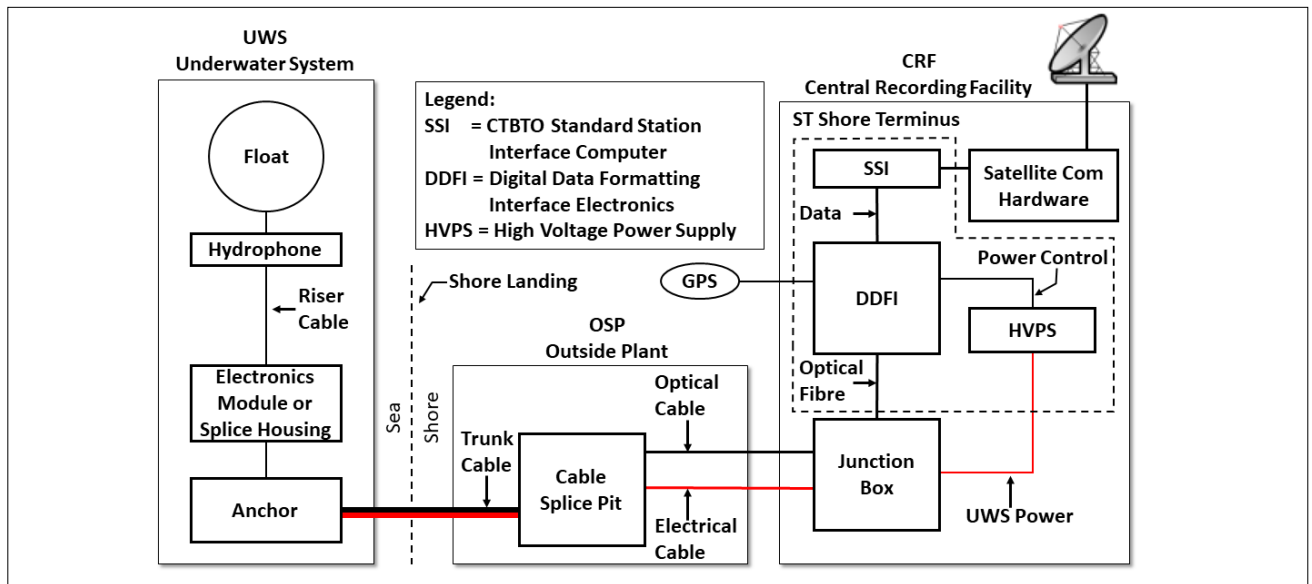
including a minimum design life of 20 years for the equipment deployed at sea, preparatory site surveys to assess suitability of the site, challenging maritime operations in remote areas under adverse weather conditions, rigorous post installation testing, certification, and finally, integration into the operations of the CTBTO.

The main components of a hydrophone station are shown in Figure 13:

- The underwater system (UWS): The UWS node design consists of a float, the hydrophone and preamplifier assembly, the electronics bottle (in node 1) or splice housing (nodes 2 and 3), an anode, and an anchor. Node 1 is the most shoreward one and is connected to the trunk cable. The electronics bottle at node 1 contains the digitizers, signal conditioning electronics and lasers. Each hydrophone channel has a separate digitizer. The three digital outputs are multiplexed into a single signal stream. The three nodes are lowered to the seafloor as a single unit. The float is then released by command received from the ship (a corrosive link is used as a backup), allowing the hydrophone sensor and riser cable to float upwards in the water column until the hydrophones reach their design depth at the SOFAR axis. The riser cables are partially covered by small flags made of polyurethane, which are designed to reduce the likelihood of strumming noise in high ocean currents. Cable strumming can shake the hydrophone and thereby induce high acoustic noise levels in the data at the lower frequencies. The turbulent fluctuations associated with water flowing over the hydrophone sensing element may also introduce noise into the system. To reduce this noise, the hydrophones are encased in a water-filled boot which provides distance between the sensing element and the water flow past the hydrophone assembly, which regularizes the water flow.

FIGURE 12.
Deployment of a hydroacoustic node from the aft deck of a ship. The large yellow sphere is the mid-water float. The riser cable can be seen wrapped around the circular anchor.

FIGURE 13.
Block diagram of hydroacoustic hydrophone station components.
Red lines denote UWS power connections, black lines are data links.

- The underwater cable: The underwater cable connecting the underwater electronics bottle to the beach splice pit can be up to 215 km long. The trunk cable is an electro-optical telecommunications type cable, with the data transmitted via optical fibres and electrical power provided by a copper sheath in the cable core. From the splice pit seaward, the near shore cable is armoured for protection and enclosed in split pipe iron casts near the shore for additional fortification and stability. The cable protection becomes lighter as the deployment depth increases so that the cable is not stressed beyond its design limits by its own weight.

- The shore terminus: The shore terminus in the central recording facility (CRF) includes a junction box, power (including conditioning and control) for the UWS, and the Digital Data Formatting Interface (DDFI). The junction box interfaces the optical and power (copper) cables from the UWS to the shore equipment. A high voltage power supply (HVPS), chosen not because the cables carry a high electrical load but because it provides stable power and operates in the constant current mode to supply power to the UWS. The DDFI receives the acoustic data frames from the UWS, demultiplexes the data stream, supplies the time tag, and passes the data to the CTBTO standard station interface computer. A Global Positioning System antenna and receiver provide an accurate time signal to the DDFI with which the signal is synchronized. The DDFI responds to commands to perform a calibration or reset of the UWS. The standard station interface provides authentication, formats the data and forwards them to the satellite communications equipment. It also provides remote access for CTBTO or station operators.

- Communications and data transmission: A communications hub in the CRF provides the interface between the station and the external communications links. The data supplied to the communications hub is formatted in CD1.1 and is authenticated. The primary data stream is provided to the IDC via the very small aperture terminal satellite antenna. Backup links may be provided via a second very small aperture terminal for legacy communications links or via a broadband global area network. In some cases, a second data stream may be sent to the station operator through a separate communication line.

- Station primary and backup power: The station is powered from the mains power where available. uninterruptible power supplies provide backup power in the case of loss of mains power. Additional backup power may be provided through an on-site diesel generator.

4.1. HA8

Station HA8 is operated by the US Air Force Technical Applications Center (AFTAC) at Patrick Air Force Base, Florida. The station was manufactured and installed by the United States of America, and it was certified by the PTS certification team in 2000. It comprises the north and south triplet with trunk cable lengths 215 km
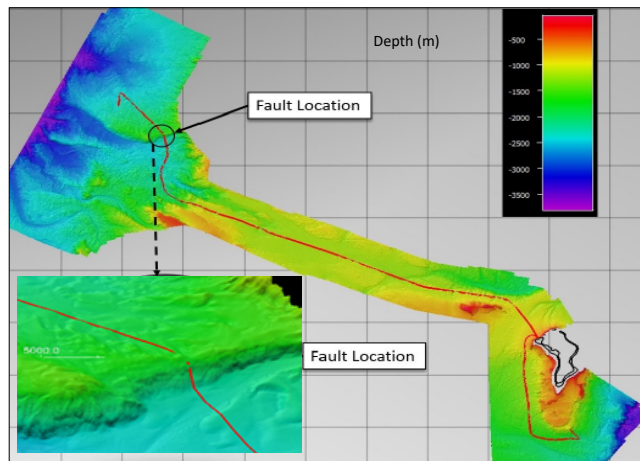
FIGURE 14.

Bathymetric map from the Naval Oceanographic Office survey, with cable routes for H8N and H8S overlaid.

Fault location at 189 km along the cable denoted by the black circle on the map.
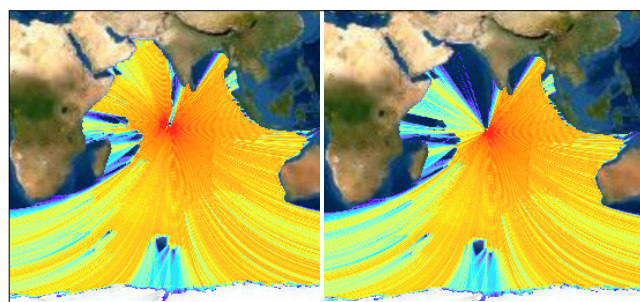
FIGURE 15.

IMS Hydroacoustic network coverage with (left plot) and without (right plot) the HA8 north triplet.

The plots represent 3-D Parabolic Equation Model Transmission Loss of IMS Hydroacoustic Station HA8. The colour scale is from -90 dB to -150 dB. (Provided by K.D. Heaney et al. Applied Ocean Sciences, USA).

and 70 km respectively. Shortly after installation, it was noticed in narrowband spectral analysis that the station has some 60 Hz interference in the data. Tests performed in 2001 showed that this noise source could be eliminated by installing a seawater ground at the splice pit on shore. Since then, all successive hydrophone hydroacoustic stations have a seawater ground.

Since March 2014, the north triplet has ceased to transmit data due to cable damage approximately 189 km from the shore. A bathymetric survey was undertaken by the Naval Oceanographic Office, USA (see Figure 14) in early 2017 and provided to the PTS as a contribution-in-kind. The data from the bathymetric survey, together with all other related information, were used in an expert evaluation study by external submarine telecommunications cable experts from France. The study, that was concluded in 2018, was financed by the United Kingdom of Great Britain and Northern Ireland to assess potential options for the re-establishment of the station. Moreover, in 2018, the PTS outsourced to the company that built the station a study regarding the status of the triplets at HA8. This study was completed in 2019. The expert evaluation study included the recommendation: "Entire new wet H8N re-establishment on initial route with minor improvements. Existing H8N triplet recovered and replaced".

The effect of this damage on the acoustic coverage in the northern Indian Ocean region is shown in Figure 15. Warm colours (red/yellow) indicate lower transmission loss, therefore higher probability of detection compared to cold colours that indicate weak or no detection capability (blue/black).

4.2. HA1

The hydrophone hydroacoustic station HA1 was installed and certified in 2001. HA1 is the only IMS hydrophone hydroacoustic station that is not located on a remote island, thus it has only one underwater cable with a single triplet of hydrophones. The triplet is positioned to provide coverage over an arc of about 240 degrees, covering large parts of both the Indian and southern oceans. The shore building is placed
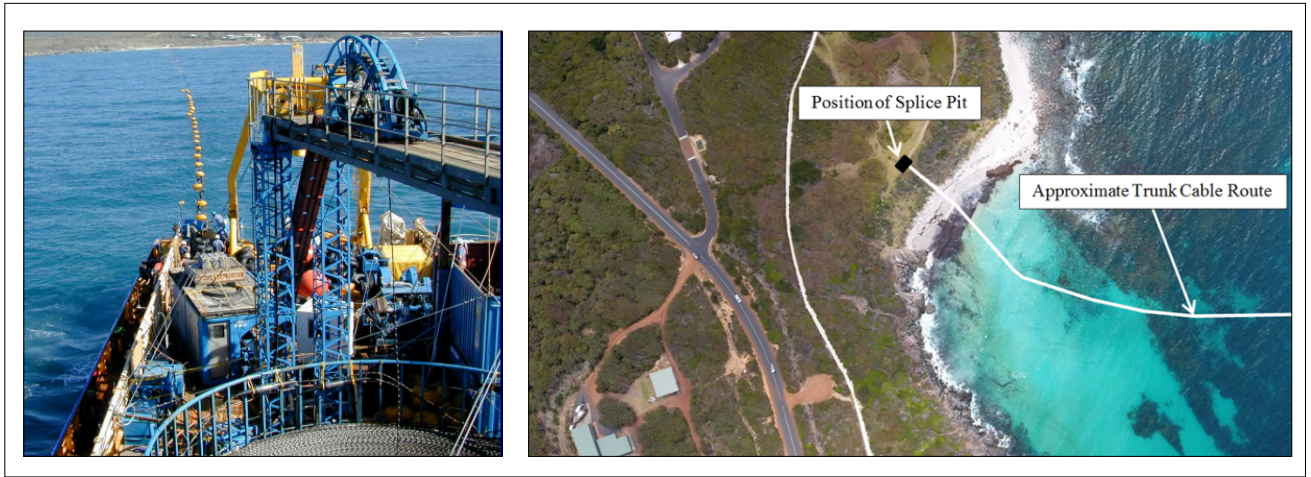
FIGURE 16.
HA1 Shore landing operations (left) and near-shore cable route (right). The CRF is located across the road, near the buildings in the left bottom corner of the image.
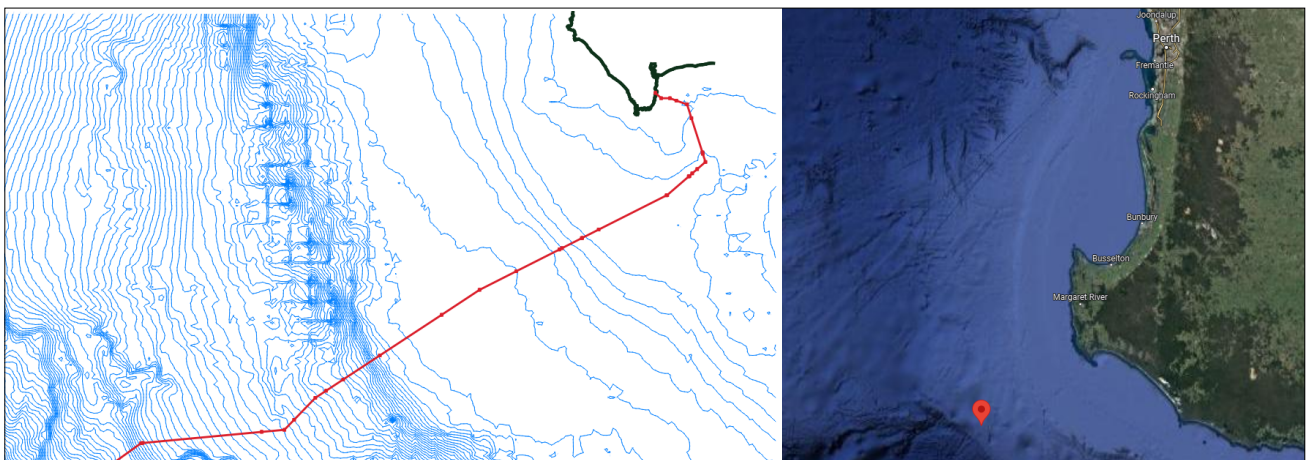
FIGURE 17.
HA1 Cable route and triplet location (left, the blue lines indicate 20 m depth contours), and triplet location relative to Western Australia (right, red pin indicates triplet centroid).

on the site of the Department of Conservation and Land Management Rangers Residence in the Leeuwin Naturaliste National Park. The underwater cable connecting the underwater electronics bottle to the beach splice pit is approximately 135 km in length (Figure 17).

4.3.   HA3

HA3 was originally installed and certified in 2003. In 2010 the station was destroyed by a tsunami which devastated Robinson Crusoe Island and claimed 16 lives. Following a major engineering and logistical undertaking that spanned four years, HA3 was re-established in 2014 and revalidated in 2015 (Figure 18). The two new hydrophone triplets were deployed not far

from the original positions. The CRF was relocated to higher ground to mitigate tsunami risks. Cable lengths for the north and south triplets are 33 km and 49 km, respectively (Figure 19).

On 1 April 2014 an 8.2 magnitude earthquake struck in northern Chile triggering a tsunami that, fortunately, did not affect Juan Fernández. The hydroacoustic signal from the earthquake was recorded by the hydrophones of HA3, as shown in Figure 20 (a). The first of the fast seismic waves travelling through the crust below the ocean and leaking acoustic energy into the water reached the hydrophone at approximately 100 seconds. Most of the acoustic energy received was contained in the sound radiated from the epicentre area into the water near the coast, which travelled as

FIGURE 18.
Initial phases of shore landing (left). Deployment of an H3N node at night (right). Both images are from the 2014 re-establishment mission.
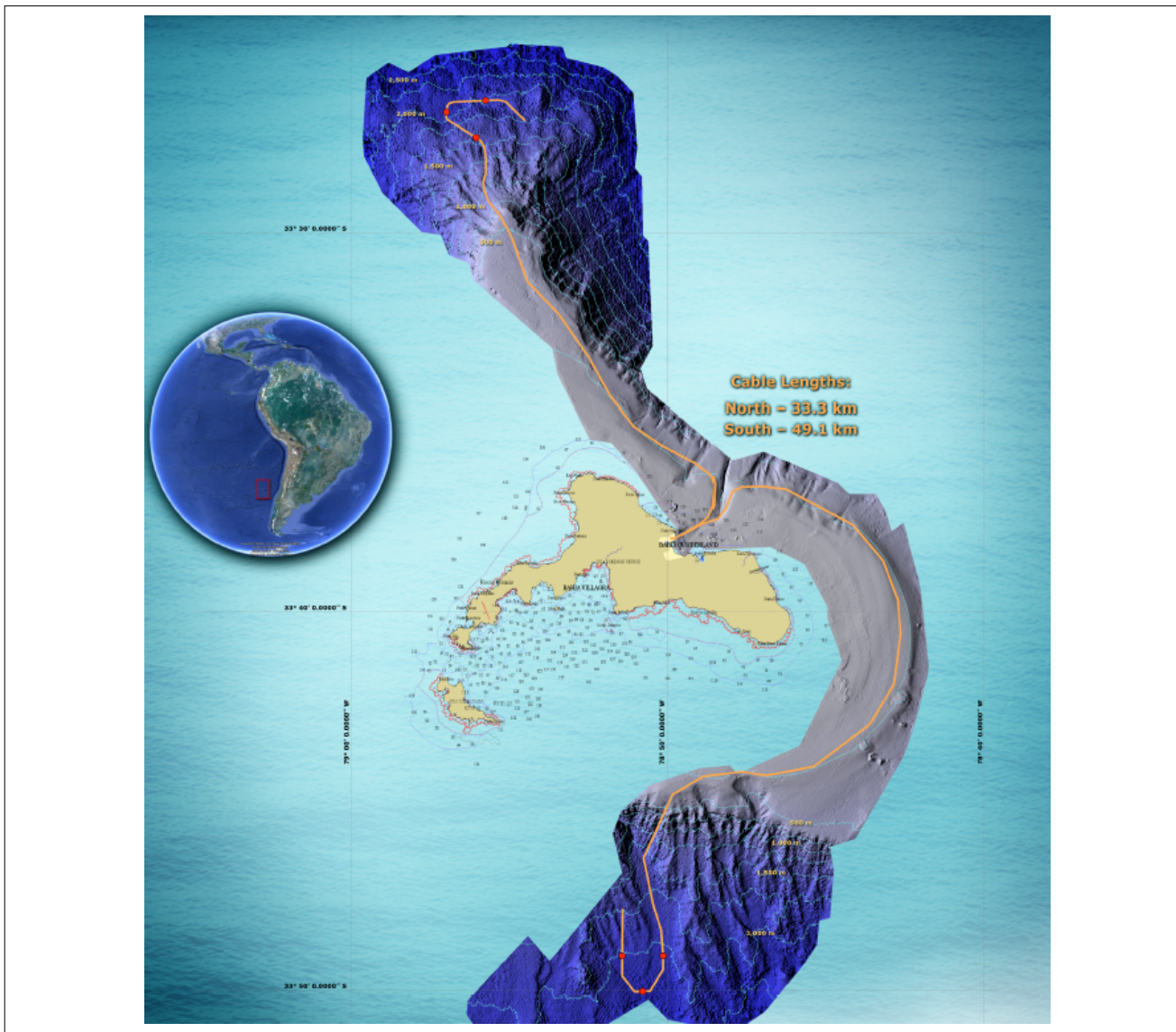
FIGURE 19.
HA3 cable routes and triplet locations, as of 2014.
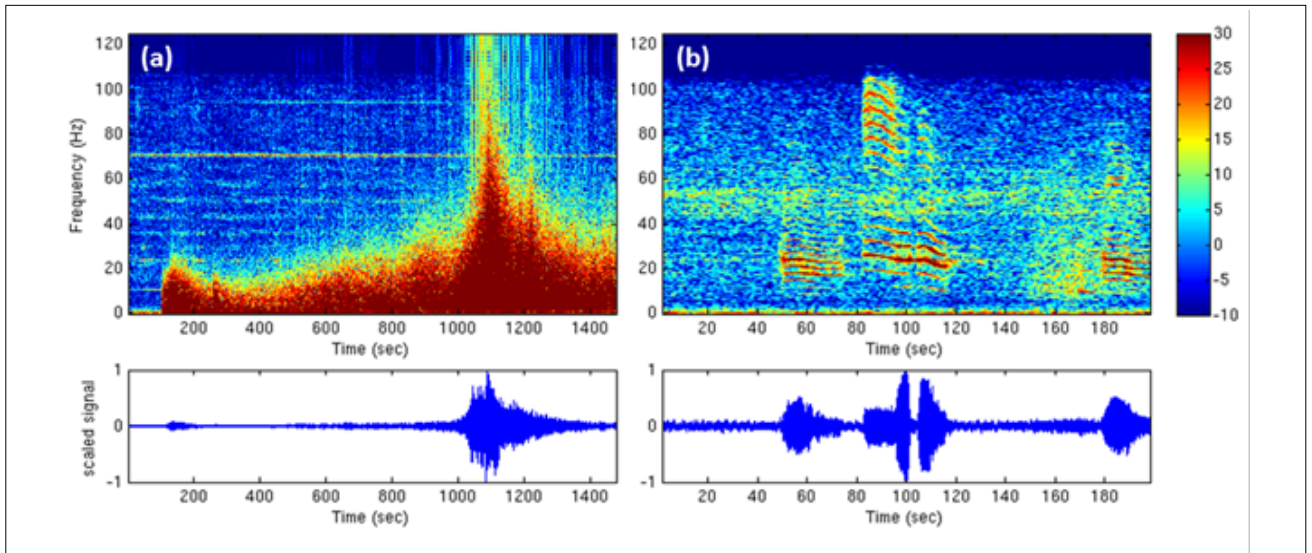
FIGURE 20.
(a) Raw data from the 1 April 2014 earthquake signal received by an HA3 hydrophone. (b) Whale vocalization recorded by HA3. The colour scale represents the spectrogram magnitude in decibels (dB) re arbitrary reference.

T wave and arrived at the hydrophone later, as shown in the same figure. Figure 20 (b) shows calls of large baleen whales in the vicinity of the stations.

The H3N3 hydrophone was taken out of IDC operations in June 2022 because of high levels of electronic noise, possibly due to riser cable or internode cable damage.

4.4. HA10

The hydrophone hydroacoustic station HA10 is situated on a mid-Atlantic ridge island, and is operated by AFTAC. In this station slant bore holes were drilled from the shore to exit points under the sea near the beach using a horizontal directional drilling technique (Figure 21). The trunk cables were ducted through these bore holes for further protection from damage by nearshore wave action and human activity. The station was certified in 2004. It has a north and a south triplet with 20 km and 127 km of trunk cable respectively (Figures 22 and 23).

Since September 2013, hydrophone H10S1 has been taken out of IDC operations because of high levels of electronic noise with intermittent crosstalk to H10S2 and H10S3. In this case, the most plausible hypothesis is that the issue is caused by damage to the H10S1 riser cable.

FIGURE 21.
HA10 cable landing (left). Node deployment (centre) and detail of cable conduits exiting the onshore splice pit (right).
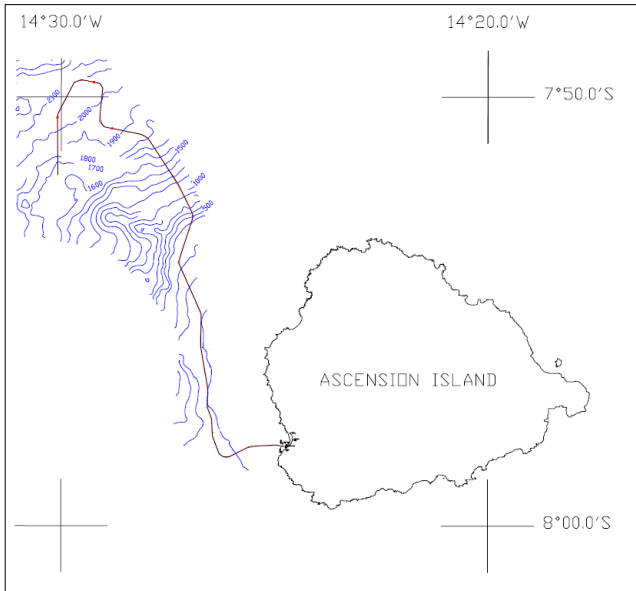
FIGURE 22.
H10N cable route, triplet location and depth contour lines (blue).
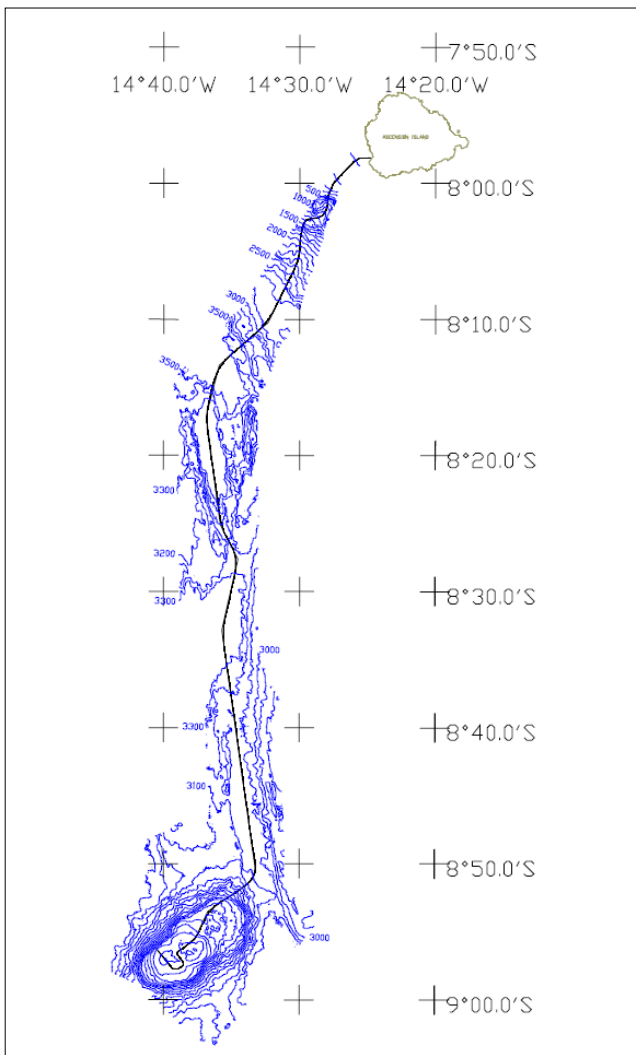
FIGURE 23.
 H10S cable route, triplet location and depth contour lines (blue).

4.5. HA11

This station is situated in the western Pacific Ocean (Figure 24). Two triplets, connected to the shore by 113 km of trunk cable to the north and 93 km to the south (Figure 25) as well as the underwater and shore hardware are essentially identical in design to the system at HA10. The HA11 trunk cable reaches depths of up to 5042 m on its way to the sea mount where the northern triplet is located, and 5185 m on its way to the

FIGURE 24.
HA11 cable landing and CRF.
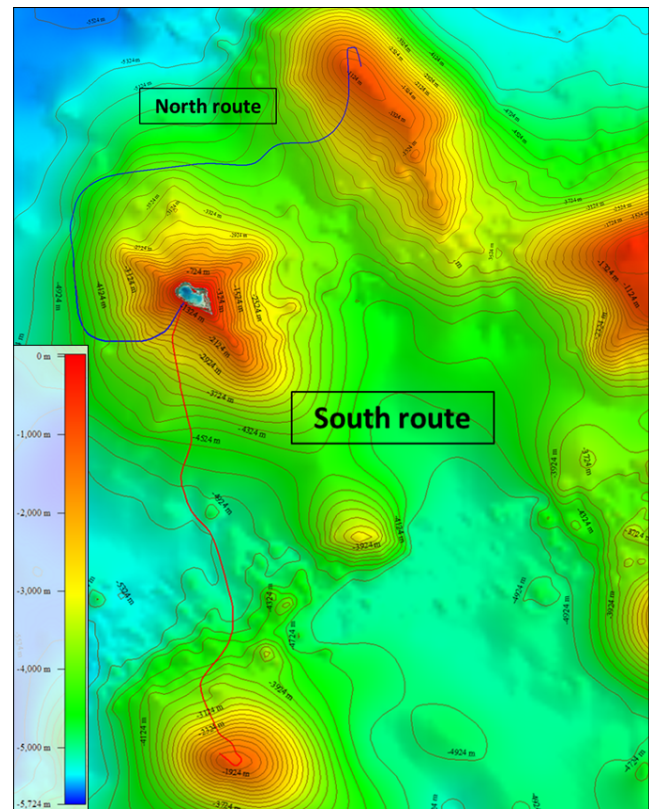
FIGURE 25.
Bathymetries and cable routes for HA11. The colour scale denotes depth on a scale from 0 m (red) to 5724 m (blue).

southern triplet sea mount. At these depths, the cable is necessarily lightweight unarmoured core cable because of the self-weight limitations for cable deployment previously discussed. These are the deepest depths reached by any IMS hydroacoustic trunk cable. The cable landing point and the shore components are located on Wilkes Island. The anchor pit is a large concrete vault that was constructed in place at the location where the cables exit the borehole tubes onto the land. The station was certified in 2007.

4.6. HA4

Station HA4 is located in the southern Indian Ocean at Île de la Possession, an island of the subantarctic Crozet Archipelago. The nearest ports are in La Réunion (France) 2800 km to the north and Durban (South Africa) 2600 km to the north-west. Antarctica is located 2200 km to the south of Île de la Possession. The Crozet Islands are administered by the Prefecture of the French Southern and Antarctic Territories (TAAF: from the French Terres Australes et Antarctiques Françaises) with headquarters in the town of Saint Pierre on the island of La Réunion. Any activity in the Crozet area must be strictly coordinated with the TAAF. The Crozet islands are very remote and are known to have one of the world's most challenging ocean climates. Lying as they do in the path of the Roaring Forties latitudes of the southern oceans, the islands are invariably windy, and the frequent depressions arriving from the west bring cold, wet and cloudy weather. On average it rains 300 days per year, and the winds exceed 100 km/hr more than 100 days of the year, seas are generally rough, and storms can lead to extreme wave heights. Deploying hydroacoustic equipment and cables in such conditions is an especially challenging undertaking.

An initial campaign was carried out from 11 February to 22 March 2000 for the installation of the underwater array and cables. Neither the initial installation effort, nor the follow-up missions including the last one conducted in December 2005, were successful.

More than 10 years later, after extensive bathymetric investigations, oceanographic and acoustic modelling studies, meticulous preparation and planning, including making use of the latest generation cable ships and modern deployment technologies, a new installation campaign took place. This time it was successful. The installation of HA4 was completed in December 2016 and the station was certified in June 2017 (Figure 26). The north trunk cable is 47 km long and the south trunk cable is 56 km long (Figure 27).

In November 2021 TAAF, in coordination with the hydroacoustics team in the IMS Engineering and Development Section, successfully completed the first nearshore cable inspection and environmental survey at HA4 using the French oceanographic research and supply vessel Marion Dufresne 2. This mission involved multiple segment remotely operated undersea vehicle surveys and diving operations.
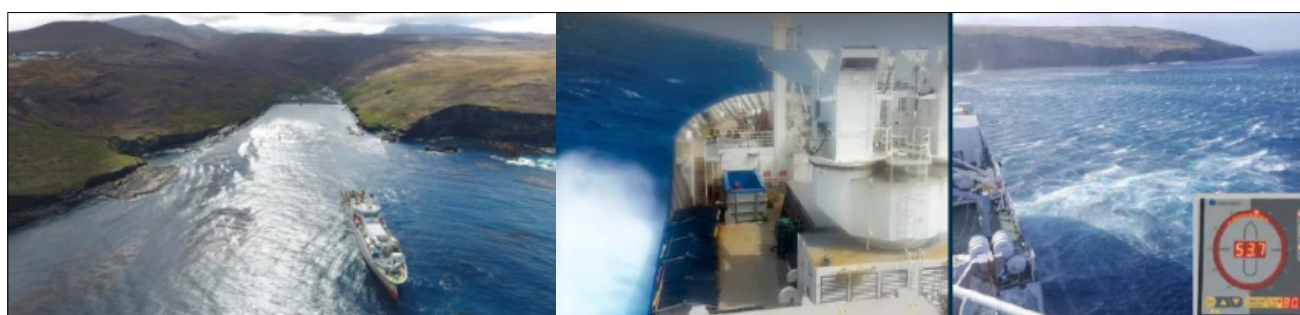
FIGURE 26.
 HA4 cable landing from cable ship C/S Decisive (left). Marion Dufresne II oceanographic and logistical supply ship en route in stormy seas (centre). Cable ship C/S Decisive holding in strong winds of 54 knots (100 km/h) with gusts of 80 knots (148 km/h).
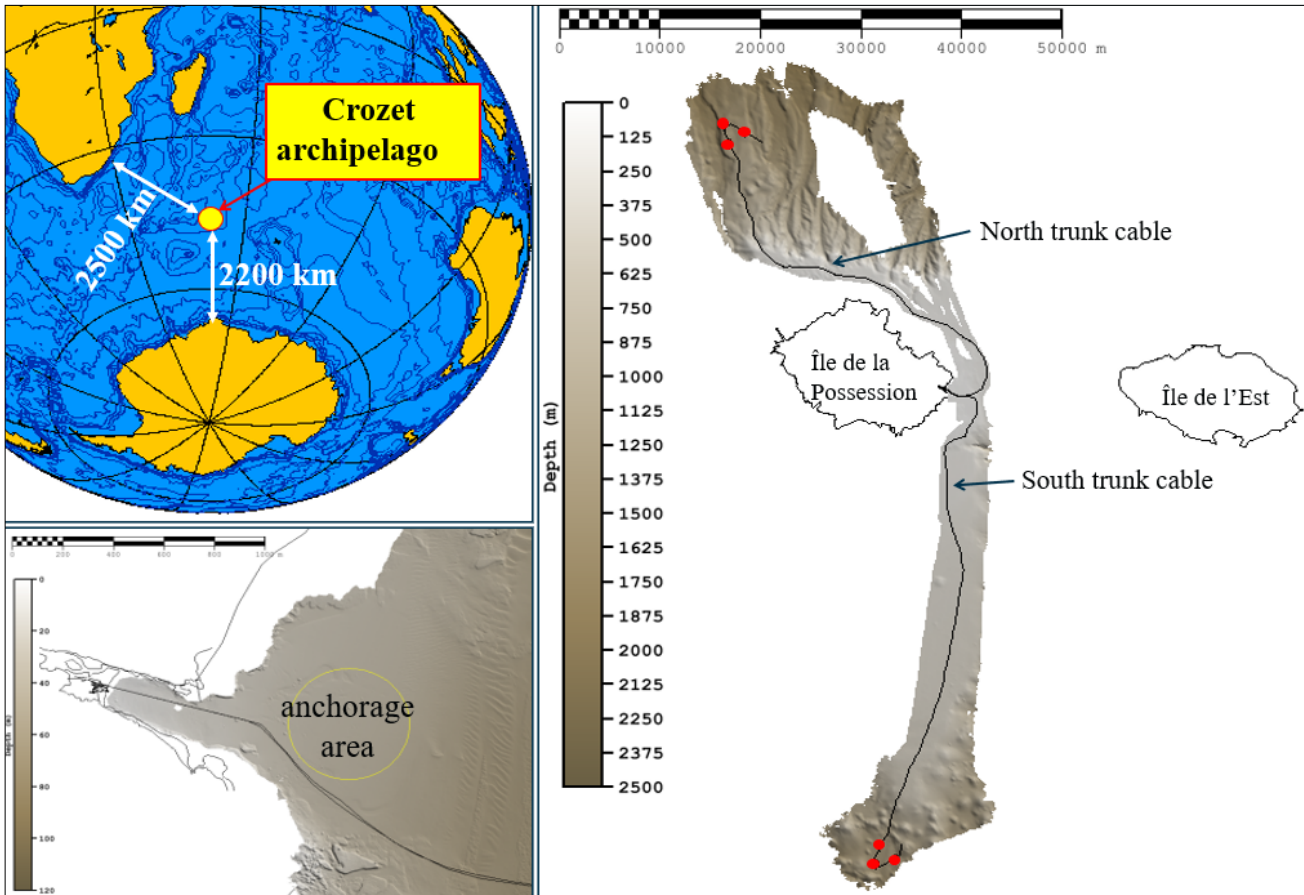
FIGURE 27.
Location of the Crozet archipelago in the southern Indian Ocean (top left).
HA4 cable routes and triplet locations (right).
Detail of the near-shore cable landing (bottom left).

5. CIVIL AND SCIENTIFIC APPLICATIONS OF THE INTERNATIONAL MONITORING SYSTEM HYDROACOUSTICS NETWORK

While the hydroacoustic network's primary purpose is to detect, locate, and identify underwater explosions, secondary benefits come from the civil and scientific applications of the data. Given the remarkable propagation efficiency of low frequency sound in the ocean, it is not surprising that the hydrophone stations detect many underwater sounds not related to nuclear explosions.

This brief and non-exhaustive overview shows how the IMS hydroacoustic network can provide an unprecedented amount of long term data for scientific research. The references cite other work which may be of interest to the reader who wishes to look more in depth into studies presented here. The section is organized in broad topics, which are not separate from each other. The subdivision is merely meant to provide a somewhat logical categorization of the topics, although it is understood that some of the literature cited could well fit into various categories. Beyond scientific use of its data, the IMS also plays an important role in emergency response and disaster risk reduction. Data from IMS hydroacoustic and seismic stations are transmitted in near real time to tsunami warning centres around the world established under the auspices of the United Nations Educational, Scientific and Cultural Organization Intergovernmental Oceanographic Commission

and contribute to tsunami emergency response plans[1]. At the time of writing of this paper CTBTO has agreements for providing real time data to tsunami warning centres in 19 countries[2].

5.1. Ocean Acoustic Tomography, Thermometry and Diffraction

Sound speed in the ocean depends primarily on temperature and hydrostatic pressure (the latter quantity being linearly dependent on depth), with salinity and acidity playing secondary roles for the frequencies and propagation scenarios such as those considered here (O'Mongain et al. 2007, Ainslie 2010). This has led to many studies investigating the relationship between hydroacoustic travel time and temperature variations of the ocean's deep layers where the SOFAR channel is usually located. The interest in such techniques is motivated by the potential of obtaining a measure of temperature variations in the deep layers of the oceans and over large areas, as opposed to near-surface measurements which are made with satellite-based observations. Earlier studies making use of precisely located and timed human-made sources led to the Acoustic Thermometry of the Oceans research programme (The ATOC Consortium 1998, Colosi et al. 1999, Dushaw et al. 2009).

The attractiveness of IMS hydrophone data in the context of thermometry and ocean acoustic tomography (i.e. the inference of properties of the propagation medium, in this case the ocean, from hydroacoustic travel path measurements) is that IMS hydroacoustic stations provide data over very long timespans in the bandwidth up to about 100 Hz covering the oceans at basin scales. Therefore, many researchers set out to identify scenarios in which sources of opportunity, such as natural events, could be used to study the relation between hydroacoustic travel times over long propagation paths and temperature variations in the ocean. These methods are referred to as passive acoustic methods because they do not rely on the intentional emission of acoustic energy into the water by anthropogenic sources.

Recently Wu et al. (2021) implemented a method using the H8S hydrophones in the central Indian ocean. Using International Seismological Centre catalogued repeating earthquakes in 2005–2016 around the Nias Island of Sumatra as precisely located and timed sources of opportunity, the authors were able to infer large scale ocean temperature changes with a high temporal resolution. Seasonal variations generally consistent with those available in oceanographic data sets such as NASA Estimating the Circulation and Climate of the Ocean consortium and Argo were detected in the IMS hydroacoustic data, along with more detailed features on shorter timescales not captured by the oceanographic data sets. More recently, Smets et al. (2022) correlated seismometer measurements from repeated volcanic activity of the Monowai seamount (southern Pacific Ocean) with IMS hydroacoustic data recorded at HA3 and HA10 to infer travel time variations, revealing consistently with other studies a linear decreasing trend in the travel time, which may be associated with increase of temperature in the deep ocean layers.

Woolfe et al. (2015) made use of noise naturally generated by the Antarctic iceshelf as sources of opportunity to obtain measurements of acoustic travel times between two hydrophone triplets at IMS stations HA10 and HA11 (south and north triplet respectively), by studying the cross-correlation between the two triplets. These measurements made it possible to infer deep ocean temperature variations locally at the hydroacoustic station's site. Evers et al. (2017) studied a similar method, forming 'end-fire beams' between hydrophones in each triplet by coherent addition with a suitable time delay, to improve the signal to noise ratio of hydroacoustic arrivals from Antarctica at HA10.

---

[1]   For more information: http://www.ctbto.org/fileadmin/user_upload/pdf/Spectrum/2012/Spectrum_18_p33.pdf

[2]   Tsunami agreements have been concluded between the CTBTO and the following countries (alphabetical order, status as of September 2022): Australia, Chile, France, Greece, Honduras, Indonesia, Italy, Japan, Madagascar, Malaysia, Myanmar, Philippines, Portugal, Thailand, the Republic of Korea, the Russian Federation, Spain, Türkiye and the United States of America.
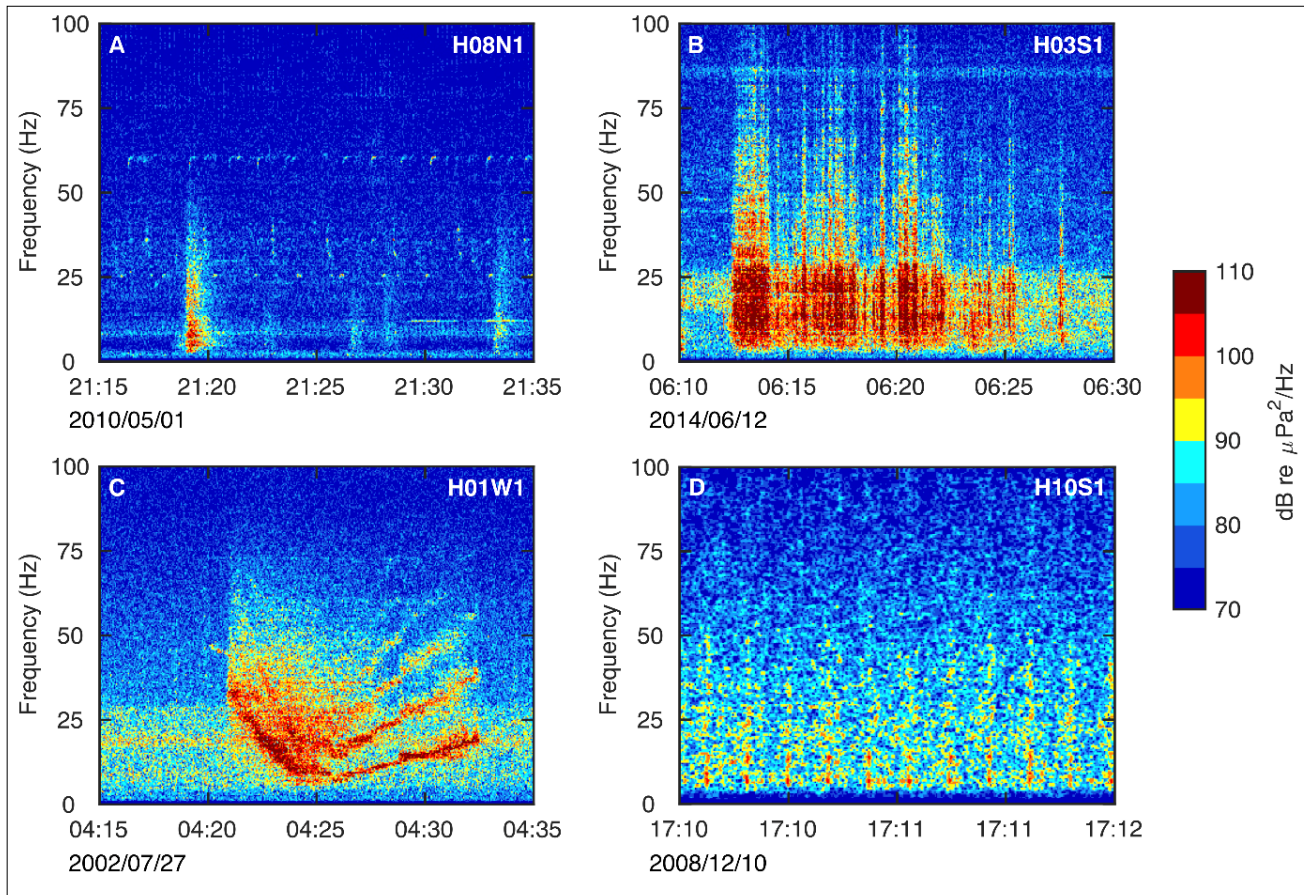
FIGURE 28.

Four examples of underwater signals received by IMS hydrophone stations. Spectrograms in (A-C) show a 20-min long excerpt from one element in the triplet; for clarity, a shorter, 2-min long excerpt is used in (D). All times are given in UTC. Note that source-receiver distances of all signals shown here are hundreds to thousands of kilometres. (A) T phase associated with seismic activity along the Central Indian Ridge. In addition, whale calls feature prominently between 25 Hz and 40 Hz, and at around 60 Hz. (B) Submarine volcanic activity at Monowai, Kermadec Arc. Arrivals create a quasi-continuous wave train up to 25 Hz, with occasional bursts up to 100 Hz. (C) Ice-generated tremor from an iceberg in the Indian Ocean, as described by Chapp et al. (2005). Note the presence of distinct overtones and 'gliding' of the fundamental between 8 Hz and 20 Hz. (D) Seismic surveying in the Equatorial Atlantic Ocean. Air gun shots are fired at regular, seconds-long intervals and populate the entire frequency range of the hydrophone.

Locations and times of anthropogenic hydroacoustic sources, such as conventional explosions or geophysical air-gun surveys, can sometimes be known precisely. Such data sets offer opportunities to evaluate the detection capabilities and accuracy of the IMS hydroacoustic stations and can be valuable for testing the IDC processing chain for hydroacoustic data and for studying potential algorithm improvements (Prior et al. 2011, Brouwer et al. 2019).

The IMS hydroacoustic data may also reveal signs of three-dimensional propagation of sound underwater, notably lateral diffraction from bathymetric features, land masses and currents/ eddies (Heaney et al. 2017, Heaney and Campbell 2016, de Groot-Hedlin et al. 2009). Lateral diffraction, reflection and refraction effects are becoming also increasingly relevant to IDC data processing, as events originating at locations assumed to be blocked under two-dimensional sound propagation assumption (as is the case for the current hydroacoustic blockage maps and travel timetables in IDC) tend to increase the workload of analysts.

5.2.   Ocean Soundscape

IMS hydroacoustic data plays a fundamental role in the study of the global ocean soundscape

thanks to continuous data acquisition for periods covering two decades, recorded at hydrophones placed permanently in some of the world's most remote ocean locations. Prior, Brown and Haralabus (2011) conducted an early investigation into the description of the main seasonal contributors to the ocean soundscape at hydrophone station HA1, identified features of microseisms, ice breaking and marine mammal noise. The characterization of the soundscape over long periods of time at different IMS hydrophone station locations continued to be studied by several groups. In some cases, a decrease of ocean noise in the 100 Hz frequency band were indicated, the reasons for which are a topic of current investigations (Sabra et al. 2013, Miksis-Olds and Nichols 2016, Harris et al. 2019). The seasonal trends in Antarctic ice-related noise recorded at HA1, HA3 and HA10 and a non-IMS autonomous mooring in the Pacific Ocean were investigated by Matsumoto et al. (2014), with comparison to remote sensing measurements of ice volume. This work showed a correlation between sound levels received at the IMS hydroacoustic hydrophone stations in the frequency bands below 40 Hz and the seasonal drift and breakup of icebergs from Antarctica, highlighting how such climate-induced distant ambient noise levels reach the hydrophones.

5.3. Marine Mammal Ecology

The frequency band up to approximately 100 Hz in which the IMS hydroacoustic hydrophones operate lends itself to recording sounds from large marine mammals, such as blue whales and fin whales. These sounds are generally related to the communication spectrum of these animals since echolocation signals have higher frequencies. Harris, et al. (2018) used HA11 recordings, including directional distribution information obtained from the back-azimuths, and predictions of call-rate frequencies, source levels, transmission loss and signal to noise ratios, to develop a method for fin whale density and distribution estimation. Such studies can be useful for the investigation of whale population seasonal migration habits.

The long term recordings provided by IMS hydrophones led to a study into the variation of the Sri Lankan pygmy blue whale calls in the Indian Ocean (Miksis-Olds et al. 2018) for over a decade. It was found that some of the call units that make up the entire vocalization appear to have consistently shifted downwards in frequency over the study period.

Notable examples of the importance of long term hydroacoustic data for marine mammal ecology are also in the recent publications by Cerchio et al. (2020), Pinto and Chandrayadula (2021) and by Leroy et al. (2021) who found acoustic evidence of a previously unknown species of Indian Ocean pygmy blue whale in multiyear hydroacoustic recordings at HA8 over the period 2002–2019.

5.4. Undersea Volcanoes, Earthquakes and Tsunamis

Sounds from submarine volcanoes and earthquakes are ubiquitous in IMS hydrophone recordings and over the years the hydroacoustic data set turned out to be an abundant resource for remote detection and study of these phenomena. Undersea volcanoes can cause destructive tsunamis that pose a high risk in many coastal regions. The CTBTO is providing real time data to 19 tsunami warning centres in 18 countries to improve their tsunami warning alert systems.

Tepp and Dziak (2021) highlighted the IMS as a global seismoacoustic network of primary importance for the study of submarine volcanic activity. Metz et al. (2018) investigated the activity of the Monowai volcanic centre, in the Kermadec Arc, southwest Pacific Ocean, over a period of 3.5 years, using recordings at HA3 which is located across the ocean basin at a distance of more than 9000 km from Monowai (Figure 28 (b)). Smets et al. (2022) later reported about arrivals from Monowai detected at HA3 and at HA10 in the Atlantic Ocean, the latter station being more than 15 000 km from the volcanic activity, essentially at the antipodes, in a study which shows how repetitive volcanic events may be used as acoustic sources of opportunity for ocean acoustic thermometry and tomography studies. Matsumoto et al. (2022) studied a tsunamigenic eruption of the Kadovar

volcano, using data from HA11 hydrophones at a distance of 3500 km from the site.

A tsunamigenic earthquake which occurred in 2015 in Chile was studied by Matsumoto et al. (2016) using data from HA3, showing the detection of primary phases, and a T phase generated by the event. This paper also showed that, in the very low frequency band up to a few tens of milli-Hertz (mHz,) it is possible to detect tsunamis passing at IMS hydrophones. Although such frequencies are far below the range 1–100 Hz used for CTBT monitoring, and little is known about the absolute accuracy of sensor calibration at these very low frequencies, the spectrograms and filtered raw sensor data show clearly the pressure fluctuations signal dispersion associated with the tsunami's passage.

At the time of writing of this paper the cataclysmic eruption and tsunami of the Hunga Volcano, Tonga, on 15 January 2022 has been studied by a multitude of authors using IMS seismic and infrasound data. Hydroacoustic arrivals of T phases and a long duration rumble associated with this event have been recorded at HA11 (4700 km from the volcano) and HA3 (9300 km from the volcano), and the very low frequency pressure fluctuations associated with the passing tsunami were detected for about one week in hydrophone recordings from HA3 and HA11 (Pacific Ocean), HA4 (southern Indian Ocean) and HA10 (central Atlantic Ocean) (Le Bras et al. 2022).

Among the early scientific uses of IMS hydroacoustic data there is the study of Tolstoy and Bohnenstiehl (2005) who used data recorded at HA8 to investigate the potential for rapid assessment of spatial extents and rupture evolution of the large Sumatra-Andaman submarine earthquake of 2004. More recently, Oliveira et al. (2021) studied the propagation of T phases from a 7.4 Mw earthquake in the Kermadec Trench, which were recorded at HA10 at a distance of 15 100 km from the source. A parabolic equation three-dimensional underwater acoustic propagation model was used by the authors to explain the observed lateral diffraction of the T phases at Drake's Passage.

5.5. Search for the ARA San Juan and Other Maritime Emergencies

The Argentine submarine ARA (Armada de la Republica Argentina) San Juan went missing on 15 November 2017, with its last confirmed location around 600 kilometres east of Comodoro Rivadavia, Chubut, Argentina. In the days following the initiation of the multinational search and rescue mission, the CTBTO analysed data recorded by the IMS for any signals that could support this effort. Two of the IMS hydrophone stations, HA10 and HA4, were found to have recorded an unusual impulsive hydroacoustic signal of unknown nature (referred to as a 'hydroacoustic anomaly'), which originated from the vicinity of the last known location of the ARA San Juan. The distance between the source location of the hydroacoustic anomaly and the hydroacoustic stations was 6000 km for HA10 and 7700 km for HA4, respectively. After extended search operations on 17 November 2018 the ARA San Juan was found at the bottom of an undersea canyon on the seabed at approximately 900 meters depth, less than 20 km from the location of the hydroacoustic anomaly provided by CTBTO (Nielsen et al. 2021). There were no survivors.

In Nielsen et al. (2021) the authors also examine several continental and bathymetric reflections of the main signal and a sound with similar spectral properties to the hydroacoustic anomaly which reached HA4 approximately 1200 sec before the main arrival, from an azimuth pointing 16 degrees more southwards than the main arrival. It was found that this arrival could be explained by considering coupling of the sound with the Antarctic icesheet, through which the sound can travel at speeds higher than the speed of sound in water, until it coupled again into the ocean waveguide south of Crozet (Figure 29).

The signal recorded at HA10 and HA4 was found to have a cepstral delay of 0.33 sec and 0.45 sec, respectively. Cepstral delay in a signal can be detected for example in case of underwater explosions, where the collapsing bubble caused by the explosion generates closely spaced impulsive sounds. More generally, a cepstral delay emerges
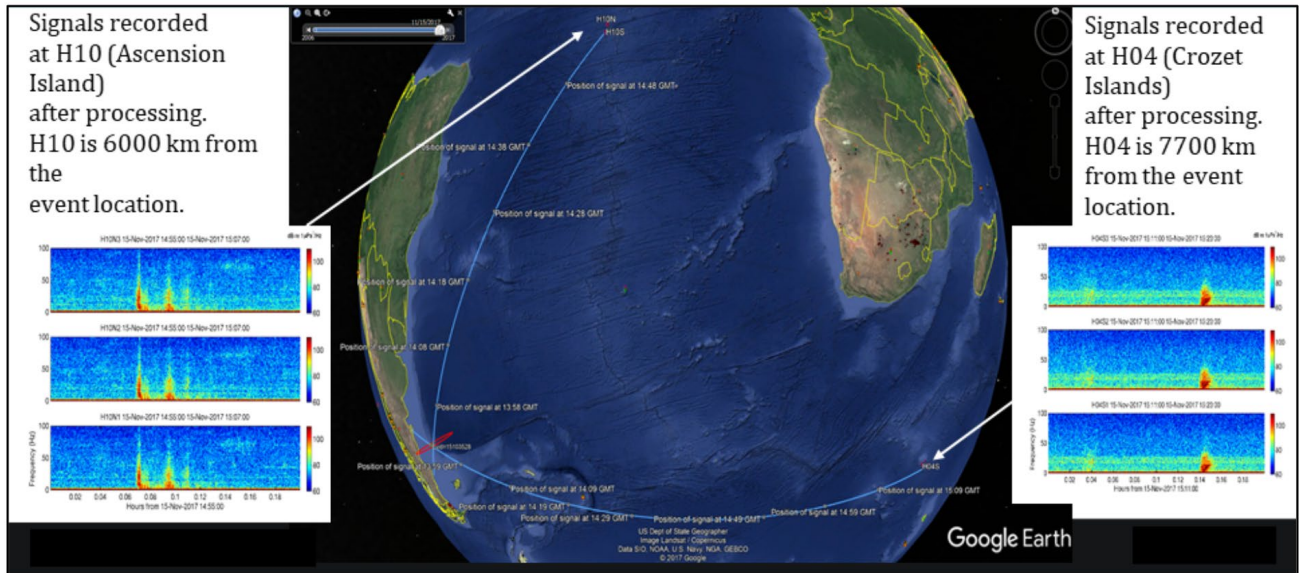
FIGURE 29.

The hydroacoustic anomaly related to the search for the ARA San Juan, recorded on 15 November 2017 by HA10 and HA4. The thin blue lines emanating from each hydroacoustic station are the back-azimuths, which cross at the estimated source location. The spectrograms show the time-frequency representation of the signals recorded by the H10N and the H04S triplets.

in the case of (closely spaced) repetitions of an impulsive signal. The difference in cepstral delays recorded at the two hydroacoustic stations is indicative of an acoustic source which is not omnidirectional. Prario et al. (2022) followed an inverse problem approach for estimating features of the impulse-like signal through the application of spectral and cepstral analyses. This analysis, in conjunction with considerations on the possible heading of the submarine and based on the navigation information known to the authorities, led to the formulation of the hypothesis of two closely spaced and successive implosions which may have occurred at 690 m depth (Prario et al. 2022).

The hypothesis of two closely spaced events and continental reflections of the hydroacoustic sound were also independently studied by Vergoz et al. (2021), Dall'Osto (2019) used the arrivals from horizontal refraction from the continental shelf break to show how such arrivals can improve source triangulation.This approach has potential beyond the study specific to the loss of the ARA San Juan, as such refracted arrivals may more generally aid in hydroacoustic source localization in cases when there is not a direct line of sight from two distinct hydroacoustic stations. Heyburn et al. (2020) used non-IMS seismic stations in addition to the IMS hydroacoustic

hydrophone stations' data to study potential refinements of the acoustic source localization.

Other maritime emergencies have been associated with signals recorded by IMS hydroacoustic hydrophones over large distances. Two recent notable examples are the studies by Metz et al. (2022), who examined IMS hydroacoustic recordings of sounds associated with the high-speed impact of a military plane on the sea surface and with the sinking of a container ship during a storm (Metz et al. 2021).

5.6. Detection of the Announced Democratic People's Republic of Korea Sixth Nuclear Test and Other Non-Nuclear Explosions Recorded by the International Monitoring System Hydroacoustic Hydrophones

The announced Democratic People's Republic of Korea underground nuclear test of 2017 was the first nuclear test to be automatically detected also by IMS hydroacoustic hydrophone stations. Seismic P phases from this event were detected in HA1 and HA11 hydrophone recordings by the IDC automatic processing system, and at HA8 and HA3 by manual detection and association. It should be noted that HA3 is almost at the antipodes of the test site of the Democratic People's Republic
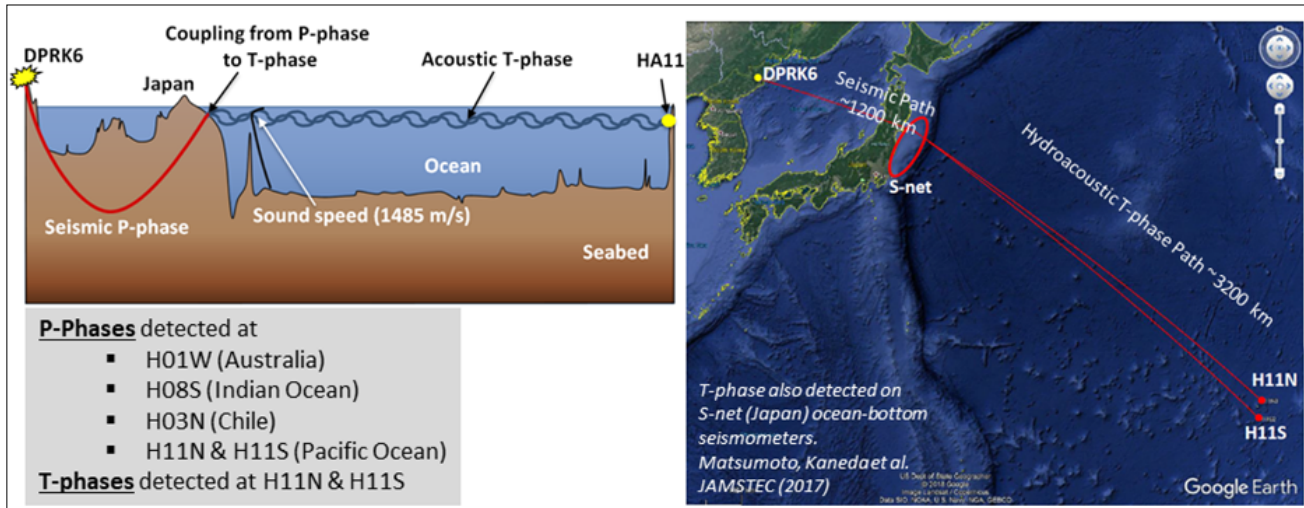
FIGURE 30.
Illustration of the DPRK6 T phase generation and propagation to HA11 (top left).
List of IMS hydroacoustic hydrophone stations where P-Phases or T phases from DPRK6 were detected (bottom left).
Seismic propagation path and T phase propagation path in the ocean from the East Japan slope to the H11N and H11S (right).

of Korea at a distance of 17 500 km. Some of the seismic P phases generated by this nuclear test coupled into the SOFAR channel along the seaward-facing slope of the Japan Trench, from where the sound propagated another 3200 km to reach the H11S and H11N hydrophones at a combined distance of 4400 km from the source, as shown in Figure 30. This signal was manually detected and associated and represents the first detection of a T phase from a nuclear test on IMS hydrophones. These findings were reported at the CTBT Science and Technology Conference in 2021 (Zampolli et al. 2021).

Non-nuclear underwater explosions are also detected at IMS hydroacoustic stations and represent valuable opportunities for assessing the sensitivity and accuracy of the hydroacoustic stations. For example, the accidental explosion of the power supply of seabed-moored oceanographic equipment on the New Jersey shelf, 175 km south-east of New York, was detected at HA10 at 8000 km distance. This event was studied by Prior and Chapman et al. (2010). A series of geophysical explosions off the shore of Japan, detected at ranges of thousands of kilometres across the Pacific Ocean were studied by Prior et al. (2011) and Prior and Brown (2010). The same series of explosions, and more recent ones with approximately 400 kg

Trinitrotoluene equivalent sources in deep water off the shore of Japan were studied using HA3 and HA11 recordings by Yamada et al. (2016), where persistence of cepstral features and effects of diffraction on the long-range propagation of the signals were studied.

Signals from conventional explosions equivalent to approximately 6700 kg Trinitrotoluene from naval shock trials off the shore of the Florida coast were studied using recordings from HA10 hydrophones and seismometers by Heyburn et al. (2018). The authors characterized the signals in terms of bubble pulses, modulation spectra and seismic magnitudes and analysed the effect of bathymetry on hydroacoustic signal distortion with numerical underwater acoustic propagation models. This study also highlighted the potential usefulness of combining hydroacoustic and seismic observations. Finally, Stevens et al. (2021) used data from the Florida explosions in a series of studies to examine the coupling of hydroacoustic phases to the Earth's crust near the shore. A parabolic equation underwater acoustic long range propagation model was coupled with a spectral finite element seismic model for the nearshore area in order to investigate mechanisms by which hydroacoustic signals are transformed to seismic waves nearshore at T phase stations.

REFERENCES

Ainslie, M.A. (2010). *Principles of Sonar Performance Modelling*, Springer-Verlag, Berlin–Heidelberg.

Brouwer, A., Le Bras, R., Nielsen, P.L. (2019). "Exploring the use of subspace detectors for seismic survey signals observed on the IMS hydroacoustic network". Paper presented at the European Geosciences Union (EGU) General Assembly, Vienna, 2019.

Cerchio, S., et al. (2020). A new blue whale song-type described for the Arabian Sea and Western Indian Ocean. *Endangered Species Research* **43** 495–515.

Chapp, E., Bohnenstiehl, D.R., Tolstoy, M. (2005). Sound-channel observations of ice-generated tremor in the Indian Ocean. *Geochemistry Geophysics Geosystems* **6** (6).

Colosi, J.A., et al. (1999). Comparison of measured and predicted acoustic fluctuations for a 3250-km propagation experiment in the eastern North Pacific Ocean. *Journal of the Acoustical Society of Am*erica **105** 3202-3218.

Dall'Osto, D.R. (2019). Source triangulation utilizing three-dimensional arrivals: Application to the search for the ARA San Juan submarine. *Journal of the Acoustical Society of Am*erica **146** (3) 2104–2112.

de Groot-Hedlin, C., Blackman, D.K., Scott Jenkins, C. (2009). Effects of variability associated with the Antarctic circumpolar current on sound propagation in the ocean. *Geophysical Journal International* **176** (2) 478–490.

Dushaw, B.D., et al. (2009). A decade of acoustic thermometry in the North Pacific Ocean. *Journal of Geophysical Research: Oceans* **114** (C7).

Evers, L.G., Wapenaar, K., Heaney, K.D., Snellen, M. (2017). Deep ocean sound speed characteristics passively derived from the ambient acoustic noise field. *Geophysical Journal International* **210** (1) 27-33.

Haralabus, G., Zampolli, M., Grenard, P. Prior M., Pautet, L., (2017). "Underwater acoustic measurements and their applications." *Applied Underwater Acoustics: Leif Bjørnø* (T. Neighbors, D. Bradley Eds.) Elsevier, Amsterdam and New York.

Harris, D.V., Miksis-Olds, J.L., Vernon, J.A., Thomas, L. (2018) Fin whale density and distribution estimation using acoustic bearings derived from sparse arrays. *Journal of the Acoustical Society of Am*erica **143** 2980-2993.

Harris, P., Sotirakopoulos, K., Robinson, S.P., Wang, L., Livina, V. (2019). A statistical method for the evaluation of long term trends in underwater noise measurements. *Journal of the Acoustical Society of Am*erica **145** (1) 228-242.

Heaney, K.D., Campbell, R.L. (2016). Three-dimensional parabolic equation modeling of mesoscale eddy deflection. *Journal of the Acoustical Society of Am*erica **139** 918–926.

Heaney, K.D., Prior, M.K., Campbell, R.L. (2017). Bathymetric diffraction of basin-scale hydroacoustic signals. *Journal of the Acoustical Society of Am*erica **141** (2) 878-885.

Heyburn, R., Nippress, S.E.J., Bowers, D. (2018). Seismic and hydroacoustic observations from underwater explosions off the east coast of Florida. *Bulletin of the Seismological Society of America* **108** (6) 3612–3624.

Heyburn, R., Bowers, D., Green, D.N. (2020), Seismic and hydroacoustic observations from recent underwater events in the South Atlantic Ocean. *Geophysical Journal International* **223** (1) 289–300.

Jensen, F.B., Kuperman, W.A., Porter, M.B., Schmidt, H. (2011). *Computational Ocean Acoustics*, 2nd edn. Springer, New York.

Le Bras, R.J., et al. (2022). The Hunga Tonga–Hunga Ha'apai eruption of 15 January 2022: Observations on the International Monitoring System (IMS) hydroacoustic stations and synergy with seismic and infrasound sensors. *Seismological Research Letters*.

Leroy, E.C., Royer, J.-Y., Alling, A., Maslen, B., Rogers, T.L. (2021). Multiple pygmy blue whale acoustic populations in the Indian Ocean: Whale song identifies a possible new population. *Nature Scientific Reports* **11** 8762.

Matsumoto, H., et al. (2014). Antarctic icebergs: A significant natural ocean sound source in the Southern Hemisphere. *Geochemistry, Geophysics, Geosystems* **15** (8) 3448-3458.

Matsumoto, H., et al (2020). Hydroacoustic Signals Originating from Marine Volcanic Activity at Kadovar Island, Papua New Guinea, Recorded by the Comprehensive Nuclear-Test-Ban Treaty International Monitoring System. *Pure and Applied Geophysics*.

Matsumoto, H., et al. (2022). Hydroacoustic signals originating from marine volcanic activity at Kadovar Island, Papua New Guinea, recorded by the Comprehensive Nuclear-Test-Ban Treaty International Monitoring System. *Pure and Applied Geophysics*.

Metz, D., Watts, A.B., Grevemeyer, I., Rodgers, M. (2018). Tracking submarine volcanic activity at Monowai: Constraints from long-range hydroacoustic measurements. *Journal of Geophysical Research: Solid Earth* **123** (9) 7877–7895.

Metz, D., Nielsen, P.L., Zampolli, M., Haralabus, G. (2021). Remote detection of hydroacoustic signals potentially associated with the sinking of SS El Faro using CTBT IMS hydrophone data. CTBT: Science and Technology Conference 2021 (SnT21). Poster P1.3-331.

Metz, D., Obana, K., Fukao, Y. (2022). Remote Hydroacoustic Detection of an Airplane Crash. *Pure and Applied Geophysics*.

Miksis-Olds, J.L., Nichols, S.M. (2016). Is low frequency ocean sound increasing globally? *The Journal of the Acoustical Society of America* **139** (1) 501–511.

Miksis-Olds, J.L., Nieukirk, S.L., Harris, D.V. (2018). Two unit analysis of Sri Lankan pygmy blue whale song over a decade. *The Journal of the Acoustical Society of America* **144** (6) 3618–3626.

Nielsen, P.L., et al. (2021). CTBTO's data and analysis pertaining to the search for the missing Argentine submarine ARA San Juan. *Pure and Applied Geophysics* **178** 2557–2577.

Oliveira, T.C., Lin, Y.-T., Kushida, N., Jesus, S.M., Nielsen, P. (2021). T-wave propagation from the Pacific to the Atlantic: The 2020 Mw 7.4 Kermadec Trench earthquake case. *The Journal of the Acoustical Society of America Express Letters* **1** (12).

O'Mongain, A., Ottemoller, L., Baptie, B., Galloway, D., Booth, D.C. (2007). Seismic activity associated with a probable submarine eruption near Tristan da Cunha, July 2004 - July 2006. *Seismological Research Letters* **78** (3) 375-382.

Pinto, N., Chandrayadula, T.K. (2021). Long-term frequency changes of a potential baleen whale call from the central Indian Ocean during 2002–2019. *The Journal of the Acoustical Society of America Express Letters* **1** (2).

Prario, I., et al. (2022). Characterization of the acoustic event associated with the loss of the ARA San Juan submarine based on long-range measurements by CTBTO's hydrophone stations. *Pure and Applied Geophysics*.

Prior, M.K., Brown, D.J. (2010). Estimation of depth and yield of underwater explosions from first and second bubble-oscillation periods. *IEEE Journal of Oceanic Engineering* **35** (1) 103-112.

Prior, M.K., Brown, D.J., Haralabus, G. (2011). Data features from long-term monitoring of ocean noise. *Proceedings of the Institute of Acoustics*.

Prior, M.K., Chapman, N.R., Newhall, A.E. (2010). "The long-range detection of an accidental underwater explosion. (Proceedings of the 10th European Conference on Underwater Acoustics, (ECUA2010), Istanbul, 2010). Proceedings of the 10th European Conference on Underwater Acoustics, ECUA 2010: Istanbul, Turkey, July 5-9, 2010, Volume 3.

Prior, M.K., Meless, O., Bittner, P., Sugioka, H. (2011). Long-range detection and location of shallow underwater explosions using deep-sound-channel hydrophones. *IEEE Journal of Oceanic Engineering* **36** (4) 703–715.

Sabra, K.G., Fried, S., Kuperman, W.A., Prior, M.K. (2013). On the coherent components of low-frequency ambient noise in the Indian Ocean. *The Journal of the Acoustical Society of America* **133** (1).

Smets, P.S.M., Weemstra, C., Evers, L.G. (2022). Hydroacoustic travel time variations as a proxy for passive deep-ocean thermometry — A cookbook. *Journal of Geophysical Research: Oceans* **127** (5).

Stevens, J.L. et al. (2021). Calculation of hydroacoustic propagation and conversion to seismic phases at T-stations. *Pure and Applied Geophysics* **178** 2579–2609.

Tepp, G., Dziak, R.P. (2021). The seismo-acoustics of submarine volcanic eruptions. *Journal of Geophysical Research: Solid Earth* **126** (4).

The ATOC Consortium (1998). Ocean climate change: Comparison of acoustic tomography, satellite altimetry, and modelling. *Science* **281** (5381) 1327-1332.

Tolstoy, M., Bohnenstiehl, D.R. (2005). Hydroacoustic constraints on the rupture duration, length and speed of the great Sumatra-Andaman earthquake. *Seismological Research Letters* **76** (4) 419-425.

Vergoz, J., Cansi, Y., Cano, Y., Gaillard, P. (2021). Analysis of hydroacoustic signals associated to the loss of the Argentinian ARA San Juan submarine. *Pure and Applied Geophysics* 178 2527-2556.

Woolfe, K. F., Lani, S., Sabra, K.G., Kuperman, W.A. (2015). Monitoring deep-ocean temperatures using acoustic ambient noise. *Geophysical Research Letters* **42** (8) 2878–2884.

Wu, W., Zhan, Z., Peng, S., Shen, Z., Callies, J. (2021). "Seismic ocean thermometry using CTBTO hydrophone data". CTBT: Science and Technology Conference (SnT21).

Yamada, T., et al. (2016). Analysis of recordings from underwater controlled sources in the Pacific Ocean received by the International Monitoring System (IMS) of the Comprehensive Nuclear-Test-Ban Treaty Organization (CTBTO). Europ. Geosc. Union Meeting (EGU2016) Vienna.

Zampolli, M., et al. (2021). "Detections at IMS hydrophone stations of Primary and Tertiary phases from the sixth announced DPRK underground nuclear test," CTBT: Science and Technology Conference (SnT21) oral presentation.

Developments in Hydroacoustic Processing for Nuclear Test Explosion Monitoring

R. Le Bras, P. Mialle, N. Kushida, P. Bittner
Comprehensive Nuclear-Test-Ban Treaty Organization, Vienna, Austria

P. Nielsen
Esbjerg, Denmark

Abstract

Since its establishment in 1997, the International Data Centre (IDC) has been receiving data continuously from an increasing number of hydroacoustic stations. These stations are at present composed of six hydrophone triplets in the ocean and five T stations (seismometers) on land monitoring for nuclear explosions in the oceans. This paper summarizes advancements in the IDC automatic processing system from the early deployment of the system receiving data from a couple of hydroacoustic stations until today's hydroacoustic network. The advancement in IDC processing of hydrophone data has been obtained in underwater signal travel time modelling, improved rule based signal classification, estimate of underwater signal detection and direction of arrival, introduction of early artificial intelligence for signal classification, and global network processing based on an advanced Bayesian framework (NET-VISA). These advances have improved the automatic signal classification, detection and event localization and therefore importantly reduced the amount of human interaction in the data processing. Further improvements of the processing are envisioned that includes detailed oceanographic models and databases, efficient complex signal propagation models, the Progressive Multi-Channel Correlation algorithm and the rapid development of machine learning algorithms.

1. INTRODUCTION

The Preparatory Commission for the Comprehensive Nuclear-Test-Ban Treaty Organization (CTBTO), located in Vienna, Austria, has been tasked to establish a global verification regime to monitor compliance with the Comprehensive Nuclear-Test-Ban Treaty (Treaty), which bans all nuclear explosions anywhere under the jurisdiction of its States Parties. The verification regime includes the International Monitoring System (IMS), a global network of 337 monitoring facilities using four different technologies (seismic, hydroacoustic, infrasound, and radionuclide), a communications infrastructure, and an IDC with the capability to carry out on-site inspections (OSI). This paper focuses on the hydroacoustic part of the IMS network and the processing done in the IDC for this technology. Outside of military applications, experience with this technology has been limited and includes only niche civil applications such as fisheries and underwater acoustic communications. The CTBTO is currently the only organization providing daily reviewed bulletins to its States Signatories that include hydroacoustic stations. Starting from very limited experience acquired in developing software and established procedures in the 1990s, the hydroacoustic network is contributing substantially to the Reviewed Event Bulletin (REB) and a hydroacoustic criterion is also used in screening out natural events. This paper reviews the progress made in the past quarter century in establishing hydroacoustic IMS stations, enhancing the processing pipeline of the IDC, and gaining experience with observations made using this unique sparse network of extremely sensitive stations.

2. THE GROUP OF SCIENTIFIC EXPERTS TECHNICAL TESTS: ORIGIN OF WHAT BECAME THE INTERNATIONAL DATA CENTRE AUTOMATIC PROCESSING SYSTEM

Leading up to the signature of the Treaty, the predecessor of the Conference on Disarmament (Conference on Disarmament 1978) established the Ad Hoc Group of Scientific Experts (GSE) in July 1976.The GSE was composed of government appointed experts, and was mandated to consider international cooperative measures to detect and identify seismic events to facilitate the monitoring of a Nuclear Test Ban. The GSE has developed several generations of data exchange systems and conducted three Group of Scientific Experts Technical Tests (GSETT) (GSETT-1, GSETT-2, and GSETT-3) to assess its system concepts in a realistic manner (Dahlman et al. 2009, Dahlman et al. 2020).

In 1984 GSETT-1 was an exchange of parameters between all participants. During GSETT-2 in 1991 selected waveform data were collected and exchanged between four global data centres (Australia, the Russian Federation, Sweden, and the United States of America (USA)). Data were collected using a sparse non-IMS network of sensors.

On 1 January 1995, GSETT-3 started to investigate new concepts for a verification system based primarily on seismic monitoring. An experimental International Seismic Monitoring System (ISMS) was set up and complemented by an experimental data centre, the Prototype International Data Centre (PIDC), hosted at the Center for Monitoring Research (CMR) in Arlington, Virginia, USA. The initial software for the processing of seismic, hydroacoustic, and infrasound monitoring data was developed for the PIDC and primarily funded by the US government. The final product of the PIDC consisted of bulletins with detailed lists of events, including contributing stations and detections of the signals at these stations. The GSETT-3 system included rapid acquisition and processing

of data from a global network of seismic sensors at a central facility with the provision of as much automation as possible in the collection, processing, and distributing of data. The GSETT-3 system established a monitoring system architecture flexible enough to allow for any technical modifications and improvements that might be needed in the future.

While GSETT-3 (Dahlman et al. 2009) was limited to seismic monitoring, its system design was flexible enough to incorporate collecting, archiving, and distributing data from non-seismic techniques, such as hydroacoustic, infrasound, and radionuclide.

The GSETT-3 test took place during Treaty negotiations (Ramaker et al. 2003) and continued during the initial build-up of the IMS, starting in 1997 at the CTBTO.

The PIDC project continued at the CMR until March 2000, while the processing system was being installed and provisional operations initiated at the IDC in Vienna, Austria. The United States generously donated the software and associated documentation to the Provisional Technical Secretariat (PTS) of the CTBTO. The first delivery of the automatic processing algorithm (release R1) at the IDC was mainly configured for primary seismic network processing. The IMS hydroacoustic network was routinely monitored during the R1 release and was composed of two hydrophones from the Sound Surveillance System (SOSUS, Castillo et al. 2020) named WK30 and WK31 at Wake Island, Pacific Ocean, located around 240 km apart and one T phase station, VIB at Queens Island, Canada, with one vertical component. The CTBT automatic processing algorithm (R1) was still in a development phase and was mainly composed of the Detection and Feature eXtraction (DFX), Station Processing (StaPro), Global Association. As of 2022 these three modules still exist in the IDC processing system. The R1 release was operational from 15 May 1998 to 28 May 1999 while a later version was running at PIDC in Arlington, USA. Release two of the automatic processing algorithm (R2) was transferred from PIDC in May 1999. Lessons carried forward as the IDC moved towards its final goal of building a system capable of fulfilling the relevant Treaty obligations of routinely receiving, processing, analysing, and reporting on IMS data. Release three of the automatic processing algorithm (R3) was more complex and included the request for auxiliary seismic stations (IMS Map, 2023). At the time release R3 was installed as part of the IDC application software, development and maintenance was taken over by the IDC. More details of the hydroacoustic processing system developed for the PIDC and a complete description of the temporary hydroacoustic network of stations that was used between 1995 and 2000 can be found in Hanson et al. (2001).

An Ad-Hoc Expert Group on the Evaluation of Hydroacoustic Data Processing at the International Data Centre met three times in 2002 and 2003 at the CTBTO and recommended six high priority areas for further improvements: station-specific processing parameters; multichannel processing of triad (or triplet) data; usage of T (Tertiary) and H (Hydroacoustic) phases in event definition and location; modelling of travel time and transmission loss; characterization of arrival time is critical to location (refinement of probability weighted time pick); and use of a spectrogram tool for interactive phase identification. In the next section, areas of development of the hydroacoustic system that occurred in the past twenty-five years are examined in the light of these recommendations.

3. DEPLOYMENT OF THE HYDROACOUSTIC COMPONENT OF THE INTERNATIONAL MONITORING SYSTEM

Figure 1 shows the 11 stations of the IMS hydroacoustic network. All stations were deployed from 2001 to 2007 and the number of sensors providing data to the IDC increased steadily during that time, contributing to the IDC operation and products. A detailed description
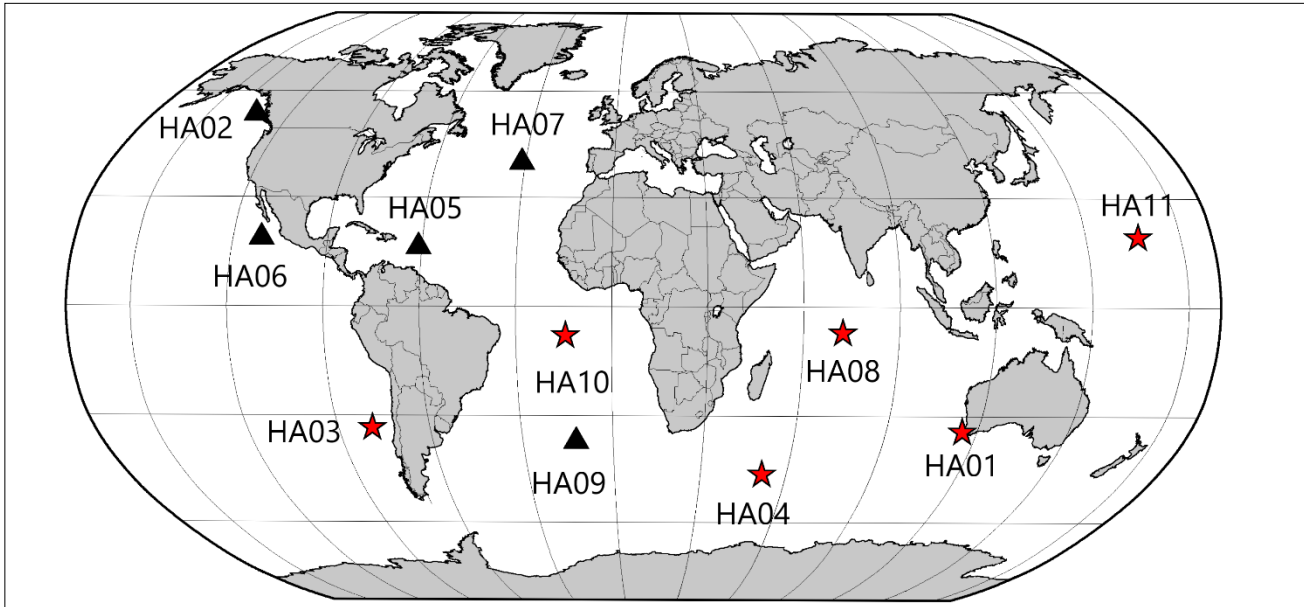
FIGURE 1.

Map of the IMS hydroacoustic network with in-water hydrophone stations represented as red stars and underground (T phase) stations as black triangles.

of the engineering involved in installing the hydroacoustic stations is beyond the scope of this paper but an example of installation is reported in Haralabus et al. (2017).

Before data from a hydroacoustic station can be used in the IDC operation, the station must be certified to fulfil the specifications as defined in the draft Operational Manual for hydroacoustic stations (Preparatory Commission for the CTBTO, 2020). Table 1 shows the dates at which each station was certified and at which it started contributing to the IDC. As of 2021, all stations in the IMS hydroacoustic network configuration have been certified and are sending data to the IDC. Five out of six hydrophone stations hosted on islands (HA3, HA4, HA8, HA10, HA11) consist of two triplets of hydrophones each covering the ocean basin to the north and south to avoid the propagation blockage by the islands. The cable transmitting the data of the sixth hydrophone station, HA1 consists of a single triplet with clear paths to large parts of the Indian Ocean and Southern Ocean.

Table 1. International Monitoring System Hydroacoustic Stations with Their Dates of Certification and Entry in the International Data Centre Provisional Operations

| Treaty Number	Station Type	Certification Date	IDC Operation Date
HA1	Hydrophone	10-DEC-2001	25-APR-2002
HA2	T phase station	20-DEC-2006	29-JAN-2007
HA3	Hydrophone	14-NOV-2003	09-JUL-2003
HA4	Hydrophone	19-JUN-2017	02-OCT-2003
HA5	T phase station	30-JAN-2002	06-MAR-2002
HA6	T phase station	22-DEC-2005	16-MAR-2006
HA7	T phase station	21-NOV-2005	28-JUL-2005
HA8	Hydrophone	18-DEC-2000	18-OCT-2001
HA9	T phase station	22-DEC-2004	23-MAR-2005
HA10	Hydrophone	15-DEC-2004	23-MAR-2005
HA11	Hydrophone	08-JUN-2007	17-DEC-2007

4.   PROCESSING OF WAVEFORM DATA AT THE INTERNATIONAL DATA CENTRE

This section provides an overview of the processing steps at the IDC, which have largely remained the same since the start, although individual modules have been enhanced and their parameters tuned in the last 20 years. The emphasis will be on the hydroacoustic part of the processing, with a few highlights of the other two waveform technologies, since the same overall steps of station and network processing, and interactive review are common to all three technologies and that the waveforms are processed together after network processing.

The IDC processing system for waveform data tightly fuses all three waveform technologies starting from the network processing stage. All three technologies are mixed when a single source has manifestations in all three media covered by the IMS, i.e. ground, ocean, and atmosphere. The products of the IDC include multi-technology automatic and reviewed event bulletins. Figure 2 shows the major steps in processing along with the approximate timing at which each product of the IDC is available.

The IDC processes the data collected by the IMS as soon as they reach the centre. The first data product, known as Standard Event List 1 (SEL1) is an automated waveform data report that lists preliminary waveform events recorded by the primary seismic and hydroacoustic stations. It is completed within one hour of the data being recorded at the station. The IDC issues a more complete waveform event list, Standard Event List 2 (SEL2) four hours after first recording the data. SEL2 uses additional data requested from the auxiliary seismic stations along with data from the infrasound stations and any other waveform data that arrived late. After a further two hours have elapsed the IDC produces the final, automated waveform event list, Standard Event List 3 (SEL3) which incorporates any additional late arriving waveform data. All these automated products are produced according to the schedules that will be required when the Treaty enters into force. IDC analysts subsequently review the waveform events recorded in SEL3 and correct the automated results, adding missed events as appropriate, to generate the daily REB. The REB for a given day contains all waveform events that meet the required criteria. During the current provisional operating mode of the IDC, the REB is issued within 10 days. After the Treaty enters into force, the REB will be released within two days of the end of the data day. An automatic stage of processing takes place after analyst review. Additional characterization parameters are computed for REB events specifically to allow screening of natural events based on a few screening criteria within these parameters. This results in the Standard Event Bulletin (SEB)
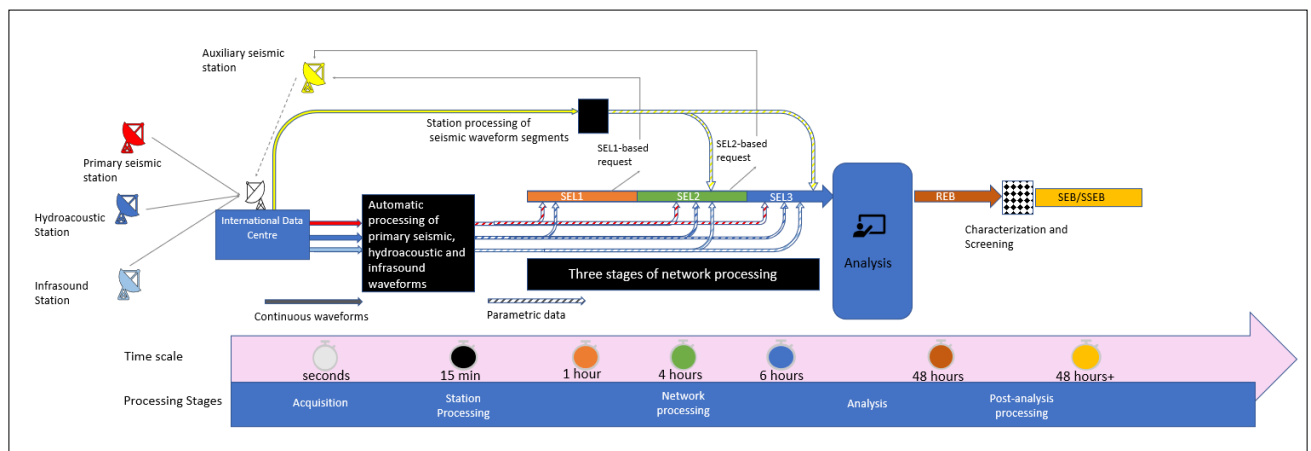
FIGURE 2.
Overall processing pipeline for waveform data, including primary seismic, auxiliary seismic, hydroacoustic, infrasound from data acquisition to production of the standard event bulletin.

which includes the characterization parameters and the Screened Standard Event Bulletin (SSEB) which is a subset of the SEB retaining events not screened out.

4.1. Data Acquisition

The primary seismic, hydroacoustic and infrasound waveform data are acquired continuously at the IDC from the stations via the Global Communication Infrastructure, which consists of a very small aperture terminal communication network to connect to a few hubs, VPN encoding, and other secure communication components.

4.2. Station Processing

Waveform data (seismic, hydroacoustic, infrasound) first undergo station processing, which includes all processing performed on waveforms from one station at the time. Detections are made on the waveforms at discrete time samples and features (time of the detection, uncertainty on time, directional parameters, uncertainty on the directional parameters, amplitudes, uncertainty on amplitudes, etc.) are extracted from the waveforms for these detections. Station processing is performed on technology-dependent time intervals and the results are available within a few minutes after receipt at the IDC (15 minutes for primary seismic and hydroacoustic

stations where processing is done in ten minutes intervals). The detections constitute the input to network processing, an automatic processing step which assembles detections from different stations into a seismoacoustic bulletin containing events which may have seismic, hydroacoustic and infrasound components. Figure 3 details the steps in station processing of the hydroacoustic waveform data. Hydrophone stations record the variations of underwater pressure with time and T phase stations record the variation of particle velocity of the ground motion at one or several seismometers. Different processing schemes are used for the two types of data as shown in Figure 3. Despite the different physical nature of the time series, the initial detection step is the same for both data types and is performed by the Detection and Features eXtraction (DFX) algorithm, using a short term average over long term average power detector (STA/LTA) with the short term average window set at 10 seconds and the long term average window at 150 seconds. This is to be compared with the standard values of respectively 1 second and 30 seconds for seismic data processing. Note that these longer time windows were adapted for the detection of horizontally propagating hydroacoustic signals which have a longer duration than the initial seismic P waves, whose detections are the most significant contributors to detecting and locating seismic events.
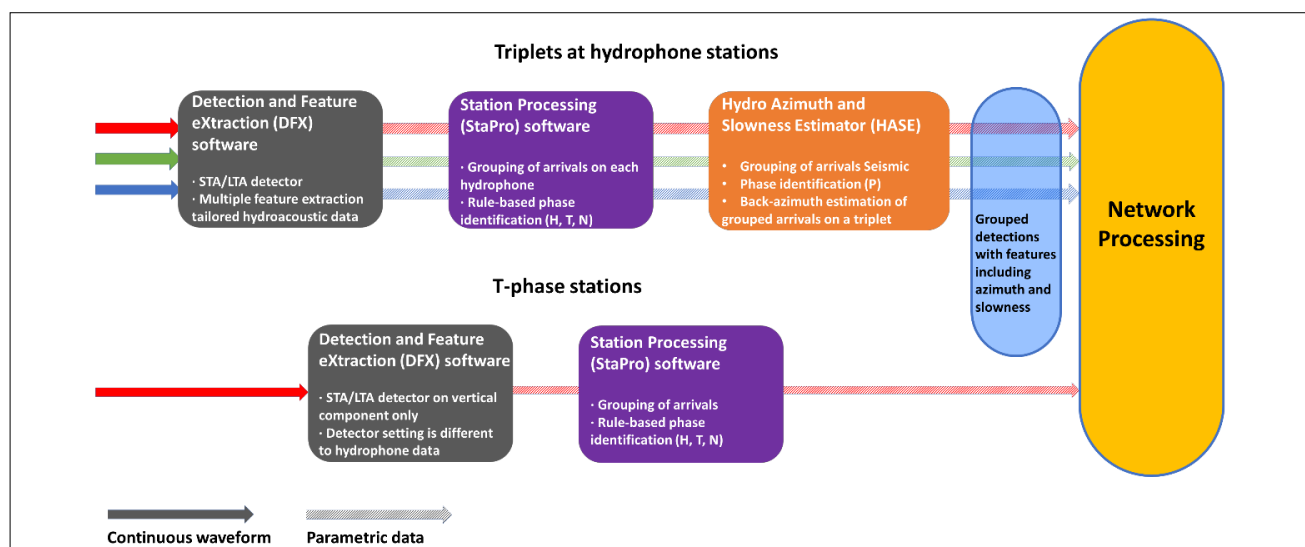
FIGURE 3.
Schema of the station processing for hydrophone data and T phase stations data showing the different steps of station processing.

Once the detections are made, the version of DFX which is used for hydroacoustic data also extracts a different set of features than the seismic version and stores them in a specialized database. These features are listed in Table 2. A series of frequency bandpass filters are used, and the features are computed for each of these filter bands.

Table 2. Frequency-Dependent Features Computed for Each Hydroacoustic Detection

Feature Name	Short Description
peak_time	time of largest absolute signal value
peak_level	pressure of largest absolute signal value
total_energy	total energy in signal
mean_arrival_time	mean arrival time of signal energy
time_spread	root mean square time spread of signal
onset_time	estimated onset time of signal
termination_time	estimated termination time of signal
total_time	total time above threshold
num_cross	number of signal threshold crossings
ave_noise	average pressure of the noise segment
skewness	skewness of the estimated signal energy
kurtosis	kurtosis of the estimated signal energy
cep_var_signal	variance of the cepstrum using spectrum
cep_delay_time_signal	bubble pulse delay time using spectrum
cep_peak_std_signal	number of standard deviations from the mean for amplitude using spectrum
cep_var_trend	variance of the cepstrum detrended using noise spectrum equalization
cep_delay_time_trend	bubble pulse delay time estimate using trend noise spectrum equalization
cep_peak_std_trend	number of standard deviations from the mean for amplitude using the trend
prob_weight_time	probability-weighted time
sigma_time	variance of the probability-weighted time

When it is possible to compute them, these features are stored for the eight frequency bands listed in Table 3. Note that the frequency bands are different between the two types of hydroacoustic stations. They include several estimates of the time pick, including the probability-weighted estimate described in Hanson et al. (2001), various amplitude and energy values, and features related to cepstral peaks, which are relevant to the identification of a possible bubble pulse due to an underwater explosion. Laney et al. (1999) document the initial implementation of this detection system. The basic system has not changed since the initial system was received as a contribution from the US government, however improvements have been made to it since and the frequency bands used in the computation have been adjusted.

Table 3. Frequency Bands Where Hydroacoustic Features are Computed.
Bands Marked Low Frequency Band (LFB), High Frequency Band (HFB), and Broad Frequency Band (BFB) are Used to Classify Hydroacoustic Arrivals

HYDROPHONES			T PHASE STATIONS SEISMOMETERS		
Band	Low Cut	High Cut	Band	Low Cut	High Cut
1	1	3	1	1	3
2	3	6	2	2	4
3 (LFB)	6	12	3	4	8
4	8	16	4	6	12
5	16	32	5	10	20
6	32	64	6	16	32
7 (HFB)	64	100	7	24	38
8 (BFB)	2	80	8 (BFB)	2	40

After the detection is made either on the vertical component of the T phase station seismometer or each hydrophone trace, an attempt is made to perform a preliminary classification of the detection as signal originating either in water (H phase) or underground (T phase), or else as noise detections (N phase). This is done by the StaPro module. Section 5 provides a more detailed explanation and improvements of the classification method. While a great deal of experience has been gained in identifying all three phase types for the hydrophone stations, further understanding of signals recorded at T phase stations is required to uniquely identify and classify these signals. Signals at T phase stations have typically undergone a complex conversion from hydroacoustic energy to seismic energy and signal classification rules at this point are applied only to identify T and N phases for signals recorded at T phase stations.

The processing after StaPro then differs between hydrophone stations and T phase stations, with hydrophone stations going through the Hydro Azimuth and (Slowness) Estimator (HAE/HASE) module which processes simultaneously the three hydrophone traces of a triplet. After the HAE/HASE step, the detections have acquired directional information. The initial name of the module was HAE because it did not include the estimate of the slowness, but only of the azimuth. The module groups detections that are made at each hydrophone of a triplet and refines the time differences between the detections using waveform cross-correlation. From these time differences, either a single back-azimuth, when three detections could be grouped together or two possible back-azimuth, when only two detections could be grouped, are computed. The slowness estimation allows for separating the vertically propagating seismic waves from the horizontally propagating hydroacoustic waves in the ocean.

Table 4 shows the main entries of the database tables that define the hydroacoustic arrival groups after processing through the HASE module. One of the tables (HYDRO_ASSOC) defines which arrivals belong to the group and the other (HYDRO_ARR_GROUP) contains the features calculated for the group and the phase name determined for the whole group.

Table 4. Tables Defining a Hydroacoustic Group

HYDRO_ARR_GROUP TABLE (one entry per group, features common to the group)		HYDRO_ASSOC TABLE (defines which arrivals belong to the group)	
hydro_id	hydro-arrival-group identifier	hydro_id	hydro-arrival-group identifier
az1	azimuth estimated from lag times	arid	arrival identifier
az2	second possible azimuth (2 arrivals)	azcontrib	azimuth contribution flag (y or n)
slow	slowness (s/km)		
delaz	azimuth uncertainty		
nhydarr	number of arrivals in hydro-arrival-group		
net	hydro network name		
hyd_grp_phase	hydro-arrival-group phase		

Section 5 details the improvements made in the upgrade from HAE to HASE. It is envisioned that this module will be superseded by using the Progressive Multichannel Cross-Correlation (PMCC) software based on the algorithm invented by Cansi (1995). It is worth noting that because the PMCC algorithm was intended for arrays of at least four elements, the progressive aspect is not used for the triplets. The three waveform traces processed together, treating the hydrophone triplet as a three-element array, addressing one of the recommendations of the Ad-hoc Expert Group on the Evaluation of Hydroacoustic Data Processing and allowing for a finer analysis of the detections with a better resolution in frequency. Section 5 also explains how PMCC is used for hydroacoustic data and demonstrates this on a few examples.

4.3. Network Processing

The next step in the pipeline is network processing, done by the Global Association module (Hanson et al. 2001). Network processing is run at several time intervals, initially to provide a bulletin including primary seismic stations and hydroacoustic stations one hour after real time, the SEL1. SEL2 is produced four hours after real time. It includes detections from all technologies, including auxiliary seismic stations. Segments from a selected group of auxiliary seismic stations are requested based on the events in the SEL1 and undergo station processing before being included as input to SEL2. The purpose of these additional data is to refine the location of the events originally formed in SEL1. SEL2 events also trigger the request of additional waveform segments from auxiliary seismic stations which are included as input to the SEL3. The input to SEL3 includes detections from all technologies. It is scheduled six hours after real time and is the automatic bulletin reviewed by analysts. A newly developed Bayesian algorithm, NET-VISA (Arora et al. 2013) has been running in parallel since 1 January 2018 to provide an alternative bulletin to SEL3, called VSEL3, and is used by analysts to complement the results of the Global Association. The analysts achieve this by loading events from the VSEL3 bulletin that were not yet presented to them for review, as they were missing in SEL3. VSEL3 has shown to contribute significantly to the REB (Le Bras et al. 2020).

4.4. Review by Analysts

The next major step in processing is the review of the automatic bulletins by analysts. This produces the REB shown in Figure 2. Analysts rectify any errors committed by the automatic system by adding missed detections, adjusting the picks for their time and directional information (back-azimuth and slowness), untangling automatic events when a single event gave rise to several automatic events or when an automatic event is formed out of detections belonging to multiple events. More specifically, for the review of hydroacoustic detections and associations, analysts use two hydroacoustic

specific tools that were developed at the PIDC. The first one allows them to check whether a path is clear from the location of an event to a hydroacoustic station to avoid making inappropriate associations of a T or H phase to an event. For a hydroacoustic detection to be associated to an event, the geodesic path to the station must be clear, meaning that there are no significant land masses along the path. This tool is integrated into the main interactive software that waveform analysts use at the IDC and gives analysts a binary answer on the blockage status of a path. The second interactive tool that was developed specifically for hydroacoustic processing is the Hydroacoustic Azimuth Review tool (HART). HART is described in some detail in Le Bras (2000) along with other aspects of augmenting the initially purely seismic processing system with components specifically adapted for hydroacoustic data. It allows the analysts to review the automatic back-azimuth calculated on groups of two or three detections picked at separate hydrophones of a triplet and estimate it for newly formed groups where detections may not have been made automatically at one or two of the hydrophones of the triplet. In addition to these two specific tools analysts have access to spectrograms which are of special value for analysing hydroacoustic data and for getting a better understanding of whether a particular signal originates from an in-water or underground source. On rare occasions where very specialized tools, such as for cepstral analysis, are needed, analysts can also access the general purpose and flexible tool Geotool (Coyne and Henson 1995). The results of analyst reviews are preserved in the Late Event Bulletin (LEB) database.

4.5. Post-Analysis Processing and Event Screening

After analysis, another phase of automatic processing is performed on the reviewed waveform data with the benefit of improved LEB parameters following the review by the IDC analysts. These steps include the filtering of the LEB into the REB. This step is performed using a weighted count per event that adds up all features contributing to the calculation of the location with weight coefficients depending on the type of the feature (time, slowness, azimuth) and the type of the station (seismic array, three-component seismic, hydroacoustic, infrasound). Auxiliary seismic stations have zero weight and their features, while they contribute to the location of an event, are not contributing to the weighted count computed in this filtering. Outside of exceptional cases of interest, a seismic event will need to consist of at least three stations to be included in the LEB, while a purely hydroacoustic event, or a purely infrasound event can be included when detected at two stations, if directional information is available.

5. HIGHLIGHTS IN ADVANCEMENTS OF AUTOMATIC HYDROACOUSTIC DATA PROCESSING OVER 25 YEARS

This section highlights the improvements to the hydroacoustic component of the processing system and the studies conducted to better understand possible further improvements in the processing.

Since the stations have been contributing data for a long time, experience using the system has been acquired and many events of special interest have been recorded by the system. A few of these events are presented later in this section. They include a summary of the analysis of the event related to the loss of the ARA San Juan submarine in 2017.

5.1. Upgrade of the Ocean Environmental Parameters

The physical properties of oceans vary with the seasons and propagation characteristics are affected by these variations. To capture at least the major variations, travel time and transmission loss tables were re-actualized around 2006 using the KRAKEN model (Porter 1992) and seasonally

varying oceanographic information. More information is available on the improvements made to the hydroacoustic part of the IDC system in Graeber et al. (2006). Due to export control restrictions, the source code for the main signal processing library for hydroacoustic data was not included in the R3 release. It was reverse engineered to comply with the IDC requirement that all source code should be available at the IDC and distributable to all States Signatories, and the software built from the version available at the IDC. Graeber et al. (2006) summarizes the improvements made prior to 2006 which included improvements to the calculations of several features.

Table 5. Features Used to Classify Single Hydrophone Detections as H, T or N Based on Rules and Thresholds Shown in Figure 4.
Note that Five out of Seven of These Parameters Necessitate Attributes Be Computed for Low Frequency Band

| Attribute and Unit	Definition or Comments
Number of frequency bands	As of 2021 attributes are computed for eight frequency bands for hydrophones and T phase seismometers. The bands differ between the station types. It is sometimes not possible to compute the features for all frequency bands
Thinness (dB)	Average overall available frequency bands of (peak_level - total_energy), both in dB
Energy Ratio (dB)	total_energy in the HFB - total_energy in the LFB
Time Spread (seconds)	Time spread in the LFB
Crossing Density (second^{-1})	(num_zero_cross / Duration) in the LFB
Fractional Time	(total_time / Duration) in the LFB
Duration (seconds)	(termination_time - onset_time) in the LFB

5.2. Tuning of Station Processing

Further improvements to station processing were made by tuning the parameters, including enlarging a frequency processing band to enhance automatic phase identification, and increasing the number of frequency bands used. Tuning of rule based phase identification based on extensive data analysis and the derived additional features resulted in fewer wrongly identified H phases that are truly T phases, and this had a beneficial impact on the automatic network processing as H phases contribute to the location of events and T phases do not. This resulted in fewer false events based on falsely identified H phases on hydrophone stations.

The parameters involved in the implementation of the rules presented in Table 5 and Figure 4 show the steps involved in the decision making process on the phase name for the detections based on the values of these parameters. The first step is to positively identify H phases when features can be computed on a sufficiently large number of frequency bands and the 'thinness' parameter, defined in Table 5, is positive. This step was introduced at the IDC and proved to be important in limiting the number of H phases in order to not overwhelm network processing. The second step involves the three parameters energy ratio, time spread, and crossing density to positively identify T phases. The third step involves the additional two parameters fractional time and duration and positively identify N phases if the conditions shown in Figure 4 are met. The detection is also identified as an N phase if any of the five parameters are missing in all frequency bands. Finally, if no identification has been made after these four steps, the detection is assigned type H. The threshold values listed in Figure 4 have been in use since December 2021.

There have been attempts to go beyond the rule based method for phase classification and explore the use of more modern classification methods, for instance Neural Net and Support Vector Machines which Tuma et al. (2016) explored. These approaches showed promise and may be applied in the future.
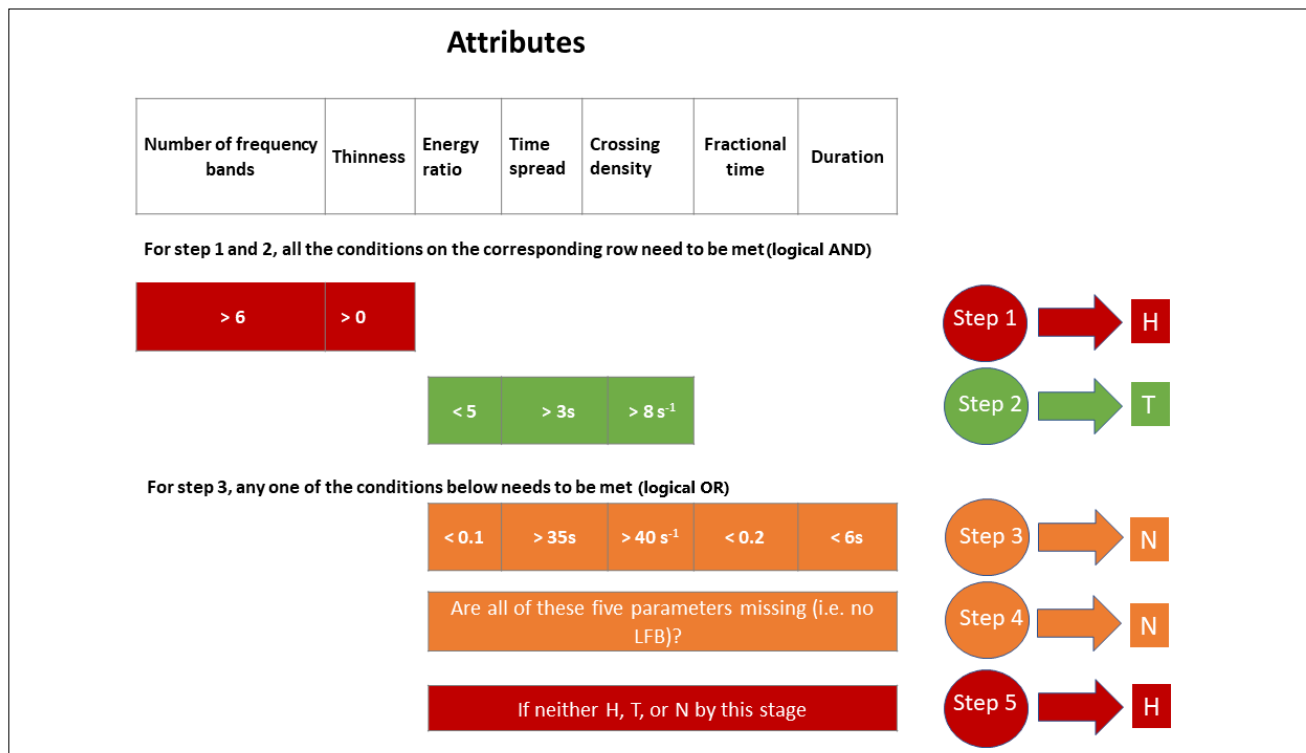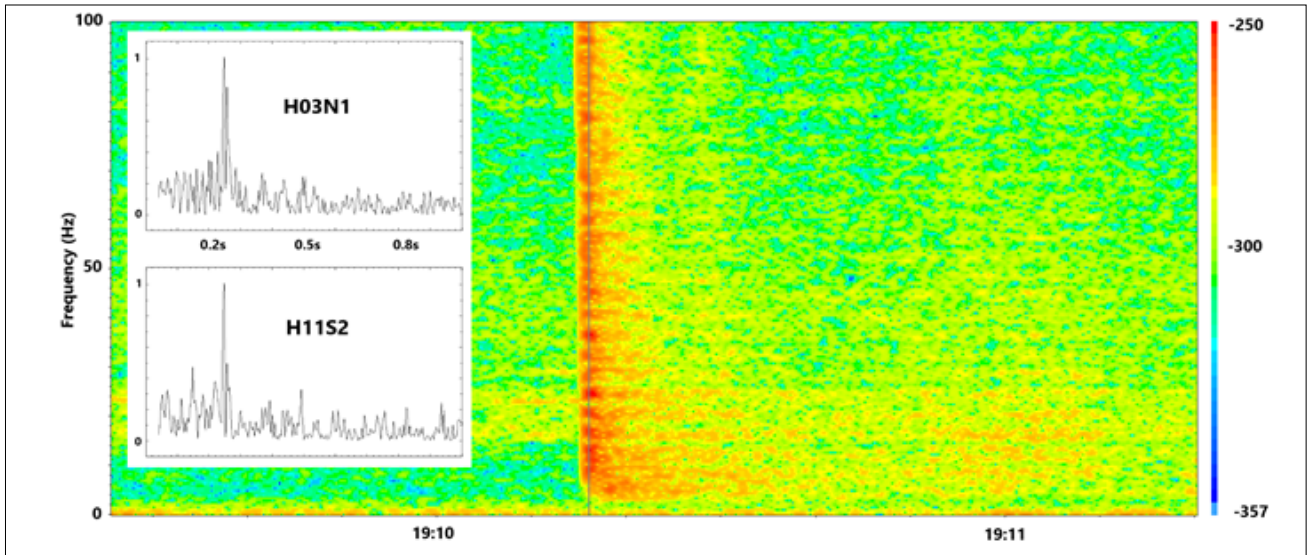
FIGURE 4.
Rule based classification of hydroacoustic detections into H, T and N on each individual hydrophone trace.

At this stage, a few illustrative real examples are presented as the results of applying this classification scheme. Figure 5 shows the spectrogram at hydrophone H3N1 around a detection identified as an H phase generated by a likely explosion of unknown origin located less than an arc degree of distance (about 111 km) away from station HA3 (see Figure 1). In that case, the H phase is broadband, all eight frequency bands are computed and available in the database and its classification as an H phase is due to its positive thinness parameter as determined in the first step of the rule based classification method (see Figure 4). In addition, scalloping of the frequency spectrum is quite apparent on the spectrogram. To confirm that this could be due to a delayed bubble pulse, the cepstrum was computed for this trace and one trace (H11S2) at station HA11 (see Figure 1) which also recorded the likely explosion at a distance of 120.7 degrees. The cepstral peak recorded for this detection has a delay of 0.244s in the broadband [2 80] Hz (parameter cep_delay_time_signal in Table 2) with an amplitude of 11.3 standard deviation above the mean (parameter cep_peak_std_signal). The event was also recorded at all HA11 hydrophones. At H11S2, the cepstral peak has a delay of 0.248 s in the broadband [2 80] Hz with an amplitude of 12.1 standard deviations above the mean. The other detections for this event have similar cepstral peaks, confirming that this feature is consistent for all recorded H phases from this event, indicating a common source, most likely an explosion.

Figure 5 shows the spectrogram of a portion of the H3N1 hydrophone trace. Note the narrow width of the arrival whose energy is mostly contained within 2 seconds. In this case the value of the thinness parameter is 7.1, which is positive, and the number of recorded frequency bands is 8, meaning that the H phase was identified in step 1 of the procedure illustrated in Figure 4. The insert shows the cepstrum of this signal and compares it to the cepstrum of the arrival at H11S2. Note how the cepstral peak around 0.24s predominates in both cepstral and that the delay is the same at a distance of 0.6 and 120.7 degrees from the source. Figure 6 shows an example of a T phase recorded at the same hydrophone on the same day as the explosion shown in Figure 5, originating from an IDC mb=4.3 event in the region of Tonga Island,
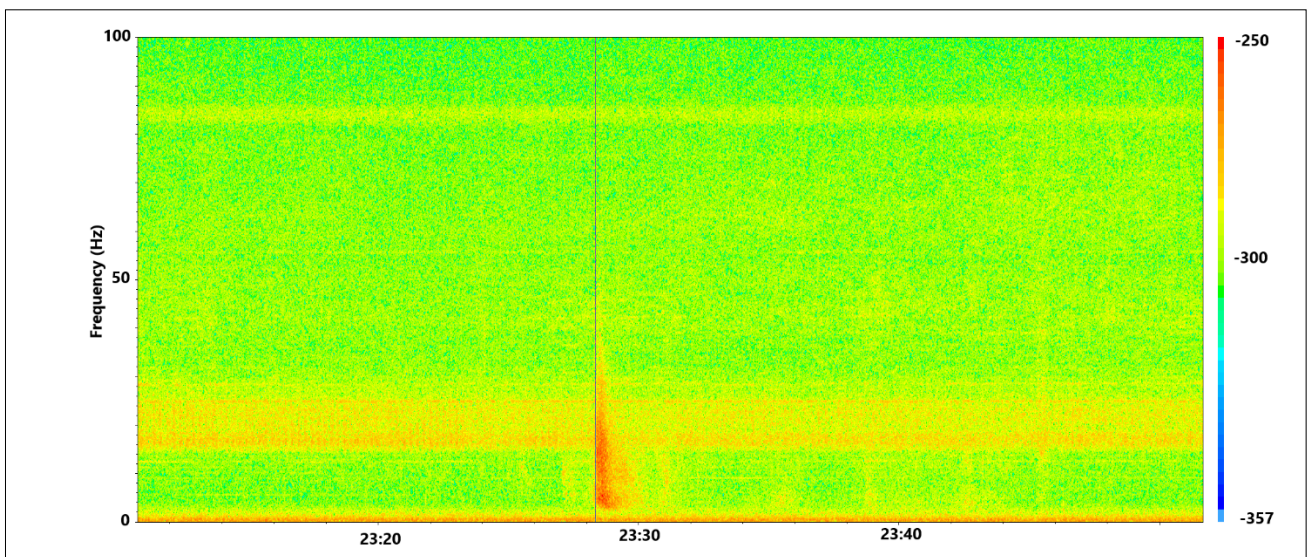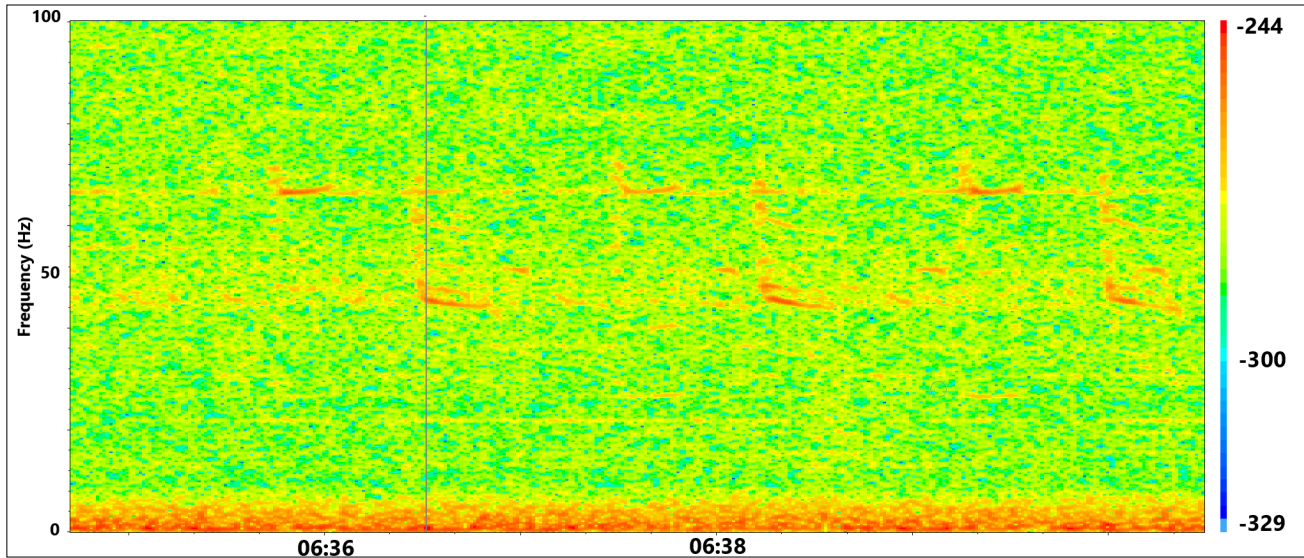
Pacific Ocean. Note that this signal is of longer duration and that the energy is concentrated at lower frequencies than for the H phase example in Figure 5. This event does not show signs of a delayed bubble pulse and therefore minimizes the likelihood for an in-water explosion (H phase). This phase is associated with an earthquake in the Tonga Islands area, confirming that the source is underground, and that the energy recorded at station HA3 has coupled into the ocean from an area close to the source and propagated a long distance in the sound fixing and ranging (SOFAR) channel.

To complete the examples of hydroacoustic phases, Figure 7 shows a spectrogram where two N phases were identified automatically on 24 February 2018. The N detections appear at 06:36:31 and 06:38:16 UTC (Coordinated Universal Time). In this instance, the signals are biological noises, likely from blue whales (McDonald et al. 2006). N phases for many kinds of noise sources can be detected. Figure 8 shows an example of the passage of a ship, giving rise to the Lloyd's mirror effect.
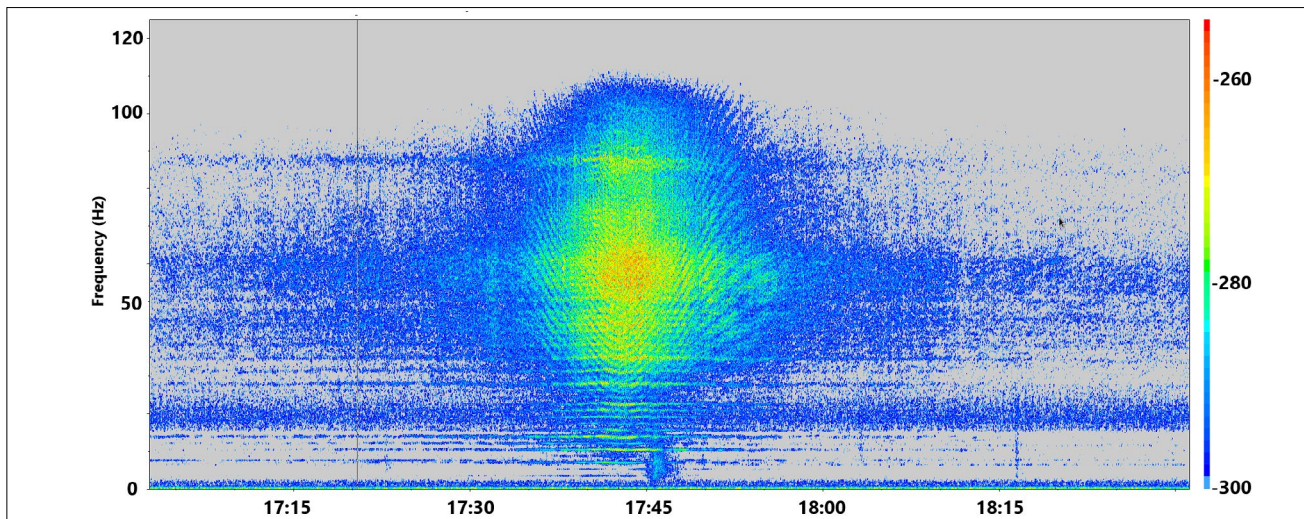
FIGURE 7.
Spectrogram containing two N phases (at 06:36:31 and 06:38:16) detected automatically on the northern triplet of station HA4 on 24 February 2018.

FIGURE 8.
Spectrogram containing an N phase just before 17:45 detected automatically on the southern triplet of station HA11. Clearly seen on this example are the U-shape fringe patterns caused by the interference of the direct and surface-reflected sound waves. This is known as Lloyd's mirror effect.

5.3. Slowness Measurement on Hydrophone Triplets and Seismic Phases Identification

The introduction of coherent processing of hydrophone triads (HASE) to simultaneously estimate the back-azimuth and the apparent wave speed for H, T, N and P (seismic) phases is one of the major enhancements to the processing of hydroacoustic data. The initial cross-correlation based implementation of the HAE module (see Figure 3) estimated only the azimuth. The introduction of the slowness is explained in detail in Graeber et al. (2006) and Graeber (2007). This enhancement allowed automatic detection of the seismic phases observed on hydrophone triplets as these phases have a vertical propagation component and have a smaller slowness value compared to the close to horizontally propagating hydroacoustic phases, which are observed to span a narrow slowness window.

Table 6 shows the features used for the criteria listed in Table 7 and applied to make

the decision on the phase type for the group of arrivals. The frequency bands where the features are computed are not necessarily the same as the ones for DFX listed in Table 4. Figure 9 shows the result of the analysis on one day in 2021 at station HA3 (see Figure 1), displayed on a polar graph, where examples of all phase types are present. That day presents an example of a P phase and several H phases on the southern triplet. The spectrogram of the hydrophone trace around the P phase is shown in Figure 10. The red shaded zone is the reject band and the orange shaded zone the slowness zone for seismic phases. The detected signals are naturally separated between horizontally propagating H, T, N and P phases with a near vertical incidence at the station. The smaller symbols are for groups with two hydrophones only while the larger ones are for groups with all three hydrophones. Figure 10 shows the spectrogram of one of the hydrophone traces where a P phase was identified.

Table 6. Features Used to Classify Detection Groups on Hydrophones as Hydroacoustic or Seismic

Attribute and Unit	Definition or Comments
VLFB (dB)	Energy in the very low frequency band. Currently [1-3 Hz]
MFB (dB)	Energy in the medium frequency band. Currently [4-12 Hz]
S (s/degree)	Slowness

Table 7. Decision Criteria to Classify a Detections Group as Either Seismic or Hydroacoustic Based on Slowness and Frequency Distribution of Energy

Type of Phase for Detections Group	Energy Ratio (dB)	Slowness S (s/degree)
Seismic	(VLFB – MFB) > 12	S <= 30 s/degree Velocity of 3.7 km/s
Hydroacoustic	N/A	S >= 70 s/degree Velocity of 1.6 km/s
None (rejected)	N/A	30s/degree < S < 70s/degree
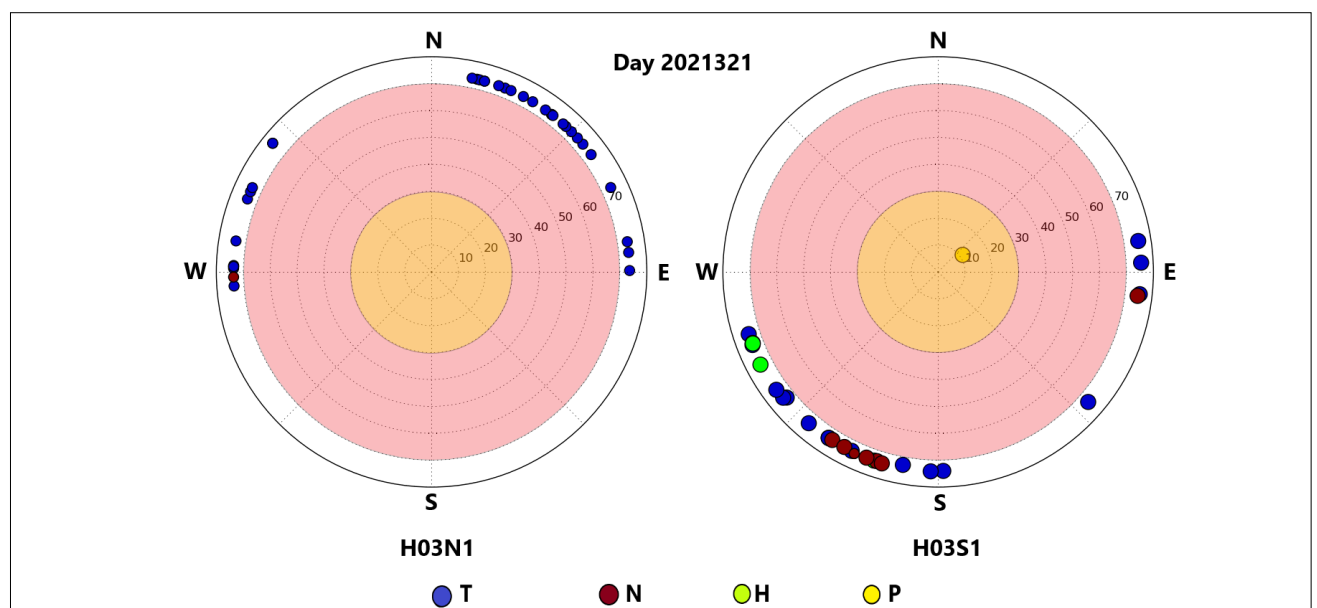
FIGURE 9.
Polar coordinate display of the seismic (<=30 degrees/s), hydroacoustic (>=70 degrees/s), and reject (30-70 degrees/s) slowness bands as implemented in December 2021. The examples are from one day of data (Julian day 2021321, 17 November 2021) at the North triplet (left) and South triplet (right) of the HA3 station.
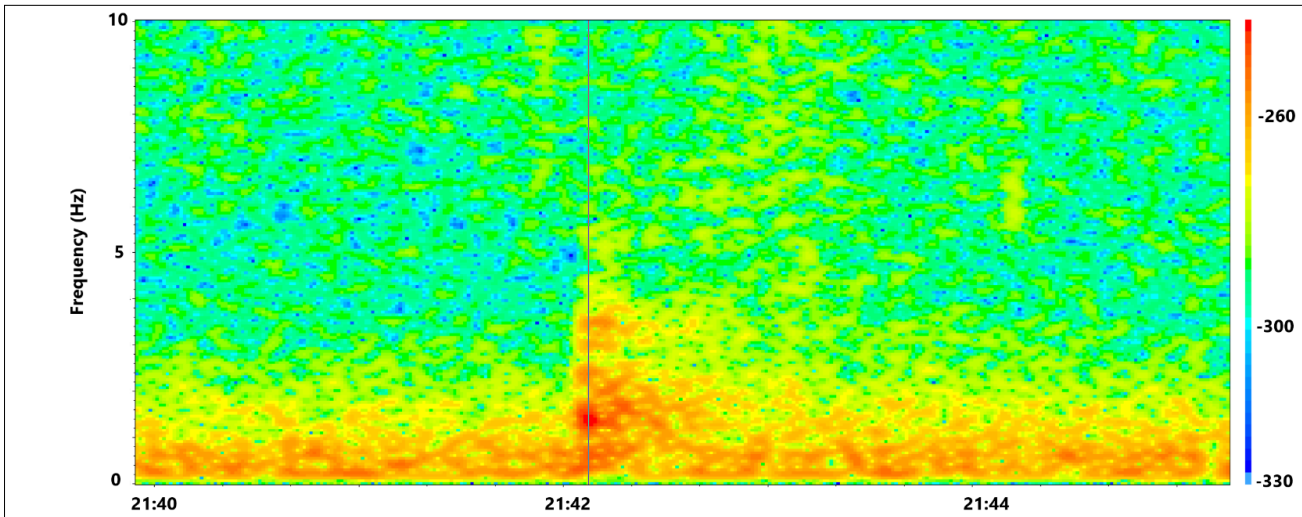
FIGURE 10.

Spectrogram and trace of a P phase recorded automatically on hydrophone H03S1 of station HA3. Note that the initial identification by StaPro of this detection was as an N phase, while the detections on other two hydrophones (H03S2 and H03S3) were identified as a T phase. It was re-classified as a P phase after grouping and new phase assignment by HASE, because of the estimated value of the slowness (11 s/degree).

5.4. Observations About Blockage and In-Water Explosions

A large amount of data has been acquired and significant experience has been gained over the past decades in the processing of hydroacoustic data. It is clear from observations and from running more sophisticated models than the one currently in use, that the modelling of propagation, particularly of blockage, could be improved. The event location algorithm used among other modules in the Global Association network processing algorithm still uses a very simple model with two dimensional (2-D) blockage maps, which do not accurately represent the reality where diffraction and refraction can occur. Hydroacoustic arrivals can be observed beyond the areas defined by this simple model. Figure 11 shows an example of diffracted arrivals which were observed at the HA10 station (see Figure 1) from earthquakes close to the South Sandwich Island. They were detected because of three dimensional (3-D) propagation effects justified by high fidelity 3-D modelling of ocean global-scale signal propagation (Heaney et al. 2017).

A typical number of detections using the PMCC algorithm (Cansi 1995) at H10N for 24 hours of acquisition is shown in the lower panel of Figure 11, with a distribution centred around azimuths of 194.5° and 199.5°. The black line shows the minimum water depth along 500 km long radial section originating at the station and centred around the South Georgia Island. The detection of signals originating from behind the island and appearing blocked by it when considering geodetic paths can be explained by 3-D diffraction of the signals. The underwater acoustic path is close to blocked for azimuths between 194.5° and 199.5° by the South Georgia Island and its underwater plateau, however relatively narrow trench-like underwater acoustic paths around these azimuths allow propagation around the South Georgia Island. The current automatic system does not take these paths into account and does not associate the detections to the earthquake sources which generate the detections.

These observations prompted the further modelling of this phenomenon of diffraction using 3-D computation of underwater signal propagation. These are presented as transmission loss maps at 5 Hz using a parabolic equation combined with split-step Fourier approach to numerical modelling. Figure 12 shows an example for the southern Atlantic area between station HA10 and the South Georgia and South Orkney Islands (Nielsen et al. 2021a). The method of
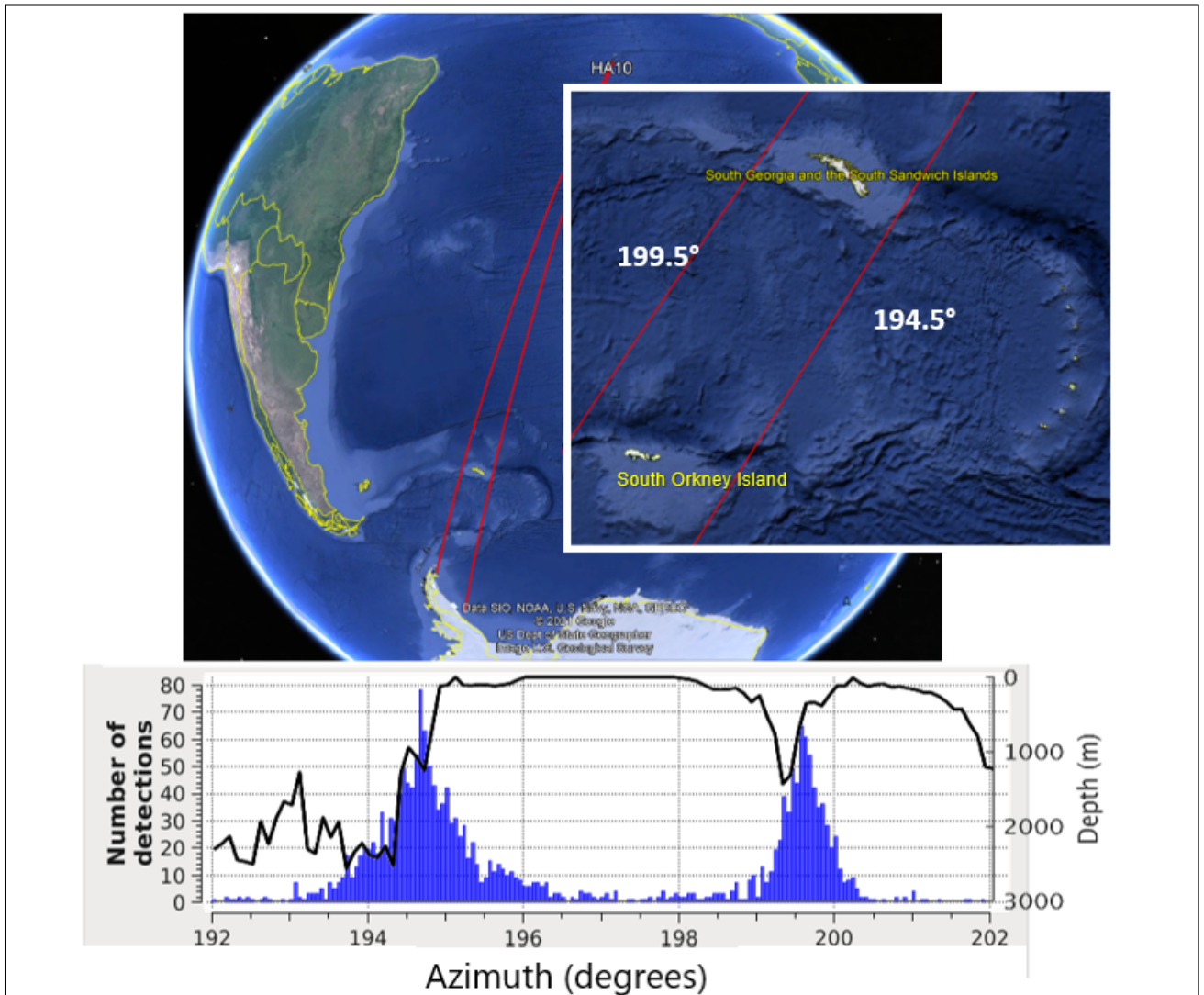
FIGURE 11.
The large map shows two geodesic paths (in red) between HA10 and the Antarctic Peninsula, skirting the South Georgia Island, with azimuth 194.5° to the east of the island and 199.5° to the west. The smaller map shows the area of South Georgia and South Orkney Islands with the two paths. The graph at the bottom shows the histograms of the number of detections as a function of azimuth at the H10N triplet superimposed on the bathymetry.

modelling the 3-D underwater signal propagation by solving the parabolic equation is explained in more detail in Lin et al. (2013) and Kushida et al. (2019).

At least 32 events from 2006 to 2014 were detected and stored in the SEL3 bulletin although they fall on the line-of-sight blockage by the South Georgia Island (white dots beyond 6000 km in the middle panel of Figure 12).

Diffraction of sound around South Georgia can make T phase arrivals visible at H10N when blockage based on 2-D computations predict they would not be seen (middle panel) (Heaney et al. 2017, Nielsen et al. 2021a). This has the potential to enhance the automatic processing and get a more accurate blockage map, transmission loss, and travel time map for the analysts.
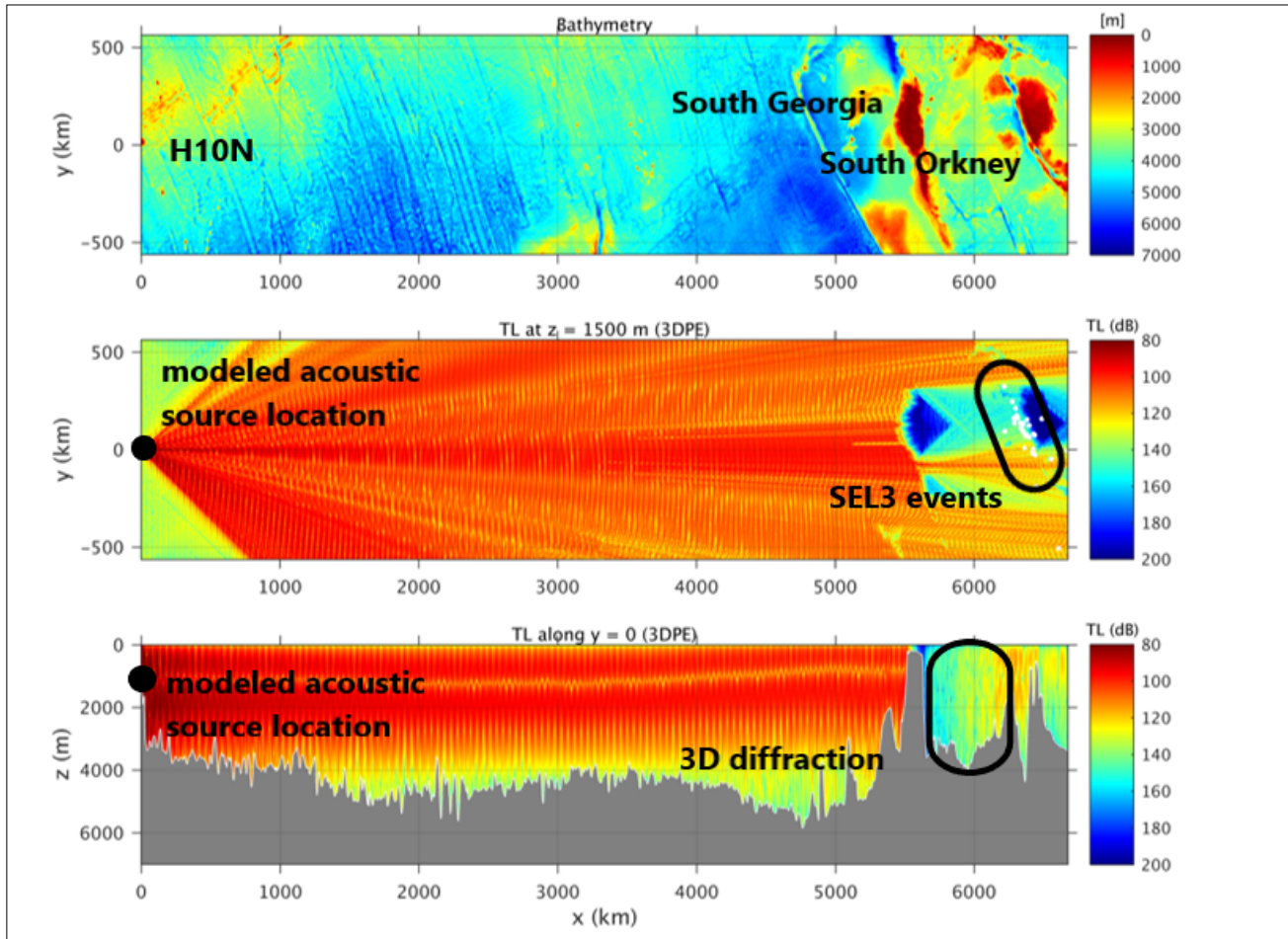
FIGURE 12.

The top panel shows the GEBCO (2021) bathymetry on cartesian coordinates from station HA10. The horizontal axis is a geodetic path from the centre location of the H10N triplet to a location close to South Orkney Island 6850 km away. The centre panel shows the value of the transmission loss over the grid at a depth of 1500 m and the bottom panel is the transmission loss on a vertical section along the horizontal axis. Note on the vertical section the consequence of the shallowing of the SOFAR channel at higher latitudes that manifests itself with the shallowing of the zone of lower transmission loss values. Calculations were performed using the COPERNICUS (2021) environmental parameters.

5.5. Experience with Progressive Multichannel Cross-Correlation on Hydroacoustic Data

The enhancements made to the HASE module for hydrophone triplets processing allowed the obtention of more complete directional information that includes the slowness, using cross-correlation on waveform segments around detections that are made by DFX. The complete waveforms of the triplets are not processed jointly as an array by HASE. In contrast, the PMCC module (Cansi 1995, Cansi and Klinger 1997, Mialle et al. 2019), conceived for infrasound arrays processing, can be adapted to the hydroacoustic data type by choosing the appropriate frequency and correlation windows. The PMCC software package allows for two modes: stand-alone, with a graphical user interface or integrated in the automatic system. The latter is used to routinely process the infrasound arrays in operations and was extended in 2018 to allow for processing of hydrophone triplets (Vergoz et al. 2021, Nielsen et al. 2021b). The results of using DTK-PMCC in the automatic system are being evaluated in a development environment. An example use of the stand-alone interactive module is shown in Figure 13. PMCC can be used in a flexible manner in interactive mode and includes many more features than HASE.

Note that the number of detections is 26 for H4N when using the PMCC algorithm compared
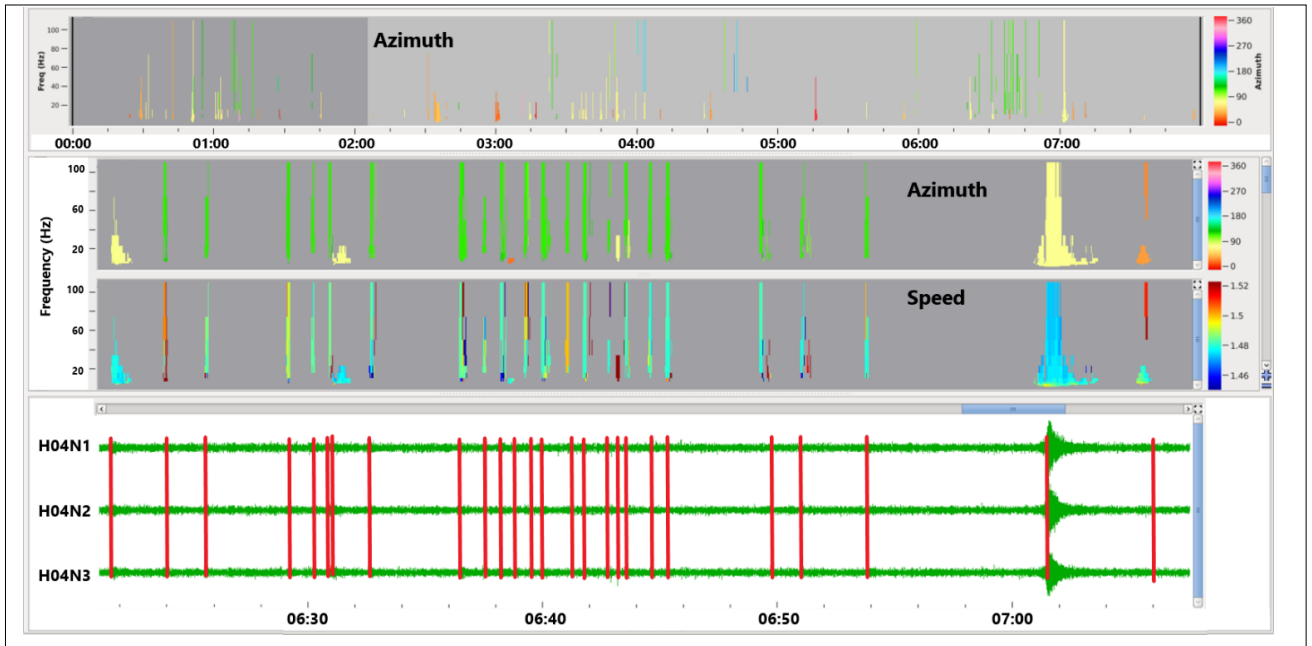
FIGURE 13.

The stand-alone version of PMCC, called DTK-(G)PMCC is delivered with a graphical user interface and an example of application on hydroacoustic data is shown here using the interactive software. The top panel shows the result of the PMCC analysis on an eight-hour segment on 24 February 2018. The vertical axis is frequency, and the detections' azimuths (degrees from North) are colour-coded. The two centre panels show a 40-minute close-up of the same results (top) and of the detections' colour-coded apparent speeds (km/s). The lower panel shows the three hydrophone traces of the H4N triplet on the close-up time window. The red bars show the 26 detections made by PMCC in the 40-minute window. Note that the detections use all three hydrophones simultaneously.
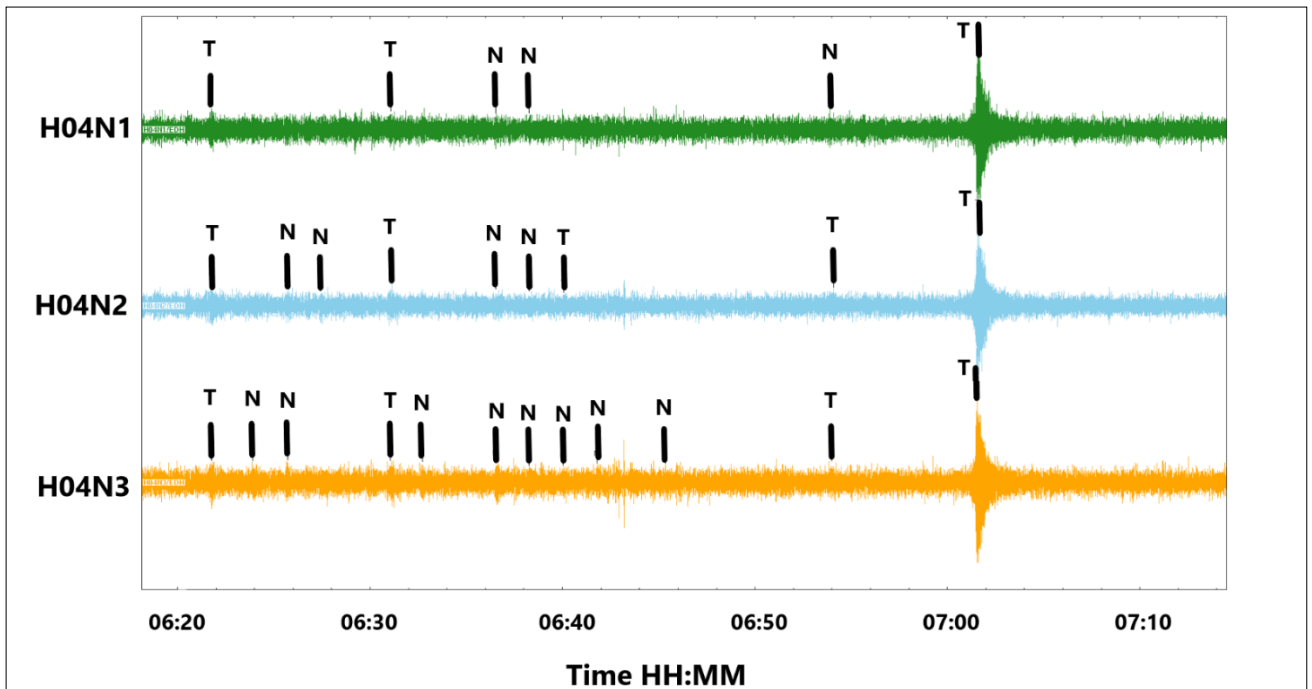
FIGURE 14.

Waveforms for the same time interval as in Figure 13, along with standard automatic detections on each of the hydrophone traces. Note that, because detections are made on each hydrophone, using an STA/LTA method, detections are not necessarily made at exactly the same time on all hydrophones and the number of detections is different for the three hydrophones. Furthermore, some detections that manifestly belong together, such as the ones identified as N on H4N1, and T on both H4N2 and H4N3 around 06:54 do not necessarily classify as the same phase.

to 12 for H4N3, 9 for H4N2, and 6 for H4N1 using the current system, as shown in Figure 14. Furthermore, the estimates of azimuth and slowness are available for all 26 detections whereas only six of the standard detections are seen on all three hydrophones of the triplet and have reliable azimuth and slowness estimate. The two methods are different, and the threshold could be adjusted in PMCC such that the total number of detections is comparable with the standard method, however there might be some benefit in keeping more detections with better parameters.

5.6. Hydroacoustic Detections for the Announced Democratic People's Republic of Korea Large Nuclear Test on 3 September 2017

As of December 2021, the largest announced nuclear test conducted by the Democratic People's Republic of Korea, named DPRK6, occurred on 3 September 2017. The test was large enough that seismic signals were visible on some of the hydrophone stations even though there are no hydroacoustic clear paths to the station from the test site (Nielsen et al. 2018). The P phases from

this test were recorded automatically at stations HA1 and HA11 and automatically associated to the SEL3 origin. The P wave signals at HA8 and HA3 were added by the analysts as part of a special study.

Adding the two additional hydroacoustic stations allowed for a location to be performed using only these four hydroacoustic stations. Figure 15 shows the location of the stations detecting (or not) the P phases from this test and Figure 16 shows the waveforms and spectrograms for the P phase at station HA1 and HA8.

The result of this is shown in Figure 17, and as it can be seen on that map, the error ellipse obtained from using only the four hydrophone stations was, as expected, larger than the REB error ellipse, but the REB error ellipse was wholly contained within the hydro-only error ellipse and the location of the DPRK6 event was only 27 km away from the REB location. In addition to adding seismic detections at hydrophone stations, there is good evidence that the HA11 station also recorded a phase that coupled to the ocean offshore of Japan and was recorded as a T phase at the station.
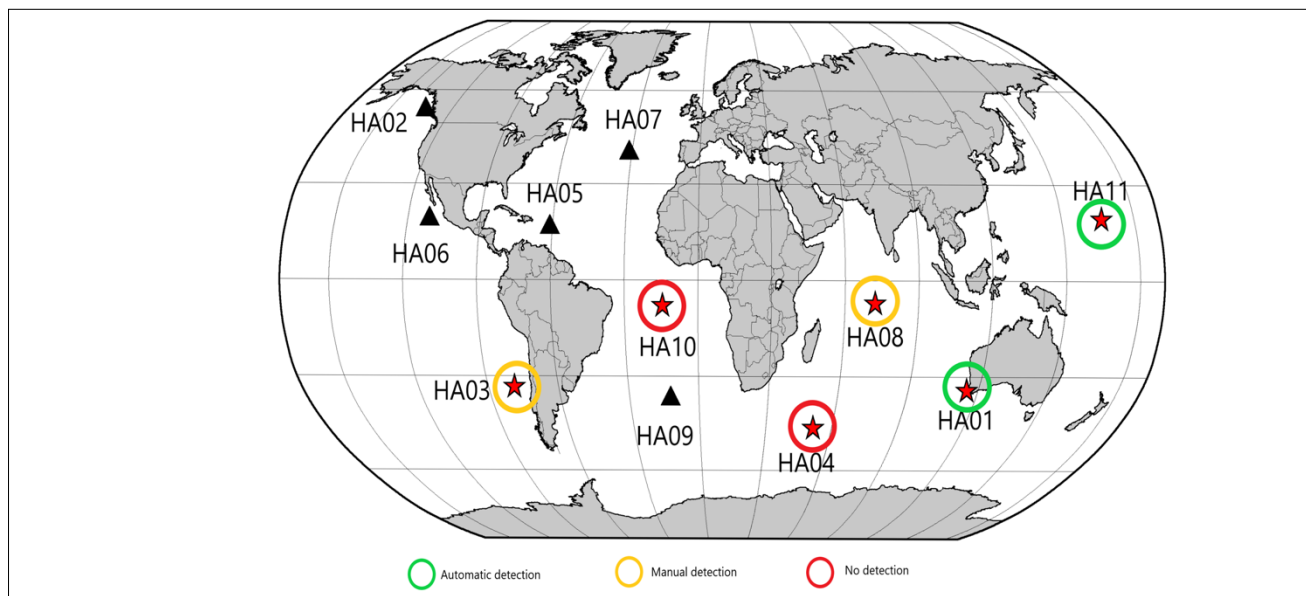
FIGURE 15.

Map of the hydroacoustic in-water stations marked by red stars. The green circles around the station symbols indicate that the P waves were associated automatically to the SEL3 event. The yellow circles indicate that the analysts added the P associations at the stations while the red circles indicate that no detections were made either automatically or manually.
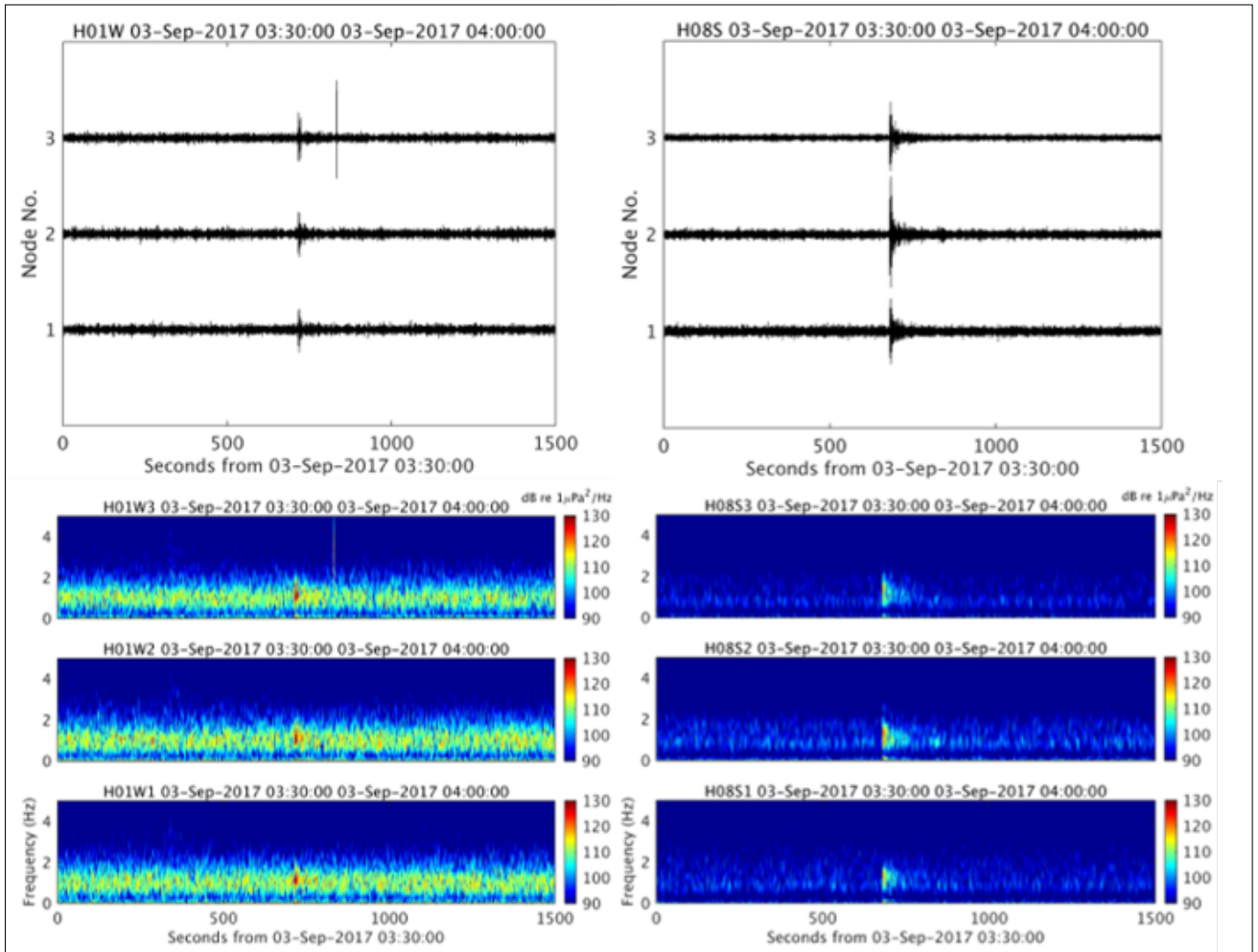
FIGURE 16.
Spectrograms of the hydrophone traces at HA1 and HA11 that recorded the P phase from DPRK6. The traces are filtered using a 3rd order Butterworth bandpass filter in the band 0.8-4.5 Hz (seismic band).
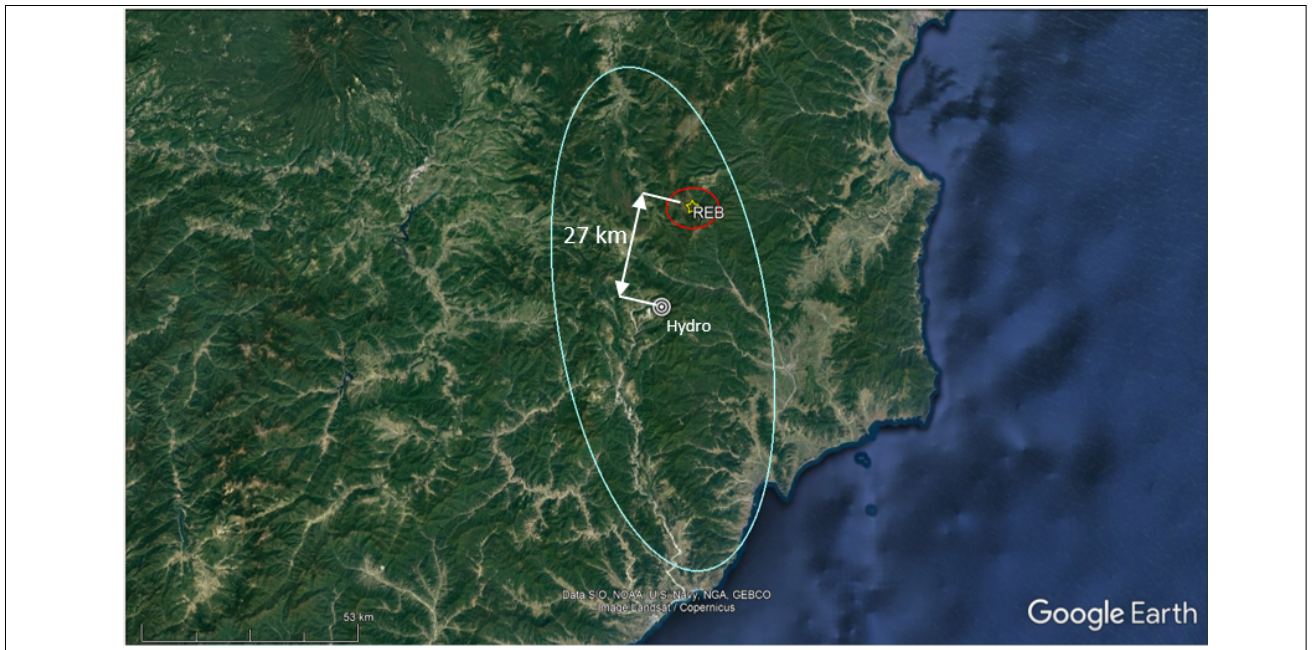
FIGURE 17.
Map showing the error ellipse (in red) for the REB location of DPRK6, the error ellipse obtained using the four in-water hydroacoustic stations (in cyan).

5.7. Integration of Hydroacoustic Processing into NET-VISA

Network processing has been undergoing a major upgrade prompted by examining the possibilities offered by machine learning approaches in improving on the current Global Association system. The problem of grouping detections from several stations into sets that are common to the same source is challenging for several reasons: travel time between any two points on Earth and the attenuation of various frequencies and wave types are not accurately known; each detector is subject to local noise that may mask true signals and cause false detections; thousands of detections are recorded per day; multiple possibilities of associating a detection to different events exist, especially for detections at teleseismic distances due to the low spatial density of the IMS network. These reasons demonstrate the problem of proposing and comparing possible events by grouping subsets of detections is daunting. It was suggested that an approach based on probabilistic inference and combinations of evidence might be effective, and early tests of the Bayesian global signal associator NET-VISA (Arora et al. 2013) proved to be promising. NET-VISA was extended to include hydroacoustic together with seismic (Arora and Prior 2014, Le Bras et al. 2020). NET-VISA uses physics-based probabilistic models and a heuristic inference algorithm. Its basic components are a generative model and an inference algorithm.

The generative model for the calculation of amplitude includes geometrical spreading and adsorption in water. The frequency of detections is modelled through a Poisson distribution and in-water events generating hydroacoustic H phases, since they are very scarce in the data. The rate of occurrence for the distribution is increased to one event per hour compared to a rate of 4.6 events per hour for seismic events.

In the case of hydroacoustic technology, the priors used as of January 2022 are static. The time, slowness and back-azimuth residuals are modelled as Laplace distributions whose parameters are derived from the large set of reviewed events. Because of the scarcity of archive data available for learning, the priors are computed on a longer time period than the seismic in order to improve the statistics. In addition to the time, azimuth and slowness that are also used in the seismic case, hydroacoustic parametrization of arrival attributes and priors include:

- The energy (in dB re. Joules/m2/Hz) in the 6-12 Hz band.
- A modified probability of detection that includes the probability that the path between the event and the station is blocked (see Figure 18).
- The fraction of time that the signal spends above the detection threshold versus the total duration of the signal measured in the 6-12 Hz frequency band. This is modelled as a beta distribution.

The inference algorithm considers all possible combinations of arrivals that maximize the likelihood of a set of hypothesized events.
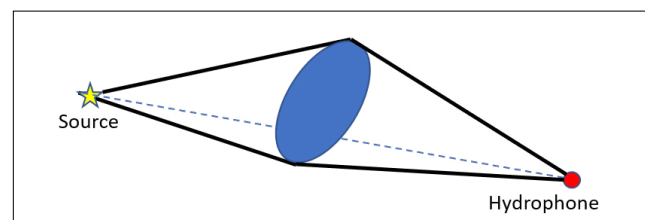
FIGURE 18.

The probabilistic model for handling blockage is more sophisticated in NET-VISA than in the rest of the IDC system. Instead of considering only direct arrivals from potential sources, NET-VISA allows the possibility of out-of-plane diffracted arrival, where the probability of detection decreases exponentially with the out-of-plane angle (Arora and Prior 2014).

NET-VISA has been used operationally since January 2018 as a complement to the Global Association. Once analysts have reviewed a time block of the SEL3 automatic bulletin, access to additional events in the VSEL3 bulletin, formed by NET-VISA using the same detections as the ones available to the Global Association at the time where the SEL3 bulletin is produced is available. These additional events do not have any detections in common with SEL3 events. It is possible to keep track of the provenance of the events in the REB bulletin, and about 10% of the analyst reviewed events originate from the VSEL3 bulletin.

5.8. Oceanographic Modelling for Hydroacoustic Processing

Mesoscale (10-100 km spatial scale) oceanographic eddies are known to impact ocean acoustic signal propagation. Figure 19 shows an example at the southern tip of Africa. The spatial and temporal behaviour of eddies are predictable by global sophisticated oceanographic models (Heaney and Campbell 2016). These predictions are computationally intensive and may require nesting to obtain sufficient resolution. The presence of eddies and their oceanographic properties predicted by the
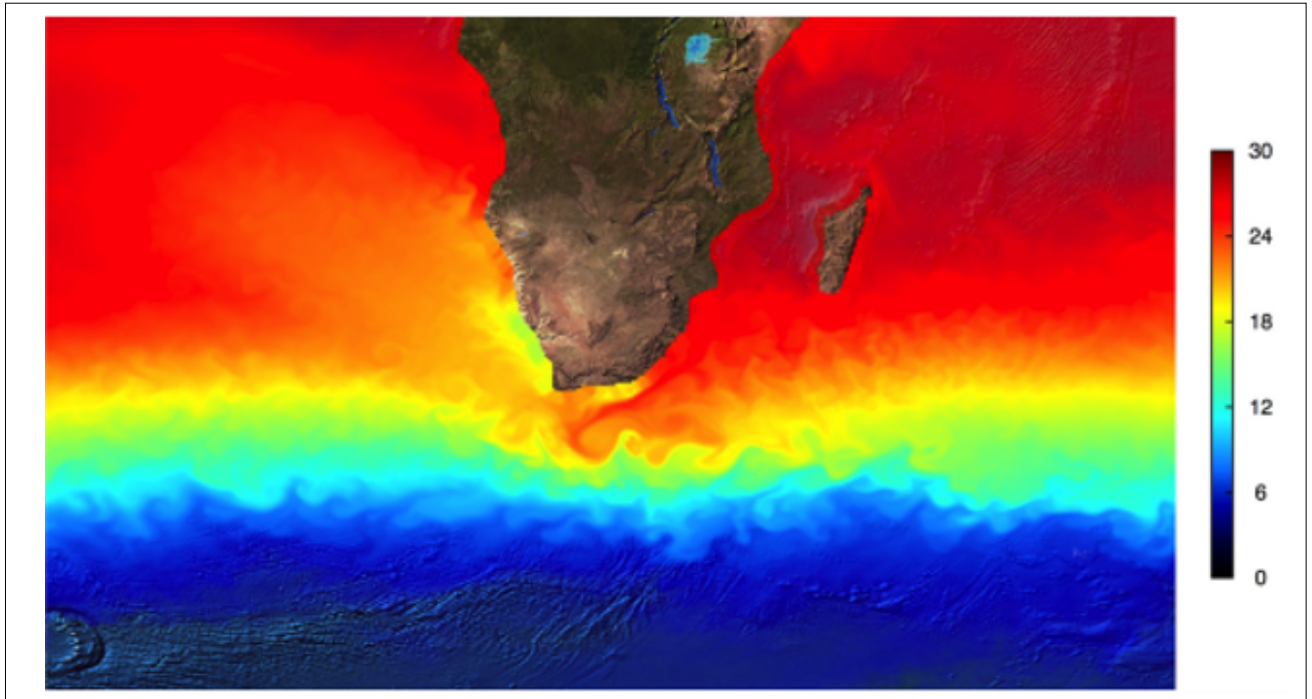
FIGURE 19.
ECCO2 (Menemenlis et al. 2008) Sea Surface Temperature in degree Celsius in the South Atlantic, South Indian Ocean, and the Southern Ocean. Note the clear eddies at the southern tip of Africa.
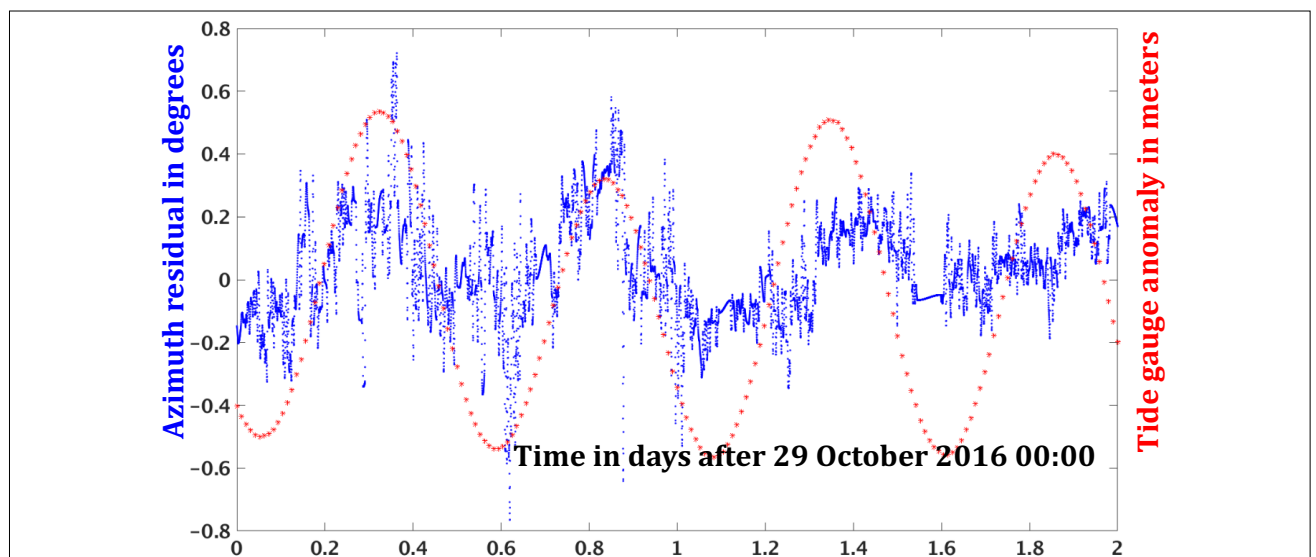
FIGURE 20.
After removing the azimuth-dependent trend and interpolating the data to a uniform 15s, there appears to be a cyclical trend within the azimuth residuals at station H3N. The red stars are tide gauge measurements anomaly (measured minus average) taken at Deep-ocean Assessment and Recording of Tsunamis (DART®) station 32404 in the same general area, showing the cyclical 12 hours 25 minutes cycle (Bernard and Meinig, 2011). The tide gauge data is time-aligned by hand to best fit the azimuth residuals.

complex oceanographic modelling efforts are essential input to global scale 3-D acoustic signal propagation models to predict arrivals at IMS hydroacoustic stations.

The oceanographic models also predict ocean currents which may cause cyclic movements of individual hydrophones in the hydroacoustic triplets, since the hydrophone are tied to floating devices anchored to the bottom of the ocean through a long riser cable. Accurate knowledge of local ocean currents may allow for corrections of temporally dependent locations of hydrophones in the IDC processing to improve the estimate of an event back-azimuth. This kind of motion was evidenced using frequent acoustic signals from a scientific seismic survey (Le Bras et al. 2019), recorded at H3N. It showed that the azimuth residual estimates exhibit a cyclical variation compatible with the action of currents around the triplet's location. While 0.5 degree of error

on a back-azimuth may appear like a small value, hydroacoustic signals can propagate efficiently far away and at a distance of 90 degrees, this apparently small error in angle leads to a difference of about 55 km for a geodetic path.

5.9. Observed Three Dimensional Refraction and Diffraction of Signals

Signals of unknown origin were detected on 15 November 2017 in the vicinity of the last known position of the lost Argentine submarine ARA San Juan. A controlled explosion test conducted by Argentine Navy was detected on 1 December 2017, with source position and time information (Nielsen et al. 2018, Nielsen et al. 2020). The 15 November signal and the 1 December test source were both detected on CTBT IMS hydrophone stations HA10 and HA4. Figure 21 shows the location of the event, the two hydroacoustic stations HA10 and HA4, and the geodesic paths

FIGURE 21.
Map showing the locations of the last contact position received from the ARA San Juan and the location of the event detected by hydroacoustic stations HA4 and HA10 on 15 November 2017.

from the estimated event locations to the stations. Note that both stations are located at considerable distance (6000 km and 7700 km) from the event.

The 15 November signal was received on H10N and analysed using a PMCC processing algorithm (Cansi 1995, Cansi and Klinger 1997). This showed the potential of this software, used routinely at the IDC, to analyse infrasound data when it is applied to hydroacoustic data.

Figure 22 shows the sequence of ten late arrivals (paths 2-11) following the direct main arrival (path number 1) identified by analysing a 15-minute time window after the main arrival. Late arrivals are attributed to reflections off underwater bathymetric features (Vergoz et al. 2021, Dall'Osto 2019a and 2019b).

5.10. Modelling of Three Dimensional Refraction and Diffraction of Signals

The data gathered after the 15 November 2017 event associated with the loss of the ARA San Juan and the interpretation that the source was powerful enough to generate multiple refraction and diffraction arrivals for up to 15 minutes after the primary arrival following the geodesic propagation path was a motivation to simulate the 3-D propagation in the southern Atlantic basin.

Figure 23 shows the simulation of the signal propagation through a limited portion of the southern Atlantic basin using the 3-D parabolic equation modelling software SSF PE (Lin et al. 2013, Lin et al. 2019, Kushida et al. 2020). The acoustic signal propagates in the SOFAR channel, interacts with the Rio Grande Rise, and is reflected off the ocean bottom to pass the rise. The signal is again trapped in the SOFAR after the Rio Grande Rise (lower panel in Figure 23). The acoustic signal propagating in the ocean after the Rio Grande Rise is a combination of 3-D refracted and diffracted propagation paths. Refraction and diffraction can be observed from the top of the Rio Grande Rise (middle panel in Figure 23). Absorption of sound in the water is not included in the computations and should add around 25 dB to the shown transmission loss in Figure 23.
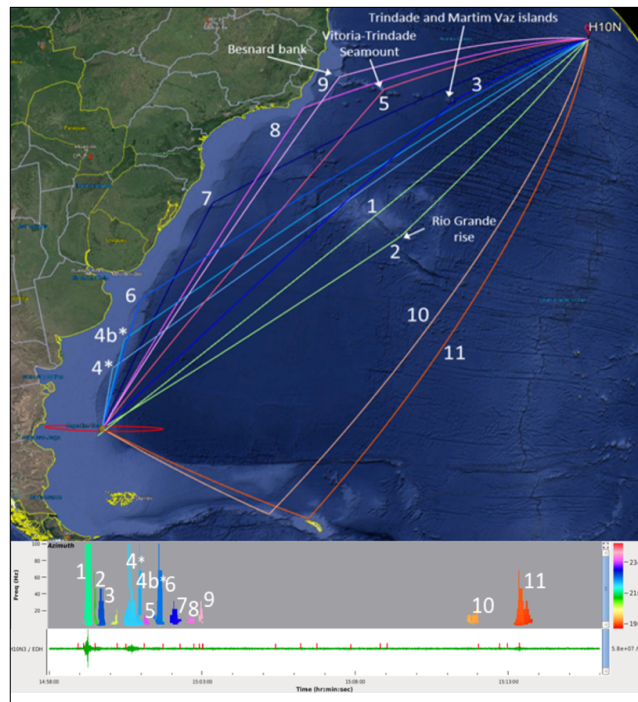
FIGURE 22.
The lower panel shows the results of processing the data from H10N, the northern triplet of HA10 with PMCC. The detections are colour-coded according to the value of the measured back-azimuth. Detections are labelled (1) to (11), (1) being the direct arrival. The map shows the interpretation of each detection as a path through the southern Atlantic basin. The features causing the refraction, reflection, or diffraction are identified thanks to the measured back-azimuth at HA10.

5.11. Signal Variability at Different Stations for the same Event

The hydroacoustic event on 15 November 2017 related to the disappearance of the ARA San Juan was well recorded at triplets H10N and H4S, however the waveform characteristics at these two stations are strongly influenced by the propagation paths. The sound profiles for the paths to the two stations are shown in Figure 24. Note that besides the longer propagation path to HA4, the path to H10N is for the most part in warm waters and exhibits a clear sound speed minimum roughly centred at a 1000 m depth which leads to a well-formed SOFAR channel, whereas the path to H4S is mostly in cold polar waters, with a minimum of the sound speed at the ocean's surface.

The differences in the propagation paths lead to differences between the signals recorded
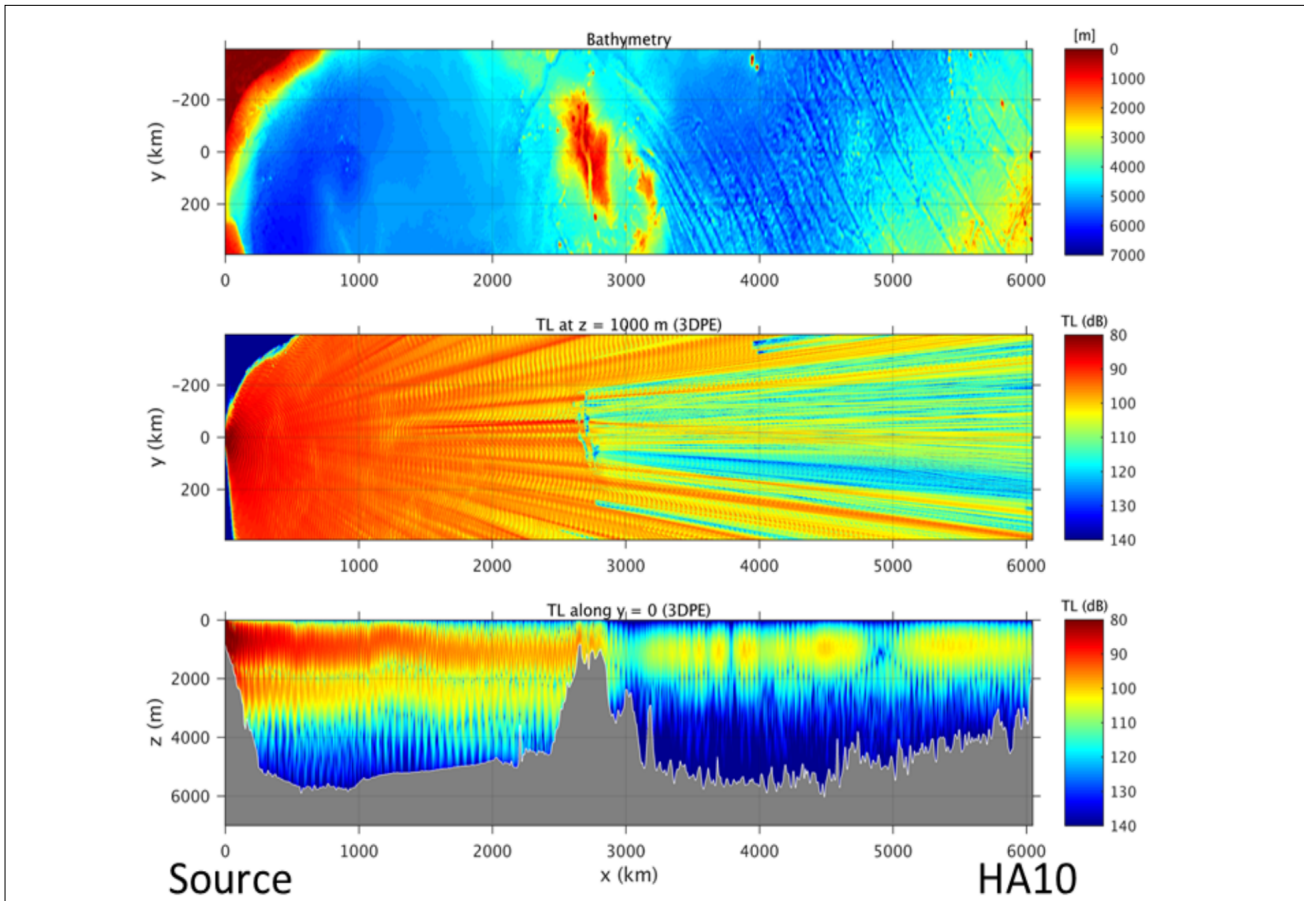
FIGURE 23.

3-D Parabolic Equation software SSF PE applied to modelling of the underwater sound propagation between the estimated location of the ARA San Juan and station HA10. The top panel is the bathymetry, the middle the value of the transmission loss on a horizontal slide of the ocean at 1000 m depth. The bottom panel is a vertical cross-section of the transmission loss on the geodesic joining source and station.
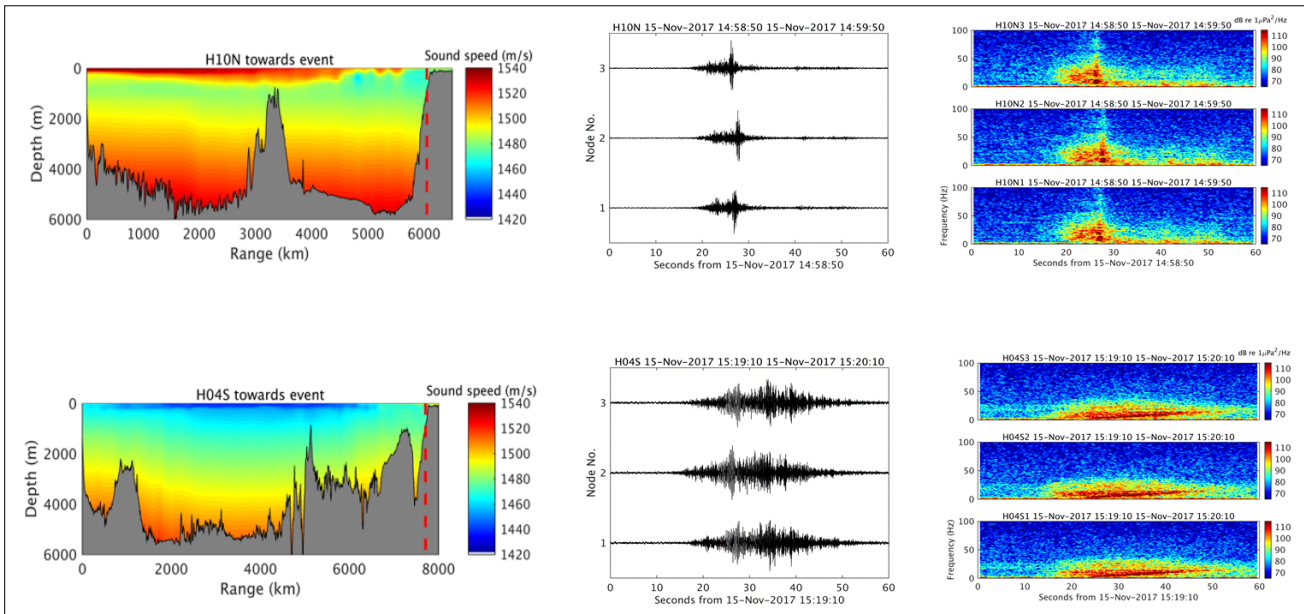
FIGURE 24.

The left side shows the sound profiles between stations HA10 and HA4 and the estimated location of the ARA San Juan. The middle panels are the observed raw waveforms at the three hydrophones of triplet H10N and H4S and the right panels are the corresponding calibrated spectrograms. The main differences are that the waveforms at HA4 are of longer duration and stripped of their high-frequency content compared to the waveforms at HA10.

at the two stations. The signal at H10N (and H10S) was correctly identified by the automatic system as an H phase emanating from an in-water event. The signal at H4S however was identified as a T phase according to the rules currently in place and explained in section 4.2 of this paper. The impulsive event from November 2017 was not formed automatically because of the false identification of the signal at HA4 as a T phase. Accurate modelling of underwater signal propagation could eliminate these false identifications by establishing more accurate phase identification rules in the automatic processing or perform numerical simulations on demand.

5.12. Estimating Transfer Function from In-Ocean Propagation to In-Ground Seismic Sensor

As mentioned in section 3 of this paper, the hydroacoustic network consists not only of the six in-water hydrophone stations but also of five T phase stations consisting of seismometers located close to ocean shores, most of them on islands. The sampling rate of the seismometer is adapted to their task and is set higher than the IMS seismic stations, at 100 samples per second. The detection capability of these stations is affected by the high seismic noise level assumed to be due to the proximity of the ocean, and the detectors used in the processing are adapted to detecting waves propagating in the oceans and coupling into the ground in the vicinity of the T
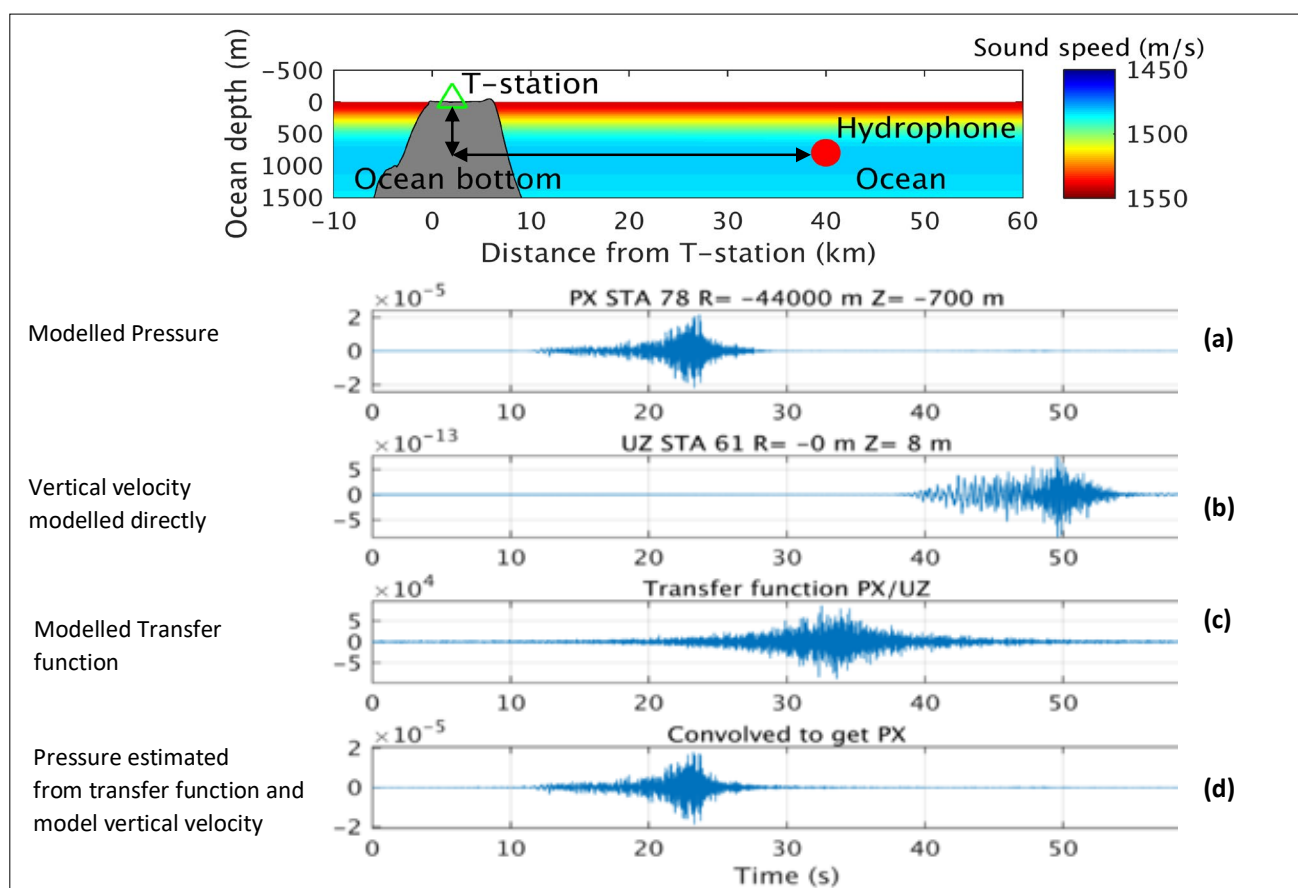
FIGURE 25.

The diagram of a hypothetical T phase station located on an island is shown on the top of the figure. Also shown is the location of a hydrophone at the depth of the SOFAR channel. A simulated multi-modal in-water acoustic wave travelling in the SOFAR from the right of the picture will first reach the in-water hydrophone. The modelled pressure is shown in (a). The acoustic wave will be converted to seismic waves at the water-ground interface and recorded at the T phase station on the island, as shown in (b). A transfer function (c) can be computed from these simulated vertical velocity and pressure records and convolving this transfer function with the pressure wave will give an estimate of the pressure expected at the hydrophone from the record of the vertical component of the velocity recorded at the T phase station, as shown in (d).
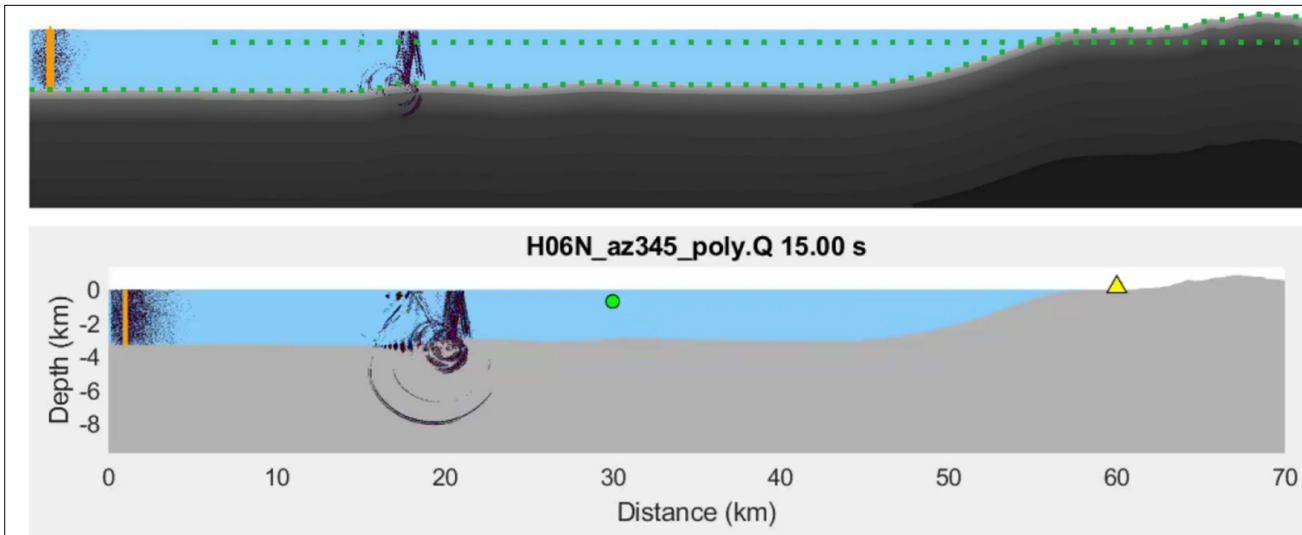
FIGURE 26.
(Adapted from Stevens et al. 2020). Both the top and bottom images show the input source location as a vertical orange bar. On the top image, the locations of all receiver points in the simulation are displayed as green dots. They are both snapshots of the acoustic and elastic waves 15 seconds after the origin time. Amplitudes of the pressure is amplified in the bottom image, which also shows the station location as a yellow triangle, and the location of a fictitious hydroacoustic station in the water (green dot). Comparison of the output at these two points is used to calculate the hydroacoustic to seismic transfer function. This example is for the T phase station seismometer site H6N on Socorro Island, Mexico.

phase stations. Efforts to maximize the use of the T phase stations for the purpose of detecting in-water explosions have taken place in the last ten years. One line of investigation was to enhance the current system by taking advantage of the multiple components of the seismometers at T phase stations to get better phase identification through the polarization analysis. Through this investigation, it was discovered that polarization appears quite random in the frequency range of interest for nuclear monitoring purposes, but that at very low frequencies (<0.05 Hz) the passage of tsunamis can be observed especially on the horizontal components (Prior et al. 2010, Poplavskiy and Le Bras 2013). Another line of investigation was to numerically model the conversion of acoustic to seismic energy at the ocean underground interface to be able to complement the very few real examples of explosion signals observed at T phase stations. Figure 25 illustrates the geometry and the resulting calculations of modelled pressure at the hydrophone and vertical velocity at the seismometer as well as the calculated transfer function that allows estimating the hydrophone signal if there is a recording of the seismic velocity at the seismometer. Stage one involved

environmental modelling at each of the 11 seismometers of the IMS T-stations and the SPECFEM2D software (Tromp et al. 2008, Xie et al. 2016) was used to model waveforms at T phase stations from H phases propagating in the ocean. A side benefit from these calculations is that transfer functions specifically adapted to each T phase station configuration, can be estimated based on the numerical calculations from each site of IMS T phase stations, using an environmental model of the bathymetry and multi-layer seismic velocity The bathymetry of the model used for the seismometer at the H6N side of the Socorro Island IMS T phase station is shown in Figure 26.

At stage two real examples of both pressure recordings and seismic recordings of large explosions at hydrophone stations HA10 and HA11 were used to refine the environmental model near these two stations by using an inversion method to match the mean energy arrival time in different frequency bands. These two IMS in-water hydrophone stations are located close to islands (Ascension in the case of HA10 and Wake in the case of HA11) with open data seismometers (stations ASCN in the case
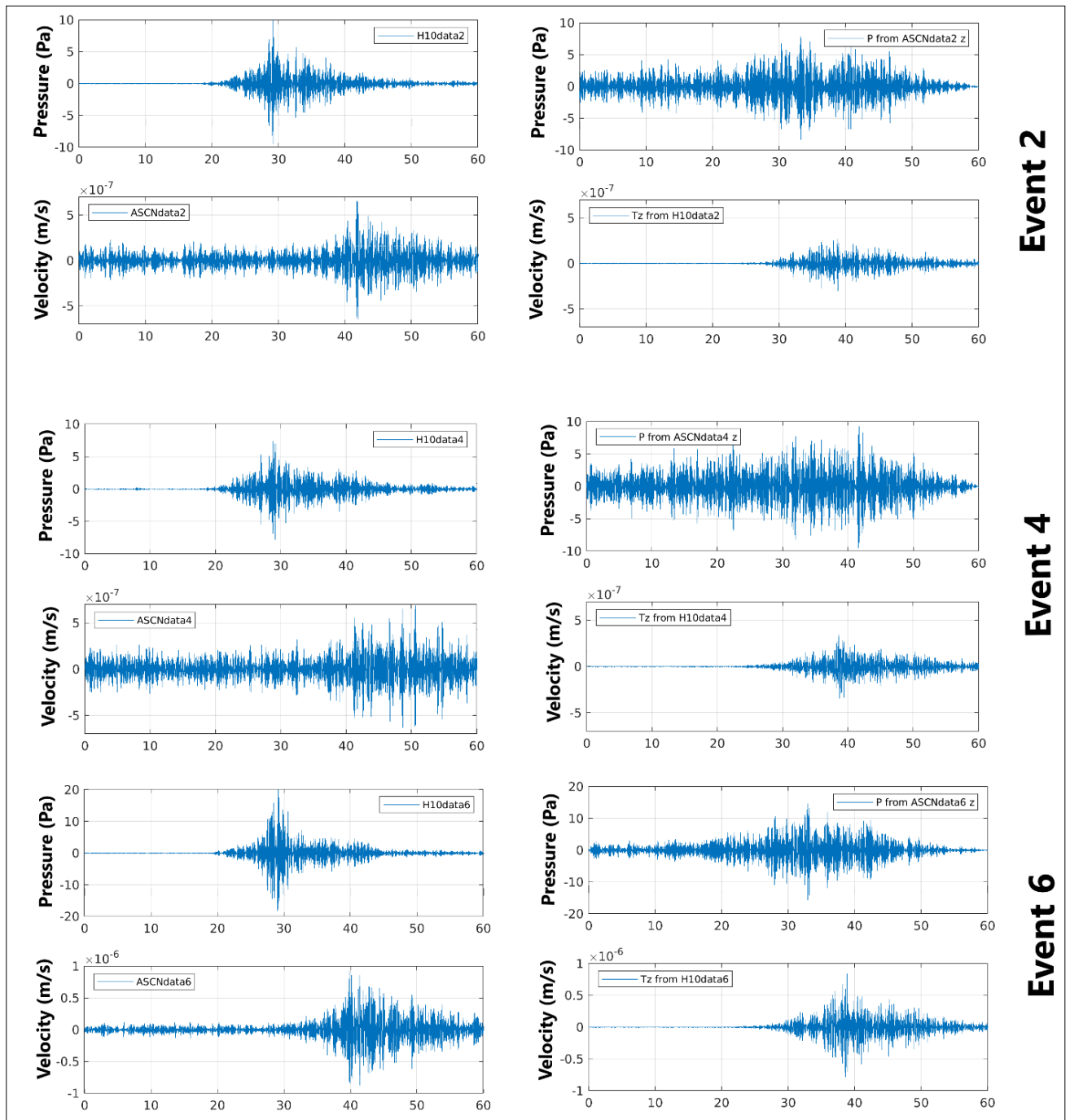
FIGURE 27.

Recordings of vertical particle velocity seismograms at ASCN and pressure at H10N are on the left column. The right column shows simulations of ASCN vertical particle velocity, calculated from the hydroacoustic recording on the H10N, and vice-versa. All waveforms are filtered in the band 6-10 Hz. The parameters for the six events are listed in Table 7. Comparable real data and simulations are placed side by side.

of Ascension Island in the South Atlantic and WAKE in the case of Wake Island in the Pacific).

Figure 27 shows real data examples of the application of the derived transfer function for HA10 after refinement through an inversion process. The real explosion events were all located off the coast of Florida, USA and their source parameters are given in Table 7.

Table 7. Time and Locations of Real Events Offshore Florida Used to Test the Effectiveness of the Transfer Function Method to Simulate Hydrophone or Vertical Seismic Velocity Traces

Event Number	Time (Y-M-D H:M:S)	Latitude	Longitude
2	2016-06-23 17:20:29.0	29.5684	-79.2866
4	2016-09-04 18:29:29.0	30.097	-79.546
6	2021-06-18 19:48:39.0	29.742	-79.347

Figure 27 shows four plots for each explosion. Data plots are in the left column and simulations using transfer functions are in the right column. The top left plot in each case is the data recorded at H10, the bottom left plot is the data recorded at ASCN. The top right is the simulated pressure record obtained by applying the appropriate transfer function on the vertical velocity seismogram and the bottom right plot is the simulated vertical velocity trace obtained by applying the appropriate transfer function on the hydrophone trace. Thus, traces are side by side comparable, although note that they are not all at the same scale. Note that the explosion associated with event 6 in 2021 had a larger yield than the 2016 explosions and it is for that explosion that the record at the seismic station ASCN has a better signal to noise ratio.

The conclusion of these challenging projects to better understand in-water explosions observed at T phase stations is that simulations allowed for much improved insight into the complexity of the conversion from underwater acoustic propagation to the propagation of seismic phases recorded by seismometers at T phase stations (Stevens et al. 2020). The limited frequency passband of the seismic records is an issue to differentiate H phases from T and N phases since the method currently used in this station processing step relies on frequency content outside of the seismic passband. It is however comforting that modelling of the transfer function can explain the general features of the simulated in-water pressure records from the seismic vertical velocity records where the frequency bands overlap.

6. FUTURE HYDROACOUSTIC DATA PROCESSING CAPABILITIES: NEAR AND LONG TERM DEVELOPMENT OF HYDROACOUSTIC DATA PROCESSING

6.1. T Phase Station Modelling and Processing

Five of the 11 IMS hydroacoustic stations are T phase stations and efforts have been made in the last few years to better understand the conversion of acoustic waves to seismic waves at the ocean ground interface. While we now have accumulated experience with this complex modelling and gained insight into the types of waves that are predicted to be observed, more work would need to be done to be able to take advantage of this better understanding and improve IDC processing of the T stations. While extensive station-adapted modelling is comforting because it allows a full understanding of the physical phenomena at play and may help identify the key parameters differentiating waves generated by in-water explosions from seismic noise, seismic signals, and T phases generated by natural causes.

Machine learning, while not allowing insight into the physics of the wave conversion, may however help seismic waves at T-stations. Observations of in-water explosions at T phases are very rare, and so far the only example has been an explosion off the coast of Florida, in 2021, with a nominal yield of nearly 30 tonnes. The modelling capabilities demonstrated to yield realistic synthetic signals at T phase stations may be used to complement the few rare observations.

Advances in machine learning methods using full waveforms point to possible gain if full waveforms contain sufficient information to differentiate between several wave types (Wei et al. 2020). Another fruitful path of investigation could be to use machine learning to denoise T phase station signals to pull out more signals from in-water events and possibly extend the frequency content at T phase stations. If machine learning methods do not yield any results on synthetic data, it may not be worth pursuing further investigations given the dearth of examples with actual observations of in-water explosion at T phase stations.

6.2. Three Dimensional Oceanic Propagation Modelling

The current operational models for seasonal varying travel times, transmission loss, and blockage modelling are 2-D and rely on dated environmental models of the ocean. Much progress has been made, for instance in making daily updates of the ocean conditions available online in the last decades. In addition, numerical computations of acoustic signal propagation involving 3-D models are now possible (Duda 2019, Heaney et al. 2017, Porter 2019). Blockage models that are still used in the IDC are 2-D and do not consider propagation phenomena such as refraction and diffraction. They may be too restrictive and it has been reported by analysts that acoustic arrivals are seen where the blockage model would not have predicted any (see Figures 11 and 12). A project has been initiated to explore oceanographic, seismoacoustic and 3-D ocean signal propagation modelling results and enhance blockage maps, travel timetables, transmission loss, probability of detection and computations of back-azimuth estimates. Automatic processing, routine interactive analysis, and expert analysis are expected to benefit from introducing the additional accuracy afforded by 3-D modelling as compared to the current 2-D models. Implementation of 3-D ocean signal propagation modelling to assist analysts and experts in interpreting recorded signals on the CTBT IMS hydroacoustic network could be run for cases of interest.

6.3. Array Processing of Hydrophone Triplets

One of the advances of the last twenty-five years, and one of the recommendations from the Ad-hoc Expert Group on the Evaluation of Hydroacoustic Data Processing (Ad-hoc Expert Group 2003), was to experiment with multichannel (array) processing of triad (or triplet). The automatic DTK-PMCC software is used operationally for the processing of infrasound arrays. It can be adapted to process the in-water hydrophone triplets. Figure 13 shows the application of the interactive version of the software, DTK(G)PMCC. Tests at the IDC over the last few years were conducted in a quasi-operational environment where the automatic detection processing was performed with DTK-PMCC. It is anticipated that further integration tests will be needed to ensure that network processing (Global Association and NET-VISA), as well as post-analysis processing (one of the screening criteria is based on hydroacoustic data) is performing at least as well as the current system. A new configuration where detection processing of hydrophone triplets is now done as an array rather than on individual hydrophones can then be proposed for the operational system. One of the potential benefits of the method may be to obtain better seismic detections at hydrophone triplets.

6.4. Machine Learning Methods

Some machine learning methods, for instance Bayesian, rely on probabilistic models that include a deterministic, physical component. Introducing more realistic and accurate seismoacoustic wave propagation physics in machine learning can only benefit these methods in their deterministic forward modelling component. An assessment of the possibility of using high fidelity seismoacoustic models to predict at least some of the measurable characteristics of hydroacoustic waveforms should be attempted. These can be applied to both hydroacoustic in-water records at hydrophones and converted waves at T phase stations.

The field of application of machine learning methods is potentially very large for high quality

hydrophone stations data. For instance, all transient signals in waveform segments might be tagged with identifiers based on either supervised or unsupervised classification methods (Russell and Norvig 2009). There are enough instances of various signals in the archives that are considered noise for the purpose of the CTBTO and whose waveforms could be specifically tagged as different types, such as blue whale calls, fin whales calls or other acoustic signals from marine creatures, underwater volcanoes, seismic survey, breaking ice, etc. It may take a while to tag enough transient signal waveforms to be able to use them in a supervised method. It may be more interesting to use the automatic detections already in place and let an unsupervised method define clusters which could then be identified by examining typical waveforms from each cluster.

Improvements in the network processing part of the pipeline have been made by analysing the problem using a probabilistic approach. NET-VISA complements the work of the analysts by bringing to their attention automatic events from the VSEL3 bulletin (see Figure 2) which they had not yet reviewed. Like the Global Association,

NET-VISA builds events by assembling sets of detections from multiple stations and estimating an origin time, size, location, and their uncertainties for these events. The concept of SIG-VISA was first discussed at the time that the NET-VISA project was conceived. The idea was to merge the steps of station and network processing and formulate a probabilistic model to build an event bulletin directly from the waveforms recorded at IMS stations, as illustrated in Figure 28. Initial research work has been accomplished using this approach (Moore and Russell 2017).

6.5. Screening Methods

One area of research which is very specific to the mission of the CTBTO is screening. This step of processing, which happens after analysis, was evoked briefly in Figure 2. One of the four methods currently in use at the IDC is based on examining hydroacoustic data. Because drilling in open seas can only be achieved up to a certain depth of water, it is very unlikely that a nuclear test would be setup under the seabed in areas where the ocean is at depths larger than a certain value (currently 500 m). The screening
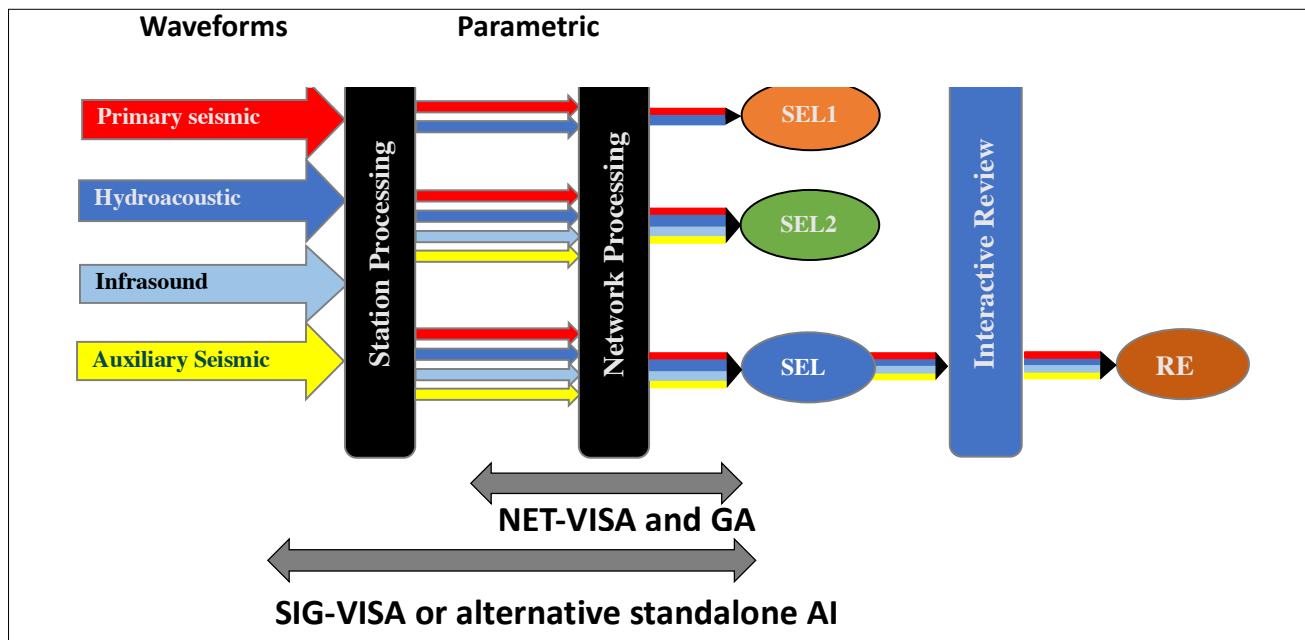
FIGURE 28.

Range of application of the NET-VISA compared to SIG-VISA. Both the Global Association and NET-VISA form automatic events from parametric data after the waveforms undergo station processing, resulting in parametric data. SIG-VISA is intended to produce an automatic bulletin directly from the waveform data, alleviating the need for an explicit stage of station processing.

criterion checks that no high frequencies are observed on hydrophone data where the paths to the hydrophone triplets is clear. If it is the case that no high frequencies are present, then the event is deemed to be of natural origin and not an explosion in the water. Because many natural events occur within oceanic areas, this criterion is very useful in classifying them as natural. As more experience has been gained with impulsive underwater events however, there may be limitations to this criterion. In at least one example, the case of the ARA San Juan signal (Nielsen et al. 2020), the high frequencies are strongly attenuated after propagation at high latitudes. This should be considered when exercising this criterion.

There may be other criteria that would work on hydroacoustic data, and this area of research may be a fruitful one.

7. CONCLUSION

This paper presented a review of the status of processing of hydroacoustic data at the IDC. It provided a history of the developments that have occurred with the IDC processing system since the early 2000s, and the outlook for the future. IDC at CTBTO has a clear path to improve the automatic processing of hydroacoustic data as continuous data acquisition had provided reference data that can be used to assess and improve the existing algorithms. With the advent of faster computational capabilities, 3-D oceanographic and acoustic 3-D modelling have become tractable and the implementation of such modelling in the automatic processing will result in measurable improvement in performance. 3-D modelling will also assist analysts in the interpretation of complex recorded data as the automatic results should improve in rendering reality.

REFERENCES

Ad-hoc Expert Group (2003). *Evaluation of Hydroacoustic Data Processing at the International Data Centre*, CTBT/EVA/EG-2/1. Preparatory Commission for the Comprehensive Nuclear-Test-Ban Treaty Organization.

Arora, N.S., Russell, S., Sudderth, E. (2013). NET-VISA: Network processing vertically integrated seismic analysis. *Bulletin of the Seismological Society of America* **103** (2a) 709–729.

Arora, N.S., Prior, M. (2014). *Testing and enhancing the NET-VISA software of the commission fusion of seismic and hydro-acoustic propagation*. Poster presented at Bayesian Logic Inc. https://bayesianlogic.com/publications/2014/05/01/Arora_RMR_14.pdf (last accessed 1 December 2021)

Bernard, E., Meinig, C. (2011): History and future of deep-ocean tsunami measurements. In Proceedings of Oceans' 11 MTS/IEEE, Kona, IEEE, Piscataway, NJ, 19–22 September 2011, No. 6106894, 7 pp.

Castillo, III, E., Holdzkom, J., Smock, J., et al. (2020). SOSUS/IUSS: Monitoring the world's oceans. *The Cable: IUSS-Caesar Alumni Association* (n.d.). Retrieved from https://www.iusscaa.org/idn.htm (Click on "History") (last accessed March 2022)

Cansi, Y. (1995). An automatic seismic event processing for detection and location: The P.M.C.C. method. *Geophysical Research Letters* **22** (9) 1021-1024.

Cansi, Y., Klinger, Y. (1997). An automated data processing method for mini-arrays. CSEM/EMSC European-Mediterranean Seismological Centre, **11** 1021-1024.

Conference on Disarmament (1978). Resolutions and Decisions adopted by the General Assembly during its Tenth Special Session. A/INF/S-10/2. UN Office for Disarmament Affairs.

Coyne J., Henson, I. (1995). Geotool User's Manual. (last accessed February 2023)

Dall'Osto, D. (2019a), How consideration of Horizontal Refraction from the Continental Shelf Break improves Source Triangulation: Application to the Search for the ARA San Juan, (2019*). The Journal of the Acoustical Society of America* **146** 2104-2112.

Dall'Osto, D. (2019b), Reducing Ambiguity in Hydroacoustic Triangulation Through Consideration of Three-Dimensional Propagation Features, (2019). Presentation T1.3 O9, CTBT: Science and Technology conference https://events.ctbto.org/sites/default/files/2019-06/SnT2019_Book_Of_Abstracts_Web_Version_with_front_cover.pdf (last accessed 1 December 2021)

Dahlman, O., Ringdal, F., Mackby, J., Mykkeltveit, S. (2020). The inside story of the Group of Scientific Experts and its key role in developing the CTBT verification regime. *The Nonproliferation Review* **27** (1-3) 181-200.

Dahlman, O., Mykkeltveit, S., Haak, H., (2009). *Nuclear Test Ban. Converting Political Visions to Reality*. Springer, Dordrecht.

Duda, T.F. (2019). Computational acoustics in oceanography: The research roles of sound field simulations. *Acoustics Today* **15** (3) 28-37.

Graeber, F.M., Coyne, J., Tomuta, E. (2006). "The current status of hydroacoustic data processing at the International Data Centre". (Proceedings of the 28th Seismic Research Review: Ground-Based Nuclear Explosion Monitoring Technologies) 717-724.

Graeber, F.M., (2007): A new version of the Hydroacoustic Azimuth and Slowness Estimator (HASE 2.0) featuring automatic identification of seismoacoustic arrivals, IDC/WI/WD, 8 March 2007.

Hanson, J. et al. (2001). Operational processing of hydroacoustics at the prototype International Data Center. *Pure and Applied Geophysics*. **158** (3) 425-456.

Haralabus, G., Zampolli, M., Grenard, P., Prior, M., Pautet, L. (2017). "Underwater acoustics in nuclear-test-ban treaty monitoring." *Applied Underwater Acoustics* **16** (T. Neighbors, D. Bradley, Eds) Elsevier, Amsterdam and New York.

Heaney, K., Campbell, R.L. (2016). Three-dimensional parabolic equation modeling of mesoscale eddy deflection. *The Journal of the Acoustical Society of America* **139** 918-926.

Heaney, K., Prior, M., Campbell, R.L. (2017). Bathymetric diffraction of basin-scale hydroacoustic signals. *The Journal of the Acoustical Society of America* **141** 878-885.

IMS Map (2023) Link to IMS map (last accessed January 2023)

Kushida, N.Y., Lin, P., Nielsen, Le Bras, R. (2019). "Acceleration in Acoustic Wave Propagation Modelling using OpenACC/OpenMP and its Hybrid for the Global Monitoring System". *Accelerator Programming Using Directives* (S. Wienke, S. Bhalachandra, S. Chandrasekaran, G. Juckeland, Eds) Springer-Verlag, Berlin.

Laney, H. et al. (1999). Automated detection of underwater explosions by the IMS hydroacoustic network. *The Journal of the Acoustical Society of America* **105** 1038.

Le Bras, R., Nielsen, P., Brouwer, A. (2019). Ground-truth observations and modeling of an extensive air-gun seismic survey recorded at two hydroacoustic stations of the IMS network. *Geophysical Research Abstracts* **21** 18354.

Le Bras, R.J. (2000). *Multi-Sensor Data Fusion Project: Final Report*. Contracted by Science Applications International Corporation under Contract No. DASG60-96-C-0151.

Le Bras, R., et al. (2020). NET-VISA from cradle to adulthood. A machine-learning tool for seismo-acoustic automatic association. *Pure and Applied Geophysics* **178** 2437-2458.

Lin, Y.-T., Duda, T.F., Newhall, A.E. (2013), Three-dimensional sound propagation models using the parabolic-equation approximation and the split-step Fourier method. *Journal of Computational Acoustics* **21** (01).

Lin, Y.-T., Oliveira, T., Nielsen, P. (2019). *Three-Dimensional Global Scale Underwater Sound Propagation Modeling*. International Hydroacoustics Workshop, 08-11 July 2019, Vienna.

McDonald, M.A., Hildebrand, J.A., Mesnick, S.L. (2006). Biogeographic characterization of blue whale song worldwide: Using song to identify populations. *Journal of Cetacean Research and Management* **8** (1) 55-65.

Menemenlis, D. et al. (2008). ECCO2: High Resolution Global Ocean and Sea Ice Data Synthesis. *Mercator Quarterly Newsletter* **31** 13.

Mialle, P., Brown, D., Arora, N., colleagues from IDC. (2019). "Advances in Operational Processing at the International Data Centre". *Infrasound Monitoring for Atmospheric Studies* (A. Le Pichon, E. Blanc, A. Hauchecorne, Eds). Springer-Verlag, Berlin.

Moore, D.A., Russell, S.J. (2017). Signal-based Bayesian Seismic Monitoring, *Proceedings of Machine Learning Research* (Proceedings of the 20th International Conference on Artificial Intelligence and Statistics (AISTATS) Fort Lauderdale, Florida, 2017). Journal of Machine Learning Research **54**.

Nielsen, P.R., Le Bras, R., Zampolli, M., Bittner, P., Haralabus, G. (2018). "Localization using P-phases recorded on the CTBT IMS hydroacoustic stations". (Presentation at the European Geosciences Union General Assembly, Vienna, Austria, 2018) *Geophysical Research Abstracts* **20.**

Nielsen, P.L. et al. (2020). CTBTO's data and analysis pertaining to the search for the missing Argentine submarine ARA San Juan. *Pure and Applied Geophysics* **178** 2557-2577.

Nielsen, P. et al. (2021a). "High-fidelity ocean seismo-acoustic propagation modelling for signal interpretation at the CTBT IMS hydroacoustic stations". (Presentation at the European Geosciences Union General Assembly, online, 19–30 Apr 2021).

Nielsen, P.L., Zampolli, M., Le Bras, R., Mialle, P., Haralabus, G. (2021b). "A self-consistent estimate of the CTBT IMS hydrophone locations using scientific airgun data from the CEVICHE trial (Chile)". (Presentation at the CTBT: Science and Technology Conference, Vienna, Austria 2021).

Poplavskiy, A.S., Le Bras, R.J. (2013). Recordings of long period fluctuations associated with the passage of three distinct tsunamis at broadband seismometers made at the International Monitoring System (IMS) Hydroacoustic T station H06 (Socorro Island, Mexico). *Seismological Research Letters* **84** (4) 567-578.

Porter, M.B. (1992). The KRAKEN normal mode program. *Provided by the SAO/NASA Astrophysics Data System.* https://ui.adsabs.harvard.edu/abs/1992knmp.book.....P (last accessed 9 December 2021).

Porter, M.B. (2019). Beam tracing for two- and three-dimensional problems in ocean acoustics. *The Journal of the Acoustical Society of America* **146** (3).

Preparatory Commission for the Comprehensive Nuclear-Test-Ban Treaty Organization (2020). Draft Operational Manual for Hydroacoustic Monitoring and the International Exchange of Hydroacoustic Data. Doc. No. CTBT/WGB/TL-11,17/16/Rev.7. Preparatory Commission for the CTBTO, Vienna.

Prior, M., Poplavskiy, A., Le Bras, R., Given, J. (2010). "Enhancing the contribution of the T-stations of the IMS hydroacoustic network to IDC processing and tsunami warning" *Monitoring Research Review: Ground-Based Nuclear Explosion Monitoring Technologies* (Proceedings of the 2010 Monitoring Research Review: Ground-Based Nuclear Explosion Monitoring Technologies) 558-564.

Ramaker, J., Mackby, J., Marshall P.D., Geil, R. (2003). *The Final Test: A history of the Comprehensive Nuclear-Test-Ban Treaty Negotiations*. Provisional Technical Secretariat of the Preparatory Commission for the Comprehensive Nuclear-Test-Ban Treaty Organization, Vienna.

Russell, S., Norvig, P. (2009). *Artificial Intelligence: A Modern Approach*, 3rd Edn. Prentice-Hall, Englewood Cliffs, NJ.

Stevens, J.L. et al. (2020). Calculation of hydroacoustic propagation and conversion to seismic phases at T-stations. *Pure and Applied Geophysics* **178** 2579-2609.

Tuma, M., Rørbech, V., Prior, M., Igel, C. (2016). Integrated optimization of long-range underwater signal detection, feature extraction, and classification for nuclear treaty monitoring. *IEEE Transactions on Geoscience and Remote Sensing* **54** (6) 3649-3659.

Tromp, J., Komatitsch, D., Liu, Q. (2008). Spectral-element and adjoint methods in seismology. *Communications in Computational Physics* **3** (1), 1-32.

Vergoz, J., Cansi, Y., Cano, Y., Gaillard, P. (2021). Analysis of hydroacoustic signals associated to the loss of the Argentinian ARA San Juan submarine. *Pure and Applied Geophysics* **178** 2527-2556.

Wei, H., Shu, W., Dong, L., Huang, Z., Sun, D. (2020). A waveform image method for discriminating micro-seismic events and blasts in underground mines. *Sensors* **20** (15) 4322.

Xie, Z., Matzen, R., Cristini, P., Komatitsch, D., Martin, R. (2016). A perfectly matched layer for fluid-solid problems: Application to ocean-acoustics simulations with solid ocean bottoms. *The Journal of the Acoustical Society of America* **140** 165.

BIBLIOGRAPHY

Database of the Technical Secretariat (DOTS) version 4, CTBTO (2021).

E.U. Copernicus Marine Service Information. http://marine.copernicus.eu/services-portfolio/access-to-products/ (last accessed 1 December 2021)

Graeber, F.M., Piserchia, P.-F. (2004). Zones of *T*-wave excitation in the NE Indian ocean mapped using variations in backazimuth over time obtained from multi-channel correlation of IMS hydrophone triplet data. *Geophysical Journal International* **158** (1) 239–256.

Heyburn, R., Nippress, S.E.J., Bowers, D. (2016). Seismic and hydroacoustic observations from underwater explosions off the east coast of Florida, *Bulletin of the Seismological Society of America* **108** (6) 3612-3624.

National Research Council (1997). Research Required to Support Comprehensive Nuclear Test Ban Treaty Monitoring. Washington, DC: *The National Academies Press*.

Prior, M. (2008b) http://wiki.idc.ctbto.org/pmwiki/pmwiki.php?n=Hydro.STAPROHonH

Prior, M. (2008a) http://wiki.idc.ctbto.org/pmwiki/pmwiki.php?n=Hydro.NeuralPhaseID

Prior, M. K., O. Meless, P. Bittner, H. Sugioka (2011): Long-Range Detection and Location of Shallow Underwater Explosions Using Deep-Sound-Channel Hydrophones, *IEEE J. of Ocean. Eng.* 36(4), pp. 703-715.

Russell, S., Vaidya, S., and Le Bras R., (2010) Machine Learning for Comprehensive Nuclear-Test-Ban Treaty monitoring, CTBTO Spectrum 14, April 2010.

The GEBCO Digital Atlas published by the British Oceanographic Data Centre on behalf of IOC and IHO, https://www.gebco.net/data_and_products/gridded_bathymetry_data/ (last accessed 1 December 2021)

Infrasound Monitoring: Achievements and Challenges

E. Blanc, A. Le Pichon, T. Farges, C. Listowski

Commissariat à l'Energie Atomique et aux Energies Alternatives, Arpajon, France

P. Mialle

Comprehensive Nuclear-Test-Ban Treaty Organization, Vienna, Austria

Abstract

The International Monitoring System (IMS) using infrasound technology is unique for atmospheric observations, due to its high capacity for long range detection and localization. Its development, starting at the end of the nineties, motivated innovations in sensors, array stations, network configuration and automatic detection algorithms. The rapidly increasing number of certified stations detected a large diversity of anthropic and natural infrasound events, well identified thanks to their accurate description. Numerical simulations, based on propagation laws and atmospheric models, determined the IMS specifications for infrasound monitoring. They were revisited at the end of the 2000s, integrating an improved representation of the variable atmospheric environment and showing the high performances of the network. Data analyses clearly demonstrated that most uncertainties originate from the middle atmosphere disturbances, which control the infrasound waveguides and are under-represented in models. Unexpectedly, relevant atmospheric parameters were identified in infrasound signals from well-known sources such as volcanoes, opening new infrasound remote sensing possibilities. The association of the infrasound IMS to complementary multi-instrument platforms provided new middle atmosphere data needed for the determination of uncertainties in atmospheric models and infrasound simulations for more precise event analyses. New methods are developed for middle atmospheric remote sensing from IMS infrasound ocean swell noise observations. Such global observations could be relevant for future data assimilation systems used in numerical weather prediction models. A remote volcano prototype information system is in development to provide notification to civil aviation in case of large eruptions of non-instrumented volcanoes. Besides the atmospheric dynamics related to wave systems recorded during 25 years, large-scale climatology systems, such as the inter-tropical convergence zone (ITCZ) of the winds and the semi-annual oscillation (SAO) of stratospheric winds were recently identified. They can provide relevant information about the evolution of climate related parameters. This shows IMS potential for weather, climate and civil safety applications.

1.   INTRODUCTION

The International Monitoring System (IMS) infrasound network is dedicated to detecting nuclear explosions with a yield of at least one kiloton in the atmosphere with two stations to monitor compliance with the Comprehensive Nuclear-Test-Ban Treaty (CTBT). The first stations were certified at the beginning of the 21st century. Today the network is composed of 53 certified stations, constituting 88% of its final structure which will be composed of 60 stations (Preparatory Commission for the CTBTO 2022). The high quality of the multicomponent station arrays, the measured parameters and processing methods, the continuity in observations and the homogeneous global station coverage make this network unique for CTBT verification and associated scientific studies. The identification of the infrasound sources, the propagation processes and the context of the atmospheric variability motivated innovative studies, essential for improving the analysis of IMS data for nuclear explosion monitoring. The objective of this paper is to describe the evolution of the infrasound technology in relation to the development of the infrasound component of the IMS, the progress and achievements performed in the last 25 years in infrasound monitoring and associated scientific studies and the related perspectives.

2.   EARLY INFRASOUND MONITORING

2.1.   Historical Context

Infrasonic waves are sound waves at a frequency lower than 20 Hz, below the frequencies audible by humans, propagating at the sound velocity (about 330 m/s at the ground surface). They propagate with low attenuation over large distances as demonstrated already by the observations in Europe of the infrasound produced by the Tunguska meteor explosion in 1908, in Siberia (Whipple 1930). This event followed the historical eruption by Krakatoa in 1883. It had been the first documented global acoustical event with a pressure wave circling the Earth many times (Symons 1888).

Early studies were dedicated to the sound propagation, using dedicated explosions. The objective was to study the long range propagation and anomalies, such as shadow zones, which were explained by reflections in the upper atmosphere (Gutenberg 1939, Cox 1949, review by Evers and Haak 2010).

The first experimental and operational observation networks were developed in the 1950s motivated by the detection and localization of atmospheric nuclear tests. This opened the 'microbarography' era. Such systems were operating in the United States (review by McKisik 1996), France (Rocard 1959) and the United Kingdom (Carpenter et al. 1961). Long range (hundreds to thousands of kilometres) propagation models were developed in the 1960s and 1970s. The recorded signals were explained by ducted atmospheric modes involving different wave frequencies and propagation altitudes (Harkrider 1964, Pierce 1965, Pierce et al. 1971, Balachandran 1970 and review by Francis 1975). The front of the ground level disturbance travelled with the speed of the Lamb mode, near 312 m/s. This mode dominates the response at large horizontal ranges with its energy concentrating near the ground surface at periods reaching several minutes to hours (Pierce and Posey 1971, Francis 1975). Gravity modes are ducted between the thermosphere and the ground. At lower periods, in the acoustic wave domain, the energy tends to concentrate near the temperature minimum of the tropopause at ~15 km and the mesopause at ~85 km. These modes are not perfect and the acoustic modes, propagating at a velocity lower than the ground sound velocity, were measured by the microbarograph networks (Francis 1975). Acoustic waves induced by explosions were observed up to the ionosphere above 100 km altitude where they can disturb the electromagnetic wave propagation (Balachandran 1972, Berthet and Rocard 1972).

The potential of such networks for atmospheric studies was suggested by Donn and Shaw (1967) and Rind et al. (1973) and a general review was published by McKisik (1997).

After the end of the atmospheric nuclear tests in the 1970s, infrasound research focused on the study of other events such as large volcanoes, meteorites and supersonic aircrafts. Experimental infrasound networks were operating in different countries such as the Palisades New York Lamont-Doherty Geological Observatory (Rind and Donn 1975, Donn and Balachandran 1981), the Swedish Infrasound Network (Liszka 1974) and the French network (in metropole and French Polynesia; Delclos et al. 1990). However the interest in infrasound technology weakened and very little efforts were performed in this field during this period following nuclear tests.

From 1985 to 1993 several large conventional explosions (few kt) were organized in the USA in the framework of the Misty Castle programme (Reed 1978). Microbarograph observations using permanent stations in New Mexico (USA) and experimental networks provided new information about infrasound propagation (Reed et al. 1987, Whitaker et al. 1990).

All this early work was relevant for the infrasound expert group mandated by the Conference on Disarmament's Ad Hoc Committee for the development of the Comprehensive Nuclear-Test-Ban Treaty verification system in the 1990s "to develop a proposal for an infrasound monitoring network system dedicated to detect approximately one kiloton explosions and to provide global coverage". The infrasound technology was clearly identified as well adapted to atmospheric monitoring. Bringing together all available expertise, the 60 stations infrasound network was proposed by the Expert group to the Ad Hoc Committee on a Nuclear Test Ban Working Group on Verification (Expert group on verification 1995).

The IMS infrasound network is well adapted to achieve verification objectives. It motivated a very large international team to develop innovative scientific and technical studies for the IMS exploitation for CTBT verification. Dahlman et al. (2009) overviewed the efforts of the Comprehensive Nuclear-Test-Ban Treaty Organization (CTBTO) to implement the CTBT and its verification regime.

2.2. Example of Infrasound Signals from Atmospheric Explosions

Infrasonic waves are produced by human activity: explosions, supersonic aircrafts, rocket launches, quarry blasts, industrial activity or natural sources: earthquakes, ocean swells, volcanic eruptions, meteorites, lightning, auroras, hurricanes and cyclones. They are ducted in the atmospheric wave guide between the ground and the increases of the temperature of the stratosphere and the lower thermosphere, which can be reinforced or reduced by the winds. Infrasonic waves can be observed in the different atmospheric layers (Figure 1, Blanc 1985).

The infrasound technology is very well adapted to the monitoring of atmospheric nuclear explosions as about 50% to 60% of the explosion's energy is released as blast waves (Glasstone 1977) and can be further detected as infrasound at a large distance, after ducting in the atmosphere.

The infrasound propagation in the stratospheric (from the ground to about 50 km) and thermospheric (from the ground to about 120 km) wave guides strongly depends on the wind variability. These winds are essentially zonal winds, blowing at about 60 m/s to 100 m/s at altitudes of about 30 km to 70 km. They are submitted to seasonal changes with a westerly component in winter and an easterly component in summer.

Figure 2 shows two examples of signals produced by a nuclear test of a few kilotons in French Polynesia and detected at distances of 440 km (a) and 450 km (b) from the explosion in the north-west and east directions, respectively. Several wave arrivals are observed in the north-west direction, while the signal is more complex with a lower amplitude and longer duration in the east direction, opposite to the zonal wind

direction. Time frequency analysis (lower panels) shows dominant periods between 2 and 30 seconds.

Kulichkov (2003) showed that for explosions of less than one to a few kilotons, the infrasonic wavelength is in the range of hundreds of meters to few kilometres, which is comparable to the scale of the temperature and wind fluctuations in the middle atmosphere, which affects the infrasound propagation and the explosion signature. The scale of high energy nuclear explosions is comparable with the vertical dimension of the atmosphere. The whole atmosphere controls the wave propagation and the characteristics of the infrasound signature. The largest nuclear explosions generate gravity
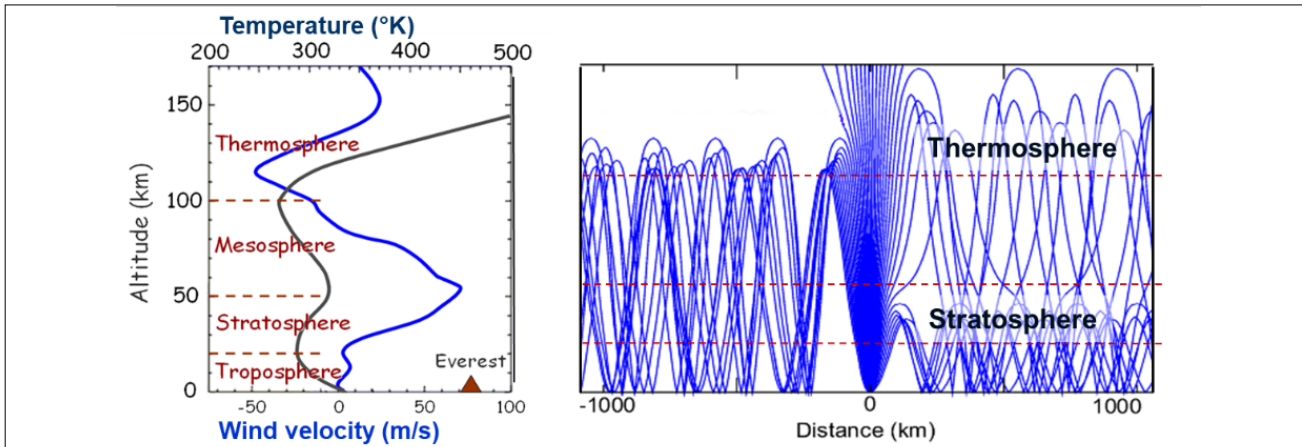
FIGURE 1.
Infrasound propagation: ray tracing showing different possible infrasound paths and corresponding typical wind and temperature profiles.
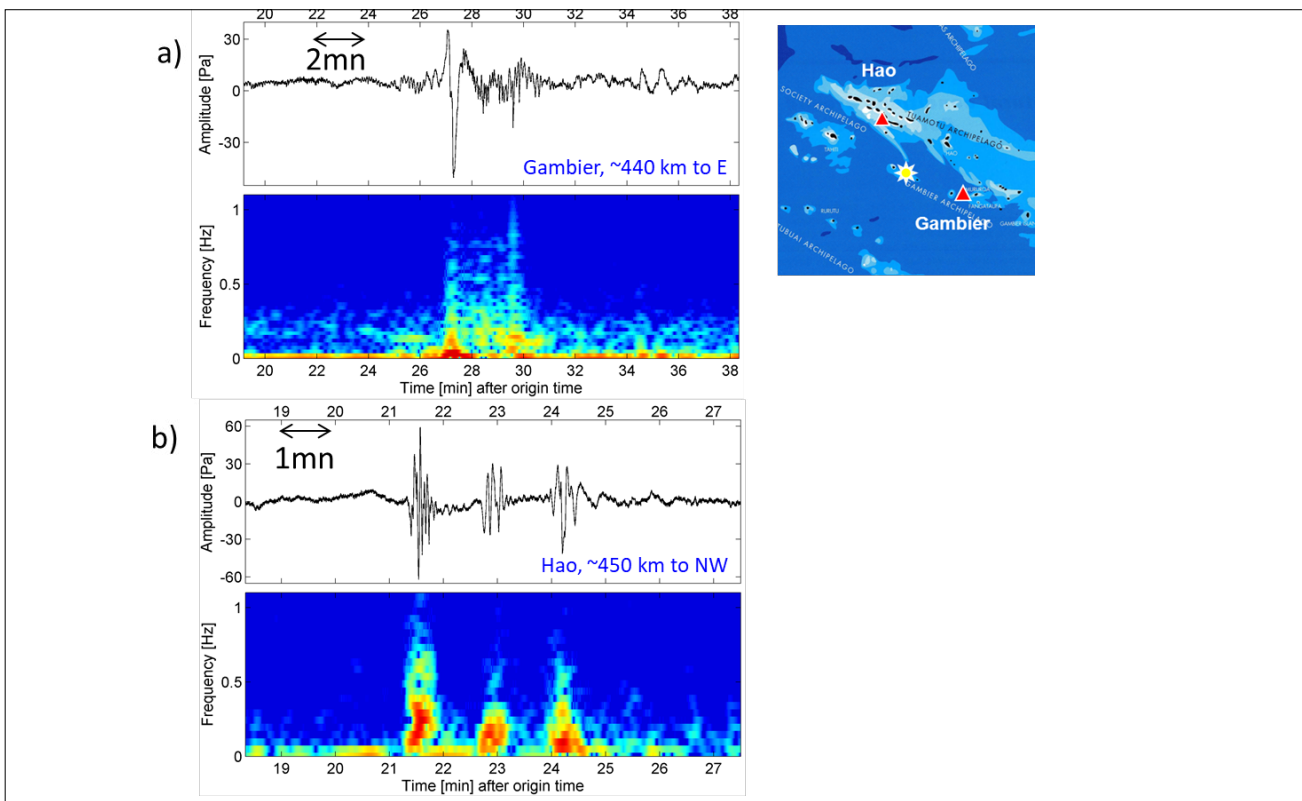
FIGURE 2.
Example of infrasound signals and time–frequency analysis from a nuclear explosion recorded in French Polynesia from a nuclear explosion with a yield of a few kt (Blanc and Ceranna 2009).

waves at frequency lower than the infrasound frequency range, corresponding to periods of about five to nine minutes up to hours.

Gravity waves are frequently observed in the atmosphere. They are excited by natural sources (large volcanic eruptions, convection, airflow over mountains, frontal systems, bolides) and affect different layers of the atmosphere.

The signal amplitude depends on the explosion yield, detection range and stratospheric winds. The first infrasound attenuation law was established from US nuclear test recordings (Reed 1969, Reed 1972, Whitaker 1995, Whitaker et al. 2003). An additional analysis using complementary data from the former Soviet Union nuclear tests was performed by Stevens et al. (2002).

As large explosions excite gravity waves, an empirical law was also established by Whitaker and Mutschlecner (2006), relating the explosion yield with the wave period.

3. CTBT VERIFICATION: RENAISSANCE OF THE INFRASOUND TECHNOLOGY, INNOVATION IN INSTRUMENTS AND METHODS

3.1. Network Configuration

Network detection and location capabilities were determined by modelling using realistic atmospheric conditions. The maps in Figure 3 show the geographical variation of the detection threshold at a global scale. This threshold corresponds to the lowest energy that would be detected by at least two stations. The methods were based on deterministic (Plantet 1996, Blanc and Plantet 1998) or probabilistic approaches (Clauter and Blanford 1997). In spite of the differences and depending on method and assumptions performed in the computations, both maps demonstrated that a 60 station network, with stations consisting in four element arrays, is well adapted to the 1 kt detection.

These maps were established using the empirical attenuation laws (amplitude versus distance) based on historical nuclear tests in the USA and France. High altitude winds were determined by atmospheric models and infrasound noise was deduced from meteorological wind observations. Computations demonstrated that high altitude winds increase detectability. They produce wind and temperature fluctuations on the atmospheric profile and partial reflections of the infrasound waves. The precision of an event location (by azimuth crossing) was estimated of about 100 km to 150 km. In any conditions, it was shown that the 60 stations network is efficient for the verification objectives of the CTBT.

3.2. Technical Challenges

Even if the basic IMS design problems were resolved, further experimental work was needed to answer technical questions that appeared during the development of the system, to ensure achievement of the verification objectives. Technical efforts were performed in different countries, at all levels from sensors to data processing. Early prototype infrasound stations were developed in France and the USA for tests and calibrations. They were described at the first Infrasound Workshops for CTBT Monitoring organized in France in 1996 and 1998[1] and in the USA in 1997[2] (Christie and Whitaker 1998). Efforts in Australia were to develop portable infrasonic arrays for experimental work in eastern and northern Australia to assess the

---

1 Infrasound Workshop for CTBT Monitoring, Bruyères-le-Châtel, France,1996 and 1998 https://digitallibrary.un.org/record/263035?ln=fr.

2 Infrasound workshop for CTBT Monitoring, CTBTO, Santa Fe, New Mexico, 1997, https://digital.library.unt.edu/ark:/67531/metadc674957/.

Deterministic approach (FR)

Probalistic approach (USA)
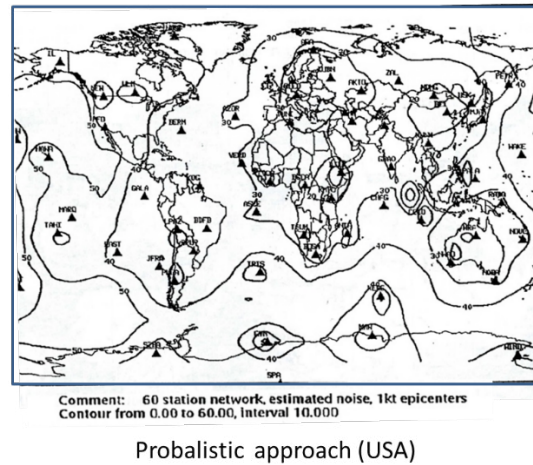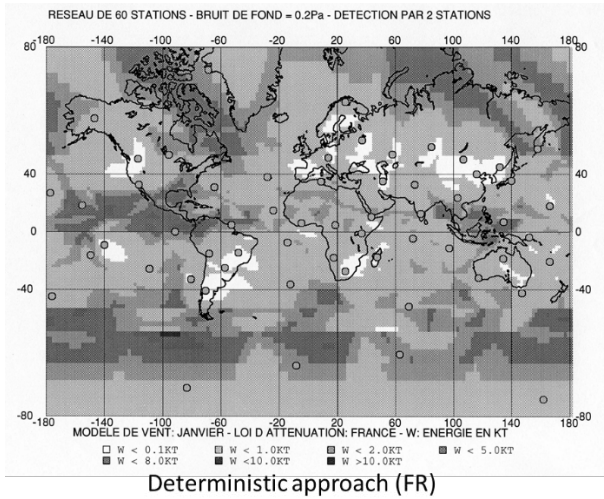
FIGURE 3.

Detection capability maps of a 60 infrasound station network, computed by using deterministic and probabilistic approaches, by the expert group to the Ad Hoc Committee on a Nuclear-Test-Ban Working Group on Verification (1995).

neighbouring IMS infrasound stations (Christie and Kennett 2007).

3.2.1. *Sensors*

Sensors are sensitive microbarometers, measuring infrasound in the range 0.02 Hz to 4 Hz, characterized by a good sensitivity (18 dB below the minimum acoustic noise) and a large dynamic (80 dB) in order to detect explosions both from short or very large distances from the explosions, without signal saturation. Two types of sensors (Figure 4) were available: the Chaparral model developed by the University of Alaska (Breding et al. 1997) and the MB2000 sensor developed by the French Alternative Energies and Atomic Energy Commission (CEA) (Ponceau and Bosca 2010), which measures both differential and absolute pressures. The frequency range of MB2000 is broader than that of the Chaparral, especially at low frequency, extending the possibilities of scientific studies. Both of these sensors are capable of detecting the smallest atmospheric pressure variations, which could be produced by a nuclear test below one millionth of the ambient pressure. The MB2000 sensors have demonstrated their excellent response stability and were deployed at over more than 90% of the network in 2012 (Marty 2019).
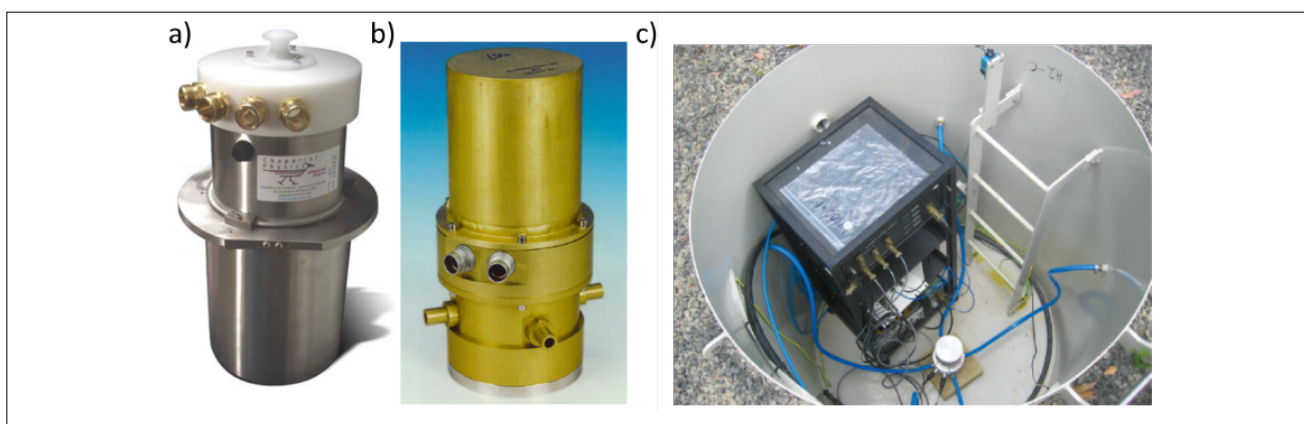
FIGURE 4.

Microbarometers used for IMS stations: a) Chaparral infrasound sensor, b) MB2000 absolute pressure sensor and c) example of infrasound equipment vault at the IS04 station, Shannon, Australia.
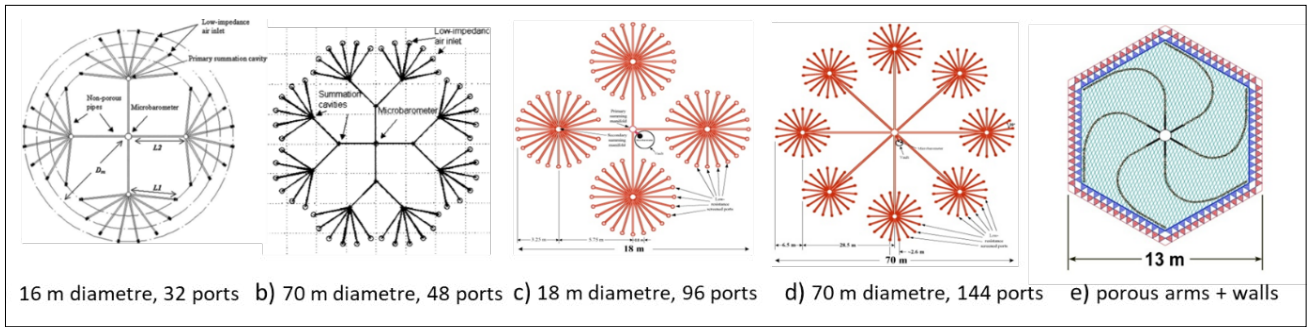
FIGURE 5.
Examples of noise filtering systems associated to the infrasound sensors for noise reduction (from Alcoverro and Le Pichon (2005) and Christie and Campus (2010)).

3.2.2. *Infrasound Noise*

Infrasound noise is mainly produced by winds, generating convective turbulences from thermal atmospheric mixing or mechanical turbulences in the presence of topographical obstacles. Noise variability has been determined experimentally by using meteorological data performed at the infrasound stations and observations using an open sensor and different system of noise acoustic filtering. Theoretical studies were also developed for better predicting the turbulence effects. A review was published by Walker and Hedlin (2010). Several filtering systems were proposed for wind noise reduction. In windy environments, dimensions of the filtering system are larger as the turbulence length scales are larger. In places when this is possible, infrasound stations are installed in forests where the vegetal cover constitutes a natural filtering system.

Figure 5a and b represent computation results showing the best configurations optimizing the filtering system for standard and high noise conditions (Alcoverro and Le Pichon 2005); the configurations of Figure 5c) and d) were experimented by Christie and Campus (2010) and configuration e) includes a wall for improving protection against turbulence. Bowman et al. (2005) established the first infrasound noise statistics using 21 globally distributed infrasound stations.

3.2.3. *Station Configuration*

The stations are arrays of sensors for optimizing the sensitivity, noise reduction and for allowing the determination of propagation parameters: azimuth and horizontal phase velocity, essential for data analyses. The sensors are located several kilometres apart. The basic arrays are composed of at least four sensors located in a triangle with a basis of 1 km to 3 km with a central point, to ensure optimal detection of the infrasound signals. These arrays form very sensitive acoustic antennas, enabling coherent signals to be detected in non-coherent noise (Christie and Campus 2010, Marty 2019).
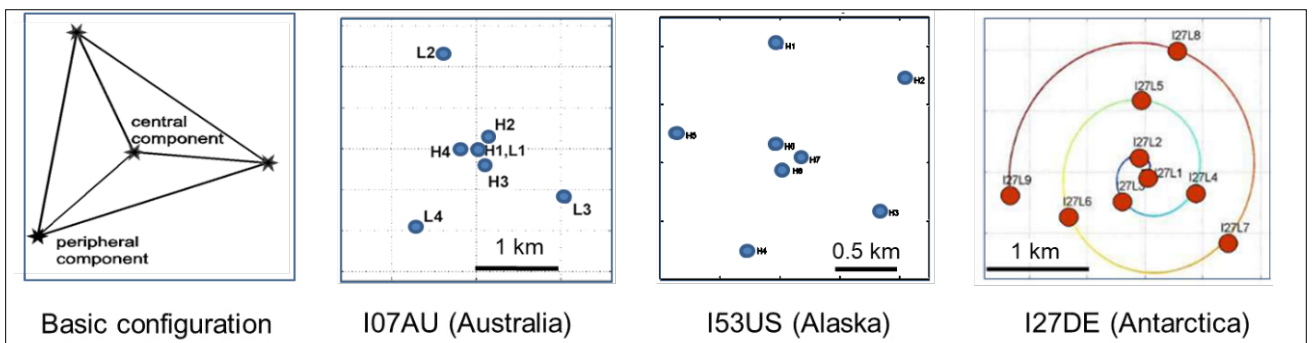
FIGURE 6.
Examples of station configurations (adapted from Christie and Kennett 2007, Olson et al. 2002, Ceranna et al. 2007).

Optimized configuration depends on atmospheric conditions. The number of station elements needs to be increased for stations submitted to extreme environmental conditions. It varies from 4 to 15. Examples of station configurations are presented in Figure 6.

3.2.4. *Data Processing*

Specific methods were developed to detect and analyse infrasound signals. The Progressive Multichannel Cross-Correlation (PMCC) algorithm computes the cross-correlation functions for each pair of signals from different station sensors (Cansi 1995). The propagation time from one sensor to another provides the propagation direction (azimuth) and the horizontal velocity. This method extracts low amplitude coherent signals from the incoherent noise (Cansi 1995), allowing signal detection, even when signals are not identified individually in the noise. This method, at first developed for seismology, was successfully adapted to infrasound technology. Figure 7 shows an example of signal processing, illustrating the infrasound signals produced by the Concorde supersonic aircraft which was currently observed at the French research station established in Flers (Le Pichon et al. 2002).

The PMCC algorithm is used for operational data processing at the International Data Centre (Brachet et al. 2006, Brachet et al. 2010).

The PMCC method is also available for National Data Centres for automatic detections and data analyses. The infrasound bulletins are edited every day, and typical infrasound events detected at the station are sorted out. For each event, the infrasound velocity and the back-azimuth of the waves (clockwise from the north) are automatically determined.

Another detection algorithm based upon the Fisher F-statistic (Fisher 1992) at first implemented for seismic arrays, was adapted to infrasound processing (Olson 2004). This method is based on the measure of the ratio of variances, which can be interpreted as the signal to noise level. Arrowsmith et al. (2008) applied this method to regional infrasound networks in Utah and Washington State and demonstrated its effectiveness for detecting, associating and locating sources of interest.
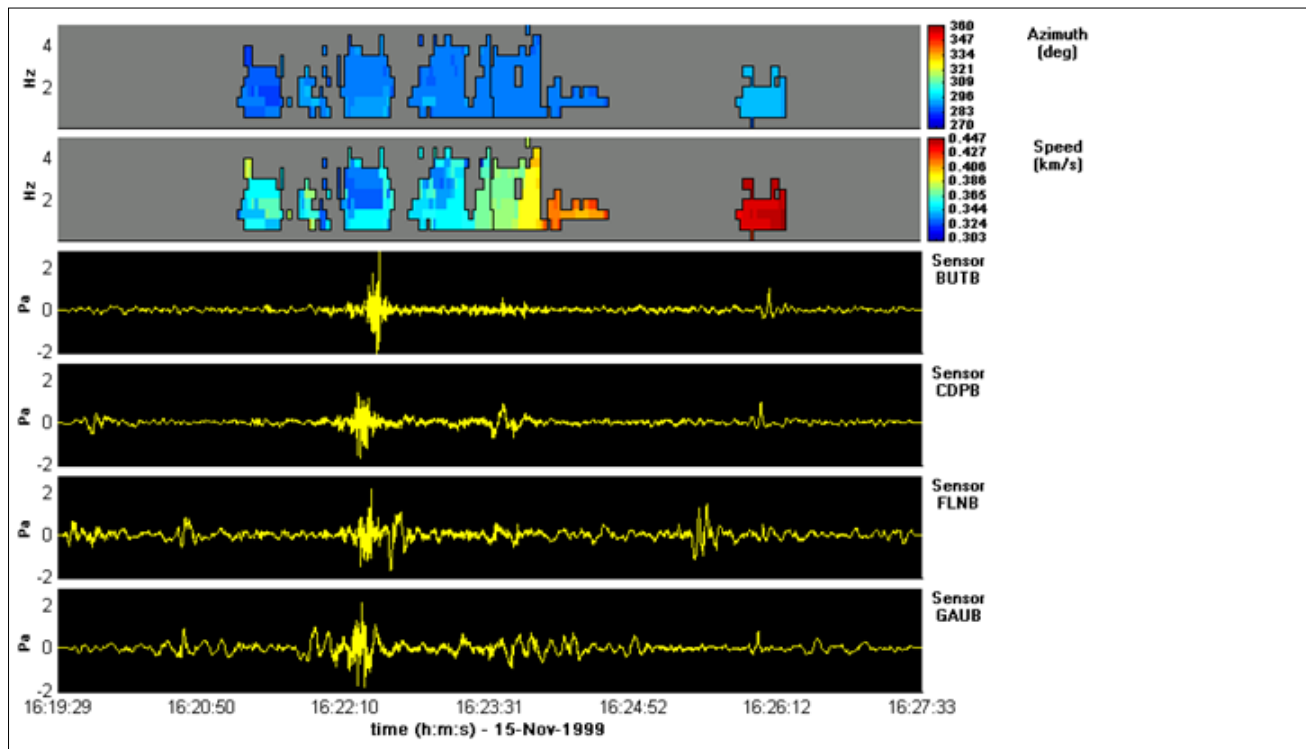
FIGURE 7.
Example of infrasound PMCC data processing showing signals produced by the Concorde supersonic aircraft in 1999.

4. DEVELOPMENT OF THE INTERNATIONAL INFRASOUND MONITORING SYSTEM

4.1. The Infrasound International Monitoring System

The infrasound IMS network when completed will consist of 60 stations located on all continents and several islands, especially in the southern hemisphere, in order to provide global coverage (Figure 8). Data and metadata are transmitted to the International Data Centre (IDC) via the Global Communications Infrastructure, where they are analysed and made available to the States Signatories through the Reviewed Event Bulletins (REB) (Mialle et al. 2019). A comprehensive description of the IMS and an analysis of its performances, from sensors to data processing, was provided by Marty (2019).

The first station, IS26 in Germany, was certified in 2001. In 2004, 17 stations were in operation, inducing a new interest for this topic (Bedard and George 2000, Hedlin et al. 2002, Bedard et al. 2004). The number of studies was increasing in relation with the challenge of the interpretation of the large set of detected events.

In the IS17 Côte d'Ivoire station, for example, 33 000 events were detected during 10 months from 2002 to 2003. Thanks to the data quality, the complementarity of the measured parameters and the location network possibilities, most of the infrasound sources were identified.

The number of publications was increasing (Figure 9). Studies were motivated by discoveries such as, for example, the oscillation of the concorde infrasound azimuth with season quantifying for the first time the effects of the stratospheric winds on the infrasound propagation paths (Le Pichon et al. 2002), or the microbarom (infrasound from ocean swell) azimuth seasonal inversion, observed at stations located in various geographical positions at distances up to ten thousand kilometers, illustrating the stratospheric wind seasonal inversion at the Earth's scale (Le Pichon et al. 2006, section 4.2).

The better understanding of the infrasound sources, propagation and atmospheric context was essential for the routine analyses performed
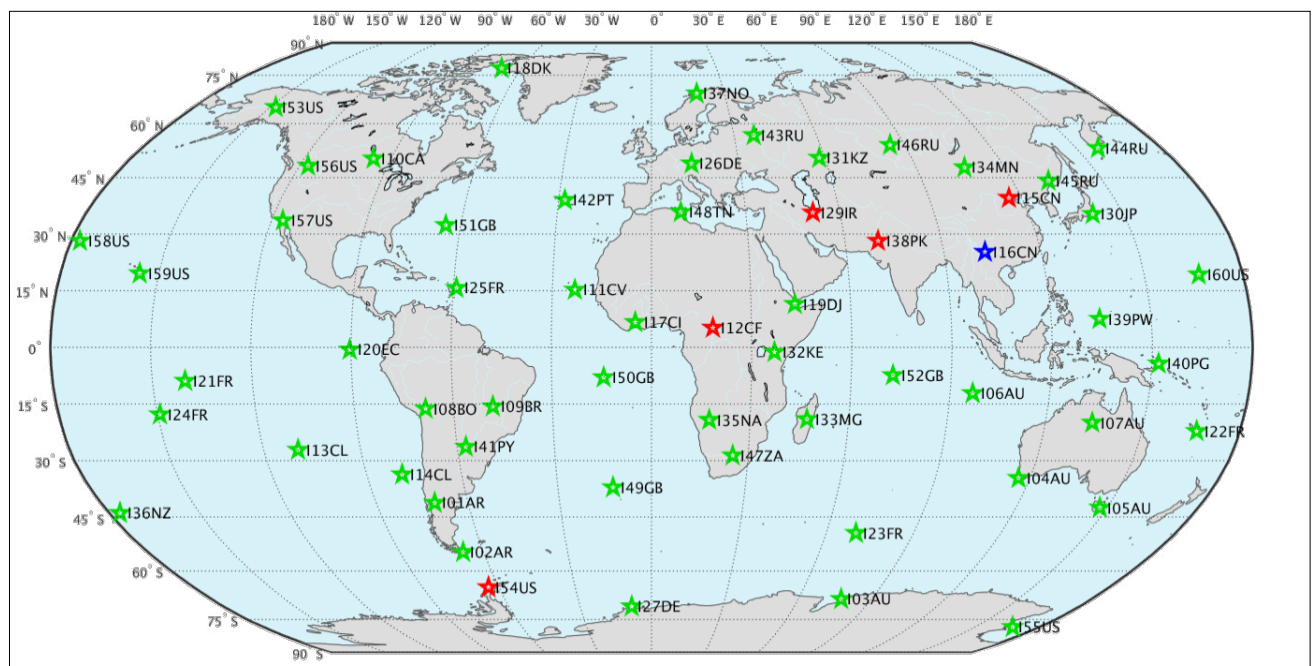
FIGURE 8.
The IMS infrasound network included 53 certified IMS infrasound stations (green stars) from 2000 to 2021 (from Mialle 2021).
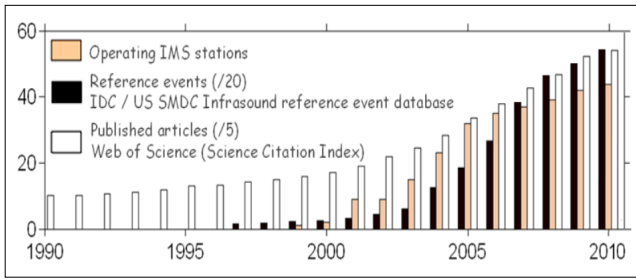
for CTBT verification purposes. Most of the infrasound events observed in the different stations were identified and further used as calibration sources for a quick control of the station health status.

In 2009, the International Scientific Studies (ISS) conference was organized by the Provisional Technical Secretariat of the CTBTO to emphasize the scientific work performed in different countries and motivate new studies (Blanc and Ceranna 2009). The increasing number of published papers highlighted the IMS scientific potential (Figure 9). Such studies are essential in maintaining the excellence of the routine technical and scientific work related to IMS data exploitation.

4.2. Identification of the Infrasound Sources

A 'zoo' of infrasound sources was observed in the different infrasound stations located in different environments. These sources are, for example, ocean waves, explosions, bolides, earthquakes, mountain associated waves, volcanoes, auroras and meteorological events such as lightning, hurricanes, cyclones.

The IMS network provides accurate description and localisation of the infrasound sources which may be differentiated by the following features:

- Microbaroms are generated at the interface between ocean and atmosphere, when ocean waves at about the same frequency

(~0.1 Hz) coming from near-opposite directions interact (Evers and Haak 2001, Garcés et al. 2004, Le Pichon et al. 2006). The microbaroms frequency is twice the frequency (~0.2 Hz) of the source waves. In the Tunisian bulletin (IS48), Atlantic Ocean swell is observed (at azimuth ~315°) in winter (Figure 10). Differently, in New Caledonia (IS22), in the Southern hemisphere, microbaroms originate from strong swell systems along the Antarctic circumpolar current. A clear seasonal variation is produced by the stratospheric general circulation changes, with westerly winds in summer and easterly winds in winter, driving the acoustic energy in the wind direction, as demonstrated by simulations (Le Pichon et al. 2006). Microbaroms constitute an infrasound noise and are observed everywhere in the world. They represent a simple calibration source for the infrasound IMS network.

- Active volcanoes such as Etna (Italy) or Lopevi and Yasur (Vanuatu) can be distinguished in the Tunisian and New Caledonia bulletins respectively. They produce persistent signals detected in
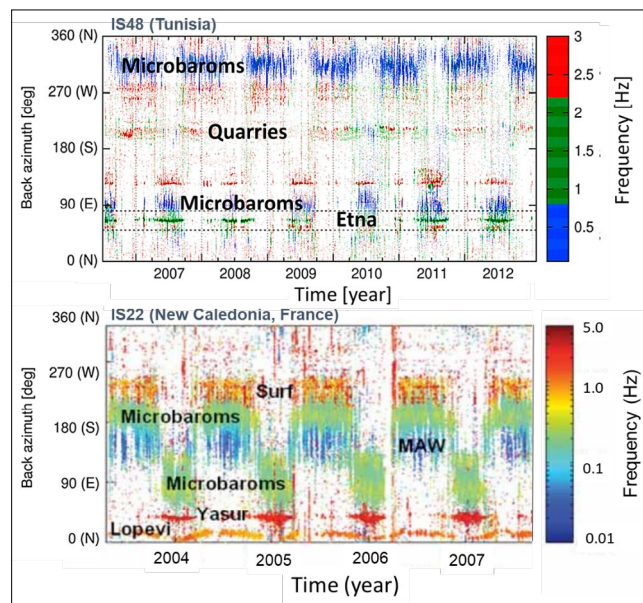
specific directions corresponding to the volcano azimuths. Small seasonal variations are observed, similar to the azimuthal variations produced by the stratospheric winds on the Concorde path (Le Pichon et al. 2002). Such fluctuations were studied by Evers and Haak (2005) and corrections of the event locations were further integrated in data processing by including the stratospheric wind effects.

- Mountain associated waves, below 0.1 Hz in blue on IS22 bulletin, are generated by the tropospheric wind flowing over mountains. The mountain sources were identified by triangulation, these signals being generally observed in several IMS stations thanks to the ability of infrasound to propagate over long distances (Hupe et al. 2019a).
- Surf: ocean waves impacting emerged reefs, generate surf signals in the 1 Hz to 5 Hz frequency band. The amplitude is proportional to the ocean wave height (Garcés et al. 2003, Le Pichon et al. 2004).
- Quarry blasts are identified at specific azimuths depending on the quarry source locations.

Other infrasound sources are auroras (Wilson 2005), severe weather (Bowman and Bedard 1971), meteors (Revelle 1976) and earthquakes (Mutschlecner and Whitaker 2005).

4.3. European Stations for Regional Calibrations and New Tools for Data Analyses

4.3.1. *New Infrasound Network in Europe and Regional Ground Truth Events*

In regions of northern Europe, a significant number of events in the industrial belt can be used for the calibration of the network capability and for testing simulations and methods.

In the 1990s the number of European stations, developed at national level, was increasing. A new European network emerged which could be considered as relevant to complement the IMS network. It mainly included the French and German experimental stations Flers and Igade and

the Swedish infrasound array (Liszka 1974). Data analyses, performed in synergy with seismology, allowed the identification of the events produced by human activity: quarry blasts, mines, supersonic aircrafts (Le Pichon et al. 2008). It showed the usefulness of this network for the discrimination between natural and anthropic sources.

These European observations were summarized by NORSAR in the "Catalogue of Ground Truth Events (GTE) from repeating sources in Europe" during the feasibility phase of the Atmospheric dynamics Research InfraStructure in Europe project (ARISE 2018), dedicated to integrating middle atmosphere observation networks as a complement to the IMS network for improving the characterization of the atmospheric disturbances.

The European network is still developing and forms a significant tool for regional studies providing a new image of regional disturbances, a way to develop and calibrate new methods for the data analysis and interpretation, and regional infrasound data well complementing the IMS global infrasound data (see section 8.2).

4.3.2. *Tools for the Parametrization of the Infrasound Propagation*

Tools were needed for rapid signal analyses, taking into account the very large data sets provided by the IMS increasing collected data and the atmospheric variability.

Using successive explosions and sounding rocket observations of wind and temperature, Kulichkov and Bush (2001) showed a large variability in the detected signals produced by changing fluctuations in the atmospheric profile, such as gravity waves. The signals were stronger and more complex in the presence of these fluctuations which increased the effective sound speed Veff (speed of sound plus along-path wind speed), above its value at the surface of the ground.

Kulichlov then proposed to use the effective sound speed ratio: Vratio, (which is the ratio of the maximum between the Veff in the stratosphere and Veff at ground level) as criterion to characterize the infrasound propagation. If Vratio >1 the propagation is possible (Kulichkov and Bush 2001, Kulichkov 2010). The ray theory requires a sound speed greater or equal to that on the ground, along the profile, (generally in the stratosphere), for ray return to ground and possible detection.

Vratio then efficiently predicts when and where the infrasound can be detected. This parameterization is very robust. It was and is still intensively used for IMS data routine interpretation and in many infrasound studies (see Figure 11 and Figure 22).

4.4. Towards Global Monitoring: Impact of Stratospheric Winds

The increasing number of IMS stations open the way to unique global scale studies. IMS data obtained from the beginning of the development
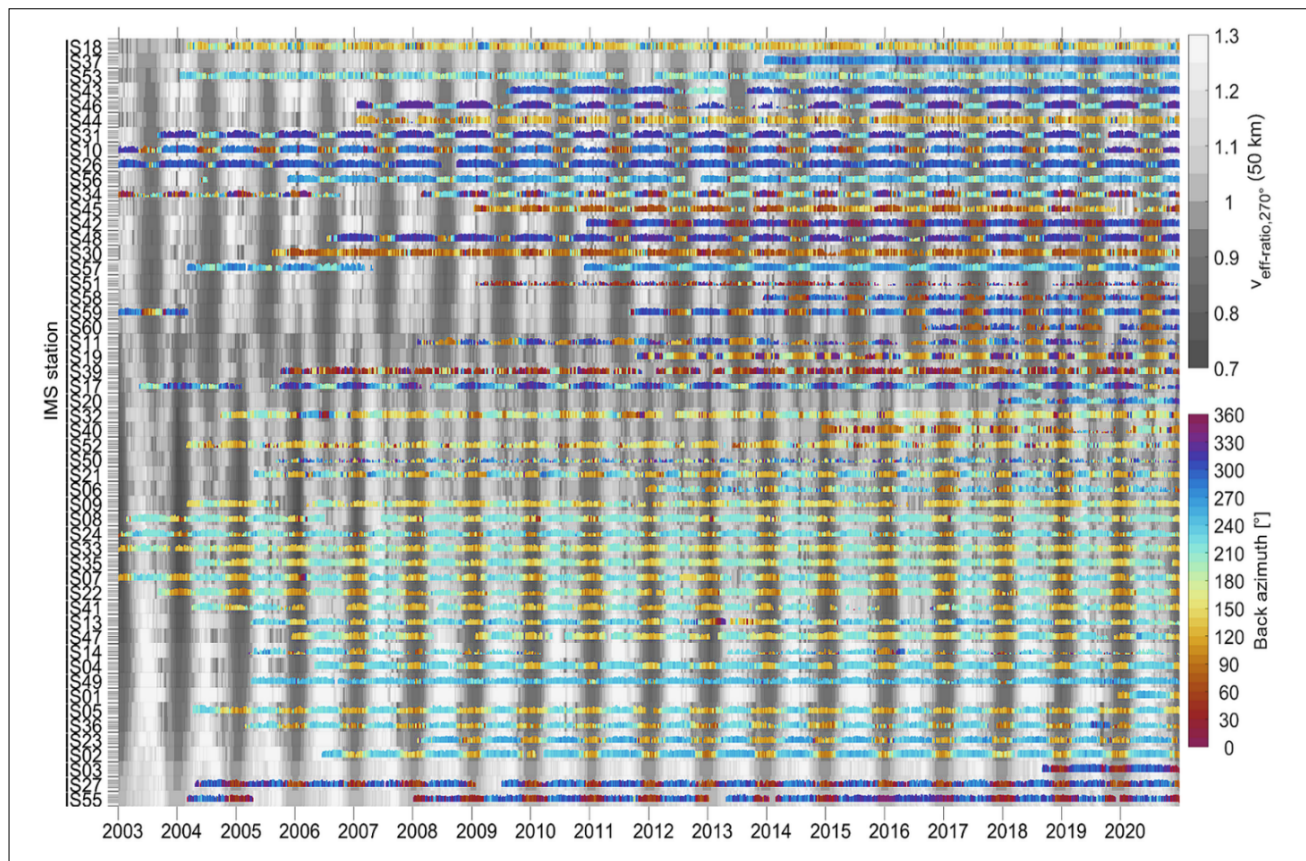
FIGURE 11.
Reprocessing of 18 years of IMS infrasound data including historical and recent data, recorded in 52 certified stations. The microbarom signals (azimuth in color) are submitted to seasonal variations controlled by the stratospheric winds (represented by Vratio in grey) (from Ceranna et al. 2019, Hupe et al. 2022).

of the network to the present were analyzed and the bulletins of all the available stations illustrated the effects of the stratospheric winds on the infrasound propagation in a global way.

Figure 11 shows the microbaroms bulletins of all stations with the azimuth represented by color and sorted by latitude. They are superimposed on the Vratio represented with grey scale (Landès et al. 2012, Ceranna et al. 2019). Vratio is defined by the ratio between the effective sound speed at 50 km and at the ground level (section 4.3.2).

When Vratio >1, the stratospheric waveguide favours eastward propagation, otherwise, propagation is inverted because of the inversion of the stratospheric wind with the season and hemisphere. Figure 11 shows the control of the microbarom propagation by the stratospheric winds. The infrasound are then tracers of the stratospheric wind activity and could provide relevant information for the assessment of the wind atmospheric models (sections 6.3.2 and 9.3).

5. INFRASOUND PROPAGATION MODELS AND CALIBRATIONS

Propagation models were developed for the representation of the infrasound propagation. The comparison between different methods: ray tracing, parabolic, 3-D HC calculations needed infrasound reference data for their validation. Well determined sources such as accidental or calibrated explosions were researched.

5.1. Comparison Between Propagation Models and Observations

During the Misty Castle high explosive tests in the USA, complementary observations were performed at distances from few up to more than thousand kilometers, providing unique calibration signals. The Misty Picture experiment consisted of the explosion of 4685 tonnes of ammonium nitrate and fuel oil carried out on 14 May 1987,
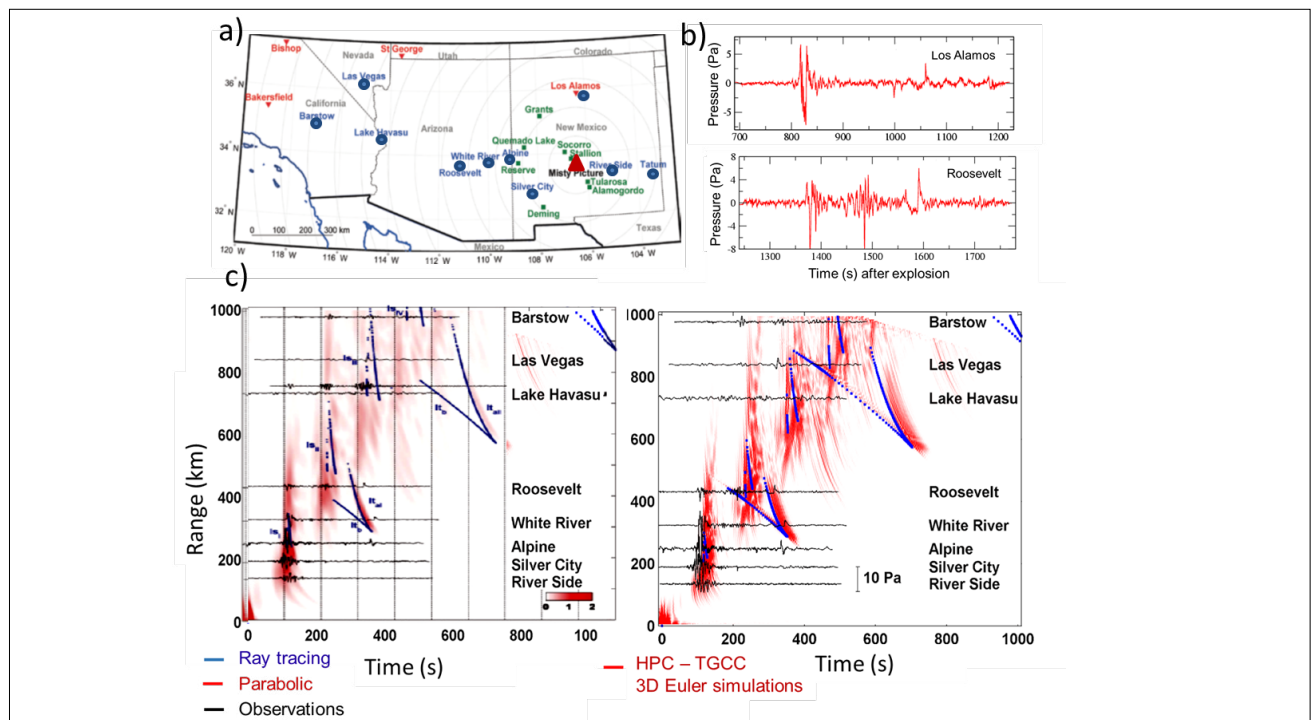
FIGURE 12.
Propagation modelling for the Misty Picture explosion. a) Map indicating the station locations, b) example of infrasound signals, c) comparison between models and observations (Gainville et al. 2010, Del Pino et al. 2009).
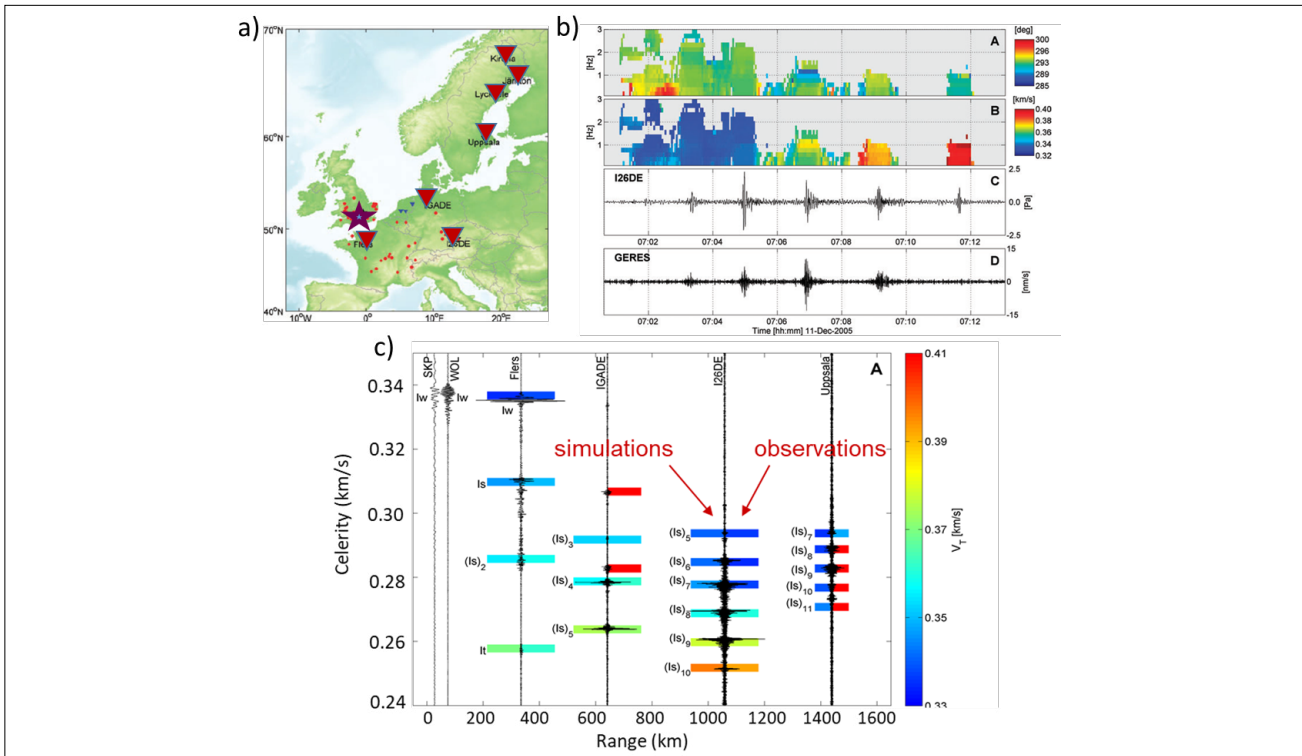
FIGURE 13.

Simulations of the infrasound propagation for the Buncefield accidental explosion (2005) using the signals recorded in the different stations indicated by a triangle in the map. (a) Examples of signals (b), in the diagram, (c) coloured bars to the right hand side of each trace represent the measured values; coloured bars to the left hand side represent the model predictions. The presented simulation used the G2S, Navy Research Laboratory model (from Ceranna et al. 2009).

in New Mexico (White Sands Missile Range), on the surface of the ground. The atmospheric profile was measured by a rocket of up to 70 km. Complementary infrasound observations were performed (Reed et al. 1987, Whitaker et al. 1990). Nine microbarometers were installed by CEA in cooperation with Los Alamos National Laboratory, as shown by the blue dots in the map of Figure 12a (Gainville et al. 2010). Ionospheric observations were also performed by Jacobson et al. (1988).

The Misty Picture infrasound signals obtained in 1987 (Figure 12b) are unique. They were used as reference signals in 2006, almost 20 years after the experiments, for the validation of the models as shown in Figure 12c: ray tracing and parabolic models (left) and 3-D simulation by using high-order finite volume discretization of the 3-D linearized convective Euler equations (right) implemented on the Bull-TERA 10 parallel high performance computer at CEA (Del Pino et al. 2009).

There is a general good agreement between observations and the model. This showed that up to 4 kt linear models well represent observations. Nonlinear effects, scattering and atmospheric absorption mainly affect the waveform evolution during the propagation and need to be integrated for specific studies. The ray tracing method is well adapted to routine analyses. The uncertainties in the representation of the infrasound propagation highly depend upon the knowledge of the atmosphere (Gainville et al. 2010).

Other calibrations used accidental explosions (Ceranna et al. 2009, Green et al. 2011). IMS infrasound station IS26 in Germany and several other European infrasound stations detected the Buncefield Oil Depot explosion in Hertfordshire, UK, in December 2005 (Figure 13). Data analysis showed that the limitations in simulations arise from uncertainties in the atmosphere rather than in the acoustic propagation modeling. The climatology model HWM-93 integrating seasonal effects without description of small scale

disturbances (scales hours, days) only predicted four phases, while the semi-empirical G2S, Navy Research Laboratory model (Drob et al. 2003) explained almost 20 infrasonic arrivals as shown by Ceranna et al. (2009) in Figure 13. This shows that one essential source of uncertainties in the propagation simulations is the poor description of the small scale disturbances in the models by lack of routine high resolution observations in the middle atmosphere.

5.2. Quantification of Gravity Wave Impact on Infrasound Detectability

The Etna volcano quasi continuously produces infrasound signals, well detected in Europe and Northern Africa, offers a relevant calibration source for multiyear studies. Such signals recorded at the Tunisian IS48 infrasound station were analyzed to quantify the effect of the small scale fluctuations on the station detection capability. The simulation uses the European Centre for Medium-Range Weather Forecasts (ECMWF) model. This model well represents the seasonal variability and large scale disturbances but is limited for including small scale

disturbances, such as gravity waves especially in the middle atmosphere where routine accurate data are rare. These sub grid scale disturbances were generally not considered by models mainly dedicated to climatological studies.

Figure 14a presents simulations of the detected amplitude using ECMWF in black, while simulations integrating atmospheric perturbations such as gravity waves along the ECMWF wind profile are in orange. The Etna detection periods are represented by a horizontal orange bar. They extend from May to September when the stratospheric ducting is efficient and occasionally in winter during sudden stratospheric warming events when the stratospheric wind is inverted. There is a first-order good agreement between the observations and the periods when the predicted detection thresholds remain smaller than the averaged source amplitude.

Statistics demonstrate that the simulation, including the wind fluctuations of the gravity waves, well represents the detection periods (Figure 14c bottom). These waves were characterized during the observation campaign
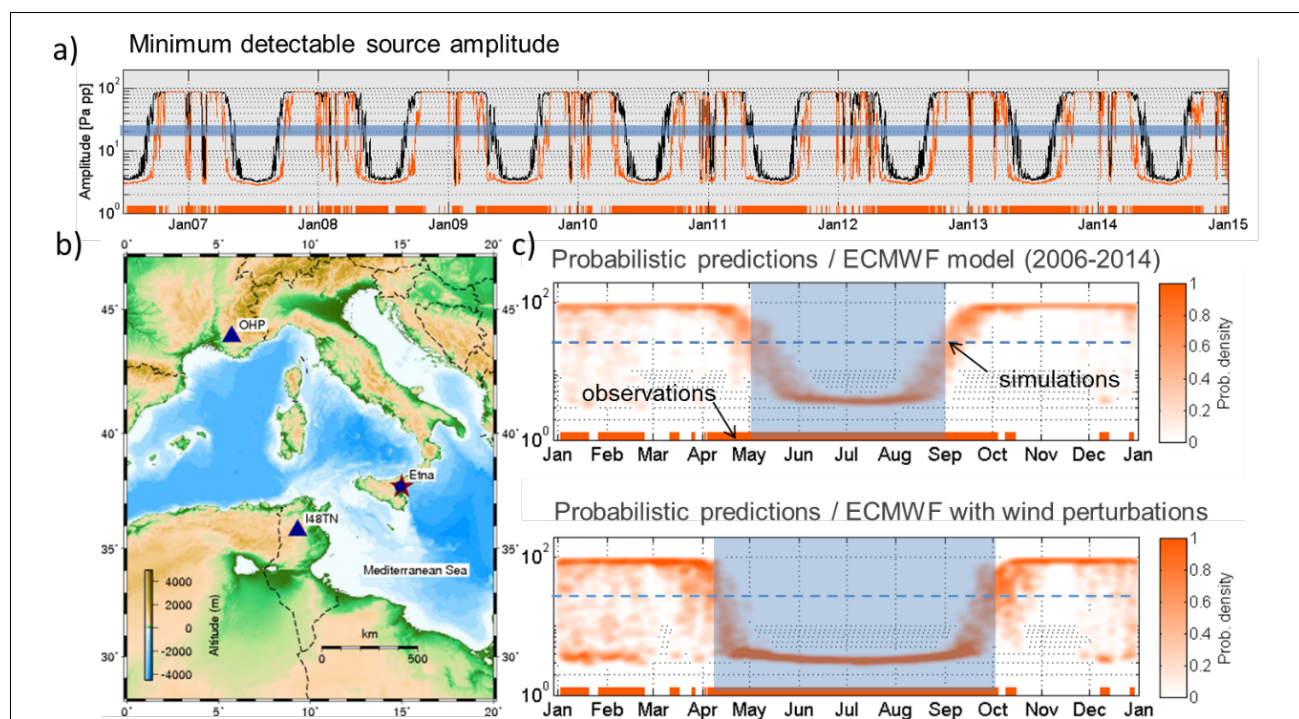
FIGURE 14.

Effects of the atmospheric small scale wind perturbations on the detection capability of IMS station IS48 to monitor explosive signals from Mt. Etna: a) Seasonal variations of the predicted detection threshold using the ECMWF HRES atmospheric model, without (black curve) and with (orange curve) incorporating these perturbations, b) statistics from 2006 to 2014 comparing the predicted detection periods (highlighted in blue) with observations.
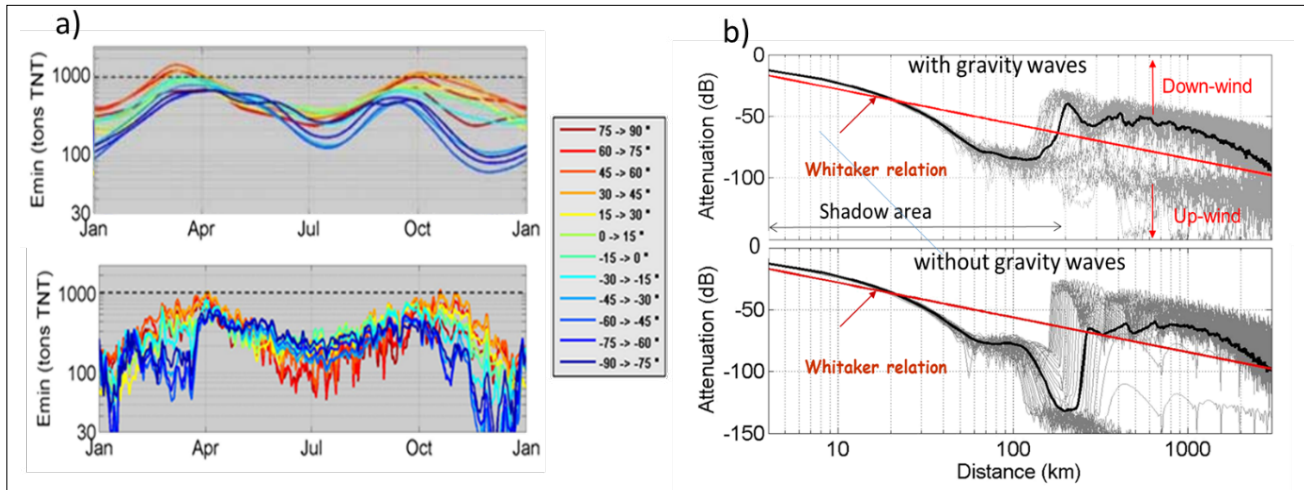
FIGURE 15.

a) Detection capability of IMS stations at different latitudes using the HWM07 model (top) and the ECMWF model better integrating the atmospheric variability at different periods of the year (bottom). The minimum detectable yield is lower than 1 kt at any latitude and any time (from Le Pichon et al. 2009). b) New attenuations laws computed with and without including gravity waves (from Le Pichon et al. 2012).

at the Observatoire de Haute Provence (OHP) France. They were statistically extrapolated up to Tunisia at 50 km altitude and incorporated into ECMWF high resolution (HRES) model. This integration significantly improves the simulations (Blanc et al. 2018).

5.3. Including Gravity Wave Effects in Detection Capability Models

Advances in simulations of the infrasound propagation, in the available atmospheric models and the increasing possibilities of calibration tests, motivated the improvement of the detection capability maps at a global scale.

The model developed by Green and Bowers in 2010, is based on the probabilistic approach (previously used by Clauter and Blandford, 1997). It demonstrated that the integration of the climatology model HWM07 (Drob et al. 2008) tends to reduce the detection threshold. This model predicts that the IMS verification objective to detect explosions is always achieved across the IMS network for a yield lower than 1 kt.

The deterministic approach developed by Le Pichon et al. in 2009, on the basis of previous studies (Plantet 1996, Blanc and Plantet 1998), used the ECMWF model and station dependent wind noise models. It determines, more precisely than previous models, the effects of the stratospheric winds on IMS detection capability (represented by the minimum detectable yield) as shown in Figure 15a. In spite of this variability, the model shows that the verification objective is achieved at all latitudes and seasons.

This study showed that the description of the atmospheric variability needs to be better understood and included in models in order to improve the determination of the uncertainties and their prediction. For this purpose, a theoretical relation predicting the attenuation versus range was developed from massive numerical simulations using the Parabolic Equation method (Le Pichon et al. 2012). This approach provides a more realistic physical description of long range infrasound propagation (Figure 15b). This new relation combines near-field and far-field terms and provides a full description of the silence zone structure in different conditions. The presence of gravity waves produces partial reflections of the infrasound, reduces the silence zone and significantly decreases the attenuation effect up to distances of thousands of kilometres.

An example of validation using the 2011 Sayarim calibration experiment coordinated by the CTBTO (Fee et al. 2013) is shown in Figure 16. The explosion yield was 100 t. More than 20 experimental infrasound stations, deployed by different countries, were associated to the existing IMS infrasound network. The stations where the
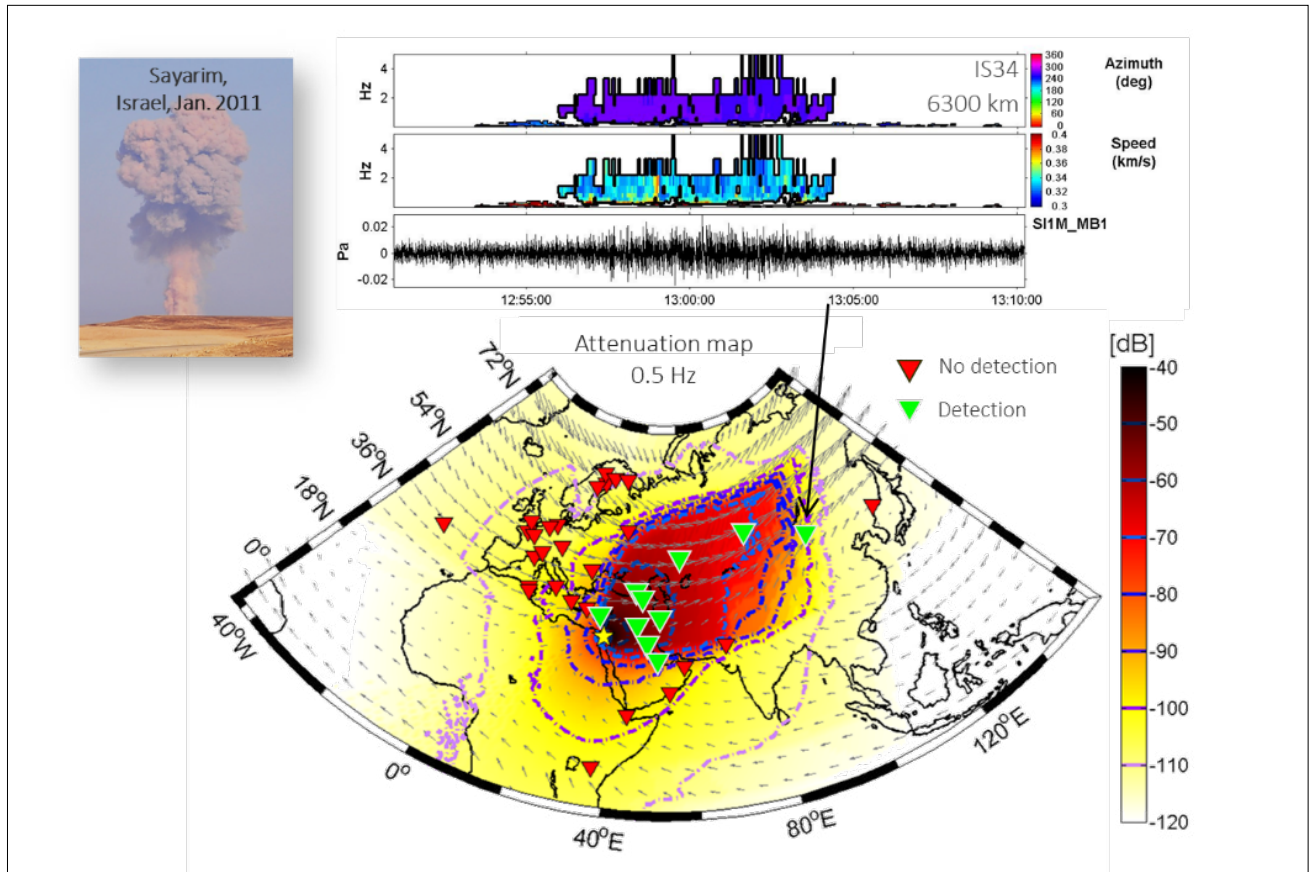
FIGURE 16.
Assessing the infrasound network detection capability map with the Sayarim calibration experiment coordinated by the CTBTO (January 2011 in Israel ~100 t TNT).

explosion was detected are represented in green in Figure 16. The winds were blowing eastward allowing detection in the IS34 station in Mongolia located at more than 6000 km from the test site. These observations are in good agreement with the simulated attenuation maps predicting detectable signal above noise in Mongolia (top of Figure 16).

The Sayarim experiment and associated simulations confirm the network high sensitivity and show its capability to detect large distance explosions with a yield one order of magnitude below the 1 kt verification threshold in favorable wind conditions.

6. IMS OBSERVATIONS FOR IMPROVING THE DESCRIPTION OF ATMOSPHERIC DISTURBANCES

6.1. Global Infrasound Disturbances Produced by Intense Natural Events

With the development of the IMS, many intense and rare natural event, such as bolides, volcanoes and earthquakes were observed (Revelle 2010) producing large disturbances at a global scale and significant damage. The infrasound IMS is well adapted to provide unique information about such atmospheric disturbances, useful for a precise event description.

The air blast and disturbances produced by the Chelyabinsk bolide on 15 February 2013 were described by Brown et al. (2013). The asteroid diameter was of about 19 meters and the
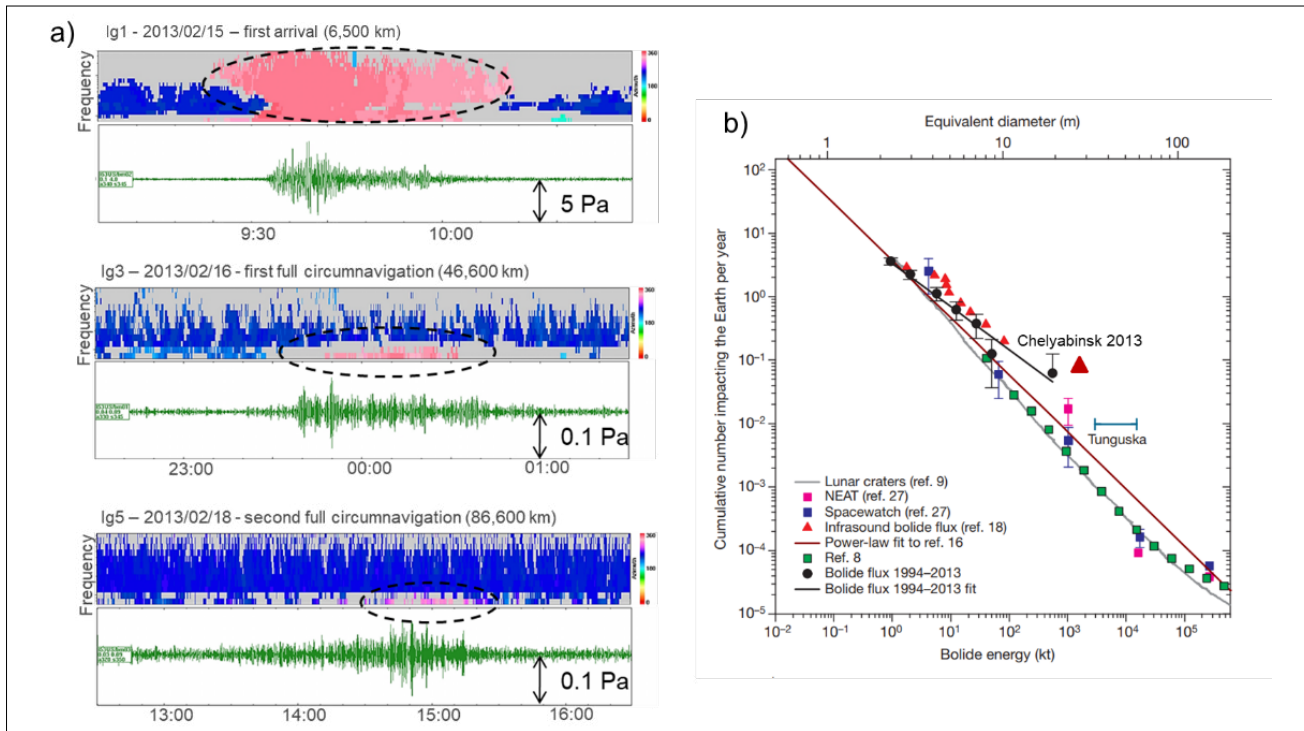
FIGURE 17.

a) Detection of the Chelyabinsk fireball on 15/02/2013 at the IS53 infrasound station. Colours represent the back-azimuth of the waves. They propagate along one and two additional full Earth revolutions (Le Pichon et al. 2013). The top time frequency diagram (lg1) illustrates the wave propagating along the short great-circle path. The second (lg3) and third one (lg5) correspond to waves that travelled along one and two additional full Earth revolutions respectively. b) Empirical relation providing the cumulative bolide number versus yield relation (Brown et al. 2013).

airburst very strong yield was about 500 kt TNT. The infrasound signals were globally detected at distances up to ~85 000 km by 20 IMS stations (Pilger et al. 2015).

Figure 17 (a) shows examples of PMCC detections at station IS53 in Alaska.

According to the expected flux rate of near-Earth objects colliding with the Earth, illustrated in Figure 17 (b) fireballs with the size of the Chelyabinsk fireball are expected to occur about once every 50-100 years, which can be compared to a return period of about 1000 years for Tunguska. The global survey of airbursts of a kiloton or more, performed by Brown et al. (2013) shows that the number of such events could be higher than estimated based on other techniques.

Since infrasound produced by such bolides can be similar to infrasound from atmospheric explosions, Pilger et al. (2019) suggested using such events detected by IMS, for long range propagation studies via stratosphere and thermosphere as reference events. Furthermore, IMS observations are relevant for meteor monitoring by providing complementary data and additional characterization parameters in complement to other meteor monitoring systems (Silber and Brown 2019).

Large volcanic eruptions also produce very large atmospheric disturbances. The recent eruption of the Hunga Tonga-Hunga Ha'apai occurring on 15 January 2022, is one of the most energetic events recorded in the last century. It can be compared in size to that of the 1883 Krakatau eruption as the measured Lamb wave amplitudes are comparable (Matoza et al. 2022). The estimated equivalent TNT yield is in the range of 100 to 200 megatons (Vergoz et al. 2022). The infrasound waves, at about 300 s period, were observed propagating around the Earth up to eight times. It represents the first event ever recorded by all IMS stations.

151
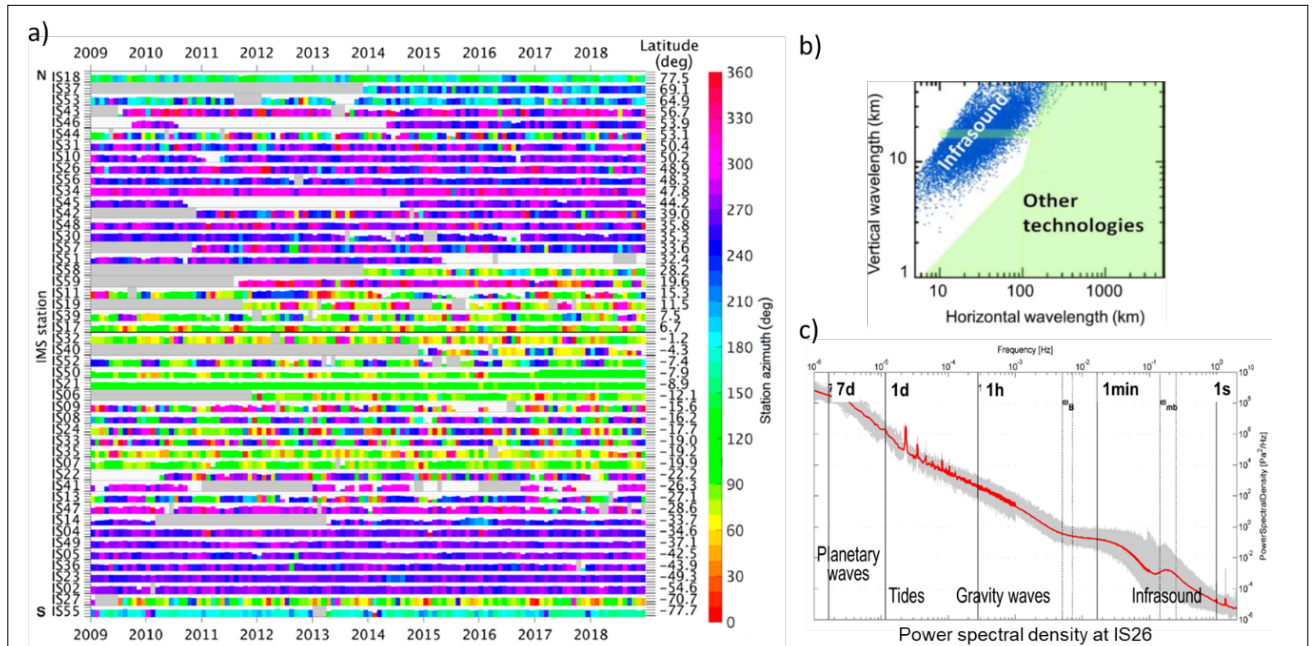
FIGURE 18.

a) Comprehensive overview of the long period gravity wave detections at 48 certified IMS stations (Hupe et al. 2019b). b) Comparison of the gravity wave scales observed by the infrasound array in Côte d'Ivoire (blue) and other technologies: infrared limb sounding, microwave sub-limb, infrared nadir viewing, super pressure balloons, radiosondes (green). c) Power spectral density of barometric data at IS26 (Hupe et al. 2018).

6.2. Gravity Wave Observations by the IMS at a Global Scale

Gravity waves are frequently observed in the atmosphere (Hauchecorne et al. 2019). They disturb the infrasound propagation and need to be integrated in the simulations for IMS data interpretation (section 5.3).

They can be continuously measured in the lower observation frequency range in most IMS stations at anytime and anywhere. They were detected in the 2010s and characterized by using the PMCC method in an adapted configuration. Marty et al. (2010) demonstrated IMS measurements capability at periods ranging from few minutes up to 24 hours, offering the possibility of worldwide gravity wave monitoring and atmospheric tide studies. The potential of IMS data for a better understanding of the dynamics of the atmosphere was suggested by Blanc et al. (2009) through different examples of observations.

For 10 years, gravity waves were observed in the lower frequency range by IMS stations and characterized by their mean back-azimuth (colour-coded) as shown in Figure 18a. These detections mainly reflect sources of deep convection, particularly in the tropics. At mid-latitudes, signals are more complex and coherent wind noise more often produces spurious detections (Hupe et al. 2019b).

Figure 18b shows the interest of these gravity waves data, which complement data provided by other instruments and assimilated in numerical weather prediction models. This result was obtained by the University of Reading in the framework of the ARISE project, by using five years of gravity wave data observed by station IS17 in the Côte d'Ivoire (blue dots), compared with typical observation ranges of other instruments (green shading taken from Alexander et al. 2010).

Gravity waves transport energy and momentum to the stratosphere and mesosphere, and therefore contribute to the atmospheric circulation. IMS global gravity wave measurements are unique. Associated to the meteorological observations performed at IMS stations, climatological data can be extracted as shown in section 7.3.1 (Marlton et al. 2019a). IMS infrasound network could thus

contribute to improving the representation and parameterization of gravity waves in numerical weather prediction models (Hupe et al. 2019b).

6.3. Middle Atmosphere Probing Using Repetitive Infrasound Sources

The possibility of atmospheric probing appeared early in 1998 when deviations of the Concorde infrasound path were related to the stratospheric wind direction changes (Le Pichon et al. 2002). The idea was to use this deviation for extracting atmospheric parameters very difficult to measure in this altitude range.

6.3.1. Using Volcanoes

As infrasound waves propagate in the upper atmosphere, the recorded wavefront characteristics reveal, in addition to information about the source, significant features of the vertical structure of the winds along the propagation path. Among other signals of natural origin, signals from permanently active volcanoes are useful to recover dynamical properties of the middle atmosphere, allowing investigations in the seasonal and diurnal fluctuations of the atmosphere. The interpretation of these data motivated studies on sources of infrasonic waves and their propagation in the upper atmosphere.
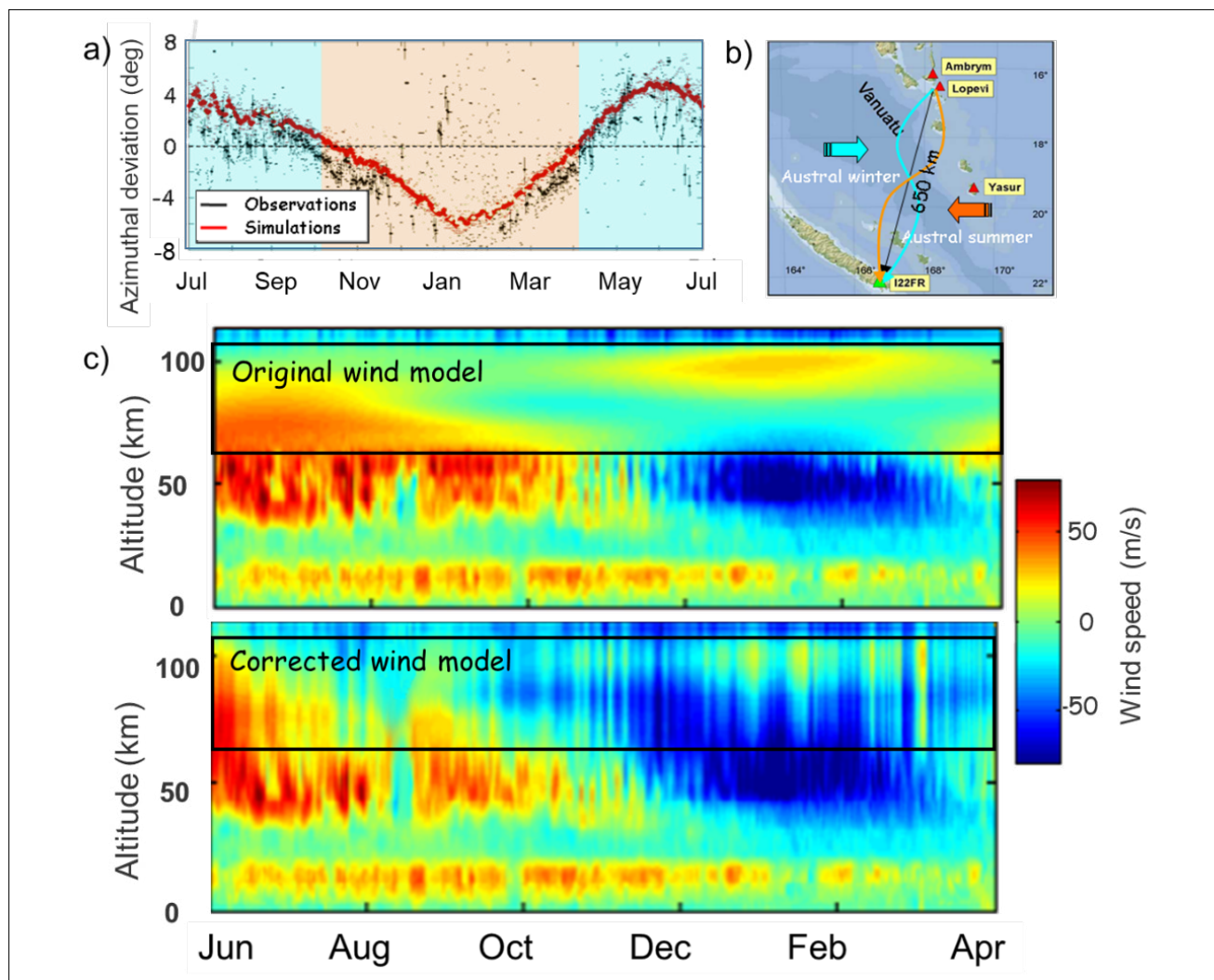
FIGURE 19.
Tomography of zonal winds in the mesosphere and lower thermosphere from continuous records of signals generated by active volcanoes in Vanuatu (Le Pichon et al. 2005). a) The diagram shows the observed and predicted deviations compared to the volcano azimuth (dotted). b) The map shows the volcano and station positions and the wind speed positive towards the east. c) Top: original wind model (G2S, Naval Research Laboratory); bottom-corrected wind model after inversion. The red rectangle delineates the study region where the winds are unknown. Bounded between 60 and 100 km altitude, this region is originally characterized by the HWM model.

Among other studies, Antier et al. (2007) showed that the Yasur volcano in the Vanuatu archipelago is an outstanding source of infrasonic waves due to its regular activity. The proposed detection and propagation modelling methods allow assessing state of the art atmospheric models up to 60 km altitude.

Le Pichon et al. (2005) studied the seasonal trends in the direction of arrival of detected signals from active volcanoes in the Vanuatu archipelago. From summer to winter, the azimuth variation reaches 15°, as the result of the reversibility of the zonal stratospheric wind with season (Figure 19). 3-D ray-tracing modeling roughly explains the observed seasonal trend in the azimuth variation but underestimates its amplitude (Virieux et al. 2004). The discrepancy between the measurements and the result of the simulation is explained by undervalued wind speeds in the upper atmosphere. Infrasonic observations are used as input of an inversion scheme for adjusting the vertical structure of the wind in the upper stratosphere and mesosphere. This study showed the added value of infrasound to correct mesospheric winds which were here found to be underestimated by at least 20 m/s throughout the year, with differences reaching 50 m/s.

Assink et al. (2013) revisited the use of infrasound as a remote sensing technique for horizontal winds in the upper atmosphere. Travel times of impulsive signals from the Tungurahua volcano in Ecuador were used to characterize atmospheric tides in the thermosphere. The results suggested that the predicted mesospheric and thermospheric arrivals, based on tidal specification provided by the empirical wind model HWM07 (Drob et al. 2008) are inconsistent with the observations. This is clearly the result of atmospheric components not represented in the horizontal wind model (HWM) and in the mass spectrometer and incoherent scatter model (MSIS) due to the lack of precision in the upper atmospheric zonal wind models.

Assink et al. (2014) further explored a Bayesian framework to estimate first-order effective sound speed model updates with a time resolution ranging from hours to multiple years using near-continuous active volcanoes. Taking advantage of efficient array processing methods (Cansi 1995), accurate wavefront parameter estimations were used to improve atmospheric estimation procedures. The proposed inversion method includes the elevation angle of arrival, travel times, which is directly related to the ray parameter.

While a first-order agreement was found between the inverted and original profiles produced by the ECMWF model this study reported significant discrepancies around some of the equinox periods and other intervals during which the atmosphere is in a state of transition. Deviations from the a priori models around the stratopause up to 30 m/s were estimated.

Such updates are in line with the results from comparisons between ECMWF analysis and ground based facilities that were collocated during the ARISE measurement campaign.

Validation of atmospheric analysis and forecast products, in regions above 30 km altitude where data coverage is sparse, are important for numerical weather prediction applications. These studies demonstrate that infrasound can provide useful additional information in the upper stratosphere, benefiting from an infrastructure that integrates independent measurement techniques of both wind and temperature in the middle atmosphere.

As atmospheric specifications in the lower and middle atmosphere are routinely used in a wide variety of atmospheric sciences and applications, continuing investigations into infrasonic signals from repetitive sources such as active volcanoes, will certainly improve our understanding of the interaction between the stratosphere and the troposphere. Furthermore, the validation of the analysis product is relevant to a broad community, such as the community involved in the verification of the Treaty, to help advance the development of automated source location procedures for operational infrasound monitoring.

6.3.2. *Using the Swell*

Continuous microbarom emission also provide a source of infrasound that can be used to probe the atmosphere. Smets et al. (2016) demonstrated the possibility of using a microbarom source model to infer the performance of forecasts with different lead-times (10-day forecast, 5-day forecast and nowcast) in terms of sudden stratospheric warming (SSW) predictions. Smets and Evers (2014) had shown beforehand how infrasound could allow for following the lifetime of an SSW. Recent investigations showed however that the microbarom source model could be improved and be more realistic (De Carlo et al. 2020, 2021). Hence, work using microbarom as a reference source to diagnose atmospheric products remain to be undertaken with a more realistic source model. Vorobeva et al. (2021) started demonstrating the use of this new model to assess the quality of analysis products during SSW events (section 9.3).

7. THUNDERSTORM IMPACTS AND NEW SCIENTIFIC CHALLENGES

7.1. Impact of Thunderstorms on Infrasound Monitoring

About one thousand thunderstorms occur every day around the world, producing about 45 lightning flashes per second (Christian et al. 2003). Lightning infrasound studies made in the 1960s and 1970s were limited because of the lack of an accurate lightning location system. The development of the IMS together with the progress made in the 1990s and 2000s in 2-D (latitude and longitude) and 3-D (latitude, longitude and altitude) lightning localization systems allowed these studies to be revived.

The effect of thunderstorms on the IMS monitoring system could be related to an increase of noise level and to false alarms from lightning infrasound producing multiple coherent impulse-like signals in the monitoring frequency range (Assink et al. 2008). However, lightning infrasound signatures differ from that of nuclear explosion signals (section 2.2) especially by their amplitude and duration (Farges 2009, Farges and Blanc 2010). The detected infrasound signals can also be correlated with results from the electromagnetic lightning detection networks, which could be used for the discrimination. This could be possible up to distances of about 50 km from the infrasound array, which is approximately the distance of successful correlations between infrasound and electromagnetic signals (Assink et al. 2008).

7.2. Probing Sprite and Lightning Structures

In 1989, sprites — very brief glows occurring in the middle atmosphere between 40 km and 80 km above thunderstorms — were discovered (Franz et al. 1990). Their origin was related to high altitude discharges and runaway avalanching processes (Roussel-Dupré and Gurevich 1996). Associated emissions gamma ray were observed by satellites in the Earth's atmosphere (Smith et al. 2005). Very quickly numerous complementary measurements completed the first optical observations everywhere in the world and from space.

Since the first sprite observation campaigns organized in Europe in the early 2000s, the challenge was to identify the acoustic waves they could generate. The origin could be weak air heating in the streamer channels of sprites on the order of several degrees K (Pasko and Snively 2007). Using observations performed at the French Flers prototype infrasound station during the 'Sprite 2003' campaign, Farges et al. (2005) highlighted that infrasound could be associated with sprites having taken place up to 1000 km from the station. Their arrival time was compatible with a source located at 60 km altitude and their duration was proportional to the horizontal extension of the sprites. The signals were characterized by a specific time
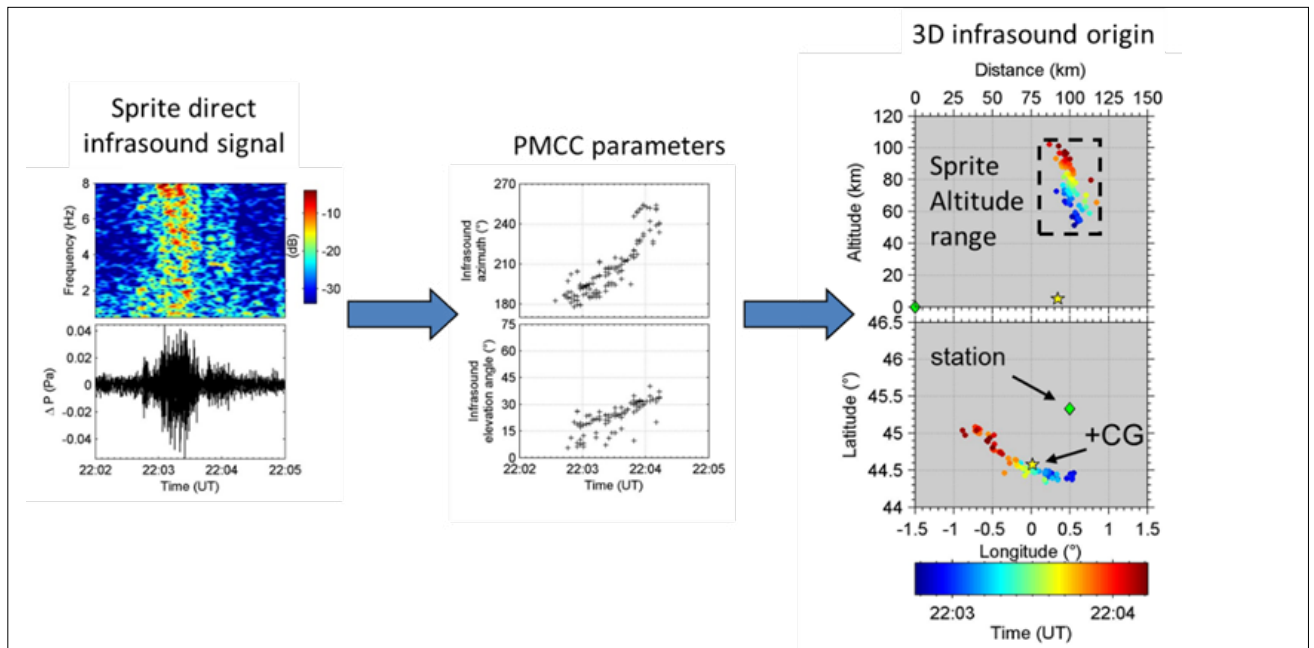
FIGURE 20.

3-D infrasound structure from sprites observed by direct transmission. PMCC processing provides the azimuth and elevation angle of the infrasound origin inside the sprite structure. The origin time is the time of the positive cloud to ground (+CG) lightning parent, recorded by electromagnetic observations. The origin distance is deduced from the sprite infrasound time by ray tracing (Farges and Blanc 2010). The origin of the sprite infrasound was determined at about 100 km altitude and at 90 km to 140 km from the Flers station.

frequency chirp signature in the 0.1-9 Hz range, confirming previous observations by Liszka (2004). Sprites were simultaneously observed by camera at the Observatoire du Pic du Midi in the Pyrenees mountains, and the first direct correlation between chirp-like signatures with optical observations was obtained (Farges et al. 2005).

The infrasound chirp sprite signature is very characteristic. A method based on diffusion entropy detection was developed by Ignaccolo et al. (2008) for automatic detection of these signals. The infrasound technology then contributed to determining the global number of sprite (Ignaccolo et al. 2006).

Measurements made two years later allowed the detection of sprites within 200 km of a temporary station. They showed that at short distance the signature is an inverted chirp (Farges and Blanc 2010).

De Larquier and Pasko (2010) demonstrated that both sprite infrasound signatures are explained by the smaller structures at lower altitudes radiating higher infrasonic frequencies that are observed first at the station, while the low frequency components are delayed because they originate at lower air densities at higher altitudes. This effect is enhanced by the stronger absorption at high frequencies at high altitudes.

Using the measured azimuth and the elevation angle deduced from the measured horizontal velocity, which represents the projection at ground of the infrasound sound speed velocity, a new method was developed to reconstruct in three dimensions the position of the infrasound source as shown in Figure 20 (Farges and Blanc 2010).

The same procedure was also used to retrieve the lightning infrasound sources at altitudes of several kilometres. The 3-D reconstruction of acoustic sources show that they are very well superimposed on electromagnetic discharges (Gallin et al. 2016). The part of the signal coming from the ionized channel connecting the ground to the cloud was isolated from the one coming from the intracloud discharges. Lacroix et al. (2018) thus highlights that the acoustic signal,

including infrasound, comes essentially from the energy point of view of the ionized channel. A new model explaining the observed spectra, proposed by Lacroix et al. (2019) reconciles the infrasound measurements and the mechanism explaining the formation of the acoustic waves by the heating to more than 40 000 K of the air inside the channel.

Infrasound from sprites were also observed by the Israel Infrasound Network (Applbaum et al. 2020) and the IS33 Madagascar station (Ramanantsoa 2019).

7.3. Low Latitude Climatology from Thunderstorm Infrasound Observations

7.3.1. *Gravity Waves from Convection and Inter Tropical Convergence Zone of the Winds*

Statistics were performed using infrasound gravity wave data measured at the IS17 station in the Côte d'Ivoire from January 2002 to December 2015. The PMCC method was used at low frequency in the gravity wave observation range (lower than the verification frequency range: section 6.2) showing that the wave activity is intense throughout the year with peak periods in May and October and less intense activity in January, in good agreement with the local keraunic level. The azimuth seasonal variations from northward direction from February to August to southward direction from August to December, follow the seasonal motion of the tropical rain belt partly related to the Intertropical Convergence Zone of the winds (ITCZ, Figure 21).

The observed gravity waves at the surface are associated to the passage of thunderstorm convective cells near the station. They are related to the flow of the tropospheric air mass in the tropics, which goes from east to west, and the seasonal north–south motion of thunderstorms with respect to the station. When they are not ducted near the surface, waves propagate upwards, and in the absence of gravity waves breaking due to wind shears and strong temperature inversions, their amplitude is amplified in the upper atmosphere and can reach the threshold value beyond which wave saturation can occur (Costantino and Heinrich, 2014). Gravity waves were observed up to the ionosphere (Blanc et al. 2018). Simulations were performed for the interpretation of lidar gravity wave observed in the stratosphere and mesosphere at the Observatoire de Haute Provence. The potential energy provided by the
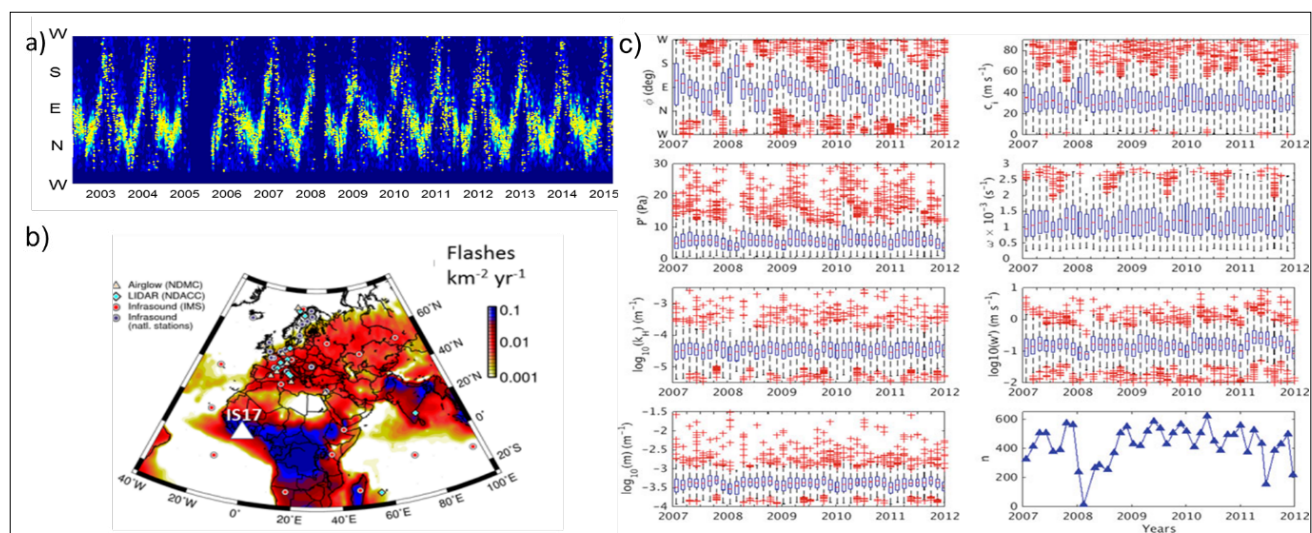
FIGURE 21.
a) Statistics over 13 years of data from the IS17 IMS station in the Côte d'Ivoire: gravity waves represent the motion of the ITCZ (Blanc et al. 2014). b) Lightning map from the World Wide Lightning Location Network observations. c) Gravity waves climatology parameters deduced from IMS gravity wave and meteorological data (Marlton et al. 2019b).

model is in good agreement with observations (Costantino and Heinrich 2014).

Marlton et al. (2019a, 2019b) showed that by combining these data with the meteorological data recorded at the infrasound station, further relevant parameters can be calculated, as shown in Figure 21c. These parameters can be used by the meteorological community to improve gravity wave parameterization in the models and improve the understanding of their variability.

7.3.2. Semi-Annual Wind Oscillation from Lightning Infrasound

The high quality and the long duration of the observations were also exploited in the infrasound frequency range to study lightning activity. Farges et al. (2021) systematically and automatically identified lightning-related detections measured from 2005 to 2019 at the IS17 IMS station in the Côte d'Ivoire. By isolating the detections at distances larger than 150 km after stratospheric propagation, it is possible to
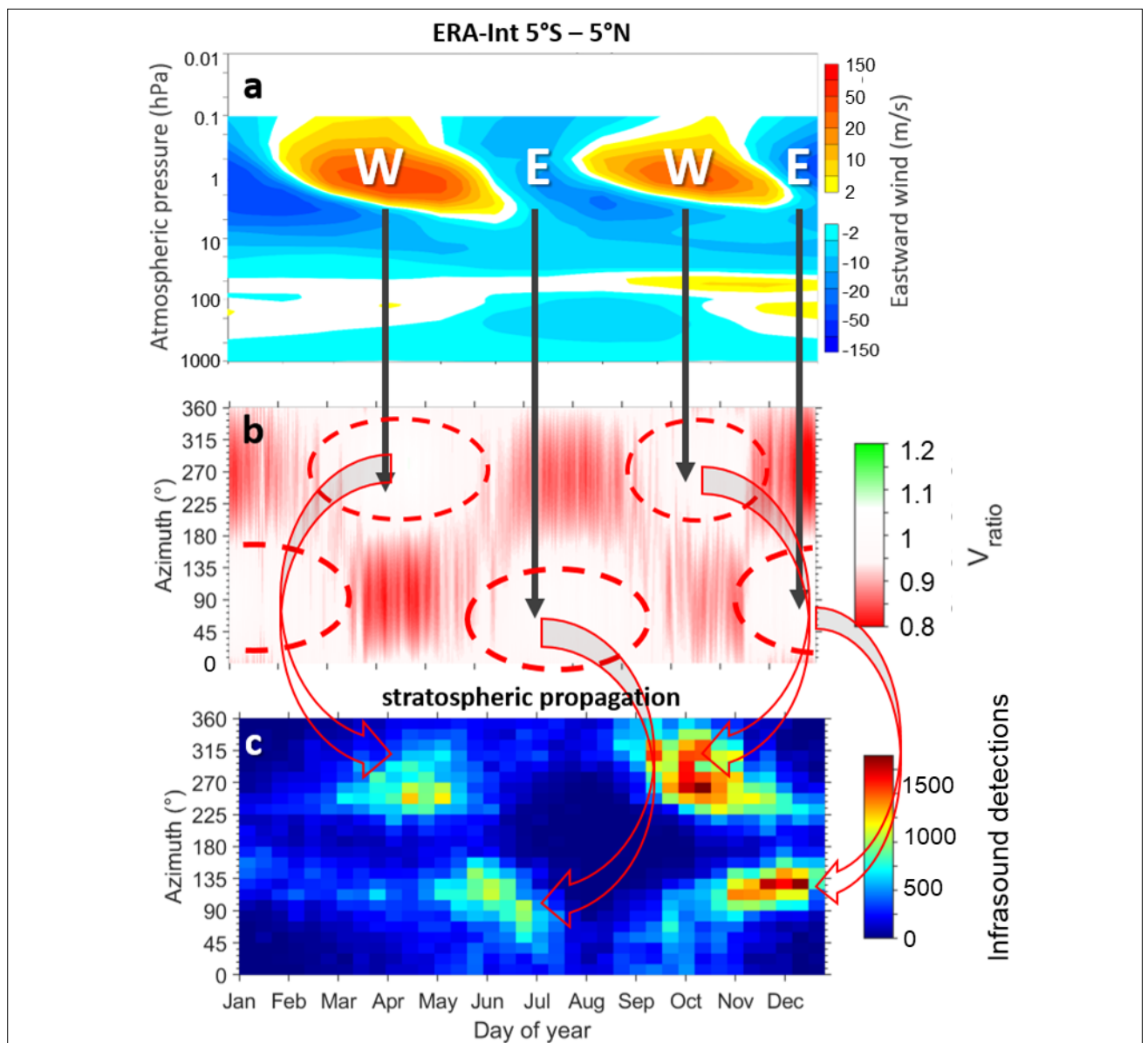
FIGURE 22.
a) Climatological monthly zonal mean, eastward wind averaged over 5S-5N, from the monthly mean in the ECMWF Integrated Forecast System ERA5. The vertical pressure scale indicates the altitude (1 hPa at about 50 km). b) Vratio (section 4.3.2) variation with time and azimuth (favorable propagation when it is white or green). c) Statistics over 15 years of infrasound signals produced by thunder in the Côte d'Ivoire. Adapted from Farges et al. (2021) and ECMWF (2021).

highlight the semi-annual wind oscillation (SAO) of the winds in the tropical stratosphere because of the change in azimuth of these detections as shown in Figure 22c.

The SAO controls the wind seasonal variability from the upper stratosphere to the upper mesosphere (Baldwin et al. 2019). The SAO is in its westerly phase from March to May and from October to November and in its easterly phase from August to October and from December to February (Figure 22a). This seasonal change controls the infrasound wave guide and is at the origin of the observations. A comparison of infrasound detection statistics (Figure 22c) with the SAO from 2004 to 2019, represented by the ECMWF's high resolution analysis (Figure 22.b), showed a general good agreement (red arrows). Some differences, possibly related to ECMWF uncertainties from gravity waves, and altitude changes of infrasound reflections in relation with

the SAO, would motivate further studies (Farges et al. 2021).

Detections of lightning infrasound and of gravity waves from convection are submitted to some modes of variability in the middle atmosphere (Farges et al. 2021) and in the troposphere (Blanc et al., 2014), respectively. These detections can be used as tracers of low latitude climatology processes acting at synoptic to planetary scales (ITCZ and SAO). The activity of extreme meteorological events (intense thunderstorms, cyclones) and, at larger scales, some low latitude climatology processes (ITCZ and SAO). The activity of extreme meteorological events (intense thunderstorms, cyclones) can also be monitored and characterized through infrasound detections (e.g. Listowski et al. 2022). 'Infrasound meteorology' is an avenue to be explored for all altitudes at a regional or global scale, in support of conventional technologies.

8. MULTI-INSTRUMENT PLATFORMS FOR THE DETERMINATION OF UNCERTAINTIES IN INFRASOUND MONITORING

This section focuses on the interest of complementary ground based multi-instrument platforms to provide a new scientific input in the understanding of infrasound sources, propagation effects and related processes. This especially leads to the quantification and reduction of uncertainties in the infrasound monitoring simulations and assessment of atmospheric models.

8.1. ARISE Middle Atmosphere Multi-instrument Observations for Improving Infrasound Monitoring and Atmospheric Models

The ARISE project (Blanc et al. 2018) consists in a multi-instrument research platform, integrating the IMS infrasound network for scientific infrasound related applications, the Network for the Detection of Atmospheric Composition Changes for lidar measurements of the wind and temperature profiles (Hauchecorne et al. 2019) and other innovative instruments such as airglow spectrometers, meteor radars and wind microwave radiometers. Routine

measurement and observation campaigns are performed in the ARISE reference stations such as the Arctic Lidar Observatory for Middle Atmosphere Research (ALOMAR) in Northern Scandinavia, the OHP in France and the Maïdo Observatory in Reunion Island. The objective is to develop innovative instruments and new methodologies for providing improved data sets needed to better characterize stratospheric disturbances and related atmospheric processes.

8.1.1. Uncertainties in Middle Atmospheric Profiles and Infrasound Simulations

During ARISE observation campaigns, specific structures difficult to be predicted and inducing local uncertainty in the ECMWF model were measured by lidar at the Maïdo observatory (Hauchecorne et al. 2019). At the same time an eastward jet around 40 km and a westward jet around 50 km produced a double atmospheric duct inducing microbarom propagation toward both west and east directions (Figure 25a).
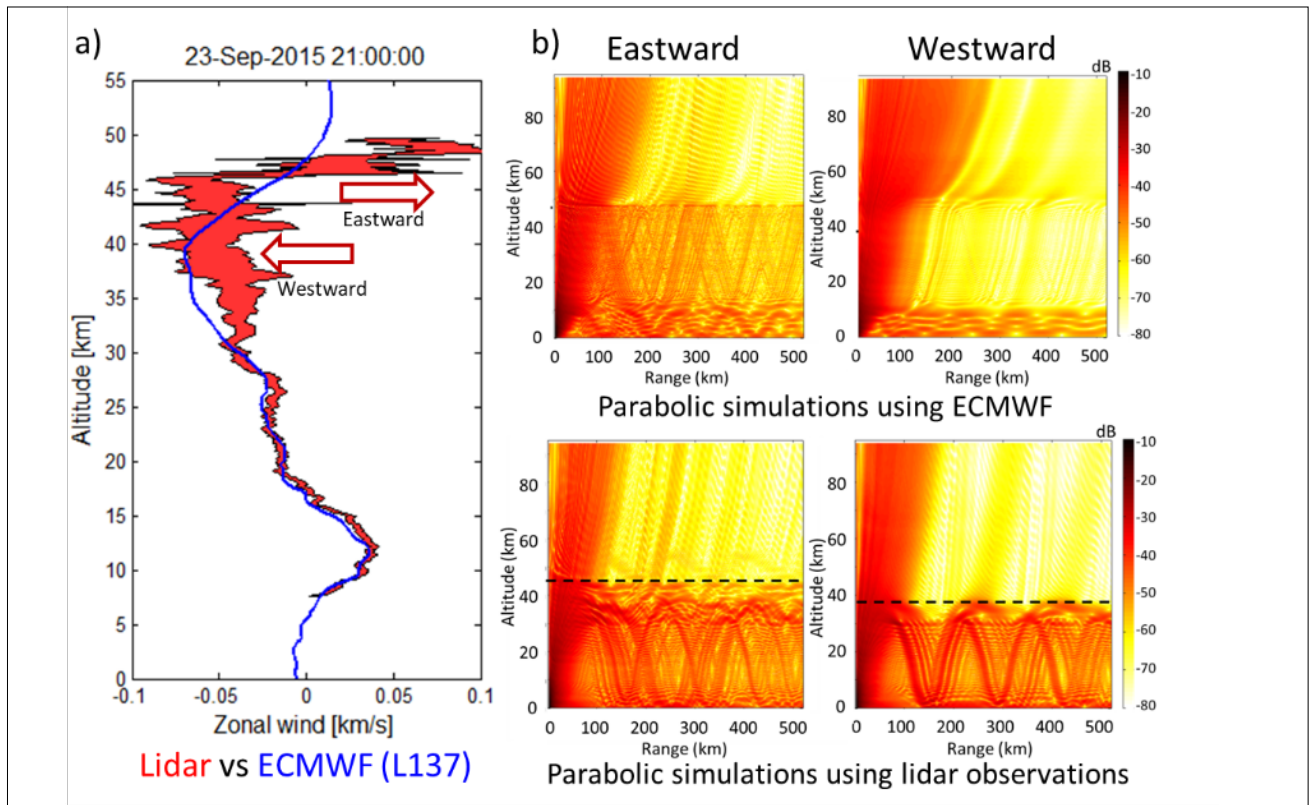
FIGURE 23.

a) Comparisons between wind profiles measured by lidar at the Maïdo observatory (instrumental error bars in red) and provided by the ECMWF model (L137, in blue) on September 25, 2013. b) Simulations of the infrasound propagation at 0.3 Hz (attenuation in dB with a reference distance of 1 km to the source) with the ECMWF profile (top) and the lidar profile (bottom) (from Blanc et al. 2019).

The simulation of the infrasound propagation performed using the lidar profile reproduces the observed double infrasound stratospheric duct well while the simulation performed with the ECMWF profile (in blue) only predicts weak eastward propagation (Figure 25b), confirming the difficulties to represent such small scale structures in routine infrasound data analyses (sections 5.2 and 5.3).

This example demonstrates the potential benefit of the association between lidars and infrasound technology for infrasound propagation simulations to locally supplant model outputs and thus limit propagation uncertainties related to atmospheric model inaccuracies.

8.1.2. *Uncertainties in Atmospheric Models*

The first ARISE multi-instrument campaign at the OHP observatory in 2013 and 2014 allowed the quantification of the ECMWF model uncertainties (Blanc et al. 2019). It showed systematic differences between modeled and observed temperature and wind fields. The mean standard deviation exceeds 5 K and 20 m/s in temperature and zonal wind speed respectively between 40 km and 60 km altitude, while the 95% confidence intervals reach 30 K and 40 m/s (Le Pichon et al. 2015). The largest deviations are observed in winter when the variability from large scale planetary waves dominates the general circulation.

Other campaigns were performed at the ALOMAR observatory for the comparisons between lidars and meteor radar observations and atmospheric models (Baumgarten 2010, Hildebrand et al. 2017). The measurements of the wind and temperature profiles were continuously performed for five days, from 20 km to 100 km altitude for the first time. They were compared with the ECMWF Integrated Forecasting System (IFS) (Figure 24). This shows that the ISF noticeably represents a
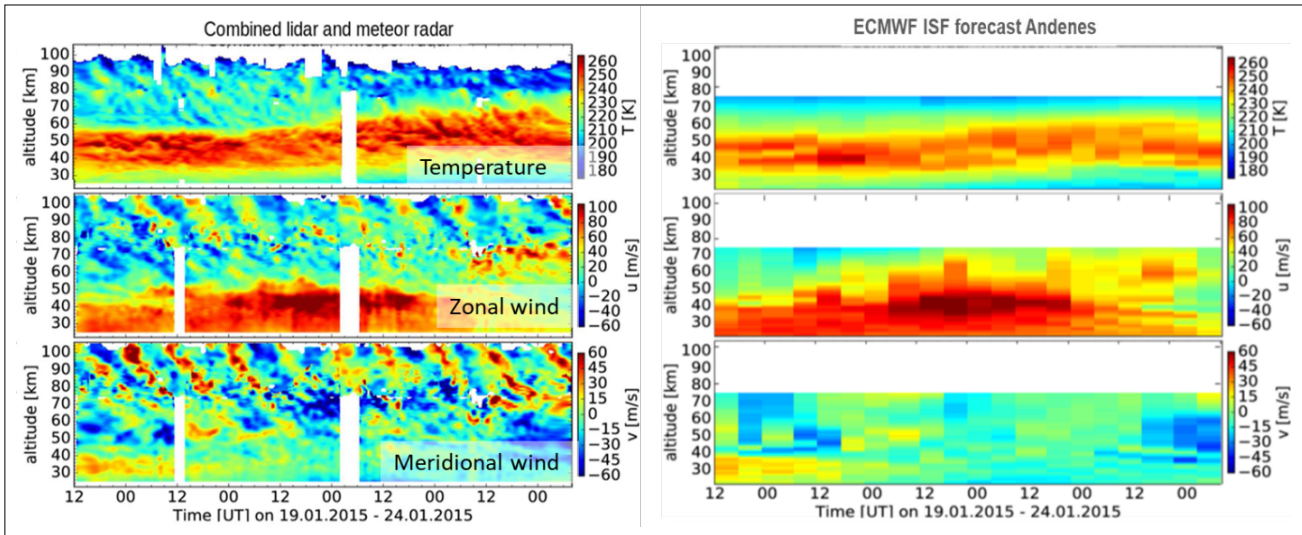
FIGURE 24.

Combined and simultaneous high resolution temperature and wind observations with the ALOMAR Rayleigh/Mie/ Raman lidar, the mobile iron resonance lidar, and the Andenes meteor radar (top panel: temperature, middle panel: zonal wind, lower panel: meridional wind), compared with the ECMWF IFS (from Blanc et al. 2019).

long period of wave activity. However, gravity waves and tidal signatures are not reproduced and gravity waves amplitudes in temperature and wind fluctuations are underestimated in ECMWF by more than a factor of 3 above 50 km.

This campaign shows the potential of such data sets to determine the origin of uncertainties and their impacts on infrasound monitoring. It also allows the assessment of the numerical weather prediction models and the preparation of future pilot stations and network observations for data assimilation in models.

8.1.3. *Example of Sudden Stratospheric Warming Events*

The largest dynamical events occurring in the stratosphere are the SSW events producing an increase of the polar stratospheric temperature up to 40 K compared to ECMWF predictions, as measured during the ARISE multi-instrument campaigns. They lead to the breaking of the polar vortex in winter and inversion of the westerly stratospheric winds, which induces summer-like infrasound propagation conditions.

The strong dynamics perturbations associated to such events can propagate downward and dramatically affect the surface temperature and pressure fields, leading to warmer and cooler temperatures in eastern North America and Northern Europe respectively (Lee et al. 2019). These events are the clearest and strongest manifestation of the stratosphere–troposphere interactions (Charlton and Polvani 2007). As reviewed by Tripathi et al. (2014) in the framework of the ARISE project, correctly predicting the evolution of these extreme events in the stratosphere can lead to improvements in tropospheric weather forecasts on monthly timescales.

These events produce an inversion of the stratospheric wind direction, which drastically change the infrasound propagation conditions. The major SSW of 6 March 2016 produced strong disturbances observed during the ARISE campaign performed in Norway. As shown in Figure 25a, the atmospheric ducting of microbaroms extracted by NORSAR from IS37 IMS station data, strongly changed during the SSW. The Pacific microbaroms were amplified while Atlantic microbaroms weakened. This is due to the sudden direction inversion of the westerly stratospheric wind at the event onset. Figure 25c shows the wind inversion in the ECMWF high resolution analyses. Figure 25b shows the lidar profiles recorded during this event at the ALOMAR station by the Leibniz Institute of Atmospheric Physics compared to the ECMWF profile.

161
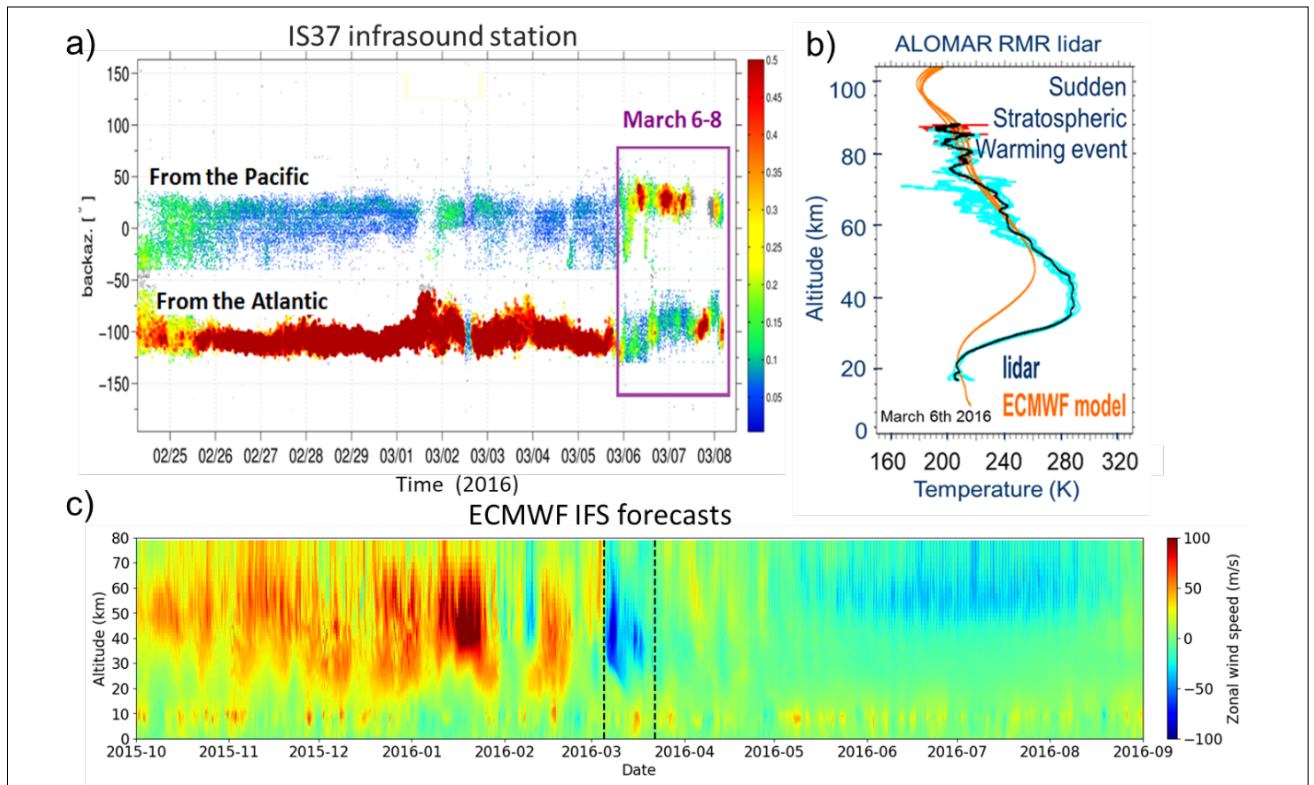
FIGURE 25.

a) Processed infrasound data recorded at the IS37 IMS station during the sudden stratospheric warming event in March 2016. The colour scale corresponds to the observed maximum array cross-correlation. b) Lidar profile measured at the beginning of the event at ALOMAR. c) ECMWF's high resolution (~9 km) analysis products, obtained with the IFS.

This example shows the potential of lidars to provide precise information about such events, whose timing and amplitude are not systematically well reproduced by the models (Figure 25b). This information is needed for infrasound data interpretation, which requests near real time knowledge of atmospheric conditions for CTBT verification purposes.

Smets et al. (2019) reviewed infrasound studies of recent SSW events. They proposed a methodology to provide information about the life cycle of these events from infrasound stratospheric remote sensing (Smets et al. 2016). New methods are developed to provide stratospheric diagnostic in the presence of such event using microbarom monitoring (section 9.3).

8.1.4. *Synergy Between Lidar and Infrasound Observations*

The development of innovative instruments such as lidar is encouraged by the ARISE project to provide direct near real time information about the middle atmosphere, as needed for infrasound data analyses. The Compact Rayleigh Autonomous Lidar lidar is the first fully autonomous middle atmosphere lidar system able to provide temperature profiles from 15 km to approximately 90 km altitude (Kaifler and Kaifler 2021). It was used during ARISE observation campaigns in 2018. Its high temporal and altitude resolutions, of 5 min and 1 km respectively, are well adapted to describe the fine structures of the middle atmosphere, which affect infrasound propagation and its variability. Its ability for fully autonomous operations allows the development of synergy with infrasound routine observations.

This lidar demonstrated its performances during the ARISE campaign in Argentina, with the description of large amplitude mountain waves in the upper stratosphere inducing temperature perturbations of 80 K. This exceeds the largest values previously measured by satellite and reveals large gravity waves activity (Kaifler et al. 2020).

162
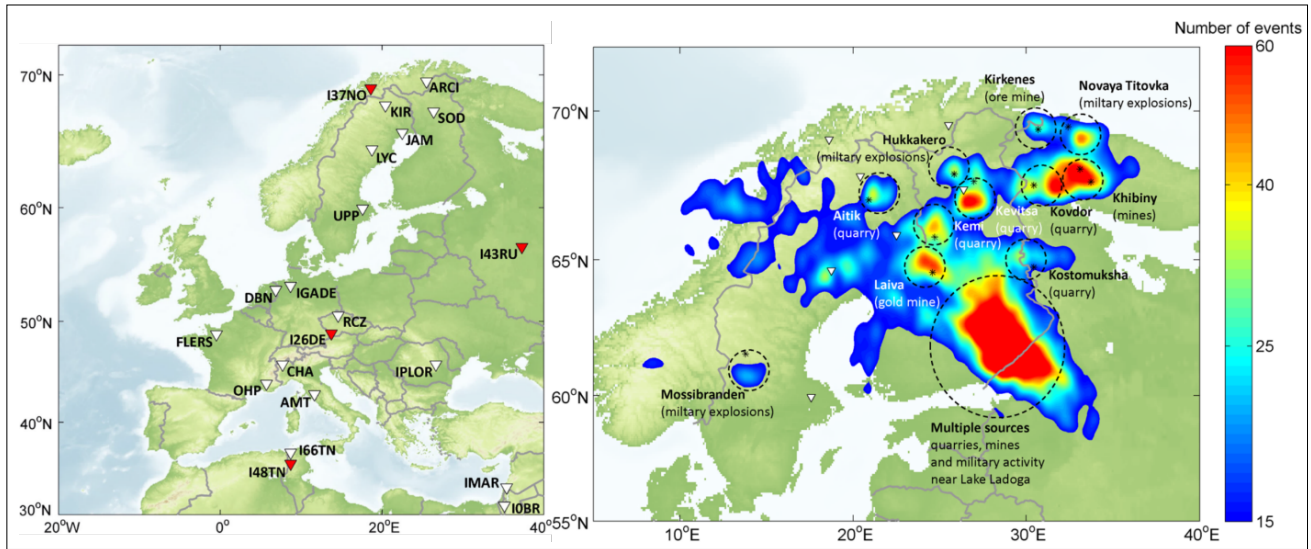
FIGURE 26.

Left: IMS and experimental infrasound arrays in and around Europe contributing to the European infrasound bulletins during the period 2000-2015. Right: Source regions of high frequency infrasound in the Fennoscandian region. Ground truth locations of seismoacoustic sources from Gibbons et al. (2015) are marked by asterisk symbols, while dashed circles highlight the associations to nearby colour-coded infrasound activities (Figure from Pilger et al. 2018).

8.2. Improving European Infrasound Bulletins

Continuous infrasound monitoring on regional scales is useful for advancing the development of automated source location procedures, as well as provides new insights into quantitative relationships between network detection capabilities and atmospheric specifications. To achieve these goals, ground truth events in regions of dense infrasound networks have been considered since the 2000s (section 4.3.1). The IMS infrasound network, while currently not fully established, has demonstrated its capability for locating infrasonic sources on a global scale, including meteorites and volcanic eruptions.

Continuous records made by dense networks, that are not part of the IMS, have a potential to improve seismoacoustic monitoring systems. A total of 24 infrasound arrays in and around Europe are now operated. IMS recordings and data contributions by international partners were collected in the course of the ARISE project to generate a European Infrasound Bulletin during 16 years of operation.

Following the work initiated by Le Pichon et al. (2008), systematic detection and event analyses were carried out. Pilger et al. (2018)

demonstrated the benefit of the dense infrasound European network to improve source localization through comparisons with complementary ground-truth seismoinformation (e.g. Gibbons et al. 2015). The authors highlighted seasonal and diurnal variations of the sources and infrasonic activity in larger detail.

Figure 26 shows event clusters mainly related to anthropogenic origins. These include industrial activities due to various mining and quarry blasts in Northern Europe, military activity in terms of regular ammunition explosions, and other military supersonic flights mainly in the North Sea. The Concorde flights near London and Paris was observed up to 2003. The use of a dense network of infrasound stations in Europe compared to the far sparser distribution of IMS stations in this area provided important insights on the detection and location capability and corresponding event identification and characterization. Additionally, investigation of the seasonal variations of source detections allowed quantifying the sensitivity of the overall network detection capability to the dynamics of the middle atmosphere in the context of CTBT verification.

Efforts are pursuing with the integration in the ARISE platform of infrasound stations located in the Eastern and central part of

Europe, which now form the Central and Eastern European Infrasound Network (CEEIN 2023) This contributes both to progress in the understanding of infrasound sources in central Europe and improving the European infrasound network performances (Bondár et al. 2022).

8.3. Synergy with Seismology

8.3.1. *The USArray*

The USArray transportable array is a wide area network of 400 seismic sensors with about 70 km spacing deployed over various regions of the USA. Most of these stations include infrasound sensors to monitor atmospheric signals (Kerr 1999). This dense infrasound array has enabled large scale infrasonic detection and source location studies using reverse time migration methods with acoustic to seismic coupled signals to locate sources.

From 2007 to 2008, about 900 infrasound sources were recorded and integrated in the Western United States Infrasonic Catalog (Walker et al. 2011). A large number of events were located in Nevada, Utah, and Idaho within active military areas. This study showed that such seismic networks fill in the gaps between sparsely located infrasound arrays by improving the regional infrasonic source location and identification and providing relevant information for propagation studies, especially above the middle stratosphere where routine high resolution observations are lacking. Another example is the study of the Antares rocket explosion observed by the USArray (Vergoz et al. 2019). The large number of infrasound signals (180 infrasound arrivals) recorded by the stations offered a unique opportunity to calibrate propagation models and localization methods.

8.3.2. *Seismoacoustic Coupling*

Arrowsmith et al. (2010) presented a review about seismoacoustic studies highlighting their potential for nuclear explosion monitoring by enhancing the performances in the detection, location and discrimination of events.

The seismoacoustic coupling was studied using infrasound earthquake observations in a wide range of earthquake magnitudes and distances by Mutschlecner and Whitaker (2005). A relation was found between their amplitude, duration and the seismic magnitude suggesting a source regions extension from the epicenter to larger distances by the seismic surface wave ground deformation. Using the infrasound arrival times and azimuths, measured for the Kunlun Mountains great China earthquake in 2001, and an appropriate propagation model, the radiating zone was precisely reconstructed by Le Pichon et al. (2003). Stump et al. (2009), deploying six infrasound arrays in association with the Utah seismic network, showed their potential to enhance the infrasound generation model, leading to a possible infrasound based depth discrimination method. Furthermore, infrasound signals observed in the Republic of Korea were associated to a deep focus (566 km) earthquake occurring in China in 2002. The source area was located near the epicenter, and also in Democratic People's Republic of Korea, the Russian Federation and Japan. This study showed the possibility of infrasound monitoring to detect such earthquakes and help in determining their depth (Che et al. 2013).

An example showing the benefit of the seismoacoustic synergy for CTBT verification is the detection of the underground nuclear explosion in Democratic People's Republic of Korea on 12 February 2013. The atmospheric conditions allowed the infrasound nuclear test detections, by the stations located in the downwind direction, in complement to seismic detections. Such infrasound signals provide relevant information, which could help for the yield and depth determination and for discrimination (Che et al. 2014 and section 9.1).

The interest to develop synergy between infrasound and seismic monitoring also appeared in the study of tsunamis. Coupling between seismic and infrasonic signals were observed in the IS52 (Diego Garcia) station and three other IMS stations during the Sumatra earthquake and tsunami by Garcés et al. (2005). They showed that the initiation and propagation of a tsunami

produce infrasound near the source and along coastlines. As the infrasound velocity (300 m/s) is higher than the tsunami velocity (200 m/s), the infrasound signal is precursor of the tsunami observation.

9. PERSPECTIVES

9.1. Progress in Data Processing for Detection and Discrimination

9.1.1. *Detection*

The need to distinguish between incoherent wind noise and real coherent infrasonic wave signals motivated the development of improved methods to continuously extract interfering coherent signals embedded in background noise (Den Ouden et al. 2020). Among them, a new expression of the likelihood function of a parametric stochastic model was implemented in the time frequency domain multi-channel maximum-likelihood method in order to avoid the presence of interfering signals (Poste et al. 2022). Extensive evaluations through simulations with synthetic signals and analyses of real signals show improved detection probability and false alarm rate in poor signal to noise ratio scenarios.

Continuing the development of such an approach may enhance the potential of the infrasound technology for verification techniques. Furthermore, applying high resolution detection techniques on a broad range of timescales will allow systematic assessments of the variability in the waveform characteristics, opening new perspectives for a growing number of applications with high civil and societal benefits.

9.1.2. *Discrimination*

The global IMS network was designed to detect large atmospheric explosions at distances of several thousand kilometers. Since the yield of anthropogenic events generally remains much below one kiloton, most of them are only reported in single-station detection lists. Combining dense regional seismic and infrasound networks like the ones operated by the Institute of Geoscience and Mineral Resources (Che et al. 2019) in the Republic of Korea or the Norwegian Seismic Array (NORSAR, Gibbons et al. 2015), allows more detailed source and propagation studies. Another example is the deployment of the USArray transportable array (Walker et al. 2011 and section 8.3) with an average interstation spacing of 70 km, which has demonstrated its capability to detect and identify much smaller sources than the ones which would be observed with much sparser station spacing. Such studies illustrate the potentiality of dense regional networks to detect local and regional small magnitude surface explosions and discriminate between natural and anthropogenic phenomena. In this new era of massive data sets, there is a unique opportunity to examine geophysical phenomena in more detail than what was possible before.

9.2. New Data for Weather Prediction Models

The analysis of the infrasound data described in the previous section led to a better description of large scale events such as SSW (section 8.1.3) which originate in the middle and upper stratosphere, influencing surface weather systems. Tripathi et al. (2014) showed that correctly predicting their evolution could lead to improvements in surface weather forecasts on weekly timescales. Other recent investigations on seasonal to sub-seasonal weather predictions demonstrate the importance of using high altitude atmospheric models for simulating surface weather (Domeisen et al. 2020a,b). Including a well resolved stratosphere appears essential to represent stratosphere–troposphere coupling and their impact on weather forecast (Gerber et al. 2012, Domeisen et al. 2020b).

Given their sensitivity to middle atmospheric temperature and wind conditions, infrasound can be used to infer atmospheric states at these high

altitudes (section 6.3). Atmospheric sounding units are used operationally by numerical weather prevision models to assimilate temperature observations in the middle atmosphere with a relatively coarse resolution. However, operational and global measurements of middle atmospheric winds are lacking, while it is known that their better representation is a major step for improved forecasts (Baker et al. 2014). Satellite Doppler wind lidar data recently demonstrated the benefit to forecast performance of assimilating global lower stratospheric wind observations (Rennie et al. 2021).

Routinely made infrasound measurements provide a novel database to further contribute to these tasks in the middle atmosphere since infrasound observations bear signatures of the stratospheric and thermospheric waveguides. Infrasound detections from the Etna volcano were used to show that ensemble forecasting could benefit from this technology to reduce the range of possible atmospheric states using Bayesian techniques (Vanderbecken et al. 2020). Aiming at a different approach and using repetitive explosions related to the destruction of old ammunition, Blixt et al. (2019) documented the systematic link between crosswinds and infrasound azimuth deviations. Key information, which can be retrieved, is crosswinds with respect to infrasound propagation. In the wake of this simple but robust systematic observation,

pioneer studies demonstrate a proof of concept for assimilating infrasound data originating from such discontinuous and localized sources (Amezcua et al. 2020) seeking information on winds. These above mentioned studies paved the way to future investigations for developing techniques using a global and continuous source of infrasound, namely the oceanic swell as shown in sections 6.3 and 9.3.

9.3. Global Microbarom Patterns: Infrasound Noise as Used for Stratospheric Diagnostic

The evaluation of infrasound ambient noise model is essential in the context of the future verification of the CTBT to reduce the number of false alarms. Microbarom signals, produced by counter-propagating surface waves at the ocean surface, propagate all around the globe through the stratosphere and dominate the coherent infrasound ambient noise with a peak around 0.2 Hz. Furthermore, monitoring these signals allows assessing atmospheric models in higher resolution in order to reduce source location errors and improve source characterization methods.

Different theoretical models have been developed to characterize the source of microbaroms, all based on the second-order nonlinear interaction of ocean waves. While early theories considered an infinite ocean depth and a
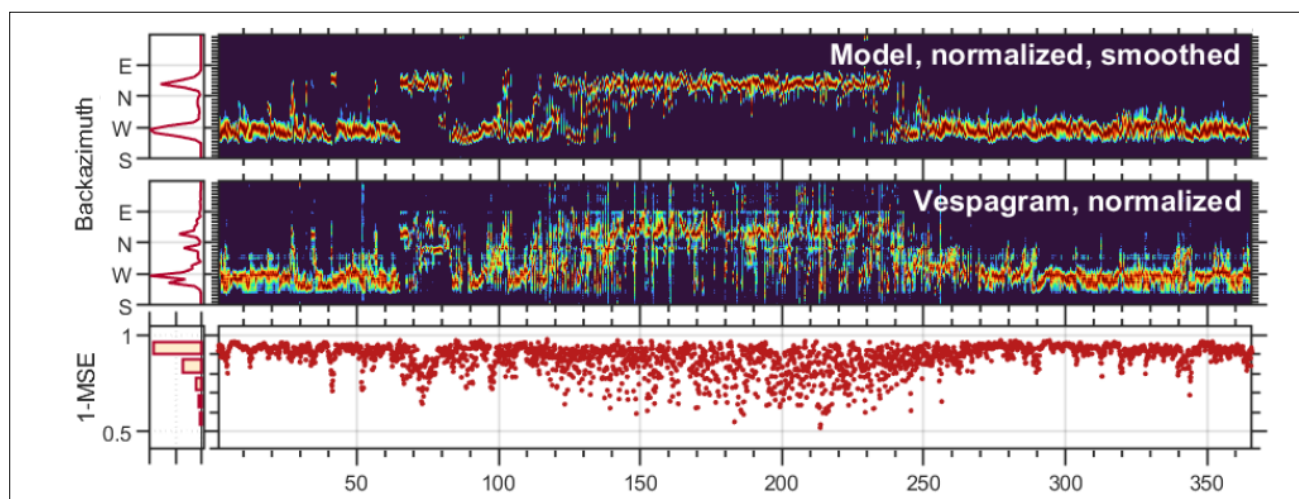
FIGURE 27.
Comparison between microbarom model (De Carlo et al. 2020; top panel) and infrasound observations (middle) in 2016 at IS37. The bottom panel shows the similarity score between the daily normalized microbarom model and vespagram (Figure adapted from Vorobeva et al. 2021).

source radiation depending on the acoustic wave elevation angle (Brekhovskikh et al. 1973), other works have approximated the radiation pattern as a monopole and found a considerable effect of the water depth (Waxler et al. 2007). De Carlo et al. (2020) extended the previous theories to the combined effects of both finite depth ocean and source directivity in both elevation and azimuth angles.

Beyond theoretical issues, efforts are pursued to validate the source model by considering ambient noise observations as recorded by the IMS. In particular, the implementation of the source model developed by De Carlo et al. (2020), based on a state of the art numerical wave model (Ardhuin 2021), is helping to build a global and time dependent reference database. Vorobeva et al. (2021) demonstrated that exploiting this source database is relevant for developing middle-atmospheric remote sensing methods. Figure 27 is an example of multidirectional comparisons between microbarom soundscapes and infrasound data recorded at IS37 in northern Norway during 2014-2019. The proposed method, computationally inexpensive, highlights seasonal variations in the microbarom azimuth distribution, amplitude and frequency, uncovers microbarom source variability and has the potential for near real time stratospheric diagnostics and improving atmospheric model as well as SSW monitoring.

Modeling microbaroms worldwide in a straightforward way is thus feasible. De Carlo et al. (2021) demonstrated that a fine reprocessing of continuous IMS waveform data in the microbarom band allows quantitative validation of the source model. This study demonstrates that the use of an updated source model improves the prediction rate of observations by around 20% against previous ocean wave models when accounting for attenuation and coastal reflection. Other works investigating offline assimilation experiments have shown promising results when applied to infrasound signals from explosions. Amezcua et al. (2020) and Amezcua and Barton (2021) demonstrated that an assimilation technique based on ensemble Kalman filter can provide crosswind estimates between the source site and the recording station with a potential

to assimilate infrasound observations. Through these experiments it is expected that a passive remote sensing method using global infrasound measurements from a well constrained natural source, in conjunction with other simultaneous atmospheric measurements, will improve estimates of the state of the middle and upper atmosphere.

9.4. New Models and Approaches for Representing Gravity Waves

The detection capability of the IMS infrasound network is controlled by middle atmospheric winds and temperatures, among other factors. Infrasound (<20 Hz) ducting is indeed affected by the seasonal changes in stratospheric winds driven by thermal wind balance, with westerly winds in the winter season and easterly winds in the summer season of both hemispheres in the extratropics, while the semiannual oscillation is mainly acting in the tropical regions (see section 7.3.2). Gravity waves are critical in this respect, at scales of hours and days, as they alter the propagation path of infrasound waves in the middle atmospheric waveguide. They cause detections at infrasound stations that remain unexplained when only large scale atmospheric features are considered (Drob et al. 2013, Hedlin and Drob 2014, Le Pichon et al. 2019). Because of the various sources and propagation conditions of gravity waves, infrasound detections at each IMS infrasound station will be affected in different ways by gravity waves activity.

Several pathways have been explored in the infrasound community to account for gravity waves in atmospheric specifications for propagation modelling: parameterizations based on the gravity waves universal spectrum (e.g. Gardner et al. 1993, Vallage et al. 2021), stochastic parameterizations accounting for the intermittency of the gravity waves field (e.g. de la Cámara and Lott 2015, Cugnet et al. 2019), gravity waves ray-tracing equations applied to a frequency spectrum (Drob et al. 2013) or 3-D gravity waves-spectrum model (Chunchuzov and Kulichkov 2019).

New paths remain to be explored. The recently developed Multi-Scale Gravity Wave Model (MS-

GWaM) is a unique parameterization accounting for non-linear non-dissipative interactions between the mean field and the gravity waves field (Bölöni et al. 2021, Kim et al. 2021). To date, most gravity waves parameterization implemented in numerical weather prevision models are stationary, meaning they ignore the effect of gravity waves before they break at the critical level where momentum is deposited into the mean flow. Other approaches try to first reconsider the launching level for gravity waves and allow for a vertical distribution of the sources (Ribstein et al. 2022). Indeed, the launching or source level is systematically set at a constant tropospheric altitude in parameterization, which does not allow for the explanation of low phase speeds measured in the mesosphere.

MS-GWaM parameterization has been developed for the state of the art Icosahedral Non-hydrostatic model (ICON, Zängl et al. 2015) which has recently been extended to the upper atmosphere (UA-ICON, Borchert et al. 2019). It allows for stimulation of the atmospheric dynamics from the surface to the thermosphere with a model top set at 150 km and a sponge layer starting at around 110 km. This multiscale model allows for coarse resolution modelling (e.g. typical of General Circulation Model ~100 km) as well as higher resolution simulations (up to ~1 km) where a large part of the gravity waves spectrum can be explicitly resolved. In the latter case, the gravity waves parameterization can be switched off. The explicit simulation of gravity waves perturbations by the dynamical core of the model allows accounting for their lateral propagation, which has significant impacts on the gravity waves field (Stephan et al. 2020). Current gravity waves parameterizations usually assume purely upward propagation. Hence, using high resolution models explicitly resolving middle atmospheric perturbations and their 3-D propagation appears as a relevant and achievable step for the infrasound community, given the increased computation means available today.

9.5. Remote Monitoring of Volcanoes

With the advent of civil aviation and the exponential growth in air traffic, the problem of a volcanic ash encounter has become an issue of paramount importance. During the last decade, the deployment of infrasound stations at local, regional and global scales has significantly increased the potential of infrasound measurements to mitigate volcanic hazards. It was demonstrated that infrasound can play a key role in supporting warning systems by notifying, the onset of explosive eruptions, thus reducing the risk of aircrafts encountering volcanic ash (Matoza et al. 2019). In particular, remote infrasound observations allows the identification of erupting volcanoes based on the characteristics of the recorded signal and well complement satellite based monitoring techniques which cannot be used to identify weak volcanic plumes when cloud cover fraction is high (Taisne et al. 2019).

Infrasound provides the clearest evidence of the direct coupling between the volcanic process and the atmosphere. Weakly attenuated in the atmospheric waveguide, infrasound signals from volcanoes can be detected up to several thousands of kilometers. The infrasound IMS network, because of its global coverage and high quality data, is well adapted to remote volcano monitoring. Figure 28 shows the example of remote infrasound detections of the stratovolcano Calbuco (South Chile) which erupted on 22 April 2015. The eruption generated an ash column spreading to an altitude of more than 15 km. A second eruption started on 23 April 2015. These eruptions were well recorded by several IMS infrasound arrays in south America at distances as large as 3700 km.

Such observations are relevant for civil aviation especially when volcanoes are not well monitored with in situ instruments. The ARISE project, recognized by Volcanic Ash Advisory Centers (VAACs) and the International Civil Aviation Organization, explored multidisciplinary approaches to support the remote monitoring of volcanic hazards at global, regional and local scales. Within ARISE, the concept of a volcanic information system has been proposed in cooperation with the CTBTO and the Toulouse VAAC. This system, applied to the IMS infrasound detections includes computation of
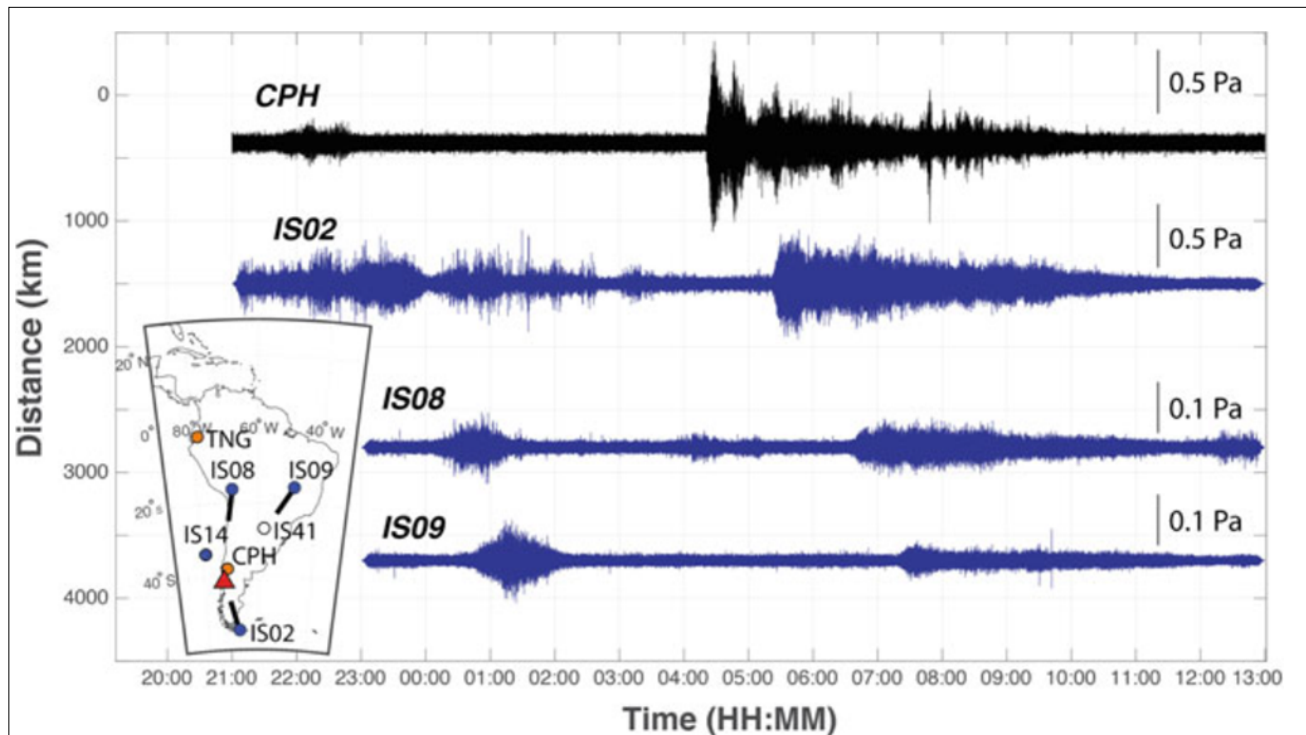
FIGURE 28.

Infrasound by the eruptions of Calbuco volcano on 22 and 23 April 2015 as recorded by the CPH infrasound array operated in Argentina by University of Firenze and by the IMS infrasound stations IS2 (Argentina), IS8 (Bolivia) and IS9 (Brazil). The inset shows the position of the Calbuco volcano, Chile (red triangle), IMS arrays (blue circles) retrieved back azimuths (black lines) and permanent arrays (from Marchetti et al. 2019).

long range propagation effects determining the detection capability of the network. It accounts for near real time atmospheric specifications as provided by ECMWF operational High spatial RESolution forecasts (HRES) between 30 km and 60 km. A volcanic information system has been successfully implemented and validated on the Virtual Data Exploitation Center platform operated by the IDC using archived infrasound processing results.

The performance of a volcanic information system has been evaluated through comparisons with the timing volcanic ash advisories issued by Toulouse VAAC and demonstrated its capability to trigger early warning notifications of Mount Etna eruptions with negligible false volcanic alerts. It is expected that the proposed proof of concept procedure might be successfully applied to other volcanoes worldwide, in particular for higher energy eruptions, thus opening new perspectives in volcano monitoring and in related support to VAACs at a global scale. The final aim of this service is to deliver timely early warning messages to VAACs of ongoing eruptions, both through local and regional observations, with an accuracy and reliability that is affected and controlled by infrasound propagation, pressure amplitude at the source and noise level at the array.

10. CONCLUSION

The IMS infrasound monitoring network is unique by its data quality, global coverage and continuity in measurements. It allows the observation of most atmospheric events in broad scales of frequency and altitude ranges. Catalogues of the selected IMS ground truth events provide the characteristics of signals from well identified sources, useful for event identification in routine

data analyses. The objective to detect and locate 1 kiloton explosion, at any time with a global coverage, is well achieved as demonstrated by the recent detection capability computations, which use state of the art atmospheric models and noise representations integrating atmospheric variability. Validations were performed by using specific events such as the Sayarim calibration explosions and natural events such as the Chelyabinsk meteorite or the Calbuco volcano. Other rare events such as the Hunga Tonga-Hunga Ha'apai recent volcanic eruption (January 2022) present a new opportunity to study the long range propagation of infrasound at global scale as this event was observed by all the operational IMS infrasound stations.

Infrasound from repetitive well identified sources, such as quasi-continuous volcanic eruptions, can be used as a probe for atmospheric wind and temperature sounding. Methods were developed for the study of SSW events, which drastically affect infrasound propagation. The new challenge is now to use microbarom noise, available at any time at global scale, for such purposes, thanks to the new observations of ocean swell by satellites and the progress in microbarom source modelling. The perspective is to provide diagnostics in near real time to numerical weather prediction models, notifying model biases or sudden stratospheric disturbances. In the future, the perspective is to use IMS data for assimilation in numerical weather prevision models at the global scale.

Unexpectedly, the infrasound network also provides information about large scale climatology systems, such as the inter tropical convergence zone (ITCZ) of the winds and the semi-annual oscillation (SAO) of stratospheric winds. This information is deduced from thunderstorm lightning and convection observations, performed for the first time by the infrasound technology at global scale and during more than 10 years in many IMS stations, opening new applications in low latitude climatology.

Multi-instrument observations, including lidars and radars were associated to infrasound technology in the framework of the Atmospheric dynamics Research InfraStructure (ARISE) project. The differences between ECMWF and observations were precisely determined in the presence of gravity waves, SSWs and other event, allowing the quantification of uncertainties in the atmospheric models and infrasound propagation simulations.

These observations showed the potential of lidars associated to infrasound stations to provide precise wind and temperature observations needed for improving propagation simulations in routine monitoring. The development of a new generation of portable automated high resolution lidars, used during ARISE campaigns, should facilitate the development of such synergy. The project sustainability is now reinforced especially by its participation in the GEOINQUIRE project (Horizon Europe for research and innovation) for access to consolidated data bases, opening enhanced possibilities.

Major scientific advances and accomplishments for infrasound technology spanning over the last 20 years are captured in the two reference books "Atmospheric monitoring for atmospheric studies" (Le Pichon et al. 2010b) and "Atmospheric monitoring for atmospheric studies, challenges in middle atmosphere dynamics and societal benefits" (Le Pichon et al. 2019). Infrasound sessions are presented in international conferences such as the American Geophysical Union (AGU), the Acoustical Society of America (ASA), the European Geophysical Union (EGU) for more than ten years and the CTBT Science and Technology Conferences, attracting a large number of scientists.

During the 25 years of IMS development, infrasound progressed from a technology limited to regional and qualitative studies to an international well recognized thematic. It provides a new image of the atmospheric dynamics and societal applications going towards natural hazard monitoring, infrasound meteorology, weather prediction and climate research.

In return the engagement of the large scientific community involved in these studies supports the CTBTO efforts aimed at improving

nuclear test monitoring with infrasound technology by providing new methods, a more accurate description of the atmospheric events and noise, complementary regional infrasound networks and multi-instrument stations.

Several perspectives are also within reach by the completion of the IMS network with the new stations, which still need to be built, and the consolidated network sustainability. This will provide the opportunity to gather a larger number of ground truth events in new geophysical areas and to extend further the cataloguing of events over climatic time scales. These progresses are essential to determine the evolution of the detected atmospheric disturbances with the climate evolution.

REFERENCES

Alcoverro, B., Le Pichon, A. (2005). Design and optimization of a noise reduction system for infrasonic measurements using elements with low acoustic impedance. *The Journal of the Acoustical Society of America* **117** (4 Pt 1) 1717–1727.

Alexander, M.J., et al. (2010). Recent developments in gravity wave effects in climate models and the global distribution of gravity-wave momentum flux from observations and models. *Quarterly Journal of the Royal Meteorological Society* **136** (650) 1103-1124.

Amezcua, J., Näsholm, S.P., Blixt, E.M., Charlton-Perez, A. (2020). Assimilation of atmospheric infrasound data to constrain tropospheric and stratospheric winds. *Quarterly Journal of the Royal Meteorological Society* **146** (731) 2634-2653.

Amezcua, J., Barton, Z. (2021). Assimilating atmospheric infrasound data to constrain atmospheric winds in a two-dimensional grid. *Quarterly Journal of the Royal Meteorological Society* **147** 3530–3554.

Antier, K., Le Pichon, A., Vergniolle, S., Zielinski, C., Lardy, M. (2007). Multiyear validation of the NRL-G2S wind fields using infrasound from Yasur. *Journal of Geophysical Research* **112** (D23).

Applbaum, D., Averbuch, G., Price, C., Yair, C., Ben-Horin, Y. (2020). Infrasound observations of sprites associated with winter thunderstorms in the eastern Mediterranean. *Atmospheric Research* **235**.

Ardhuin, F. (2021). Ocean waves in geosciences. Laboratoire d'Oceanographie Physique et Spatiale, France.

Atmospheric dynamics Research InfraStructure in Europe (ARISE) (2018).

Arrowsmith, S.J., et al. (2008). Regional monitoring of infrasound events using multiple arrays: application to Utah and Washington State. *Geophysical Journal International* **175** (1) 291–300.

Arrowsmith, S.J., Johnson, J.B., Drob, D.P., Hedlin, M.A.H. (2010). The seismoacoustic wavefield: A new paradigm in studying geophysical phenomena. *Reviews of Geophysics* **48** (4).

Assink, J.D., Evers, L.G., Holleman, I., Paulssen, H. (2008). Characterization of infrasound from lightning. *Geophysical Research Letters* **35** (15).

Assink, J.D., et al. (2013). Passive acoustic remote sensing and anomalous infrasound propagation studies. *The Journal of the Acoustical Society of America* **134** (5) 4161-4161.

Assink, J.D., Le Pichon, A., Blanc, E., Kallel, M., Khemiri, L. (2014). Evaluation of wind and temperature profiles from ECMWF analysis on two hemispheres using volcanic infrasound. *Journal of Geophysical Research: Atmospheres* **119** (14).

Baker, W.E., et al. (2014). Lidar-measured wind profiles: The missing link in the global observing system. B*ulletin of the American Meteorological Society* **95** (4) 543-564.

Balachandran, N.K. (1970). Effects of winds on the dispersion of acoustic-gravity waves. *The Journal of the Acoustical Society of America* **48** (1B).

Balachandran, N.K. (1972). "Acoustic-gravity waves in the neutral atmosphere and the ionosphere". *Effects of atmospheric acoustic gravity waves on electromagnetic wave propagation* (Proceedings of the Advisory Group for Aerospace Research and Development, Paris, France, 1972). AGARD Advisory Group for Aerospace Research and Development Conference Proceedings No. 115.

Baldwin, M.P., et al. (2019). 100 years of progress in understanding the stratosphere and mesosphere. *Meteorological Monographs* **59**.

Baumgarten, G. (2010). Doppler Rayleigh/Mie/Raman lidar for wind and temperature measurements in the middle atmosphere up to 80 km. *Atmospheric Measurement Techniques* **3** (6) 1509–1518.

Bedard, A.J. Jr, Georges, T.M. (2000). *Atmospheric infrasound. Physics Today* **53** (3) 32–37.

Bedard, Jr. A.J., Bartram, B.W., Keane, A.N., Welsh, D.C., Nishiyama R.T. (2004). "The infrasound network (ISNET): Background, design details, and display capability as an 88D adjunct tornado detection tool". Paper presented at the 22nd Conf. On Severe Local Storms by the American Meteorological Society, Hyannis, MA, 2004.

Berthet, C., Rocard, Y. (1972). "The theory of atmospheric acoustic propagation". *Effects of atmospheric acoustic gravity waves on electromagnetic wave propagation* (Proceedings of the Advisory Group for Aerospace Research and Development, Paris, France, 1972). AGARD Advisory Group for Aerospace Research and Development Conference Proceedings No. 115.

Blanc, E. (1985). Observations in the upper atmosphere of infrasonic waves from natural or artificial sources: A summary. *Annales Geophysicae* **3** 673–687.

Blanc, E., Plantet, J.L. (1998). "Detection capability of the IMS infrasound network: A more realistic approach". Infrasound Workshop on infrasounds, Bruyères-le-Châtel, France, 21– 24 July 1998.

Blanc, E., Ceranna, L. (2009). "Infrasound". *Science for Security, Verifying the Comprehensive Nuclear Test Ban Treaty*, International Scientific Studies Conference, 10-12 June, Vienna, Austria, 2009.

Blanc, E., Pichon, A.L., Ceranna, L., Farges, T., Marty, J., Herry, P. (2009). "Global scale monitoring of acoustic and gravity waves for the study of the atmospheric dynamics". I*nfrasound Monitoring for Atmospheric Studies* (A. Le Pichon, E. Blanc, A. Hauchecorne, Eds). Springer, Dordrecht.

Blanc, E., Farges, T., Le Pichon, A., Heinrich, P. (2014). Ten year observations of gravity waves from thunderstorms in western Africa. *Journal of Geophysical Research: Atmospheres* **119** (11) 6409-6418.

Blanc, E., et al. (2018). Toward an improved representation of middle atmospheric dynamics thanks to the ARISE project. *Surveys in Geophysics* **39** (2) 171-225.

Blanc, E., et al. (2019). "Middle Atmosphere Variability and Model Uncertainties as Investigated in the Framework of the ARISE Project". *Infrasound Monitoring for Atmospheric Studies, Challenges in Middle-Atmosphere Dynamics and Societal Benefits* (A. Le Pichon, E. Blanc, A. Hauchecorne, Eds). Springer, Cham.

Blixt, E.M., et al. (2019). Estimating tropospheric and stratospheric winds using infrasound from explosions. *The Journal of the Acoustical Society of America* **146** (2) 973-982.

Bölöni, G., Kim, Y.H., Borchert, S., Achatz, U. (2021). Toward transient subgrid-scale gravity wave representation in atmospheric models. Part I: Propagation model including non-dissipative direct wave–mean-flow interactions. *Journal of the Atmospheric Sciences* **78** (4) 1317-1338.

Bondár, I., et al. (2022). Central and eastern European infrasound network: Contribution to infrasound monitoring. *Geophysical Journal International* **230** (1) 565–579.

Borchert, S., et al. (2019). The upper-atmosphere extension of the ICON general circulation model (version: ua-icon-1.0). *Geoscientific Model Development* **12** (8) 3541–3569.

Bowman, J.R., Baker, G., Bahavar, M. (2005). Ambient infrasound noise. *Geophysical Research Letters* **32** (9).

Bowman, H.S., Bedard, A.J. (1971). Observations of infrasound and subsonic disturbances related to severe weather. *Geophysical Journal International* **26** (1-4) 215–242.

Brachet, N., Coyne, J., Le Bras R. (2006). Latest developments in the automatic and interactive processing of infrasound data at the IDC, in Infrasound Technology Workshop, 2006.

Brachet, N., et al. (2010). "Monitoring the Earth's Atmosphere with the Global IMS Infrasound Network". I*nfrasound Monitoring for Atmospheric Studies* (A. Le Pichon, E. Blanc, A. Hauchecorne, Eds). Springer, Dordrecht.

Breding, D.R., Kromer R.P., Whitaker, R.W., Sandoval, T. (1997). *Test report for the infrasound prototype for a CTBT IMS station.* Rep. No. SAND97-2741 UC-700. Sandia National Laboratories, Albuquerque, NM and Livermore, CA.

Brekhovskikh, L.M., Goncharov, V.V., Kurtepov, V.M., Naugolmy, K.A. (1973). Radiation of infrasound into atmosphere by surface-waves in ocean. Izvestiya Akademii Nauk SSSR Fizika Atmosfery i Okeana, **9** (9) 899-907.

Brown, P.J., et al. (2013). A 500- kiloton airburst over Chelyabinsk and an enhanced hazard from small impactors. *Nature* **503** (7475) 1–24.

Cansi, Y. (1995). An automatic seismic event processing for detection and location: The PMCC method. *Geophysical Research Letters* **22** (9) 1021–1024.

Carpenter, E.W., Harwood, G., Whiteside, T. (1961). Microbarograph records from the Russian large nuclear explosions. *Nature* **192** 857.

Central and Easter European Infrasound Network (CEEIN), (2023).

Ceranna, L., Le Pichon, A., Blanc, E. (2007). "Listen to the Sounds of the Antarctic". Presentation at the Atmosphere Infrasound Technology Workshop, Tokyo, 2007.

Ceranna, L., Le Pichon, A., Green, D. N., Mialle, P. (2009). The Buncefield Explosion: A benchmark for infrasound analysis across central Europe. *Geophysical Journal International* **177** (2) 491–508.

Ceranna, L., Matoza, R., Hupe, P. Le Pichon, A., Landès M. (2019). "Systematic array processing of a decade of global IMS infrasound data". *Infrasound monitoring for atmospheric studies: Challenges in middle-atmosphere dynamics and societal benefits* (A. Le Pichon, E. Blanc, A. Hauchecorne, Eds). Springer, Cham.

Charlton, A.J., Polvani, L.M. (2007) A new look at stratospheric sudden warmings. Part I: Climatology and modeling benchmarks. *Journal of Climate* **20** (3) 449–469.

Che, I.-Y., Kim, G., Le Pichon, A. (2013). Infrasound associated with the deep M 7.3 northeastern China earthquake of June 28, 2002. Earth Planets and Space **65** 109–113.

Che, I.-Y, Park, J., Kim, I. Kim, T.S., Lee, H.I. (2014). Infrasound signals from the underground nuclear explosions of North Korea. *Geophysical Journal International*, Volume 198, Issue 1, July, 2014, 495–503.

Che, I.-Y., Park, J., Kim, T.S., Hayward, C., Stump, B. (2019). "On the use of a dense network of seismo-acoustic arrays for near-regional environmental monitoring". *Infrasound monitoring for atmospheric studies: Challenges in middle-atmosphere dynamics and societal benefits* (Le Pichon, A., Blanc, E., Hauchecorne, A. Eds.). Springer, Cham.

Christian, H.J., et al. (2003). Global frequency and distribution of lightning as observed from space by the Optical Transient Detector. *Journal of Geophysical Research Atmospheres* **108** (D1).

Christie, D., Whitaker, R. (1998). "Infrasound workshop for CTBT monitoring: Proceedings". *Office of Scientific & Technical Information Technical Reports,* University of North Texas Libraries, UNT Digital Library, UNT Libraries Government Document Department, 1998.

Christie, D., Kennett, B.L. (2007). *Detection of Nuclear Explosions Using Infrasound Techniques.* Report No. AFRL-RV-HA-TR-2007-1151. Air Force Research Laboratory, Hanscom AFB, MA.

Christie, D.R., Campus, P. (2010). "The IMS Infrasound Network: Design and establishment of infrasound stations". I*nfrasound monitoring for atmospheric studies,* (Le Pichon, A., Blanc, E., Hauchecorne, A. Eds.). Springer, Dordrecht.

Chunchuzov, I., Kulichkov, S. (2019). "Internal gravity wave perturbations and their impacts on infrasound propagation in the atmosphere". *Infrasound monitoring for atmospheric studies: Challenges in middle-atmosphere dynamics and societal benefits* (Le Pichon, A., Blanc, E., Hauchecorne, A. Eds.). Springer, Cham.

Clauter, D.A., Blandford, R.R. (1997). "Capability modeling of the proposed International Monitoring System 60-station infrasonic network", Infrasound workshop for CTBT Monitoring, Comprehensive Nuclear-Test-Ban Treaty Organization, Santa Fe, New Mexico, 25– 28 August 1997, Proceedings, pp 227-234.

Costantino, L., Heinrich, P. (2014). Tropical deep convection and density current signature in surface pressure: Comparison between WRF model simulations and infrasound measurements, *Atmospheric Chemistry and Physics* **14** (6) 3113–3132.

Cox, E.F. (1949). Abnormal audibility zones in long distance propagation through the atmosphere. *The Journal of the Acoustical Society of America* **21** (1) 6-16.

Cugnet, D., De la Cámara, A., Lott, F., Millet, C., Ribstein, B. (2019). "Non-orographic gravity waves: Representation in climate models and effects on infrasound". *Infrasound monitoring for atmospheric studies: Challenges in middle-atmosphere dynamics and societal benefits* (Le Pichon, A., Blanc, E., Hauchecorne, A. Eds.). Springer, Cham.

Dahlman, O., Mykkeltveit, S., Haak, H. (2009). *Nuclear Test Ban: Converting Political Visions to Reality*. Springer, Dordrecht.

De Carlo, M., Ardhuin, F., Le Pichon, A. (2020). Atmospheric infrasound radiation by ocean waves in finite depth: Unified theory and application to radiation patterns. *Geophysical Journal International* **221** (1). 569–585.

De Carlo, M., Hupe, P., Le Pichon, A., Ceranna, L., Ardhuin, F. (2021). Global microbarom patterns: A first confirmation of the theory for source and propagation. *Geophysical Research Letters* **48** (3).

De la Cámara, A., Lott, F. (2015). A parameterization of gravity waves emitted by fronts and jets. *Geophysical Research Letters* **42** (6) 2071-2078.

De Larquier, S.V., Pasko, P. (2010). Mechanism of inverted chirp infrasonic radiation from sprites. *Geophysical Research Letters* **37** (24).

Del Pino, S., Després, B., Havé, P., Jourdren, H., Piserchia, P.F. (2009). 3D Finite Volume simulation of acoustic waves in the earth atmosphere. *Computers & Fluids* **38** (4) 765–777.

Delclos, C., Blanc, E., Broche, P., Glangeaud, F., Lacoume, J.L. (1990). Processing and interpretation of microbarograph signals generated by the explosion of Mount St. Helens. *Journal of Geophysical Research* **95** (D5) 5485-5494.

Den Ouden, O.F.C., et al. (2020). CLEAN beamforming for the enhanced detection of multiple infrasonic sources. *Geophysical Journal International* **221** (1) 305–317.

Domeisen, D.I.V., et al (2020a). The role of the stratosphere in subseasonal to seasonal prediction: 1. Predictability of the stratosphere. *Journal of Geophysical Research: Atmospheres* **125** (2).

Domeisen, D.I., et al. (2020b). The role of the stratosphere in subseasonal to seasonal prediction: 2. Predictability arising from stratosphere-troposphere coupling. *Journal of Geophysical Research: Atmospheres* **125** (2).

Donn, W.L., Shaw, D.M. (1967). Exploring the atmosphere with nuclear explosions. *Reviews of Geophysics* **5** (1) 53-82.

Donn, W.L., Balachandran, N.K. (1981). Mount St. Helens eruption of 18 May 1980: Air waves and explosive yield. *Science* **213** (4507) 539-541.

Drob, D., Picone, J.M., Garcés, M. (2003). Global morphology of infrasound propagation. *Journal of Geophysical Research: Atmospheres* **108** (D21).

Drob, D., et al. (2008). An empirical model of the Earth's horizontal wind fields: HWM07. *Journal of Geophysical Research: Space Physics* **113** (A12).

Drob, D.P., Broutman, D., Hedlin, M.A., Winslow, N.W., Gibson, R.G. (2013). A method for specifying atmospheric gravity wavefields for long-range infrasound propagation calculations. *Journal of Geophysical Research: Atmospheres* **118** (10) 3933-3943.

Evers, L.G., Haak H.W. (2001). Listening to sounds from an exploding meteor and oceanic waves. *Geophysical Research Letters* **28** (1) 41–44.

Evers, L.G., Haak, H.W. (2005). The detectability of infrasound in the Netherlands from the Italian volcano Mt. Etna. *Journal of Atmospheric and Solar-Terrestrial Physics* **67** (3) 259–268.

Evers, L.G., Haak, H.W. (2010). "The characteristics of infrasound, its propagation and some early history". *Infrasound monitoring for atmospheric studies,* (Le Pichon, A., Blanc, E., Hauchecorne, A. Eds.). Springer.

Expert group to the Ad Hoc Committee on a Nuclear Test Ban Working Group on Verification (1995). "International Monitoring System Infrasound Network Design" CD/NTB/WP.283, Conference on the disarmament, 15 December 1995.

Farges, T., Blanc, E., Le Pichon, A., Neubert, T., Allin T.H. (2005). Identification of infrasound produced by sprites during the Sprite2003 campaign. *Geophysical Research Letters* **32** (1).

Farges, T. (2009). "Infrasound from lightning and sprites". *Lightning: Principles, Instruments and Applications* (Dieter Betz H, Schumann U, Laroche P., Eds) Springer, Dordrecht, pp 417–432.

Farges, T., Blanc, E. (2010). Characteristics of infrasound from lightning and sprites near thunderstorm areas. *Journal of Geophysical Research* **115** (A6).

Farges, T., et al. (2021). Infrasound thunder detections across 15 years over Ivory Coast: Localization, propagation, and link with the stratospheric semi-annual oscillation. *Atmosphere* **12** (9) 1188.

Fee, D., et al. (2013). Overview of the 2009 and 2011 Sayarim Infrasound Calibration Experiments. *Journal of Geophysical Research: Atmospheres* **118** (12) 6122–6143.

Fisher, R.A. (1992). "Statistical methods for research workers". *Breakthroughs in Statistics: Methodology and Distribution* (Kotz, S., Johnson, N.L. Eds) Springer, New York, pp. 66–70.

Francis, S.H. (1975). Global propagation of atmospheric gravity waves: A review. *Journal of Atmospheric and Terrestrial Physics* **37** (6-7) 1011-1030.

Franz, R.C., Nemzek, R.J., Winckler, J.R. (1990). Television image of a large upward electrical discharge above a thunderstorm system. *Science* **249** (4964) 48–51.

Gainville, O., et al. (2010). "Misty picture: a unique experiment for the interpretation of the infrasound propagation from large explosive sources". *Infrasound monitoring for atmospheric studies* (Le Pichon, A., Blanc, E., Hauchecorne, A. Eds) Springer, Dordrecht.

Gallin, L-J., et al. (2016). Statistical analysis of storm electrical discharges reconstituted from a lightning mapping system, a lightning location system, and an acoustic array. *Journal of Geophysical Research: Atmospheres* **121** (8) 3929–3953.

Garcés, M., Hetzer, C., Merrifield, M., Willis, M., Aucan, J. (2003). Observations of surf infrasound n Hawai'i, *Geophysical Research Letters* **30** (24).

Garcés, M., Willis, M., Hetzer, C., Le Pichon, A., Drob, D. (2004). On using ocean swells for continuous infrasonic measurements of winds and temperature in the lower, middle, and upper atmosphere. *Geophysical Research Letters* **31** (19).

Garcés, M., et al. (2005) Deep infrasound radiated by the Sumatra Earthquake and Tsunami. Eos, Transactions, *American Geophysical Union* **86** (35) 317–320.

Gardner, C.S., Hostetler, C.A., Franke, S.J. (1993). Gravity wave models for the horizontal wave number spectra of atmospheric velocity and density fluctuations. J*ournal of Geophysical Research: Atmospheres* **98** (D1) 1035-1049.

Gerber, E.P., et al. (2012). Assessing and Understanding the Impact of Stratospheric Dynamics and Variability on the Earth System. B*ulletin of the American Meteorological Society* **93** (6) 845-859.

Gibbons, S.J., et al. (2015). The European Arctic: A Laboratory for Seismo-acoustic Studies. *Seismological Research Letters* **86** (3) 917–928.

Glasstone S., Dolan, P.J. (1977). *The Effects of Nuclear Weapons*, 3rd edn. Washington D.C., USA.

Green, D.N., Bowers, D. (2010). Estimating the detection capability of the International Monitoring System infrasound network. J*ournal of Geophysical Research: Atmospheres* **115** (D18).

Green, D.N., Vergoz, J., Gibson, R., Le Pichon, A., Ceranna, L. (2011). Infrasound radiated by the Gerdec and Chelopechene explosions: Propagation along unexpected paths. *Geophysical Journal International* **185** (2) 890–910.

Gutenberg, B. (1939). The velocity of sound waves and the temperature in the stratosphere above Southern California. *Bulletin of American Meteorological Society* **20** 192-201.

Harkrider, D.G. (1964). Theoretical and observed acoustic-gravity waves from explosive sources in the atmosphere. *Journal of Geophysical Research* **69** (24) 5295-5321.

Hauchecorne, A., Khaykin, S., Keckhut, P., Mzé, N., Angot, G., Claud, C. (2019). "Recent dynamic studies on the middle atmosphere at mid- and low-latitudes using Rayleigh lidar and other technologies". *Infrasound monitoring for atmospheric studies: Challenges in middle-atmosphere dynamics and societal benefits* (A. Le Pichon, E. Blanc, A. Hauchecorne, Eds) Springer, Cham.

Hedlin, M., et al. (2002). Listening to the secret sounds of earth's atmosphere. *Eos, Transactions, American Geophysical Union* **83** (48) 564-565.

Hedlin, M.A., Drob, D.P. (2014). Statistical characterization of atmospheric gravity waves by seismoacoustic observations. *Journal of Geophysical Research: Atmospheres* **119** (9) 5345-5363.

Hildebrand, J., Baumgarten, G., Fiedler, J., Lübken, F.J. (2017). Winds and temperatures of the Arctic middle atmosphere during January measured by Doppler lidar. *Atmospheric Chemistry and Physics* **17** (21)13345-13359.

Hupe, P., Ceranna, L., Pilger, C. (2018). Using barometric time series of the IMS infrasound network for a global analysis of thermally induced atmospheric tides. *Atmospheric Measurement Techniques* **11** (4) 2027–2040.

Hupe, P., et al. (2019a). Mountain-associated waves and their relation to orographic gravity waves. *Meteorologische Zeitschrift* **30** (1) 59-77.

Hupe P., Ceranna, L., Le Pichon, A. (2019b). How can the International Monitoring System infrasound network contribute to gravity wave measurements? *Atmosphere* **10** (7).

Hupe, P., Ceranna, L., Le Pichon, A., Matoza, R.S., Mialle, P. (2022). Infrasound broadband bulletin products of the IMS for atmospheric studies and civilian applications. *EGU General Assembly 2022* (Vienna, Austria, 23–27 May 2022).

Ignaccolo, M, et al. (2006). The planetary rate of sprite events. *Geophysical Research Letters* **33** (11) 1-4.

Ignaccolo, M., Farges, T., Blanc, E., Füllekrug, M. (2008). Automated chirp detection with diffusion entropy: Application to infrasound from sprites. *Chaos, Solitons and Fractals* **38** (4) 1039–1050.

Jacobson, A.R., Carlos, R., Blanc, E. (1988). Observation of ionospheric disturbance following a 5-kt chemical explosion: 1. persistent oscillation in the lower thermosphere after shock passage. *Radio Science* **23** (5) 820-830.

Kaifler, N., Kaifler, B. (2021). A Compact Rayleigh Autonomous Lidar (CORAL) for the middle atmosphere. *Atmospheric Measurement Techniques* **14** 1715–1732.

Kaifler, N., et al. (2020). Lidar observations of large-amplitude mountain waves in the stratosphere above Tierra del Fuego, Argentina. *Scientific Reports* **10**.

Kerr, R.A. (1999). NSF Proposes Marriage of Rocks and Waves. *Science* **286** (5445).

Kim, Y.-H., Bölöni, G., Borchert, S., Chun, H.-Y., Achatz, U. (2021). Toward transient subgrid-scale gravity wave representation in atmospheric models. Part II: Wave intermittency simulated with convective sources. *Journal of the Atmospheric Sciences* **78** (4) 1339-1357.

Kulichkov, S.N., Bush G.A. (2001). Rapid variations in infrasonic signals at long distances from one-type explosions. *Izvestiya Atmospheric and Oceanic Physics* **37** (3) 306–313.

Kulichkov, S.N., (2003). Long-range propagation and scattering of low-frequency sound pulses in the middle atmosphere. *Meteorology and Atmospheric Physics* **85** 1-14.

Kulichkov, S.N. (2010). "On the prospects for acoustic sounding on the fine structure of the middle atmosphere". *Infrasound monitoring for atmospheric studies* (A. Le Pichon, E. Blanc, A. Hauchecorne, Eds) Springer, Dordrecht.

Lacroix, A., Farges, T., Marchiano, R., Coulouvrat, F. (2018). Acoustical measurement of natural lightning flashes: Reconstructions and statistical analysis of energy spectra. *Journal of Geophysical Research: Atmospheres* **123** (21) 12040-12065.

Lacroix, A., Coulouvrat, F., Marchiano, R., Farges, T., Ripoll, J.-F. (2019). Acoustical energy of return strokes: A comparison between a statistical model and measurements. *Geophysical Research Letters* **46** (20) 11479–11489.

Landès, M., Ceranna, L., Le Pichon, A., Matoza, R.S. (2012). Localization of microbarom sources using the IMS infrasound network. *Journal of Geophysical Research: Atmospheres* **117**.

Lee, C., et al. (2019). "The potential impact of upper stratospheric measurements on sub-seasonal forecasts in the extra-tropics". I*nfrasound monitoring for atmospheric studies* (A. Le Pichon, E. Blanc, A. Hauchecorne, Eds) Springer, Cham, pp. 889-907.

Le Pichon, A., Garcés, M., Blanc, E., Barthélémy, M., Drob, D.P. (2002). Acoustic propagation and atmosphere characteristics derived from infrasonic waves generated by the Concorde. *The Journal of the Acoustical Society of America* **111** (1) 629–641.

Le Pichon, A., Guilbert, J., Vallée, M., Dessa, J.X., Ulziibat, M. (2003). Infrasonic imaging of the Kunlun Mountains for the great 2001 China earthquake. *Geophysical Research Letters* **30** (15).

Le Pichon, A., Maurer, V., Raymond, D., Hyvernaud, O. (2004). Infrasound from ocean waves observed in Tahiti. *Geophysical Research Letters* **31** (19).

Le Pichon, A., Blanc, E., Drob, D. (2005). Probing high-altitude winds using infrasound. *Journal of Geophysical Research: Atmospheres* **110** (D20).

Le Pichon, A., Ceranna, L., Garcés, M., Drob, D., Millet, C. (2006). On using infrasound from interacting ocean swells for global continuous measurements of winds and temperature in the stratosphere. *Journal of Geophysical Research: Atmospheres* **111** (D11).

Le Pichon, A., Vergoz, J., Herry, P., Ceranna, L. (2008). Analyzing the detection capability of infrasound arrays in Central Europe. *Journal of Geophysical Research: Atmospheres* **113** (D12).

Le Pichon, A., et al. (2009). Assessing the performance of the International Monitoring System's infrasound network: Geographical coverage and temporal variabilities. *Journal of Geophysical Research: Atmospheres* **114** (D8).

Le Pichon, A., Matoza, R., Brachet, N., Cansi, Y. (2010a). Recent enhancements of the PMCC infrasound signal detector. *Inframatics*.

Le Pichon, A., Blanc, E., Hauchecorne, A. (Eds.) (2010b). I*nfrasound Monitoring for Atmospheric Studies Springer*, Dordrecht.

Le Pichon, A., Ceranna, L., Vergoz, J. (2012). Incorporating numerical modeling into estimates of the detection capability of the IMS infrasound network. *Journal of Geophysical Research: Atmospheres* **117** (D05).

Le Pichon, A., et al. (2013). The 2013 Russian fireball largest ever detected by CTBTO infrasound sensors. *Geophysical Research Letters* **40** (14) 3732-3737.

Le Pichon, et al. (2015). Comparison of co-located independent ground-based middle atmospheric wind and temperature measurements with numerical weather prediction models. Journal of Geophysical Research: *Atmospheres* **120** (16) 8318-8331.

Le Pichon, A. Blanc, E. Hauchecorne, A. (Eds) (2019). *Infrasound Monitoring for Atmospheric Studies: Challenges in Middle Atmosphere Dynamics and Societal Benefits*, Springer Cham.

Listowski, C., et al. (2022). Remote monitoring of Mediterranean hurricanes using infrasound. R*emote Sensing* **14** (23) 6162.

Liszka, L. (1974). Long distance propagation of infrasound from artificial sources, *The Journal of the Acoustical Society of America* **56** (5) 1383– 1388.

Liszka, L. (2004). On the possible infrasound generation by sprite. *Noise Notes* **23** (2) 85-93.

Marchetti E., et al. (2019). "Infrasound monitoring of volcanic eruptions and contribution of ARISE to the Volcanic Ash Advisory Centers". *Infrasound monitoring for atmospheric studies, Challenges in middle-atmosphere dynamics and societal benefits* (A. Le Pichon, E. Blanc, A. Hauchecorne, Eds) Springer, Cham.

Marlton, G.J., et al. (2019a). Meteorological source variability in atmospheric gravity wave parameters derived from a tropical infrasound station. *Journal of Geophysical Research: Atmospheres* **124** (8) 4352–4364.

Marlton, G. Charlton-Perez, A. Harrison, G. Lee, C. (2019b). "Calculating atmospheric gravity wave parameters from infrasound measurements". *Infrasound monitoring for atmospheric studies, Challenges in middle-atmosphere dynamics and societal benefits* (A. Le Pichon, E. Blanc, A. Hauchecorne, Eds) Springer, Cham.

Marty J. (2019). "The IMS infrasound network: current status and technological developments". *Infrasound monitoring for atmospheric studies, Challenges in middle-atmosphere dynamics and societal benefits* (A. Le Pichon, E. Blanc, A. Hauchecorne, Eds) Springer, Cham.

Marty, J., Ponceau D., Dalaudier F. (2010). Using the international monitoring system infrasound network to study gravity waves. *Geophysical Research Letters* **37** (19).

Matoza, R., Fee, D., Green, D., Mialle, P. (2019). "Volcano infrasound and the International Monitoring System". *Infrasound monitoring for atmospheric studies, Challenges in middle-atmosphere dynamics and societal benefits* (A. Le Pichon, E. Blanc, A. Hauchecorne, Eds) Springer, Cham.

Matoza, R.S., et al. (2022). Atmospheric waves and global seismoacoustic observations of the January 2022 Hunga eruption, Tonga. *Science* **377** (6601).

McKisik, J.M. (1996). Infrasound and the infrasonic monitoring of atmospheric nuclear explosions: past monitoring efforts. Rep. No. PL-TR-96-2190. Hanscom AFB, MA.

McKisik, J.M. (1997). Infrasound and the infrasonic monitoring of atmospheric explosions: a literature review. Phillips Laboratory, Rep. No. PL-TR-97-2123. Hanscom AFB, MA.

Mialle, P., et al. (2019). "Advances in operational processing at the International Data Centre". *Infrasound monitoring for atmospheric studies, Challenges in middle-atmosphere dynamics and societal benefits* (A. Le Pichon, E. Blanc, A. Hauchecorne, Eds) Springer, Cham.

Mialle, P., et al. (2021). Infrasound processing system at the IDC, from rudimentary to maturity. CTBT: Science and Technology Conference 2021 (SnT2021).

Mutschlecner, J.P., Whitaker, R.W. (2005). Infrasound from earthquakes. *Journal of Geophysical Research* **110** (D1).

Olson, J.V., Wilson, C.R., Szuberla, C.A., Osborne, D. (2002). Infrasound signals observed at I53US and I55US. Presentation at the Infrasound Technology Workshop, De Bilt, Netherlands, 2002.

Olson, J.V. (2004). Infrasound signal detection using the Fisher F-statistics. *Inframatics* **6** 1-7.

Pasko, V.P., Snively, J.B. (2007). Mechanism of infrasound radiation from sprites, *American Geophysical Union, Fall Meeting* 2007AGUFMAE23A0899P.

Pierce, A. (1965). Propagation of acoustic-gravity waves in a temperature-and-wind stratified atmosphere, *The Journal of the Acoustical Society of America* **37**, 218-227.

Pierce, A.D., Posey, J.W., Iliff, E.F. (1971). Variation of nuclear explosion generated acoustic-gravity wave forms with burst height and with energy yield. *Journal of Geophysical Research* **76** (21).

Pierce, A.D., Posey, J.W. (1971). Theory of the excitation and propagation of Lamb's atmospheric edge mode from nuclear explosions. *Geophysical Journal International* **26** (1-4) 341-368.

Pilger C, Ceranna L, Ross JO, Le Pichon A, Mialle P, Garce´s MA (2015) CTBT infrasound network performance to detect the 2013 Russian fireball event. Geophys Res Lett 42:2523–2531.

Pilger, C., et al. (2018). The European Infrasound Bulletin. *Pure and Applied Geophysics* **175**, 3619-3638.

Pilger C., Ceranna, L., Le Pichon, A., Brown P. (2019). "Using large meteorite as global infrasound reference events". *Infrasound monitoring for atmospheric studies, Challenges in middle-atmosphere dynamics and societal benefits* (A. Le Pichon, E. Blanc, A. Hauchecorne, Eds) Springer, Cham.

Plantet, J.P. (1996). "Evaluation of infrasound network capability". (Presentation at the Infrasound Workshop for CTBT Monitoring, Comprehensive Nuclear-Test-Ban Treaty Organization, Paris, France, 1996).

Ponceau, D., Bosca, L. (2010). "Low-noise broadband microbarometers". I*nfrasound monitoring for atmospheric studies* (A. Le Pichon, E. Blanc, A. Hauchecorne, Eds). Springer, Dordrecht.

Poste, B., et al. (2022). The Multi-Channel Maximum-Likelihood (MCML) method: a new approach for infrasound detection and wave parameter estimation. *Geophysical Journal International* **232** (2) 1099-1112.

Preparatory Commission for the Comprehensive Nuclear-Test-Ban Treaty Organization (2022). (accessed on January 2023).

Ramanantsoa, A.H. (2019). V*alorisation des infrasons et étude des effets des conditions météorologiques locales sur la détectabilité de la station I33MG*. PhD Thesis, Université d'Antananarivo, Madagascar.

Reed, J.W. (1969). *Climatology of airblast propagations from Nevada Test Site nuclear airbursts*. Rep. No. SCRR-69-572, Sandia Laboratories. Albuquerque.

Reed, J.W. (1972). Airblast overpressure decay at long ranges. *Journal of Geophysical Research* **77** (9) 1623-1629.

Reed, J.W. (1978). P*roject Misty Castle: distant airblast effects predictions.* Rep. No. SAND; 78-0271, Sandia Laboratories. Albuquerque.

Reed, J.W, Church, H.W., Huck, T.W. (1987). Misty picture weather-watch and microbarograph project: Experiments 9412-14-18. Sand-87-2978c, Sandia Laboratories.

Rennie, M.P., et al. (2021). The impact of Aeolus wind retrievals on ECMWF global weather forecasts. *Quarterly Journal of the Royal Meteorological Society* **147** (740) 3555-3586.

Revelle, D.O. (1976). On meteor generated infrasound. *Journal of Geophysical Research* **81** (7) 1217-1230.

Revelle, D.O. (2010). "Acoustic-gravity waves from impulsive sources in the atmosphere". *Infrasound monitoring for atmospheric studies* (A. Le Pichon, E. Blanc, A. Hauchecorne, Eds) Springer, Dordrecht.

Ribstein, B., Millet, C., Lott, F., de la Cámara, A. (2022). Can we improve the realism of gravity wave parameterizations by imposing sources at all altitudes in the atmosphere? *Journal of Advances in Modeling Earth Systems* **14** (2).

Rind, D., Donn, W.L., Dede, E. (1973). Upper air wind speeds calculated from observations of natural infrasound. *Journal of the Atmospheric Sciences* **30** (8) 1726–1729.

Rind, D., Donn, W.L. (1975). Further use of natural infrasound as a continuous monitor of the upper atmosphere. *Journal of the Atmospheric Sciences* **32** (9) 1694-1704.

Rocard, Y. (1959). Propagation atmosphérique à longue portée des signaux acoustiques puissants, Comptes rendus à l'Académie de Sciences, 1959. Gauthier-Villars editions.

Roussel-Dupré, R., Gurevich, A.V. (1996). On runaway breakdown and upward propagating discharges. J*ournal of Geophysical Research: Space Physics* **101** (A2) 2297-2311.

Smets, P.S.M., Evers, L.G. (2014). The life cycle of a sudden stratospheric warming from infrasonic ambient noise observations. *Journal of Geophysical Research: Atmospheres* **119** (21).

Smets P.S.M., Assink, J.D., Le Pichon, A., Evers, L.G. (2016). ECMWF SSW forecast evaluation using infrasound. *Journal of Geophysical Research: Atmospheres* **121** (9) 4637–4650.

Smets, P., Assink, J., Evers, L. (2019). "The study of sudden stratospheric warmings using infrasound". *Infrasound monitoring for atmospheric studies, Challenges in middle-atmosphere dynamics and societal benefits* (A. Le Pichon, E. Blanc, A. Hauchecorne, Eds) Springer, Cham.

Silber, E., Brown, P. (2019). "Infrasound monitoring as a tool to characterize impacting near-Earth objects (NEOs)". *Infrasound monitoring for atmospheric studies, Challenges in middle-atmosphere dynamics and societal benefits* (A. Le Pichon, E. Blanc, A. Hauchecorne, Eds) Springer, Cham.

Smith, D.M., Lopez, L.I., Lin, R.P., Barrington-Leigh, C.P. (2005). Terrestrial gamma-ray-flashes observed up to 20 Mev. *Science* **307** (5712) 1085–1088.

Stephan, C.C., Schmidt, H., Zuelicke, C., Matthias, V. (2020). Oblique gravity wave propagation during sudden stratospheric warmings. *Journal of Geophysical Research: Atmospheres* **125** (1).

Stevens, J.L., Divnov, I.I., Adams, D.A., Murphy, J.R., Bourchik, V.N. (2002). Constraints on infrasound scaling and attenuation relations from Soviet explosion data. *Pure and Applied Geophysics* **159** 1045–1062.

Stump, B.W., et al. (2009). "Infrasound from earthquakes: Signal characterization". *Ground-Based Nuclear Explosion Monitoring Technologies* (Proceedings of the 2009 Monitoring Research Review: Ground-Based Nuclear Explosion Monitoring Technologies, Denver, CO, 2007).

Symons, G.J. (1888). *The Eruption of Krakatoa and Subsequent Phenomena.*, Trübner & co., London.

Taisne, B., Perttu, A., Tailpied, D., Caudron, C., Simonini, L. (2019). "Atmospheric controls on ground- and space-based remote detection of volcanic ash injection into the atmosphere, and link to early warning systems for aviation hazard mitigation". *Infrasound monitoring for atmospheric studies, Challenges in middle-atmosphere dynamics and societal benefits* (A. Le Pichon, E. Blanc, A. Hauchecorne, Eds) Springer, Cham.

Tripathi, O.P., et al. (2014). The predictability of the extra-tropical stratosphere on monthly time-scales and its impact on the skill of tropospheric forecasts. *Quarterly Journal of the Royal Meteorological Society* **141** (689) 987-1003.

Vallage, A., et al. (2021). Multitechnology characterization of an unusual surface rupturing intraplate earthquake: the ML 5.4 2019 Le Teil event in France. *Geophysical Journal International* **226** (2) 803-813.

Vanderbecken, P.J., Mahfouf, J.-F., C. Millet (2020). Bayesian selection of atmospheric profiles from an ensemble data assimilation system using infrasonic observations of May 2016 Mount Etna eruptions. *Journal of Geophysical Research: Atmospheres* **125** (2).

Vergoz, J., Le Pichon, A., Millet, C. (2019). "The Antares explosion observed by the USArray: An unprecedented collection of infrasound phases recorded from the same event". *Infrasound monitoring for atmospheric studies, Challenges in middle-atmosphere dynamics and societal benefits* (A. Le Pichon, E. Blanc, A. Hauchecorne, Eds) Springer, Cham.

Vergoz, J., et al. (2022). IMS observations of infrasound and acoustic-gravity waves produced by the January 2022 volcanic eruption of Hunga, Tonga: A global analysis. *Earth and Planetary Science Letters* **591**.

Virieux J., Garnier N.B., Blanc E., Dessa J.-X. (2004). Paraxial ray tracing for atmospheric wave propagation. *Geophysical Research Letters* **31** (20).

Vorobeva, E., De Carlo, M., Le Pichon, A., Espy, P., Näsholm, S.P. (2021). Benchmarking microbarom radiation and propagation model against infrasound recordings: a vespagram-based approach *Annales Geophysicae* **39** (3) 515–531.

Walker, K.T., Hedlin, M.A. (2010). "A review of wind-noise reduction methodologies". *Infrasound monitoring for atmospheric studies* (A. Le Pichon, E. Blanc, A. Hauchecorne, Eds) Springer, Dordrecht.

Walker, K.T, Shelby, R., Hedlin, M.A.H., de Groot-Hedlin, C., Vernon, F. (2011). Western U.S. infrasonic catalog: illuminating infrasonic hot spots with the USArray. *Journal of Geophysical Research: Solid Earth* **116** (B12).

Waxler, R. (2007). "The effect of the finite depth of the ocean on the microbarom signal". *Theoretical and Computational Acoustics 2007*. (Proceedings of the 8th International Conference on Theoretical and Computational Acoustics, Crete, 2007).

Whipple, F.J.W. (1930). The great Siberian meteor and the waves, seismic and aerial, which it produced. *Quarterly Journal of the Royal Meteorological Society* **56** 287–304.

Whitaker, R.W., Mutschlecner, J.P., Davidson, M.B., Noel S.D. (1990). "Infrasonic observations of large scale HE events". (Proceedings of the 14th long range sound propagation symposium, Virginia, 1990) pp 133-141.

Whitaker, R.W. (1995). "Infrasonic monitoring". (Proceedings of the 17th Annual Seismic Research Symposium on Monitoring a Comprehensive Test Ban Treaty (CTBT), Scottsdale, 1995).

Whitaker, R.W., Sandoval, T.D., Mutschlecner, J.P. (2003). "Recent infrasound analysis". *Nuclear Explosion Monitoring: Building the Knowledge Base* (Proceedings of the 25th Seismic Research Review - Nuclear Explosion Monitoring: Building the Knowledge Base, Tucson, 2003).

Whitaker, R.W., Mutschlecner, J.P. (2006). "Revisiting yield, direction, and signal type". *28th Seismic Research Review: Ground-Based Nuclear Explosion Monitoring Technologies*.

Wilson, C.R. (2005). Infrasound from auroral electrojet motions at I53US. *InfraMatics* **10** 1-13.

Zängl, G., Reinert, D. Rípodas, P., Baldauf, M. (2015). The ICON (ICOsahedral Non-hydrostatic) modelling framework of DWD and MPI-M: Description of the non-hydrostatic dynamical core. *Quarterly Journal of the Royal Meteorological Society* **141** (687) 563-579.

Infrasound Processing System at the International Data Centre: From Rudimentary to Maturity

P. Mialle

Comprehensive Nuclear-Test-Ban Treaty Organization, Vienna, Austria

Abstract

In 2001, when the first data from an International Monitoring System infrasound station started to arrive in near real time at the International Data Centre (IDC), its infrasound processing system was in a premature state. The IDC then embarked on a multiyear design and development of its dedicated processing system, which led to operational IDC automatic processing and interactive analysis systems in 2010. Over the next ten years the IDC produced more than 40 000 infrasound events reviewed by expert analysts. To continue advancing its methods, improving its automatic system and providing software packages to Comprehensive Nuclear-Test-Ban Treaty Organization users, the IDC focused on several projects. First, the automatic system for the identification of valid signals was redesigned with the development of DASE Tool-Kit Progressive Multi-Channel Correlation (DTK-PMCC), which is made available to CTBTO users within NDC in a box. Second, an infrasound model was developed for automatic waveform network processing software NET-VISA with an emphasis on the optimization of the network detection threshold by identifying ways to refine signal characterization methodology and association criteria. Future improvements of the IDC processing system are planned to further reduce analyst workload that includes atmospheric propagation modeling and enhancements of the automatic pipeline components.

1. STATUS OF INFRASOUND TECHNOLOGY AT THE INTERNATIONAL DATA CENTRE

The International Data Centre (IDC) of the Comprehensive Nuclear-Test-Ban Treaty Organization (CTBTO) Preparatory Commission receives and processes in near real time data from the International Monitoring System (IMS), a globally distributed network of seismic, hydroacoustic, infrasound and radionuclide stations.

Once completed, the IMS network will comprise 60 infrasound stations of which 53 have been installed and certified as of 2022 (Figure 1). The infrasound stations are arrays of measurement systems that are sensitive to acoustic pressure variations in the atmosphere in the IMS frequency band between 0.02 to 4 Hz. The array configurations include 4 to 15 elements, with typical designs of 4 to 8 elements, and with apertures between one- and three-kilometres following IMS requirements (Marty 2019).

1.1. The International Data Centre Processing System

After a design and development phase of more than 10 years, the IDC automatic processing system and interactive analysis has been fully operational for infrasound technology since February 2010. After reception, storage and referencing in the IDC database, the station data are automatically processed individually, e.g. at the station processing stage (Coyne et al. 2012). Based on the results of the station processing the network processing is initiated to form events with all three waveform technologies. The event information is then reported in IDC products (or bulletins) referred to as Standard Event Lists (SELs). Since 2010, the bulletin production deadlines have been revised and accommodate late arriving data and the signal propagation times for all waveform technologies (Brachet et al. 2010). The final automatic bulletin containing infrasound signals associated to waveform events is the SEL3, which is reviewed by IDC analysts.
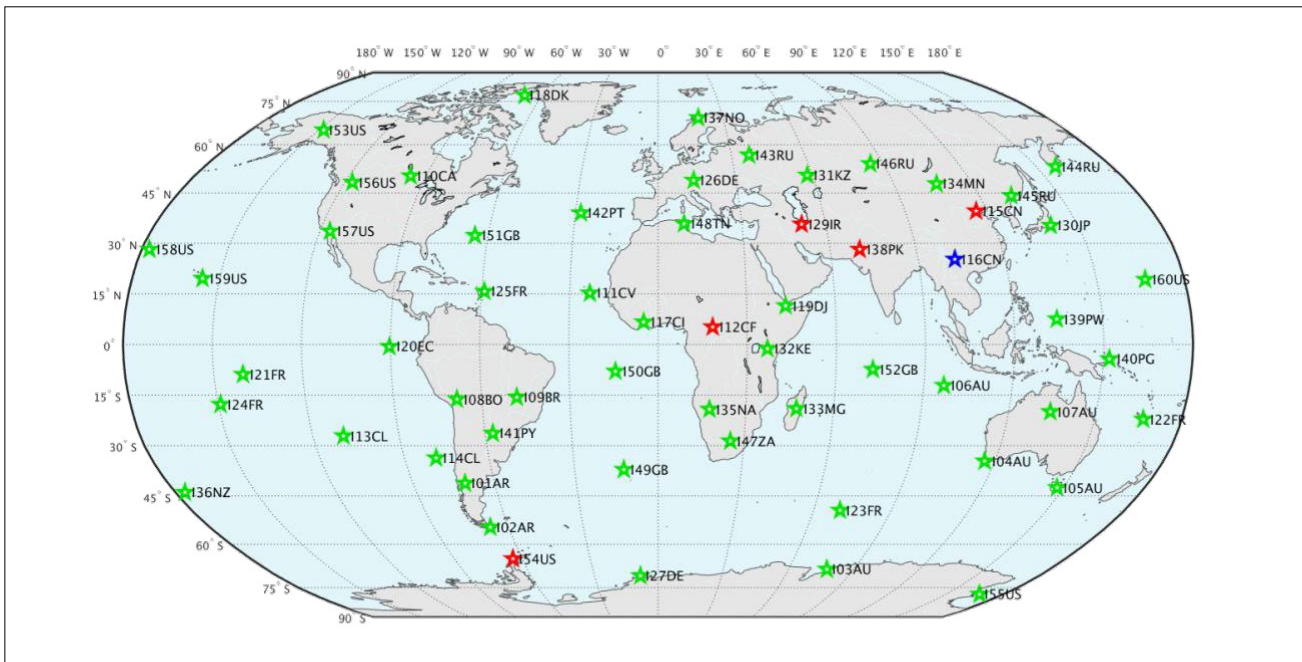
FIGURE 1.
From 2000 to 2022, 53 IMS infrasound stations have been installed and certified out of the planned 60 stations. The IMS infrasound network has reached 90% completeness.
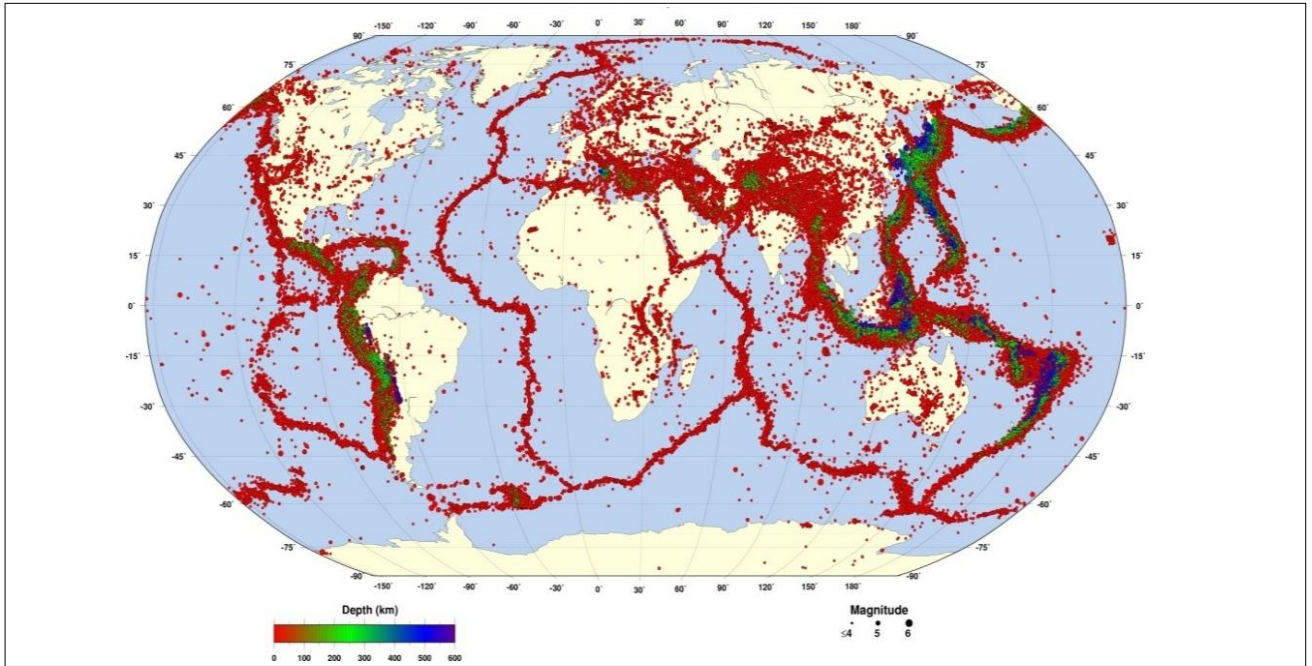
FIGURE 2.

REB continues to grow (contains seismic, hydroacoustic and infrasound): Since February 2000 — Over 688 000 REB events; 845 000 LEB and 545 000 since February 2010; about 130 events per day.

The result of the interactive review process is the Late Event Bulletin (LEB) on which event definition criteria are applied to produce the Reviewed Event Bulletin (REB).

The REB (Figure 2) is the final waveform product of the IDC and currently, during provisional operations, the target timeline for publishing the REB is within 10 days of real time. After entry into force (EIF) of the Treaty, the target timeline will be reduced to 48 hours. Specialized software has been developed for every processing stage at the IDC to improve signal to noise ratio, detect infrasound signals, categorize and identify relevant detections, form automatic events and perform interactive review analysis.

1.2. International Data Centre Bulletin Production Over the Last 12 Years

For the period 2010 to 2017, thousands of waveform events containing infrasound associations appear in IDC bulletins, in particular the REB and the LEB (Figure 3). This demonstrates

the sensitivity of the IMS infrasound component and the IDC ability to globally monitor the infrasound activity.

The unique information gathered by the IMS systems have been widely used for civil and scientific studies and have resulted in numerous publications: on meteor impacts such as the largest ever infrasound recorded event that is the Chelyabinsk meteor in February 2013 (Brown et al. 2013, Pilger et al. 2015, Le Pichon et al. 2013) as well as other observed fireballs and meteors (Caudron 2016), on powerful volcanic eruptions (Matoza et al. 2017, 2018, 2022, Vergoz et al. 2022, Gheri et al. 2023), on controlled explosions (Fee et al. 2013), on announced underground nuclear tests (Che et al. 2014), on accidental explosions (Pilger et al. 2021) or on atmospheric dynamic research (Le Pichon et al. 2015), on characterizing the infrasound global wavefield (Matoza et al. 2013), or on gravity waves study (Hupe et al. 2019) that could lead to deriving a space and time varying gravity wave climatology.
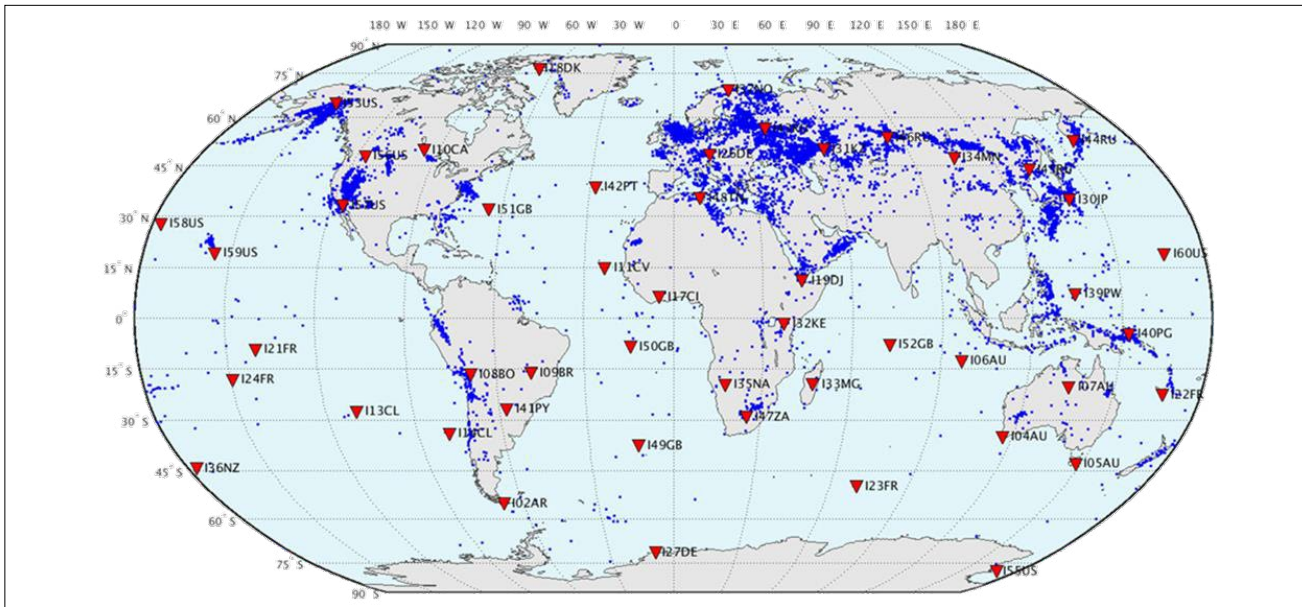
FIGURE 3.
2000–2021: LEB since infrasound technology fully in IDC operations: Since February 2010 – Over 41 000 LEB infrasound events; 9.9 events/day with infrasound association.

2. THE JOURNEY: HISTORY OF INFRASOUND PROCESSING SYSTEM AT THE INTERNATIONAL DATA CENTRE

It took several years for the IDC to evaluate the legacy system from the Prototype-IDC (pIDC) (Le Bras et al. 1999, Brown et al. 2002), to test new methods[1], to prepare the requirements for a full processing system for infrasound technology specifically adapted to IDC needs and to then go on to develop and implement the system. During this time the infrasound segment of the IMS was growing and evolving quickly with new stations coming online every year, bringing new challenges in terms of station design and signal variety being registered. These progresses forced the IMS to constantly re-evaluate requirements, while development of methods and software was happening to reach the expectations of the IDC and experts from States Signatories.

2.1. A Rudimentary System

Before the IDC was established in Vienna, efforts were ongoing at the pIDC to implement, test, evaluate or develop various algorithms, methods or software packages applicable to all verification technologies. In 1998, the *LibInfra* (Brown et al. 2002) station detection algorithm was in development at the pIDC, while the recently published Progressive Multi-Channel Correlation (PMCC) (Cansi 1995) algorithm was being considered for testing and comparison purposes. During that period, evaluation was carried out on data from research and development stations. In 2001, the development of the IDC system moved to Vienna to the IDC and the first data from an IMS infrasound station (Figure 4) was processed by the IDC. This milestone achievement is the prototype of an infrasound data processing system.

In 2003 as new IMS stations were certified and sending data, the number of infrasound events produced by the IDC system reached an alarming level. This emphasized the immaturity of the system inherited from the pIDC for infrasound technology (Figure 5) therefore efforts to develop verification technologies continued. After monitoring the performance of the IDC system, the IDC quickly decided to stop the 'pollution' of the IDC automatic bulletin by

---

1 Historical progress and results from IDC were presented during the Infrasound Technology Workshops organized or co-organized yearly by the Provisional Technical Secretariat since the late 1990s.
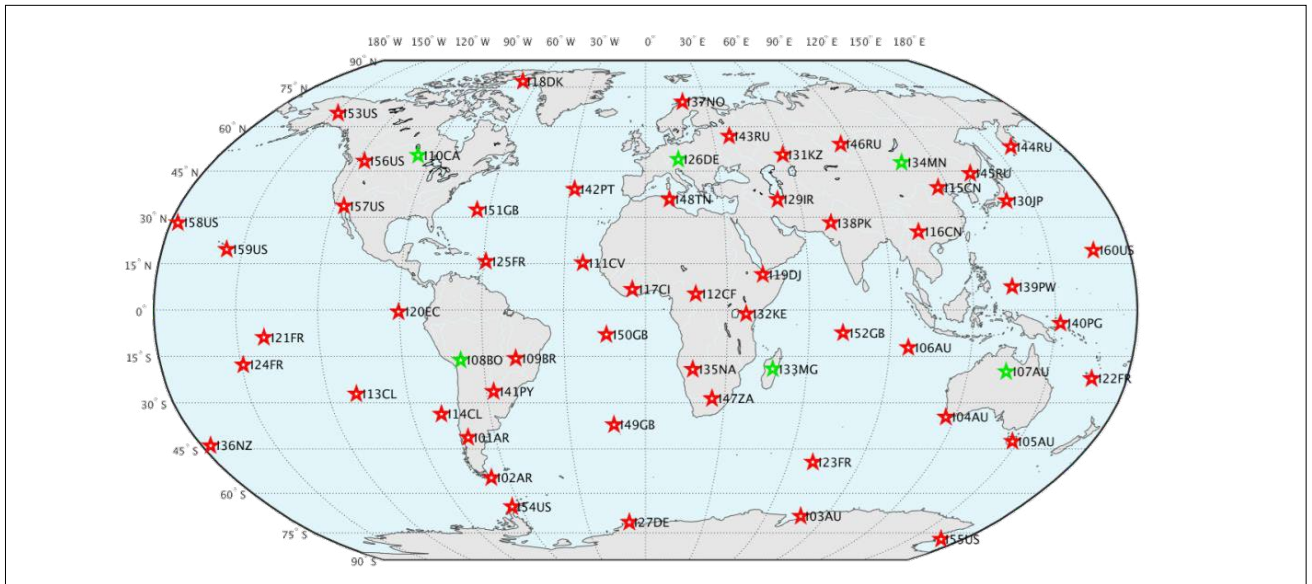
FIGURE 4.
IMS infrasound network in 2001 with six stations installed, certified and sending data to the IDC.
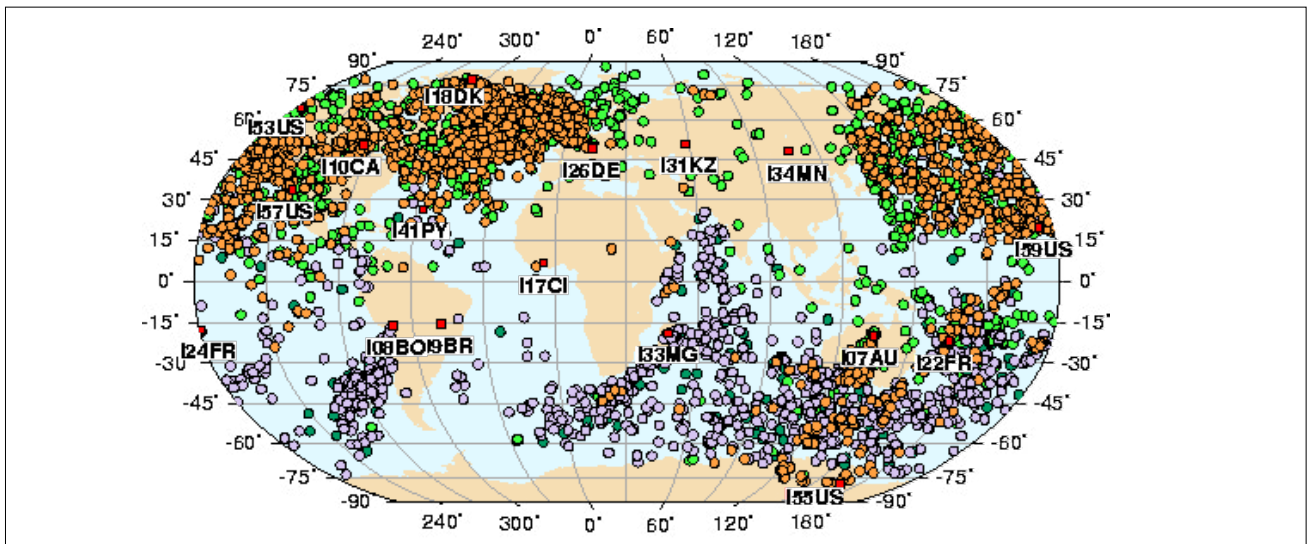
FIGURE 5.
Alarming network processing results of the prototype infrasound data processing system of the IDC (2003-2004).

infrasound data in 2004. Infrasound data were then disconnected from IDC operations and development on infrasound technology at the IDC continued the development pipeline with the objective to promote the recently developed station processing software, *DFX-PMCC*, and replace the legacy *LibInfra* system.

The design and development process of this updated IDC infrasound system was carried out during the early establishment of the IDC (2000-2010) (Brachet et al. 2010). The stations in the IMS network send data to the IDC according to the formats and protocols specified in the corresponding draft IMS operational manual (Marty 2019). Stations in the primary seismic, hydroacoustic, and infrasound networks send data continuously to the IDC and are processed automatically, while stations in the auxiliary seismic network are processed in response to a data request received from the IDC based on IDC data processing results from stations in the primary seismic, hydroacoustic, and infrasound networks. IMS data, also referred to as raw data, received at the IDC are parsed and are accessible through the IDC relational database management system. The data are then stored in the IDC database and are available for automatic

processing. The communication between IMS stations and the IDC, and between the IDC and users is done over the Global Communications Infrastructure.

2.2. Towards the First International Data Centre Processing System

Waveform data are automatically processed once they arrive at the IDC. Waveform station processing for continuous data stations is done in fixed time intervals with duration according to technologies, 10 minutes for primary seismic and hydroacoustic stations, and 30-minute intervals for infrasound stations accounting for the slower propagating medium. Once a time interval has elapsed, each interval is processed as soon as 95% of data used for station processing from that station has arrived in the IDC database. This threshold is set-up in order to optimize availability of results for further processing and not delay processing due to the arrival of very late data. Data from auxiliary seismic stations are processed once the requested data segments have been parsed into the IDC database.

Common to all waveform technologies is the pre–processing to perform quality control checks with Data Feature eXtraction – Quality Control (DFX-QC), that is being upgraded by *libwaveformqc* that allows for more transparency of the quality control checks implemented. While the quality control and masking logic remain unchanged, *libwaveformqc* brings several improvements for quality control of seismic data that is out of the scope of this paper and fixes several issues from DFX-QC), in particular with the spike detector (described in Brachet et al. 2010). The waveform station processing performed after the quality control checks is then technology dependent with Data Feature eXtraction - Progressive Multi-Channel Correlation (DFX-PMCC in use for infrasound technology, while DFX runs for seismic data and Hydroacoustic Azimuth and Slowness Estimator (DFX-HASE) for hydroacoustic technology. The PMCC algorithm (Cansi 1995) implemented in DFX-PMCC (described in detail in Brachet et al. 2009) is based on the 2004 version of PMCC algorithm. PMCC is an array processing method originally designed for processing data from seismic arrays, which proved to be efficient for extracting coherent signals with low signal to noise ratio among non-coherent noise that characterize infrasound signals propagating at a regional or global range.

PMCC performs several computations from band-pass filtering, cross-correlating data from station channels to aggregating time–frequency signal features to improve the signal to noise ratio and detect signals in the processed data interval. The objective of the feature extraction is to compute wave attribute resulting, among others, in detection time, amplitude, azimuth, trace velocity and then added to the IDC database. For infrasound technology, the final stages of station processing is performed by the *StaPro* (Le Bras et al. 1999) algorithm and includes signal grouping and initial phase identification. This software combines criteria for all waveform technologies and signal types.

The arrivals resulting from station processing are the input in network processing, currently performed with Global Association (Le Bras et al. 1994) software. At the network processing stage, the arrivals are combined to form events which are published in the automatic bulletins, named Standard Event List (SEL) 1, 2 and 3. After the final automatic bulletin is produced, the data are ready for review by the IDC waveform analysts using specialized software for interactive review analysis. The analysts correct mistakes in the automatic bulletin, refine the results, and scan IDC results and raw data to try to add events missed by the network processing algorithm. To illustrate this stage, the infrasound processing pipeline currently operational at the IDC is summarized in Figure 6.

The result of the review process by the analysts is the LEB on which event definition criteria are applied to produce the REB. The REB is the final waveform product of the IDC available to States Signatories. Currently, during provisional operations, the target timeline for publishing the REB is within 10 days of real time. After EIF of the Treaty, the target timeline is reduced to 48 hours.
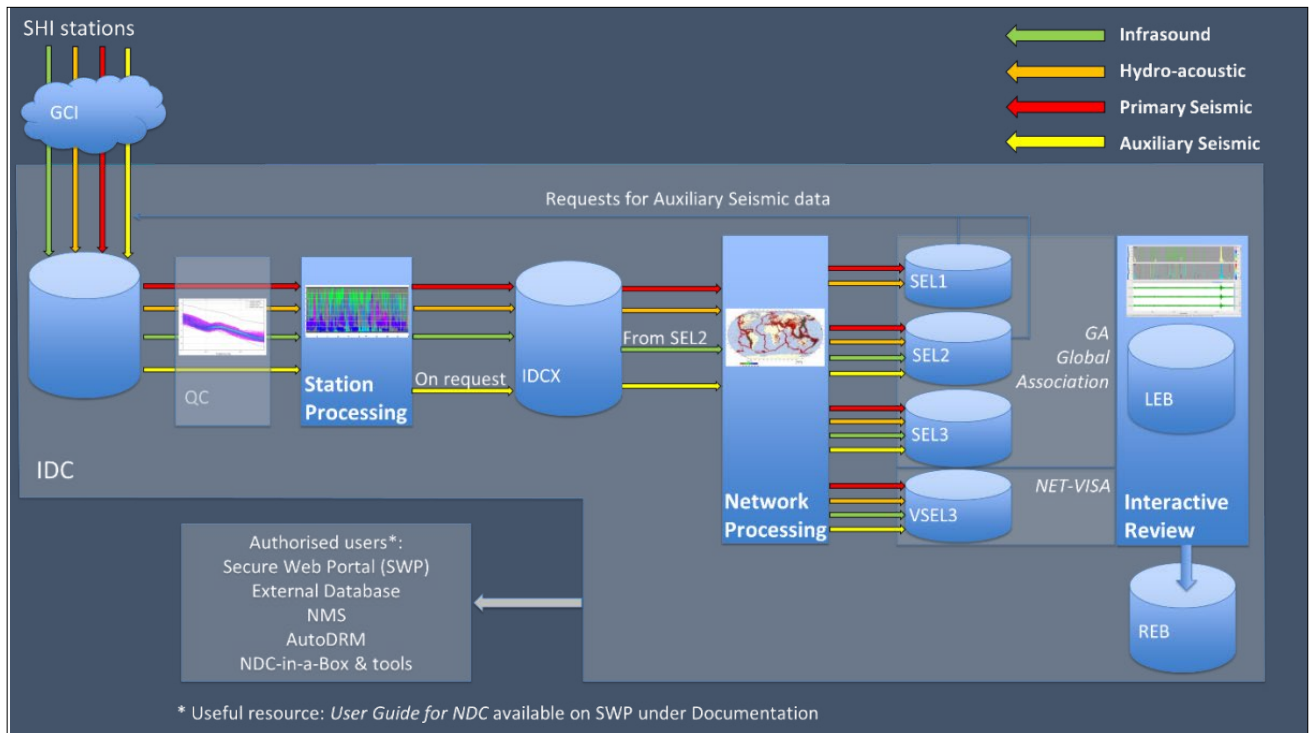
FIGURE 6.
Operational waveform processing of the IDC.

In 2005, the IDC focused on near term development for the waveform technologies with the main goal of reinstating infrasound processing in the operations of the IDC within a year . However, a year later progress was insufficient as the IDC realized methods and analysis procedures needed more work before promotion. A side project to support this endeavour was then initiated by compiling a catalogue of ground truth events with infrasound detections from IMS stations analysed in the IDC development area. This catalogue called Infrasound Reference Event Database (IRED) (Brachet 2006) rapidly grew and then captured 160 reference events. Over the next couple of years, the IRED would grow from 311 events in 2007 to nearly 600 in 2009, while the IDC developed the graphical interface accompanying DFX-PMCC. This allowed the preparation of a preliminary procedure for associating infrasound phases to seismoacoustic event and for saving infrasound events thanks to the newly produced interactive review tool: *Geotool-PMCC*.

With this progress, the IDC then felt ready to tackle the challenge of updating its Global Association network association method to reduce the false association rate with infrasound phases that forced the IDC to remove infrasound technology from its operations in the first place. This task was jointly carried out with better characterizing the nuisance sources being registered at each station, in particular signals originating from microbaroms or local human-made or natural activity (such as for instance, respectively, activity at hydroelectric dam or waterfalls).

In 2009, the IDC was closer to its goal and decided to reconnect infrasound data to IDC operations after its merge to a new Linux based operating system. This is also the time when the 2009 Sayarim Infrasound Calibration Experiment (Fee et al. 2013) was scheduled, a large scale international collaboration aimed at assessing the performance of the IMS infrasound component and provide ground truth data. This experiment provided an opportunity for the IDC to test its redesigned infrasound system on a real case scenario. The success of the experiment cemented further the readiness of the IDC and infrasound data and event analysis returned to the IDC operations on 10 February 2010.
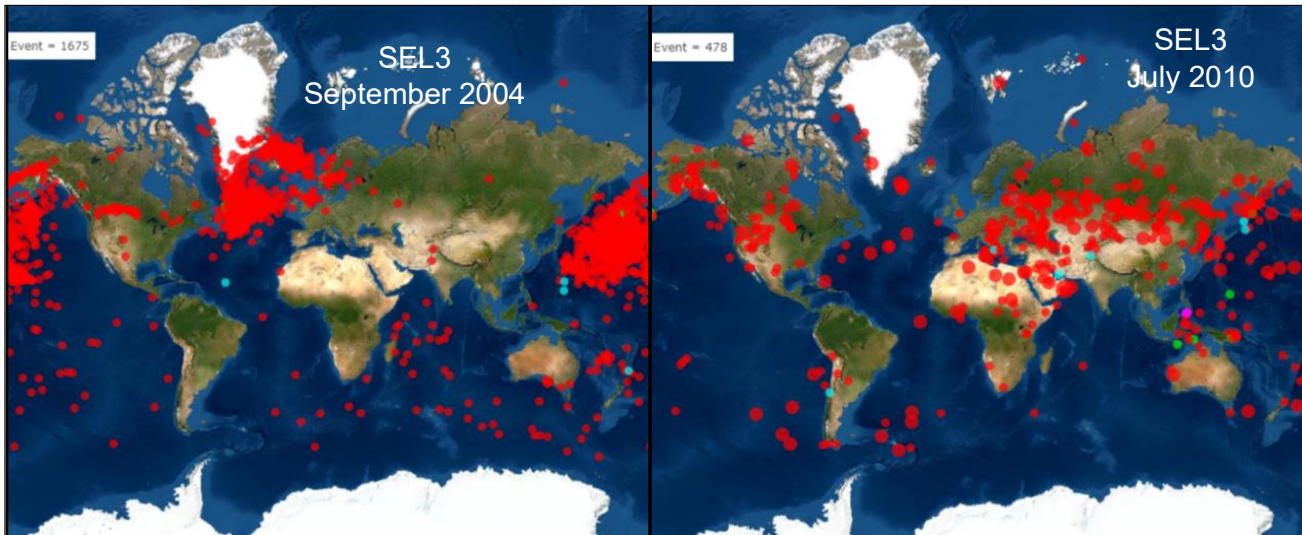
FIGURE 7.
SEL3 comparison of events with infrasound phases associated from September 2004 to July 2010.

2.3. A System in Progress: Overview of the Results of International Data Centre Automatic and Interactive Analysis – (Alternative: Introduction of Infrasound Technology in International Data Centre Bulletin Production)

The IDC processes seismoacoustic data from the global network of the IMS for the three waveform technologies. Automatic data analysis is done in near real time. The detection framework, composed of DFX-PMCC followed by *StaPro*, produces high quality detection lists for IMS infrasound data, and the network association algorithm, Global Association, aggregates event bulletins containing infrasound and seismoacoustic events enriched with infrasound detections. The outcome of this fully automated process is then methodically examined by expert analysts.

IDC analysts perform their review activities using the analyst review station (ARS) following predetermined sets of IDC procedures. ARS provides access to a few display panels and functionalities such as raw data from IMS waveform stations, results of the automatic station processing (phase attributes and time picking in particular) and tools to visualize or compute waveform attributes, modify or add event hypothesis and save the results of analyst review in the LEB.

Specifically for infrasound technology, the review of infrasound signals detected by station processing has been made available in ARS through a specific graphical module integrated within the IDCs Geotool software (Geotool-PMCC). Geotool-PMCC could only be used to visualize existing results and it did not allow the user to interactively process or re-process infrasound data using a different set of detection parameters.

At the time of the introduction of infrasound technology in IDC operations, resources were dedicated to ease the infrasound related activities. The efforts concentrated on:

- Continuously assessing the performance of the automatic system to ensure that results were in alignment with those of the IDC test environment (also known as IDC testbed);
- Updating the IDC procedures for interactive analysis of infrasound only events and seismicacoustic events. This task included the training of IDC analysts to prepare them for the review of infrasound detections and infrasound events, but also the support of the infrasound analysis group for routine analysis and the inclusion of high quality events in IDC products;
- Creating procedures for the inclusion in IDC operational environment of newly installed IMS infrasound stations or IMS stations going through upgrade activities. To
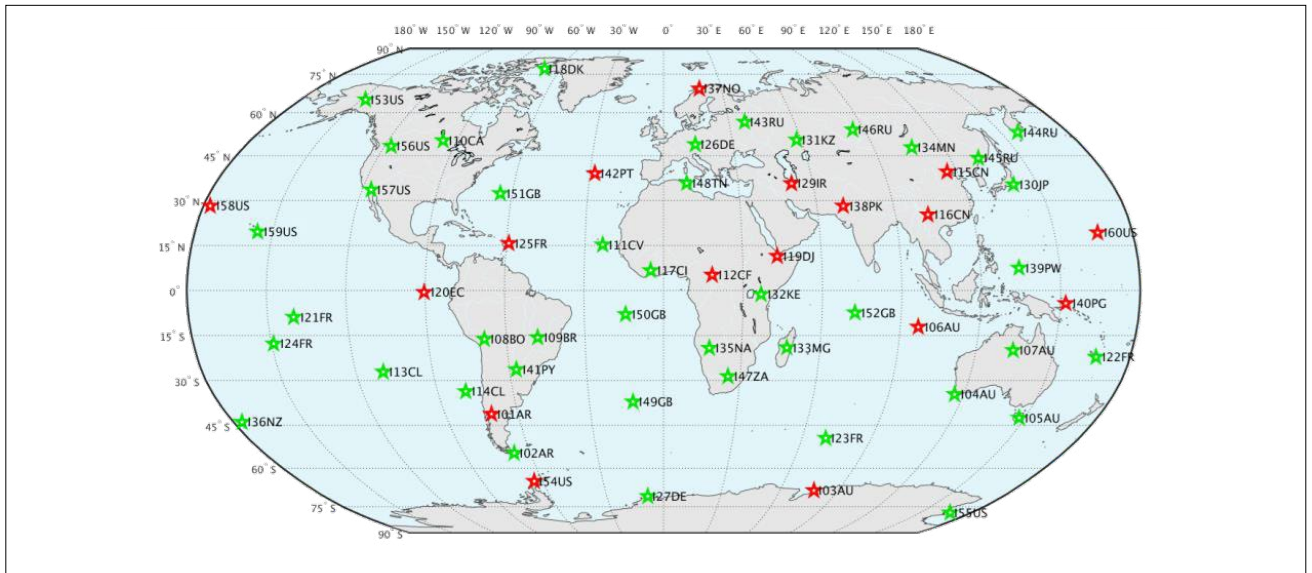
facilitate this activity, the infrasound station configuration and processing is installed or updated in the IDC testbed for testing, and after a period of a few weeks an assessment is made by the IDC to support the decision to promote the station to IDC operational environment;

- Updating station parameters and processing configuration to account for station performance changes (such as loss of sensor data or change in station behaviour), to optimize the quality of the detection bulletin and ease routine analysis;
- Preparing system enhancements based on the performance assessment and with the goals to reduce analyst workload and raise the quality of IDC products.

This motivated the IDC to conduct several projects such as the infrasound only pipeline project to upgrade the network processing stage, which ended in the development of an infrasound model for NET-VISA and a project to develop a new detection and interactive display package.

IDC analysts recognize the value of the infrasound legacy system, from the results of the automatic system (station and network processing) to the set of specialized software used for interactive review and have developed working habits to efficiently review event hypothesis from the SEL3. This includes modifying them and possibly scanning for missed events by the network processing software in order to produce final IDC products. The infrasound system of the IDC produces high quality products over several years, which constitutes a unique and unmatched data set of infrasound events.

3. REDESIGN AND OPERATIONS: AND IT CONTINUED WITH ANOTHER 10-YEAR TRIP

## 3.1. Infrasound Technology Fully Part of International Data Centre Operations

Since February 2010, the IDC has compiled the first global infrasound catalogue of events (Figure 3) continuously enriched at the IDC by interactive analysis performed by IDC analysts. In over twelve years the IDC has reviewed over 700 000 waveform events of which over 60 000 contained infrasound phase associated,

i.e. infrasound detections are being used to enrich the event solution (origin time and localization).

After review, during the first seven years of infrasound technology in operation, IDC analysts have saved over 11 000 events with associated infrasound arrivals in the REB and nearly twice as many (over 21 000) in the LEB.

In 2010, the full inclusion of infrasound technology in IDC operational activities was made possible by a multiyear effort that led to the complete redesign of the IDC infrasound automatic and interactive software, the rewriting of interactive review procedures and the thorough redefinition of IDC analyst activities. Furthermore, since the IDC infrasound catalogue was the first global near real time bulletin produced for infrasound technology, the internal IDC criteria for the LEB production were relaxed in order to save and archive pure infrasound technology events made of only two infrasound associated arrivals (figure 9). It should be noted that the events not matching event definition criteria for the REB are part of the LEB, but not published in the REB. While the concept of the event definition criteria was introduced, considering the mission of the CTBTO, to look for evidence of potential Treaty violations (Coyne et al. 2012), there were multiple reasons for relaxed criteria for infrasound bulletins to:
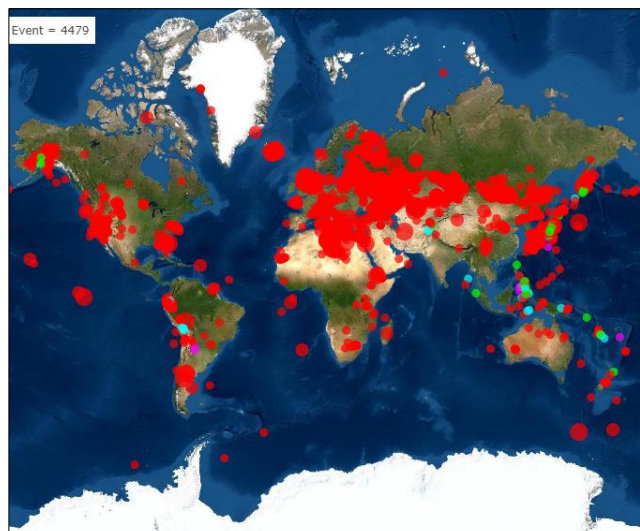
FIGURE 9.
Infrasound associations in the LEB in 2010 and 2011 (about eight events saved per day in IDC products).

1. Build as complete as possible an infragenic picture during the CTBTO provisional status to ensure optimum global coverage;
2. Compensate for the sparsity of the network as there was 42 certified IMS stations in 2010 covering the Earth (Figure 8);
3. Allow for a fast-tracked learning process at the IDC;
4. Obtain in a limited time span a statistically significant infragenic picture for the next generation of network association algorithm that was in the proof of concept phase;
5. Increase the understanding of the technology and its capacity as compared to design period of the network in 1996.

As the IMS infrasound component continues to expand, up to 53 certified stations by 2023 (Mialle et al. 2021) , the relaxed LEB criteria remain in place at the IDC under provisional operations. This deliberate choice is justified by the continuity in the learning phase of the IDC about global infrasound sources while the IMS infrasound network remains in its installation phase. The IMS infrasound component is now reaching over 90% completion rate.

3.2. Infrasound Station Processing Re-Engineering

In 2010, the IDC completed the introduction of infrasound technology in every aspect of its operation activities. In the following years, efforts rapidly shifted to ensure a smooth transition of IDC activities to include infrasound technology. These efforts focused on the assessment the performance of the infrasound processing and the reporting to CTBT States Signatories, the training and preparation of IDC analysts for routine operations and the update of procedures and guidelines for analysis at the IDC, the support for requests from National Data Centres on newly available infrasound related information, and the preparation of procedures for testing newly installed and certified IMS infrasound stations or upgraded facilities. In 2012, the IDC identified areas for improvement of its infrasound system to address software limitation in the legacy system from pIDC. And in 2013, the Provisional Technical Secretariat (PTS) Midterm Strategy

197
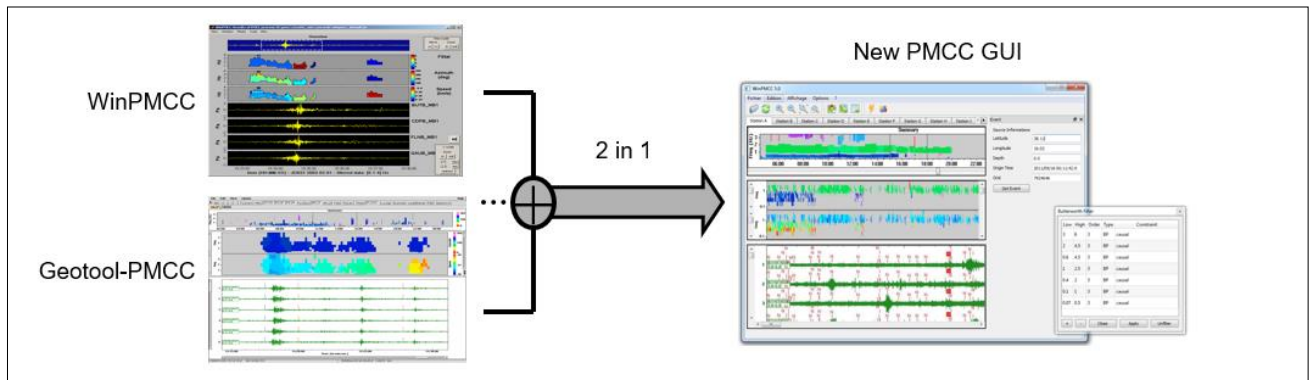
FIGURE 10.
Develop an upgraded infrasound software package for IDC and National Data Centre (NDC).

was published stating that "As part of its re-engineering effort, the IDC Division will deploy new signal processing, event association and analyst tool to increase valid events detected and reduce the analyst workload".

This provided a mandate for the IDC to continue its work on the review of its station and network processing algorithms and on the redesign of the interactive software. In addition, to keep abreast of new developments from the research community and pursue enhanced collaboration with IMS for introducing (or re-introducing) stations in IDC operations.

After 2004 and its initial inclusion in the IDC method list, numerous updates and improvements have been implemented in the PMCC software developed at Commissariat à l'énergie atomique et aux énergies alternatives (CEA). With the significant advancements in infrasound technology since the design and the installation of the first IMS station, the PTS worked on a programme to upgrade its methods for infrasound processing from the control of data quality to the automatic association of infrasound phases for bulletin production and on a framework for station processing with integration of the interactive review modules. As the PMCC algorithm and graphical interface have proven to have satisfactory performance and fulfils all need of the IDC for its automatic system and routine analysis and it is widely used in the infrasound user community, the DTK-PMCC and DTK-GPMCC (respectively station processing and related graphical user interface) were developed based on research community

and IDC operational needs (Figure 10). This software library is specifically designed for multipurpose usage within the IDC operational system for automatic and interactive analysis and for the IMS engineering team during potential site surveys and station installation or upgrade. In its standalone version, the software gives the ability to the user to re-compute the PMCC results, which is valuable for NDC activities and in the field use.

Notable enhancements and specific developments of DTK-PMCC software is described in Mialle et al. 2019. The package has then been introduced in NDC in a box at the early stage in 2016 and in the IDC development environment in 2017. It is currently up and running in all environments of the IDC and it is being used for special event analysis for hydroacoustic and for automatic and routine analysis for infrasound technology. After multiyear efforts, it replaced the legacy system in 2022.

This achievement was made possible thanks to the partnership of the IDC with the CEA and with the support of the European Union Council Decisions. It allowed the PTS to develop a software package for the IDC that could be delivered to NDCs for them to process the data available from the IMS for both Treaty monitoring and for national purposes. These efforts have created a strong NDC user base and the project results helped NDCs trust in the credibility of the verification system as it gives all NDCs the chance to become active contributors to the CTBT verification process.

The IDC continues to remain dedicated to further developing the software package for the IDC and for the NDC in a box users. Updates of the packages continue to be rolled out towards NDCs as they become available and dedicated training ensures the continuous support of the user base.

3.3. An Infrasound Model for NET-VISA

In its effort to sustain IDC capacities and continuously improve its methods, the IDC has been working on the replacement of its network association software, Global Association, and decided to evaluate possible improvement by developing a Bayesian inference system that computes the most likely global event history given the record of local sensor data.

In 2015, NET-VISA was extended to incorporate infrasound data from the IMS. However, infrasound technology presents additional challenges as many signals are produced by nuisance sources, that are not of interest for the verification regime. Despite efforts to identify and categorize detections from such sources, the repetitive nature of this clutter and its variability in wave attributes leads to a significant number of false event hypotheses due to the true or random matching of clutter at multiple stations. A probabilistic model of clutter is then built and used as part of NET-VISA (Le Bras et al. 2021).

The IDC collects waveforms from a global network of infrasound sensors maintained by the IMS, and automatically detects signal onsets and associates them to form event hypotheses. However, many signal onsets are due to local, regional or global clutter sources such as microbaroms (from standing waves in the oceans), waterfalls, dams, gas flares, surf (ocean breaking waves) etc. These sources are either too diffuse or too local to form events. Adding to the difficulty of this task, the repetitive nature of this clutter leads to a large number of false event hypotheses due to the random matching of clutter at multiple stations. Several studies focus effort on categorization of clutter using long term trends on detection azimuth, frequency, and amplitude at each station. Continuing the reasoning, a probabilistic model of clutter is

then created within NET-VISA. The resulting model is a fusion of seismic, hydro-acoustic and infrasound processing built on a unified probabilistic framework.

NET-VISA incorporate several infrasound specific features due to the nature of infrasound signals and infrasound processing. Those are:

- Static prior using a whole year's worth of data;
- Clutter model to avoid building events from gas flares;
- Disentangling seismoacoustic versus pure infrasound associations;
- Identification of useful infrasound detection features.

The infrasound model is an integral part of NET-VISA and it originates from processing results gathered in 2012, which was then tested in 2013 against the results of the IDC automatic system, the SEL3 produced by Global Association (that contained 54 327 events), and of the reviewed bulletins, the LEB (that contained 42 782 events). NET-VISA runs in the IDC environment for all waveform technologies and for the year 2013 it produced 60 904 events of which 3383 events contain infrasound phases associated. The evaluation of the infrasound model considers that two events in two different bulletins are identical if they share two similar arrivals where the arrivals are detected at the same station and if they separated in time and space (back-azimuth) with specific criteria. Additional information on the features implemented and the comparison are provided in (Mialle et al. 2019).

While NET-VISA is implemented in the IDC environment and operates in real time to assist IDC for bulletin production, its results are continuously scrutinized for testing and evaluation and for complete integration in routine operation as the primary network processing system of the IDC.

For infrasound technology, the IDC notes that the NDT-VISA infrasound model outperforms the current operational system, Global Association. Global Association produces relatively high ratio of spurious seismoacoustic associations, which is not observed with NET-VISA. Further to that

NET-VISA reduces spurious associations, while retaining a similar level of overlap compared to the REBs.

While the IDC remains focused on optimizing the performance of the detection and association algorithms, it also remains committed on sustaining and updating existing operational capabilities with respect to its evolving station network.

3.4. Additional Projects to Advance Infrasound Technology at the International Data Centre

While the IDC continues to advance its methods to better detect signals and characterize them and enhance the association of infrasound signals with those from other waveform technologies, it also remains committed to serve and support its user base and add important components to its operational systems.

Several research and development projects have been carried out over the years with internal and external stakeholders to integrate tools for evaluating the detection capabilities of the infrasound network with contributions from France (DTK-NetPerf developed by CEA) and the United States of America (NetMOD developed by Sandia National Laboratories). Those methods are still under development, evaluation, and integration at the PTS.

Similarly, the IDC continues to closely monitor the progresses in numerical weather prediction of the middle atmosphere and in the development and open source distribution of propagation modelling methods for infrasound technology. The current performance of such methods for in-depth analysis of event of interest could soon open capabilities for the IDC real time operational system to further improve the seismoacoustic association task.

The IDC also remains strongly committed to supporting its authorized user by providing them with modern and user-friendly software packages, which are based on their requests to the PTS. Such software packages are made available via NDC in a box and allow NDCs to reproduce
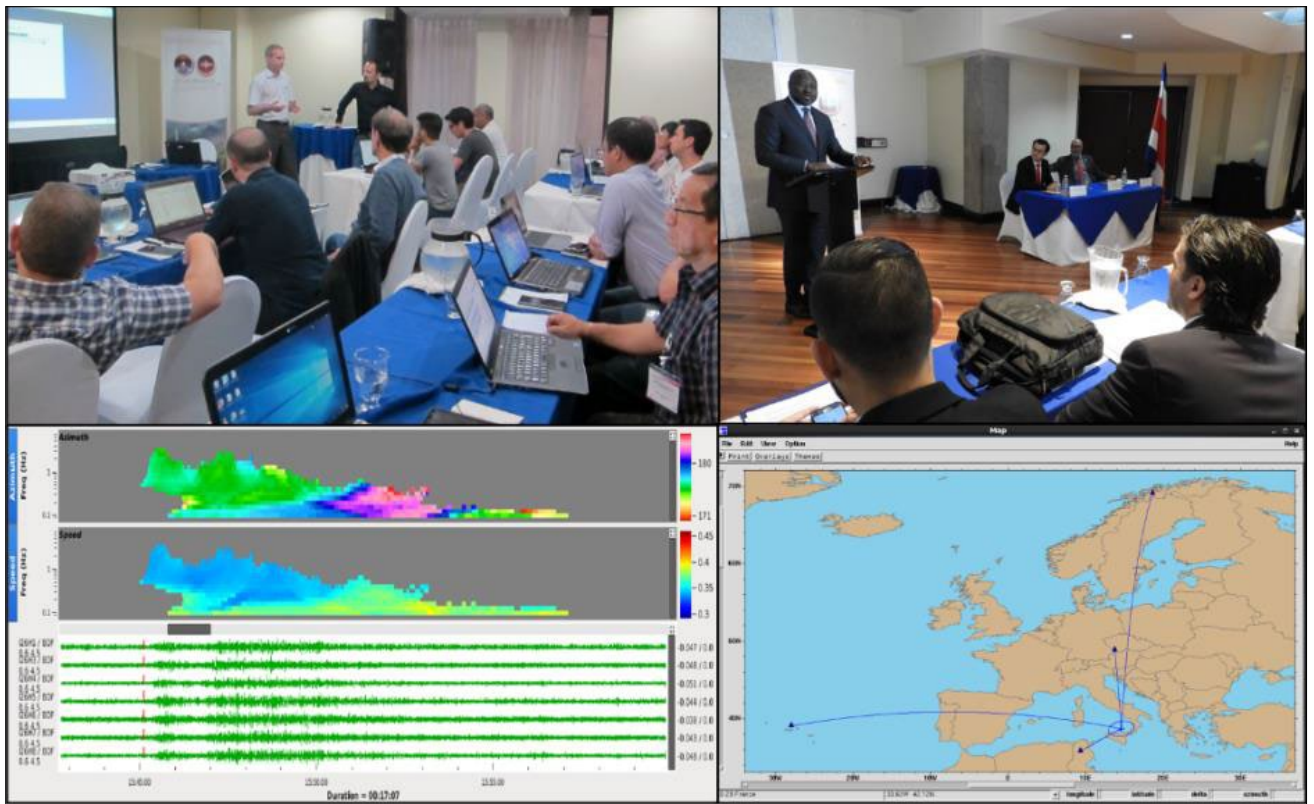
FIGURE 11.
Top pictures: training and workshop rooms in Costa Rica in 2019, and bottom images: training material produced at the intermediate level training in Romania in 2019.

IDC automatic and interactive results thus further advancing the trustworthiness in IDC products. The efforts on NDC in a box continues, with the support and contractual resources from external stakeholders and methods with the integration of infrasound technology in the SeiComp3 model and the donation of the detection browser, DTK-DIVA, which are both used on a regular basis by the authorized users.

To support those projects the IDC also developed an infrasound technology training cycle composed of several elements (Figure 11), which are:

- Introduction to infrasound technology in various NDC courses, including training in languages other than English, since 2017;
- Introductory courses and regional infrasound workshop and integrated trainings (RIWIT) – such as the African RIWIT in February 2018, the Latin American and Caribbeans RIWIT in February 2019 and the Southeast Asia Pacific and Far East RIWIT originally scheduled to take place in Indonesia in March 2020 and postponed until 2024;
- Intermediate and advanced level trainings. The first of its kind intermediate infrasound training was held in Bucharest, Romania in July 2019 and a second was postponed in 2020 until a later date;
- Series of expert trainings that are co-organized with CEA. The first event of the series was organized in October 2019 in France, a second training was postponed due to the Covid-19 pandemic.

3.5. The January 2022 Volcanic Eruption of Hunga, Tonga: A Benchmark Event

While the redesigned IDC infrasound system was receiving its final touch prior to introduction to the IDC operational system, a large eruption took place in early 2022, which produced unprecedented recordings and findings. The 15 January 2022 climactic eruption of the undersea Hunga volcano, Tonga, produced an explosion in the atmosphere of a size that had not been documented in the modern geophysical record (Matoza et al. 2022, Vergoz et al. 2022, Donner et al. 2023). The eruption generated tsunamis, regional ashfall and plume that reached stratospheric height (55 km) despite the eruption being triggered underwater. The event generated a broad range of atmospheric waves observed globally by various ground based and spaceborne technologies and instrumentation networks.

The most notable atmospheric wave was the surface guided Lamb wave (≲0.01 Hz, which is an acoustic gravity wave that is associated with extremely large atmospheric explosions). The Lamb wave was detected on barometers, infrasound sensors, seismometers, and satellites. Internal gravity, acoustic gravity, and infrasound waves were captured in detail by the entire operational at the time infrasound component of the IMS network, comprised of 53 stations, with periods from ~1 h to a few Hz (Figure 12).

The Lamb wave propagated around the globe numerous times, observations of at least four, plus three antipodal, passages around Earth over six days were extracted (Figure 13). The Lamb wave contributed to fast arriving, hazardous tsunamis that were not forecasted. The Hunga Lamb wave resembled the Lamb wave produced by the 1883 Krakatau eruption (Le Bras et al. 2023), but it was observed by a much denser instrument network. The Hunga eruption produced atmospheric waves that dwarfed the previously largest infrasound event recorded by the IMS that was the created by the impact of the Chelyabinsk meteor in the atmosphere on 15 February 2013 (detected by 20 of the 42 operational infrasound IMS stations at the time).

The Hunga eruption produced remarkable globally detected infrasound (0.01 to 20 Hz), long-range audible sound, and ionospheric perturbations. Infrasound waves also propagated around the globe numerous times and audible acoustic waves were heard out to New Zealand and to Alaska at about 9000 km, which was unprecedented. Current wave propagation models do not sufficiently explain these observations.

The estimation of an equivalent yield for the eruption is possible, however remain challenging

FIGURE 12.
The eruption was detected by 53 out of 53 operational IMS infrasound stations at the time of the event.
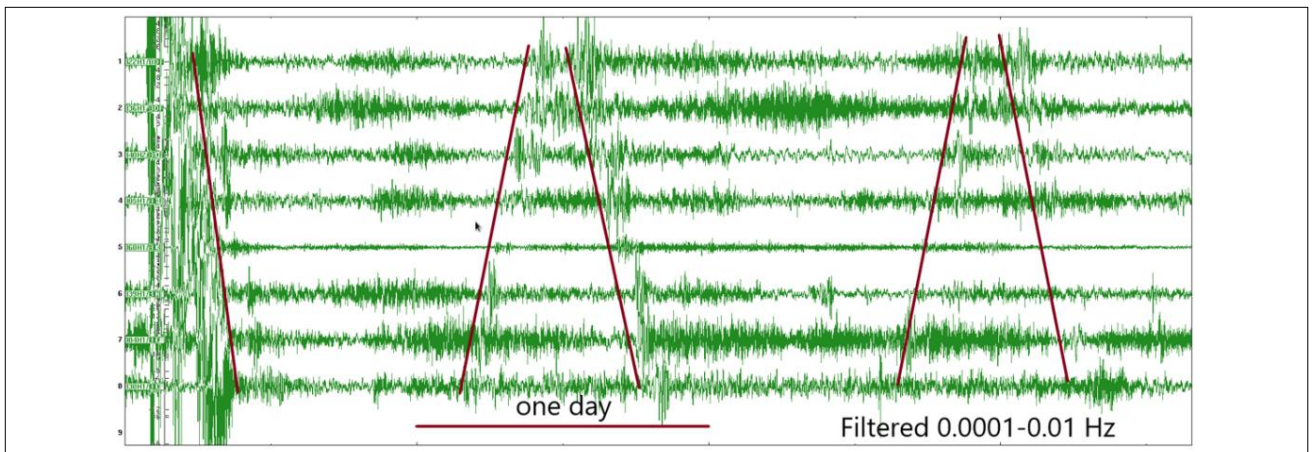
FIGURE 13.
Passage of the Lamb waves on eight IMS infrasound stations, located from New Caledonia about 1860 km away to Japan over 8000 km away, over four days.

due to the inherent properties of the source, which is a long duration source time function.

The atmospheric waves from this eruption provide a landmark data set for scientists to study for many years, with the IMS network being a key element to understand global wave phenomenon. This set of observations is helpful for disentangling the event and understanding the propagation of waves through the atmosphere and ocean. The

202

eruption has captured global attention and many research groups have published and presented their findings (Matoza et al. 2022, Vergoz et al. 2022, Donner et al. 2022, Le Bras et al. 2023).

4. OUTLOOK AND CONCLUDING REMARKS

Infrasound technology is an integral part of the work of the IMS with station installation, maintenance, sustainment, and technological progresses (Marty 2019). It is also preponderant in IDC operational and development activities over the last 26 years and more so since the introduction of infrasound technology in IDC products in February 2010. Since the early days of the PTS, the IDC strives to develop a complete, efficient, and accurate infrasound system. A step further was achieved in recent years with progresses at the network association level and with the completion of the redesign of the infrasound station processing system and interactive analysis tools. The uniqueness of the IMS infrasound network and the IDC operational processing system continue to place the CTBTO as a cornerstone of infrasound technology research and development for nuclear test verification and for civil and scientific applications.

Among the latest achievements, the most notables were attained on one side with the progress on the network association method, NET-VISA, that equally consider the three waveform technologies and offers improved performance over its predecessor. On the other side, the station processing and interactive review platform, DTK-PMCC and DTK-GPMCC, now offers the same platform to the IDC analysts and to the experts from NDCs thanks to NDC in a box framework. Indeed, as requested by CTBT States Signatories expert for a number of years, the CTBTO user community recently acquired the ability to accurately reproduce IDC results obtained with IMS infrasound data, which further enhance the verification regime and advance the capabilities of NDCs. These efforts have created a strong NDC user base and the resulting NDC in a box project help gaining NDC trust in the credibility of the verification system.

Beyond these achievements, the IDC aims to pursue efforts for infrasound technology with a multiyear horizon to enhance its capabilities with the final goal to produce a complete and high quality bulletin. Several research and development area, of interest to the infrasound community are considered by the IDC. To name a few the use of atmospheric specifications in infrasound network processing captures most interest, with several approaches being considered for the extension of the infrasound model in NET-VISA to either use real time atmospheric specifications or derived products produced by an infrasound propagation algorithm. However, challenges remain as the inherent unpredictability of the atmosphere makes it a complex task, in particular in the context of fully automated real time system operated by the IDC. On a shorter timeframe, the IDC could revisit the phase categorization by building on the experience from the current IDC station processing system and the effort and knowledge gained by the recently developed clutter model for NET-VISA. A few more projects have been ongoing for several years, such as the pursuit of developing and implementing a framework for detector evaluation for the IDC that could extended to all waveform technologies. In addition, the development and implementation of a state of the art platform for special event analysis, including for infrasound technology in the content of the special studies and expert technical analysis project initiated by the IDC.

The commitment of the PTS to improve the IDC system ensures the sustainment and enhancement of the existing capabilities of the IDC in order to continue building a trustworthy and credible verification system and support the preparation for EIF of the CTBT.

REFERENCES

Brachet, N., Coyne, J. (2006). The Current Status of Infrasound Processing at the International Data Centre. https://api.semanticscholar.org/CorpusID:53515655.

Brachet, N., Brown, D., Le Bras, R., Cansi, Y., Mialle, P., Coyne, J. (2010). Monitoring the Earth's Atmosphere with the Global IMS Infrasound Network. In: Le Pichon, A., Blanc, E., Hauchecorne, A. (eds) Infrasound Monitoring for Atmospheric Studies. Springer, Dordrecht.

Brown, D.J., et al. (2002). Infrasonic signal detection and source location at the Prototype International Data Centre. *Pure and Applied Geophysics* **159** (5) 1081-1125.

Brown, P.G., et al (2013). A 500-kiloton airburst over Chelyabinsk and an enhanced hazard from small impactors. *Nature* **503** 238-241.

Cansi, Y. (1995). An automatic seismic event processing for detection and location: The P.M.C.C. method, *Geophysical Research Letters* **22** (9) 1021-1024.

Coyne, J., et al. (2012). "CTBTO: Goals, networks, data analysis and data availability". *New Manual of Seismological Observatory Practice 2 (NMSOP-2)* (P. Bormann, Ed.). Deutsches GeoForschungsZentrum GFZ, Potsdam, pp. 1-41.

Donner, S., Steinberg, A., Lehr, J., Pilger, P., Hupe, P., Gaebler, P., Ross, I.O., Eibl, E.P.S., Heimann, S., Rebscher, D., Plenefisch, T., Ceranna, L. (2023) The January 2022 Hunga Volcano explosive eruption from the multitechnological perspective of CTBT monitoring, Geophysical Journal International, Volume 235, Issue 1, Pages 48–73, https://doi.org/10.1093/gji/ggad204.

Fee, D., et al. (2013). Overview of the 2009 and 2011 Sayarim infrasound calibration experiments. *J. Geophys. Res. Atmos.* 118. https://doi.org/10.1002/jgrd.50398.

Gheri, D., et al. (2023). Monitoring of Indonesian volcanoes with the IS06 infrasound array. *Journal of Volcanology and Geothermal Research* **434** 107753.

Hupe, P., Ceranna, L., Le Pichon, A. (2019). How can the International Monitoring System infrasound network contribute to gravity wave measurements? *Atmosphere* **10** (7) 399.

Le Bras, R.J., Guern J.A., Brumbaugh D.A., Hansen J.A., Sereno T.J. (1999). "Integration of seismic, hydroacoustic, infrasound and radionuclide processing at the Prototype International Data Centre". Paper presented at the 21st Seismic Research Symposium, Las Vegas, NV, 1999.

LeBras, R, Swanger, H, Sereno, T, Beall, G, and Jenkins, R. (1994) Global association. Final report, May-November 1994. United States. https://www.osti.gov/biblio/256532 (Accessed on 2 January 2024).

Le Bras, R.J., et al. (2021). NET-VISA from cradle to adulthood. A machine-learning tool for seismo-acoustic automatic association. *Pure and Applied Geophysics* **178** (5) 2437–2458.

Le Bras, R. et al. (2023). "Timing statistics of the multiple passages of the pressure wave generated by the 2022 Hunga Tonga- Hunga -Ha'apai and comparison with the 1883 Krakatoa pressure wave". E-poster presented at the CTBT: Science and Technology Conference 2023, Vienna, Austria, 2023.

Le Pichon A., et al. (2013). The 2013 Russian fireball largest ever detected by CTBTO infrasound sensors. *Geophysical Research Letters* **40** (14) 3732–3737.

Le Pichon A, Assink J., Heinrich P, Blanc E, Charlton-Perez A, Lee C., Keckhut P, Hauchecorne A, Rüfenacht R, Kämpfer N, Drob D., Smets P., Evers L., Ceranna L, Pilger C, Ross O, Claud C (2015) Comparison of co-located independent ground-based middle atmospheric wind and temperature measurements with numerical weather prediction models. J Geophys Res Atmos 120:8318–8331.

Marty, J. (2019). "The IMS infrasound network: current status and technological developments". *Infrasound monitoring for atmospheric studies* (A. Le Pichon, E. Blanc, A. Hauchecorne Eds). Springer, Cham, 3–62.

Matoza, R.S., Landes, M., Le Pichon, A., Ceranna, L., Brown, D. (2013). Coherent ambient infrasound recorded by the International Monitoring System. *Geophysical Research Letters* **40** (2) 429–433.

Matoza, R.S., et al. (2017). Automated detection and cataloging of global explosive volcanism using the International Monitoring System infrasound network. *Journal Geophysical Research: Solid Earth* **122** (4) 2946-2971.

Matoza, R., Fee, D., Green, D., Mialle, P. (2018). "Volcano infrasound and the International Monitoring System". *Infrasound Monitoring for Atmospheric Studies: Challenges in Middle Atmosphere Dynamics and Societal Benefits*, Springer, NY.

Matoza, R.S., et al. (2022). Atmospheric waves and global seismoacoustic observations of the January 2022 Hunga eruption, Tonga. *Science* **377** (6601) 95-100.

Mialle, P., et al. (2019). "Advances in operational processing at the International Data Centre". in *Infrasound Monitoring for Atmospheric Studies: Challenges in Middle Atmosphere Dynamics and Societal Benefits* Springer, NY.

Mialle, P., et al. (2021). Infrasound processing system at the IDC, from rudimentary to maturity, CTBT: Science and Technology Conference 2021 (SnT2021), Vienna, Austria https://conferences. ctbto.org/event/7/contributions/1419/(Accessed on 5 January 2024).

Pilger C. Ceranna L. Ross J. O. Le Pichon A. Mialle P., and Garcés M. A. (2015). CTBT infrasound network performance to detect the 2013 Russian fireball event, Geophys. Res. Lett. 42, 2523–2531.

Pilger, C, et al. (2021). Yield estimation of the 2020 Beirut explosion using open access waveform and remote sensing data. *Scientific Reports* **11** (1) 14144.

Vergoz, J., et al. (2022). IMS observations of infrasound and acoustic-gravity waves produced by the January 2022 volcanic eruption of Hunga, Tonga: a global analysis. *Earth and Planetary Science Letters* **591** 117639.

Machine Learning for Automatic Seismic, Hydroacoustic and Infrasonic Data Processing at the International Data Centre: Past, Present and Future

C. Saragiotis, R. Le Bras, V. Miljanovic-Tamarit

Comprehensive Nuclear-Test-Ban Treaty Organization, Vienna, Austria

Abstract

The International Data Centre (IDC) has been making limited use of machine learning methods in its automatic processing pipeline since its inception. With the recent advances of machine learning and artificial intelligence methods however, the IDC has been scanning the scientific literature to find methods that can potentially enhance its technical capabilities, testing and evaluating them. This paper presents machine learning algorithms used in the IDC processing pipeline such as phase identification for three component stations and classification of regional S phases. Methods like NET-VISA and the generalised F detector that are currently underway and some methods that can potentially improve IDC processing that are or are scheduled to be evaluated are also presented.

1. HISTORICAL BACKGROUND

The idea of artificial intelligence (AI) was arguably born in 1950 when Alan Turing proposed what we today call the 'Turing test', according to which machines were deemed intelligent or unintelligent. Machine learning is a subfield of AI and perhaps what most associate with AI due to its learning and decision making abilities. In 1952 the first machine learning application was developed by IBM; it was a checkerboard program that learned to play better the more it played. From that point on, machine learning saw some development with the introduction of Bayesian methods for probabilistic inference, but this development was not as rapid as was anticipated. This led to the 'AI winter', a period of reduced funding and interest in AI research. The term was coined by the analogy to the idea of a nuclear winter, a severe and prolonged global climatic cooling effect that is expected to occur after a large scale nuclear war.

In the 1970s and early 1980s AI research focused on using logical, knowledge-based approaches rather than algorithms. Artificial neural networks (ANNs) were seen as infeasible and a dead end due to limits in network depth, the lack of computing power and difficulty in collecting enough training data. The 1980s and 1990s saw some developments again, especially thanks to the popularization of ANNs, in particular recurrent neural networks. Also, in the 1990s machine learning shifted from a knowledge-driven approach to a data-driven approach as scientists began creating programs for computers to analyse large amounts of data and draw conclusions, that is, to 'learn' from the data.

In machine learning, there was eventually a shift from developing the perfect AI to solving practical problems and providing decision making services. Focus shifted from approaches inherited from AI research to methods and tactics used in probability theory and statistics. In the 2000s support-vector clustering (and other kernel methods) and unsupervised machine learning methods became widespread and in the 2010s deep learning became feasible. This led to machine learning becoming integral to many widely used software services and applications. To put the Comprehensive Nuclear-Test-Ban Treaty (CTBT) into perspective, the CTBT was signed in 1996 and routine data analysis started in 2000, during the regeneration of interest and developments in machine learning and AI.

2. MACHINE LEARNING IN THE EARLY IDC PROCESSING

Since the beginning of the operation of the IDC, machine learning has been used in the automatic processing pipeline for phase identification, as accurately identified phases significantly improve the quality of the automatic bulletin Standard Event List 3 (SEL3), the input to analyst review It has been and is still being used for a) phase identification in three component (3-C) stations and b) identification of regional S type phases during station processing.

2.1. Phase Identification at 3-C Stations

Automatic phase identification at 3-C stations is a much more challenging task compared to phase identification at array stations. A lot of research was carried out in the late 1980s and 1990s on this task using parameters that are distinctly different for the P and S phases, such as deflection angle, degree of polarization, and the ratio between transverse and total energy (Cichowicz 1993), auto- and cross-correlation of the three components (Roberts et al. 1989), polarization analysis (Jurkevics 1988, Suteau-Henson 1991), neural networks (Sereno and Patnaik 1993, Wang 2002, Wang and Teng 1997), the wavelet transform (Anant and Dowla 1997) and others.

The prototype IDC employed the ANN developed by Sereno and Patnaik (1993) to

automatically classify seismic phases. ANNs are inspired by biological neural networks in the nervous system of organisms in which neurons use electrical impulses and chemical signals to transmit information between different areas of the brain, and between the brain and the rest of the nervous system, in other words they act as information messengers. ANNs are constructed by interconnecting artificial neurons with weights. Artificial neurons act like biological neurons; they collect input which is either external to the neural network or the output of one or more other neurons and direct their output to other neurons. The neurons' output is eventually communicated to a decision making centre. The typical architecture of a neuron is shown in Figure 1, in which n inputs, $x_1,\ldots,x_n$ are weighted using pre-specified weights, $w_1,\ldots,w_n$ and summed. The result, $x= \Sigma_i\, w_i\, x_i$, is inserted into an activation (or transfer) function typically of the form $F(x) = \frac{1}{1+e^{-\beta x}}$ (β is a parameter that controls the steepness of the sigmoid F function) or similar sigmoid function.

One of the simplest forms of an ANN is the multilayer perceptron (MLP). It consists of neurons such as those in Figure 1 and has at least three layers: a) an input layer that takes input external to the ANN, b) an output layer that yields one of more outputs and c) one or more intermediate (or hidden) layers that take as input the output of other neurons and feed their output again to other neurons. MLPs are feedforward (the neuron connections do not form cycles) and typically partially connected (not all neurons are connected to all neurons). A three-layer MLP is shown in Figure 2.

Training of an ANN consists of computing the weights with which the artificial neurons are interconnected. A widely used algorithm for multilayer feedforward ANNs is the backward error propagation algorithm, in which an iterative least-squares error minimization strategy is used to find the weights that minimize the difference between the output of the neurons of the rightmost (output) layer from a desired (target) output.

In the IDC, phase identification is used to classify detections into one of four initial phases:
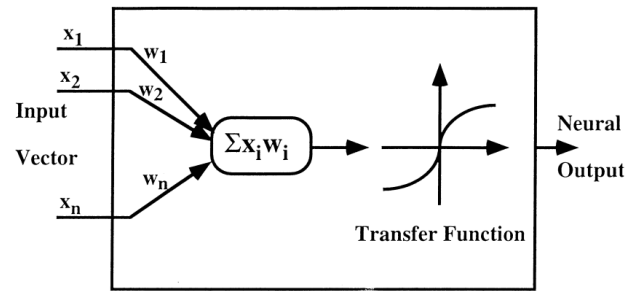
FIGURE 1.

Architecture of an artificial neuron. The inputs $x_1,\ldots,x_n$ are weighted using pre-specified weights, $w_1,\ldots,w_n$ and summed and the result is inserted into the activation or transfer function. From Wang and Teng (1997).

teleseismic (T), regional P (P), regional S (S) and noise (N). This classification is made using three cascaded MLPs like that of Figure 2 and is based on 15 features extracted from the signal waveform around the detection time. These features are:

a) Seven polarisation attributes (Jurkevics 1988): rectilinearity, planarity, long-axis and short-axis incident angle, ratio of the maximum to minimum horizontal amplitude, ratio of horizontal-to-vertical power at the time of maximum rectilinearity and at the time of the maximum amplitude;

b) Horizontal-to-vertical power ratios in five different frequency bands;

c) The difference between the number of arrivals before and after the detection within a fixed time window of 60 s;

d) Mean time difference between the detection and the arrivals before and after it within a fixed time window of 60 s;

e) The dominant period.

All three MLPs have 15 neurons at the input layer (one for each signal feature), six neurons in the hidden layer and two layers at the output layer. The first MLP classifies a detection between noise (N) or signal. The second classifies signals as regional or teleseismic (T). Finally, the third distinguishes regional signals as P or S. P-type regional phases are further classified into P and PKP, and S-type regional phases are further classified into S_n, L_g, R_g and S_x using other programs (for the latter, see subsection 2.2).
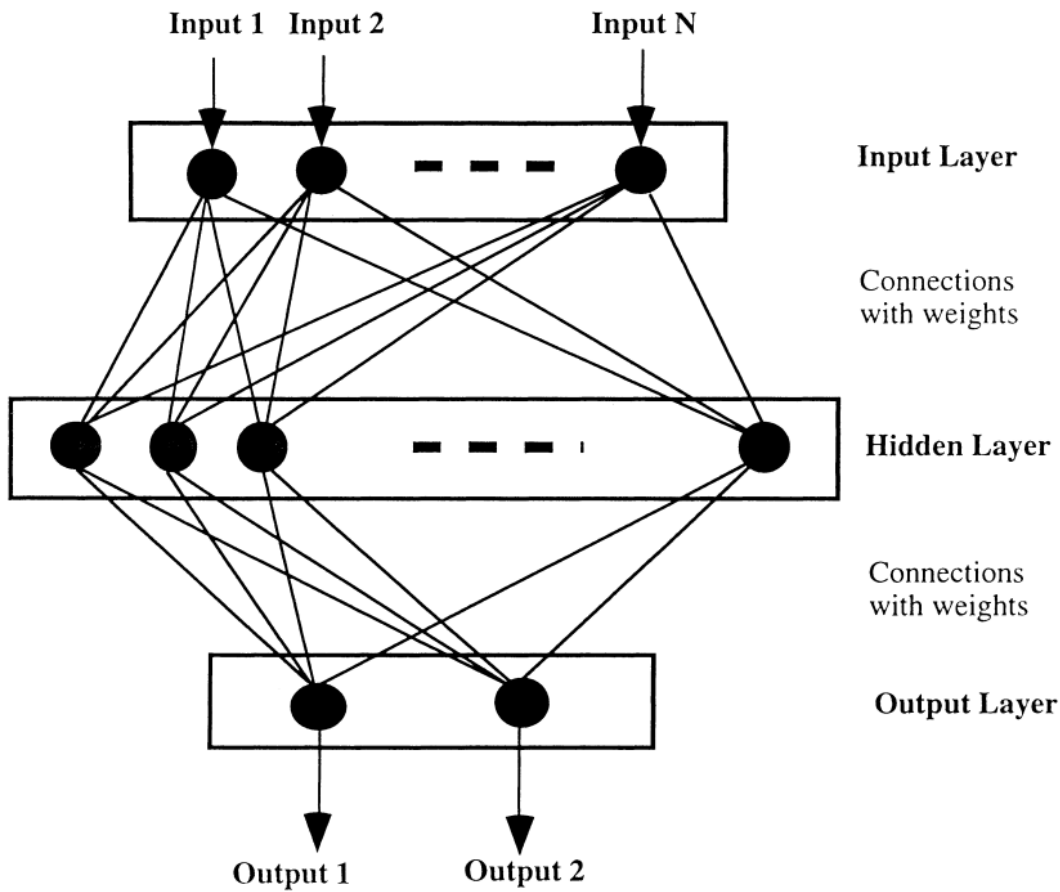
FIGURE 2.
Architecture of an MLP (feedforward, partially connected) network. From Wang and Teng (1997).

2.2. Identification of S-Type Regional Phases

The identification of either the first or the largest S in a group of S-type regional phases (S_n, L_g, R_g and S_x) is done using Bayesian inference. Bayesian inference is a method of statistical inference at the heart of many machine learning algorithms. It employs Bayes' theorem to update the probability for a hypothesis as more information or evidence becomes available. Bayes' theorem is usually be formulated as

$$\mathbb{P}(H|E) = \frac{\mathbb{P}(E|H)\,\mathbb{P}(H)}{\mathbb{P}(E)} \qquad (1)$$

where

- H denotes the hypothesis the probability of which is affected by the evidence E;
- E denotes the evidence that affects the probability of H occurring or having occurred;

- $\mathbb{P}(H)$ is the probability of H happening and often called the prior probability because it is the estimate of the probability of H happening before the evidence E is observed. It is also often interpreted as the inherent likelihood of the hypothesis H;
- Analogously, $\mathbb{P}(H|E)$ is called the posterior probability because it is the estimated probability of H having happened or happening after the evidence E is observed;
- $\mathbb{P}(E|H)$ is usually called the likelihood of observing the evidence given the hypothesis and usually called the likelihood of the evidence and is often interpreted as the compatibility of the evidence with the hypothesis;
- Finally, $\mathbb{P}(E)$ is called the inherent likelihood of the evidence or the marginal likelihood of the evidence because it is the probability of the evidence assuming all hypotheses and therefore does not depend on any specific hypothesis.

211

Usually, a number of competing hypotheses exist and the task is to determine which is the most probable given the evidence. From eq. (1) it is evident that the higher the inherent likelihood, $\mathbb{P}(H)$, of a hypothesis is and the higher the compatibility of the evidence with the hypothesis is, the higher the posterior probability is, a conclusion that agrees with intuition as well. Also, from eq. (1) it is evident that inherent likelihood of the evidence affects in the same way (it is inversely proportional) the posterior probability of all the alternative hypotheses, it is therefore often ignored in the calculation of the latter.

In the context of the regional S-type identification, the competing hypotheses are the types of the regional phases, H, and the evidence is signal features, F, and contextual information, C. Available values for H are S_n, L_g, R_g and S_x. Features are measurements, made either directly or indirectly by DFX, that describe an arrival's attribute, such as S–P time multiplied by frequency, frequency, velocity and horizontal-to-vertical power ratio. Contextual information of an arrival is station specific and includes a description of the arrival pattern (for example, only-S, first-S-of-two, first-S-of-many, or largest-S).

The probability sought is $\mathbb{P}(H|F,C)$, therefore eq. (1) becomes

$$\mathbb{P}(H|F,C) = \frac{\mathbb{P}(F,C|H)\,\mathbb{P}(H)}{\mathbb{P}(F,C)}$$

and after some manipulation,

$$\mathbb{P}(H|F,C) = \frac{\mathbb{P}(F|H,C)\,\mathbb{P}(H|C)}{\mathbb{P}(F|C)} \qquad (2)$$

The values of the conditional probabilities on the right hand side of eq. (2) are empirically determined and the phase type, H, for which the largest posterior probability $\mathbb{P}(H|F,C)$ is computed, is assigned to the unclassified regional phase.

The regional S phases identified by the cascaded MLPs further undergo a stage of Bayesian inference stage to distinguish between Sn, Lg, Rg and Sx phases. This inference is based on the maximization of the probability for each phase given specific seismological features (time difference between the arrivals of P and S phase, dominant frequency, velocity, horizontal to vertical power ratio) and contextual features.

3. RECENT AND CURRENT EFFORTS IN MACHINE LEARNING

The IDC continued to have interest in machine learning methods and algorithms even after it was formally established. In 2009 the Preparatory Commission for the Comprehensive Nuclear Test-Ban-Treaty Organization (CTBTO) organized the International Scientific Studies Conference, in which scientists and diplomats from all over the world gathered to present and discuss ideas and results regarding the treaty verification regime. The extensive data mining session included technologies such as NET-VISA, the Generalized F Detector (GenF) and false event identification (FEI), that are described in the following sections. The biannual publication of the CTBTO, the *CTBTO Spectrum*, also featured an article that introduced machine learning concepts and assessed techniques that could provide value for event detection and on-site inspection (Russell et al. 2010).

3.1. NET-VISA: A Bayesian Approach to Network Processing

As seen in the preceding section, Bayesian inference has been used successfully starting in the 1990s to identify regional S-wave types. Another problem which is amenable to this probabilistic approach is network processing, the stage in the processing where detections at multiple stations are interpreted as arrivals of various types of seismic and acoustic phases originating from the same source and their features used to determine the origin time and locate the event. The legacy and current system used at the CTBTO is called Global Association and is based on an exhaustive grid search for potential events that explain the observed detections. Global Association implicitly uses a basic forward model to deduce

the arrival time, amplitude, existence of phases at a given location, based on travel-time tables, transmission losses and blockage maps for hydroacoustic data.

Starting in 2009, a machine learning research effort culminated in the publication of the paper (Arora et al. 2013). Development efforts ensued and the NET-VISA software has been in operation at the IDC since January 2018 as a complement to the legacy Global Association system. Figure 3 shows the current configuration of network processing at the IDC. The detections present as input to Global Association at the time the SEL3 bulletin is built are also available to NET-VISA and the NET-VISA Standard Event List 3 (VSEL3) bulletin is built by NET-VISA from the same detection set. Once analysts have finished their review of the SEL3, they examine additional events from VSEL3 that were not formed by Global Association, adding about 10% of the events that end up in the Reviewed Event Bulletin (REB). Le Bras et al. (2021) explain the algorithms used by NET-VISA and the testing stages undergone until it could be used operationally.

The NET-VISA software has shown to produce fewer random associations and the automatic events it produces follow the seismicity more accurately. When the bulletins it produces are compared to the analyst-produced bulletins, the overlap (percentage of analyst-reviewed events that are also in the automatic bulletin) is consistently better, meaning that fewer events are missed by NET-VISA than by Global Association, and inconsistency (percentage of automatic events that are not in the analyst-reviewed bulletin) is comparable but slightly lower overall when NET-VISA is used in all three automatic pipelines (SEL1, SEL2 and SEL3) of the IDC. This
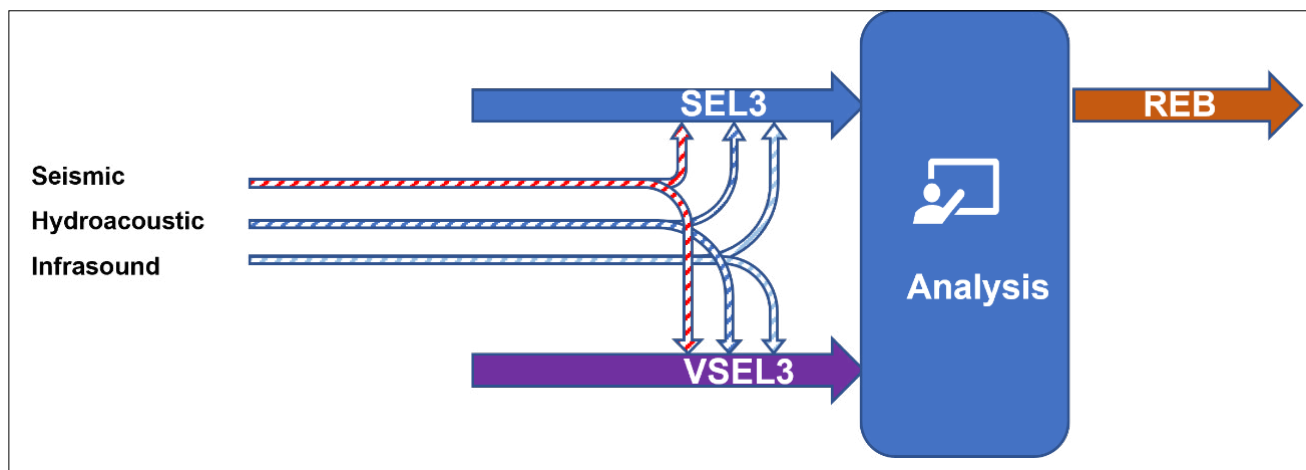
FIGURE 3.
Illustration of the current (2022) configuration of network processing at the IDC.
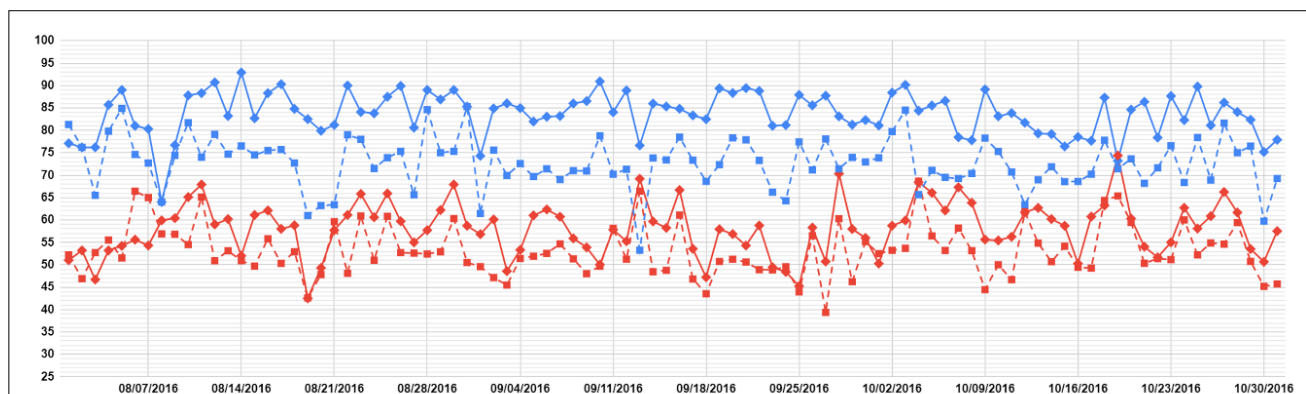
FIGURE 4.
Daily overlap (blue) and inconsistency (red) percentages for SEL3 (Global Association) and VSEL3 (NET-VISA) during the period August-October 2016. The solid lines with lozenge symbols correspond to NET-VISA numbers and the dashed lines with square symbols to Global Association.
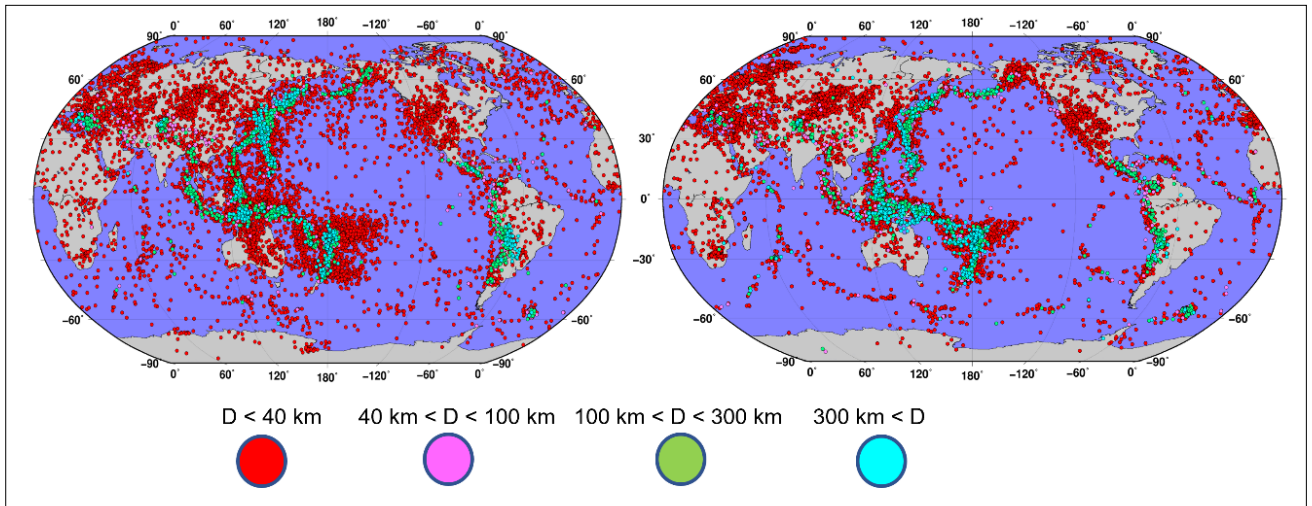
FIGURE 5.
Automatic events for three months (August–October 2016). Left: SEL3 events (produced by Global Association).
Right: VSEL3 events (produced by NET-VISA).
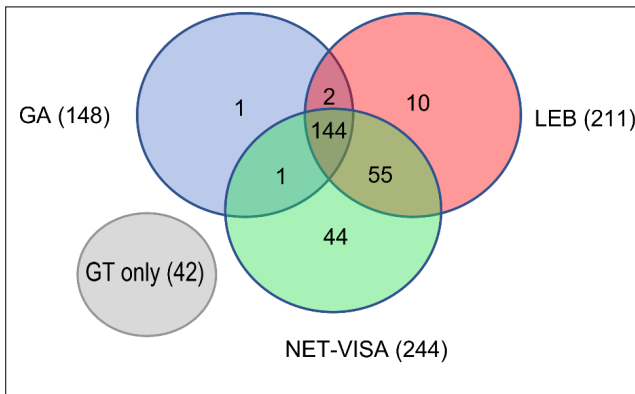
FIGURE 6.
Number of ground truth events obtained by each of the LEB, SEL3 and NET-VISA for the period August–October 2016 (for a total of 299 events).

is illustrated in Figure 4 for a test conducted on historical data from August to October 2016. The maps of the automatic events produced by the test are compared to the standard SEL3 on Figure 5. When this comparison of both the NET-VISA results and Global Association results are made to the analyst-reviewed bulletin, it is important to note that the reviewed bulletin may be influenced by its automatic bulletin starting point, and therefore biased towards Global Association, especially for the estimation of false alarms. Had the analysts the opportunity to review the automatic bulletin produced by NET-VISA, some of the event classified as false alarms may have turned out to be real.

Another comparison which is independent of the results of the IDC analysts is to compare both SEL3 and NET-VISA results to the 299 ground truth events published by the ISC (Bondár and McLaughlin 2009) for that period and assess how many of them are obtained by each of the SEL3, Late Event Bulletin (LEB), or NET-VISA instance running as a test. Figure 6 illustrates that NET-VISA significantly outperforms both Global Association and LEB (analyst-reviewed) events using this criterion. It is noted that 42 of the ground truth events were not obtained by any of the methods.

3.2. Generalized F Detector

GenF is based on the F-detector (Blandford 1974). GenF generalizes the F detector in that it uses a priori information about signal and noise. Essentially it assumes that the noise is correlated, it models the noise, and accounts for this noise model in the calculations of the beam and corresponding F statistic. The theoretical framework and a frequency domain implementation is described in Selby (2008). In Selby (2011) the method is extended to teleseismic signals and in Selby (2013) a hybrid time-frequency-domain multiple-filter approach is implemented. The detector currently used at the IDC is Detection and Feature Extraction (DFX). GenF is computationally more complex but has several advantages over the DFX, such as:
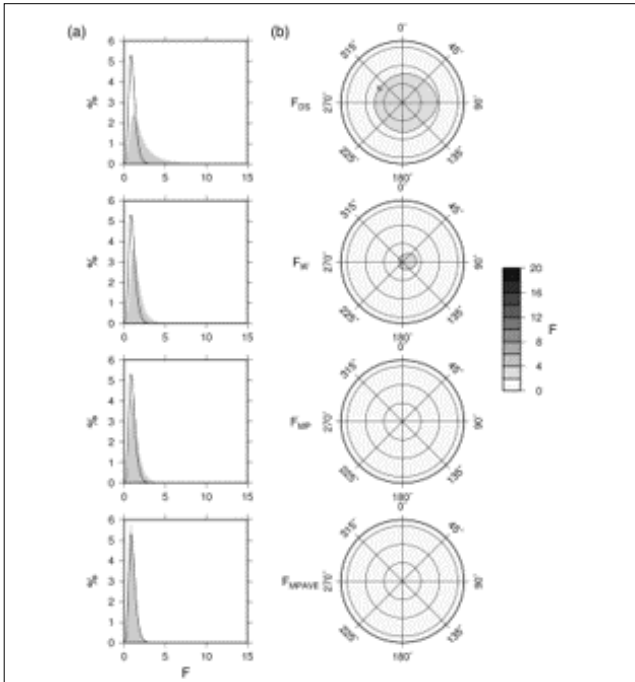
FIGURE 7.
F distributions for varying assumptions about noise power spectrum and correlation for the MKAR array, Kazakhstan. (a) Observed (shaded) and theoretical (heavy line) F distributions, (b) Mean F as a function of azimuth and slowness (from Selby 2011).

- It requires a much less time-consuming tuning;
- It makes much fewer false detections than DFX while keeping the number of associated arrivals at a similar level (see Figure 8);
- The F statistic is statistically convenient in that it follows a well known distribution and can thus be converted to a probability of detection for a given prior SNR.

FIGURE 8.
Number of detections made by DFX (red), GenF (green) and number of associated detections in the REB (blue) for the period 1 to 14 January 2022.

The GenF has been extensively tested at the IDC since 2013 with promising results and has recently been integrated in the IDC DFX detector framework that allows configuration based switching between the DFX and GenF and defaults to DFX for stations not suitable (i.e. single-station 3-C stations) or not configured for GenF. Although it is not yet part of the operational pipeline, it has been configured in the development pipeline (DevLAN) and is expected to be operationalized soon.

4. FALSE EVENT IDENTIFICATION

False event identification refers to events created by the automatic processing pipeline (SEL3 events) that are later discarded either by the system due to their not fulfilling the event definition criteria as specified in the Draft Operational Manual for the International Data Centre (Preparatory Commission for the CTBTO 2020) or by the analysts due to physical reasons (invalid associations or detections, discrete events that had been joined into one etc.). Rejecting, splitting, or merging events is a time intensive process for the analyst, therefore a tool was sought by the IDC to automatically identify such false events.

False event identification is a Java program written by Mackey et al. (2009). It uses a machine learning approach, in particular support vector machines to automatically determine whether SEL3 events will be either discarded or

retained by the analysts. It is therefore framed as a supervised binary classification problem ('discard'/'retain') accompanied by a confidence score. FEI was trained on SEL3 and LEB events, that is, automatically created events that had also been reviewed by analysts. Training features included:

- Arrival parameters, such as station, time initial phase, slowness, azimuth, arrival quality, amplitude SNR etc.;
- Origin parameters, such as time, location, error ellipse direction and dimension, associated arrivals etc.

Testing of FEI took place from 2009 until 2011 and showed that FEI does an excellent job at classifying/categorizing events (Le Bras et al. 2011). The results presented to analysts as the process currently stands should add comfort to their decisions and help in identifying obviously wrong associations that form false events. The few misses (events that fell into the 'wrongly retained') category seemed to actually be correct assessments of split events/coda detection events. The events in the 'wrongly rejected' category (false negatives) show a large variance in the final association set for the event id being tracked, suggesting that the initial assessment (rejection) was correct for the composition of the event at the time of evaluation. This suggests that work on the association process itself should bring improvement into the overall process. As it currently performs, FEI shows great promise. If additional optimization can be accomplished, it could be a powerful tool to build on and revisit in the future once NET-VISA is operational.

5. FUTURE PLANS

In the last few years, there have been many developments in the field of machine learning methods in seismology. Following its mandate, in particular to "[. . .] progressively enhance its technical capabilities as experience is gained in the operation of the International Monitoring System" (para. 18, of the Protocol to the Treaty, CTBT 1996), the IDC plans to exploit these advancements so as to enhance the IDC processing pipeline as far as parameter accuracy and uncertainty, and computational efficiency are concerned.

5.1. Back Azimuth Prediction in 3-C Stations

Back azimuth estimation (value and uncertainty) at 3-C stations are things that can be significantly improved in the IDC pipeline. At array stations back azimuth is estimated using beam forming, a well established method that yields back azimuth estimates that are both accurate and with high confidence. On the other hand, at 3-C stations using polarization analysis (Jurkevics 1988) back azimuth estimation is based on polarization analysis that essentially consists of estimating the rectilinear and elliptical polarization directions by applying eigenanalysis on the three components of the recorded seismograms. Polarization analysis is very unstable therefore back azimuth estimates from 3-C stations suffer from both high error and low confidence. Erroneous back azimuth estimates may lead to false associations or even false events, thus aggravating the quality of the automatically created event lists and adding to the workload of analysts during interactive processing/review of events. This issue is particularly significant in regions where the IMS network consists of only (South America) or mostly (Africa) 3-C stations. BazNet (Dickey et al. 2021) is a temporal Convolutional Neural Network (CNN) that makes single-station azimuth predictions accompanied by a certainty measure on these predictions. The latter allows the exclusion of bad back azimuth predictions from the association algorithm and will therefore enhance its speed and performance.

Its three structural components are the input layer, the feature extraction structure and the output layer (Figure 9). The input layer is fed with 3-C waveforms; the output layer yields
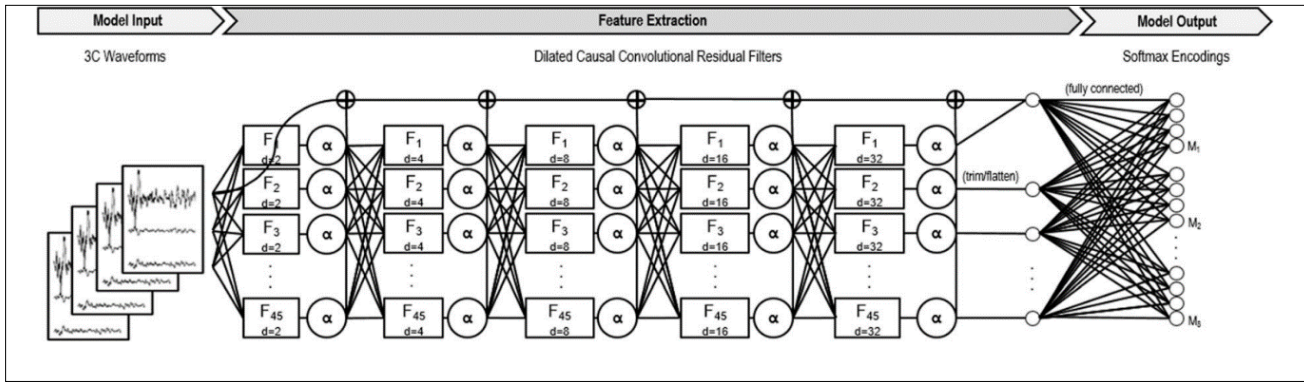
FIGURE 9.
BazNet architecture (from Dickey et al. 2021).

probabilities for a predefined set of back azimuth classes. The intermediate structure consists of four convolutional layers that essentially perform multi-resolution analysis on 3-C waveforms. BazNet has been trained and tested on nine IMS stations (Dickey et al. 2021) using 10 years of data. Although the back azimuth estimate accuracy is only slightly better than a finely tuned polarization algorithm, the certainty measure it assigns to these estimates correlates strongly with the prediction accuracy. This allows a robust selection of high confidence back azimuths to be passed on to the associator. BazNet is scheduled to be further tested and evaluated at the IDC.

5.2. Arrival Time Refinement

Another issue that can lead to significant gains as far as processing time is concerned is automatically picked arrival times refinement. In 2020 more than 300 000 automatically picked arrivals (73% of the all the automatically picked arrivals) were retimed during the interactive processing stage. Retiming refers to the manual shifting by IDC analysts, of an arrival pick to up to 10 sec. Some of these retimings require fk analysis and can therefore be very time consuming. Assuming a modest 10 sec retiming effort per arrival, that gives 875 person hours which is about 1 a person year. A tool that reliably refines the automatically picked arrivals will therefore
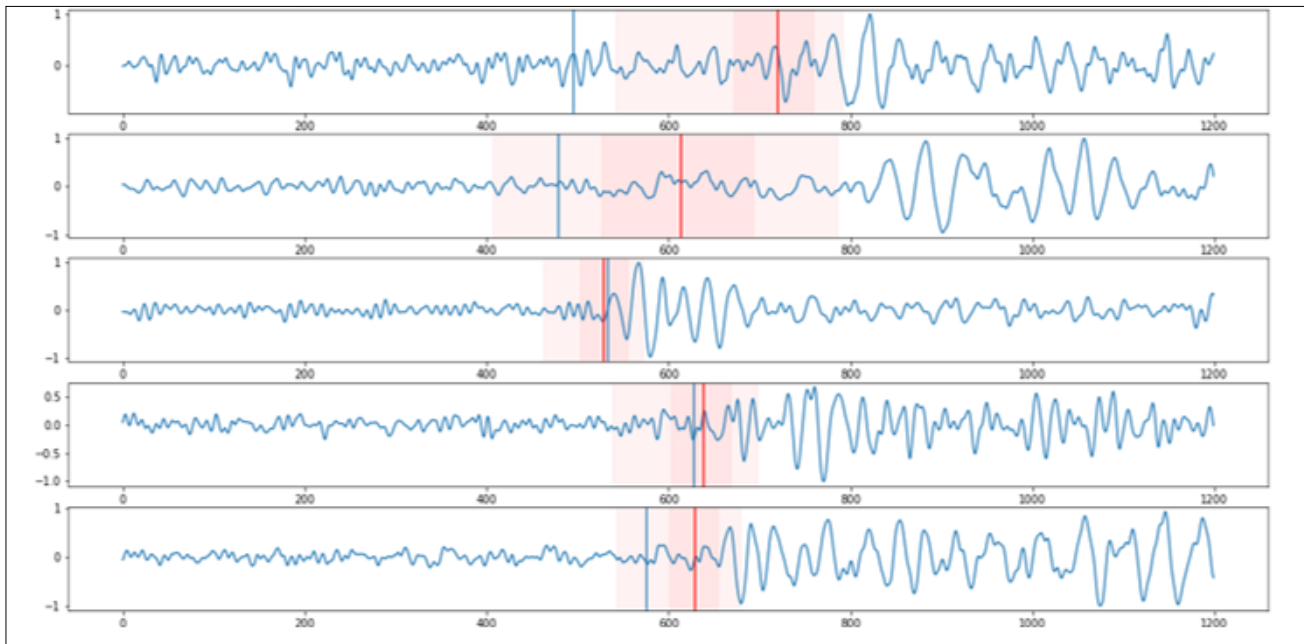
FIGURE 10.
Arrival refinement with ArrNet. Blue lines denote automatic arrival picks, red lines with red patches denote picks refined by ArrNet and their uncertainties (from Peña and Dickey 2021).

217

improve the quality of automatically created event lists and consequently reduce interactive review time.

A tool the IDC plans to evaluate is the ArrNet (Peña and Dickey 2021), a temporal CNN presented at the Science and Technology Conference (SnT) 2021. The ArrNet structure is similar to that of BazNet, the only difference being that the output layer yields a new arrival time and confidence intervals for various confidence levels (Figure 10). Results from initial tests presented at the SnT 2021 have been promising not only in refining the arrival time but also providing a robust uncertainty for this interval.

5.3. Waveform Denoising

Seismic waveform data are generally contaminated by noise from various sources. Suppressing this noise effectively so that the remaining signal of interest can be successfully detected is an evergreen problem for the seismological community. At the IDC noise suppression for signal to noise ratio (SNR) enhancement is based on bandpass filtering, that eliminates any undesired signals outside the frequency band of interest and leaving untouched any noise within the frequency pass band. Elimination of this noise is essentially a source separation problem and could potentially significantly increase the SNR of the waveform.

Tibi et al. (2021) have developed a method to perform such source separation using a deep CNN to decompose waveforms into signal of interest and noise (see Figure 11). This is achieved via a signal and a noise time-frequency mask that are applied on the input signals. This approach has been tested on signals recorded at regional distances and claims an SNR improvement of 2 to 5 over simple band pass filtering. It is currently tested on signals recorded at teleseismic distances. Improving the SNR of arrivals will have a direct impact on the associated rate (i.e. the ratio of automatically detected arrivals associated to events in the REB over all the associated arrivals.

5.4. Waveform Methods for Network Processing

One major advance made in IDC processing within the last few years, NET-VISA, has been described in subsection 3.1 of this paper.
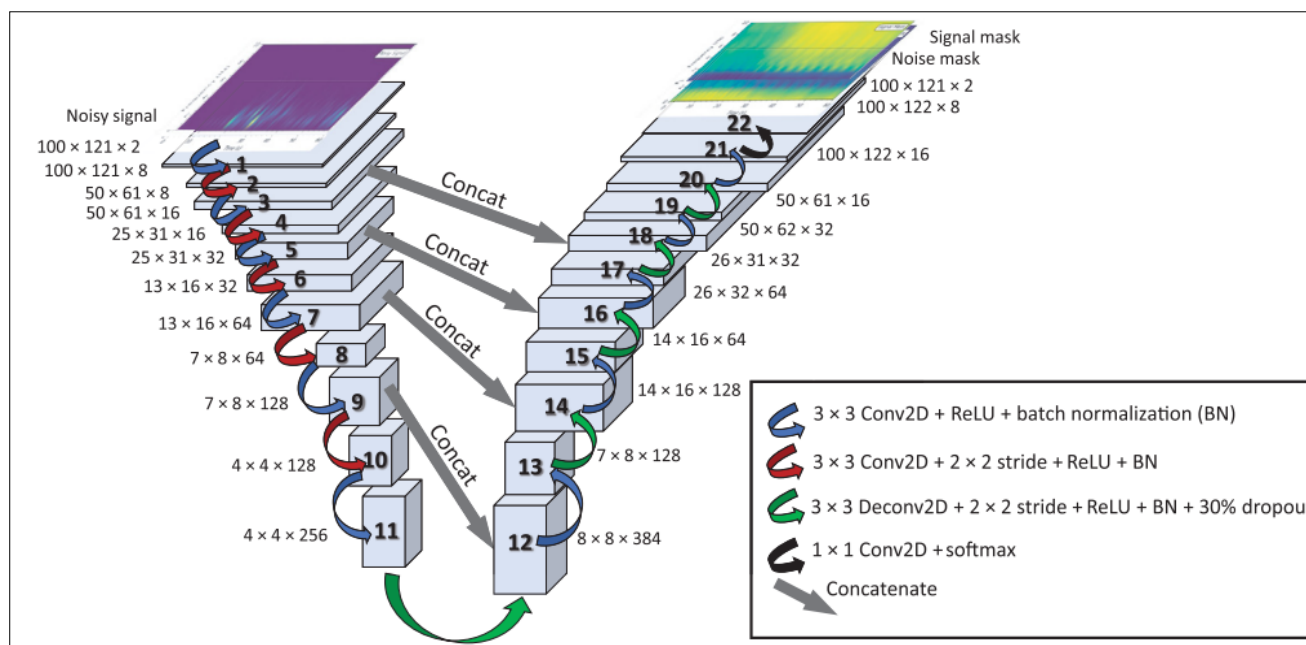
FIGURE 11.

Architecture of the denoiser CNN. The input signal (top left) is successively analysed in the t f domain using various t f filters. The signal and noise masks are then constructed by appropriately shifting superposing the outputs of these filters (from Tibi et al. 2021).
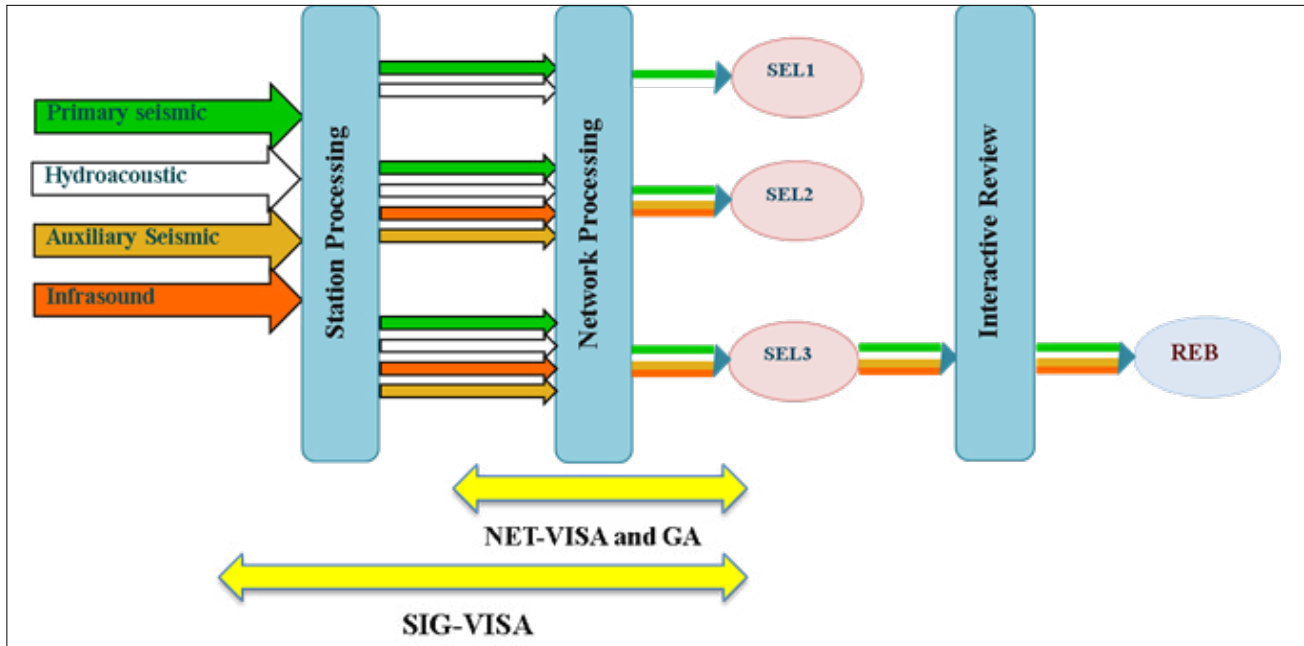
FIGURE 12.
This figure illustrates that SIG-VISA would allow a direct extraction of automatic event bulletins (standard events lists) from the waveforms as opposed to the NET-VISA approach which uses features extracted from the waveforms as an intermediate step (from Le Bras et al. 2021).

Functionally, NET-VISA is an exact replacement of Global Association, using as its input the same parametric features extracted from the waveforms.

Extending the model to include the extraction of features, a Bayesian generative model can be elaborated directly from the waveforms, and this is the approach taken in SIG-VISA (Moore et al. 2012, Moore et al. 2017, Moore and Russell 2017). This is a promising way to go; it takes advantage of the archive of full waveforms acquired since the inception of acquisition of data at the CTBTO, is more sensitive than a features based approach in detecting smaller events and has the capability of providing a physics based generative model explaining the details of the observations at IMS stations. The approach would benefit from further testing and proof of concept exercises simulating operational applications of the method and validation by seasoned analysts.

5.5. Other Methods

There are many other machine learning algorithms that can potentially benefit the IDC processing pipeline. The IDC is always scanning the scientific literature for such opportunities. Testing, evaluation, and integration of any of these methods, however, is time and resource intensive. National Data Centres as well as independent scientists and researchers would benefit by using IMS data to validate methods in the treaty verification context. Sharing IMS data can be done through the IDC product dissemination services methods (subscription, electronic, web) as well as the Virtual Data Exploitation Centre, a data sharing platform that has been used for more than 10 years by scientists and researchers around the world for various purposes.

The containerization of the IDC pipeline, a deliverable of the IDC re-engineering project will also allow simultaneous testing and will therefore reduce implementation, integration and testing time of candidate algorithms.

REFERENCES

Anant, K.S., Dowla, F.U. (1997). Wavelet transform methods for phase identification in three-component seismograms. *Bulletin of the Seismological Society of America* **87** (6) 1598-1612.

Arora, N.S., Russell, S., Sudderth, E. (2013). NET-VISA: Network processing vertically integrated seismic analysis. *Bulletin of the Seismological Society of America* **103** (2A) 709-729.

Blandford, R.R. (1974). An automatic event detector at the Tonto Forest Seismic Observatory. *Geophysics*, **39** (5) 633-643.

Bondár, I., McLaughlin, K.L. (2009). A new ground truth data set for seismic studies. *Seismological Research Letters* **80** (3) 465-472.

Cichowicz, A. (1993). An automatic S-phase picker. *Bulletin of the Seismological Society of America* **83** (1) 180-189.

Dickey, J., Borghetti, B., Junek, W. (2021). BazNet: A deep neural network for confident three-component backazimuth prediction. *Pure and Applied Geophysics* **178** (7) 2459-2473.

Jurkevics, A. (1988). Polarization analysis of three-component array data. *Bulletin of the Seismological Society of America*, **78** (5) 1725-1743.

Le Bras, R. et al. (2021). NET-VISA from cradle to adulthood. A machine-learning tool for seismo-acoustic automatic association. *Pure and Applied Geophysics* **178** (7) 2437-2458.

Le Bras, R.J., Russell, S.J., Arora, N.S., Miljanovic, V. (2011). "Machine learning at the CTBTO. testing and evaluation of the false events identification (FEI) and vertically integrated seismic association (VISA) projects. *Monitoring Research Review* 2011 (Proceedings of a Conference on Ground-Based Nuclear Explosion Monitoring Technologies, Tucson, Arizona, 2011) 313-321.

Mackey, L., Kleiner, A., Jordan, M.I. (2009). Improved automated seismic event ex- traction using machine learning. Eos Trans. AGU, 90(52), 2009. Fall Meet. Suppl., Abstract S31B-1714.

Moore, D.A., Mayeda, K., Myers, S., Joon Seo, M., Russell, S.J. (2012). "Progress in signal-based Bayesian monitoring". *Monitoring Research Review* 2012 (Proceedings of a Conference on Ground-Based Nuclear Explosion Monitoring Technologies, Albuquerque, New Mexico, 2012) 263-273.

Moore, D.A., Mayeda, K., Myers, S., Russell, S.J. (2017). *Initial evaluations of signal-based Bayesian seismic monitoring (SIGVISA)*. CTBT: Science and Technology 2017 Conference, Vienna.

Moore, D.A., Russell, S.J. (2017). "Signal-based bayesian seismic monitoring". *Machine Learning Research.* (Proceedings of 20th international conference on artificial intelligence and statistics, Fort Lauderdale, FL, 2017) PMLR 54:1293-1301.

Peña, R., Dickey, J. (2021) *Arr-Net: A deep neural network for confident arrival time estimation.* CTBT: Science and Technology 2021 Virtual Conference.

Preparatory Commission for the Comprehensive Nuclear-Test-Ban Treaty Organization (2020). *Draft operational manual for the International Data Centre (Rev. 7).* Preparatory Commission for the CTBTO, Vienna.

Preparatory Commission for the Comprehensive Nuclear-Test-Ban Treaty Organization (1996). *Nuclear Test-Ban-Treaty.* Preparatory Commission for the CTBTO, Vienna.

Roberts, R.G., Christoffersson, A., Cassidy, F. (1989). Real-time event detection, phase identification and source location estimation using single station three-component seismic data. *Geophysical Journal International* **97** (3) 471-480.

Russell, S.J., Vaidya, S., Le Bras, R. (2010). Machine learning for Comprehensive Nuclear-Test-Ban Treaty monitoring. Preparatory Commission for the Comprehensive Nuclear-Test-Ban Treaty Organization. *CTBTO Spectrum* **14** 32-35.

Selby, N.D. (2008). Application of a generalized F detector at a seismometer array. *Bulletin of the Seismological Society of America* **98** (5) 2469-2481.

Selby, N.D. (2011). Improved teleseismic signal detection at small-aperture arrays. *Bulletin of the Seismological Society of America* **101** (4) 1563-1575.

Selby, N.D. (2013). A multiple-filter F detector method for medium-aperture seismometer arrays. *Geophysical Journal International* **192** (3) 1189-1195.

Sereno, T.J., Patnaik, G.B. (1993). *Initial wave-type identification with neural networks and its contribution to automated processing in IMS version 3.0.* Rep. No. SAIC-93/1219. Science Applications International Corporation, San Diego, California.

Suteau-Henson, A. (1991). Three-component analysis of regional phases at NORESS and ARCESS: Polarization and phase identification. *Bulletin of the Seismological Society of America* **81** (6) 2419-2440.

Tibi, R., Hammond, P., Brogan, R., Young, C.J., Koper, K. (2021). Deep learning denoising applied to regional distance seismic data in Utah. *Bulletin of the Seismological Society of America* **111** (2) 775-790.

Wang, J. (2002). "Adaptive training of neural networks for automatic seismic phase identification". *Monitoring the comprehensive nuclear-test-ban treaty: Data processing and infrasound* (Zoltan, A. Der, Shumway, R.H., Herrin, E.T., Eds) Birkhäuser Basel, Basel, pp. 1021-1041.

Wang, J., Teng, T.-l. (1997). Identification and picking of S phase using an artificial neural network. *Bulletin of the Seismological Society of America* **87** (5) 1140-1149.

New Applications at the International Data Centre for Seismic, Hydroacoustic and Infrasound Expert Technical Analysis

I. Kitov

Comprehensive Nuclear-Test-Ban Treaty Organization, Vienna, Austria

M. Rozhkov

Instrumental Software Technologies, Inc, New York, United States of America

Abstract

There are many principal challenges for the Comprehensive Nuclear-Test-Ban Treaty (CTBT) monitoring regime and tasks related to the work of the International Data Centre (IDC). The objectives of the expert technical analysis (ETA) stem from these challenges and tasks. The Provisional Technical Secretariat (PTS) of the Comprehensive Nuclear-Test-Ban Treaty Organization (CTBTO) routinely operates software to process time series data from seismic, hydroacoustic and infrasound (SHI) stations from around the world. The data are transmitted to the IDC and processed to detect, build, locate and screen events that may be nuclear explosions. The observation and processing systems are required to be sensitive to small events, especially in unusual locations. Data with the highest resolution are typically provided by array stations. Advanced signal processing methods can significantly improve detection of monitoring relevant signals, effectively associate them with events and locate these events more accurately and with lower uncertainty for the purposes of the CTBT. Several advanced techniques aimed at improving the estimation accuracy and consistency of the most important seismic parameters: detection threshold, characterization parameters of detected signals, event hypocentre, event magnitude and focal mechanism as well as identification of sources of all found events are discussed.

1. INTRODUCTION

One of the International Data Centre (IDC) services to the States Parties is expert technical analysis (ETA). Paragraph 19 of the Protocol to the CTBT (Part I) says: "The International Data Centre shall carry out, at no cost to States Parties, special studies to provide in-depth, technical review by expert analysis of data from the International Monitoring System, if requested by the Organization or by a State Party, to improve the estimated values for the standard signal and event parameters". Paragraph 20 (c) provides that the methods for supporting data access and the provision of data shall include the following service: "Assisting individual States Parties, at their request and at no cost for reasonable efforts, with expert technical analysis of International Monitoring System data and other relevant data provided by the requesting State Party, in order to help the State Party concerned to identify the source of specific events. The output of any such technical analysis shall be considered a product of the requesting State Party, but shall be available to all States Parties."

According to Annex 2 to the Protocol, one of the defining parameters estimated by the IDC is the hypocentre solution based on seismic, hydroacoustic and infrasound (SHI) data, which includes the origin epicentre coordinates and depth. One of the characterization parameters for IDC standard event screening mentioned in the same Annex is focal mechanism. In routine IDC processing, source location is calculated with the globally robust and steady technique providing quasi-uniform location accuracy and uncertainty which depends on the quality of relevant detections. For ETA advanced and state of the art techniques should be used to enhance automatic and interactive location.

This paper covers seismic applications where there is some experience and tangible results showing potential improvements and enhancements related to the objectives previously mentioned:

- Finding small events;
- Finding events in unusual locations;

- Achieving higher absolute and relative accuracy and lower uncertainty of epicentral location and depth;
- Estimation of standard and advanced event characteristics;
- Estimation of focal mechanisms for the monitoring related events with magnitudes (mb or Ms) above, around four, spectral ratios of phases;
- Comparative measures to other events and groups of events.

All these applications have to improve the completeness, accuracy and consistency of the Reviewed Event Bulletin (REB), Standard Event Bulletin (SEB), Standard Screened Event Bulletin (SSEB) and Executive Summary - the IDC principal deliverables for the States Parties. This paper discusses the following applications:

- Interactive and automatic Spot Check Tool (SCT) based on waveform cross-correlation (WCC) (REB/SSEB completeness and consistency);
- Depth determination based on moment tensor estimation (MTE), Parametrical Moment Tensor Estimator (ParMT) (location, depth, focal mechanism);
- Spectral discrimination of the explosions and aftershocks by the Democratic People's Republic of Korea (nature of events);
- Detection of weak aftershocks from the tests by the Democratic People's Republic of Korea (focus on small events);
- Signals separation with the independent component analysis (ICA) (source identification);
- Multidimensional approach to the CTBTO data processing (comparative measures of group events);
- N-Dimensional structures: tensors and quaternions, principal component analysis and dimensionality and noise reduction (detection enhancement);
- Ambient noise tomography (seismic array resolution).

2. INTERACTIVE SPOT CHECK TOOL (EXPERT TECHNICAL ANALYSIS SUITE PROTOTYPE FOR SEISMIC, HYDROACOUSTIC AND INFRASOUND DATA)

The basic idea behind the SCT is to use information from the historical events in the REB, historical nuclear tests data and new detection and phase association algorithms. The underlying methodology of the SCT is WCC, which provides an optimal detection procedure for signals from repeating events. Due to plate tectonics, natural seismicity is concentrated within long but relatively narrow zones and more than 95% of earthquakes in the REB can be considered as repeated. This proportion increases in time with increasing number of REB events. A larger part of the observed artificial seismicity belongs to mining areas, and thus, is highly repetitive. For standalone events, synthetic seismograms with various source functions can be used. For underground nuclear explosions, the source functions are accurately modelled in many rock types based on the historic events, and synthetic seismograms are an efficient way to predict WCC.

There are several processing stages of the SCT: master event selection, detection using the matched filter technique, local association, conflict resolution and comparison with other bulletins. There are two SCT modes: interactive and automatic. The interactive mode provides wider flexibility of processing scenarios as needed by the independent reviewers to assess the accuracy and completeness of IDC products. In the automatic mode, a cross-correlation standard event list (XSEL) is calculated at a daily rate.

Routine automatic processing based on the WCC method also includes proactive creation of XSEL, which is similar to the Standard Event List (SEL) 3 – a standard IDC automatic product, and a comprehensive check of the IDC events in the SEL3 and REB against the historical REB. This activity matches the Protocol task "comparative measures to other events and groups of events". The interactive mode is aimed at exclusive processing of a small subset of SEL3 (also SEL1, SEL2 and Local Event Bulletins) and REB events with a crafted set of parameters. The interactive mode is governed by a Spot Check interface, which is designed to match diverse requirements of a broad range of roles/customers.

Figure 1 demonstrates the main screen of the front end interface (SCT Web graphical user interface (GUI) as a Secure Web Portal
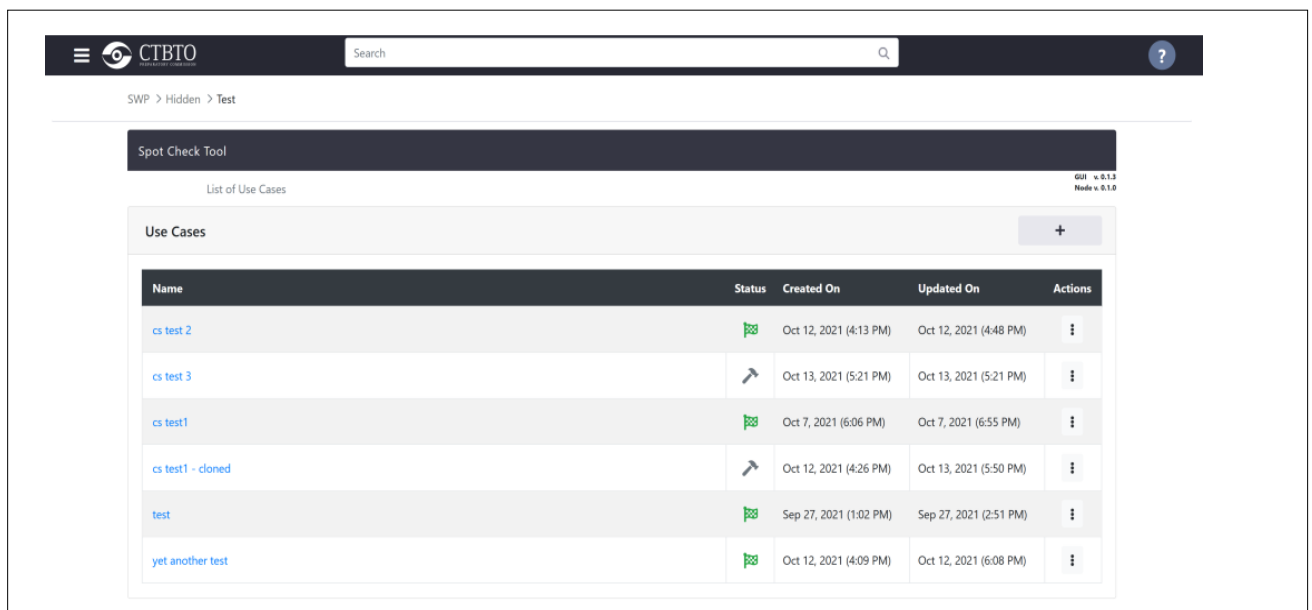
FIGURE 1.
The main screen of the SCT to select new or available use case.
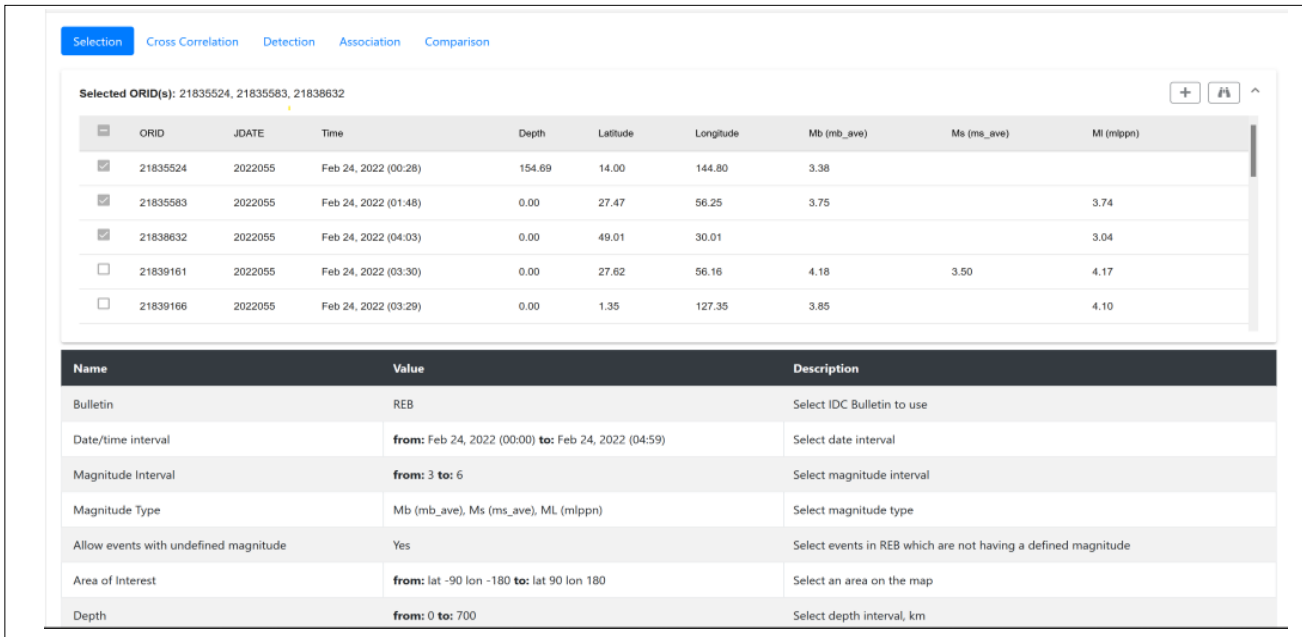
FIGURE 2.
Five steps of SCT processing.

Liferay Portlet) where a new use case can be started or any of the previous use cases with a specific set of parameters can be selected. Figure 2 presents a control panel for a given use case with five processing steps: event selection (event origin identification), cross-correlation, detection, association with conflict resolution and bulletin comparison. There is also a control panel, which allows handling various technical parameters. Any successful parameter sets aimed at solution of repeating seismic events can be saved as presets and used when needed. There are also generic presets for specific roles based on experience with the automatic Spot Check.

The SCT processing includes numerous defining/control parameters. Some of them are used often and have a smooth and gradual
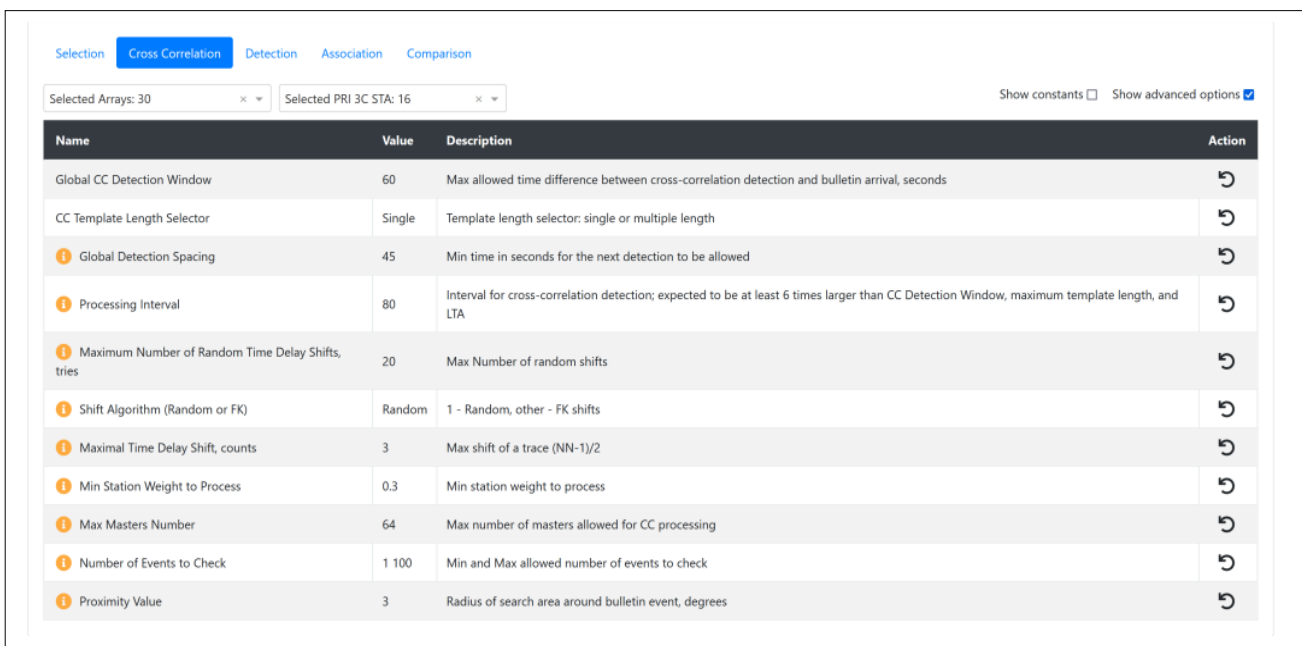
FIGURE 3.
Advanced parameters of the cross-correlation panel.

influence on processing. Others may introduce dramatic changes to the SCT performance, even in the allowed range. Therefore, some SCT parameters are for basic use and other advanced parameters are hidden in pop-up windows. Figure 3 shows parameters of the advanced cross-correlation mode. For example, the time interval around an arrival associated with the studied event can be defined. Since one cross-correlation trace from the original set of real traces is needed, it is important to have the real data interval much larger than the length of the cross-

correlation window. It allows for accommodation of the length of the long term average window in signal to noise ratio (SNR) estimates and the recursive character of the SNR calculation. A master event set is available and can be tailored to the necessary preferences. Most important for nuclear test monitoring, the master event nature can be selected: natural, mining, nuclear test (like the Democratic People's Republic of Korea or Nevada Test Site events), synthetic as obtained from historical nuclear tests or different sources, and fully synthetic.

3. DEPTH DETERMINATION BASED ON MOMENT TENSOR ESTIMATION (ETA SUITE PROTOTYPE FOR SHI DATA)

A twofold software processing framework for ETA is aimed at issuing the Updated Event Bulletin and can be used in the special studies. The first component of the processing is a single station event depth estimation procedure, which is optimized for an event depth and attenuation parameter, t^*. After applying the first component to many stations, a suitable depth-search range and event station specific attenuation parameter are available for use as prior information in

the second component: MTE. MTE is a suitable strategy for inferring the depth and magnitude of the event, subject to the plausible constraint that the event's source mechanism is not necessarily known prior to source identification.

MTE is analogous to a hypothesis test whereby an event depth, magnitude and moment tensor are proposed then the corresponding synthetic seismograms at regional and teleseismic
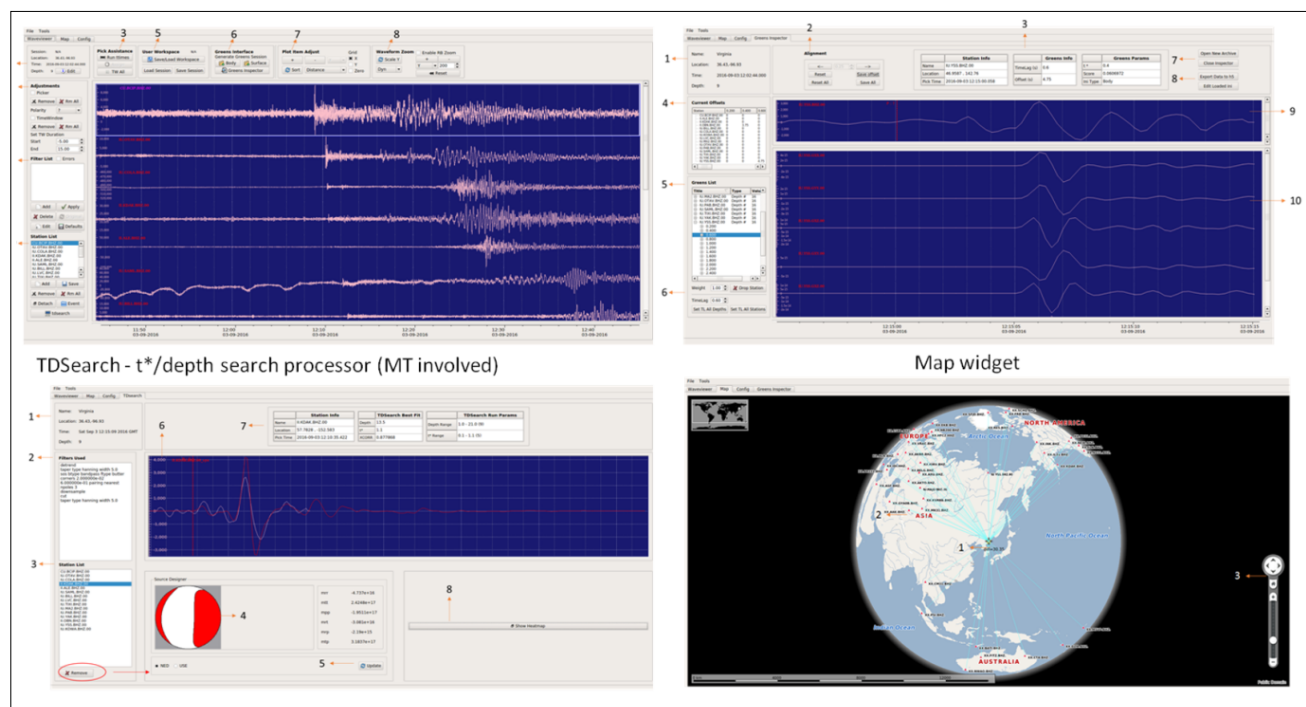
FIGURE 4.
Processing stages: Data selection and preparation, Green's function calculation, depth and MTE and results presented on a map.
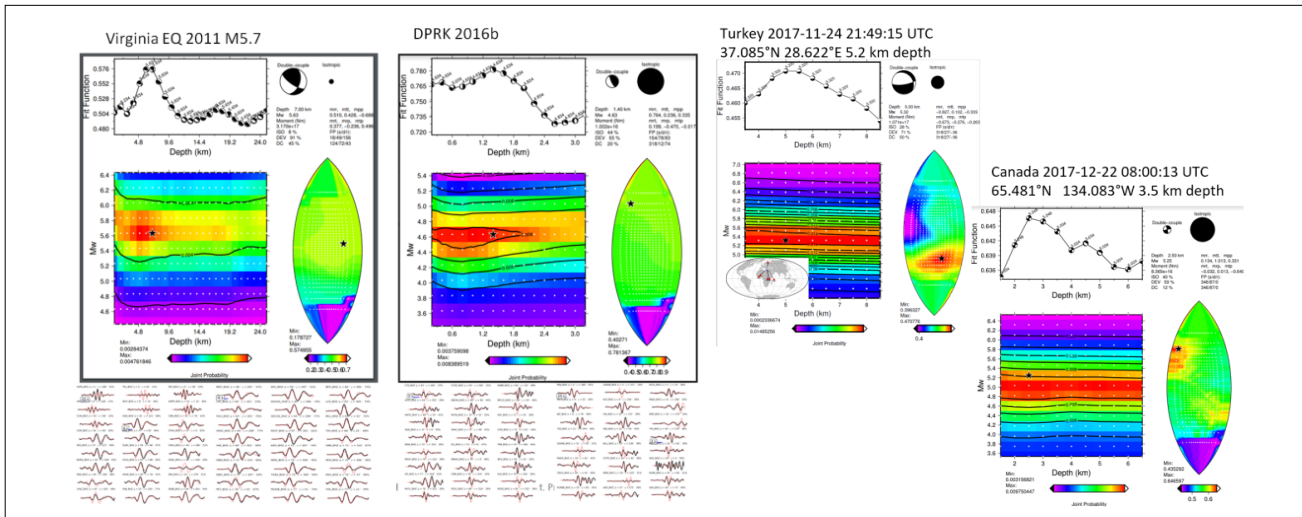
FIGURE 5.
Four cases of depth and MTE: Three earthquakes and DPRK-5 (2016b).

distances are computed and scored against the observed waveforms. After many candidate events are generated from a uniform prior search space and their waveform fits are tabulated, a post-processing step is performed which selects the best-fitting event and presents distributions of likely magnitudes, depths and source mechanisms. The framework is then applied to multiple earthquakes and explosions and the methodology's efficacy in inferring event depth and magnitude is assessed. A powerful GUI is developed, allowing for the framework extension and introducing more functionality. Additionally, a synthetic seismogram generator is introduced into the workflow. This synthetic data can then be channeled into the MTE framework and the seismic network's sensitivity to a known solution can be judged.

The testing procedure involves the estimation of the moment tensor and depth for events of various natures to match the Protocol screening criteria – depth of burial and focal mechanism. Figure 5 presents four cases: three shallow earthquakes and the fifth underground nuclear test announced by the Democratic People's Republic of Korea. These examples show the difficulties in interpretation of the nature of the source: the DPRK-5 has a predominant isotropic part, as expected for an underground nuclear test. However, the Canadian earthquake, at a depth of

3.5 km with the estimated magnitude Mw=5.25, is also characterized by a predominant isotropic component. The probability distribution plots show the depth, magnitude and focal mechanism estimation process.

Two underground nuclear tests conducted by India and Pakistan are presented in Figure 6. The Chagai-I explosion conducted by Pakistan is a greater challenge to event screening using the focal mechanism approach – the double-couple component is larger than the isotropic one and the MTE solution is moved from the population of explosions closer to the population of earthquakes. There were likely five charges in the Chagai-I event, with one bigger than the other four. The estimated depth of burial is around 1 km. The merging of the earthquake and explosion populations seems to be an important issue when using focal mechanism as a screening parameter.

For the ParMT application however the main goal is the depth estimate with the constraints from the focal mechanism. Depth is a powerful event screening parameter. Currently the uncertainty in depth estimates is constrained by depth-sensitive phases. Only arrival times of these phases are used. Inclusion of the focal mechanism allows the use of full waveforms to constrain depth in the source solution.
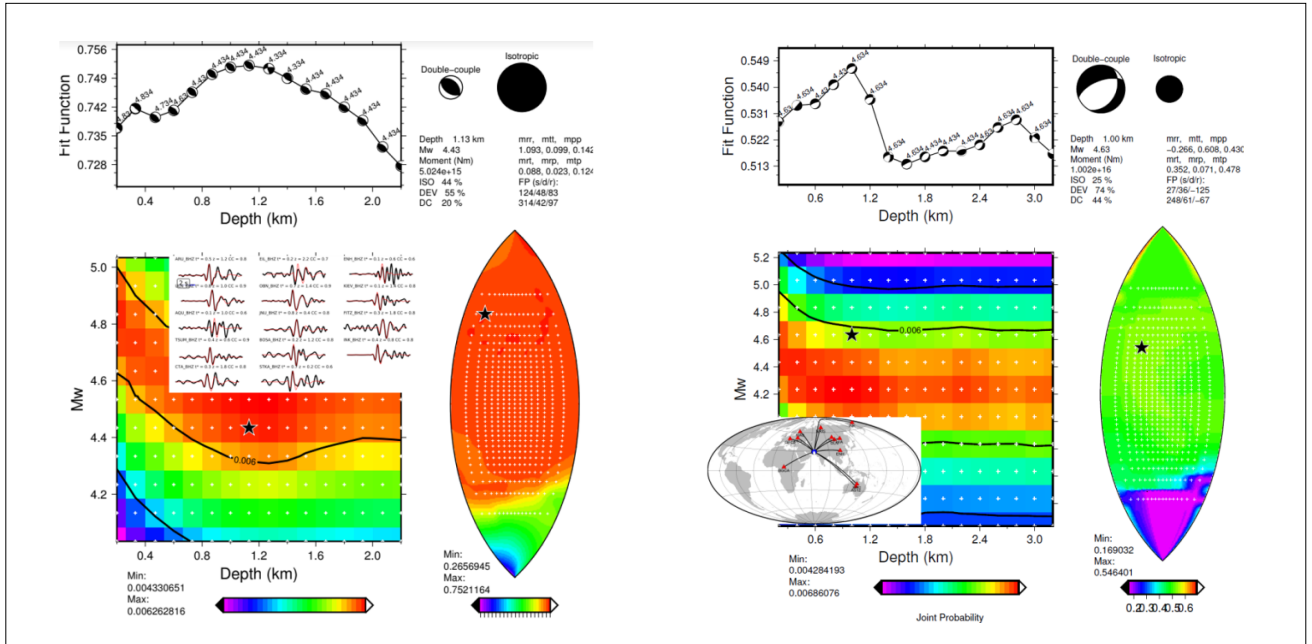
4. SPECTRAL DISCRIMINATION OF THE DEMOCRATIC PEOPLE'S REPUBLIC OF KOREA EXPLOSIONS AND AFTERSHOCKS

The main difference between seismic sources of underground explosions and earthquakes, which is useful for discrimination, is related to the relative efficiency of P- and S- wave generation. Explosions demonstrate more efficient generation of compressional waves, whereas earthquakes generate shear waves of relatively higher amplitude. As a result, the difference between body (P-) wave, mb and surface (related to S-) wave, Ms, magnitudes measured at teleseismic distances successfully serves for discrimination between earthquakes and underground explosions.

At regional distances, seismic wavefield is characterized by a much higher fluctuation in amplitudes of P- and S- waves because of the inhomogeneous velocity and attenuation structures of the crust and the uppermost mantle. No reliable magnitude scale can be derived for discrimination purposes. Therefore, finer characteristics are needed to distinguish between earthquakes and explosions. It has been found that the spectrum of P-wave falls faster for earthquakes than that of explosion sources.

Based on this observation, a spectral discriminant was introduced as a frequency dependent ratio of P- and S-wave spectral amplitudes. In this study, the focus was on the comparison of the tests by the Democratic People's Republic of Korea and their aftershocks considered as natural earthquakes due to the similarity in their source mechanisms.

To estimate the frequency dependent P/S spectral amplitude ratios, first, time windows best representing the groups of P- and S- waves were selected. Then 150-second records in 10-second-long segments were divided. The root-mean-square amplitudes in each segment in all frequency bands were then calculated. For arrays, first the root-mean-square amplitude using all individual traces was estimated. Then individual traces were steered to the reference channel with the slowness corresponding to the Democratic People's Republic of Korea test site, creating a single beam trace to calculate the root-mean-square amplitude. One problem with such an approach is that group and phase velocity in the secondary phases are prone to

changes relative to those of the primary P_n-wave. To match the changing slowness, beams with slowness adjusted to the corresponding seismic phase along the trace were calculated. Both approaches give approximately the same result. The averaging over all individual traces was used. For three component (3-C) stations, two versions were calculated: only Z-component and all three components. No large difference was observed and the 3-C version was used.

Figure 7 presents P/S (P_n- and L_g-waves) spectral ratios from six explosions and six aftershocks as measured at two International Monitoring System (IMS) array stations KSRS (Republic of Korea) and USRK (Russian Federation) and at two non-IMS 3-C stations MDJ (China) and SEHB (Republic of Korea). The number of detected events varies from station to station. One can see that for frequency of 4Hz, the P/S curves from the nuclear test deviate from the corresponding aftershock curves.

Figure 8 displays the mean values as obtained by averaging all individual P/S ratios for a given source type at a given frequency for KSRS and USRK. The error bars for each mean value represent standard deviations for a given station/source-type/frequency-band combination. The mean value and standard deviation obtained for the explosions prohibits their wrong interpretation as aftershocks.

When there are several stations, discrimination becomes even more statistically significant. Since USRK and KSRS are two IMS stations detecting all aftershocks, their measurements were merged using the Mahalanobis distance method. This method allows for measuring the distances between populations in various directions using various standard deviations as measurement units.

In Figure 9, the distance of explosions and aftershocks from the average explosion (left) and the average aftershock (right) are presented. The Mahalanobis distance has a logarithmic scale. The distance of aftershocks from the average explosion is above 100 (up to 20 000) and the distance of the explosions from the average explosion is just a few units of distance. The critical $\alpha=0.001$ corresponds to Mahalanobis distance $=16.3$. The
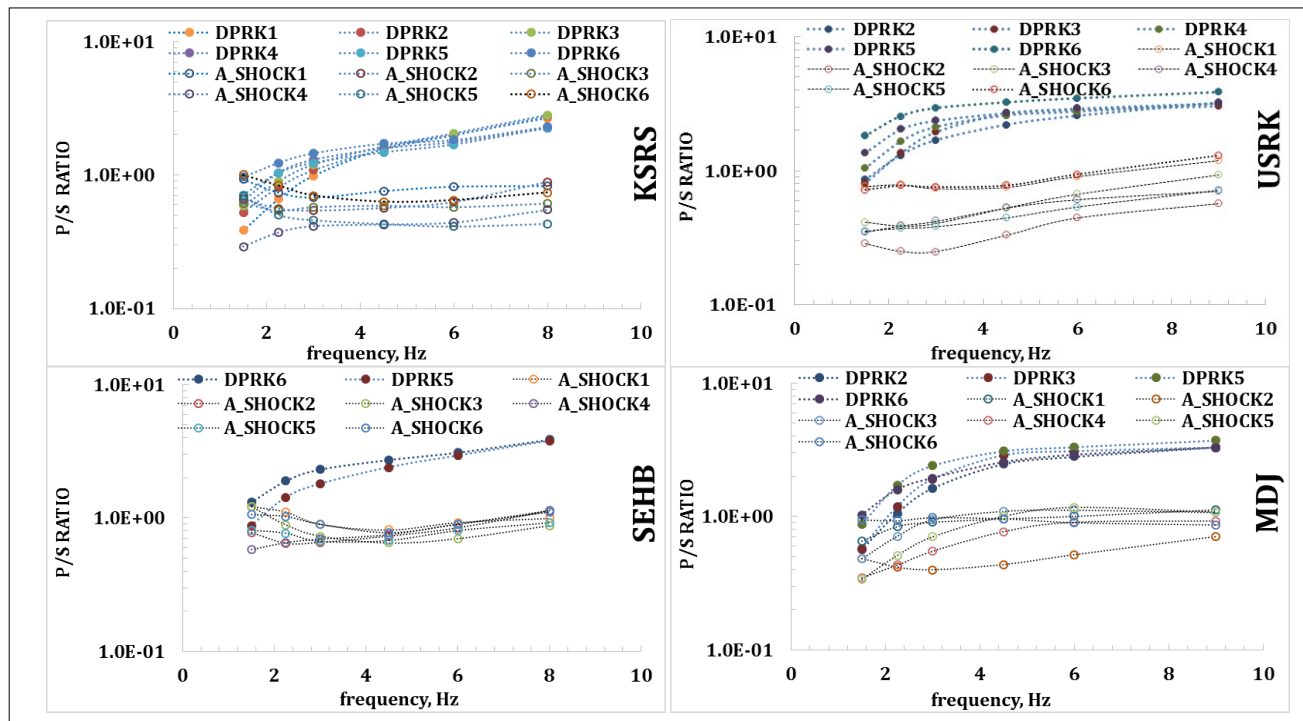
FIGURE 7.
Dependence of the P/S ratio on frequency for stations KSRS, USRK, SEHB and MDJ. There are six Democratic People's Republic of Korea nuclear tests and six aftershocks (A_SHOCK1 to A_SHOCK6). The number of detected explosions and aftershocks varies with station. Notice the lin-log scale.
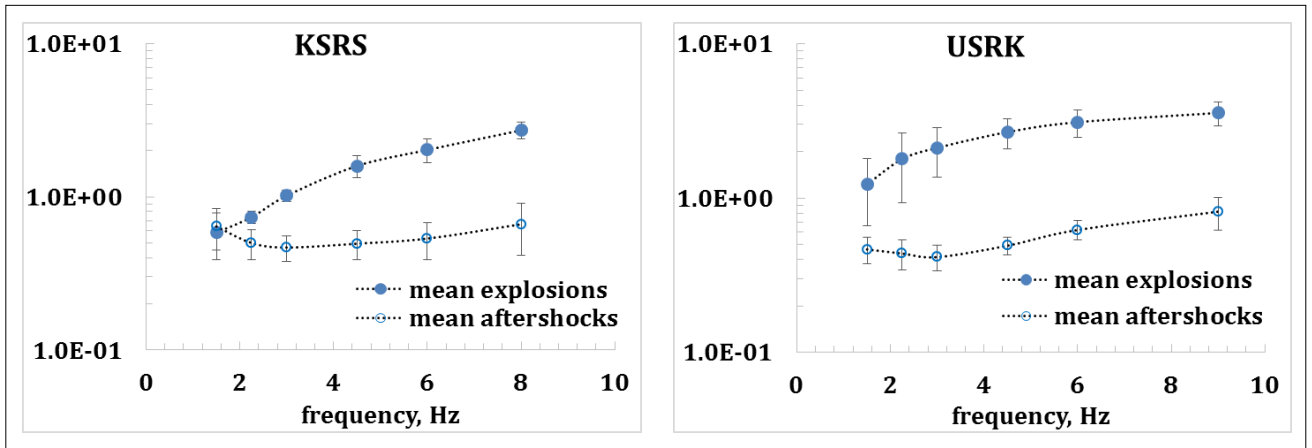
FIGURE 8.

The mean values of the P/S ratio for the aftershocks (open circles) and explosions (solid circles) together with the standard deviations calculated for each frequency band. Left panel: station KSRS, where six aftershocks and six explosions were measured. Right panel: station USRK with five Democratic People's Republic of Korea explosions and six aftershocks.
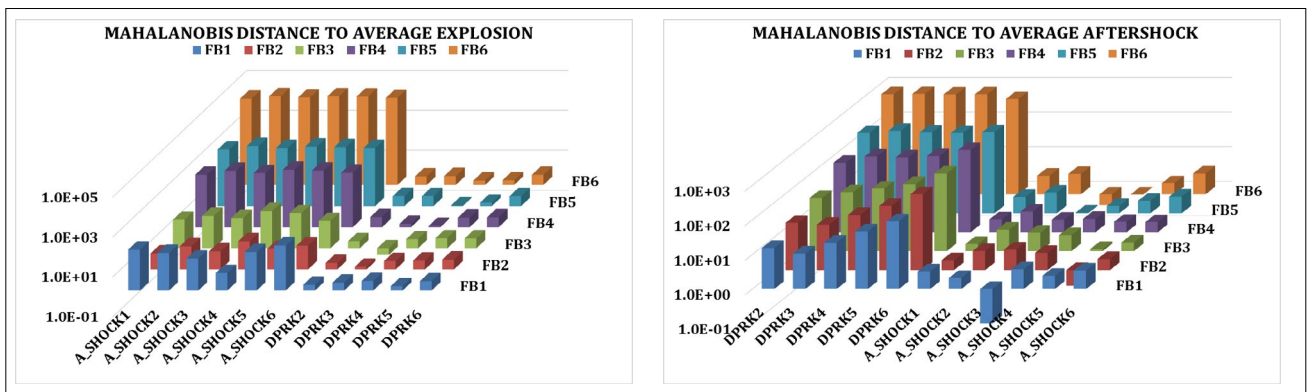
FIGURE 9.

Squared Mahalanobis distances calculated using the P/S ratios at stations KSRS and USRK from five tests conducted by the Democratic People's Republic of Korea (2 to 6) and six aftershocks. Six frequency bands are presented. Left panel: Mahalanobis distances to the average explosion. Notice the logarithm scale.
Right panel: Mahalanobis distances to the average aftershock.

outcome is clear and it is not possible to confuse explosions and aftershocks. The same result is obtained for the average aftershock, where larger scattering between aftershocks was observed.

The importance of discrimination for the Democratic People's Republic of Korea test site is defined by the possibility of a clandestine or partially failed nuclear test with low-amplitude signals at regional seismic stations. The P/S spectral ratio serves as a powerful tool to discriminate weak explosions and weak natural events like aftershocks. The next section describes the finding of weak aftershocks of the DPRK-3 and DPRK-4, which were found using the multi-master method based on the WCC processing.

5. DETECTION OF WEAK AFTERSHOCKS OF THE DEMOCRATIC PEOPLE'S REPUBLIC OF KOREA TESTS (FOCUS ON SMALL EVENTS)

Detection of weak aftershocks of the Democratic People's Republic of Korea tests is a challenge for the IDC. WCC is used for detection of signals with amplitudes at the microseismic noise level. There are several well detected aftershocks, which can be used as more effective master events for the detection of aftershocks weaker than the Democratic People's Republic of Korea explosions. Table 1 lists 23 aftershocks used as master events. Together with the signals measured from six explosions, there are 57 waveform templates.

Table 1 shows the number of associated detections NassR (routine) and NassF (final) processing at stations KSRS and USRK. The relative magnitude is estimated by averaging all associated templates. In some cases, there are several aftershocks per day and they are ordered by time (#). The aftershocks are divided into two clusters: DPRK-5 (red) and DPRK-5 (black). The first aftershock found by cross-correlation (DPRK-5) aftershock is highlighted in bold.

For repeated events, the same physical signal can be counted several times if it is detected by templates from close but different events. The intuition behind this procedure is a higher similarity of signals from spatially close events than the similarity of remote events, especially at array stations or seismic antennas. Moreover, a slight variation in the template shapes between master events can be useful for discrimination if this variation has a physical origin. The number of detections obtained by a given set of templates at a given station is a good measure of the reliability of the corresponding physical signal, which is possibly hidden in the ambient seismic noise and not seen by analysts.

The share of successful templates with detections within the predefined arrival time interval is somewhat similar to the rate of successful detections of reflected signals for a given radar pulse rate as the defining parameter of the radar performance. The difference in the

Table 1. List of 23 Aftershocks Used as Master Events in the Multi-Master Method

Jdate	Time	#	NassR	NassF	KSRS	USRK	RM
2017246	03:38:30	1	36	37	17	20	3.81
2017266	4:42: 58	1	42	42	21	21	3.01
2017266	*8:29: 14*	*2*	48	49	25	24	3.61
2017285	16:41:07	1	43	43	18	22	3.25
2017304	10:20:12	1	18	20	5	15	2.46
2017335	22:45:54	1	32	35	18	17	2.90
2017339	14:40:50	1	42	40	19	21	3.14
2017340	16:20:04	1	23	31	14	17	2.61
2017343	06:08:39	1	22	30	11	19	2.78
2017343	6:13: 32	2	41	35	17	18	3.42
2017343	06:39:59	3	39	37	18	19	3.11
2016255	**1:50: 48**	1	36	37	19	18	2.87
2017246	09:31:28	2	31	41	19	22	2.67
2018036	10:32:30	1	36	36	12	24	2.66
2018036	20:07:29	2	28	37	14	23	2.76
2018036	21:57:35	3	23	27	8	19	2.75
2018037	04:49:36	1	22	24	5	19	2.64
2018037	10:12:30	2	17	25	5	20	2.59
2018037	10:53:52	3	49	47	23	24	3.02
2018038	21:46:23	1	47	33	17	16	3.38
2018039	17:39:17	1	41	42	19	23	2.74
2018112	19:25:09	1	36	47	22	25	2.71
2018112	*19:31:18*	*2*	50	45	25	20	2.99

shape of the templates is somewhat similar to the change in the pulse frequency content or pulse width. Therefore, the multi-master association is applied, based on two stations and tens of templates generated by different master events, as a version of radar, with the cross-correlation-detections representing the matched reflections. Using the multi-master method, a retroactive re-processing at stations KSRS and USRK was conducted starting from 1 January 2009 to 9 May 2022. More than 100 reliable aftershocks were found. Figure 10 presents a list of reliable the Democratic People's Republic of Korea aftershocks. There have been 105 aftershocks detected since 11 September 2016 (after DPRK-5) and no events similar to the Democratic People's Republic of Korea aftershocks were found between 1 January 2009 and 29 May 2013.

The overall aftershock activity of the Democratic People's Republic of Korea after 11 September 2016 can be divided into two clusters related to DPRK-5 and DPRK-6. The first

FIGURE 10.

No	Date	#	Time	KSRS	USRK	RM	Nass
1	2013149	1	13:53:08	16	24	2.65	40
2	2013200	1	13:23:50	10	18	2.63	28
3	2013203	1	15:50:16	6	16	2.40	22
4	2014145	1	04:56:56	8	18	2.69	26
5	2014145	2	06: 1: 27	18	25	2.82	43
6	2014145	3	06:43:03	23	25	2.91	48
7	2016050	1	00:28:07	6	24	2.80	30
8	2016184	1	19:52:27	19	19	2.61	38
9	2016255	1	01:50: 48	19	18	2.87	37
10	2016257	1	03:57:42	7	18	2.61	25
11	2017246	1	03:38:30	17	20	3.81	37
12	2017246	2	09:31:28	19	22	2.67	41
13	2017266	1	04:42: 58	21	21	3.01	42
14	2017266	2	08:29:14	25	24	3.61	49
15	2017285	1	16:41:07	18	22	3.25	43
16	2017303	1	23:37:48	10	17	2.71	27
17	2017304	1	10:20:12	5	15	2.46	20
18	2017335	1	22:45:54	18	17	2.90	35
19	2017339	1	14:40:50	19	21	3.14	40
20	2017339	2	19:55:53	16	24	2.75	40
21	2017339	3	23:30:10	10	15	2.83	25
22	2017340	1	16:20:04	14	17	2.61	31
23	2017343	1	06:08:39	11	19	2.78	30
24	2017343	2	6:13: 32	17	18	3.42	35
25	2017343	3	06:39:59	18	19	3.11	37
26	2018036	1	10:32:30	12	24	2.66	36
27	2018036	2	20:07:29	14	23	2.76	37
28	2018036	3	21:57:35	8	19	2.75	27
29	2018037	1	04:49:36	5	19	2.64	24
30	2018037	2	10:12:30	5	20	2.59	25
31	2018037	3	10:53:52	23	24	3.02	47
32	2018038	1	21:46:23	17	16	3.38	33
33	2018039	1	17:39:17	19	23	2.74	42
34	2018112	1	19:25:09	22	25	2.71	47
35	2018112	2	19:31:18	25	20	2.99	45
36	2018161	1	15:53:04	11	12	2.57	25
37	2019001	1	22:20:27	16	19	3.19	35
38	2019011	1	21:34:28	8	22	2.60	30
39	2019011	2	23:15:46	19	25	2.81	44
40	2019011	4	23:19:21	5	15	2.59	20
41	2019078	1	08:32:36	11	16	2.78	27
42	2019079	1	19:41:03	17	17	3.13	34
43	2019080	1	01:55:35	17	18	2.99	35
44	2019080	2	10:45:36	10	13	2.69	23
45	2019117	1	22:37:16	10	10	2.65	20
46	2019158	1	03:49:30	16	22	2.91	38
47	2019158	2	05:18:39	25	22	3.20	47
48	2019158	3	07:45:43	17	22	2.91	39
49	2019218	4	04:05:31	12	14	2.83	26
50	2019233	1	03:36:52	16	17	2.86	34
51	2019270	1	19:01:31	22	22	2.65	44
52	2019310	1	23:51:34	19	21	3.00	40
53	2019323	1	21:59:46	17	25	2.81	42
54	2019323	2	22:02:29	23	23	2.93	46
55	2019323	3	22:49:36	8	20	2.77	28
56	2020029	1	00:33:46	24	22	3.15	46
57	2020029	2	02:48:28	11	19	3.01	30
58	2020030	1	00:50:00	13	22	2.97	35
59	2020046	1	17:05:05	12	13	2.63	25
60	2020071	1	17:09:01	12	8	2.52	20
61	2020092	1	15:14:59	12	14	2.66	26
62	2020220	1	12:27:41	23	25	3.06	48
63	2020263	1	11:22:26	12	8	2.64	20
64	2020273	1	20:23:29	14	16	2.66	30
65	2020282	1	21:49:37	7	21	2.71	28
66	2020308	1	10:12:17	11	16	2.70	27
67	2020308	2	10:13:52	8	20	2.66	28
68	2020308	3	10:30:32	20	21	2.74	41
69	2020308	4	11:28:06	9	18	2.69	27
70	2020309	1	10:18:42	22	17	2.85	39
71	2020319	1	14:45:35	18	20	3.00	38
72	2020319	2	15:40:26	16	7	2.67	23
73	2020321	1	9:11: 28	13	10	2.91	23
74	2020321	2	13:38:34	10	11	2.73	21
75	2020321	3	18:10:28	14	10	3.35	24
76	2021013	1	19:29:30	9	16	2.68	25
77	2021030	1	15:07:45	17	8	3.03	25
78	2021031	1	5:10: 31	11	10	2.80	21
79	2021031	2	06:18:12	11	9	2.76	20
80	2021078	1	12:48:50	9	12	2.67	21
81	2021108	1	23:20:03	12	21	2.79	33
82	2021109	1	06:48:48	24	22	3.49	46
83	2021110	1	17:12:31	21	16	2.64	37
84	2021164	1	14:57:30	20	22	3.39	42
85	2021169	1	19:45:57	9	13	2.53	22
86	2021175	1	17:09:32	22	13	2.65	43
87	2021209	1	13:20:45	13	18	2.66	31
88	2021224	1	07:42:59	8	12	2.83	20
89	2021225	1	04:35:30	9	17	2.81	26
90	2021227	1	03:46:45	10	18	2.71	26
91	2021242	1	20:33:25	11	22	2.56	33
92	2021242	2	20:51:11	5	17	2.65	22
93	2021244	1	09:39:49	23	27	2.95	50
94	2021244	2	17:05:32	13	18	2.62	30
95	2021253	1	18:16:41	14	19	2.69	33
96	2021253	2	18:47:25	16	17	2.80	33
97	2021254	1	04:17:02	18	9	2.79	27
98	2021284	1	12:58:59	12	10	3.00	22
99	2021284	2	13:00:49	20	13	3.10	33
100	2021364	1	01:45:36	9	18	2.85	27
101	2021364	1	05:21:30	11	19	2.87	30
102	2021364	3	08:54:51	15	15	2.86	30
103	2022042	1	01:35:23	21	18	3.86	39
104	2022045	1	05:33:21	15	15	3.01	30
105	2022045	2	10:47:24	14	17	2.91	31
106	2022045	3	21:52:24	15	11	2.81	26
107	2022049	1	02:44:57	17	19	3.05	36
108	2022049	2	03:38:18	16	15	2.96	31
109	2022053	1	21:07:04	7	18	2.76	25
110	2022059	1	12:22:48	15	16	2.69	31
111	2022059	2	12:32:00	16	9	2.94	25
112	2022062	1	17:15:33	16	9	2.98	25

List of the Democratic People's Republic of Korea aftershocks found after 1 January 2009 using the multi-master method.

DPRK-5 aftershock defines the DPRK-5 cluster and the events within a few weeks after the DPRK-6 defines the set of DPRK-6 samples (see Table 1 for details). The quantitative difference between DPRK-5 and DPRK-6 aftershocks is determined by the maximum signal to noise ratio at the cross-correlation trace (SNRcc) among all templates from one group and the average SNRcc value in each group of templates (as defined in Table 1). The duration of the DPRK-5 and DPRK-6 aftershock sequence is almost 5 years. Omori's law that accurately describes the decay of natural aftershock activity is clearly violated: magnitudes and the occurrence rate of the Democratic People's Republic of Korea aftershocks do not change in time as Figure 11 demonstrates. These features make the Democratic People's Republic of Korea aftershocks sequence a very specific one. It is highly unlikely that such behaviour will be repeated in the future elsewhere. Therefore, a strict statistical assessment of the discrimination procedure would be excessive. The preliminary physical interpretation of two different sequences is based on the mechanism of the release of gravitational energy caused by the interaction of the DPRK-5 and DPRK-6 damaged zones, which have different sizes and depth of burial.

A simple discrimination graph may be useful for a better understanding of the difference in the distribution of the DPRK-5 and DPRK-6 parameters. Figure 12 presents the difference between the sum of the maximum SNRcc at KSRS and USRK for the DPRK-5 and DPRK-6 templates as well as the difference of the corresponding mean SNRcc values. The decision line is the x-axis. The events above the decision line belong to the DPRK-5 cluster and those below

FIGURE 11.

Left panel: the relative magnitude of the aftershocks measured after 1 January 2016. Right panel: the number of associated templates, Nass (from 57), of the same sequence. No significant decay in the relative magnitude and Nass is observed. Open circles -DPRK-5 aftershocks, solid diamond – DPRK-6 aftershocks. There are poor events which cannot be reliably attributed to one cluster.
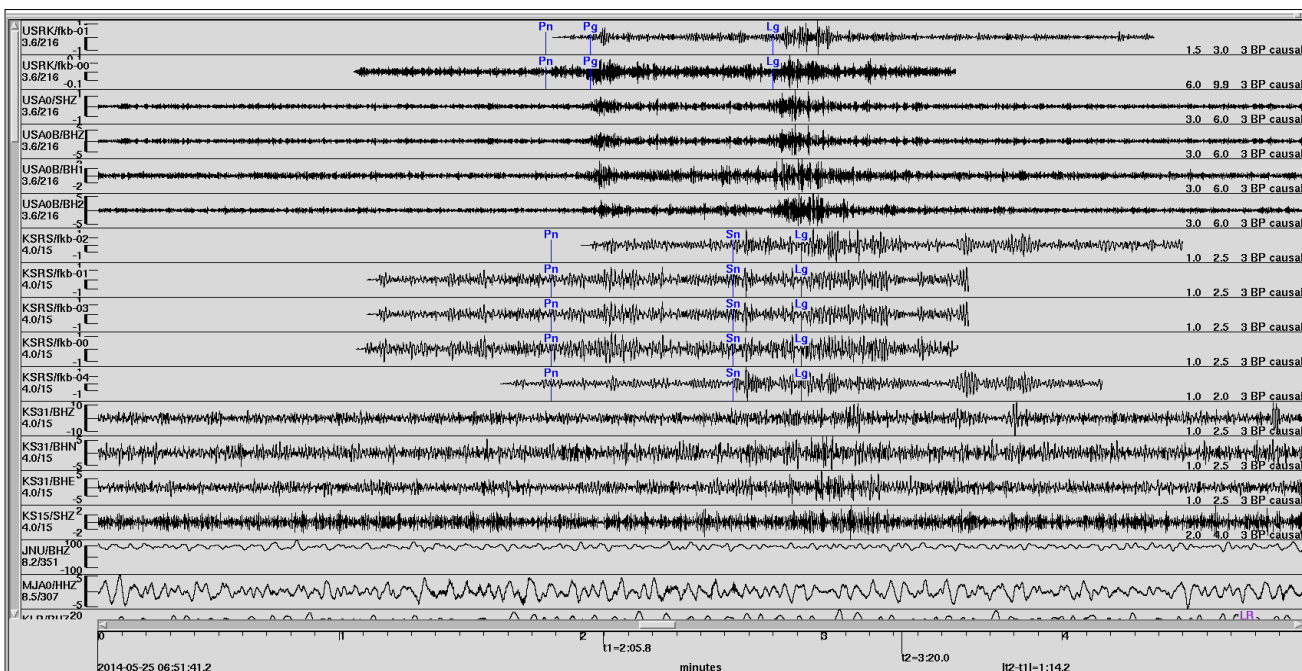
FIGURE 12.

The decision line for the difference between the sum of the max (left) and the mean (right) SNRcc values. The DPRK-5 aftershock found on 11 September 2016 defines its own cluster. The DPRK-6 immediate (several weeks) aftershocks define another cluster. The poor events with low SNRcc values are not classified.

the line are the DPRK-6 aftershocks. Poor events are also shown. They are closer to the decision line than most of the identified aftershock, but some DPRK-6 aftershocks are also close to the decision line. The poor events include three examples of the LEB-like hypotheses with Nass<20. The decision that the event is poor is taken when there are contradicting identification by various parameters or very low Nass (around 20), as illustrated in Figure 12. For example, the identification changes with the parameter (max and mean SNRcc) at two stations for 2018161_1. The events 2019011_1, 2020095_1, and 2020105_1 are considered poor and are also

not included in the XSEL due to low Nass<20. However these events have relatively high max and mean SNRcc and are likely real aftershocks.

The retroactive reprocessing of the KSRS and USRK data with the multi-master method has found several aftershocks of the third (DPRK-3) and the fourth (DPRK-4) announced underground nuclear tests conducted by the Democratic People's Republic of Korea on 12 February 2013 and 6 January 2016, respectively. The second Democratic People's Republic of Korea test had no reliable aftershock hypotheses at the level of the method sensitivity and resolution. The largest

FIGURE 13.

IDC interactive solution for DPRK-3 aftershock observed on 25 May 2014.

235

aftershocks of the DPRK-3 and DPRK-4 are close in magnitude to the first aftershock of DPRK-5 on 11 September 2016, and many aftershocks of DPRK-6. Three big aftershocks of DPRK-3 occurred on 25 May 2014, i.e. 467 days after the mainshock. The DPRK-3 aftershock found at 6:43:03 UTC had a relative magnitude of 2.91, as shown in Figure 13.

Two aftershocks from DPRK-4 were found: on 19 February 2016 (0:28:07 UTC) and on 02.07.2016 (19:52:27 UTC). The largest aftershocks from DPRK-3 and DPRK-4 could be interpreted as related to the cavity collapse process likely followed by a chimney collapse, not reaching the free surface, however. Seismic signals from all events found before DPRK-5 (09.09.2016), had a high level of cross-correlation with the waveform templates from DRPK-5 and DPRK-6. These signals prove the shape similarity and thus the close spatial proximity of the seismic events after DPRK-3/DPRK-4 to DPRK-5/DPRK-6 aftershocks.

6. SIGNALS SEPARATION WITH THE INDEPENDENT COMPONENT ANALYSIS

Blind source separation methods used in signal recovery applications are attractive because they use minimal a priori information about the signals they are dealing with. ICA implying non-Gaussianity of the underlying processes signal's mixture is a blind source separation method that was applied to examine three scenarios of interest to the CTBTO: (1) separation of two almost co-located explosions conducted within fractions of seconds, (2) separation of regional earthquakes and (3) extraction of nuclear explosion signals merged with wave trains from a strong earthquake. The importance of resolving the problem related to case 1 is related to correct explosion yield estimation. Case 3 is a well known scenario of conducting clandestine nuclear tests. ICA was tested with synthetic waveforms, seismic data from the explosions by the Democratic People's Republic of Korea and mining blasts conducted within the Eastern European platform as well as with signals from strong teleseismic events (Sumatra, April 2012 Mw=8.6, and Tohoku, March 2011 Mw=9.0 earthquakes). The data was recorded by seismic arrays of the IMS and by the small aperture seismic array Mikhnevo (MHVAR) operated by the Institute of Geosphere Dynamics, Russian Academy of Sciences. ICA demonstrates a good ability to separate seismic sources with very close origin times and locations (hundreds of metres), and/or having close arrival times (fractions of seconds) and recovering their waveforms from the mixture.

In Figure 14 solid arrow lines indicate input waveforms for the actual example (mixture and decomposition on the right). The dashed line indicates a typical waveform used to produce a similar signal separation result. In the first case, the primary phase of Q#1 event falls onto the secondary phase of Q#2 event making them visually inseparable. In the second case, all arrivals of both events fall at the same time producing visually a new event. A section with separation results consists of (bottom-right): (1) a pair of input signals (from the same channels) composing the mixture, (2) separated signals and (3) the first principal components of the array seismograms corresponding to each signal. The principal components were presented to emphasize that the restored signals inherit the property of the whole array, not just some single component since the best similarity is provided between the first principal components of the input array and the best independent component. The black vertical rounded lines indicate corresponding signals (omitted on the right panel). Correlation coefficients between the original and restored signals are in a range (0.84, 0.92).

Figure 15 shows that the independent components on the right are the restored signals of both earthquakes. Principle components of the array are given for illustration. Figure 16 illustrates the separating of events with close azimuths from the mix: DPRK-3, February 2013 mb=4.9 (scaled up to mb=7) test, and Tohoku,
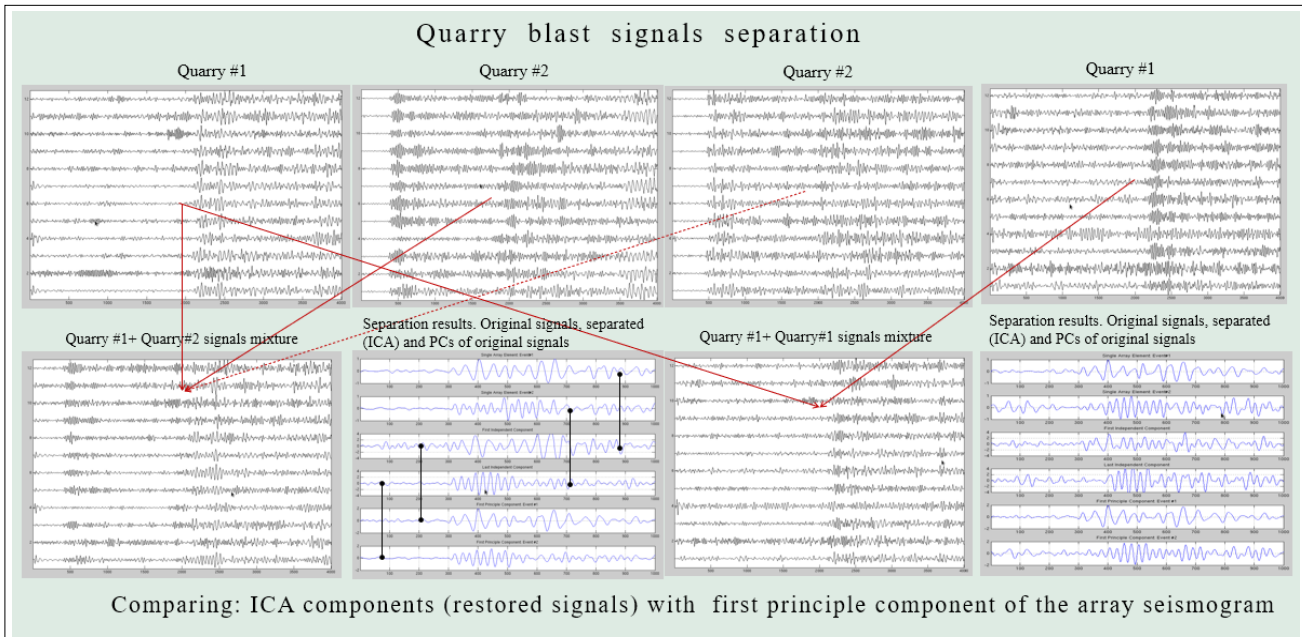
FIGURE 14.
Separation of signals from different quarries by the ICA method.
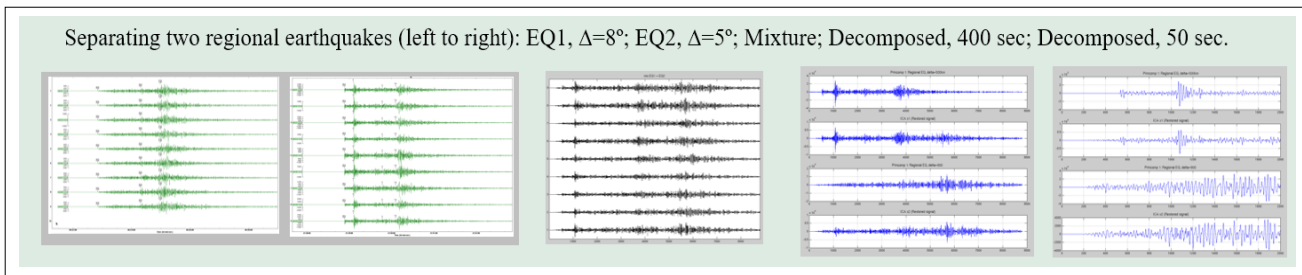
FIGURE 15.
Separating two regional earthquakes with Δ=8º and Δ=5º recorded at MKAR IMS array station.
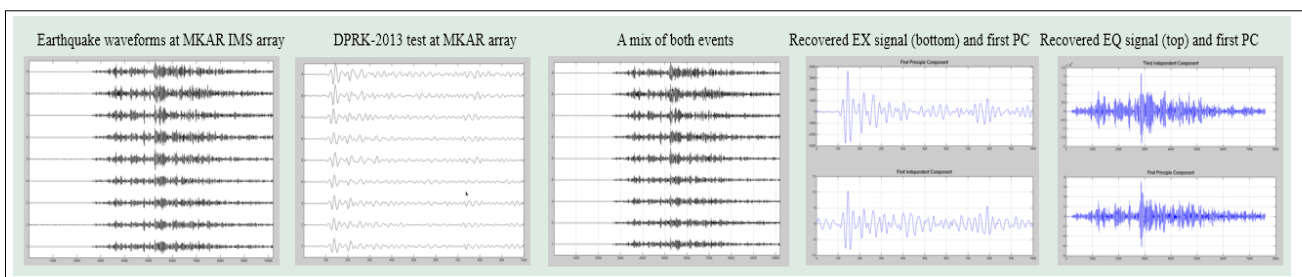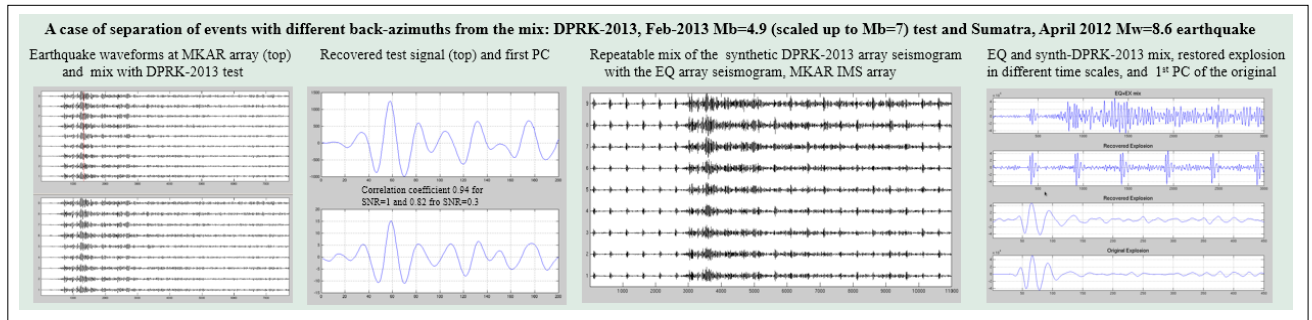

FIGURE 16.
Separating events with close azimuths from the mix: DPRK-3, February 2013 mb=4.9 (scaled up to mb=7) test and Tohoku, March 2011 Mw=9.0 EQ.

March 2011 Mw=9.0 EQ recorded at MKAR IMS array station. The explosion is very well extracted from the mix as well as the earthquake as independent components 1 and 3 show.

Figure 17 demonstrates good separation of the DPRK-3 explosion hidden in Sumatra, April 2012 Mw 8.6 earthquake. Examples are made for SNR 1 and 0.3 (signal is the Democratic People's Republic of Korea explosion and the noise is the earthquake). A red line on the left indicates a P-arrival of a hidden explosion by the Democratic People's Republic of Korea. The repeatable mix is given for the synthetic record of DPRK-3, as well as the recovered explosion in different time scales.

FIGURE 17.
Separation of events with different back-azimuths from the mix: DPRK-3, February 2013 mb=4.9 (scaled up to mb=7) test and Sumatra, April 2012 Mw=8.6 earthquake.

7. MULTIDIMENSIONAL APPROACH TO CTBTO DATA PROCESSING

The multidimensional approach is a promising way in modern experimental science and engineering. In this section, a hypercomplex and high-order (tensorial) representation of multichannel seismic data as they are recorded by the IMS was considered with further processing within the context of the corresponding multidimensional model. In particular approaches to construct multidimensional master event templates for further cross-correlation based detection and location with the data recorded at multichannel seismic installations, such as IMS 3-C seismic stations and arrays were discussed. Hypercomplex number systems are the natural cases of representing 3-C digital seismogram samples requiring special attention to the underlying axioms. Dealing with the composite observations (3-C arrays) may demand higher than four dimensional algebras, or some specific grouping of them, so the tensor representation of seismic wavefield looks natural in this case (details in Figure 18).

Data processing would be conducted not on separate waveform projections but on a fuller multidimensional object and tensor representation of the data from the 3-C arrays that would utilize joint volumetric (sensor) and spatial (array) information. Further dimensionality reduction of tensor and hypercomplex (e.g. quaternion in Figure 19) data produces lower order principal components, a basis for the multidimensional waveform templates. Highly effective master events built with the hypercomplex and multilinear singular value decomposition

(SVD) provide a good example of introducing multidimensional data models into CTBT practice (Witten and Shragge 2006).

This is not a full list of the hypercomplex applications in geophysics and seismology:

- Master event method extension with the quaternion based 3-C cross-correlation;
- Subspace method extension based on the quaternion singular value decomposition (4-D SVD, or quaternion-based singular value decomposition (QSVD)/SVDQ in different implementations) introducing this approach into the semi-empirical master event location (Le Bihan and Mars 2002);
- 4-D – homomorphic analysis and deconvolution based on the quaternion elementary functions properties allowing for the Q–Fourier transform (QFFT), Q-convolution, etc.;
- Focal mechanism description and simple comparing different seismic events based on the quaternion approach (Kagan's angles);
- Direct analytical solution for the optimal reorientation of two dimensional or three dimensional (3-D) geophysical time series data (sensor reorientation);
- Polarized wave separation, in ambient noise tomography methods and ellipticity recovery for shallow and intermediate depths seismic impedance estimation;
- The SVDQ technique may also be used to recover the component of a polarized signal that is lost in the noise;
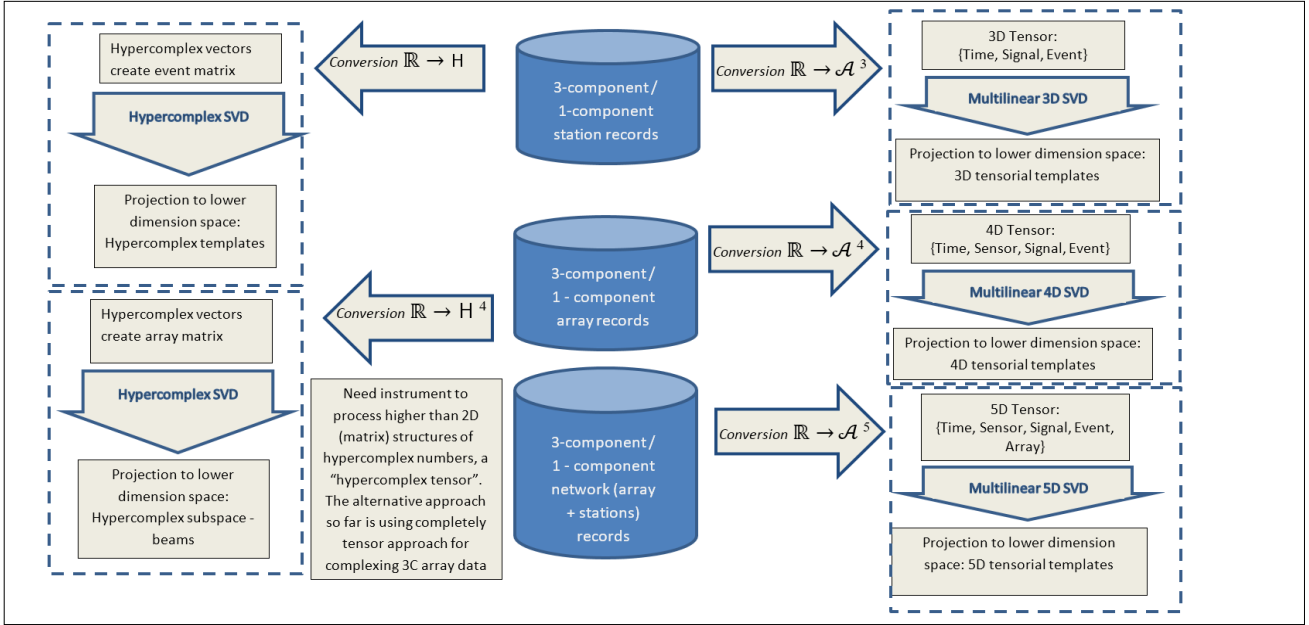
FIGURE 18.
Generalized schema of multidimensional CTBTO data processing.

- A natural extension of the proposed method would include higher-order statistics (ICA-like technique) in order to enhance the separation results and release the constraint of uncorrelation to higher-order independence;

- SVDQ is in fact linked with principal component analysis and could be seen as the standardization step in a blind polarized source separation algorithm. As a perspective, the study of sensors/arrays with an arbitrary number of components *l* could be investigated, with further use of hypercomplex numbers of dimension *l* could then be used, as well as the use of Clifford Algebras. These algebras have already been used to develop pattern recognition algorithms on hyperspectral images.

For the quaternions, which are a 4-D $\mathbb{R}$-algebra, with the multiplication table:

$$ij = -ji = k,\ jk = -kj = i,\ ki = -ik = j,\ i^2 = j^2 = k^2 = -1.$$

a quaternion SVD can be defined,

$$\mathbf{A} = \sum_{n=1}^{r} \mathbf{u}_n \mathbf{v}_n^{\triangleleft} \sigma_n,$$

where u_n are the left singular vectors and v_n the right singular vectors, σ_n are the real singular values, and the quaternion principal components can be extracted from the pure-quaternion (i-j-k) seismic records to be used in a hypercomplex master event template design (see Figure 19).
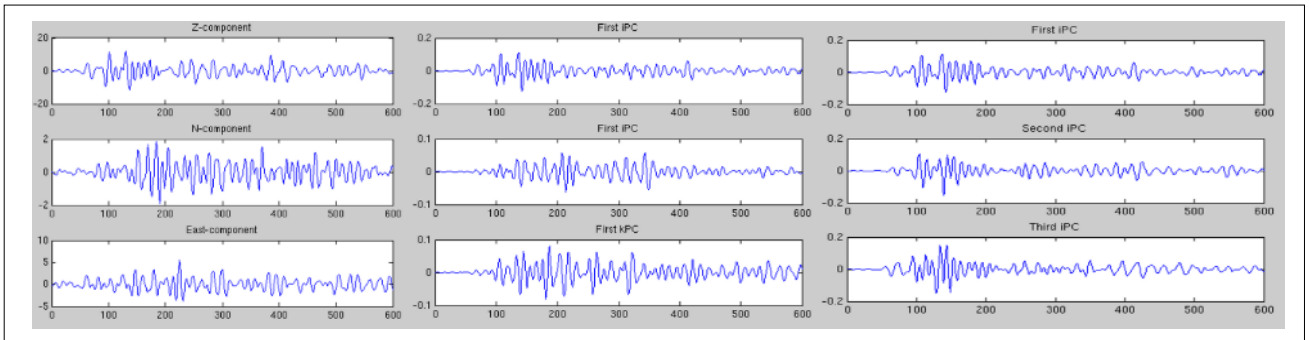
FIGURE 19.
Example quaternion principal components. Left: input 3-C seismogram, center: pure quaternion i, j, and k components of first principal component, right: first complex quaternion component of first three principal components.

8. N-D STRUCTURES: TENSORS, QUATERNIONS, PRINCIPAL COMPONENT ANALYSIS, DIMENSIONALITY AND NOISE REDUCTION

For any tensor

$$\mathcal{A} = \mathcal{S} \times_1 U^{(1)} \times_2 U^{(2)} \dots \times_N U^{(N)} ,$$

the multilinear principle component analysis objective is to define a multilinear transformation that maps the original tensor space

$$R^{I_1} \otimes R^{I_2} \dots \otimes R^{I_N}$$

into a tensor subspace

$$R^{P_1} \otimes R^{P_2} \dots \otimes R^{P_N}$$

(with $P_n < I_n$ for $n = 1, \dots N$) (Lu et al. 2008).

Then the dimensionality reduction can be performed through the truncation of U and $\mathcal{S}$ terms and building the restored tensor $\mathcal{A}_{red}$ through the block term decomposition which approximates a tensor by a sum of low multilinear rank terms (https://www.tensorlab.net/doc/btd.html, Vervliet et al. 2016).

$$\mathcal{A}_{red} = \sum_{r=1}^{R} \mathcal{S}^{(r)} \bullet_1 U^{(r,1)} \bullet_2 U^{(r,2)} \bullet_3 \dots \bullet_1 N U^{(r,N)}$$

A tensor containing records of N events from the M arrays of vertical sensors can be thought of as a 3-D cube sliced to N slices, and the reduced tensor – to R slices where R corresponds to the meaningful part of eigenevent. A 4-D cube can represent the same of 3-C array, or a network of L arrays. Such N-D reduction provides significant N-D noise reduction (compare left and right panels in Figure 20).

A consequence of processing seismic sensor components separately is that the relations between the signal components are not considered. In the quaternion approach, component-wise and long vector techniques are avoided and the aim is to process vector signals in a concise way using quaternionic signals. Such a model allows extending the concept of modulus and phase to vector signals having samples evolving in 3-D space. The module is linked with signal magnitude while the 3-D phase is directly representative of
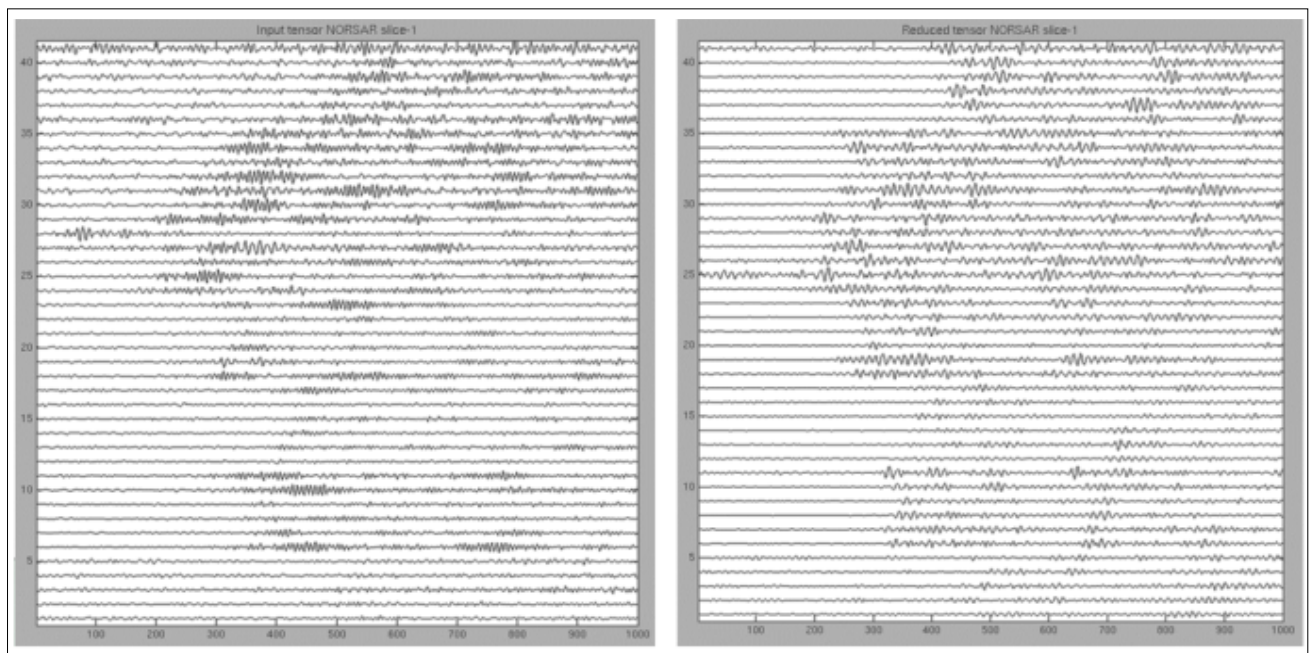
FIGURE 20.
An example of noise reduction resulting from dimensionality reduction.

the 3-D Lissajous (particle motion) plot. For the signal-noise subspace decomposition, the data matrix would be arranged as a quaternion matrix, each element of which is a quaternion. The SVDQ would produce 3-C noise reduced signal vectors and, applying principal component analysis or ICA, effective extension of principal component analysis and ICA on the N-component data would be provided, for example for master event template design. SVDQ provides sharper descending of the eigenvalues sequence; QFFT provides more prominent secondary picks in cepstrum – also ETA branch.

9. AMBIENT NOISE-BASED METHODS FOR REFINING LOCAL VELOCITY MODELS AT IMS STATIONS: AMBIENT NOISE TOMOGRAPHY, HORIZONTAL-TO-VERTICAL SPECTRAL RATIO

One of the beam forming problems is the absence of empirical arrival times (except NOA seismic array) at sensors of the array. Theoretical time delays between channels, based on theoretical slowness, in many cases are not accurate because of the complex velocity structure below the array. Low velocity inclusions may introduce significant disturbances in the relative arrival times and amplitudes as the example of the Nevada Seismic Array shows (Figure 21). Variations in amplitude and arrival time delays are related to geology below the sensors (limestone, tuff, granite, sandstone, basaltic lava) and lead to potentially significant beam loss as driven by the absence of signal synchronization in time and amplitude.

The IDC needs empirical arrival time delays for the whole set of detection beams, i.e. a set of azimuth/scalar slowness pairs. Velocity model can be estimated using various methods. Results of velocity recovery by the ambient noise-based methods, which might be useful for enhancements in IDC processing are explored in this paper.

Passive seismic techniques based on ambient noise analysis procedures (inversion of the dispersion curves produced by the seismic interferometry or horizontal-to-vertical spectral ratios (HVSR) to velocity profiles) comprise an efficient toolbox for refinement of velocity models underneath sensors deployment. This tool
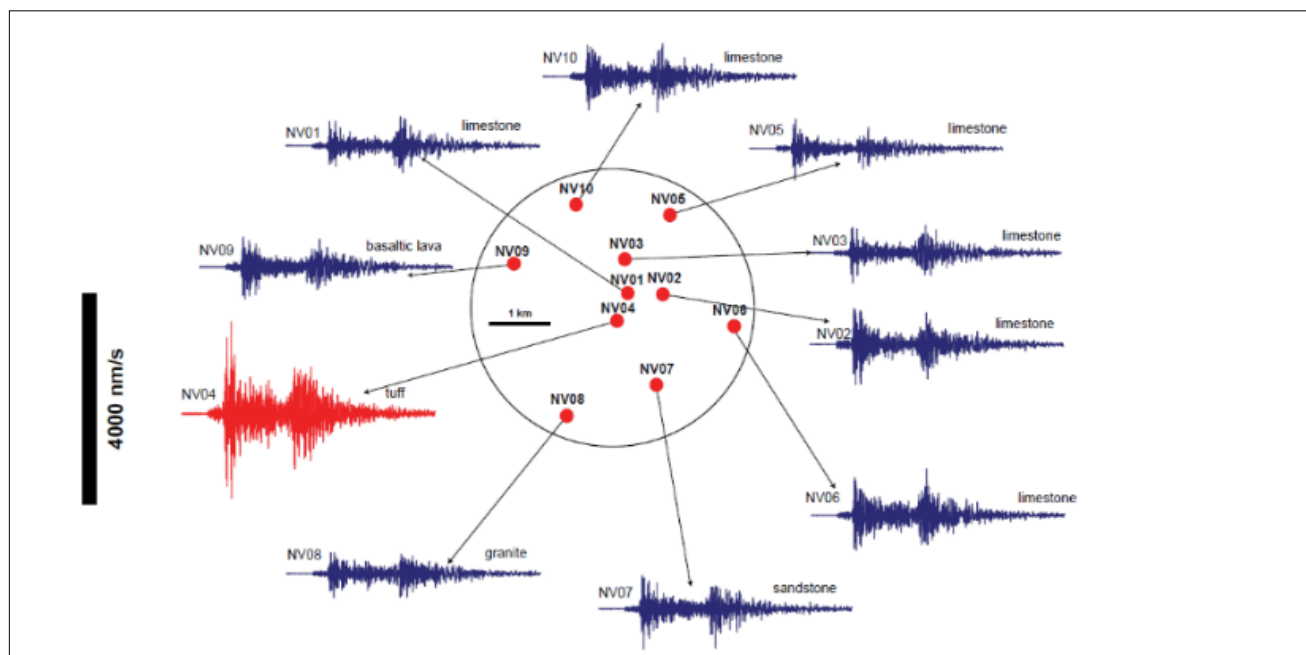
FIGURE 21.
Different shapes of the wave trains at the Nevada Seismic Array station due to local heterogeneities.

is useful for the enhancement of ParMT results, as well as for the improvement of IDC regional locations and the OSI Seismic Aftershocks Monitoring System. It could be widely utilized for IMS seismic arrays for restorations of the velocity model of the underlying crust. In recent decades the application of these methods has led to restoration of the Earth interior models at vast spatial ranges from tens of metres to continental scales.

9.1. Geological and Tectonic Settings of the ARCES Array Station, Norway

The ARCES array station is situated in a very specific area, to the north of Karasjok (Karasjok coordinates 69.47306, 25.507394, and 69.5349 25.5058 for the central ARCES station ARA0). Geologically and tectonically, it belongs to the Karasjok-Levajok area and the Karasjok-Kittila Greenstone Belt. Recent mapping, isotopic dating and metamorphic and structural observations from the Karasjok-Levajok area lead to a tectonic interpretation that is similar

in many ways to Phanerozoic plate tectonic models. Three major belts of Early Proterozoic rocks lie between two Archean Gneiss complexes: the Jergul Gneiss Complex on the west and the Baitvarri Gneiss Complex on the east. The E-dipping Early Proterozoic belts are, from west to east: the Karasjok Greenstone Belt, the Tanaelv Migmatite Belt and the Levajok Granulite Belt.

According to the maps in Figure 22, Karasjok sits just by the intersection of the profiles Y-Y' and A-A', and the geological information from Figure 22 could be used to build the impression of the generalized structure of the area surrounding and including ARCES. The complexity of the Karasjok-Kittila Greenstone Belt site, which includes thrusting, clines, sloping and intrusions with well-expressed layering within the first ~200 m, then 400 m, 800 m and 1300 m inter-formation interfaces (bedrocks) is noticeable. It would not be a surprise to see the seismic velocity anomalies, lower density intrusions or sequencing within the whole stratigraphy section.

Cross-sections of the Lakselv Valley.

Schematic E-W cross-section of the Karasjok area.

Stratigraphic section from the Lakselv area
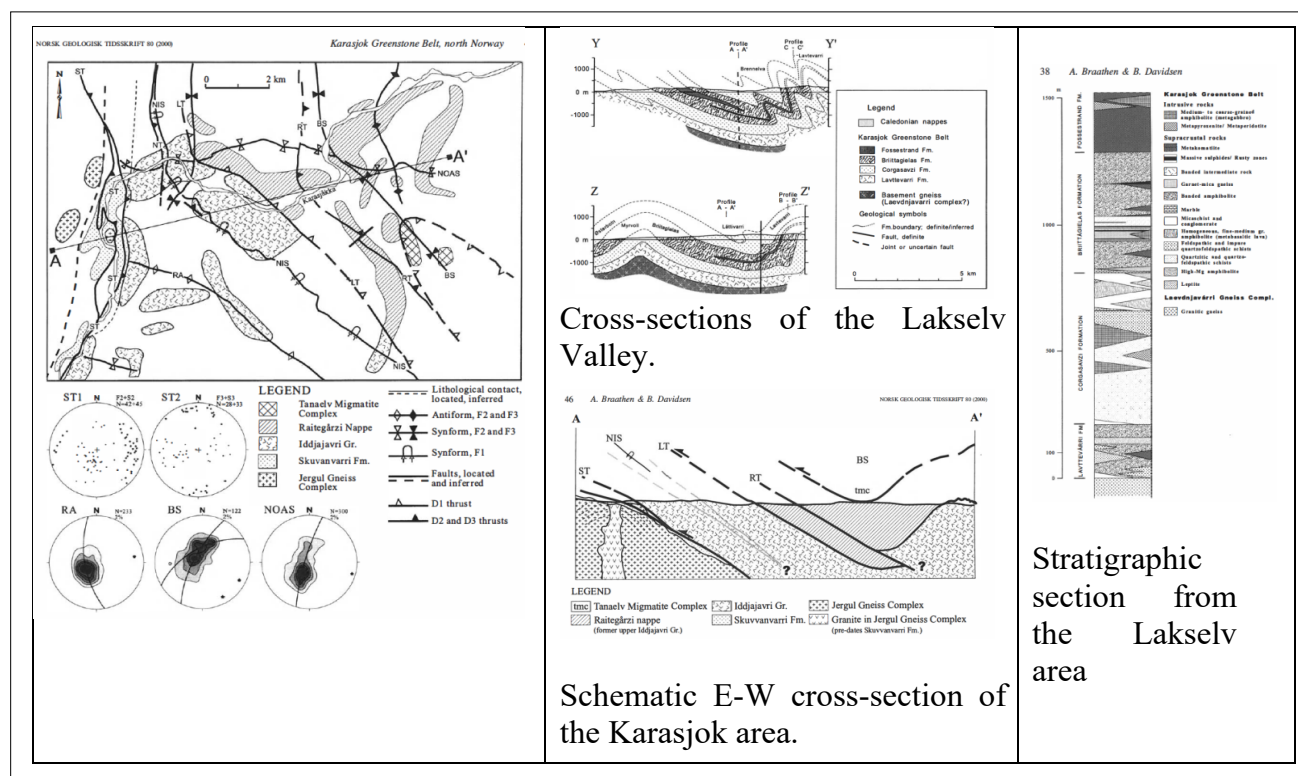
FIGURE 22.
The profile A-A' on a map above crosses the Karasjok area NE-SW, while Y-Y' profile has a NW-SE direction (Braathen and Davidsen 2000).
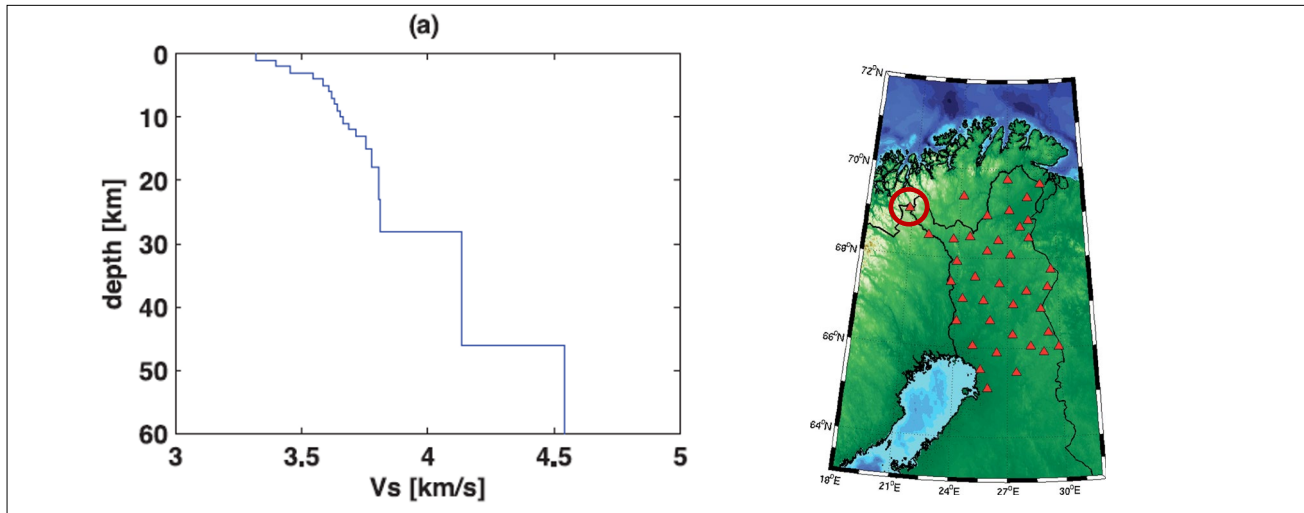
9.2.   Seismic Velocity Structure

So far seismologists use the high level generalized models for Fennoscandia, produced either within the CRUST-1 project by the local researchers or international teams. There's no more detailed seismic velocity model for this area. Before starting to model the paper by Poli et al. 2012 was analysed. They built an average crustal shear velocity model based on the inversion of the dispersion curve produced from the seismic data continuously recorded during the POLENET/LAPNET temporary experiment in northern Fennoscandia. The array configuration was an approximately two dimensional grid with station separations that span from ~50 km to ~600 km (see the inlay in Figure 23). The broadband data was pre-filtered at 0.01–2 Hz, resampled to a common sample rate (5 Hz) and deconvolved from the instrumental responses. Data from the ARCES, the most northwest station of the array, was also used.

The model they present is finer than the traditional ones and is yet to be considered for CTBTO applications, but still does not resolve layers thinner than 1 km.

9.3.   Horizontal-to-Vertical Spectral Ratio Inversion

Originally based on a simple layer over half-space subsurface, computational methods for the evaluation of the Horizontal-to-Vertical Spectral Ratio (HVSR, or H/V, or HV) curve have recently become available for multilayer systems where the subsurface is modelled as a stack of infinite homogeneous layers and using different approaches such as computation of mechanical transfer functions (Aki and Richards 2002, Ben-Menahem and Singh 1981, Tsai and Housner 1970) or even exploiting the statistical approach (Sánchez-Sesma et al. 2011, Lunedei and Albarello 2015). HVSR involves analysing measurements of ambient seismic noise in 3-D to determine the fundamental site resonance frequency. Resonance is excited by the interaction of Rayleigh and Love surface waves and body waves (vertically incident shear) with the high contrast acoustic impedance boundary at the bedrock-sediment interface. This site characterization has been successfully used to determine the thickness of unconsolidated sediments in sedimentary basins throughout the world (Ibs-von Seht and Wohlenberg 1999). The HVSR method is a passive seismic method, so it relies on the measurement of ambient noise caused by wind, ocean waves and human activity. The seismic noise is recorded with a single broadband 3-C seismometer and processed after collection to determine the resonance frequency. The resonance frequency is determined by calculating the spectral ratio of horizontal over vertical (H/V) ground motion in the seismic record. Resonance frequency has been shown to be proportional to the thickness

of unconsolidated sediments (Nakamura 1989, Bonnefoy-Claudet et al. 2006, Van der Baan 2009). For example (Haefner et al. 2015).

$$Z = a f_{r0}{}^{b}$$

where Z is the sediment thickness; f_{r0} = seismic resonance frequency, in Hz; a, b = empirically determined fitting parameters from non-linear regression of fr0 data at sites where Z is known.

In addition, resonance frequency can be expressed through the average shear wave velocity and thickness of the sedimentary package:

$$Fr = \frac{V_S}{4H}$$

where Fr is a resonant frequency, H is the thickness of the sedimentary package, given an average shear wave velocity (Vs).

It is well known that consideration of H/V solely at the surface is insufficient to characterize shallow properties uniquely due to a trade-off between layer velocity and thickness that leads to similar H/V curves. It should be noted, that for the IMS applications this might be not a significant problem since all seismic contrasts are very prominent. For instance, learning the geological reports of the surrounding area, we can acknowledge that ARCES sits on a hard rock pie (granulites thrusted westward over migmatites, which were in turn thrust over the greenstones and a coarse-grained gabbro).

Additionally, the forward problem is highly non-linear and depends on several uncorrelated parameters (Hobiger et al. 2012, Lontsi et al. 2015). For example, the HV-Inv, an HVSR inversion software based on the diffuse field assumption (DFA) approach, better constrain the inversion by inverting jointly the phase dispersion curve and the HVSR observations using a priori shear wave velocities for a certain location. While the HVSR is mainly sensitive to sharp impedance contrasts and vertical travel time, it has poor sensitivity to the absolute value of the velocities. Alternatively, dispersion curves are only weakly sensitive to the depth of structural variations due to the broad sensitivity kernels of surface waves with depth, but they are highly sensitive to the absolute velocity of the medium. The complementary nature of these measurements makes it a powerful combination for subsurface characterization (e.g. Picozzi et al. 2005). In the inversion, both the shear wave velocity and the layer thickness in HV-Inv are free parameters. A combination of Monte Carlo sampling and downhill simplex optimization was used to adjust the theoretical dispersion curve and HVSR (Bignardi et al. 2016, Pina-Flores et al. 2016).

In this preliminary research, the following software packages were incorporated: (1) Geopsy, (2) RayDec, (3) DFA HV-Inv and (4) OpenHVSR and the proprietary data processing toolbox for multidimensional data processing. We also applied the methods implemented for the linear architectures (profiles) of recording networks developed for the surface microseismic hydrofracturing monitoring.

9.4. Geopsy

Geopsy contains tools that allow for building HVSR curves, including directivity diagrams, and provides a pipeline framework for inverting the dispersion curves and sets of spatial correlations into velocity models that are based, in particular, on spatial autocorrelation (SPAC) (Aki,1957) and modified for the microtremor SPAC (MSPAC) method – spatial correlation approach, allowing for the irregular structures network data inversion (Molnar et al, 2018). Though this kind of inversion provides us with only an average model for a site like ARCES, some work was conducted in order to subdivide the network into independent segments providing consistent results providing us with the refined velocity model. Due to the lack of information for the initial models (the standard Fennoscandia model and the CRUST-1 model are rather rough), we dug into the seismic profiling and passive seismic research for the area adjacent to ARCES, including learning of the historical geological maps. We also studied Poli, et al. (2012) on the passive seismic resolution of Fennoscandia with broadband sensors, including ARCES broadband data. This data does not, however, give information on the very upper crust structure allowing to refine

velocities in the upper few hundred meters. It does give the constraints for the half-space and average velocity for the uppermost crust of the investigation.

Initially, HVSR methods provided single station results for the single bedrock depth, connected via a simple formula with the pick frequency of the horizontal to vertical spectral estimates. Then second and more depths were involved for high contrast interfaces, and the depths were also connected with the secondary picks on the HVSR curve. Recently more complex methods were developed involving forward and inverse modelling and aimed at more complex depth profiles (OpenHVSR, for instance) and inverting network data for 1-3-D velocity models. Per se, they also utilize the underlying idea of a simple link between the depth, S-waves velocity Vs, and fundamental frequency of the single layer. However, they consider the possibility of the complex interference of the reverberations of each layer and packs of layers. This is very important since the manifestation of complex interference as a specific rippling on the HV curve may force a researcher to assign corresponding maxima to the income of the certain layer while this is just the consequence of the constructive or destructive interference and a higher grade spectral resolution may be required rather than simple Fast Fourier Transform (FFT).

9.5. Diffuse Field Assumption Approaches

As mentioned in 9.3, one of the software packages used in this research is the HV-Inv, which is based on the Diffuse Field Assumption approach (DFA), that better constrain the inversion by inverting jointly the phase dispersion and the HVSR curves. During the last decade there was a switch from just the prominent HV pick discrimination to the modelling of complex interference wave sequences, better allowing for more detailed subsurface velocity structure resolution. In HV-Inv, this is Monte Carlo and simulated annealing modeling for global simulation and downhill simplex and interior-point for local simulation. HV-Inv takes advantage of the recently found connection

between the HVSRN (N stands for noise) and the elastodynamic Green's function which arises from the ambient noise interferometry theory.

9.6. RayDec – Rayleigh Wave Ellipticity Estimation Using the Random Decrement Technique

Rayleigh wave ellipticity as a function of frequency is closely linked to underground structure, i.e. shear wave velocity profile and sediment thickness. The possibility to calculate these underground properties by inverting ellipticity curves has recently been shown. RayDec is a new technique enabling the Rayleigh wave ellipticity to be recovered over a wide frequency range by using ambient noise recordings. Based on the random decrement technique commonly used to characterize dynamic parameters of buildings, this method eliminates all wave types except Rayleigh waves. While many scientists and geotechnical engineers believe that the HVSR expression provides the true value for the Rayleigh waves ellipticity (which is not always the case because of the presence of the wide nomenclature of waves), the RayDec eliminates all wave types except Rayleigh waves. The ellipticity curve can be loaded in Dinver module (Geopsy package, http://www.geopsy.org/) and inverted for the velocity profile. With this, an ellipticity curve alone is not sufficient to retrieve the velocity profile without additional constraints (e.g. Love/Rayleigh wave dispersion curves, interface depths, constraints on the velocities of certain layers).

9.7. Preliminary Results of ARCES Ambient Noise Data Processing

In this paper some preliminary results are presented for the 24-hour noise data inversion at ARCES. HVSRN were computed using functionalities of the following packages: Geopsy, OpenHVSR and RayDec. DFA software was also tested in order to check the feasibility of joint processing of the dispersion curves produced with Geopsy and the HV curves produced with all the above products, including different forms of the HV spectral representation ('clear' ellipticity following RayDec methodology, or using

quaternion based SVD decomposition polarized eigenvectors). Geopsy provides a powerful set of tools for HVSR analysis but is not robust, and the lack of completed documentation makes some tools hard to tune and use.

Figure 24 characterizes the distribution of the main HVSR peak over ARCES stations and the depth of the most prominent bedrock in the general case through some empirical relation.

It can be clearly seen on a summary HV figure with the picks distributed between 1 and 18 Hz (Nyquist is 18 Hz). In general, when multiple peaks are present, the significant peak with the lowest frequency is sought associated with the fundamental resonance frequency (f_0) of the sedimentary cover, for example, $f_0 = Vs/(4*H)$ or using a function where Vs increases with depth. A station map indirectly characterizes bedrocks with the highest impedances below each station,
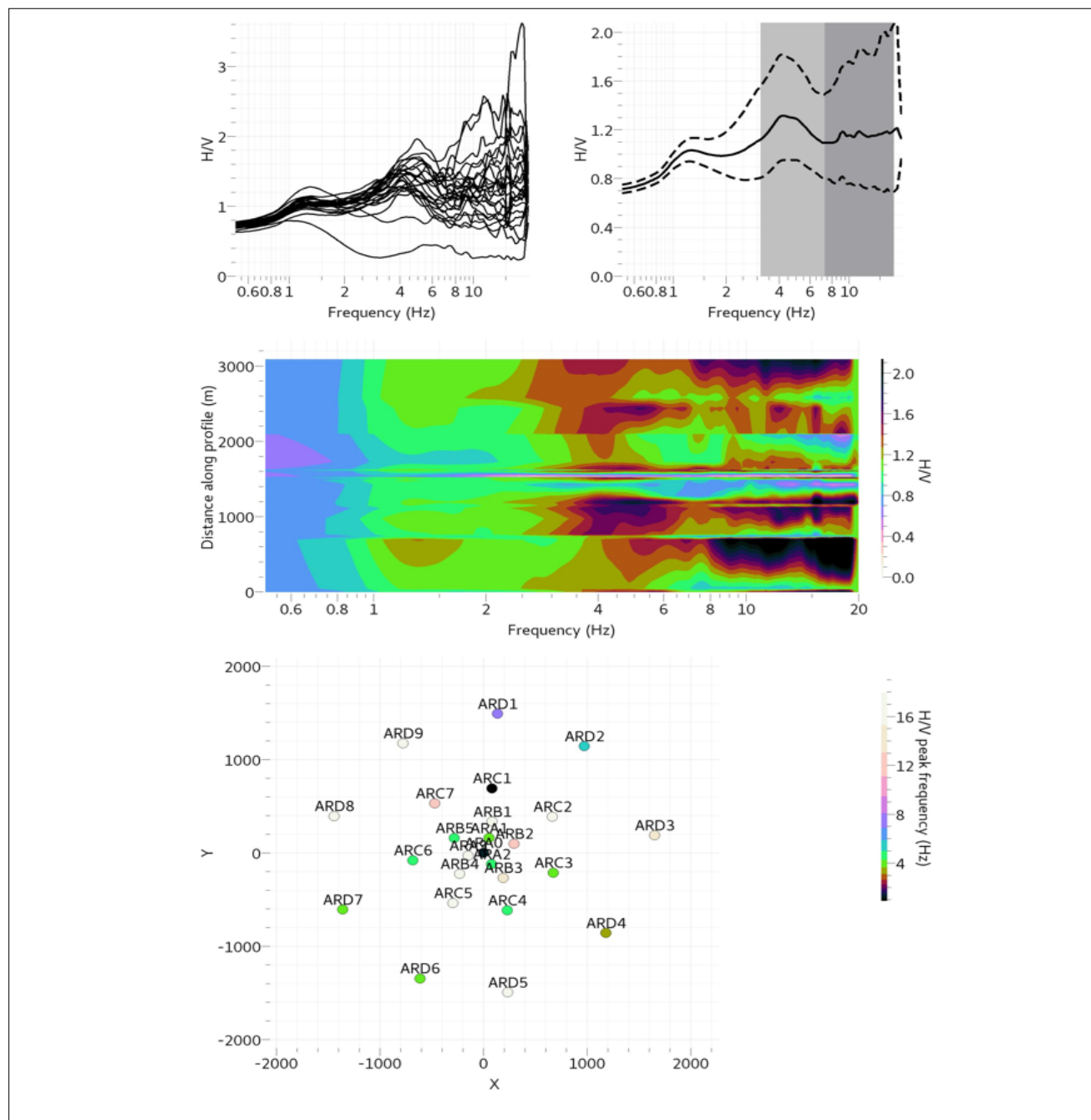
FIGURE 24.
HVSR (Geopsy) for all ARCES stations (top) and distribution of main HVSR peak (+- std) over ARCES array. Colour codes on the map (bottom) correspond to the HV frequency peaks, represented on the directivity diagram (middle) and on the top part of the figure.
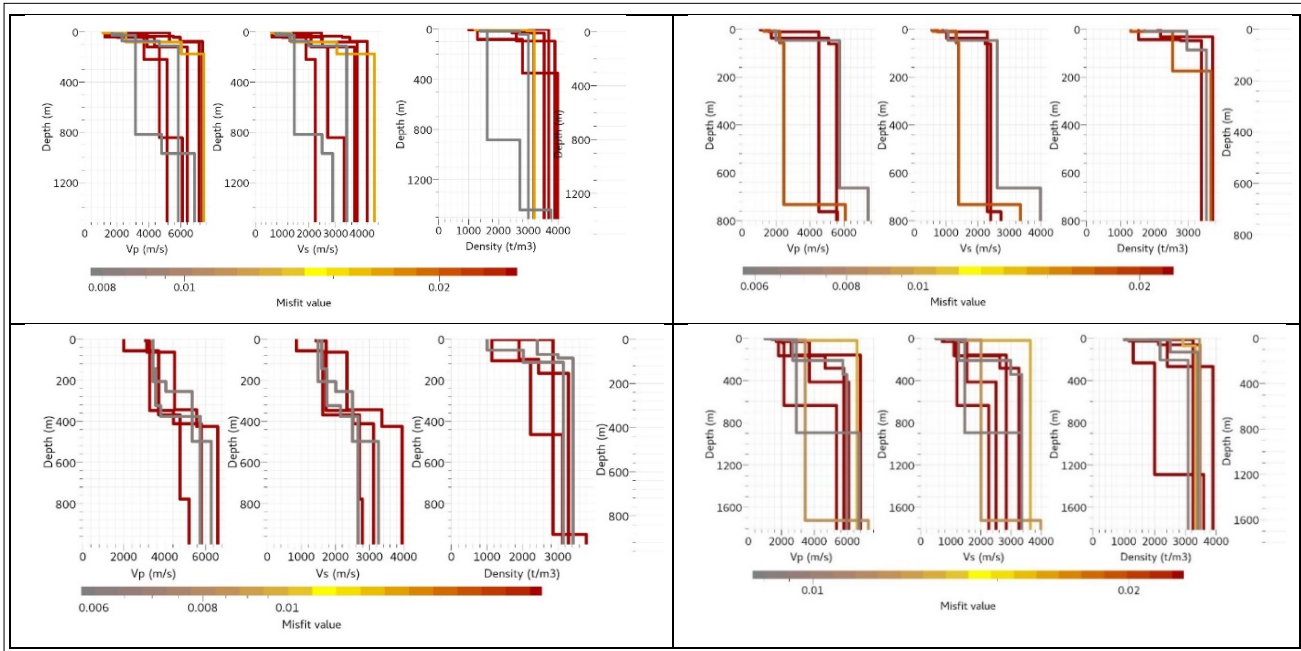
FIGURE 25.
Ellipticity inversion for the ARCES stations ARA0, ARA1 (top) and ARA2 and ARA3 (bottom).

where black code corresponds to the lowest resonance frequency and white to the highest. For example, the most prominent interface under stations ARA0 and ARC1 can be mapped at the deepest depths, while white coded stations have very shallow contrast better sought (which does not mean the absence of the lower high impedance layers).

Geopsy allows for further H/V curves inversion to velocity but as mentioned before more correct inversion is based on the inversion by the Dinver component of Geopsy of ellipticity produced by random decrement technique, RayDec (Hobiger et al, 2009). Such velocity models for ARCES are presented in Figure 25. Joint inversion of ellipticity and dispersion curves is needed for the non-ambiguity solution.

Most of the stations expose seismic contrasts at approximately 400 m and 800 m, same as the MSPAC provides (Starovoyt 2022).

9.8. HVSR Inversion with the OpenHVSR

A more detailed analysis with the OpenHVSR showed the same resonant frequency distribution and similar directional diagrams as for the Geopsy. Figure 26 shows that different resonance picks can be clearly seen for different stations as well as different shapes of curves. On the left for each station is the map of profiles created by us for 2-D processing, the main HVSR curve follows, with spectra for each component and different spectral ratios (standard horizontal to vertical H/V, North to vertical N/V, South to vertical S/V). Some stations can 'focus' only on big depths (lower frequencies), some on shallow (high frequencies) and some on both (several prominent picks).

Figure 27 is a comparison of H/V ratios for different IMS stations. For NV31 and NV11 broadband Nevada Seismic Array stations, the same resonance frequency near 3.5 Hz, 0.5 Hz and 12 Hz is clearly seen indicating the possibility of deep and shallow interfaces. Both stations sit at the same location, but a much longer time interval for NV11 (24 hours) allows for noticing longer resonance periods (out of picture range). TX31 at Lachitos array indicates sharp shallow contrast beneath it, and PD32 at Pinedale demonstrates a rather complex mostly shallow multilayer structure.

The HVSR curve can also be inverted to infer the visco-elastic properties of the subsurface. In the approach implemented in OpenHVSR (Herak 2008), the vertical axis from frequency
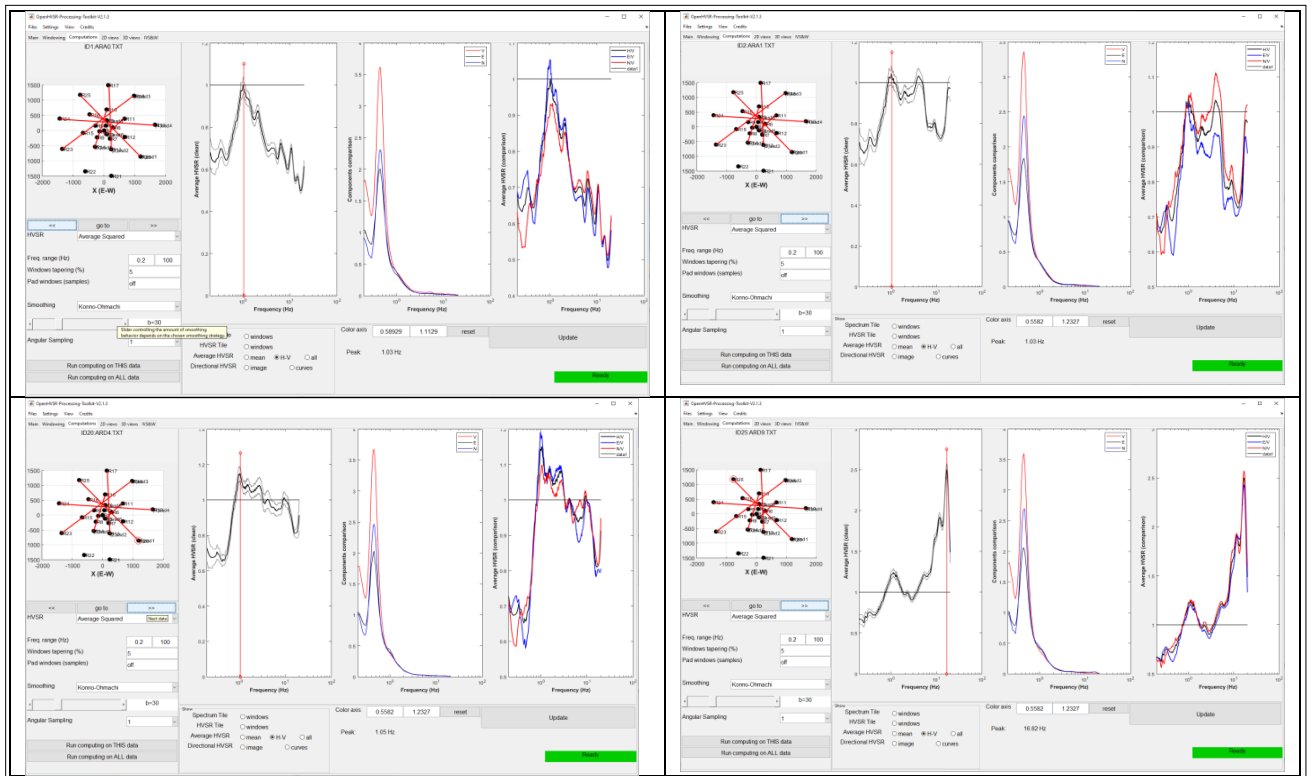
FIGURE 26.

Eight HVSR results for four ARCES stations in OpenHVSR (ARA0 and ARA1 from the inner circle and ARD4 and ARD9 from the outer circle). Due to good smoothing, very specific spectral features characterize each station as very stable for 24 hours. Red-line profiles on the left of each inlay figure are used for plotting a velocity section map used for further 2-D velocity profile mapping.
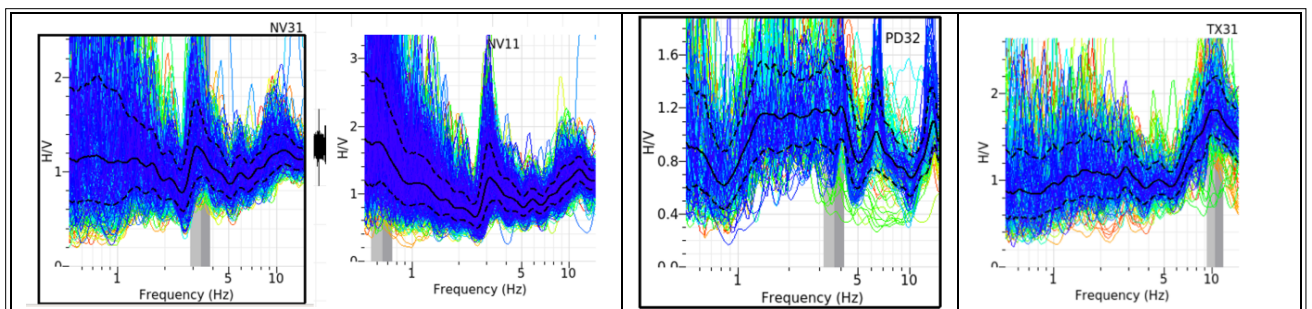
FIGURE 27.

H/V curves (Geopsy) for different IMS stations (each line is for each H/V time window).

is transformed into 'pseudo-depth' using an approximated average velocity of the soft sedimentary stack, as well as 'bedrock mapping' introduced by Ibs-von Seht and Wohlenberg (1999) which can be seen in Figure 28.

This data can be used as a starting inversion model, producing a consistent 3-D velocity model for the entire cube underneath the array site (Figures 29 and 30). Within the OpenHVSR project, it can be done with the OpenHVSR inversion component.

9.9. Perspectives for Improvement of HVSR Analysis at Intermediate Depths with Hypercomplex Surface Waves Decomposition

This paper has shown that hypercomplex data decomposition may help in polarized wave separation in ambient noise tomography methods and ellipticity recovery for shallow seismic impedance estimation. Technically, the QSVD technique may be used to recover the component of a polarized signal that also can be lost in the
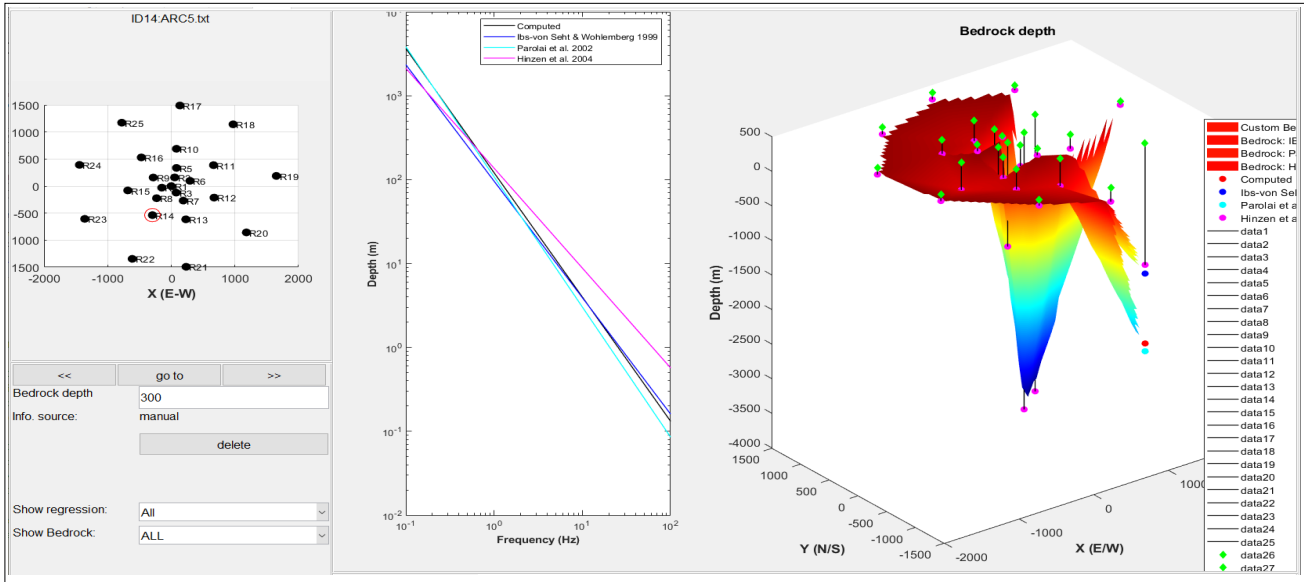
FIGURE 28.

Frequencies were inverted into depths according to the three approaches shown in the box of the middle figure. For all stations, we adjusted the bedrock depth manually due to a lack of the local well data. With this the computed regression line (black, middle figure) is in good agreement with the three given theoretical regressions. The depth distribution produced with the Monte Carlo inversion reflected on the right panel is close enough to the distribution of real bedrock interfaces.
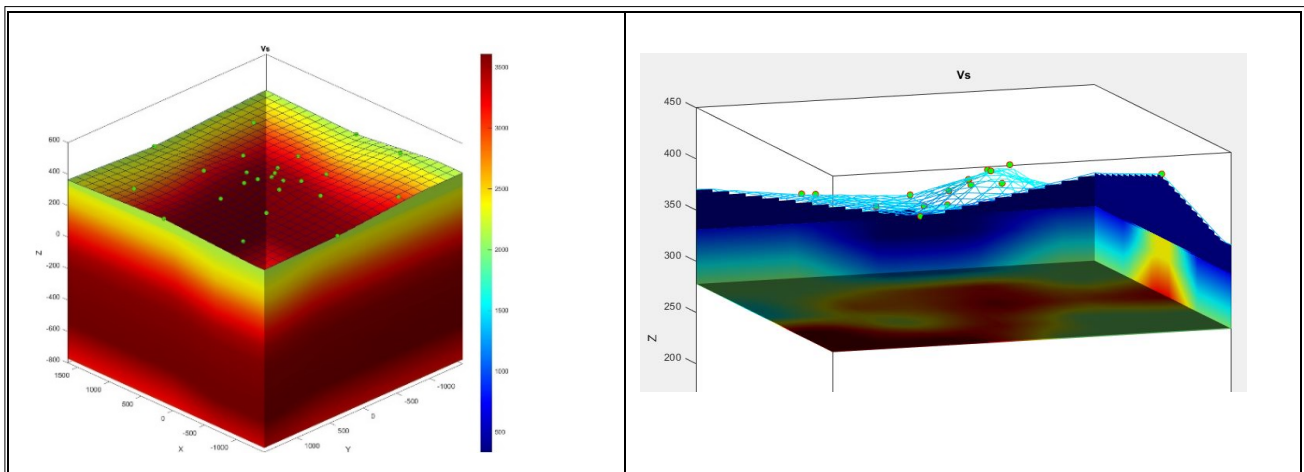
FIGURE 29.

3-D representation of ARCES deep (average model correlated with the SPAC computation until 1200 m) and shallow model (right, first 100 m). Note that the ARCES heights are between 331 and 414 above sea level.
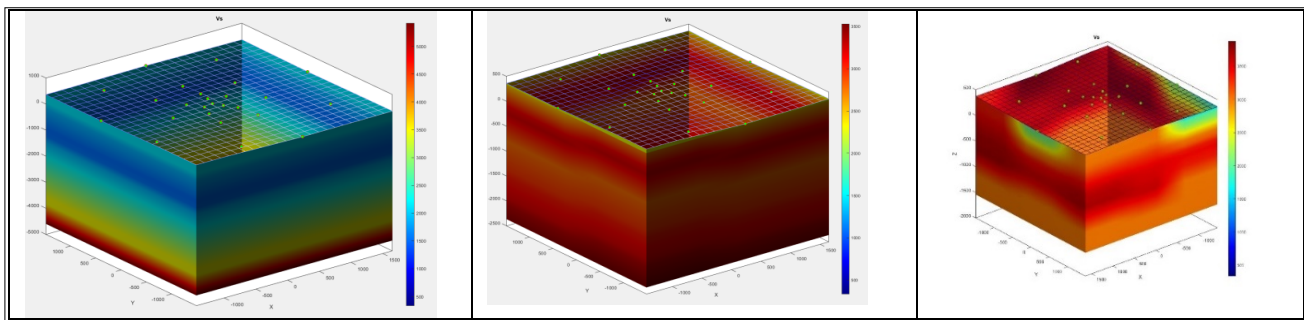
FIGURE 30.

Different ARCES models for different geological constraints. The left and middle models are average models, the right – a model with possible intrusions depicted in the chapter 9.1 covering Geological and Tectonic Settings.

noise. Figure 31 presents a QSVD decomposition of the ARA0 station noise record.

Several experiments were conducted with the HV-ratios built from the pure quaternion parts of the second principal component. The results are more consistent with the associated information than the raw data (see Figure 32). More experiments with the synthetic data are to be fulfilled. See also (Hobiger 2011) for the related quaternion formalism.
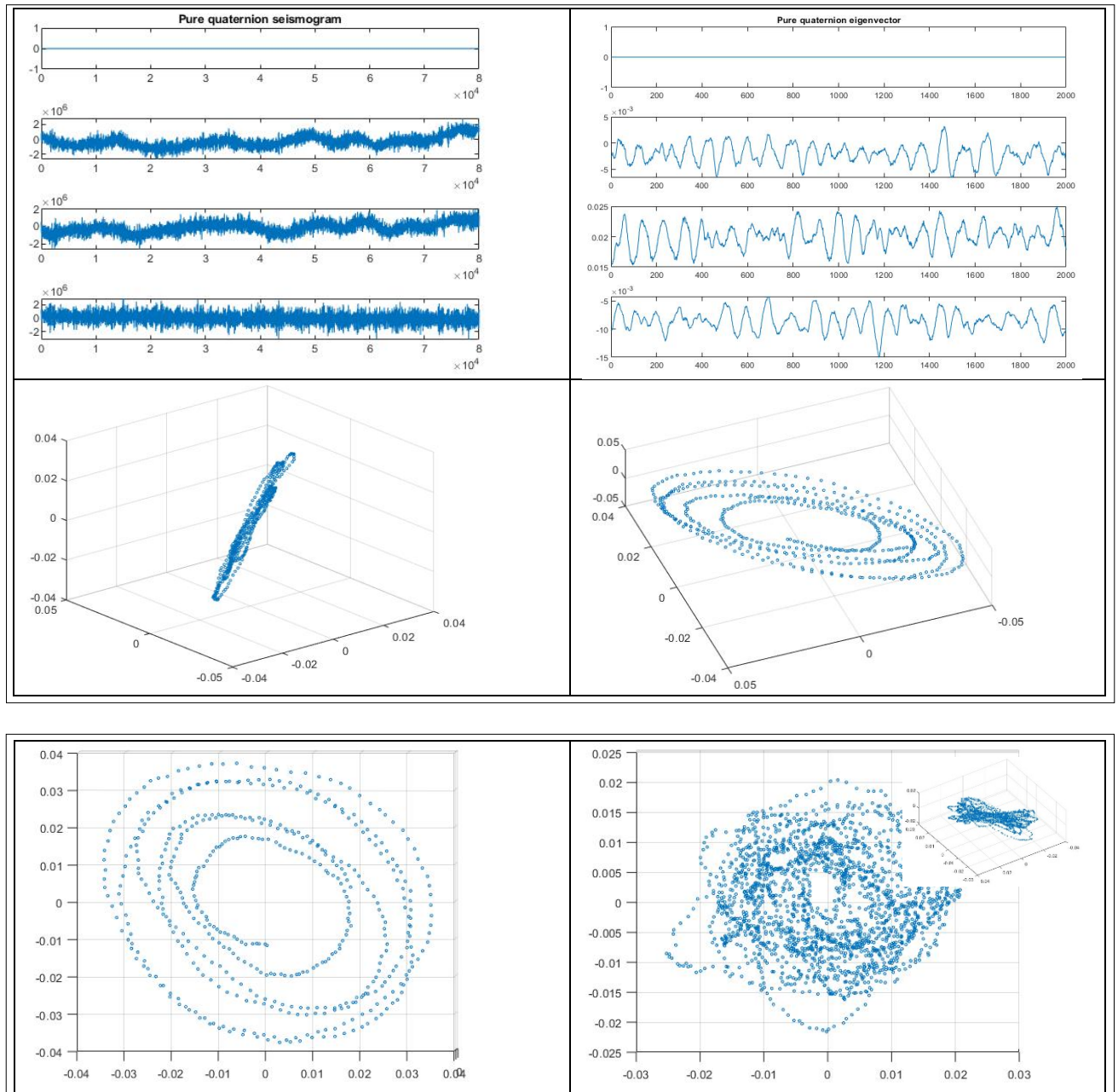
FIGURE 31.

Stacking one-by-one 3-C seismic record windows as columns form a Q-matrix, each row of which is a fully imaginary part of the 4-D structure (hypercomplex) with zeroed scalar part (upper left). The upper right is the best polarized eigenvector of the 0-mean non-filtered data, which can be considered as a second principal component of the input data. Its different isometric representation is shown in middle left and right. Comparison of the flat view of the Q-decomposed seismogram vs input of ARA0 with the dumbbell-like isometric inlay.
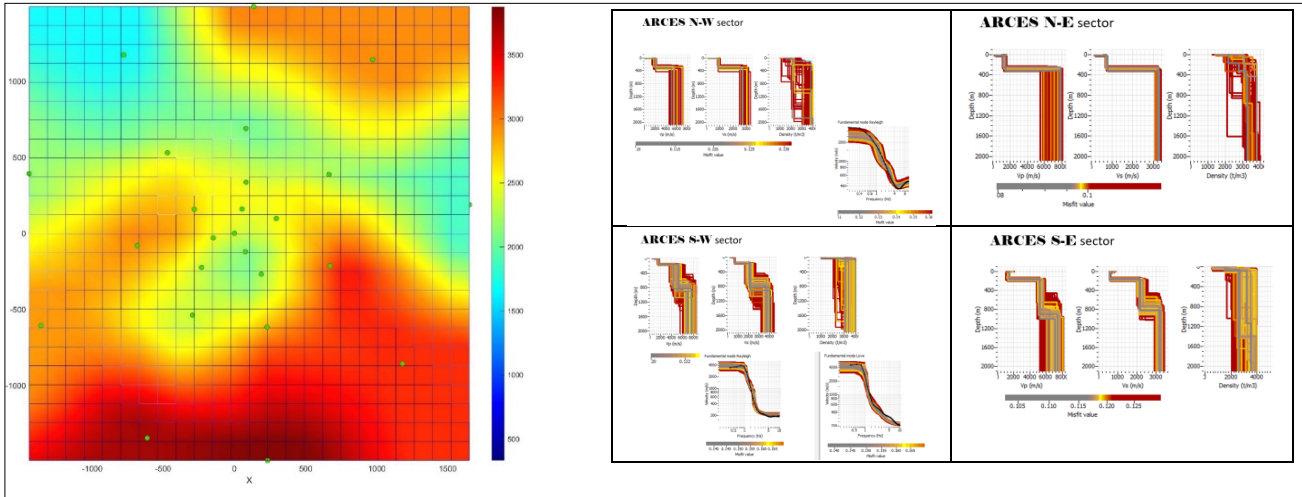
FIGURE 32.
Left, the lateral distribution of velocities at ~800 m depth beneath the ARCES seismic array corresponds to this distribution produced by the SPAC method presented on right (see also (Starovoyt 2022) for better resolution). Green dots are the ARCES array stations. Right panel shows, that the average Vs velocities are higher for the north-east quadrant of the left figure then for the north-west quadrant for the ~900 m depth, and the highest velocities are for the south-east quadrant, with the south-west velocities higher than for both northern sectors.

10. CONCLUSION

There is a wide set of tools that allow for the crustal velocity model restoration beneath the CTBTO array stations. Depending on the type of sensors (one dimensional or 3-D) different methods can be applied. The new generation of the state of the art software is required which would take into account described features of different approaches, with a strong machine learning component. The software would allow to some extent, a switch from the run time simulation to the template matching, to avoid the sometimes extremely tedious work of model adjustment in the absence or lack of additional observation data.

REFERENCES

Aki, K. (1957). Space and time spectra of stationary stochastic waves, with special reference to microtremors. *Bulletin of the Earthquake Research Institute* **25** 415–456.

Aki, K., Richards, P.G. (2002). *Quantitative Seismology*, University Science Books, Sausalito, California.

Ben-Menahem, A., Singh, S.J. (1981). *Seismic Waves and Sources*, Springer New York, New York.

Bonnefoy-Claudet, S., Cotton, F., Bard, P.-Y. (2006). The nature of noise wavefield and its applications for site effects studies. *Earth-Science Reviews* **79** (3-4) 205-227.

Bignardi, S., Mantovani, A., Abu Zeid, N. (2016). OpenHVSR: imaging the subsurface 2D/3D elastic properties through multiple HVSR modeling and inversion, *Computers & Geosciences* **93** 103-113.

Braathen, A., Davidsen, B. (2000). Structure and stratigraphy of the Palaeoproterozoic Karasjok Greenstone Belt, north Norway - regional implications. *Norsk Geologisk Tidsskrift* **80** (1) 33-50.

Haefner, R.J., Sheets, R.A., Andrews, R. (2010). Evaluation of the horizontal-to-vertical spectral ratio (HVSR) seismic method to deter- mine sediment thickness in the vicinity of the South Well Field, Franklin County, OH. *The Ohio journal of science* **110** (4) 77-85.

Herak, M. (2008). ModelHVSR—A Matlab® *tool to model horizontal-to-vertical spectral ratio of ambient noise. Computers & Geosciences* **34** (1) 1514-1526.

Hobiger, M. (2011). *Polarization of surface waves: characterization, inversion and application to seismic hazard assessment*. Thesis.

Hobiger, M., Le Bihan, N., Cornou, C., Bard, P.-Y. (2012). Multicomponent signal processing for Rayleigh wave ellipticity estimation: Application to seismic hazard assessment. *IEEE Signal Processing Magazine* **29** (3).

Hobiger, M., Bard, P.-Y., Cornou, C., Le Bihan, N. (2009). Single station determination of Rayleigh wave ellipticity by using the random decrement technique (RayDec). *Geophysical Research Letters* **36** (14).

Ibs-von Seht, M., Wohlenberg, J. (1999). Microtremor measurements used to map thickness of soft sediments. *Bulletin of the Seismological Society of America* **89** (1) 250-259.

Le Bihan, N., Mars, J. (2002). "Quaternion subspace method for vector-sensor wave separation". *11th European Signal Processing Conference* (Proceedings of the 11th European Signal Processing Conference, Toulouse, France, 2002). Institute of Electrical and Electronics Engineers, Piscataway, NJ, pp. 1-4.

Lontsi, A.M., *Sánchez*-Sesma, F.J., Molina-Villegas, J.C., Ohrnberger, M., Krüger, F. (2015). Full microtremor H/V(z,f) inversion for shallow subsurface characterization. *Geophysical Journal International* **202** (1) 298-312.

Lunedei E., Albarello D. (2015). HVSR curve by a full-wavefield model of ambient vibrations generated by a distribution of correlated surface sources. *Geophysical Journal International* **201** 1140-1153.

Lu, H., Plataniotis, K.N., Venetsanopoulos, A.N. (2008). MPCA: Multilinear principal component analysis of tensor objects. *Institute of Electrical and Electronics Engineers Transactions on Neural Networks* **19** (1) 18-39.

Molnar, S., et al. (2018). Application of Microtremor Horizontal-to-Vertical Spectral Ratio (MHVSR) analysis for site characterization: State of the art. *Surveys in Geophysics* **39** (2).

Nakamura, Y. (1989). A method for dynamic characteristics estimation of subsurface using microtremor on the ground surface. *Quarterly Report of Railway Technical Research* **30** 25-33.

Picozzi, M., Parolai, S., Richwalski, S.M. (2005). Joint inversion of H/V ratios and dispersion curves from seismic noise: Estimating the S-wave velocity of bedrock. *Geophysical Research Letters* **32** (11) 308.

Pina-Flores, J., et al. (2016). The inversion of spectral ratio H/V in a layered system using the diffuse field assumption (DFA). *Geophysical Journal International* **208** (1) 577-588.

Poli, P., Pedersen, H.A., Campillo, M., the POLENET/LAPNET Working Group (2012). Noise directivity and group velocity tomography in a region with small velocity contrasts: the northern Baltic shield. *Geophysical Journal International* **192** (1) 413–424.

Sánchez-Sesma, F.J., et al. (2011), A theory for microtremor H/V spectral ratio: application for a layered medium. *Geophysical Journal International* **186** (1) 221-225.

Starovoyt, Y. (2022). Deployment of different types of equipment in the IMS seismic networks. Current CTBTO 25th Anniversary Book. 2022.

Tsai, N.C., Housner, G.W. (1970). Calculation of surface motions of a layered half-space. *Bulletin of the Seismological Society of America* **60** (5) 1625-1651.

Van Der Baan, M. (2009). The origin of SH-wave resonance frequencies in sedimentary layers. *Geophysical Journal International* **178** (3) 1587-1596.

Vervliet, N., Debals, O., De Lathauwer, L. (2016). "Tensorlab 3.0 — Numerical optimization strategies for large-scale constrained and coupled matrix/tensor factorization". *2016 50th Asilomar Conference on Signals, Systems and Computers* pp. 1733-1738.

Witten, B., Shragge, J. (2006). Quaternion-based signal processing. *SEG Technical Program Expanded Abstracts* **25** (1).

Radionuclide Measurements of the International Monitoring System

M.A. Goodwin

Atomic Weapons Establishment, Reading, United Kingdom

A.V. Davies, R. Britton

Comprehensive Nuclear-Test-Ban Treaty Organization, Vienna, Austria

H.S. Miley, P.W. Eslinger

Pacific Northwest National Laboratory, Richland, United States of America

K. Ungar, I. Hoffman, P. Mekarski, A. Botti

Health Canada, Canada

Abstract

The International Monitoring System (IMS) is a unique global network of sensors tuned to measure various phenomenology, with the common goal of detecting a nuclear explosion anywhere in the world. One component of this network collects measurements of radioactive particulates and gases present in the atmosphere; through this, compliance with the Comprehensive Nuclear-Test-Ban Treaty can be verified. The radionuclide sub-network consists of 120 sensors across 80 locations, supported by 16 measurement laboratories. All radionuclide stations make use of a form of gamma ray spectroscopy to measure radionuclides from samples. This remains largely unchanged since the network was first established 20 years ago. Advances in sampling and spectroscopy systems can yield improvements to the sensitivity of the network to detect a nuclear explosion. This paper summarizes the status of the IMS radionuclide network, the current suite of technology used and reviews new technology that could enhance future iterations, potentially improving the verification power of the IMS.

1. INTRODUCTION

1.1. The Comprehensive Nuclear-Test-Ban Treaty

When it enters into force, the Comprehensive Nuclear-Test-Ban (Treaty) will ban all nuclear explosions anywhere in the world, be they in the atmosphere, underground or underwater. The Treaty, which was adopted by the United Nations General Assembly in 1996 and formally opened for signature on 24 September 1996, has been underpinned by a requirement for verification. Such verification requires a network of sensors to detect potential violations of the Treaty. A nuclear explosion can produce a variety of signals, such as seismic, infrasound, hydroacoustic and radionuclide signals. Therefore, these signals require continuous monitoring such that deviations from background noise, potentially caused by a nuclear explosion, can be identified.

Each of these monitoring capabilities is utilized in a network of 337 facilities known as the International Monitoring System (IMS). One such phenomena arising from a nuclear explosion is the creation and emission of radionuclides (radioactive isotopes) produced during the explosion. The IMS includes two types of radionuclide monitoring systems — particulate (or aerosol) and noble gas. This paper reviews the progress made in developing and deploying a system of radionuclide sensors around the globe and discusses the future of this one of a kind verification tool.

1.2. Radionuclide Monitoring

Radionuclides are predominantly produced during fission of heavy fuel actinides (such as ^{235}U or ^{239}Pu) or the neutron activation of other materials (such as stable isotopes present in steel), producing a range of radioactive 'activation products'. Depending on the level of containment, particularly for underground nuclear tests, such materials may escape from the explosion site and disperse into the atmosphere where they can be transported around the world. These radionuclides can be collected by either using high volume air sampling (HVAS) onto filter papers, or through separation of special elements. One such element is xenon, of which there are four radioactive fission product isotopes that are sufficiently long lived and produced in large quantities during a nuclear explosion to be detectable with current technologies. These form the basis of the noble gas monitoring network — a subset of the IMS radionuclide network. When complete, the current configuration of the IMS will consist of 80 particulate monitoring stations and 40 noble gas monitoring stations. Once the Treaty enters into force, the number of noble gas stations may increase to 80. As of November 2022, there were 72 particulate stations and 26 noble gas stations operating (see Table 1).

Table 1. Current International Monitoring System Radionuclide Network Status, Correct as of December 2022

Technology	Certified	Installed (not certified)	Under construction	Under negotiation	Not started	Total
Radionuclide — particulate	72	0	1	2	5	80
Radionuclide — noble gas	26	6	2	0	6	40
Total	98	6	3	2	11	120

Data from the IMS is sent to the International Data Centre (IDC). IMS data is made available to States Parties through their National Data Centres (NDCs) — designated technical organizations tasked with providing evaluations of IMS data to their respective governments.

Since the 1990s States have invested heavily in developing technology for automatic sampling and measurement of radionuclides in the IMS. Such systems include those used in particulate stations — radionuclide aerosol sampler analyser (RASA), CANA, Cinderella, Petrianov (see
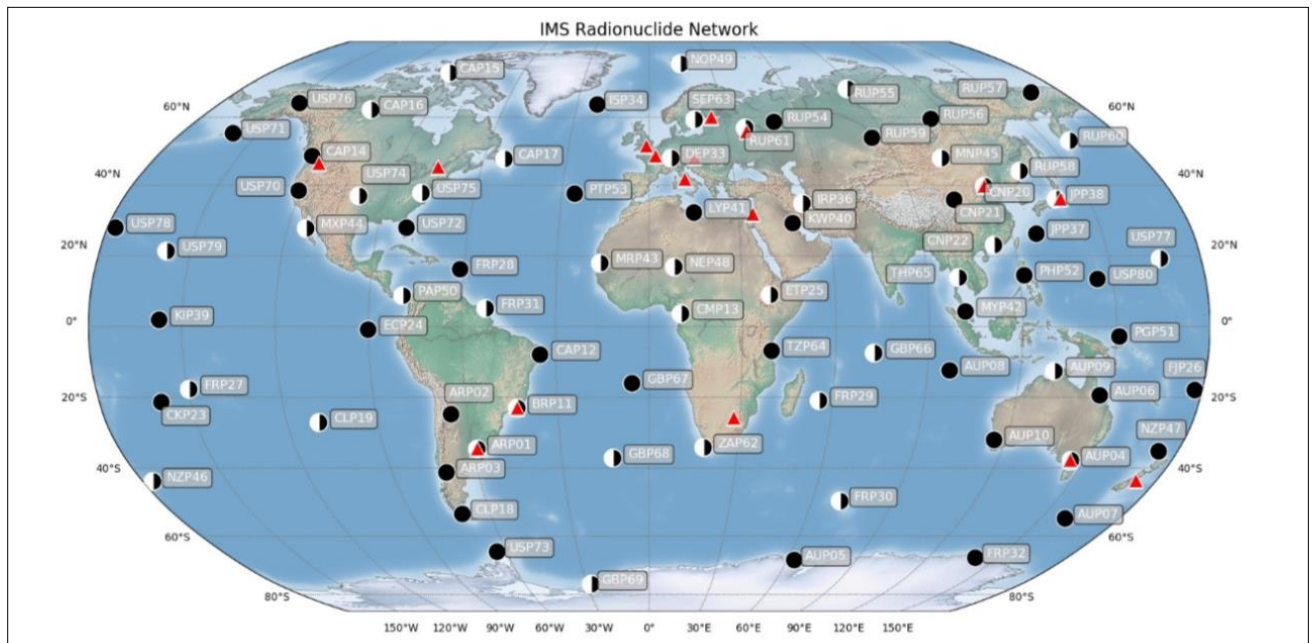
FIGURE 1.

Map showing the radionuclide IMS – black points show particulate radionuclide stations, half-filled circles show particulate plus noble gas combined stations and red triangles show radionuclide laboratories (from Goodwin et al. 2022a).

Section 2.1) and those for noble gas monitoring —ARSA (Reeder et al. 1998), SAUNA (Ringbom et al. 2003 and 2017), SPALAX (Fontaine et al. 2004, Topin et al. 2020), Xenon International (Hayes et al. 2015), ARIX (Dubasov et al. 2005) and MIKS. All station systems use measurement technology based on gamma spectrometry and produce spectral data which, when analysed, can report activity concentrations (Bq/m^3) of radionuclides in the atmosphere. Some current systems can measure to a sensitivity of μBq/m^3 (one decay every one million seconds, per cubic metre of air) for some radionuclides and the ultimate measure of a system is the 'detection limit'. The detection limit is often referred to as the minimum detectable activity (MDA) or, in the case of these air-sampling systems, minimum detectable concentration (MDC), i.e. the minimum quantifiable activity per cubic metre of air sampled.

Another important aspect to radionuclide monitoring is the sampling time. In order to collect a sufficiently large volume of air (corresponding to a larger sample) the stations must sample from the atmosphere for periods of up to 24 hours. This means that there is a limit on the temporal resolution of sampling data. New systems are improving the measurement technologies (see

Sections 2.5.2 and 3.2) and collection techniques used (see Section 2.5.1).

Section 4 describes how improving the temporal resolution of radionuclide data can enhance the probability of detection and constrain a possible source region. New source reconstruction techniques can make use of this data, but must also account for background signals which, in the case of radioxenon, are present in significant (and dynamic) quantities in some parts of the world (Achim et al. 2016). Studies to characterize and understand the radioxenon background improve the ability to distinguish between civilian and non-civilian (weapon) sources of atmospheric and environmental radionuclides, which is primarily achieved by comparing isotopic ratios (Kalinowski et al. 2010).

For radioxenon the background signal from civil nuclear facilities is a problem for nuclear explosion monitoring since the isotopes produced in a reactor are largely the same as those produced from a fission based nuclear explosion (although some significant differences can occur). Noble gases are the most difficult isotopes to abate from release and as such these civil radioxenon emissions cause false positive detections on the IMS (Bowyer 2021). Only through networks such

as the IMS is this background quantified and monitored daily.

Through the CTBT verification community several working groups have been established, such as the International Noble Gas Experiment (INGE) and the Workshop on Signatures of Man-Made Isotope Production (WOSMIP). Expertise is developed and shared both within the radionuclide monitoring community and with those outside, such as medical isotope production Facilities (MIPFs). Such outputs have included advances in xenon mitigation technology, improved radioxenon background simulations through atmospheric transport calculations and stack monitoring of civil nuclear facilities, such as the Source Term Analysis of Xenon (STAX) project (Metz et al. 2019). The radionuclide network is supported by 16 radionuclide measurement laboratories (14 of which are currently operational). These laboratories specialize in the measurement of IMS samples, which can be sent to any of the laboratories once they have been certified for operations. All CTBT radionuclide laboratories measure particulate samples (in the form of filter papers) and five laboratories are also currently certified for noble gas measurements (Schroettner et al. 2010, Foxe et al. 2021' Douysset et al. 2017, Goodwin et al. 2020). Radionuclide laboratories play a key part in verifying the performance of the network (through an extensive quality assurance/quality control programme) and verifying the global compliance to the CTBT by re-measuring samples of interest. The laboratories can operate at greater levels of sensitivity than IMS stations, sometimes by using underground facilities (Aalseth et al. 2012) or advanced technologies such as coincidence detection and cosmic veto systems (Britton et al. 2019). Section 5 discusses recent advances in this area.

1.3. History

Environmental monitoring for radionuclides began at the dawn of the nuclear age. One example is the monitoring of a nuclear production site in the 1940s (Singlevich 1948). While monitoring of that era was crude by modern standards, the monitoring was sufficient to detect remote atmospheric testing (Friedman et al. 1996). By the early 1960s continuous monitoring of the atmosphere had begun (Perkins et al. 1990). The early approach to atmospheric monitoring employed a very high volume (500-1000 cfm or 874-1748 m^3/h) aerosol sampler collecting aerosols on a filter for up to a month, followed by a period of decay for radon daughter[1] isotopes, then two weeks of measurement on a large, dual-crystal sodium iodide (NaI) radiation detector (Figure 2). Figure 3 shows that this approach yielded excellent results detecting nuclear explosions in the atmosphere of the northern hemisphere for decades. In the early years dual NaI detectors were employed in coincidence mode on 500 cfm (874 m^3/h) samples, and in later years, dual high purity germanium (HPGe) detectors were employed on 1000 cfm (1874 m^3/h) samples. One disintegration per minute per thousand standard cubic meters (1 dpm/kSCM) is about 17 μBq/m^3. By comparison, IMS sensitivity range is 10-30 μBq/m^3 (see Figure 3), but operate with vastly improved selectivity, which can resolve far more complex spectra in a much shorter time frame.

The manual system in use from the 1960s to the 1980s was more sensitive than the particulate stations developed for the IMS owing to the longer sampling periods. IMS aerosol stations operate on a daily regimen in a network of 1000 km station separation rather than the 10 000 km source to sampler distance employed by earlier systems.

By the 1990s the news cycle had become a 24-hour phenomenon and it was far from acceptable to have a month-long response time to satisfy leadership decision-making processes. During the same period it also became apparent that aerosol collection and measurement functions could be automated. Using large modern germanium detectors, daily samples could be measured at sensitivities similar to the original one-month samples on dual NaI detectors (Miley 1997). The original sample collection time period

---

[1] Aerosol collections filter particles from the air, not radon. The solid decay products of the ^{222}Rn decay chain diminish with a half-life of less than 30 minutes. But the solid decay products of the ^{220}Rn decay chain diminish with the 10.6 hour half-life of ^{212}Pb. These products are greatly reduced at one day and undetectable at one week.
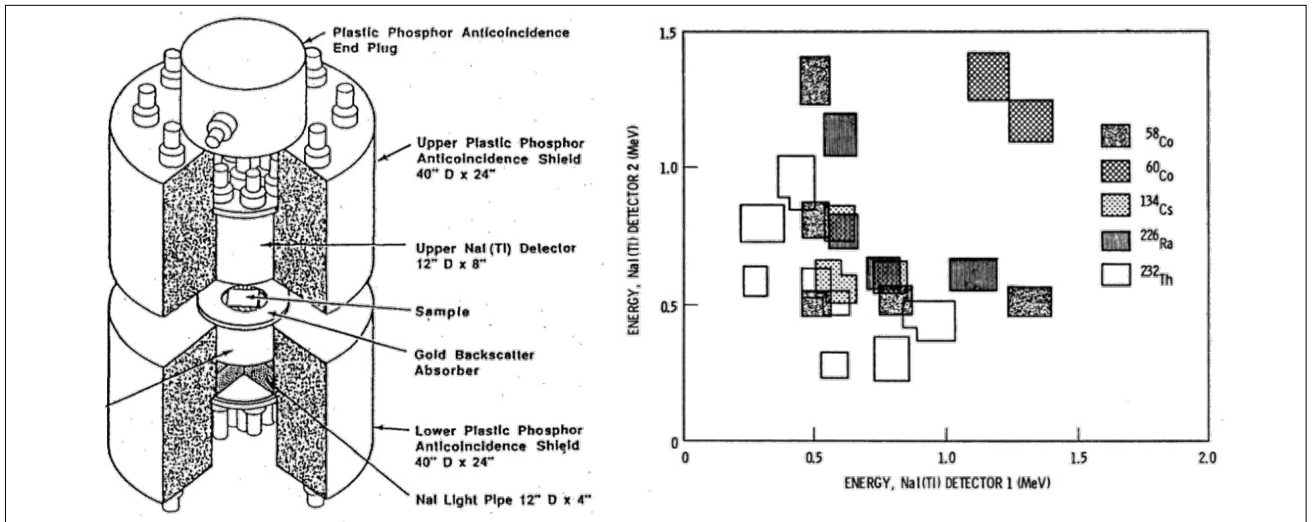
FIGURE 2.
A dual sodium iodide (NaI) detector system in use before HPGe detectors were prevalent (Reeves 1992, Wogman et al. 1969) and analysed with a multidimensional scheme (Brauer et al. 1975).
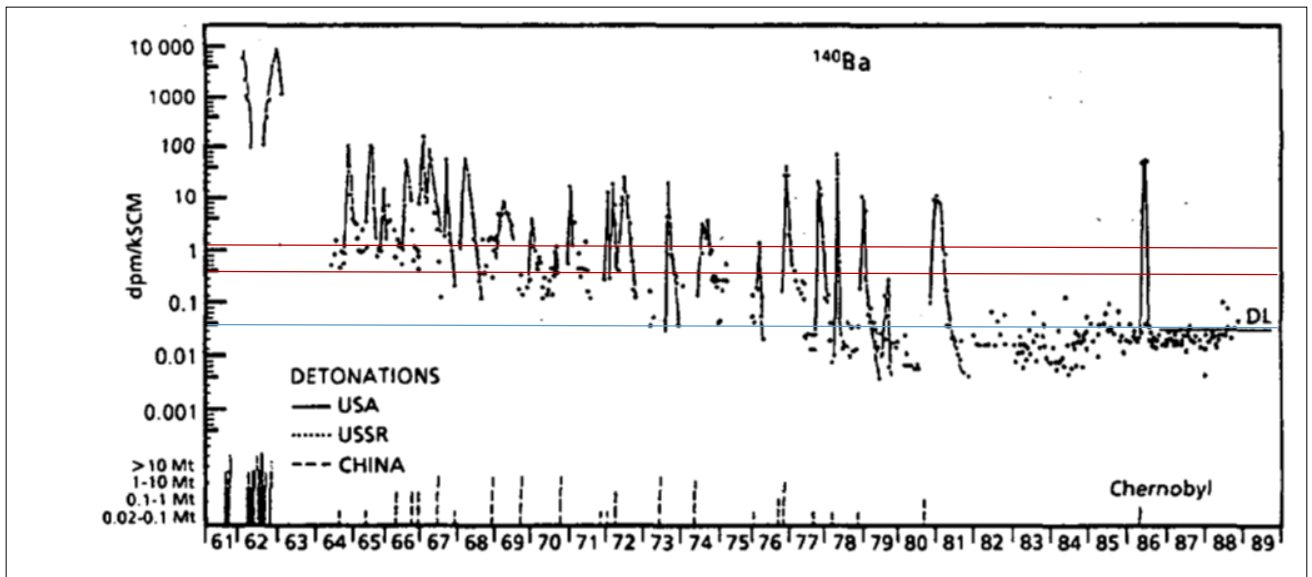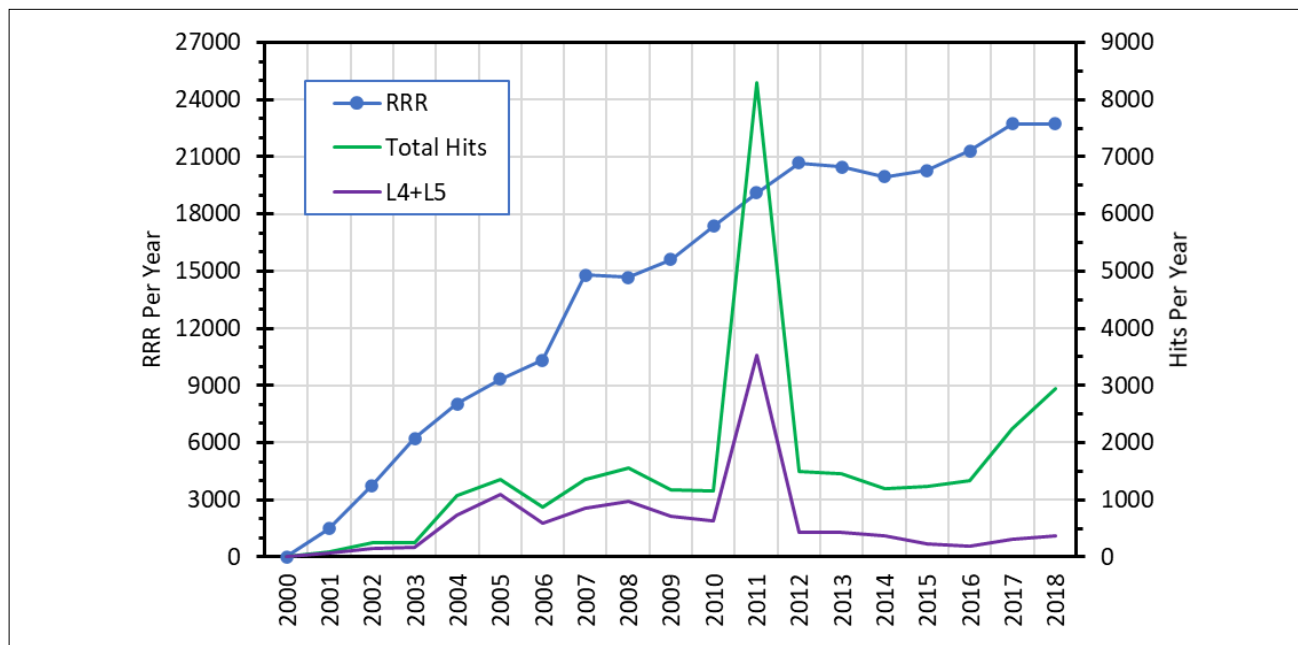

FIGURE 3.
[140]Ba versus time (Perkins et al. 1990) showing correlation with atmospheric or venting 'leaky' underground nuclear tests. The approximate 0.05 dpm/kSCM detection limit (blue line) for these systems was about 1 µBq/m³. By comparison IMS sensitivity range is 10-30 µBq/m³ (red lines).

(two weeks) was selected to boost sensitivity and it could not worsen the location capability of atmospheric collections because of the poor knowledge of the movement of the atmosphere. Event identification was based on age dating methods using two or more isotopes in conjunction with seismic observations. In the 1990s, a faster collect-decay-measure scheme gave higher quality nuclear results and was reasonably matched to atmospheric transport modelling, with one day each for collections, natural radioactivity decay, and nuclear measurement. Seismic location uncertainty of approximately 1000 km² was dwarfed by atmospheric location uncertainty of approximately 100 000 km². So, radionuclide measurements contributed to seismic signals as before. However, in the early days of nuclear monitoring of the atmosphere reactors and civilian nuclear processes were rare. Today this is not the case and as a result, isotopic ratios are valuable for discriminating nuclear explosions from, for instance, operational civilian reactor releases.

In 1995 the IMS Expert Group reported on concepts, goals, and approaches for CTBT verification monitoring (Conference on Disarmament 1995).

FIGURE 4.

The growth of the number of RRRs is shown with the evolution of hits per year. Total hits are the sum of sample RRRs with levels L3, L4 and L5 (Miley et al. 2021, PNNL-SA-32446). The peak is due to emissions from the Fukushima Daiichi nuclear reactor accident.

For aerosol signals in the atmosphere this group adopted the goal of a detection probability of 90% for a non-evasive 1 kt release (2×10^{14} Bq of ^{140}Ba) within 10 days by a network of ~75 stations. The stations were estimated to require an MDC for ^{140}Ba of about 10 µBq/m^3.

The measurement goals for xenon are more ambitious — to detect xenon leaking from underground nuclear tests. For these the scenario assumed a 10% release of gas emitted at ground level with no buoyancy, then travelling at low surface wind speeds.

Many phenomena and challenges have been observed since (Conference on Disarmament 1995). For example, the Fukushima Daiichi nuclear reactor accident occurred in 2011 and medical isotope production of xenon has emerged as a major global phenomenon. Several industrial releases of iodine have happened and there have been numerous background detections of medical isotope usage (^{99}Mo). Additionally, because many seismic bulletins are not resolved, there is greater opportunity for radionuclide monitoring to return an improved location estimate (smaller plausible region) of a radionuclide release.

Figure 4 shows the rate of daily Reviewed Radionuclide Reports (RRR) per year as the system accumulated additional aerosol systems. Level 4 and Level 5 detections are the most interesting detections as they contain one (L4) or two or more (L5) isotopes from a list of high priority radionuclides. About 300 000 such RRRs have been produced at the time of this writing. During this time period (2000-2018), the number of stations in operation went from zero to almost 70.

2. PARTICULATE NETWORK

The original rationale of radionuclide aerosol monitoring in the IMS was to detect small atmospheric explosions. In this case waveform sensing modalities would give a precise time of the explosion and a good location estimate. Aerosol systems need only confirm that the triggering waveform event was nuclear in nature. Thus the network was

designed to robustly detect a sub1-kt explosion in the atmosphere (Conference on Disarmament 1995) based on a single isotope, identify sources using isotopic ratios and be available in a timely way for on-site inspections (OSI) (total IMS reporting time, 72 hours). The key isotope for detection was settled as ^{140}Ba, which is among the most highly produced and easily detected isotopes from nuclear fission.

2.1. Current Systems

From the detection requirements the number of stations and their required sensitivity was determined, providing the basis for the detection of Treaty-relevant radionuclides in the IMS. To meet these criteria a minimum network of 80 stations located around the globe was required, which was defined in the Treaty. All 80 of these stations shall have a particulate monitoring system. The equipment for a typical particulate station consists of an HVAS with a flow rate greater than 500 m^3 per hour and a HPGe detector system with a relative efficiency of at least 40%[2].

Currently there are 72 radionuclide IMS stations installed and certified by the Provisional Technical Secretariat (PTS). There are two main types of equipment, manual and automatic systems, which currently operate on the same collection-decay-measurement cycle (see Figure 5). The following sub-sections give information on each radionuclide station type.

2.1.1. Radionuclide Aerosol Sampler Analyser

The radionuclide aerosol sampler analyser (RASA) was designed in 1995 by Pacific Northwest National Laboratory (USA) to automatically sample and measure trace levels of radionuclides in large atmospheric air samples. It was first installed at an IMS location in 1998 and is subsequently on the fourth-generation model. The RASA contains a large blower that forces air through a polypropylene filter at a flow rate of about 1000 m^3/hr. The daily sample consists of six filter sections which are sealed in a mylar strip and after the decay period, it is transferred to the detector system and wrapped around the HPGe crystal. Measurement and state of health data are automatically transmitted to the IDC.

2.1.2. Snow White

The Snow White sampler units (now built by Senya) were developed to be part of the Finnish national network for monitoring radioactive fallout after the Chernobyl accident. This work also formed the basis for the determination of IMS minimum requirements for particulate samplers. The filter is placed inside a sampling head consisting of two hemispherical covers 91 cm in diameter. Air is drawn through the filter at approximately 800 m^3/hr, trapping particulates in a filter consisting of 3M polypropylene. After 24 hours of sampling, filters are compressed to disks with a diameter of 50 mm and a height of

Collection	Decay	Measurement
24 hours	24 hours	24 hours
particles are collected on a filter with a particulate collection efficiency of ≥ 80% at ∅ = 0.2 μm	the filter is left to allow the decay of NORM, specifically Rn progenies from the U and Th decay series	measurement on a HPGe, after the preparation of a reproducible geometry
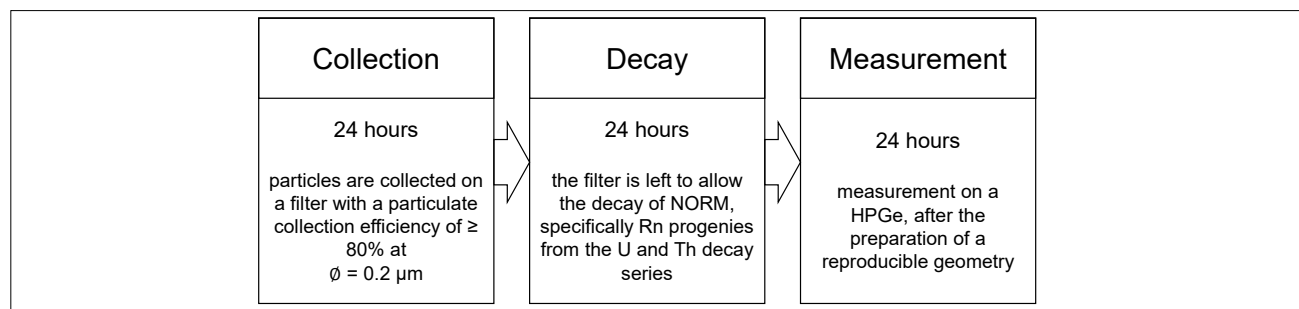
FIGURE 5.
Schematic diagram showing the process of particulate filter from collection to measurement. NORM: Naturally occurring radioactive material.

---

2   Efficiency relative to a 3 in × 3 in (diameter × height) NaI(Tl) crystal, based on the 1332 keV peak of a ^{60}Co source positioned 25 cm from the detector. These criteria, while a useful metric based on technology available at the time of its definition, can also be 'substantially met', especially for planar HPGe crystal types, which will typically outperform co-axial designs for this application, but not quite meet this requirement.

FIGURE 6.
RASA system at JPP38.

FIGURE 7.
A Snow White HVAS situated at RN67.

5 mm and packaged in PVC containers for storage and measurement. Measurements are completed by placing the compressed filter disc onto a HPGe detector and the measurement data is transmitted to the IDC.

2.1.3. Cinderella

The Cinderella sampler units (now built by Senya) were developed to be a fully automated system operating on either a 6-hour or 24-hour sampling cycle. For CTBT purposes the sample filter is changed daily. The system is designed to be autonomous for 15 days after which an operator is required to mount fresh filters[3]. The system is comprised of an air sampling unit which has a flow rate between 500 m^3/h and 1000 m^3/h and a filter manipulator unit comprised of a 3-D robot arm. Filter cassettes are loaded into the system and manipulated into the flow. After collection for 24 hours, the sample preparation is performed by the 3-D arm. A cutting head cuts the filter into 15 filters 84 mm × 82 mm and then uses vacuum to transfer the filters into a plastic holder. They are then located in an area for 24 hours decay before transfer to the detector for measurement. All stages of the process are followed by scanning the filter barcode. Samples are measured on an HPGe p-type detector and spectra and state of health data are automatically sent to the IDC.

2.2. Detector Systems

Since the first installation of stations in the IMS the detection principles have been the same as those used in the early 1990s. The introduction of electrically cooled systems has undergone continual improvement from the early 'CryoTIGER' and 'X cooler' offerings. The current generation of coolers are far more reliable and offer improved efficiency ('CP5' and 'ICS' systems from Mirion and Ortec respectively) as they are based on Stirling coolers in comparison to the early pulse tube refrigeration units.
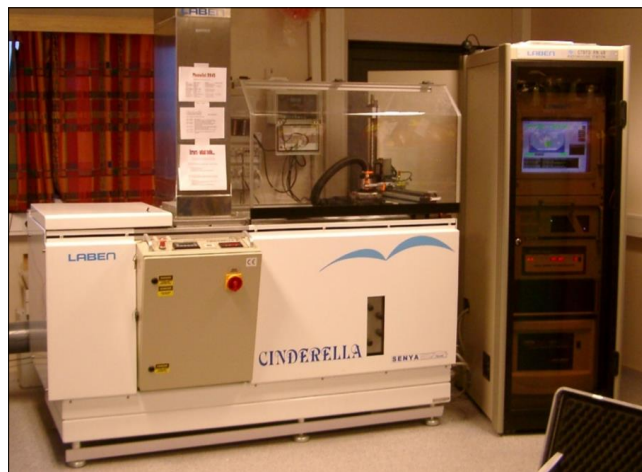
FIGURE 8.
Cinderella installed at NOP49.

---

[3]   New versions can go up to 60 days between refills.

The initial detector systems installed in the IMS were comprised of analogue multichannel analysers. These have been upgraded to the latest digital signal processing units commercially available, offering superior performance and greatly reduced complexity.

As the detector signal is now digitized very early in the signal processing chain (compared to analogue systems) drift and resolution instability are greatly reduced. Digital systems can record the time of the event giving more analysis power than conventional standard pulse height analysis (PHA) modes used within gamma spectrometry. This type of acquisition mode is not yet implemented in the IMS but is discussed in section 2.5.2 of this paper.

There has been significant development in the manufacturing of germanium crystals with major manufacturers offering planar crystals, optimizing the counting efficiency for geometries counting on the end cap and photon energy ranges typical of IMS samples. They also both deploy a low noise back-contact to the crystal that reduces noise and improves resolution. These crystals have benefits when counting samples from a manual station that are compressed into a puck, but for the RASA that relies on the wrapping of the sample around the crystal, a standard (coaxial) detector configuration is still the optimal solution.

2.3.   Minimum Detectable Concentration Discussion

To calculate the MDC for an isotope, the minimum detectable counts are converted to a concentration using the gamma branching fraction, *Br*, the collected air volume, *V*, the measurement time, t_c, and the efficiency and solid angle, $\varepsilon\delta\Omega$. Making a simplifying assumption that only ^{212}Pb Compton scatter events, $[^{212}$Pb], are responsible for the background in the energy region of interest, the width of which is some multiple of the full width at half-maximum (FWHM) of the spectrometer and collecting a

number of terms into a leading constant (*k*), the MDC equation has the following form (Miley et al. 2019) as shown in Equation 1.

$$MDC \cong k\sqrt{\frac{[^{212}Pb] \times FWHM}{V \times t_c \times \epsilon\delta\Omega}} \qquad (1)$$

Possible ways to shorten the integration and measurement time from 24 h while maintaining about the same MDC, include increasing *V* or $\varepsilon\delta\Omega$, or decreasing the measured background with more decay. With electrostatic precipitation, it may be possible to increase *V* and decrease power simultaneously. If the sample collection media is substantially thinner and more foldable than current RASA filters, an additional improvement in $\varepsilon\delta\Omega$ could be realized. If the design still used the maximum 72 h allowed by the IMS from the start of sample collection to the end of measurement, the time for decay of radon progeny could be substantially increased. Thus, an optimal design could potentially simultaneously shorten the measurement time *t*, increase *V* or $\varepsilon\delta\Omega$, and decrease the measured background.

The relative effect of different design configurations on the MDC is shown in Table 2 (Miley et. al. 2019), where the current RASA performance is in row A. The MDC factors also use the assumption that the background counts are dominated by the presence of ^{212}Pb. This has been experimentally verified for continental stations, but there is less ^{212}Pb present in samples taken at island stations. Preparing a 7.5 × 7.5 cm compact, folded sample directly to the detector face will improve $\varepsilon\delta\Omega$ by more than a factor of two, and doubling then tripling the air flow, results in a much better (lower) MDC in rows B, C and D. Rows A and E show that with a compact, folded sample geometry, a sampler could operate in a 12-hour mode with the same MDC as the current 24-hour mode. Doubled airflow and the compact, folded geometry make the 8-hour results in row F almost equivalent to today's MDC, where tripling the airflow as in row G improves over today's MDC.

Table 2. Possible Measurement Schemes and the Impact on MDC for Samples with ^{212}Pb Contributions to the Background Concentrations
(The air flow rate and the MDC have been scaled to 1 for the current RASA, and $\epsilon d\Omega$, or the efficiency of the sample-detector geometry, is scaled to the efficiency of a point source on the detector face. Current RASA performance is given in Row A)

Row	Geometry $\epsilon\delta\Omega$	Flow Rate	Sample & Count (h)	Decay Time (h)	MDC Factor	MDC Factor with Added Detector
A	0.2	1	24	24	1.00	NA[a]
B	0.5	1	24	24	0.63	0.45
C	0.5	2	24	24	0.45	0.32
D	0.5	3	24	24	0.37	0.26
E	0.5	1	12	48	1.00	0.71
F	0.5	2	8	56	1.07	0.76
G	0.5	3	8	56	0.88	0.62

[a.]The current filter wrap-around geometry in the RASA does not support adding an additional detector.

Component failures are a considerable concern for the IMS where 95% availability is required. At the core of an aerosol monitoring system is an HPGe detector. While these detectors have a very good mean time to failure, when a failure does occur, it can take weeks or months to get a new detector into place and is thus detrimental to a station's yearly uptime requirement. For these and other reasons, it is valuable to run a second detector simultaneously, providing a modest improvement to the MDC, but allowing the station to substantially meet MDC requirements when one detector fails.

2.4. Particulate Monitoring Following the Fukushima Daiichi Nuclear Accident

An interesting example of the power of the aerosol monitoring network is the Fukushima Daiichi nuclear accident. While there are estimates that the xenon release from the affected nuclear plants was near complete (Schöppner et al. 2012, Eslinger et al. 2012) the aerosol release was suppressed greatly by the safety systems of the plants: released gases had to cross a large tank of water, thereby removing most particles (Achim et al. 2014). The three elements released in large quantities, Caesium (Cs), Iodine (I), and Tellurium (Te) are all gases at high temperature. Thus, the release fraction of these elements was perhaps as much as 100 times less than the xenon isotopes. That would put the release of these elements in the range of a 10 kt to 50 kt explosion, with all other elements essentially missing. These three elements were seen all over the northern hemisphere. One study of North American signals focused on the ratio of two iodine isotopes (Biegalski et al. 2012). Iodine has a complicated chemical reaction with the atmosphere and is difficult to compare to other elements, but the ratio within iodine isotopes avoids most of that issue. In Figure 9, the ratio of ^{133}I to ^{131}I is graphed vs model estimates for reactor production of iodine isotopes and an instantaneous production from fission of uranium.

This analysis works because the half-life for decay of these two isotopes is quite different: ^{133}I ($T_{1/2}$ = 20.8 h) vs ^{131}I ($T_{1/2}$ = 8.02 days). In instantaneous production nuclear physics alone dictates the ratio of these isotopes and they immediately begin to decay at different rates. In a reactor the fission production of these would be quite similar, although the thermal neutron energies of reactors produce slightly different fission product composition compared to fission spectrum energies. As the reactor continues to operate, these fission atoms accumulate, but also decay away. The longer-lived isotope would accumulate to higher levels, predicted simply by the inverse ratio of the half-life of the pair. Thus, after collection and detection, if short lived isotopes are detected along with longer lived isotopes of the same element, reactors and explosions can be objectively discriminated.
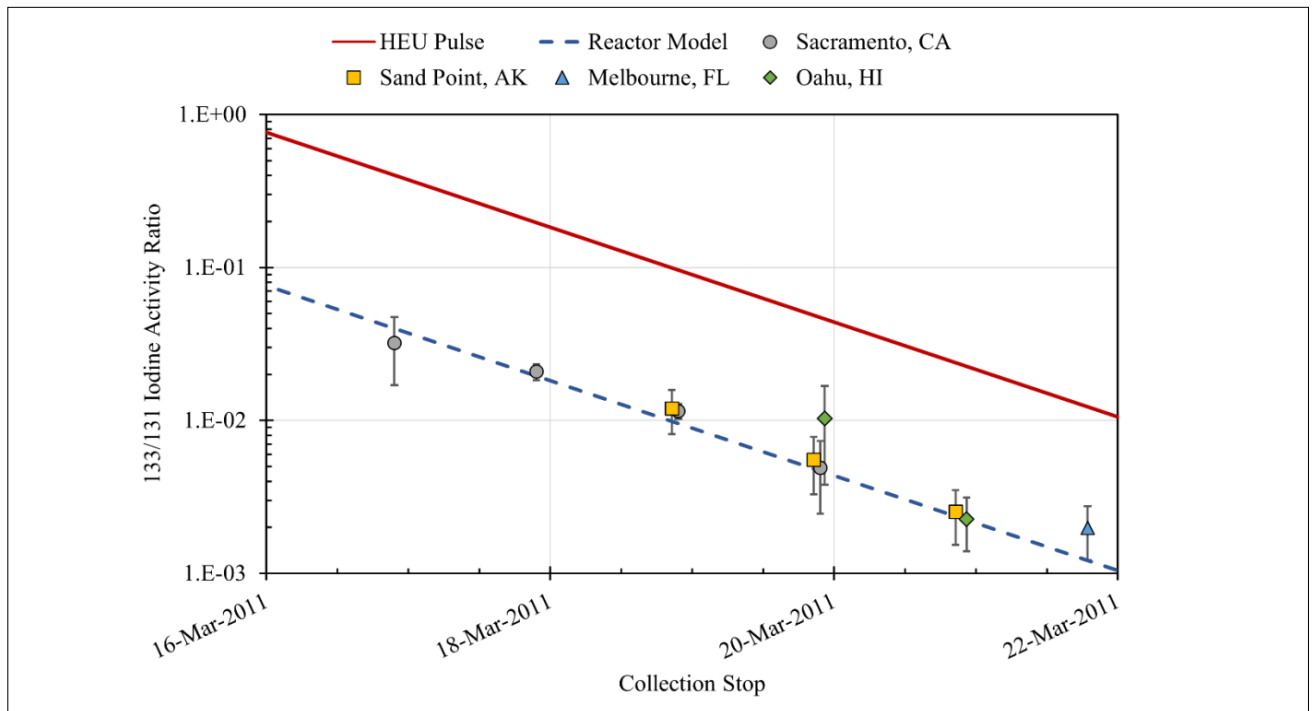
FIGURE 9.

Ratio of iodine concentrations from IMS stations in the United States with two sigma uncertainties plotted. These show consistency with slow reactor fission of uranium and inconsistency with a sudden fission of highly enriched uranium pulse on 11 March 2011.

On the vertical axis of Figure 9, the reactor model and pulse curves are separated by about one order of magnitude. The isotope ^{132}I has a half-life of 2.30 hours. If this isotope was detected, the separation of the models for the ^{132}I/^{131}I would probably be another order of magnitude apart.

2.5. Next Generation Systems

2.5.1. Next Generation Air Sampler Systems

There are various new capabilities desired for aerosol systems. Some are motivated by the Fukushima disaster, some by the desire for the 79 aerosol systems to augment the 39 xenon systems planned so far for the IMS, and others for radionuclide monitoring to support waveform event screening[4]. These new capabilities cannot come at the expense of the original capability foreseen in (Conference on Disarmament 1995).

In the 1990s the original aerosol design approach was for a moderately low-level mission (Kalinowski and Schulze 2002). In other words, the signals of interest (e.g. a leaking underground nuclear test at a great distance) were expected to be weaker than the signals created by the decay products of natural radon found in the atmosphere: ^{212}Pb, ^{212}Bi, ^{214}Pb, ^{214}Bi and ^{208}Tl. The network design criteria included a 90% probability of detection within about two weeks (Conference on Disarmament 1995). The time period was driven in part by slow air transport in equatorial regions. The low-level scenario required three days to complete any sample. With improvement, this signal scenario could be updated using modern technology to achieve the same sensitivity as the original RASA from a 12-hour or perhaps 8-hour collection, thus driving a significantly smaller location uncertainty (Eslinger et al. 2016).

---

[4] There are currently 79 locations identified for the IMS radionuclide network, which when complete will comprise of 80 locations.

Table 3. Capability Set Desired for a Next Generation Aerosol Monitoring Capability and Drivers

Capability	Reason
True real-time gross radiation measurement of collected sample	• Consequence management for nuclear emergencies • Location refinement from plume time of arrival for remote explosion monitoring
Early isotopic measurement for high level emissions	• High level event characterization within hours after collection, more than two days sooner • Increased sensitivity to short half-life isotopes, like ^{133}I ($T_{1/2}$ = 20.8 h) or ^{132}I ($T_{1/2}$ = 2.3 h)
Measurement after modest radon decay, the original IMS mission	• Balanced sensitivity and timeliness
Very low background measurement after one week of decay	• Confirmatory measurement for early-time or IMS detections • May add isotopes for low level event characterization • Ten times more sensitivity to longer-lived isotopes, like ^{131}I ($T_{1/2}$ = 8 days)
Improved measurement sensitivity	• Improvements in sensitivity are possible, such as using coincidence detector systems (see 2.5.2)
Improved robustness	• Adding a secondary detector as a 'hot spare' would improve robustness of the station and decrease down-time during equipment failures

The Fukushima disaster provides an example of how consequence management interests are aligned with verification interest. Timeliness was considered only from the perspective of an OSI, and only the time from the arrival of a plume to data transmitted to Vienna (Conference on Disarmament 1995). Fukushima revealed that responsible authorities wished to have current information and regretted even the transport time of the atmosphere from the source to the station. This is quite a different situation to the period between the 1940s and 1990s, where weeks and months passed before radionuclide data was obtained.

The Fukushima disaster, which released on the order of 10-kilotons worth of some fission products, signals were many times stronger than natural radioactivity, and the measurement results were substantially later than desirable by responsible authorities. Waiting 24 hours for negligible radon-related signals to decay was counterproductive in this situation. Consequence management and verification interests could be simultaneously accommodated by a radiation detector measuring radioactivity on the filter as aerosols accumulated on it. This would give an indication of the arrival of gross radioactivity in the air in real time. Linked to local, national, or global emergency management, the information would be invaluable in directing actions to protect life and property (Burnett et al. 2017).

Atmospheric or surface nuclear explosions are classic IMS aerosol missions and yet the Fukushima disaster showed that IMS aerosol systems were not optimally designed for high-level samples one would obtain from those sources. For this signal scenario, the arrival time information obtained from the consequence management detector mentioned would be valuable, but it is important to discriminate and quantify the isotopes detected to differentiate explosion signals from a reactor accident, as in
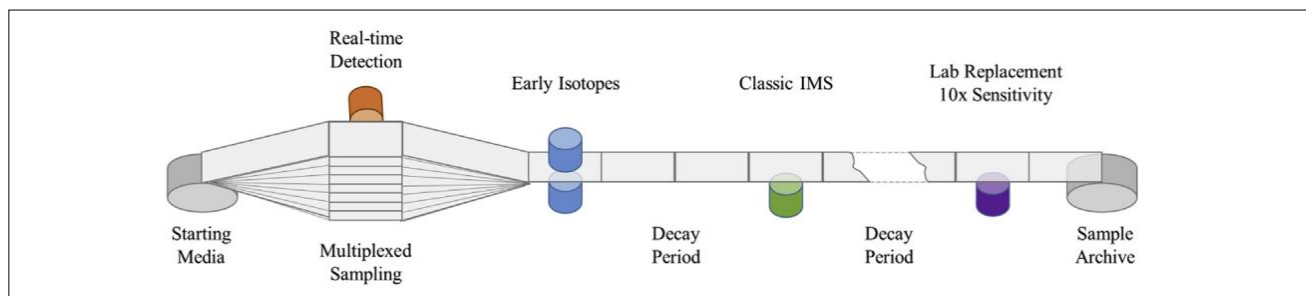
FIGURE 10.
A notional concept from Miley et al. (2019) for making measurements that meet needs for real time data, early isotopic data for high level signals, classic IMS signals and high sensitivity low level signal scenarios.

Figure 9, but for other, more powerful isotope pairs. High activity, short-lived isotopes worked well for this in Fukushima samples and showed that fission had stopped. One good solution to obtain this capability in a next generation aerosol system could be a detector (or detector pair) measuring activity on the filter just after the end of sample collection, in the decay position. This isotopic measurement could be executed in a short period of time for a hot sample, and a variable-aperture shield for the detector could protect against very high radiation samples.

A third signal scenario for future aerosol systems is for slight leakage from a well-contained underground test, or a similarly sized leakage from civilian nuclear activity. Very low background emissions like this would benefit from a long sample collection time and very low background detection. It has been shown that a one-week decay time for natural radioactivity before RASA measurement would allow detection limits for fission products to be improved by a factor of 10. A study calculated that an improvement of this magnitude would have allowed the detection of ^{131}I, in the average US underground nuclear test that vented/leaked (Aalseth et al. 2009).

The MDC equation provides scientific clues for how to achieve the same IMS performance available today, but with additional location capability and timeliness (shorter sample integration). It is impossible to change physics (gamma branching fraction) or environmental values (background radioactivity concentration), but the rate at which air is sampled can be relatively easily changed. Thus, a sample from a shorter integration time might have the same or greater amount of atmospheric aerosol collected as the original design.

One obvious solution is to simply acquire a more powerful air pump for existing aerosol systems. This would lock in the use of filtration for collection. Filters have been used for nuclear fallout monitoring since the 1940s, but electrostatic precipitation has been shown to meet efficiency requirements (80% at 0.2 micron particle size) at high volumes and with lower power requirements (Miley et al. 2019). A lesson from the Fukushima accident was that power outages were common for hours and days during the crisis. Keeping power levels down would allow some degree of battery backup allowing for the flow of real time data and samples.

Electrostatic collection has a variety of benefits besides higher flow at lower power. Electrostatic collection cells have lower flow resistance and require less blower power than a filtered system. It is possible to electronically reduce collection efficiency in case of a very high-level sample. The collection media, aluminized mylar, is far thinner than a filter and can fold to a smaller size. Aluminized mylar is easier to cut, for splitting samples, and can be sealed or cut readily by the application of a hot, non-stick bar or non-contact laser. Because of several benefits a shift to electrostatic collection seems likely in the future (Miley et al. 2019).

Even with a larger sample collection rate, a shorter collection time likely implies a shorter measurement time for the classic IMS mission, if the progression of sample movement includes only one measurement system. By contrast, some automated Xe systems have more than one detector and can measure for a longer time than the collection time (Hayes et al. 2015). To offset the shorter collection time a more efficient measurement of each decaying fission product atom is needed.

Two terms in the MDC equation can be adjusted to reflect improved detection probability of each atom in the sample decaying: improving the efficiency of the detector, ε, and improving the detector source geometry, $\delta\Omega$. Detector efficiency can be expensive to increase as it involves purchasing a different HPGe. At a simple level, it means purchasing a bigger detector with more mass of germanium that is sensitive to gamma rays. However, a key concept is the solid angle the detector subtends. From the point of view of a radioactive atom, the highest probability of detection is when every direction a departing gamma ray can take ($\delta\Omega \rightarrow 4p$) is covered by active detector material of sufficient density and thickness for the gamma ray to deposit all its energy in the detector ($e \rightarrow 1$). Thus, the optimum detector configuration would be for a point-like sample in the well of a

large, well-type detector, or between the faces of two large diameter cylindrical detectors. The latter option is favoured most often because the sample preparation and data analysis can be much simpler. For example, one desirable configuration would be two 10 cm diameter broad energy HPGe detectors, each of ~90% relative efficiency (actual gamma detection efficiency might be 5%) with a $7.6 \times 7.6 \times 0.2$ cm square sample between.

If the sample collection medium is aluminized mylar (available in thicknesses from 2 to 200 microns thick) instead of many layers of filters around 1 mm thick, sample preparation, manually or via automation, would be conceptually simple. In such a setup, the efficiency for collecting a given gamma ray in the detector pair might be twice that of an existing manual system and up to five times that of a RASA system (Miley et al. 1998).

For samples in which radon decay products potentially cover a signature of interest, samples can be remeasured days later when the radon daughters are essentially absent due to nuclear decay. This would be scientifically identical to the historical approach reported above. Whether

accomplished via automation in the station (the right-most detector in Figure 10), or by using specialized ultra-low background systems at laboratories, substantial gains can be made by waiting for [212]Pb to decay away for a week, as reported in (Miley et al. 2009).

Figure 11 shows the gamma ray spectrum resulting from a normal IMS aerosol sample measurement, the background of the IMS system with no sample at all, and the gamma ray spectrum measured on the sample eight days later in an ultra-low background (ULB) detector. The ULB detector was not underground and similar detector systems can simply be purchased today.

A simulation study was used to examine IMS network performance if shorter sampling periods were used but the MDCs were not changed (Eslinger et al. 2023). This study used 10^5 release points spaced equidistant across the earth and eight releases per day for an entire year. The detection statistics shown in Figure 12 are based on 2.92×10^8 hypothetical releases. The detection probabilities improve modestly with decreasing sample collection length, but much of the
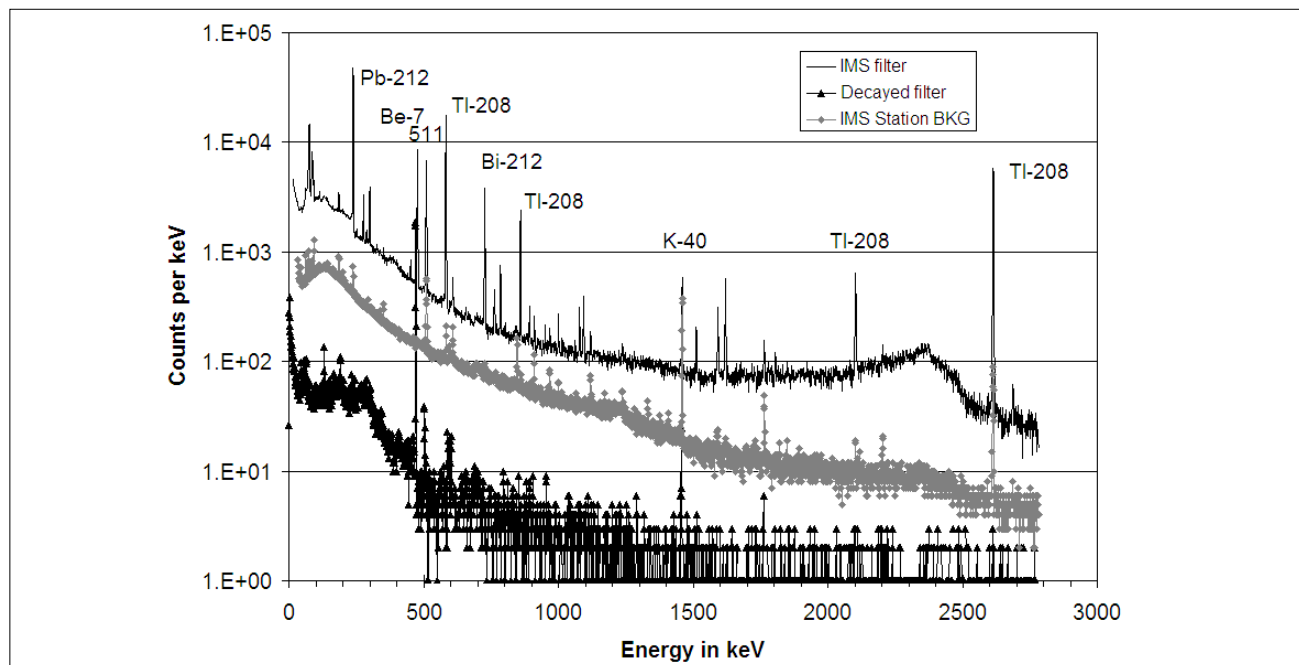
FIGURE 11.
The gamma spectrum measurements of an IMS sample (particulate filter) are shown (solid line) about two orders of magnitude higher in counts than the same sample decayed by eight days (black triangles). In between is the blank sample measurement of the IMS system itself. This shows that as currently designed, the IMS system could not register an ultra-low background result, regardless of decay. A specialized ULB detector is needed with appropriate shielding.
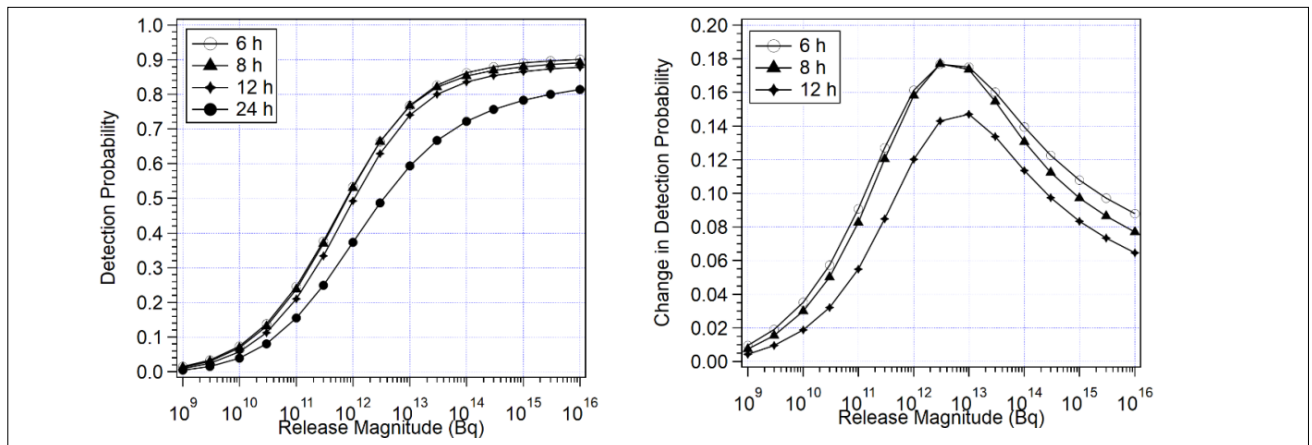
FIGURE 12.

Network detection probability for ^{140}Ba averaged over a year using different sample durations where each sample duration has the same MDC. The left pane shows the detection probability, and the right pane shows the improvement in the detection probability compared to a 24 h sample duration.

improvement came from 12h samples. Additional improvement is seen for eight-hour samples, and little change occurs if the sample collection time is decreased to six hours.

Unsurprisingly most of the improvement came in the number of samples that would register a detection above MDC, and some improvement was needed in the number of stations that would detect an event. These improvements are valuable for location, confidence, and resilience against station outages.

2.5.2. Next Generation Detector Systems

While the majority of particulate detector systems look (extremely) similar to the systems first deployed 20+ years ago, there have been incremental advances. Current systems are far more reliable than their predecessors and are also far simpler to operate. Unfortunately the nature of the threat has also evolved, while the design goal of the IMS has remained static.

The monitoring community has begun to acknowledge this disconnect with IMS laboratories taking the lead in system development. Dual detector systems have emerged, based on commercial off the shelf technology, that offer far greater reliability and insights into sample inhomogeneity that typically simple single sensor systems cannot resolve (Zhang et al. 2018). More advanced, coincidence-based systems have also

been built (Britton et al. 2015a) and deployed in-field, with fully automated analysis chains (Britton et al. 2015b).

A full discussion of next generation systems (those providing a significant improvement in capability) is available in (Britton et al. 2019b). To summarize:

- Multi-detector coincidence based systems offer a range of advantages over traditional systems;
- Multiple detectors retain the ability to make a Treaty measurement, even when one instrument fails. Such a capability would greatly improve the data availability from IMS systems, which remain vulnerable to the loss of a single detector;
- The sensitivity gains possible with next generation systems range from a factor of 2, to a factor of 100. Crucially, sensitivity is improved for all signatures measured, as list-mode data recording and processing allows for simultaneous production of anti-coincidence spectra, and gain-matched sum spectra;
- Such advanced systems used to be within the purview of large collaborations, as they required significant resources to both process and analyse the data. Today, such systems can be managed and analysed on an embedded computer, such as a Raspberry Pi;

- The sensitivity gains possible due to next generation systems are crucial to maintaining an effective IMS – many signatures simply cannot be detected with the technology currently deployed;
- Next generation particulate sensors work hand in hand with next generation sampling technologies and next generation noble gas systems. Certain signatures are only possible to detect with a particulate monitor at the station – without a prompt measurement, that information is lost forever.

Electronics

A number of solutions have been published, ranging from the synchronized use of multiple multichannel analysers (MCAs) to the use of advanced modules with multiple inputs. Ultimately, there are many suitable desktop digitizers, and the choice should be guided by the application and level of programming experience locally available.

Data Processing

Typically the data produced by multi-sensor systems is orders of magnitude larger (and more complex) than from single systems. This, however, is more a reflection of the choices made by developers of these systems, who typically want the finest granularity to extract trace signatures.

Instead of offline processing of list-mode data (the gold standard for current systems utilizing fully digitized MCAs), online processing could be used, greatly reducing the bandwidth required (and directly producing the coincidence matrices alongside traditional spectra).

Analysis

For multiple detectors, the analysis is typically more complex than traditional spectra, however many of the concepts remain similar. Alongside traditional analysis of gain matched summed spectra, and anti-coincidence spectra, analysis of coincidence signatures typically requires one extra step before peak fitting – the selection of a gate energy and the projection of this range to extract a peak that is in coincidence with the energy range of interest.

Once the peak/signal is identified, it must be characterized. The first step is to calculate the γ-cascade probability, which is possible from standard ENSDF data sets (Bhat 1992). Typically, software is used to calculate the cascade probabilities automatically and fold in efficiency values to yield a detection probability (Britton et al. 2015, Britton et al. 2016). Note that the automation of this step is crucial as it allows the analysts to optimize their analysis based on the most probable (detectable) signatures.

To properly characterize the geometry (and therefore the peak and total efficiencies) complex Monte-Carlo simulations were often used. Now, however there are commercial and open source tools available that can produce accurate efficiency characterizations (Gheddou 2021).

The Potential

Next generation systems have the potential to revitalize the particulate component of the IMS, enabling a multi-isotope, multi-technology combination of events. While this is of interest for identifying anomalies, it is also of great use when explaining more commonly detected events. Coincidence analysis can dramatically reduce the number of false positives on the network, reducing analyst load. Enhanced MDAs can also result in clear rejections of hypotheses (see Figure 13).

In example measurement data shown in Figure 13 and 14 an anomalous signature is detected and quickly confirmed to be ^{106}Rh. If an analyst wanted to check whether the signature also contained ^{134}Cs, typically produced from ^{133}Cs in a reactor over a long period of neutron exposure, the MDA is limited by the ^{106}Rh continuum. When operating in coincidence mode, almost all noise is eliminated, dramatically lowering the MDA and allowing the analyst to better characterize the event.
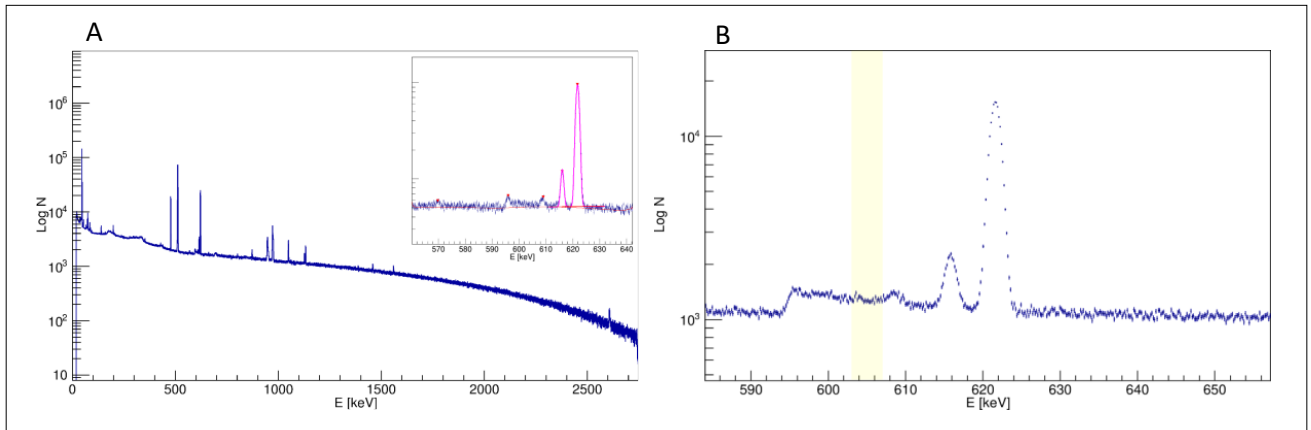
FIGURE 13.

Measurement results from traditional gamma spectrometry (A) shows a singles gamma spectrum summed from two gain-matched gamma detectors with a Compton suppression system in place. With gamma emissions from ^{106}Rh at 616.2 keV and 621.9 keV. (B) highlights the region where ^{134}Cs would be detected if present. There are many thousands of counts from the Compton continuum of ^{106}Rh. (Adapted from Britton et al. 2019a).
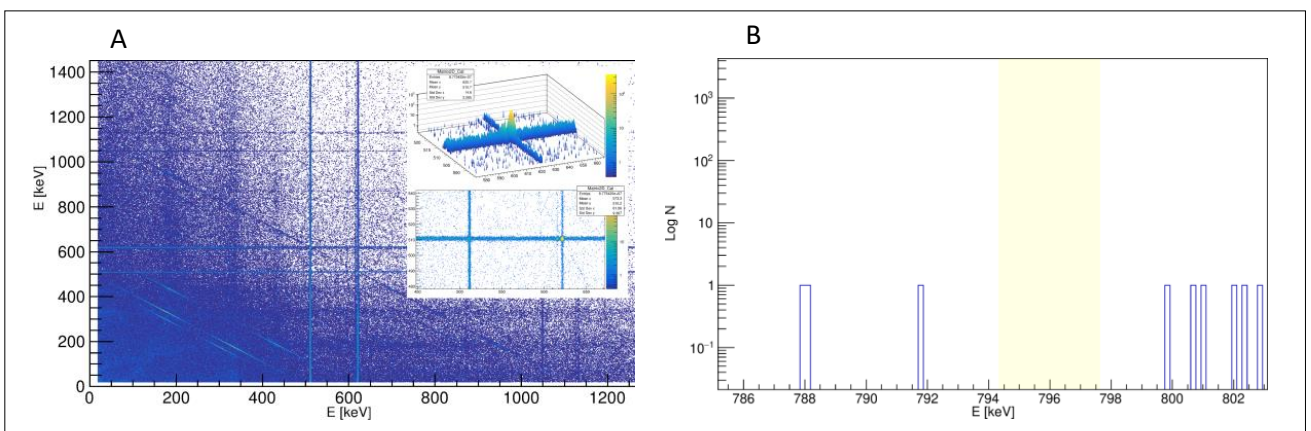
FIGURE 14.

Coincidence based gamma spectrometry shows (A) correlated emissions in each detector where the insert shows a cascade from ^{106}Rh; with 616.2 keV and 621.9 keV in coincidence with the 511.9 keV gamma ray. In (B) the selectivity of the ^{134}Cs 604.7 keV gamma cascade almost completely eliminates the background in the region where ^{134}Cs would be detected. (Adapted from Britton et al. 2019).

The Future

Next generation systems are already present in many IMS laboratories. They have been proven to work in-field and have even been remotely deployed in deep underground mines (Britton et al. 2019c). The ultimate limits of the technique have been explored and point to a further factor of 10-1000 being possible (albeit with vastly more complex and expensive systems) (Britton et al. 2019a).

3. NOBLE GAS NETWORK

3.1. Current International Monitoring System Station Systems

There are historical examples of lengthy campaigns to measure isotopes of radioxenon (especially ^{133}Xe) from the atmosphere (C. Schlosser 2017) but the first scientific paper demonstrating that environmental radioxenon can be sampled, separated, and measured on a daily time scale (Bowyer 1999) showed that in New York City there was a significant atmospheric background of radioxenon present.

The system used in this work was the automatic radioxenon sampler/analyzer (ARSA), developed at Pacific Northwest National Laboratory (PNNL) in the USA. The ARSA used a NaI(Tl) and plastic scintillator–based beta–gamma coincidence detector to measure the radioxenon isotopes of interest (Bowyer et al. 1996). The ARSA system was capable of measuring as low as 0.2 mBq/m³ of ^{133}Xe. In 2003 the Swedish Automatic Unit for Noble Gas Acquisition (SAUNA) paper was published by scientists from the Swedish Defence Research Agency (FOI), which used a similar detector system but improved the sampling system. In 2010 the SAUNA II system was released commercially, improving the sample size and reliability.

SAUNA II systems have been deployed at IMS stations around the world and various iterations of the system have been used, such as the transportable xenon laboratory (TXL) system, used for temporary measurement campaigns in regions of interest. Ringbom et al. used such a system to detect radioxenon from the Democratic People's Republic of Korea nuclear test in October 2006 (Ringbom et al. 2009). SAUNA is the most prevalent system used in the IMS. The second most prevalent IMS noble gas system is the Système De Prélèvement Automatique En Ligne Avec L'analyse Du Xénon (SPALAX) — developed by the French Alternative Energies and Atomic Energy Commission (CEA, France). This system uses high resolution gamma spectroscopy to measure radioxenon isotopes. This is inherently less efficient than scintillator detectors but the high energy resolution can mean less interference between signals. Unfortunately without coincidence spectrometry, measurement of the long lived isomers ^{131m}Xe and ^{133m}Xe is challenging as they have the same X ray energies and relatively low gamma ray emission probabilities. It is generally agreed that beta–gamma coincidence spectrometry is the method of choice for measurements of radioxenon. This is reflected by the decision to move the next generation SPALAX system (SPALAX-NG) to coincidence detectors, which utilises a state of the art high resolution beta–gamma coincidence detector (Le Petit et al. 2015, Cagniant et al. 2018).

One challenge that has been overcome in recent years is that of the xenon memory effect. Plastics, adhesives and other materials used in detector construction can allow the xenon gas to migrate into the material. If the sample contains isotopes of radioxenon, then the decay of the now immobile xenon will cause an increased count rate in the detector. The original solution to this was to introduce a so-called 'gas background' measurement – an empty cell detector acquisition that follows the sample measurement. Any residual radioxenon can be quantified, decay-corrected and then subtracted from the sample measurement. This process is completed on all beta–gamma coincidence systems where the plastic cells used in the SAUNA systems were most affected. Blackberg et al. (2013) designed a coating process to prevent the migration of xenon into the SAUNA gas cells. The 0.4 μm coating of Al_2O_3 reduced the memory effect to a very low level, but if the coating is too thick, it can degrade the beta resolution of the plastic scintillator.

The current IMS noble gas network has identified a significant global radioxenon
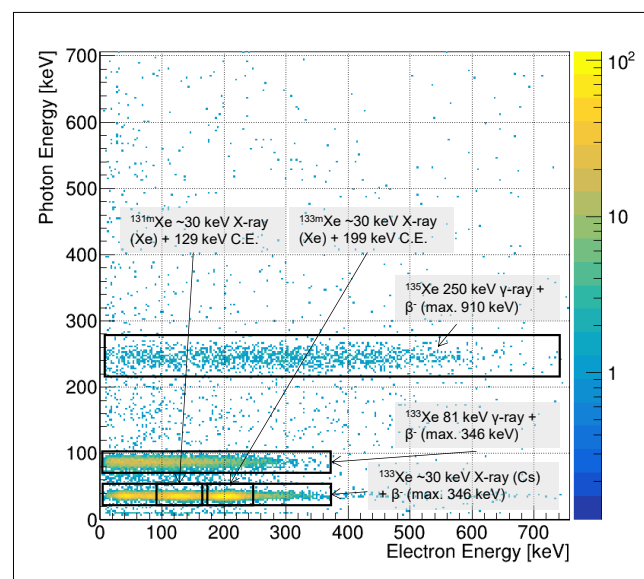
FIGURE 15

A beta–gamma (or electron–photon) coincidence energy histogram, from the measurement of an environmental sample of purified xenon using a SAUNA system. This sample contains ^{133}Xe (81 keV γ ray β⁻ coincidences), ^{135}Xe (250 keV γ ray β⁻ coincidences), ^{131m}Xe (30-35 keV Xe X(K) ray - 129 keV conversion electron coincidences) and ^{133m}Xe (30-35 keV Xe X(K) ray - 129 keV conversion electron coincidences).

background from civil nuclear facilities, which hinders the ability to detect radioxenon from a nuclear explosion. Other work, such as the STAX project (see Friese et al. 2019) is ongoing in this area to better understand, predict and account for this background. Identifying which detections are associated with a nuclear explosion is a complicated challenge, but one way in which it can be made easier is through enhancements to the current IMS systems. Eslinger (2022) showed that there is a benefit to the explosion detection probability from reducing collection periods from 12 to 24 hours to six to eight hours. Sampling enhancements mean it is possible to sample more air and extract more xenon to increase sample sizes. Spectroscopy enhancements mean it is possible to measure the decay emissions with higher resolution, lower interference and/or improved detection efficiency. All these improvements mean the potential detection limits for each isotope are lower than the current systems can achieve. With lower detection limits and more samples collected per day, the number of detections of radioxenon on the IMS will increase significantly. Section 3.2 provides more information on the next generation systems being installed and discusses how enhancements will make the next generation of IMS noble gas network a more effective verification tool.

3.2. Next Generation Noble Gas International Monitoring Systems

At the time of this writing the IMS runs 32 noble gas systems (26 are certified for operation), which include SAUNA II and SPALAX systems. Over the next 10 years, the rollout of a new generation of noble gas systems will be completed. These third generation systems will sample over shorter collection intervals, collect more xenon gas per sample, measure lower MDCs for all four isotopes of interest and aim to improve reliability and maintainability of the systems once installed.

There are three main next generation noble gas systems all of which have been tested in a station environment as part of the acceptance testing process. These systems are SAUNA-III (Scienta Envinet, Sweden), SPALAX-NG (CEA, France) and Xenon International ("XeInt", PNNL and Teledyne Brown, USA). A fourth system is being developed (MIKS) but there is limited published information available for this system. Table 4 summarizes the specifications of second and third generation noble gas stations.

Table 4. Summary of Second and Third Generation Noble Gas IMS Systems

Gen.	System name	Xe Vol. (mL) / Sampling length (hrs)	Isotope MDC (mBq/m^3)			
			^{133}Xe	^{135}Xe	^{131m}Xe	^{133m}Xe
II	SAUNA-II	1.5 / 12	0.2	0.5	0.2	0.2
II	SPALAX	2.5 / 24	0.15	0.65	4.0	1.0
III	SAUNA-III	3.25 / 6	0.2	0.36	0.12	0.12
III	SPALAX-NG	4.0 / 8	0.2	0.2	0.2	0.2
III	XeInt	2.5 / 6	0.17	0.19	0.17	0.14

MDC data from: Eslinger et al. 2022.

As shown in Table 4, the sampling periods for Generation III systems are shorter (six to eight hours) so there are more samples collected per day but the new systems also collect more xenon gas. This demonstrates a great improvement in xenon sampling and processing capability. Eslinger et al. (2022) demonstrated that such improvements have increased the probability of detecting radioxenon based on multiple release scenarios.

3.2.1. SAUNA-III

SAUNA-III is designed as an upgrade to the current SAUNA-II system. This system uses the same plastic scintillator/NaI(Tl) β-γ coincidence detector system as the SAUNA-II, with the exception of a larger plastic scintillator gas cell that is now a 18 cm^3 active volume compared to the previous size of 6.3 cm^3. While the detectors are broadly similar, the xenon sampling and processing system is improved by using a larger

sampling pump, improved xenon trap material (Ag-ETS 10) and more readily available carrier gas (N_2 instead of He).

3.2.2. SPALAX-NG

The next generation of SPALAX system has shown a big change to the spectroscopy system, with the innovation of a PIPSBox– a gas cell with carbon fibre windows, containing two planar silicon detectors for beta/electron detection, used in coincidence with a HPGe detector.

3.2.3. Xenon International

The Xenon International system was developed at PNNL and manufactured at Teledyne Brown Engineering (USA). The system uses a cryo-cooled charcoal trap to collect xenon (cooling the charcoal makes it a more effective gas trap). The detector setup is similar to that of the SAUNA (and previously ARSA) systems – NaI(Tl) gamma detector and plastic scintillator gas cells.

4. SAMPLE ASSOCIATION AND THE NEXT GENERATION NETWORK

Using multiple samples, rather than one sample, allows an analyst to constrain the size of the possible source location. Figure 16 contains contours from a Bayesian posterior probability distribution on the location of a release associated with samples related to the announced nuclear test in 2013 by the Democratic People's Republic of Korea, based on several samples of ^{133}Xe taken in Takasaki, Japan. The model used to calculate the probabilities is explained in Eslinger and Schrom (2016). In this case the analysis framework provides a reasonable location estimate that improves with the number of samples. One feature of next generation xenon systems under development is that they provide more samples per day than the current systems, increasing the potential number of detections, or associated non-detections.

Since the introduction of xenon systems over 20 years ago many lessons have been learned about xenon radioisotopes in the atmosphere (Kalinowski et al. 2010).

The first has been that xenon is measured in the atmosphere frequently, especially in the northern hemisphere. An aspect of that is that the prevalence of ^{133}Xe background, which is the favoured isotope for explosion monitoring, means that other xenon isotopes are much more important than originally envisioned (Conference on Disarmament 1995). The ratios of these isotopes vary substantially between reactor releases and explosions, but medical isotope production has been determined to be a far greater contributor to the ^{133}Xe background (Miley et al. 2022).

Upon identification of samples containing radionuclides of interest, fusion between radionuclide and ATM data is required to better describe the original source. By generating source–receptor sensitivity fields for each sample measurement, and knowledge of the measured activity concentrations at known locations, it is possible to perform a Bayesian calculation to calculate the source parameters (location [lat, lon], release time [start, stop] and release magnitude) (De Meutter and Hoffman 2020). A Bayesian source reconstruction tool known as 'FREAR' has been developed and shared with the community.

A recent study utilized FREAR during the analysis of ^{131}I detections at IMS radionuclide stations of the Russian Federation in Dubna and Kirov (Goodwin et al. 2022a). The reconstruction showed that the release of ^{131}I likely originated from an isotope production facility in Obninsk. More recent work has assessed the power of source reconstruction for events where there is a background signal present (Chester et al. 2022). In other work it has been shown that a simulated radionuclide event with multiple detections is reconstructed, even in the presence of a background signal. It highlights the importance of identifying the anomalous signal amongst
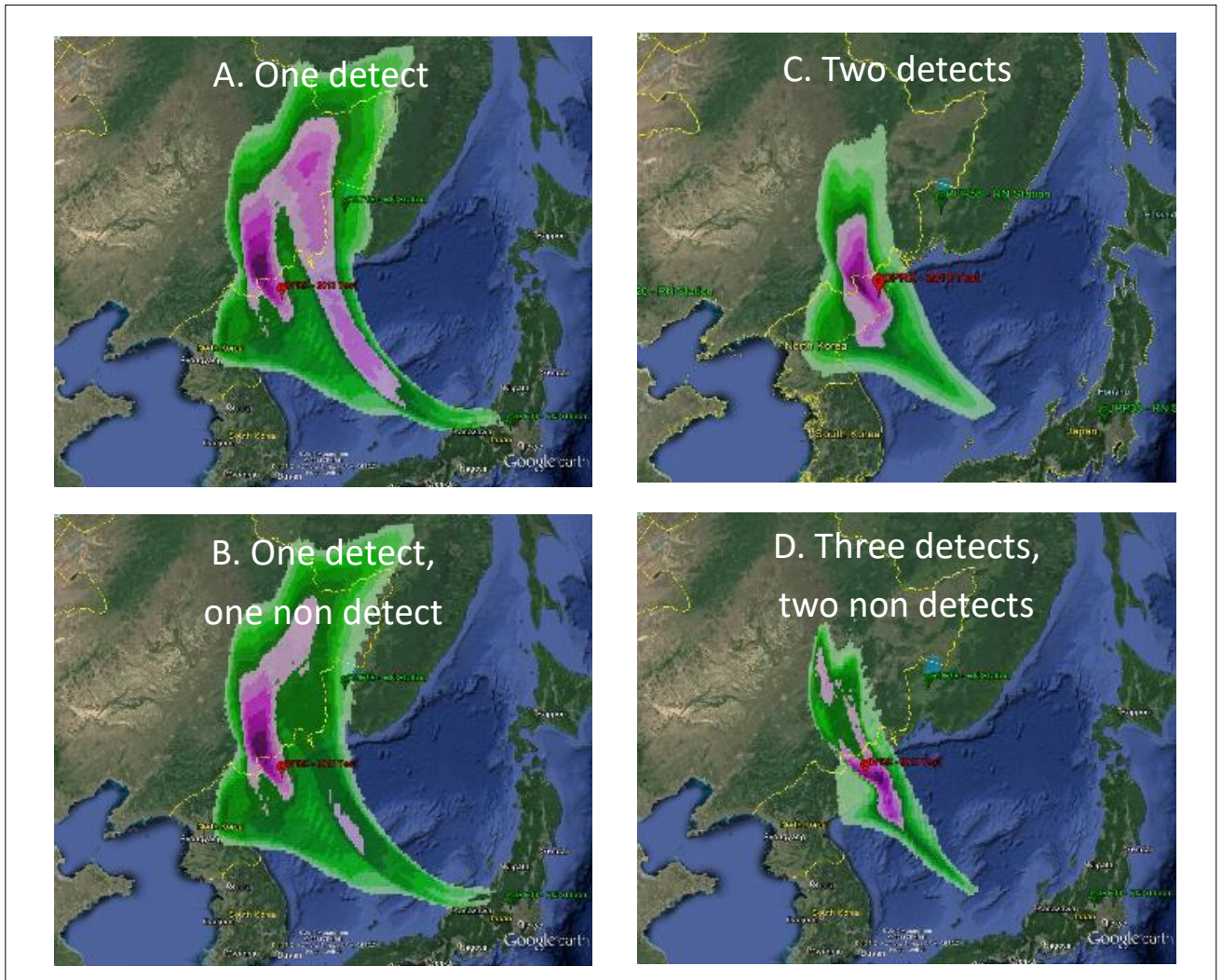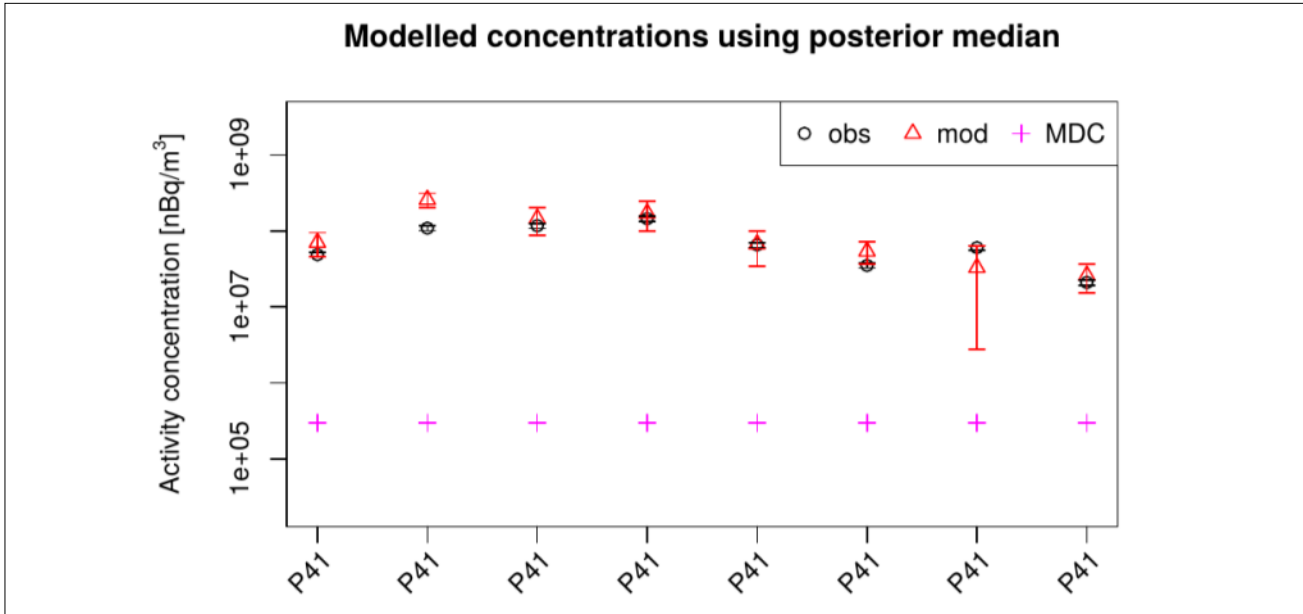
FIGURE 16.
Location power of associated samples illustrated by the posterior probability distribution of the source location for the Democratic People's Republic of Korea announced test in 2013.

the background and correctly associating the samples with the radionuclide event. In the case where the main detections are associated with the event, Figure 17 shows how the detections can be recreated ('simulated') by the model during the reconstruction. In this instance there is excellent agreement between simulated and 'real' detections (Goodwin et al. 2022b).

In this case the samples are associated with one another by running inverse simulations from each sampler with a high category detection. Those with the highest degree of overlap (spatially and temporally) are used to reconstruct the source parameters using FREAR. Figure 18 shows the probability distribution of each source parameter. The location is represented in Figure 19.

It can be understood from Figure 20 that the time of release from an explosion, medical isotope production process or reactor will have a marked impact on the ratios among the isotopes and possibly the connection of iodine detections to xenon detections. The improvement in multiple isotope detections using next generation systems are summarized in Figure 21 for the three release scenarios from (Eslinger et al. 2022). There are few 4 isotopes detections for release in scenario A because it has a low activity release of ^{131m}Xe. There are no 4 isotopes detections for release in scenario C because it has a very low release of ^{135}Xe (decayed away before release). However, there is a significantly higher probability of detecting multiple isotopes across the network for a 1% release of the xenon activity of a 1 kt inventory in all three release scenarios.
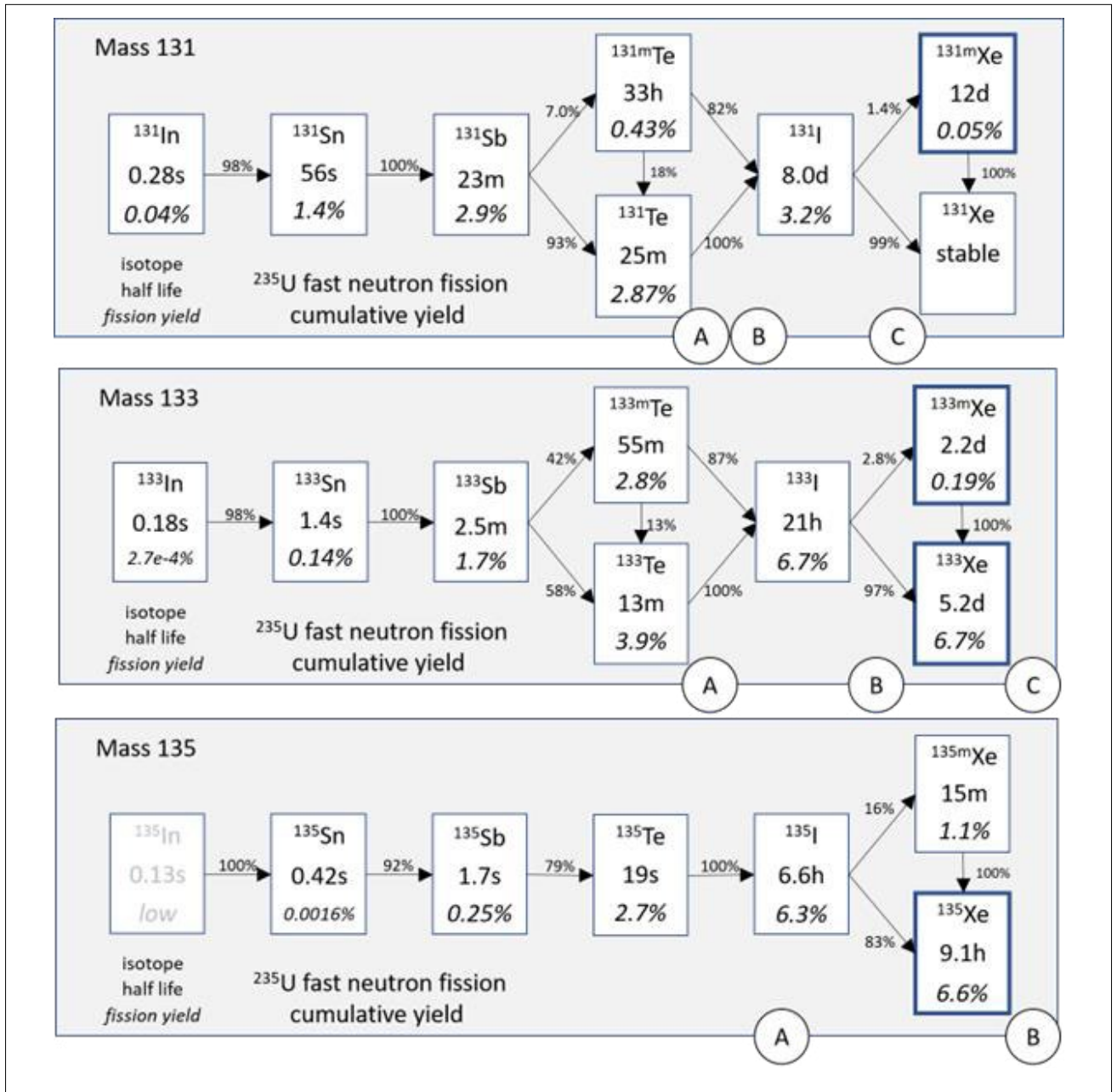
FIGURE 17.
Observed (real, 'obs') activity concentrations compared to modelled ('mod') value, based on the reconstruction of a hypothetical source from multiple detections at the same station (RN41).
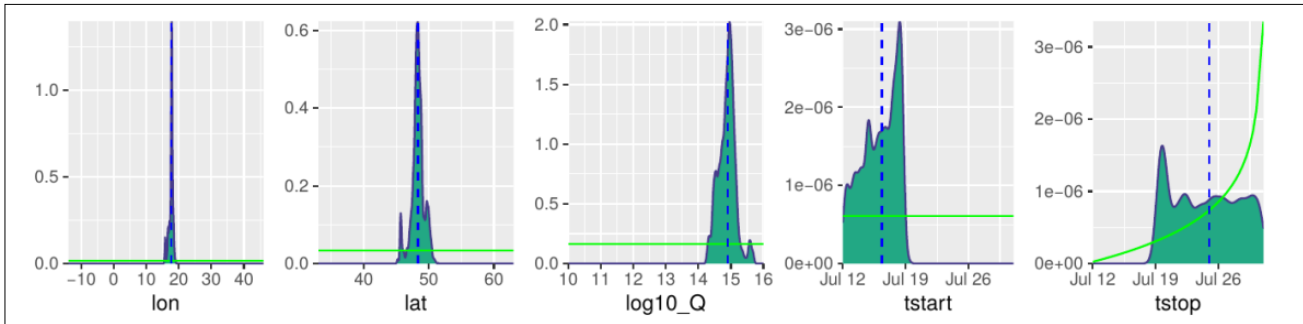
FIGURE 18.
Source parameter probability distributions based on the reconstruction of the source.
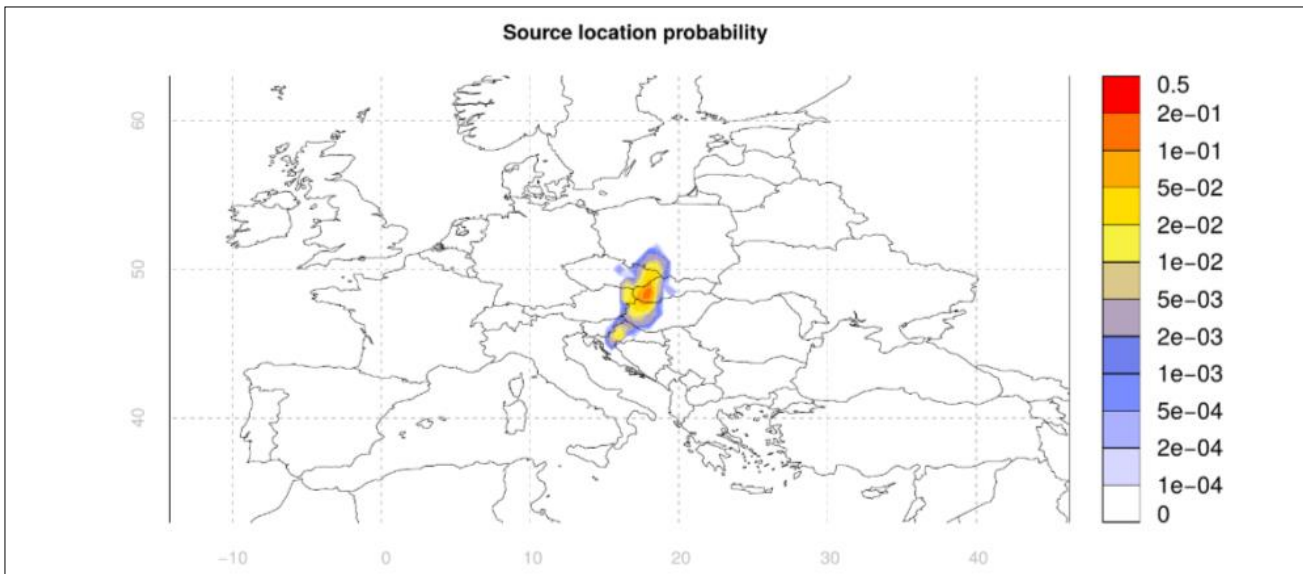
FIGURE 19.
*Mapped probability distribution for the hypothetical release.*

FIGURE 20.
Simplified nuclear decay chains for mass chains 131, 133 and 135 with half-life, cumulative fission yield and decay percentages indicated. Data are from England and Rider (1994). The curves in Figure 21 presume all the isotopes are kept together, whereas the cumulative fission from left to right shows what would be lost from the highlighted xenon signature if the mass chain atoms were segregated from each other. The symbols A, B and C indicate a rough idea of where one hour, one day and 10 days might fall, respectively.

5. LABORATORY ANALYSIS – SUPPORTING THE INTERNATIONAL MONITORING SYSTEM

5.1. Current Capability Summary

The 80 station radionuclide network is supported by 16 radionuclide laboratories. Currently 14 of these laboratories are certified for particulate analysis and five for noble gas analysis. For particulate analysis their main function is the reanalysis of samples categorized as Level 5 (i.e. that contain multiple anthropogenic radionuclides, with at least one of which is a
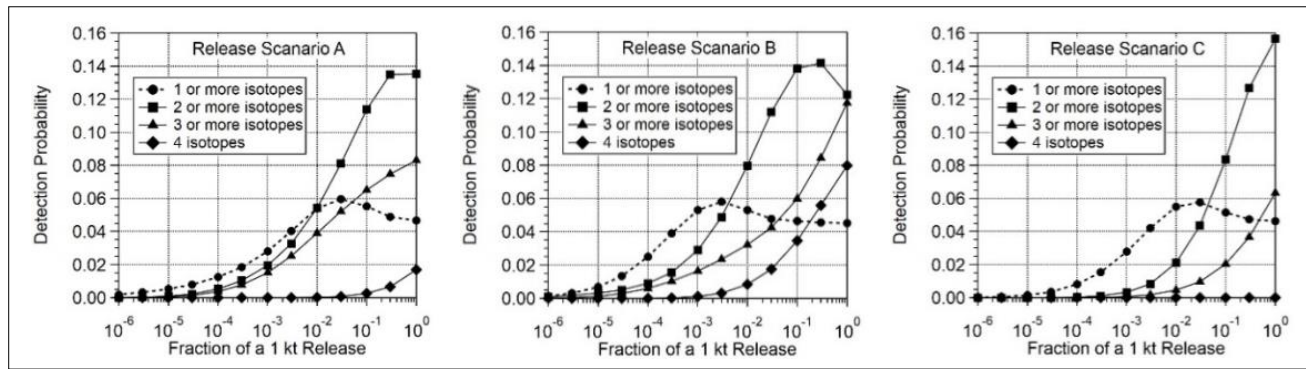
FIGURE 21.
Improvement in the network detection probability for next generation systems at 39 stations for different numbers of detected isotopes in each sample for three release scenarios.

fission or an activation product). Additionally, samples from stations are sent to laboratories for reanalysis as part of a quality control programme for the results produced by the stations.

There are a combination of (mainly commercial off the shelf) detectors used at the laboratories. These systems utilize the latest developments offered by the main manufacturers of germanium crystals (Mirion and Ortec). Around half of the laboratories use wider diameter ('planar') crystals, optimizing the counting efficiency for geometries counting on the end cap and photon energy ranges typical of IMS samples according to the database of the PTS. The components in the manufacture and assembly of these detectors have been selected for low intrinsic background. The preamplifier is situated outside of the detector shield to reduce line of sight from components that may contain trace levels of anthropogenic radionuclides. The laboratories have installed improved shields compared to IMS radionuclide stations with an increased thickness of lead, including a layer of low background lead that has been refined from aged lead, reducing the ^{210}Pb content. Typically other materials used in the shielding (copper, cadmium and tin) have been selected from radiopure materials. The typical count time for the laboratory is from five to seven days, which is required to meet the CTBT requirements (MDA of 24 mBq for ^{140}Ba for a compressed air filter with dimensions of 70 mm diameter and 6 mm height). To improve detection limits a number of laboratories have also installed Cosmic Veto systems to suppress coincident events that originate outside the detector and are

normally detected by a plastic scintillator and the HPGe inside the lead shield (Burnett et al 2014, Shroettner et al. 2004). These systems improve detection limits for CTBT relevant nuclides by ~50% as the main contribution to the background when counting a sample after the decay of short-lived radon daughters are the radionuclides themselves or backgrounds from environmental or cosmogenic radiation. This is not the case when samples are counted at the station where the main interference to the nuclides of interest in the sample is from radon daughters (Davies et al. 2020).

US CTBT-certified Radionuclide Laboratory (USL16, based at PNNL) has had the opportunity to locate some of their detectors in a shallow underground laboratory reducing the fast neutron flux. This has shown to improve the net background rate by a factor of 100 when compared to the standard, commercially available detectors used at the above ground location (Greenwood et al. 2017).

5.2. Noble Gas Laboratories

Of the 14 certified IMS radionuclide laboratories five are certified for measurements of noble gas radioisotopes. Between the five radionuclide labs, the detector technologies utilised vary (see Table 5). Since the inception of the noble gas network the IMS radionuclide laboratories have been involved in further developing the laboratory analysis through INGE.

Table 5. International Monitoring System Radionuclide Laboratories Operating Noble Gas Measurement Systems, Showing the Systems Available at Each Laboratory as Part of the CTBT-Certified Process and for Research and Development (R&D) Purposes

IMS Laboratory	Certified Measurement System	Other Systems / R&D
ATL03	HPGe	Anti-coincidence systems (Schroettner et al. 2010)
FRL08	Dual HPGe	Dual HPGe + PIPSBox, coincidence (Delaune et al. 2018)
CAL05	Dual HPGe	HPGe, SAUNA II
GBL15	SAUNA II (NaI(Tl)+plastic)	Dual HPGe + PIPSBox, coincidence (Goodwin et al. 2022c)
USL16	Custom beta–gamma	Various (Foxe et al. 2016)

FIGURE 22.

The UK CTBT radionuclide noble gas laboratory (GBL15), which uses a SAUNA II IMS lab system to process and measure radioxenon samples from the IMS noble gas station network.

New and improved spectroscopy at the radionuclide noble gas laboratories can improve the effectiveness of the IMS radionuclide network by offering more sensitive measurements for some radionuclides. With a 9.1 h half-life measurement of ^{135}Xe is not improved upon at a laboratory when accounting for the delays due to shipment of the sample. However it is possible that ^{133}Xe, ^{131m}Xe and ^{133m}Xe detection limits can be lower at a laboratory even after allowing some time for shipment of the sample. This means that there is more information to be gained from laboratory remeasurement than is currently being realized. Quantification of an otherwise unmeasured isotopic ratio may significantly impact the analysis of a radionuclide event.
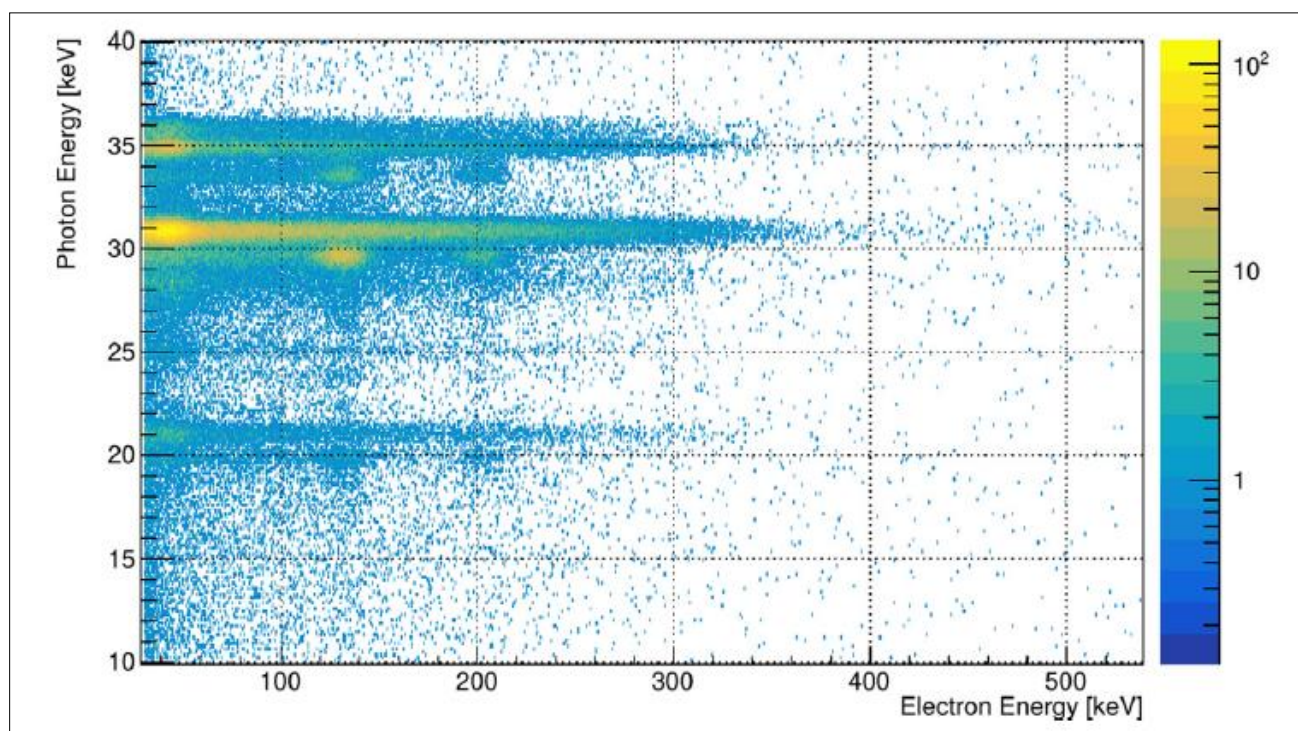
FIGURE 23.

β-γ/e⁻-X ray coincidence energy matrix showing coincidences between the β⁻ emissions of ^{133}Xe and ^{135}Xe with X rays of Cs and the conversion e⁻ transitions of ^{131m}Xe and ^{133m}Xe with X rays of Xe. Figure from (Goodwin et al. 2020).

The noble gas community are faced with a challenge – the detection of radioxenon from a nuclear explosion within an atmosphere polluted with radioxenon from civil nuclear facilities (Bowyer 2020). One way the community is addressing this is through the development and use of new types of spectroscopy, such as high resolution beta–gamma coincidence spectroscopy (Goodwin et al 2020, Goodwin et al. 2022c). High resolution spectroscopy offers lower background signals due to reduced interference between coincidence signatures in the coincidence energy matrix (see Figure 23).

The effect of reduced backgrounds is improved sensitivity in real world samples especially for the metastable isomers (^{131m}Xe and ^{133n}Xe), the activity ratio of which, is the best discriminant between a civil nuclear facility and a nuclear explosion.

Section 5.3 summarizes some advanced measurement techniques offered by radionuclide laboratories.

5.3. Advanced Laboratory Analysis

5.3.1. Advanced Laboratory Analysis Summary

For many decades gamma ray spectrometry has been a key technology employed by laboratories for the identification of radionuclides. Through this method the detection of specific radionuclides can be indicative of nuclear events or the process history and origin of nuclear materials and by-products. Over the past decade there have been significant advancements in this method where state of the art laboratory systems are now combining multiple detectors and exploiting various technologies to detect smaller amounts of radioactivity.

5.3.2. Benchmarking Laboratory Systems

In 2019 an international effort took place to evaluate the performance of gamma ray spectrometers for the support of these nuclear forensic applications. Carefully selected environmental samples measured by various laboratories across a multitude of detector technologies served as a benchmarking exercise to illustrate the radiation detection capabilities of these systems. Participants included Canadian laboratories at the Canadian Nuclear Safety Commission, Defence Research and Development Canada, Health Canada and SNOLAB, along with the Atomic Weapons Establishment in the United Kingdom. In addition to the traditional detectors, advances between these laboratories included: (1) active background suppression (in the form of cosmic veto systems), (2) dual gamma ray spectrometers, (3) coincident event detection/ analysis and (4) deep underground laboratories.

As part of this study a blank sample was circulated among the participants enabling them to determine the detection limits of their systems, shown in Figure 24 for two CTBT-relevant radioisotopes. The requirement for a laboratory to enter certified operations within the CTBTO IMS is included for comparison, defined as a specific MDA for ^{140}Ba that must be attained or bettered. This exercise demonstrates the impacts of the various advances, where employing an additional detector in combination with cosmic suppression and/or coincidence analysis results in roughly a 5-fold improvement over traditional laboratory systems. Exploiting the ultra-low background environments offered by the Boulby Underground Laboratory (1.1 km overburden) and the SNOLAB Underground Laboratory (2 km overburden) further improves this performance by an order of magnitude or greater.

By incorporating one or more of these complimentary advances, multi-detector systems along with those located in deep underground laboratories are pushing the limits of gamma ray spectroscopy for the identification of radioisotopes in the environment. This evolution results in a precise non-destructive method that enables the unambiguous identification of the nature of nuclear events or origin of nuclear materials. Ultimately this advances multiple domains, including inspections for illicit nuclear materials, nuclear explosion monitoring, nuclear safeguards and nuclear non-proliferation monitoring.
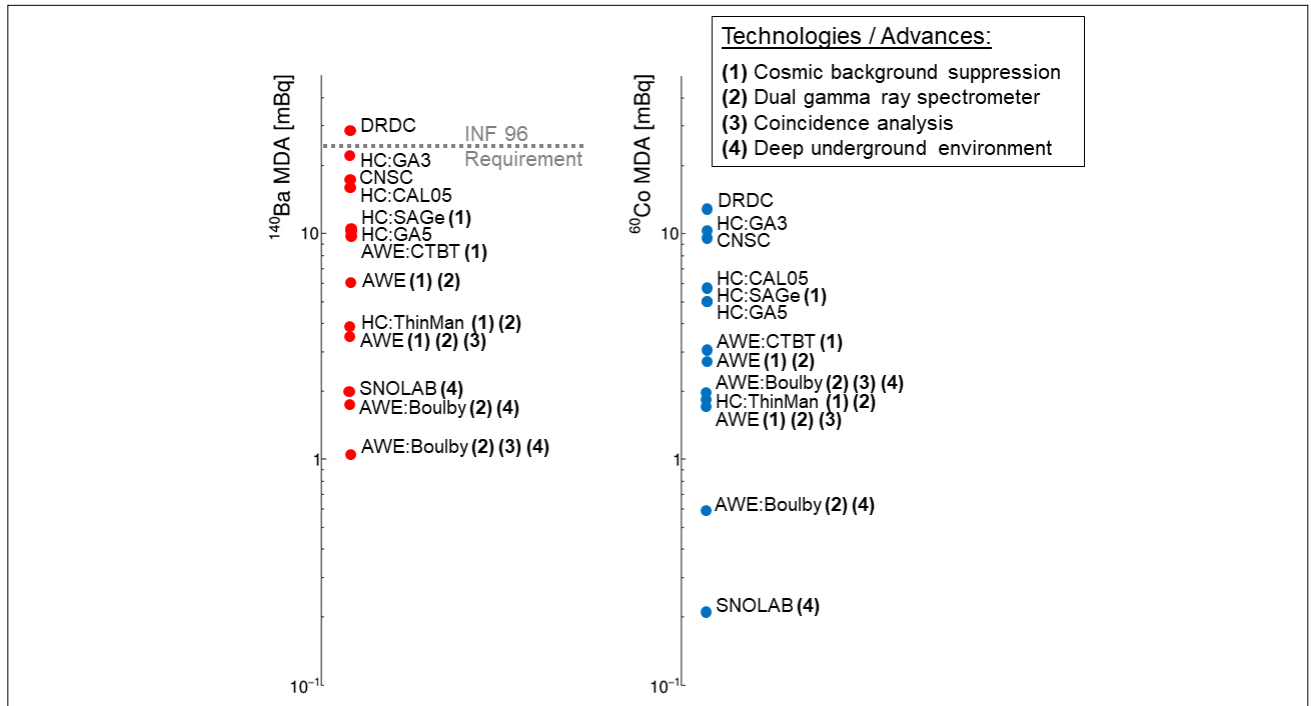
FIGURE 24.

Sensitivity comparison as a part of a 2019 performance benchmarking exercise, determined as the MDA for ^{140}Ba and ^{60}Co. Each data point corresponds to a detector system with its various employed advances identified, if applicable. The requirement to operate as a certified laboratory within the CTBTO IMS is displayed, corresponding to a maximum permitted MDA for ^{140}Ba.

With more advanced spectroscopy come questions around the sample composition, specifically the distribution of radionuclide particles across a sample (such as a filter paper). section 5.3.3 discusses real measurements using digital radiography to improve the understanding of the activity distributions within a sample.

5.3.3. Digital Radiography

Modern autoradiography techniques based on phosphor-imaging technology using image plates and digital scanning can identify heterogeneities in activity distributions and reveal material properties, serving to inform subsequent analyses (Parsons-Davis et al. 2017). Image plate autoradiography can image large 2-D areas often with relatively low detection limits for fission and activation products relevant to CTBT verification, with sensitivity to a wide dynamic range (10^5) of activity density in a single image and with excellent linearity in response to radiation emissions. Distributions of radioactivity in nuclear debris can be generated with a raw spatial resolution of approximately 50

µm using image plate autoradiography and digital scanning. Sample preparation requirements are minimal and the analytical method does not consume or alter the sample. The dynamic range and linearity of response facilitate calibration and simulation in support of quantitative and semi-quantitative analysis not readily achieved in classical autoradiography (Berg et al. 2016, Zeissler et al. 2013). These advantages make image plate autoradiography ideal for routine characterization of nuclear debris and for the identification of areas of interest for subsequent micro-characterization methods.

An example of the insight afforded by this simple technique may be drawn from experience garnered in examination of samples collected in relation to the undeclared release and subsequent detection of ^{106}Ru throughout Europe from late September to early October 2017 (Cooke et al. 2020). The image of a blank filter and sample from the Cottbus station of the German Weather Service (Deutscher Wetterdienst) collected from 25 September to 2 October 2017 shows an almost uniformly dispersed material on the sample
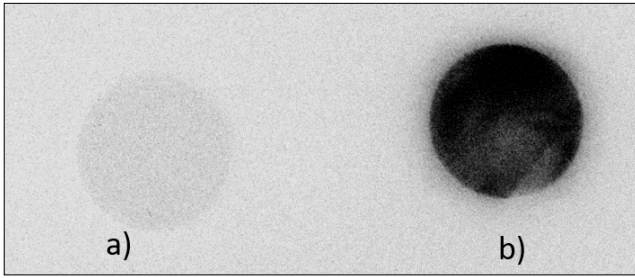
FIGURE 25.
Image plate response of a) filter blank and b) filter collected by the German Weather Service in Cottbus, Germany from 25 September 2017 to 2 October 2017 containing 18.7 Bq of ^{106}Ru.
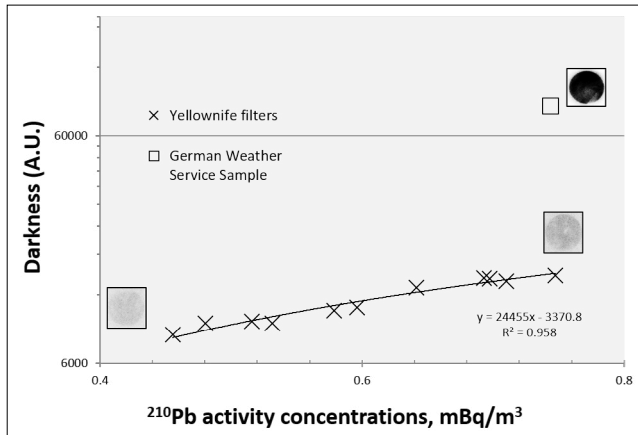
FIGURE 26.
Image plate response of a series of Yellowknife Northwest Territories filter samples at different ^{210}Pb levels and response of a ^{106}Ru containing filter from Cottbus, Germany at comparable ^{210}Pb levels as Yellowknife.

image (Figure 25). In typical filter samples of environmental aerosols, such as the series of filters from Yellowknife, Northwest Territories used to develop the ^{210}Pb to the image plate darkening relationship of Figure 25, the dominant image plate signal arises from emissions of the ^{210}Pb decay chain with neither emissions from ^{7}Be or ^{22}Na decay strongly contributing to image plate darkening. The ^{210}Pb in these samples is likewise highly dispersed having been continuously attached to ambient aerosols by decay of radon gas. The Cottbus filter caused significantly stronger darkening of the image plate considering its sample activity concentration of ^{210}Pb of 0.74 mBq/m^3. This is even more striking given its similar sample activity for ^{210}Pb and ^{106}Ru, 17.2 Bq and 18.3 Bq respectively, which results from the higher energy betas released by ^{106}Ru as it decays.

The high degree of dispersion of ^{106}Ru contrasts significantly with the discrete particles observed in emissions from the Fukushima Daiichi accident aerosols of 2011 (Zeissler et al. 2013) and the debris from a 2012 Canadian radioactive dispersal device experiment characterized for particle size in deposition (Berg et al. 2016). This speaks to a different phenomenology in the creation and history of the observed aerosols and provides (at least qualitative) insight into these processes. Such characterization provides additional considerations as to the plausible origins of the observed material. In the particular case of ^{106}Ru chemical speciation studies indicate a fuel reprocessing origin where ruthenium tetroxide (RuO$_4$) likely had a central role and was able to contribute to effective dispersion of ^{106}Ru as a vapour (Cooke et al. 2020). In this example image plate radiography was able to support the hypothesis by providing new information not available from γ-spectroscopy measurements. While image plate radiography cannot replace γ-spectroscopy it is useful during an event analysis.

Using advanced γ-spectroscopy techniques it is possible to better understand the distribution of radionuclides within a sample. Similar to how noble gas laboratory measurements can impact the event analysis, remeasurement of particulate filters using multi-dimensional detector setups can impact the key radionuclide discriminators – isotopic ratios. Section 5.3.4 shows how a dual detector system can be used to improve the output of the IMS laboratories.

5.3.4. Dual Gamma Detector Systems

Dual gamma spectroscopy offers many advantages over the current standard single detector gamma spectroscopy. The advantages offered fall into two categories – the measurement process itself and equally important the interpretation of the sample in the context of the release process or event.

In the measurement process itself dual gamma spectroscopy offers benefits to sensitivity as more photons interact with the detection system. This is useful for isotopes that are present near
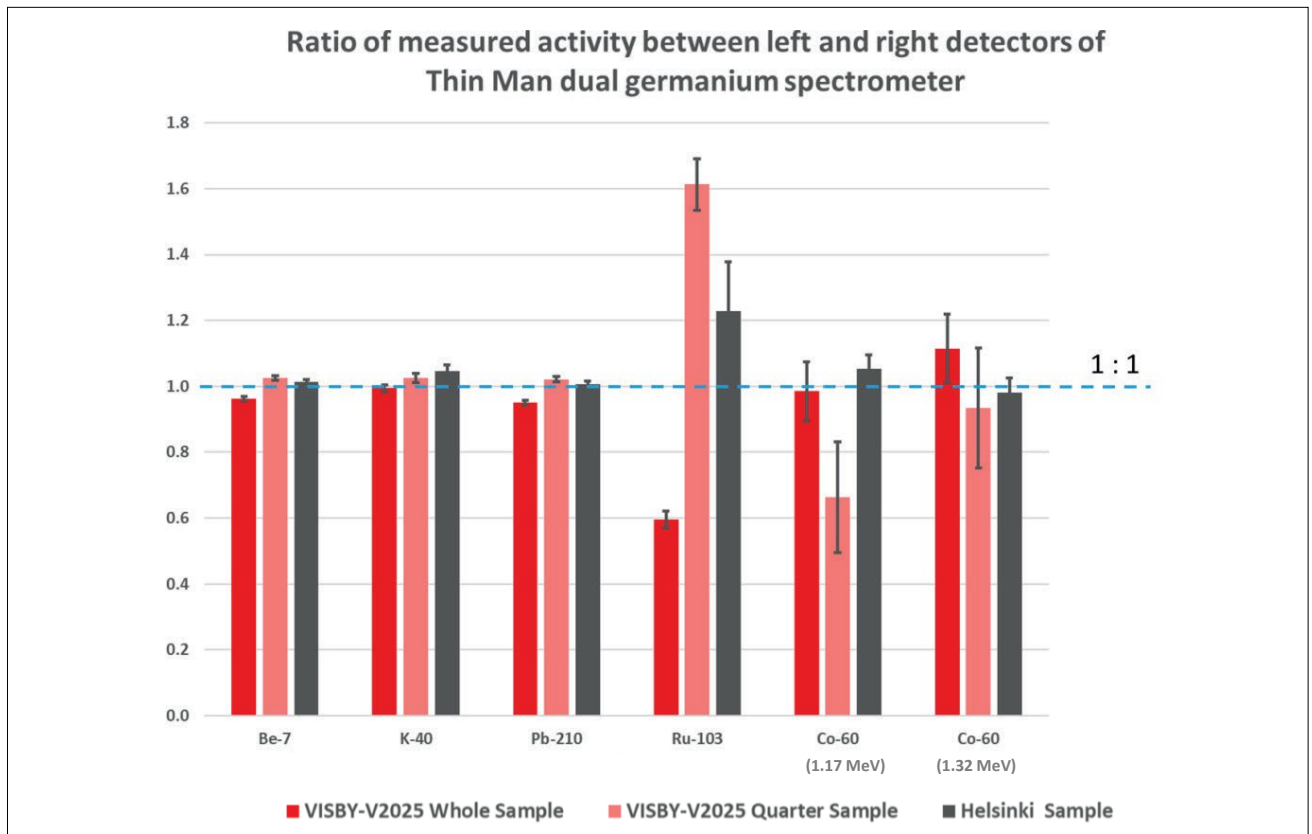
FIGURE 27.

Analysis of samples from a recent radionuclide event. The Visby sample was measured wholly and as a single quarter. The three natural radionuclides on the left were homogeneous over the filter while the fission and activation products measured showed a bias to the right or left detector, depending on how the hot particles were collected on the filter. Results from both gamma lines of ^{60}Co are shown.

or below the limits of detection. The use of dual detectors also allows for improvements in isotopic identification as specificity is enhanced by using knowledge of the decay process itself to aid in nuclide identification. By setting up the detectors with time-synchronized electronics, it is possible to measure coincidences between detectors (see Section 2.5.2). This means it is possible to remove peak interferences and significantly improve the signal to noise ratio, providing certainty in nuclide identification.

The other important advantage with dual gamma spectroscopy is related to the additional knowledge gained by inferring the physical deposition process on the sample. Often many samples are inhomogeneous, which presents challenges in their interpretation. Isotopic ratios between pairs of radionuclides is useful information in source discrimination (isotopic clock, production of blocked radioisotopes, etc.). When samples are inhomogeneous, they can give inaccurate isotopic ratios without multiple measurements to average sample inhomogeneity. A dual detector system when used to sum the response of both detectors is much more robust against sample inhomogeneity and allows for a better understanding of the sample.

Aerosol samples from the undeclared release of ^{106}Ru throughout Europe from late September to early October 2017 (Cooke et al. 2020) measured on the dual gamma spectrometer (Thin Man) of Health Canada's Radiation Protection Bureau illustrate some of these advantages. Figure 27 illustrates that the apparent activities of highly and evenly dispersed natural nuclides (^{7}Be, ^{212}Pb) and the inherent ^{40}K in the glass fibre were equally balanced between individual detectors of the dual gamma system. In contrast there can be significant differences in response of each detector due to heterogeneous distribution, for example in the sporadic detections of the fission product ^{103}Ru and the activation product

^{60}Co. Significantly the spectrum from combining the two detector signals pulse by pulse (i.e. both detectors populate the same histogram) and the average activity from each detector agreed in all cases, demonstrating how dual gamma spectrometry compensates for bias in activity and activity ratio due to sample heterogeneity.

Furthermore the apparent activities of the activation product ^{60}Co and the fission product ^{103}Ru were split differently between the left and right detectors as might be expected if each nuclide was concentrated on different particles than the other.

6. DISCUSSION

The radionuclide measurement capability of the IMS is unique when it comes to global coverage, system sensitivity, system reliability and data quality. However, this does not mean the network cannot be improved from its current generation. While the number of stations and their locations are determined by the Treaty text, new technologies are being continuously developed and as such, new detector systems have been demonstrated to improve the performance of this network. Given the importance of the nuclear component of the verification regime in the increasingly complex global security landscape, the IMS must continue to develop in order to remain sustainable and avoid obsolescence.

While the development of sensor technologies improves, confirming the presence or activity ratio of species that are otherwise undetected, the work to analyse and report on the data in the context of the CTBT gets more difficult. The circumstances which (may) lead to the release of radionuclides from an underground cavity are speculative and there is more to learn about the physical and chemical processes involved during such a release. The methods for associating one sample detection with another are complex, meaning that identifying radionuclide events from a network of sensor data is a great challenge. New software is making it easier to combine associated signals to identify a source location and reconstruct its parameters within a Bayesian framework (De Meutter and Hoffman 2020).

With an ever developing global nuclear infrastructure the effect of civil nuclear facilities on the IMS remains largely unpredictable and actively interferes with verification measurements. Civil nuclear facility emissions remain one of the great challenges to the verification power of the IMS. The newly developed next generation noble gas systems provide improved sensitivity, shorter sampling time integrals and improved reliability. These will improve the likelihood of sampling and measuring radioactive isotopes originating from a nuclear test. The reduced sampling times mean sample association and event analysis is improved.

In the field of particulate radionuclide measurements, new ideas mean that a new generation of high resolution gamma spectrometry detector systems can improve the sensitivity of stations in the IMS by orders of magnitude. Multi-detector systems and utilizing coincidence spectrometry can improve sensitivity and selectivity of the spectroscopy (Britton and Davies 2022). By modernizing the sample collection process it is possible to get more data at a faster rate (Miley et al. 2019).

Radionuclide laboratories are pioneering new technologies and measurement developments to improve sensitivity for both particulate and noble gas measurements, such as the developments in multi-detector, high resolution and multi-technologies setups, some using coincidence analysis techniques to improve detection limits by orders of magnitudes.

7. CONCLUSION

The CTBT, when it enters into force, faces a tremendous challenge – verification. IMS provides the operational means to verify the Treaty and deter states from violating the agreements within. Monitoring radionuclides in the atmosphere is a crucial part of the verification regime and scientific and engineering developments to the IMS radionuclide network will mean this can continue for many years to come.

8. ACKNOWLEDGEMENTS

APPENDIX

List of 84 CTBT-relevant radionuclides. Bold gamma energies denote the radionuclide is detected from measurements of the short-lived daughter. Reproduced from Appendix V of the Draft IDC Operational Manual.

Fission Product	Half-life	Primary γ ray Energy (keV)	Activation Product	Half-life	Primary γ ray Energy (keV)
^{91}Sr	9.63 h	1024.3	^{24}Na	14.96 h	1368.6
^{91}Y	58.51 d	1204.8	^{42}K	12.36 h	1524.7
^{93}Y	10.18 h	266.9	^{46}Sc	83.79 d	889.3
^{95}Zr	64.02 d	756.7	^{47}Sc	3.349 d	159.4
^{95}Nb	34.98 d	765.8	^{51}Cr	27.7 d	320.1
^{97}Zr	16.91 h	743.4	^{54}Mn	312.1 d	834.8
^{99}Mo	65.94 h	140.5	^{57}Co	271.8 d	122.1
^{99m}Tc	6.01 h	140.5	^{58}Co	70.82 d	810.8
^{103}Ru	39.26 d	497.1	^{59}Fe	44.5 d	1099.2
^{105}Ru	35.36 h	319.1	^{60}Co	5.271 y	1332.5
^{106}Ru	373.59 d	621.9	^{65}Zn	244.3 d	1115.5
^{111}Ag	7.45 d	342.1	^{69m}Zn	13.76 h	438.6
^{112}Pd	21.03 h	617.5	^{72}Ga	14.1 h	834.1
^{115m}Cd	44.6 d	933.8	^{74}As	17.77 d	595.8
^{115}Cd	53.46 h	336.2	^{76}As	1.078 d	559.1
^{125}Sn	9.64 d	1067.1	^{84}Rb	32.77 d	881.6
^{125}Sb	2.76 y	427.9	^{86}Rb	18.63 d	1076.7
^{126}Sb	12.46 d	695	^{88}Y	106.7 d	1836.1
^{127}Sb	3.85 d	685.7	^{89}Zr	78.41 h	909
^{128}Sb	9.01 h	743.2	^{102}Rh	207 d	475.1
^{129m}Te	33.6 d	695.9	^{106m}Ag	8.28 d	717.2
^{130}I	12.36 h	536.1	^{108m}Ag	418 y	722.9
^{131m}Te	30 h	773.7	^{110m}Ag	249.8 d	657.8
^{131}I	8.02 d	364.5	^{120}Sb	5.76 d	1171.7
^{132}Te	3.2 d	772.6	^{122}Sb	2.724 d	564.2
^{133}I	20.8 h	529.9	^{124}Sb	60.2 d	602.7
^{135}I	6.57 h	1260.4	^{132}Cs	6.479 d	667.7
^{136}Cs	13.16 d	1048.1	^{133}Ba	10.52 y	356
^{137}Cs	30.07 y	661.7	^{134}Cs	2.065 y	604.7
^{140}Ba	12.75 d	537.3	^{152m}Eu	9.312 h	841.6
^{140}La	1.678 d	1596.2	^{152}Eu	13.54 y	1408
^{141}Ce	32.5 d	145.4	^{168}Tm	93.1 d	816
^{143}Ce	33.04 h	293.3	^{187}W	23.72 h	685.7
^{144}Ce	284.9 d	133.5	^{190}Ir	11.78 d	186.7
^{147}Nd	10.98 d	531	^{192}Ir	73.83 d	316.5
^{149}Pm	53.08 h	286	^{196}Au	6.183 d	355.7
^{151}Pm	28.4 h	340.1	^{196m}Au	9.7 h	147.8
^{153}Sm	46.27 h	103.2	^{198}Au	2.695 d	411.8
^{155}Eu	4.761 y	105.3	^{203}Pb	51.87 h	279.2
^{156}Sm	9.4 h	203.8	^{224}Ra	3.66 d	241
^{156}Eu	15.19 d	1153.7	^{237}U	6.75 d	208
^{157}Eu	15.18 h	370.5	^{239}Np	2.357 d	277.6

REFERENCES

Aalseth, C.E., et al. (2009). Ultra-low background measurements of decayed aerosol filters. *Journal of Radioanalytical and Nuclear Chemistry* **282** (3) 731-735.

Aalseth, C.E., et al. (2012). A shallow underground laboratory for low-background radiation measurements and materials development. *Review of Scientific Instruments* **83** (11) 113503.

Achim, P., et al. (2014). Analysis of radionuclide releases from the Fukushima Dai-ichi nuclear power plant accident part II. *Pure and Applied Geophysics* **171** (3) 645-667.

Achim, P., et al. (2016). Characterization of Xe-133 global atmospheric background: Implications for the International Monitoring System of the Comprehensive Nuclear-Test-Ban Treaty. *Journal of Geophysical Research: Atmospheres* **121** (9) 4951-4966.

Berg, R., Gilhuly, C., Korpach, E.P., Ungar, K. (2016). Particle density using deposition filters at the full scale RDD experiments. *Health Physics* **110** (5) 471-480.

Bhat, M.R. (1992). "Evaluated nuclear structure data file (ENSDF)". *Nuclear Data for Science and Technology* (S.M. Qaim, Ed.) Springer, Berlin/Heidelberg, pp. 817-821.

Biegalski, S.R., et al. (2012) Analysis of Data from Sensitive U.S. Monitoring Stations for the Fukushima Daiichi Nuclear Reactor Accident. *Journal of Environmental Radioactivity* **114** 15-21.

Blackberg, L., et al. (2013). Memory effect, resolution, and efficiency measurements of an Al_2O_3 coated plastic scintillator used for radioxenon detection. *Nuclear Instruments and Methods in Physics Research A* **714** 128–135.

Bowyer, T.W., et al. (1996). *Automatic Radioxenon Analyzer for CTBT Monitoring*. Rep. No. PNNL-11424, Pacific Northwest National Laboratory, Richland, Washington.

Bowyer, T.W., et al. (1999). Field testing of collection and measurement of radioxenon for the Comprehensive Test Ban Treaty. *Journal of Radioanalytical and Nuclear Chemistry* **240** (1) 109-122.

Bowyer, T.W. (2021). A Review of Global Radioxenon Background Research and Issues. *Pure and Applied Geophysics* **178**.

Brauer, F.P., Kaye, J.H., Fager, J.E. (1975). NaI(Tl)-Ge(Li) Coincidence Gamma-Ray Spectrometry for Radionuclide Analysis of Environmental Samples. *IEEE Transactions on Nuclear Science* **22** (1) 661-670.

Britton, R., Burnett, J., Davies, A., Jackson, M. (2015a). A high-efficiency HPGe coincidence system for environmental analysis. *Journal of Environmental Radioactivity* **146** 1–5.

Britton, R., Jackson, M., Davies, A. (2015b). Quantifying radionuclide signatures from a γ-γ coincidence system. *Journal of Environmental Radioactivity* **149** 158–163.

Britton, R., Davies, A., Jackson, M. (2016). Incorporating X–ray summing into gamma–gamma signature quantification. *Applied Radiation and Isotopes* **116** 128–133.

Britton, R., Davies, A.V. (2019). Limits of detection — Enhancing identification of anthropogenic radionuclides. *Nuclear Instruments and Methods in Physics Research* **A 947.**

Britton, R., Davies, A.V. (2022). Next generation particulate monitoring. *Applied Radiation and Isotopes* **184.**

Burnett J.L., Davies, A.V. (2014). Cosmic veto gamma-spectrometry for Comprehensive Nuclear-Test-Ban Treaty samples. *Nuclear Instruments and Methods in Physics Research*, Section A: Accelerators, Spectrometers, Detectors and Associated Equipment, **747** 37-40.

Cagniant, A., et al. (2018). SPALAX NG: A breakthrough in radioxenon field measurement. *Applied Radiation and Isotopes* **134** 461-465.

Chester, D.L., Goodwin, M.A. (2022). "Using a Bayesian Framework to Reconstruct Radioxenon Source(s) using Measurements in the UK" Poster presented at the WOSMIP conference, Stockholm, Sweden, 2022.

Conference on Disarmament (1995). International Monitoring System Expert Group: Report based on technical discussions held from 6 February to 3 March 1995. CD/NTB/WP.224.

Cooke, M.W., Botti, A., Zok, D., Steinhauser, G., Ungar, K. (2020). Identification of a chemical fingerprint linking the undeclared 2017 release of 106Ru to advanced nuclear fuel reprocessing. *Proceedings of the National Academy of Sciences of the United States of America*. **117** (26) 14703–14711.

Davies, A.V., Britton, R. (2020). Improving the sensitivity and reliability of radionuclide measurements at remote IMS stations. *Journal of Environmental Radioactivity* **216.**

Delaune, O., et al. (2018). Low-level laboratory measurement of xenon radionuclides: Electron-photon versus photon measurements. *Applied Radiation and Isotopes* **134** 450-454.

De Meutter, P., Hoffman, I. (2020). Bayesian source reconstruction of an anomalous Selenium-75 release at a nuclear research institute. *Journal of Environmental Radioactivity* **218**.

Douysset, G., Gross, P., Fontaine, J.P., Delaune, O. (2017). "Laboratory Analysis of Radioxenon Samples as a support of the IMS network" Poster presented at the CTBT: Science and Technology Conference, Vienna, Austria, 2017.

Dubasov, Y.V., et al. (2005). The automatic facility for measuring concentrations of radioactive xenon isotopes in the atmosphere. *Instruments and Experimental Techniques* **48** (3) 373–379.

Eslinger, P.W., et al. (2014). Source term estimation of radioxenon released from the Fukushima Dai-ichi nuclear reactors using measured air concentrations and atmospheric transport modeling. *Journal of Environmental Radioactivity* **127** (1) 127-132.

Eslinger P.W., Schrom, B.T. (2016). Multi-detection events, probability density functions, and reduced location area. *Journal of Radioanalytical and Nuclear Chemistry* **307** (3) 1599-1605.

Eslinger, P.W., Ely, J.H., Lowrey, J.D., Miley, H.S. (2022). Projected network performance for multiple isotopes using next generation xenon monitoring systems. *Journal of Environmental Radioactivity* **251-252**.

Eslinger, P.W., et al. (2023). Projected network performance for next generation aerosol monitoring systems. *Journal of Environmental Radioactivity* **257** 107088.

Fontaine, J.P., Pointurier, F., Blanchard, X., Taffary, T. (2004). Atmospheric xenon radioactive isotope monitoring. *Journal of Environmental Radioactivity* **72** (1–2), 129–135.

Foxe, M., et al. (2016). Characterisation of a Commercial Silicon Beta Cell, PNNL-25297, Pacific Northwest National Laboratory.

Foxe, M., et al. (2021). Design and Operation of the U.S. Radionuclide Noble Gas Laboratory for the CTBTO. *Pure and Applied Geophysics* **178** 2741–2752.

Friedman, H., Lockhart, L.B., Blifford, I.H. (1996). Detecting the Soviet Bomb: Joe 1 in a Rain Barrel. *Physics Today* **49** (11) 38-41.

Friese, J. (2019). *The STAX project. A new data source to aid in treaty monitoring*. Report No. PNNL-SA-143481, Pacific Northwest National Laboratory.

Gheddou, A. (2021). "Novel IDC software applications for radionuclide data analysis" Presented at CTBT: Science and Technology Conference, Vienna, Austria, 2021.

Goodwin, M.A., et al. (2020). A High-Resolution Beta–gamma Coincidence Spectrometry System for Radioxenon Measurements. *Nuclear Instruments and Methods in Physics Research* **978**.

Goodwin, M.A., Davies, A.V., Britton, R. (2021). Analysis of environmental radioxenon detections in the UK. *Journal of Environmental Radioactivity* **234**.

Goodwin, M.A., Chester, D.L., Davies, A.V., Britton, R. (2022a). Analysis of radionuclide detection events on the International Monitoring System. *Journal of Environmental Radioactivity* **242** 106789.

Goodwin, M.A., Chester, D.L. (2022b). "Reconstructing radioxenon sources in a high-background environment" Presented to the CTBTO Working Group B Joint Expert Group, Vienna, Austria 2022.

Goodwin, M.A., Bell, S.J., Regan, P.H., Britton, R., Davies, A.V. (2022c). Enhancing the Detection Sensitivity of a High-Resolution β – γ Coincidence Spectrometer. *Journal of Environmental Radioactivity* **250**.

Greenwood, L.R, et al. (2017). Low-background gamma-ray spectrometry for the international monitoring system. *Applied Radiation and Isotopes* **126**.

Hayes, J.C., et al. (2015). *Requirements for Xenon International*, Report No. PNNL-22227 Rev.1. Pacific Northwest National Laboratory.

Kalinowski, M.B., Schulze, J. (2002). Radionuclide monitoring for the Comprehensive Nuclear-Test Ban Treaty. *Journal of Nuclear Materials Management* **30** 57-67.

Kalinowski, M., et al. (2010). Discrimination of nuclear explosions against civilian sources based on atmospheric xenon isotopic activity ratios. *Pure and Applied Geophysics* **167** (4) 517–539.

Le Petit, G., et al. (2015). Spalax™ new generation: A sensitive and selective noble gas system for nuclear explosion monitoring. *Applied Radiation and Isotopes* **103** 102-114.

Metz, L., et al. (2022). Source term analysis of xenon (STAX): An effort focused on differentiating man-made isotope production from nuclear explosions via stack monitoring. *Journal of Environmental Radioactivity* **255** 107037.

Miley H.S., et al. (1997). Automated aerosol sampling and analysis for the Comprehensive Test Ban Treaty. *1997 IEEE Nuclear Science Symposium Conference Record* **1** 779-785.

Miley H.S., et al. (1998). A description of the DOE Radionuclide Aerosol Sampler/Analyzer for the Comprehensive Test Ban Treaty. *Journal of Radioanalytical and Nuclear Chemistry* **235** (1-2) 83-87.

Miley H.S., et al. (2009). Alternative treaty monitoring approaches using ultra-low background measurement technology. *Applied Radiation and Isotopes* **67** (5) 746-749.

Miley, H.S., et al. (2019). Design considerations for future radionuclide aerosol monitoring systems. *Journal of Environmental Radioactivity* **208-209**.

Miley, H.S., Eslinger, P.W. (2022). Impact of Industrial Nuclear Emissions on Nuclear Explosion Monitoring. *Journal of Environmental Radioactivity*. **257**.

Perkins R.W., Robertson, D.E., Thomas, C.W., Young, J.A. (1990). "Comparison on nuclear accident and nuclear test debris." Presented at the International Symposium on Environmental Contamination Following a Major Nuclear Accident. IAEA-SM--306/125, International Atomic Energy Agency, Vienna, Austria, 1989.

Reeder, P.L., Bowyer, T.W. (1998). Delayed coincidence technique for 133gXe detection. *Nuclear Instruments and Methods in Physics Research - Section A* **408** 573-581.

Reeves J.H., Arthur, R.J., Brodzinski, R.L. (1992). "Sensitivity of LDEF Foil Analyses Using Ultra-low Background Germanium vs. Large NaI(Tl) Multidimensional Spectrometers." Presented at the Second LDEF Post-Retrieval Symposium June 1-5, 1992, San Diego, California.

Ringbom, A., Larson, T., Axelsson, A., Elmgren, K., Johansson, C. (2003). SAUNA—a system for automatic sampling, processing, and analysis of radioactive xenon. *Nuclear Instruments and Methods in Physics Research* **508** (3) 542–553.

Ringbom, A., et al (2009). Measurements of radioxenon in ground level air in South Korea following the claimed nuclear test in North Korea on October 9, 2006. *Journal of Radioanalytical and Nuclear Chemistry* **282** 773-779.

Ringbom, A., et al. (2017). "Analysis of Data from an Intercomparison between a Sauna II and a Sauna III System" Presented at the CTBT: Science and Technology Conference, Vienna, Austria, 2017.

Schlosser, C., et al. (2017). Analysis of radioxenon and Krypton-85 at the BfS noble gas laboratory. *Applied Radiation and Isotopes* **126** 16–19.

Schöppner, M., et al. (2012). Estimation of the time-dependent radioactive source-term from the Fukushima nuclear power plant accident using atmospheric transport modelling. *Journal of Environmental Radioactivity* **114** 10-14.

Schroettner, T., Schraick, I., Furch, T., Kindl, P. (2010) A high-resolution, multi-parameter, β–γ coincidence, μ–γ anticoincidence system for radioxenon measurement, Nuclear Instruments and Methods in Physics Research Section A: Accelerators, Spectrometers, Detectors and Associated Equipment, Volume 621, Issues 1–3, 2010, Pages 478-488, ISSN 0168-9002, https://doi.org/10.1016/j.nima.2010.06.227.

Singlevich, W. (1948). *Radioactive contamination in the environs of the Hanford Works for the period April - May - June, 1948*. HW-11333, General Electric Company, Hanford Works, Washington.

Topin, S., et al. (2020). 6 months of radioxenon detection in western Europe with the SPALAX-New generation system – part 1: metrological capabilities. *Journal of Environmental Radioactivity* **225**.

Wogman, N.A, Perkins, R.W., Kaye, J.H. (1969). An all sodium iodide anticoincidence shielded multidimensional gamma-ray spectrometer for low-activity samples. *Nuclear Instruments and Methods* **74** (2) 197-212.

Zeissler, C.J., et al. (2013). Radio-microanalytical particle measurements method and application to Fukushima aerosols collected in Japan. *Journal of Radioanalytical and Nuclear Chemistry*. **296** 1079–1084.

Zhang, W., Lam, K., Ungar, K. (2018). The development of a digital gamma-gamma coincidence/anticoincidence spectrometer and its applications to monitor low-level atmospheric ^{22}Na/^{7}Be activity ratios in Resolute Bay, Canada. *Journal of Environmental Radioactivity* **192** 434–439.

The International Monitoring System Radionuclide Network – A Unique Machine Not Yet Fully Exploited

A. Ringbom

Swedish Defence Research Agency, Stockholm, Sweden

Abstract

The International Monitoring System radionuclide network for Comprehensive Nuclear-Test-Ban-Treaty verification is unique. It is the only global system for detection of atmospheric radioactivity, and with a capability to measure both aerosols and noble gases using state of the art technology. The purpose of this paper is to illustrate the status of the International Monitoring System radionuclide network by giving some examples of observations made so far. In addition, some ideas and concepts for future development will be discussed. The paper also includes a general discussion on the radionuclide verification mission and the expected radionuclide signal from a nuclear explosion, as well as different background sources.

Three main paths for future development of the measurement systems are identified: increased measurement sensitivity, decreased sample collection time, and increased number of sampling points, and/or optimization of sampling locations. Examples of current work addressing these points are given. In addition, it is argued that the future development of the network would benefit from an approach that optimizes the aggregated network capability, which also includes the analysis process.

1. INTRODUCTION

The radionuclide network of the International Monitoring System (IMS) for Comprehensive Nuclear-Test-Ban-Treaty (CTBT) verification is the only one of its kind. It is the only global network for detection of airborne radionuclides, and data is distributed to all members of the CTBT, which at the time of writing includes 186 States (Preparatory Commission for the CTBTO 2022).

The IMS radionuclide network consists of 80 station locations intended for monitoring atmospheric radioactive aerosols (particulate stations). In addition, 40 of these sites are also intended for measuring atmospheric noble gases (xenon). The IMS was equipped with radionuclide monitoring systems around the year 2000, and today 73 certified particulate stations are installed (see Figure 2). Out of these, 27 systems perform fully automatic sampling, filter preparation, and activity measurements using two different technologies (Miley et al. 1998, CINDERELLA 2022). Certification of noble gas stations started about ten years later, but the first systems were installed several years before that. At present, 26 noble gas stations are certified using two different technologies (Ringbom et al. 2003, Fontaine et al. 2004).

There are important differences between the IMS and national radionuclide networks used in many countries, mainly related to their purposes. Most national networks are intended for emergency preparedness, i.e. to monitor the impact from nuclear accidents and to calculate and predict radiation dose to the population. This function can also be performed by the IMS on a coarser but global scale, as was demonstrated very well during the Fukushima accident in 2011, see for example Bowyer et al. (2011).

However, the main purpose of the IMS radionuclide network is a different one: to timely *detect, locate and categorize* a radionuclide release to be able to discriminate a release from a nuclear test against potential background sources. Location and categorization of releases are generally not the main priority for national emergency preparedness networks.

The timeliness requirement is one reason that IMS measurements generally have shorter air collection time compared to systems in national networks (less than or equal to 24 hours, compared to several days or up to one week). A short collection time also allows for better source location when backward atmospheric transport modelling is used, although this motivation was not a main design criterion when the network was designed.

Another important difference is the higher degree of automation. The requirements of the IMS prompted in the 1990s the development of a new generation of fully automatic measurement systems, and today a large fraction of the IMS radionuclide sites are equipped with technology performing automatic air sampling, sample preparation, activity measurement, and data transfer.

Another unique feature is the noble gas subnetwork, manly intended to detect releases from underground nuclear tests, which is considered the most likely method used by a potential treaty violator. Measurements of atmospheric radioxenon has been performed since the 1940s (Ziegler and Jacobson 1995), but before the IMS was established, all systems were manual or semi-automatic. Although noble gas detection is a suitable early warning detection technique, noble gas monitoring is generally not used in the radiation protection community. On a national level, routine measurements are conducted only at a few places. One reason for this in the past was the complex and labour demanding measurement procedures. However, today this situation might change, with the appearance of reliable, very sensitive, and fully automatic noble gas measurement systems, a development driven by the CTBT-verification community.

However, the IMS radionuclide network was designed more than thirty years ago using technology and knowledge at the time, and the experience from twenty-five years of operation can now be used to further increase the network verification capability. Today we know that the
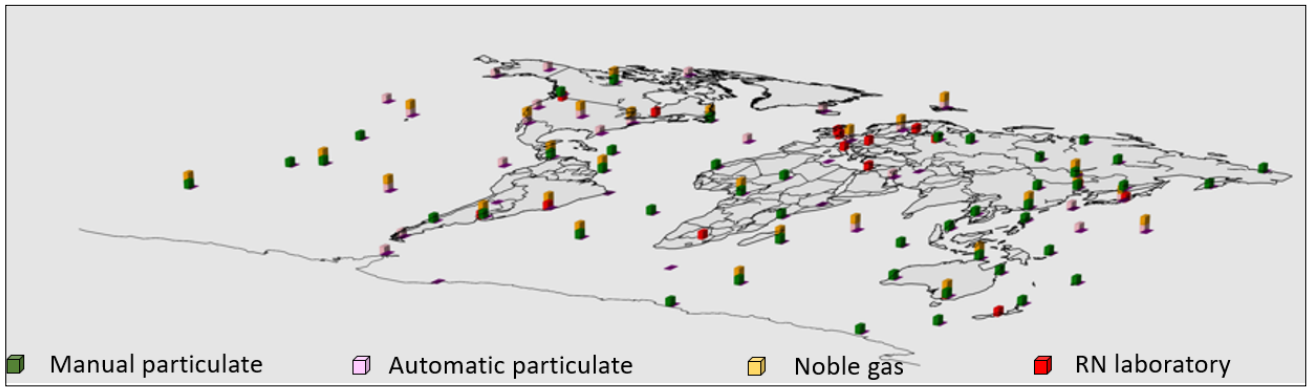
FIGURE 1.
Certified measurement systems in the IMS radionuclide network as of 2021.
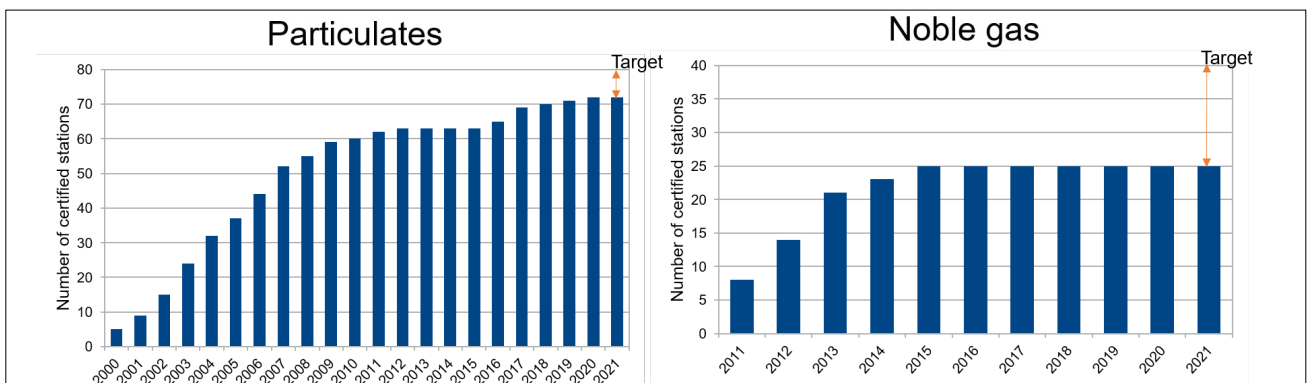
FIGURE 2.
Time development of the number of certified particulate and noble gas stations in the IMS.

release scenarios for underground explosions used in the design phase of the IMS were orders of magnitude higher than what has been observed or estimated from the tests made by the People's Democratic Republic of Korea. In addition, the network design was largely driven by detection performance, and to a lesser extent by location and categorization capabilities (CD 1995). The number of stations, as well as their locations, was partly, and by necessity, a result of political negotiations and practical circumstances, and not based on science alone. Finally, the knowledge of the radionuclide background thirty years ago was limited compared to what we know today. The last two points are particularly true for noble gases.

Although the IMS radionuclide network has proven itself to be a very capable verification tool, experience from system operation and data analysis show that there is room for improvement to further increase its capability.

The paper will illustrate the status of the IMS radionuclide network by giving some examples of observations made so far. In addition, some ideas and concepts for future development of IMS radionuclide sites will be discussed.

The paper is intended for both experts and non-experts in the field. Section 2 is devoted to a general discussion on the radionuclide verification mission and the expected radionuclide signal from a nuclear explosion, as well as different background sources. Section 4 provides examples using observations made over the last 25 years. Possible developments in view of the status is discussed in Section 5, and summary and conclusions are given in Section 6.
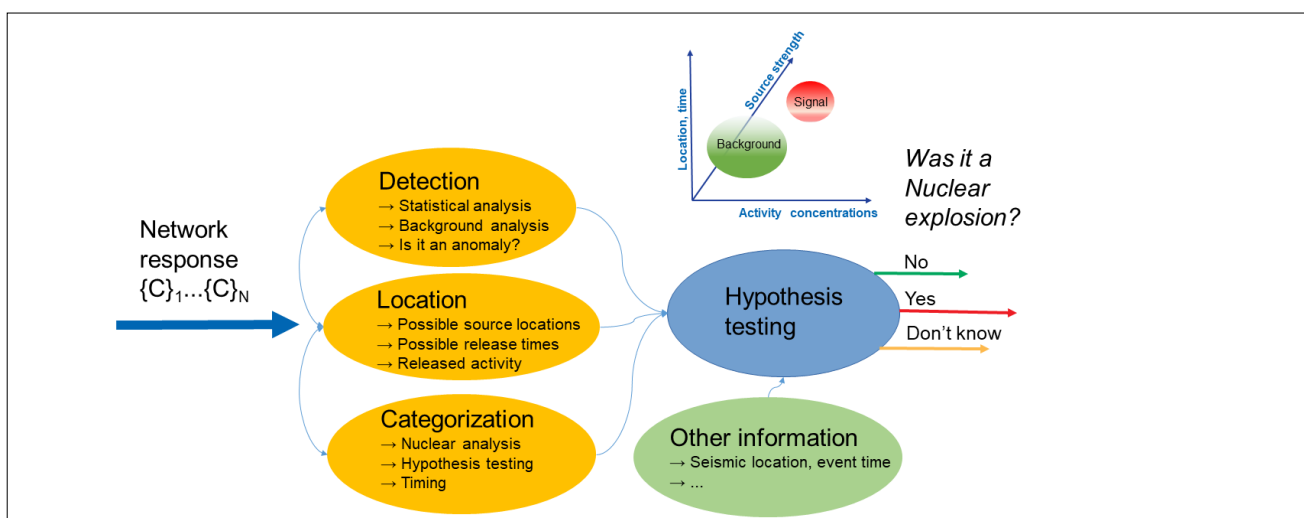
2. THE RADIONUCLIDE VERIFICATION MISSION

The task of the IMS radionuclide network is to deliver data that maximizes the possibility to detect, locate, and characterize nuclear releases to provide evidence with enough confidence that a nuclear explosion has occurred. This scientific problem is best formulated by considering measurement and analysis as a single system. Given a certain analysis method, the data that the network delivers should be tailored to minimize the uncertainty of the result of the analysis. Since resources for equipment, network operation, and analysis is limited, compromises have to be made, for example regarding number and placement of measurement stations. In the case of CTBT verification, political considerations also come into play.

One way to view the radionuclide verification process is presented in Figure 3. Given a certain network response consisting of a set of isotopes and measured activity concentrations from stations, $\{C\}_1,\{C\}_2,\ldots,\{C\}_N$, which also can include non-detections, an analysis in three steps is performed. Here, the first step, *detection,* does not refer to the spectral analysis used to establish whether a nuclide is detected, but rather to a statistical analysis, which compares the network response to the normally observed background. The analysis attempts to establish whether the observed isotopes, activity concentrations, and isotopic ratios, are caused by background sources or if the observations constitutes an

anomaly. The *location* analysis uses backwards atmospheric transport modelling in combination with different source location techniques to identify possible regions in space and time where a release might have occurred, as well as released activity for each observed isotope. Also here, it is established whether the results are anomalous or not (for example: did the release occur at a place not observed before?). The third analysis step is the *categorization*, which is a nuclear analysis comparing the observed isotopic ratios with modelled release scenarios from various potential release sources (e.g. nuclear explosions, isotope production facilities, or nuclear power plants). The nuclear analysis also has the potential to put limits on the time of fission. Finally, all analysis results are combined, and hypothesis testing is conducted in the multidimensional observable space consisting of activity concentrations, possible source locations, release times, released activity, nuclear scenarios, as well as other information. When performing the hypothesis testing, it is very important not to only search for a nuclear explosion scenario that can explain the observations. One way to reduce such confirmation bias is to compare the results against a set of pre-defined criteria, which all should be fulfilled to be able to report that a nuclear explosion occurred.

When viewing the verification process in this way it can be concluded that, for a given budget,

FIGURE 3.
An illustration of the radionuclide verification process.

it is not obvious how to design the network to maximize the verification capability of the aggregated sensor-analysis system. The goal of the design should be to maximize the signal to background ratio in the multidimensional observable space indicated in Figure 3, which includes not only the capability to detect radioactive isotopes in the atmosphere, but also location and characterization capabilities. When discussing possibilities of future development of the IMS to increase its verification capability, this perspective can be helpful.

3. THE RADIONUCLIDE SIGNAL

In a nuclear explosion, more than 1200 fission products are formed instantly or later by decay. In addition, isotopes are formed by the activation of surrounding material, and some of the original bomb fuel might escape the explosion. The possible isotopic composition of the radionuclide signal from a nuclear explosion considered in IMS is defined by the CTBT-relevant radionuclide list (Matthews 2005). The isotopes in the list have been selected according to a few criteria: They should be formed in high enough quantities, the half-life should be long enough to allow for transport, collection, and detection, and they should have detectable gamma radiation. In addition, the list should be agreed upon among the CTBT States Signatories. This has resulted in a list of 88 isotopes, of which 46 are formed in fission, and 42 in activation.

The distribution of half-life of the CTBT-relevant nuclides ranges between 6 hours (^{99m}Tc) and 418 years (^{108m}Ag). The fission product with the longest half-life is ^{137}Cs (30 years). Although only 46 fission products out of the more than 1200 produced are considered CTBT-relevant, they constitute about 50% of the remaining fission product activity after one day.

Clearly, not all CTBT-relevant nuclides are equally probable to be detected. The detection probability depends on many factors, such as produced amount, intensity and energy of the decay radiation, decay rate (related to half-life), environmental conditions, and volatility. For atmospheric explosions, Matthews (2005) calculates a "detection probability index", showing that the five most "significant" radionuclide aerosols in an atmospheric explosion after three days are ^{99}Mo, ^{133}I, ^{143}Ce, ^{132}Te, and ^{140}La. In an underground nuclear explosion, the xenon isotopes are by far the most significant due to their chemical inertness (making them more likely to escape the cavity) and large fission yields, followed by isotopes of iodine.

The background, i.e. detections not related to a nuclear explosion, are either natural or anthropogenic. Natural background includes members of the uranium and thorium series such as ^{212}Pb, nuclides in resuspended soil like ^{40}K, and cosmogenic nuclides like ^{7}Be and ^{24}Na.

Anthropogenic sources include industrial isotope production facilities, nuclear power plants, research facilities, other civil uses of radioactive material and nuclear accidents and historical nuclear tests.

4. EXAMPLES OF RADIONUCLIDE OBSERVATIONS IN THE INTERNATIONAL MONITORING SYSYTEM OVER THE LAST 20 YEARS

The database of the Comprehensive Nuclear-Test-Ban Treaty Organization International Data Centre (IDC) contains about 326 000 categorized aerosol samples measured during the period 2000-2021, and about 111 000 categorized noble gas samples, collected during 2011-2021. This

data constitutes an immense resource of scientific information. Some aspects of the content of the database are illustrated in Figure 4 using nuclide charts. Excluding ^{212}Pb and ^{7}Be, which are always present, 45 098 detections from the particulate stations were reported by the IDC, distributed over 118 different nuclides.

Table 1 lists the ten most abundant particulate nuclides during 2013-2021 (the period was chosen to reduce the effect of the Fukushima accident, which is a special case). We note that seven of the ten most detected nuclides are CTBT-relevant, and that all nuclides are anthropogenic, except for ^{24}Na.
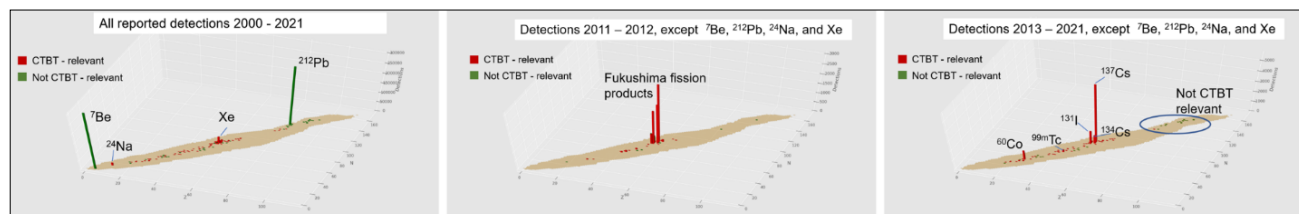
FIGURE 4.

Nuclide charts illustrating radionuclide detection statistics measured by the IMS. The left panel shows all data during the period 2000-2021 (including the always present ^{212}Pb and ^{7}Be). The middle panel shows data strongly affected by the Fukushima accident, and the left panel shows data collected later.

Table 1. The Ten Most Abundant Particulate Nuclides During the Period 2013-2021, Excluding ^{212}Pb And ^{7}Be

Nuclide	Fraction of 185 834 samples (%)	CTBT-relevant
^{24}Na	5.3	Y
^{137}Cs	3.1	Y
^{131}I	0.69	Y
^{60}Co	0.51	Y
^{134}Cs	0.45	N
^{99m}Tc	0.12	Y
^{133}I	0.030	Y
^{54}Mn	0.027	Y
^{241}Am	0.025	N
^{122}Sb	0.022	N

Following the long lived ^{137}Cs, mainly coming from previous nuclear accidents and test explosions, ^{131}I is the second most detected anthropogenic nuclide in the IMS. Another isotope of iodine, ^{133}I also on the top ten list, and a large part of the origin of these detections goes unidentified (this is true also for most other detected nuclides). Iodine is the aerosol most likely to escape an underground nuclear test, and this stresses the importance to continue to identify iodine background sources, to increase the possibility of correctly assigning iodine coming from an underground nuclear explosion; see Eslinger et al. (2022). The geographical distribution of the iodine detections for three time periods (pre- during- and post Fukushima) are shown in Figure 5. As expected, the distribution shortly after the Fukushima accident was evenly distributed across the northern hemisphere, while the pattern is more irregular during other time periods.

The knowledge of the atmospheric radioxenon background has increased tremendously thanks to the establishment of the IMS. Earlier, it was generally believed that the main radioxenon background contributor was nuclear power plants and would consists of ^{133}Xe only. We now know that globally, 95% of the atmospheric radioxenon comes as a bi-product from production of ^{99}Mo used in medical applications (Achim et al. 2016) and that all four CTBT-relevant isotopes ($^{133, 131m, 133m, 135}$Xe) are regularly observed. The background is global, but the variation between stations is high. There are low background stations at the southern hemisphere with almost
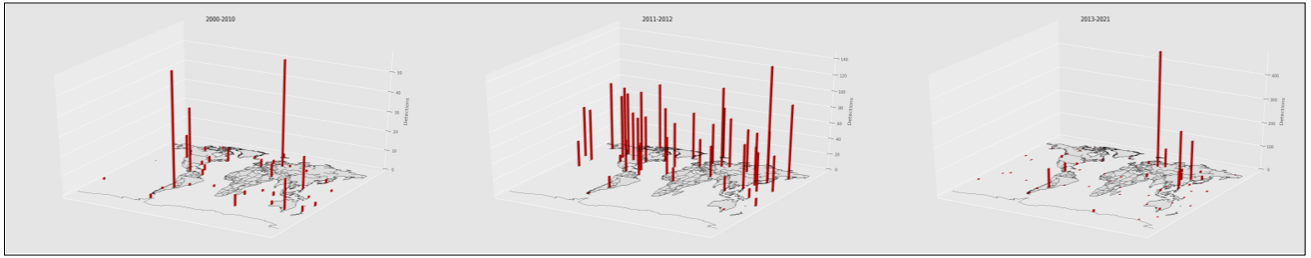
FIGURE 5.
The geographical distribution of iodine detections for three time periods. From left to right: pre-, during- and post Fukushima.

no detections, and there are sites averaging several mBq/m³ of ^{133}Xe. Some stations have a relatively large fraction of ^{131m}Xe. Many sources are known, but several are still not identified. Releases from isotope production can mix with a nuclear explosion release and disturb the isotopic ratios, leading to a wrong categorization. This is particularly true for releases of ^{99}Mo production, where shorter neutron irradiation times lead to isotopic ratios more similar to nuclear explosion ratios, compared to nuclear power plants. It is therefore important to have detailed release data and to reduce the radioxenon emissions from medical isotope production. See Bowyer (2021) for a more detailed discussion on the radioxenon background.

Since xenon, opposite to aerosols, is regularly emitted from nuclear facilities in relatively large amounts, and is routinely monitored at the plants, radioxenon data can play an important part in the development of atmospheric transport models and source location methods. It is now possible to predict the average behaviour of the

observed radioxenon levels observed by IMS stations using forward modelling in combination with generic release data (Achim et al. 2016). For individual cases, however, model and data may differ substantially due to impact from local sources and uncertainties in the atmospheric transport models (see Figure 6). It is therefore important to continue to measure the spatial and temporal distribution of atmospheric radioxenon and to further develop atmospheric transport calculations, including quantifiable associated uncertainties.

The announced nuclear tests made by the People's Democratic Republic of Korea performed in 2006, 2009, 2013 and 2017 have been crucial tests of the IMS. A few conclusions from this experience with respect to radionuclides are:

- Radioxenon could firmly be associated with only two out of the six tests, 2006 and 2013. In the former case, an IMS observation was compatible with a release from the test (Saey et al. 2007), and a national measurement
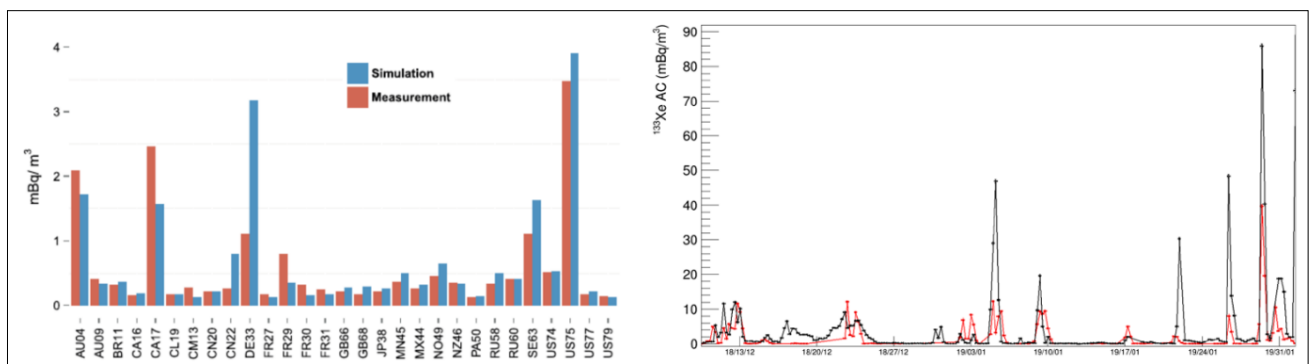
FIGURE 6.
Left panel: Simulated and measured annual averaged ^{133}Xe activity concentrations at IMS sites (Achim et al. 2016). Right panel: Simulated and measured ^{133}Xe activity concentrations from Stockholm air. The simulations were calculated using release data from the nearby Forsmark nuclear power plant (Ringbom et al. 2020).

further strengthened the case (Ringbom et al. 2009). In 2013, releases were detected at two IMS stations almost two months after the test (Ringbom et al. 2014).

- No particulate radioactivity (for example iodine) was observed from any of the tests.
- The ^{133}Xe activity estimate from the test in 2013 are about 1012 Bq, which is two orders of magnitudes lower than assumed in the network design (CD 1995).
- Atmospheric transport calculations using non-detects from two of the tests indicate a maximum prompt release of ^{133}Xe of about 10^{11} Bq.
- There are indications of later seepage from a few of the tests (Gaebler et al. 2019, De Meutter et al. 2017), but no conclusive evidence of this has been found.

5. FUTURE DEVELOPMENT

On a high level, one may identify three main development paths for the radionuclide measurement systems in the IMS to improve verification capability:

1) Increased measurement sensitivity of the individual stations.
2) Decreased sample collection time.
3) Increased number of sampling points, and/or optimization of the station locations.

Increased detection sensitivity will also improve location and characterization performance through the increased number of samples containing detected nuclides and reduced measurement uncertainties. Detection sensitivity and collection time may affect each other negatively so a trade-off is necessary. Increasing the number of sampling locations will increase detection probability, as well as the signal, through decreased average source-receptor distance. If the current number of forty sampling coordinates are used, an optimization of the positions, using detection coverage studies, will have the same effect, but to a lesser extent. In addition to technical improvements of the measurement network itself, the knowledge of background sources is crucial to the verification capability as input to the signal interpretation and should be a central part of the continued development. A few examples on recent developments and ideas in measurement technologies show a promising increase in the performance of IMS-RN. However, there is continued work on analysis methods and background studies, which are equally important in order to obtain an effective verification process.

In contrast to radioxenon, the methods used to measure particulate radioactivity has stayed essentially the same since the installation of the first systems in the late 1990s. Recently there has been several studies and suggestions aiming to further improve this capability. Design considerations for the next generation aerosol monitoring systems are discussed for example in Miley et al. (2019). Other ideas for development include increased sensitivity to measure short lived isotopes (which now is impaired by the 24-hour ^{212}Pb decay preceding the activity measurement), more efficient air collection using electrostatic sampling, decreased collection time, and improved detection efficiency by modifying sample geometry and optimizing the radon decay time.

At present, the activity measurement in both manual and automatic IMS aerosol systems are performed using one HPGe-detector in singles mode. One way to improve the measurement sensitivity, also at radionuclide laboratories, is to use two detectors in a gamma-gamma coincidence configuration (Britton et al. 2015. This technique has several benefits. The spectral background can be greatly reduced, biases from sample inhomogeneities are reduced, and the redundancy will increase, since one detector still can measure the sample if the other one breaks.

While next generation aerosol sampling systems remain to be developed, next generation noble gas systems have already been developed. The first system, the SAUNA III at station RN63 Stockholm, is already installed and certified.
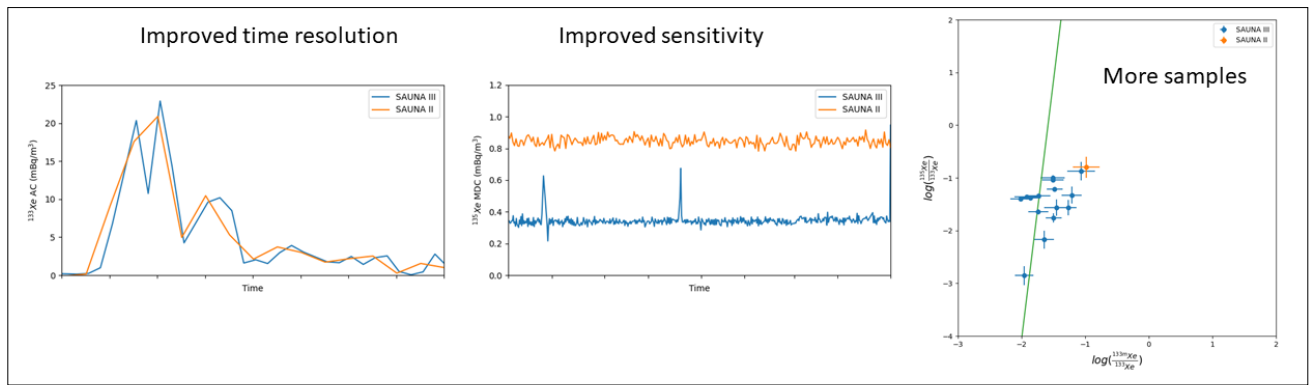
FIGURE 7.

An illustration of improved verification capability obtained by a next generation radioxenon system made by comparing data from SAUNA II and III. The left panel shows the effect of increased time resolution. The middle panel illustrates the improved sensitivity by comparing the minimum detectable concentrations, while the right panel shows the additional number of samples obtained in a multi-isotope plot used for source characterization.

New generation noble gas systems address both measurement sensitivity and collection time enhancing detection, location, and characterization (see Figure 7).

Another new development in the field of radioxenon detection is *radioxenon arrays*; a new measurement concept resulting from an optimization analysis of the total verification performance of a detection network. This analysis concluded that a cost-effective verification network can consist of many less sensitive sampling and analysis units connected into an array system. A proof of concept radioxenon array, consisting of five so called SAUNA Q_B – units is currently operating in Sweden, and preliminary data indicate a high verification performance. Multiple sampling locations spread out across an entire country make possible source regions generally smaller, where local sources can be excluded. Location is further improved using non-detections and the ATM-uncertainties are reduced by shorter plume travelling times, as on average, the signal is increased.

6. SUMMARY AND CONCLUSIONS

Being the only global system for detection of atmospheric radioactivity, and with its capability to measure both aerosols and as noble gases using state of the art technology, the IMS radionuclide network is unique. Data collected during the last 20 years contain a wealth of scientific information and has resulted in an increased knowledge of the radionuclide background signal. However, much of this information remains to be explored, and the origins of many of the observations are still unknown. Important examples include observations of ^{131}I, ^{133}I, and samples containing almost pure ^{131m}Xe and ^{135}Xe.

The network was designed almost 30 years ago with a large focus on detection capability, giving less importance to location and characterisation capabilities. The future development of the system would benefit from an approach that optimizes the aggregated network capability, which also includes the analysis process.

Three main paths for future development of the measurement systems have been identified: Increased measurement sensitivity, decreased sample collection time, and increased number of sampling points and/or optimization of sampling locations.

Some of these aspects have already been addressed by the next generation noble gas systems, which has an increased time resolution to provide better data for source location and provides an increased number of samples

which has the potential to improve source characterization. Initial ideas for next generation aerosol systems also takes this into account. Other ideas for future aerosol measurements include improvement of measurement sensitivity using gamma-gamma coincidence measurements.

The IMS radionuclide network fulfils its purpose well but the experience gained from 20 years of operation, used in combination with the development of new measurement technologies and analysis methods, will make CTBT-verification even more efficient.

REFERENCES

Achim, P., et al. (2016). Characterization of Xe-133 global atmospheric background: Implications for the International Monitoring System of the Comprehensive Nuclear-Test-Ban Treaty. *Journal of Geophysical Research: Atmospheres* **121** (9) 4951-4966.

Bowyer, T.W. (2021). A Review of Global Radioxenon Background Research and Issues. *Pure and Applied Geophysics* **178** 2665-2675.

Bowyer, T.W., et al. (2011). Elevated radioxenon detected remotely following the Fukushima nuclear accident. *Journal of Environmental Radioactivity,* **102** (7) 681-687.

Britton R., et al. (2015). Quantifying radionuclide signatures from a γ–γ coincidence system. *Journal of Environmental Radioactivity*, **149** 158-163.

CD 1995. United Nations Conference on Disarmament Ad Hoc Committee on a Nuclear Test Ban. Working Group on Verification (1995). *International Monitoring System Expert Group: Report based on technical discussions held from 6 February to 3 March 1995*. United Nations, Geneva.

CINDERELLA (2022). Automated Air Sampling Station; see https://www.senya.fi/cinderellag2.php (accessed Dec. 2022).

De Meutter, P., Camps, J., Delcloo, A., Termonia, P. (2017). Assessment of the announced North Korean nuclear test using long-range atmospheric transport and dispersion modelling. *Scientific Reports* **7** 8762.

Eslinger P.W., et al. (2022). Impact of Environmental Backgrounds on Atmospheric Monitoring of Nuclear Explosions. *Pure and Applied Geophysics*.

Fontaine, J.-P., Pointurier, F., Blanchard, X., Taffary, T. (2004). Atmospheric xenon radioactive isotope monitoring. *Journal of Environmental Radioactivity,* **72** (1-2) 129-135.

Gaebler, P., et al. (2019). A multi-technology analysis of the 2017 North Korean nuclear test. *Solid Earth* **10** 59–78.

Matthews, K.M. (2005). *The CTBT Verification Significance of Particulate Radionuclides Detected by the International Monitoring System*. Ministry of Health National Radiation Lab Report, Christchurch, New Zealand.

Miley, H.S., et al. (1998). A description of the DOE radionuclide aerosol sampler/analyzer for the Comprehensive Test Ban Treaty. *Journal of Radioanalytical and Nuclear Chemistry* **235** 83–87.

Miley, H.S., et al. (2019). Design considerations for future radionuclide aerosol monitoring systems. *Journal of Environmental Radioactivity* **208-209**.Preparatory Commission for the comprehensive Nuclear-Test-Ban Treaty Organization (2022). *Website of the Preparatory Commission for the Comprehensive Nuclear-Test-Ban Treaty;* see http://www.ctbto.org/ (accessed Dec. 2022).

Ringbom, A., et al. (2014). Radioxenon detections in the CTBT International Monitoring System likely related to the announced nuclear test in North Korea on February 12, 2013. *Journal of Environmental Radioactivity* **128** 47–63.

Ringbom, A., et al. (2020). Radioxenon releases from a nuclear power plant: Stack data and atmospheric measurements. *Pure and Applied Geophysics* **178** 2677-2693.

Ringbom, A., et al. (2009). Measurements of radioxenon in ground level air in South Korea following the claimed nuclear test in North Korea on October 9, 2006. *Journal of Radioanalytical and Nuclear Chemistry* **282** 773-779.

Ringbom, A., et al. (2003). SAUNA – a system for automatic sampling, processing, and analysis of radioactive xenon. *Nuclear Instruments and Methods in Physics Research Section A: Accelerators, Spectrometers, Detectors and Associated Equipment* **508** (3) 542-553.

Saey, P.R.J. et al. (2007). A long distance measurement of radioxenon in Yellowknife, Canada, in late October 2006. *Geophysical Research Letters* **34** (20).

Ziegler, C.A., Jacobson, D. (1995). *Spying Without Spies: Origins of America's Secret Nuclear Surveillance System.* Praeger Publishers, Westport, CT.

Screening of Nuclear Test Explosions Using Radionuclide Measurements

T.W. Bowyer

Pacific Northwest National Laboratory, Richland, Washington, USA

M.B. Kalinowski

Comprehensive Nuclear-Test-Ban Treaty Organization, Vienna, Austria

Abstract

For the International Monitoring System (IMS) to be effective, it is vital that nuclear explosion signals can be distinguished from natural and man-made radioactivity in the atmosphere. The International Data Centre (IDC) applies standard event screening criteria, with the objective of characterizing, highlighting, and thereby screening out, events considered to be consistent with natural phenomena or non-nuclear, human-made phenomena. This paper looks back to the initial understanding of possible screening methods in the early years of Comprehensive Nuclear-Test-Ban Treaty negotiations, summarizes the development of the categorization schemes and screening flags applied in the IDC reports for each particulate and noble gas sample, and reviews new proposals and open issues for discriminating nuclear explosion signals from normal radioactivity background in the atmosphere. There is still high need and ample room for enhancing radionuclide screening methodologies. This paper sketches out what methods that were already demonstrated can be enhanced and implemented in the coming years, which novel methods appear promising to be developed and it creates a vision of highly effective screening for the longer future.

1. INTRODUCTION

The Comprehensive Nuclear-Test-Ban Treaty (CTBT) specifies that standard bulletins will be created by the International Data Center (IDC) with the objective to characterize and thereby 'screen out' events considered to be consistent with natural phenomena or non-nuclear human-made phenomena. For radionuclide detection technology, this amounts to determining whether detections are consistent with non-nuclear explosive events by analyzing the isotopes present in either noble gas or particulate radionuclide Spectra elected in International Monitoring System (IMS) stations so that analysts can quickly determine from the IDC analysis whether the spectra is likely to be of interest for further review by a National Data Centre (NDC). There are several techniques that can be used to screen out non-interesting events and this paper reviews current and possible future screening techniques for radionuclide analyses.

Currently, radionuclide screening is the 'categorization' of radionuclide spectra collected from IMS stations and analysed at the IDC. Each spectrum collected by an IMS station is analysed and categorized according to its isotopic concentration, and a level is assigned to the spectrum according to preset criteria considering the history of detections at the station, and whether key isotopes consistent with a nuclear explosion are detected and if not, the spectra will be screened out. Spectrum categorization is performed separately for noble gas and particulate-borne radionuclides and the categorization criteria are not currently combined. Figures 1 and 2 show the categorization schemes for radioactive particulate-borne and noble gas radionuclides, respectively.

The philosophy of the screening process is to flag spectra collected by the IMS and analysed by the IDC for closer inspection by NDCs. Additional analyses that could be performed by NDCs include the checking of the analysis performed by the IDC, performing atmospheric transport modeling (ATM) and comparing the results to models and/or other information potentially important to the determination of whether the spectrum is consistent with a nuclear explosion. Under the current categorization scheme, the Provisional Technical Secretariat (PTS) sends Level 5 particulate samples to laboratories for reanalysis to perform confirmatory analysis and detect additional relevant radionuclides that may have not been detected in the spectrum at the IMS station. This is because short lived background from natural isotopes has decayed for only 24 hours and the acquisition time is limited to 24 hours.

The CTBT allows for additional special studies and expert technical analyses (ETA) that could be conducted as well, upon request and based on the results from the collected spectra. Although not currently instituted, additional analyses could be performed such as the sending of samples to laboratories under a wider variety of conditions such as the detection of a seismic event or detection of radionuclides at adjacent stations and other options. The purpose of the ETA of IMS and other relevant data provided by the requesting State Party is to assist the State Party concerned to identify the source of specific events. A suite of methodologies is being developed and implemented for characterizing an event as part of the ETA. These methods could go beyond anomaly detection because a nuclear explosion signal might appear as quite normal. Instead, these methods either check for sample characteristics that might be consistent with a nuclear explosion signal or they make additional assumptions such as explosion time and location-based on which it is investigated whether the sample is in agreement with these assumptions. Many of these methodologies are suitable for routinely screening the daily radionuclide data to highlight samples that have a characteristic matching a possible signal from a nuclear test. The idea of empowering NDC users implies that these methodologies shall be applied as much as possible to fully explore IDC products in routine operations for the generation of the screened radionuclide results.

The particulate and noble gas categorization schemes differ primarily because of the fewer

number of noble gas (radioactive xenon) isotopes (^{131m}Xe, ^{133}Xe, ^{133m}Xe, and ^{135}Xe) that are consistent with nuclear explosions. In the case of particulates, the PTS currently uses 84 radionuclides for particulates (De Geer 2001). The list of particulate-relevant radionuclides into 42 activation and 42 fission products that when detected could be indicative of a nuclear explosion and therefore the non-detection of these radionuclides would cause a spectrum to be screened out from further analysis.

2. RADIOACTIVE XENON ISOTOPES CATEGORIZATION

The xenon noble gas spectrum categorization scheme is shown in Figure 1. This categorization scheme allows xenon spectra to 'advance' in importance from A to C as at least one isotope of the four isotopes noted above is detected at the station at a concentration above what is typical for the station. As in the case of particulates, 'anomalous for station' is defined as a concentration, C, exceeding the medium concentration plus three times the difference between the upper and lower quartiles for one or more isotopes:

where $\ C > \langle C \rangle + \ 3(C_1 - C_3)$

$\langle C \rangle$ = the median concentration over the past 365 days,

C_1 = the first (upper) quartile concentration over the past 365 days, and

C_3 = the third (lower) quartile concentration over the over the past 365 days.

It was suggested in the 1990s that xenon isotopic ratios could be used for the screening of noble gas spectra (Bowyer et al 1998). In that simple formulation, it was proposed that the xenon airborne activity isotopic ratios ^{133m}Xe/^{133}Xe and ^{135}Xe/^{133}Xe could be used to assist in the determination of whether a nuclear explosion had occurred. This technique extended in 2006 when it was proposed to base screening on the correlation between these ratios and other combinations of the radioxenons of interest for nuclear explosions (Kalinowski and Pistner 2006). A few years later, it was shown how this proposal works with IMS observations (Kalinowski et al. 2010). In the 'Kalinowski' or multi-isotope ratio correlation plots in Figure 2, an arbitrary discrimination line can be drawn that clearly indicates the region between nuclear explosive versus the ratios expected from other nuclear processes. Unfortunately it was also recognized that both nuclear power reactors during startup and shutdown conditions (Ringbom et al. 2021) and fission-based medical isotope production can cause events to be difficult to discriminate (Biegalski et al. 2010, Saey et al. 2010). In case of nuclear power plants this occurs when the three-isotope plot is used without ^{131m}Xe and for medical isotope production facilities stack release data and environmental observations show that it is not as difficult as anticipated from the theoretical calculations (Goodwin et al. 2021). Nevertheless, even with multiple radioxenon isotopes being available, event type discrimination is not a save screening method. Another problem is that mixing in of ^{131m}Xe left over from earlier releases, a fresh plume from a nuclear test moves the signal on the four isotope plot from the nuclear explosion domain into the nuclear reactor region. This occurred with the nuclear test announced by the Democratic People's Republic of Korea in 2006 (Ringbom et al. 2009).

Both screening concepts assume that more than one xenon isotope is detected, and optimally all four of the important radioxenons. However, it may not be the case that even more than one isotope is detected from any given event, including from a nuclear explosion. In fact, the first published detection of radioxenon arising from a nuclear explosion detected in the IMS reported only a single isotope used for screening (Saey et al. 2007, Becker et al. 2010). Following the experience of several years of detections of radioxenon isotopes in the IMS
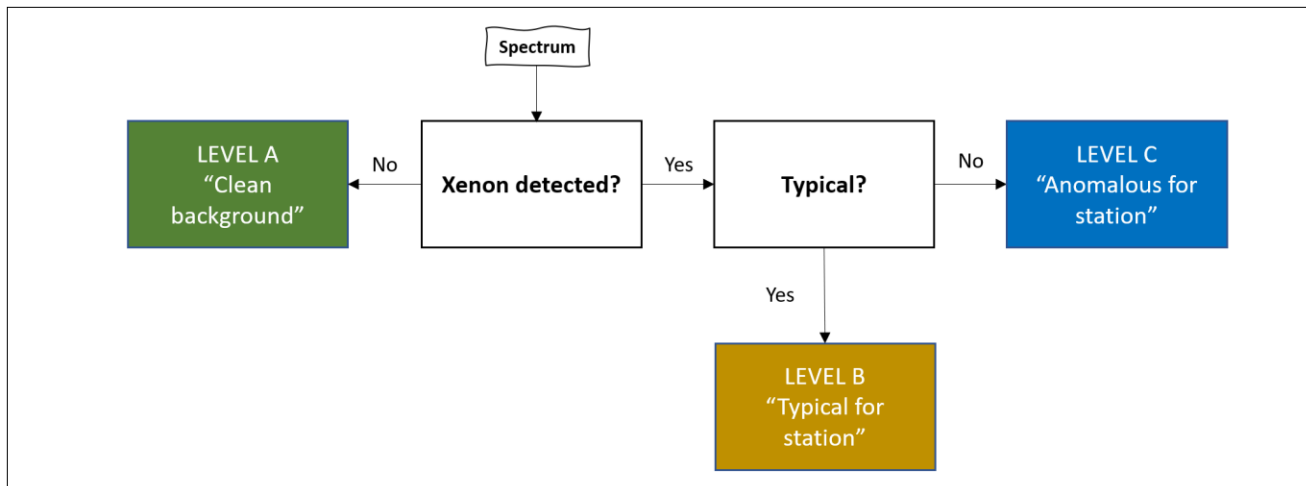
FIGURE 1.
Xenon noble gas spectrum categorization scheme currently used by the IDC.

including detection of nuclear explosions, the categorization scheme in Figure 1 is in use today.

The noble gas categorization scheme is not perfect and there are scenarios in which an event from human-made processes could be identified as a nuclear explosion using the scheme and flags outlined above. For example, xenon isotopes created during the startup of a nuclear reactor or in the production of fission based isotopes are similar in proportions (ratios) to those expected from a nuclear explosion. As mentioned before in the case that only a single isotope is detected, the categorization scheme shown in Figure 1 will have limitations since without additional information it is impossible to discriminate a single isotope detection from normal backgrounds. Combining noble gas information with other types of information such as ATM can improve these false positive and negative rates and is discussed more below.
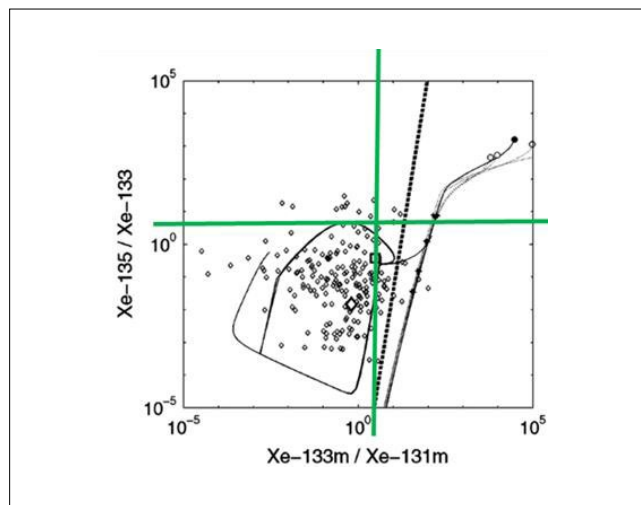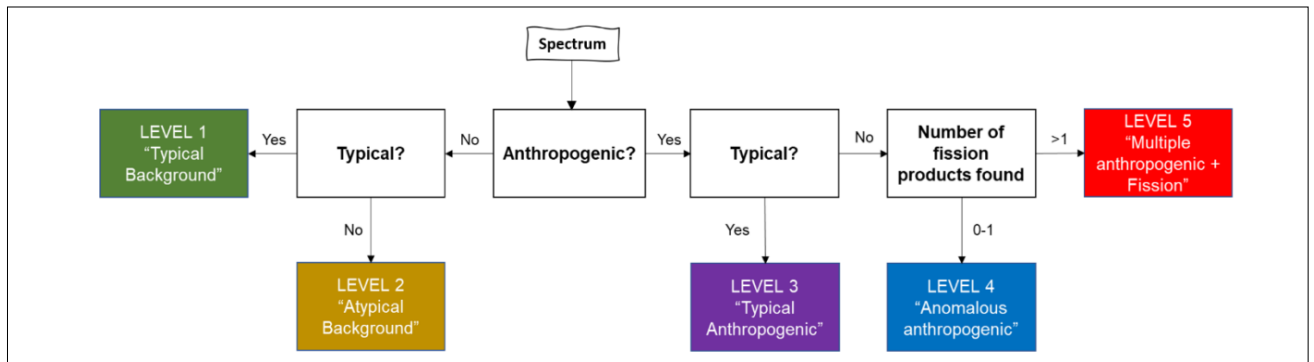

FIGURE 2.
Xenon isotopic correlation plot showing a possible discrimination line that could be used to screen out non-explosive events.

3. RADIOACTIVE PARTICULATE CATEGORIZATION

The current particulate categorization scheme shown in Figure 3 is comprised of five levels, with increasing levels indicating interest levels. For Level 5 samples, the PTS sends the air filter to a laboratory for confirmation of results and longer count times to improve detection levels for radionuclides with half-lives in the range of days to weeks. The particulate spectrum categorization scheme is based on the detection of either activation or fission products. While it is possible for activation products to be produced, released and detected in a nuclear test, fission products are generally considered to be much more detectable in almost every conceivable scenario and detectable even if there are specific scenarios in which activation products are more

FIGURE 3.
Particulate radionuclide categorization scheme currently used by the IDC.

detectable than fission products, such as in the case of some types of atmospheric detonations. Therefore, an obvious improvement to the categorization scheme for particulates may be to remove most activation products from the list of relevant radionuclides and therefore decrease the number of false positives that arise from long lived radionuclides such as ^{60}Co.

Due to chemical fractionation expected from nuclear explosions (Bourret et al. 2021, Carrigan et al. 2020), it is generally not advisable to rely on cross-elemental airborne isotopic ratios to calculate details about the event, such as vent time. The use of some intra-elemental isotopic ratios may be partially or completely void of fractionation effects, however, due to parent daughter relationships that can be affected by fractionation and/or volatility differences in parents leading to differences in vent times, even this can be a misleading practice without significant study.

4. COMBINED PARTICULATE AND NOBLE GAS CATEGORIZATION SCHEMES

The IMS radionuclide technologies are comprised of 80 particulate systems and initially 40 noble gas stations, and the noble gas systems are always co-located with particulate systems at the IMS stations. The combining of noble gas and particulate spectra into a single screening scheme has been discussed, however, no single scheme has been identified that seems to fit all the desires for a combined scheme. While work continues in this area, there are several reasons why a combined scheme has not been trivial to design. For example, 1) noble gas and particulate collection systems are generally not time synchronized (and even when synchronized) there will be multiple noble gas samples during a single particulate sampling time that complicate combining the measurements, 2) the variety of venting mechanisms for noble gas and particulate radionuclides means that a noble gas only, a particulate only or a combined detection is possible, 3) noble gases are thought to be mostly resistant to environmental chemistry effects such as rainout, whereas particulates are subject to these effects and 4) the environmental backgrounds of radioactive noble gases and particulate differ by many orders of magnitude in some places on earth and the mechanisms for the detected background are not the same in many cases.

A combined scheme could have value if it either highlights events that would otherwise be missed or somehow decreases the workload for analysts. For example, detect of a single volatile radionuclide such as ^{131}I from a particulate system and a temporally coincident of ^{133}Xe may raise a concern level if the air mass from each of these detections at a single station originate from the same region as determined from ATM. On the other hand, it is possible that a combined scheme may lead to false positive and even false negatives if there is an over emphasis on a combined scheme. Although we have previously argued that interpretation of unsynchronized atmospheric measurements may

312

be difficult to interpret, there are also possible benefits for a combined scheme when the systems are *not* time-synchronized, since in principle the time-granularity of the measurements may be improved. However, combining particulates and noble gases information in this way assumes that the release times and points for these radionuclides are the same, and that is generally not the case since many particulates are created as the daughters of noble gas precursors and the venting mechanisms may be different. Work is continuing to create an acceptable combined particulate and noble gas scheme.

Atmospheric transport modeling has traditionally been used in an a posteriori approach as in hypothesis testing to test the consistency between a detection and given scenario. However, the use of an a priori approach in which ATM models are used in the screening itself, some false positives and negatives could be avoided. For example, if ATM models are combined with the detection of a single xenon isotope and it is calculated that the event originates from the broad open ocean area where there are no known nuclear facilities, then the event in question may avoid being screened out even if the IMS station routinely detects xenon isotopes from nearby nuclear facilities. Likewise, events might be screened out if ATM is used to ascertain that isotopes originate from known frequent emitters of xenon isotopes.

5. FUSION OF RADIONUCLIDE AND WAVEFORM DATA

There has been a significant amount of thought put into the fusion of radionuclide and seismoacoustic (seismic, hydroacoustic and infrasound) technology measurements. The purpose of fusion is to identify radionuclide and seismoacoustic events that may have the same source event by showing correlation in space and time. One of the obvious issues related to the formal, procedural fusion of the two technologies is the time difference between the detection of events of interest. In the case of detection of seismic waves from a suspect nuclear explosion, the detection may happen in a few seconds following the energy release into the subsurface, while in the case of radionuclide detection, it is most likely that radionuclides would not be detected for a few to several days following a nuclear explosion, due to the potential delay in venting for the radionuclides from the subsurface, the transport time through the atmosphere and the counting times used for radionuclide systems.

Atmospheric transport modeling can be used to combine radionuclide detections and seismic detections since ATM backtracking can determine a release location when combined with other information such as isotopic ratios, or a location determined from other means such as the seismic detection (Kalinowski 2001, Kuśmierczyk-Michulec et al. 2022). Unfortunately, the location uncertainty with backtracking of atmospheric transport modeling is much larger than seismic detection in most cases and the uncertainty in the fields of regard for atmospheric transport models are not easily quantifiable (Becker et al. 2007). In the future, the use of ensemble atmospheric transport modeling may help with the determination of ATM uncertainties.

6. SCREENING FLAGS

In addition to a categorization value (1-5 for particulates or A-C for noble gases), there are a series of 'flags' that have been added to the screening levels designed through the detection of presence or absence of certain radionuclides. These flags are used only to give more information to users on the likelihood that the event should be screened out (ignored) or given a higher priority. Table 1 shows a list of the flags that are currently used by the IDC in the analysis of data from the IMS. There are a few flags that could be used in the future that may be

useful to consider, such as the use of more xenon isotopic ratios, most notably the ^{133}Xe/^{131m}Xe ratio or particulate ratios. It should be taken into consideration that the isotopic ratios flags would only be raised in case of a prompt release that is detected within a few days at most. An aged prompt release and a delayed release have ratios that are below the thresholds for raising the flag. Another drawback of the use of flags is that under certain circumstances, it may be difficult for NDCs to reproduce the results from the IDC, such as the use of a flag that notes that a station might be influenced by a known source.

Table 1. Screening Flags Used for Particulates and Noble Gas Spectra Collected by the International Monitoring System and Analysed by the International Data Centre

Technology	Screening Flag	Values
Particulate	Activation products present in the spectrum?	Yes/No
Particulate	Only one fission product in the spectrum?	Yes/No
Particulate	Two or more fission products in the spectrum?	Yes/No
Particulate	^{137}Cs present in the spectrum?	Yes/No
Xenon noble gas	Isotopes present in the spectrum?	Yes/No
Xenon noble gas	Only one Xenon isotope in the spectrum?	Yes/No
Xenon noble gas	Number of days since last Xenon detection.	#Number
Xenon noble gas	Two or more Xenon isotopes present in the spectrum?	Yes/No
Xenon noble gas	^{133}Xe present in the spectrum?	Yes/No
Xenon noble gas	Number of times ^{133}Xe seen in last 365 days.	#Number
Xenon noble gas	Short term flag – Xenon within the typical range for the station (applies to category B).	Yes/No
Xenon noble gas	^{133m}Xe/^{131m}Xe activity ratio > 2.	Yes/No
Xenon noble gas	^{135}Xe/^{133}Xe activity ratio > 5.	Yes/No
Xenon noble gas	^{133m}Xe/^{131m}Xe activity ratio > 0.3.	Yes/No
Xenon noble gas	ATM backtracking to known sources	Tbd (not yet implemented)

7. STATISTICS OF THE CURRENT CATEGORIZATION SCHEME

The current categorization scheme produces approximately four to 10 Level 5 samples per year across the 70 stations that collect a total of 25 000 samples per year. The average for the past 10 years is 9.5 as seen in Figure 4 but was slightly elevated in the years following the Fukushima accident. This number might be considered a type of false positive rate. Some Level 5 samples are due to relevant isotopes being likely a false positive, whereas other Level 5 events show the coincidental appearance of two radionuclides at anomalous concentrations that appear frequently at certain sites such as ^{137}Cs and ^{131}I.
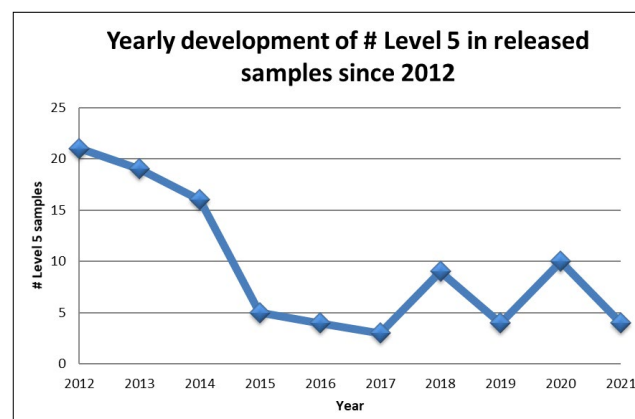
FIGURE 4.
Number of Level 5 samples in the IMS since 2012. The higher levels in 2012 were due to residual fallout from the Fukushima nuclear accident in 2011.

314

7.1. Backgrounds and How They Confound the Screening Process

Even under an optimal categorization scheme, if there are radionuclides in the atmosphere that arise from fission, the degree to which a scheme can be effective is limited, leading to a type of false positive rate that cannot easily be overcome. For example, in the case of radioactive xenon noble gases, the detection of individual xenon isotopes such as ^{133}Xe are the same isotopes as are being targeted in the categorization scheme. The use of isotopic ratios and correlation between the isotopic ratios among xenon isotopes can be useful when three or four xenon isotopes are detected, such as shown in Figure 3, however when the isotopes arise from a peaceful nuclear activity, such as the production of ^{99}Mo from medical isotope production (Biegalski et al. 2010, Saey et al. 2010), even this technique is not foolproof. In fact, since medical isotope production creates such a large amount of radioactive noble gases in the atmosphere, this is a serious issue that have received a large amount of attention (Bowyer 2021). Medical isotope production can make the detection of a single isotope such as ^{133}Xe useless, in cases in which a suspect detonation is near an area of high background, and the use of multiple isotopes is not available or being analyzed in correlation is problematic.

One solution that has been proposed to mitigate the effluents from fission-based medical isotope production is to employ measurements at the origin point of the emissions to determine the amount and isotopic composition of the releases and through atmospheric transport modeling, determine the amount of signal that is expected from the well known source at a nearby station so that its effect can be removed and the observed signal be explained (Generoso et al. 2022, Goodwin et al. 2021). Stack measurements could be used for a sample categorization scheme in several ways.

First, through stack measurements and atmospheric transport modeling, events detected by IMS stations could be 'flagged' to indicate whether the station was potentially or likely influenced by isotope production (or a nuclear power reactor) during the time of the detection (Eslinger et al. 2015, Gueibe et al. 2017, Maurer et al. 2018). The advantage of this scheme would be that especially accurate atmospheric transport models are not necessarily needed to know whether a station potentially is influenced and that is arguably the case with the current state of the art models today. However a downside is that some stations are often affected by fission-based isotope detection and that could effectively make those stations nearly useless for extended periods from the perspective of categorization of the events. In effect, the categorization results would indicate that the station results cannot be used a large part of the year.

Second, detailed regional or global atmospheric transport models may be used in combination with the measurements at stacks of nuclear facilities to subtract the effect at the station and determine an effective concentration of the radionuclide. Therefore background-subtracted (net) results can then be categorized much in the same way as the current noble gas 3-level categorization scheme if the net value exceed zero beyond expected uncertainties. The advantage of this scheme is that it is the best way to determine the effect at a station from a hypothetical nuclear explosion and therefore may significantly decrease false positives. The disadvantage of this scheme is that high fidelity operational regional and/or global models require significant computational resources and the determination of uncertainties in the models in still in development (De Meutter et al. 2016, Maurer et al. 2021).

Lastly, a simpler model that combines aspects of the last two techniques might be useful as well. For example, an alternate approach might have categories of influence expected from atmospheric modeling such as low influence expected, moderate influence expected or high influence expected. While this choice adds some flexibility, it suffers from subjective definitions of low, moderate, etc. Ultimately, the options mentioned above could be tested on data sets already in existence from the IMS and/or operationally on data coming in.

Background measurements at locations other than the current IMS stations have been performed for over a decade (Saey et al. 2013, Baré et al. 2022) to better understand the sources of emissions from nuclear facilities that emit radionuclides that interfere with IMS measurements. Issues such as 1) the magnitude of releases, 2) expected isotopic release profiles, 3) expected release times and 4) cooperative studies to better understand how to mitigate emissions have been explored and solutions suggested and tested. The treaty specifies that background measurements are usable for the screening procedures.[1]

8.   LIMITATIONS TO SPECTRUM CATEGORIZATION

The current schemes used for radionuclide screening have several assumptions built into their construct. For example, the inter-quartile average used for determining whether a radionuclide is anomalous for the station assumes that there is no or little temporal variability in the backgrounds observed at the station over the past 365 days. While there is no a priori expectation that backgrounds will change on an annual basis, there are seasonal variations expected for some radionuclides due to changes in weather patterns. In addition, it is well known that nuclear facilities can and do change operating schedules, startup and shutdown on timescales that can be shorter than 365 days. Since backgrounds are location dependent (i.e. nuclear facilities are not uniformly spread across the globe) the current radionuclide categorization scheme is location dependent and that may show as false positive and negative rates that are location dependent.

In addition, the current schemes rely on detection of airborne radionuclides that are limited by the detection levels of the instruments (i.e. the IMS air samplers) that collect and measure the debris. This means that radionuclides could be present in samples from nuclear explosions, though their levels may be below detection limits. In other words, referring to Figure 2, if only a single radionuclide was detected above the system detection limit, there still could be radionuclides in the sample that are explosion-like, and subsequent measurement in a laboratory could 'recategorize' the sample, say from Level 4 to Level 5 if additional radionuclides were detected with a longer counting time. This argues that more extensive use of the IMS certified laboratories may be useful especially with the current categorization scheme.

As a conclusion, the current spectrum categorization is *proscriptive* by having only Level 5 samples being sent to laboratories for further analysis (could lead to false negatives). Another shortcoming is that analysts have little freedom for interpreting results in order to be conservative and leave a final decision up to the States Signatories (being over conservative in avoiding false negatives leads to false positives). Analysts are required to report the detection of isotopes consistent with gamma ray detection peaks, but there can be many mechanisms for creating those lines like statistical effects and interference with peaks caused by other radionuclides.

An example is the detection of a short-lived, low abundance fission-product near detection level with no other fission products. This should be screened out; however, IDC analysts are not 'authorized' to do so. Giving analysts more authority to screen out radionuclides under certain conditions could reduce the false positive rate.

Even if the methods for implementing the radionuclide categorization scheme were enhanced to address the above described limitations, it will never avoid a large rate of false negatives because it is merely a classification of observations characterizing the background variability rather than an attempt of highlighting events of possible relevance to nuclear explosion monitoring. For any frequently observed radionuclide, the categorization scheme highlights

---

[1] Annex 2 to the Protocol to the CTBT.

anomalous concentrations, but it is missing signals from nuclear weapons that are present but in the normal range of concentrations. Regarding radioxenon, this means that level B samples may contain a signal of a nuclear test just as well as level C samples. This categorization scheme is misleading, if level B samples are ignored and only level C samples further investigated for possibly indicating a nuclear test. Nuclear explosion signals at level B concentrations would be missed events. Accepting such false negatives is a result of having chosen a simple approach when the monitoring operations were in their infancies. However, more sophisticated screening methods are possible and capable of revealing nuclear explosion signals even if they seem to be hidden by the background. Actually, there is a tremendous opportunity for reducing the false negative rate significantly and the development and validation of the appropriate methods is the task for coming years.

Many of the ingredients needed for such sophisticated screening methods are already used for the screening flags. These are all focusing on single samples and the parameters reported in their analysis. Other approaches are using multiple samples and ancillary data like information on the background and its sources, ideally stack release data. Clear evidence has been provided that understanding backgrounds may assist in the screening of radionuclide spectra. For example, following the Fukushima nuclear accident, it was well known that ^{134}Cs could resuspend and be detected in IMS stations again later from that same source. More studies on the variability of backgrounds and specific cases of sources will help in creating enhanced screening methods. Also, more studies about characteristics of all kinds of radioxenon sources including nuclear explosions are needed to refine and to validate screening methods. This includes full understanding of nuclear facilities including those not belonging to the dominant fission sources (e.g. neutron activation sources, molten salt reactors) as well as full understanding of the fractionation effects underground and in the atmosphere of all kinds of nuclear explosion signal evolvement scenarios (Liu et al. 2022).

9. CONCLUSIONS

The current radionuclide procedures used by the IDC for the screening of particulate and noble gas spectra are effective tools for determining which radionuclide spectra should be investigated further by national data centers. However, due to limitations presented by complex backgrounds, unknown parent daughter relationships due to unknown venting times, and fractionation, improvements to the screening criteria should continue to be investigated, extended, and made operational by the PTS. Specifically, the use of stack monitoring data available on a voluntary basis by some isotope producers and nuclear reactors, combined with atmospheric transport modeling may improve both the false positive and false negative rates associated with the current screening procedures. A global atmospheric model that can predict the radionuclide context at IMS stations is also being explored that will one day improve screening immensely.

In addition to improving radionuclide screening, expanding the use of radionuclide laboratories, which have better detection sensitivities than IMS stations will generally improve the detection of debris emitted by nuclear explosive testing and improve the verification of the CTBT, after entry into force.

REFERENCES

Baré, J., Gheddou A., Kalinowski, M. (2022). Overview of temporary radioxenon background measurement campaigns conducted for the CTBTO between 2008 and 2018. *Journal of Environmental Radioactivity* **257** 107053.

Becker, A., et al. (2007). Global backtracking of anthropogenic radionuclides by means of a receptor oriented ensemble dispersion modelling system in support of Nuclear-Test-Ban Treaty verification. *Atmospheric Environment* **41** (21) 4520-4534.

Becker, A., et al. (2010). Backtracking of noble gas measurements taken in the aftermath of the Announced October 2006 event in North Korea by means of PTS methods in nuclear source estimation and reconstruction. *Pure Applied Geophysics* **167** 581–599.

Biegalski, S.R., Saller, T., Helfand, J., Biegalski, K.M.F. (2010). Sensitivity study on modeling radioxenon signals from radiopharmaceutical production facilities. *Journal of Radioanalytical and Nuclear Chemistry*, **284** 663-668.

Bourret, S.M., Kwicklis, E.M., Stauffer, P.H. (2021). Evaluation of several relevant fractionation processes as possible explanation for radioxenon isotopic activity ratios in samples taken near underground nuclear explosions in shafts and tunnels. *Journal of Environmental Radioactivity* **237** 106698.

Bowyer, T.W., et al. (1998). "Xenon radionuclides, atmospheric: monitoring". *Encyclopedia of Environmental Analysis and Remediation* (R.A. Meyers, Ed). John Wiley & Sons, Hoboken, NJ 1998.

Bowyer, T.W. (2021). A review of global radioxenon background research and issues. *Pure and Applied Geophysics* **178** (7) 2665-2675.

Carrigan, C.R., Sun, Y., Pili, E., Neuville, D.R., Antoun, T. (2020). Cavity-melt partitioning of refractory radionuclides and implications for detecting underground nuclear explosions. *Journal of Environmental Radioactivity* **219** 106269.

De Geer, L.E. (2001). Comprehensive nuclear-test-ban treaty: relevant radionuclides. *Kerntechnik* **66** (3) 113-120.

De Meutter, P., Camps, J., Delcloo, A., Deconninck, B., Termonia, P. (2016). On the capability to model the background and its uncertainty of CTBT-relevant radioxenon isotopes in Europe by using ensemble dispersion modeling. *Journal of Environmental Radioactivity* **164** 280-290.

Eslinger, P.W., et al. (2015). Source term estimates of radioxenon released from the BaTek medical isotope production facility using external measured air concentrations. *Journal of Environmental Radioactivity* **148** 10-15.

Generoso, S., Achim, P., Morin, M., Gross, P., Douysset, G. (2022). Use of STAX data in global-scale simulation of ^{133}Xe atmospheric background. *Journal of Environmental Radioactivity* **251-252** 106980.

Goodwin, M. A., et al. (2021). Production and measurement of fission product noble gases. *Journal of Environmental Radioactivity* **238-239** 106733.

Gueibe, C., et al. (2017). Setting the baseline for estimated background observations at IMS systems of four radioxenon isotopes in 2014. *Journal of Environmental Radioactivity* **178-179** 297-314.

Kalinowski, M.B. (2001). Atmospheric transport modelling related to radionuclide monitoring in support of the Comprehensive Nuclear-Test-Ban Treaty verification. *Kerntechnik* **66** (3) 129-133.

Kalinowski, M.B., Pistner, Ch. (2006). Isotopic signature of atmospheric xenon released from light water reactors. *Journal of Environmental Radioactivity* **88** (3) 215-235.

Kalinowski, M.B., et al. (2010). Discrimination of nuclear explosions against civilian sources based on atmospheric xenon isotopic activity ratios. *Pure and Applied Geophysics* **167** (4-5) 517-539.

Kuśmierczyk-Michulec, J., et al. (2024). Advancements in Atmospheric Transport Modelling at the International Data Centre and plans for the future". *Twenty-Five Years Progress of the Comprehensive Nuclear-Test-Ban Treaty´s Verification System.* CTBTO, Vienna.

Liu, B. et al. (2024). "The Comprehensive Nuclear-Test-Ban Treaty Hydroacoustic Network". *Twenty-Five Years Progress of the Comprehensive Nuclear-Test-Ban Treaty´s Verification System.* CTBTO, Vienna.

Maurer, C., et al. (2018). International challenge to model the long-range transport of radioxenon released from medical isotope production to six Comprehensive Nuclear-Test-Ban Treaty monitoring stations. *Journal of Environmental Radioactivity* **192** 667-686.

Maurer, C., et al. (2021). Evaluating the added value of multi-input atmospheric transport ensemble modeling for applications of the Comprehensive Nuclear Test-Ban Treaty organization (CTBTO). *Journal of Environmental Radioactivity* **237** 106649.

Ringbom, A., et al. (2009). Measurements of radioxenon in ground level air in South Korea following the claimed nuclear test in North Korea on October 9, 2006. *Journal of Radioanalytical and Nuclear Chemistry* **282** 773-779.

Ringbom, A., et al. (2021). Radioxenon releases from a nuclear power plant: Stack data and atmospheric measurements. *Pure and Applied Geophysics* **178** 2677-2693.

Saey, P.R.J., Bowyer, T.W., Ringbom, A. (2010). Isotopic noble gas signatures released from medical isotope production facilities—Simulations and measurements. *Applied Radiation and Isotopes* **68** (9) 1846-1854.

Saey, P.R.J., et al. (2007) A long distance measurement of radioxenon in Yellowknife, Canada, in late October 2006. *Geophysical Research Letters* **34** (20).

Saey, P.R.J., et al. (2013). Worldwide measurements of radioxenon background near isotope production facilities, a nuclear power plant and at remote sites: the "EU/JA-II" Project. *Journal of Radioanalytical and Nuclear Chemistry* **296** 1133-1142.

Radionuclide Expert Technical Analysis Based on Isotopic Activity Ratios of Comprehensive Nuclear Test-Ban-Treaty-Relevant Isotopes

B. Liu, M. Kalinowski, J. Kunkle, R. Schoemaker, Y. Kijima

Comprehensive Nuclear-Test-Ban Treaty Organization, Vienna, Austria

Abstract

Radionuclide measurements in the International Monitoring System (IMS) network, especially radioxenon detections, serve as a 'smoking gun' for the discrimination of nuclear explosions compared to waveform technologies. Radioxenon isotopes measured at radionuclide stations of the IMS may indicate releases from underground nuclear explosions (UNEs) but are normally due to emissions from nuclear facilities. Characterization of Comprehensive Nuclear-Test-Ban Treaty-relevant nuclear events may use the evolution of isotopic activity ratios over time, which goes from the release of an assumed UNE, through atmospheric transport, to sample collections and measurements. This can be investigated in two ways; activity concentrations at an IMS station can be estimated using an assumed release scenario regarding a UNE and atmospheric transport modelling. The activities are directly determined by spectral analysis of collected samples and used to estimate activity concentrations in the air passing over an IMS station, often using an assumption of constant concentration during sampling. The isotopic ratios of activities released from a UNE can be related to the isotopic ratios of activity concentrations in the plume of air crossing the IMS station, resulting in a function of the isotopic activity ratio over the time from detonation to sample measurement. This function is used for discrimination of a nuclear test, such as a four radioxenon plot of the activity ratio relationship of ^{135}Xe/^{133}Xe versus ^{133m}Xe/^{131m}Xe and estimation of the time of detonation.

1. INTRODUCTION

The International Monitoring System (IMS) network is comprised of several types of detection technologies including waveform technologies (hydroacoustic, infrasound, seismic) and technology to measure airborne radionuclides that can be liberated into the atmosphere during either an atmospheric or underground nuclear detonation (typically at lower levels for the latter) (Kalinowski and Liu 2020). Measurement of radionuclides in the IMS is used to confirm whether an event detected by waveform technologies was of nuclear origin, but also as a primary detection technology if there are events that have no waveform signature.

The radionuclide detection technologies are further broken down into the detection of radioactive particulates and noble gases. There have been 72 of 80 planned particulate systems and 25 of 40 planned noble gas systems put in operation as of May 2021. There are two main types of noble gas systems. Pure gamma spectra are acquired by SPALAX systems with high purity germanium (HPGe) detectors, ten of these systems are in operation. Beta–gamma coincidence spectra are taken by the Swedish Automatic Unit for Noble Gas Acquisition (SAUNA II) systems with NaI(Tl) and plastic detectors, with 15 systems in operation. The new generation of noble gas systems, SAUNA III, the Système De Prélèvement Automatique En Ligne Avec L'analyse Du Xénon (SPALAX NG), Xenon International and MIKS all use the beta–gamma coincidence method, some of them with high resolution spectrometers.

There are 84 fission and activation products used for particulate spectrum categorization within the International Data Centre (IDC), and four radioxenon isotopes (^{131m}Xe, ^{133m}Xe, ^{133}Xe and ^{135}Xe) for noble gas (De Geer 2001). Radioisotope activities collected and measured in samples are converted to activity concentrations under an assumption of constant concentration profile in the sampling duration. The spectra of the samples from IMS stations are a time integrated snapshot of each collected sample; although there are also multiple preliminary spectra, showing the evolution of the measurement. Analysis results are reported in standard IDC products as output from automatic and interactive analyses. Some samples, such as those that contain one or more abnormal activity concentrations of Comprehensive Nuclear-Test-Ban Treaty (CTBT) relevant radionuclides (Level 4 and 5 for particulate samples, Level C for noble gas samples) are sent to IMS laboratories for reanalysis.

For both discrimination of a nuclear explosion source and estimation of the time of detonation, the first step is to estimate the isotopic activity ratio at the time of collection stop, which is based on activity concentrations in the plume of air. The isotopic ratio of two activity concentrations can be expressed by a non-linear model. Estimating the ratio value and associated uncertainty requires high order Taylor expansion terms, such as the second-order polynomial. Therefore, the ratio and associated uncertainty are dependent not only on concentrations but also on their uncertainties and covariances. For isotopic activity ratio analysis, it would be more practical to use the Monte Carlo method (MCM) based on activities measured in the sample or associated peak counts in the spectrum analysis directly, especially for uncertainty estimation related to the elapsed time since the detonation time. The isotopic ratios of activities measured at acquisition start time will likely be different from the isotopic ratios of activities at the release time and activity concentrations in the plume of air at the end of sample collection. Atmospheric transport modelling (ATM) can aid the analyst in connecting the activity and ratio evolution by providing estimated times over which the aforementioned evolution would occur. Prospective event dating can therefore be based on the unique function of the isotopic activity ratio over time under an assumed scenario. If the same decay chain is assumed both before release and during atmospheric transport, the elapsed time can be estimated numerically by solving the evolution function. The uncertainty estimation can be performed using the MCM because of non-linear functions involved. All of this, of course, assumes no additional sources that could affect the ratios to be analysed.

The purpose of a radionuclide expert technical analysis (ETA-RN) is to assist State Parties to identify the source of a specific event. The output of an ETA-RN is part of a State Requested Methods Report (SRMR), which builds on routinely generated results from standard IDC products like the radionuclide reviewed report and radionuclide laboratory report. The various functionalities in this ETA-RN software suite are all based on isotopic activity ratios detected in samples collected in the IMS network. The analysis modules include the event definition based on radioxenon detections at IMS radionuclide stations, calculations of isotopic activity ratios using different methods, sample association based on consistency analysis of isotopic activity ratio evolution, simulations of release scenarios using Bateman equations, event discrimination based on relationship plots of four/three radioxenon detections, event timing using a function of isotopic activity ratios over time, and ultimately, SRMR generation (Liu et al. 2023).

- This paper gives an overview on the procedures of ETA regarding Treaty-relevant events from IMS measurements, through IDC spectrum analyses and ATM simulations, to the characterization of CTBT-relevant nuclear events. The analysis functionalities of the ETA-RN are demonstrated via typical case studies, such as the announced 2013 event of the Democratic People's Republic of Korea, consecutive Level C samples and observations made during the Fukushima Daiichi accident.

2. INTERNATIONAL MONITORING SYSTEM MEASUREMENTS AND INTERNATIONAL DATA CENTRE ANALYSES

2.1. Radionuclide Measurements in the International Monitoring System Network

Eighty radionuclide monitoring stations within the IMS host particulate samplers. These samplers efficiently filter particulate from a minimum of 500 cubic meters of air per hour, continuously for 24 hours. After leaving the filter for a 24-hour decay period to allow the decay of short lived natural radionuclides, the filter is measured using a HPGe detector to determine the radionuclides present in the sample. The data from these systems is sent to the IDC where the spectra are analysed and categorized to differentiate between spectra from samples containing only natural or non-relevant radionuclides and those from samples containing anthropogenic radionuclides relevant to verification of compliance with the Treaty. All categorization and analysis products are made available to States Signatories, along with the raw IMS data.

Currently there are two types of particulate systems on the network, manual and automatic. These both operate on the same collection, decay and measurement cycle (Goodwin et al. 2023). Forty of these stations, in addition to particulate monitoring, will also host the equipment and means to measure noble gasses, specifically xenon. In the IMS there are two types of noble gas systems, SAUNA II and III and SPALAX. These utilize different technologies. SAUNA uses a plastic scintillator/sodium Iodide beta–gamma coincidence detector, with the air sampled for 12 hours and xenon trapped on activated charcoal. The xenon is further processed and the stable xenon quantified. Finally the radioactive isotopes are measured by the beta–gamma coincidence detectors. The SAUNA III system operates with two parallel 6-hour cycle and can therefore achieve 24 hours of uninterrupted sampling. It passed system acceptance testing in 2020. In 2021 the latest version of SAUNA III was rolled out on the network, improving both source localization and the minimum detectable concentration of xenon radioisotopes. SPALAX utilizes a semi-

permeable membrane to enrich the xenon which is trapped and purified on activated carbon and molecular sieve traps. The radioactive xenon isotopes are measured on an HPGe detector and then the stable xenon is quantified. The current version of the SPALAX on the network has a 24-hour collection cycle. The SPALAX NG that passed system acceptance applies an 8-hour sampling scheme. In 2022 Xenon International became the third variant that passed system acceptance testing. The MIKS system is still undergoing system acceptance testing.

2.2. Spectrum Analyses at the International Data Centre

2.2.1. Particulate Samples

The spectrum analysis method of single channel analyser curve (SCAC) was developed for gamma spectrum analysis of particulate samples (De Geer 2004). It is a unique algorithm for automatic processing of IMS gamma spectra. The concept of the SCAC method is based on Currie's approach regarding the estimation of critical limit (Currie 1968), in addition to the critical level curve (LCC) and baseline (B). However, the uncertainty estimation is based on Bayesian statistics.

- Numbers of counts in each channel ($SCAC_i$) are the average of original counts measured over a specified range. The Poisson distribution is applied to the numbers of counts in each single channel, both the original number of counts and the average number of counts. That means that the variances of the average numbers of counts are equal to the values themselves, which are different from the variances derived based on the uncertainty propagation. This approach is based on Bayesian statistics instead of conventional frequentist statistics, despite the concept of the critical limit, as defined by Currie, being based on the latter.
- The baseline curve (B_i) is based on a 'lawn mower' algorithm. Each peak identified within a given energy range is removed with respect to the slope of the selected spectrum area. Before and after applying the lawn mower algorithm, the selected part of the spectrum is smoothed. The number of times the lawn mower algorithm is applied depends on the part of the spectrum that is considered.
- The critical limit curve (LCC_i) is estimated using the concept of critical limit defined by Currie (1968), on top of the defined baseline curve (B_i).
- The gamma peaks are then identified using the difference between the critical limit curve and baseline curve, i.e. the detectability criterion.
- The peak areas are estimated based on the numbers of counts in a single channel ($SCAC_i$) and the energy resolution at the peak channel (R_i). This is a unique approach to fitting low count spectra where peak shapes may not be well defined.

An advanced interactive algorithm and software are needed to deal with small peaks and complicated baselines as well as an interactive calibration procedure for analyst review at the IDC. Calibration presents another issue. The energy and efficiency calibration at IMS stations are typically carried out using commercial off the shelf (COTS) analysis software from equipment providers. The calibration analysis performed at the IDC uses the SCAC method, and as a result there are some systemic deviations between the algorithms.

2.2.2. High Purity Germanium Gamma Spectra of Noble Gas Samples

The SCAC method is not used to determine radioxenon activities for pure gamma spectra from noble gas systems with high resolution detectors. The least squares fitting method for gamma and X ray peaks of radioxenon isotopes is used instead. This regression analysis was designed to operate where gamma peak areas of metastable xenon were below their decision thresholds, but the relevant X ray peak were above due to relatively higher detection efficiencies and decay branch intensities.

The fitted peak counts are compared to gamma peaks of each radioxenon. Decision

thresholds estimated based on baselines in the SCAC, however, are not available for metastable xenon in the regression analysis. False positives of ^{133m}Xe were occasionally observed due to a bump around 233 keV, resulting in negative values of ^{131m}Xe, although both were not detected via the SCAC method.

2.2.3. Beta–Gamma Coincidence Spectra of Noble Gas Samples

The net count calculation (NCC) method is used in analysis of two dimensional beta/gamma coincidence spectra, quantifying the presence of ^{131m}Xe, ^{133m}Xe, ^{133}Xe and ^{135}Xe in noble gas samples from beta–gamma coincidence measurement systems (De Geer 2007).

The classic NCC method was used at the IDC until 2018. This included binary decisions on interference corrections from higher to lower Regions of Interest (ROIs) and memory corrections were always performed. This proved problematic as subtracting negative values of memory corrections could cause decision thresholds to be underestimated, resulting in false positive detections (Cooper et al. 2019, Liu et al. 2020).

A modified version of the classic NCC method was deployed at the IDC in 2018. All binary decisions were discarded. As a result false detection rates of metastable xenon isotopes were reduced. Removing the binary decision tree is not without implications, however. It could result in under or overestimation of decision thresholds due to negative net numbers of counts in higher ROIs and the gas background spectrum.

Along with new generation systems different variations of the NCC method were developed. Net numbers of counts are the same in between, but the associated uncertainties might be different with respect to analysis algorithms (Cagniant et al. 2018, Cooper et al. 2016, 2019a, 2019b, Deshmukh et al. 2017, Liu et al. 2020, Ringbom and Axelsson 2020).

Beta–gamma coincidence measurements in a 4pi detector geometry can be calibrated using an absolute measurement method and the coincidence efficiency is equal to the product of efficiencies of the beta and gamma singles. The efficiency calibration is based on the numbers of radioxenon decays amongst the three measurement channels of beta–gamma coincidences, beta singles and gamma singles. Gas spikes of ^{131m}Xe, ^{133m}Xe, ^{133}Xe and ^{135}Xe as well as radon are generally used to unify the calibration procedures for the different systems. Gamma singles are typically only used for gamma energy and resolution calibrations, and beta energy and resolution calibrations are performed and checked via single and double peak fitting in both the beta singles and beta projections of the beta–gamma coincidences. Efficiencies of 30 keV X rays and 129 keV conversion electrons are determined by ^{131m}Xe first and the efficiency of 30 keV X rays is assumed the same for all radioxenon isotopes. Gamma efficiencies of 81 and 250 keV are derived based on the efficiency of 30 keV. Efficiencies of beta–gamma coincidences can then be determined based on the gamma singles and gamma projections accordingly.

2.3. Atmospheric Transport Modelling

Atmospheric transport modelling (ATM) simulations support radionuclide technology by providing a link between radionuclide detections and the regions of their possible source. In a data fusion process ATM computations can therefore link the radionuclide detections with waveform events that could indicate a possible source. In the process of verifying whether a given detection can be associated to a specific event, ATM results play a crucial role, particularly around the declared and un-declared nuclear weapons tests of the Democratic People's Republic of Korea.

ATM simulations add value to the radionuclide pipeline by estimating the path of particulates or noble gases through the atmosphere, back to their possible source regions. ATM simulations also support data fusion by highlighting and linking potential waveform events to these same source domains. The IDC aims to establish a world-class ATM system to meet the needs of an integral CTBT verification system. The ATM pipeline of the IDC includes four major elements:

acquisition of meteorological data, modelling, post-processing and visualisation (Stohl et al. 2005, Wotawa et al. 2003, Becker et al. 2007, Kuśmierczyk-Michulec et al. 2021). The current operational ATM pipeline is based on a Lagrangian particle dispersion model driven by global meteorological fields provided by the European Centre for Medium-Range Weather Forecasts and the National Centres for Environmental Prediction at a resolution of 0.5 degrees. For each sample at each radionuclide measurement station, the pipeline computes global source–receptor sensitivity (SRS) data for a two-week timeframe (back in time). This backward mode yields daily files that include information about geocoordinates (latitude, longitude), time step and dilution values, pointing the receptor to probable regions of interest for source localization. However, in the case a source location is known beforehand, for example an announced nuclear test by the Democratic People's Republic of Korea or the Fukushima nuclear accident, both historical forward modelling and near real time forecasting are possible in ATM's forward mode, enabling predictions as to which IMS radionuclide stations are likely to be affected by a potential radioactive release in the transported plume. A final step utilizes both ATM's backward and forward output by visualizing several products in the WEB-GRAPE, which is a post-processing platform designed and developed at the IDC.

Moreover, one of the ATM products is processed as a daily visual operational product, the field of regard (FOR), which is a first estimate on the possible source region reflecting the backward SRS data in a one to one manner. The FOR is currently available in automatic/reviewed radionuclide report (A/RRR) as well as standard screened radionuclide event bulletin (SSREB).

2.4. Characterization of Comprehensive Nuclear-Test-Ban Treaty-Relevant Nuclear Events

During routine operations each sample is categorized according to the question whether CTBT-relevant isotopes are detected and whether the concentrations are normal or anomalous. It should be noted that this categorization is meant to highlight samples of special interest, but it is not suitable as a screening method which would eliminate samples that are clearly not CTBT-relevant events. Samples with normal concentrations of CTBT-relevant concentrations don't get a high category (4, 5 or C) assigned but may just as well contain a signal from a nuclear test. The only method that has a screening power and is implemented as screening flags in standard IDC products is the isotopic activity ratio analysis.

Activity ratios of CTBT-relevant radionuclides detected in particulate and noble gas samples can be used to discriminate a nuclear explosion source against the releases originating from other nuclear facilities. In case all four radioxenon isotopes are detected, the most discriminating plot is the activity ratio relationship between $^{133m}Xe/^{131m}Xe$ and $^{135}Xe/^{133}Xe$. An important feature is that observation data can be mapped onto the chart for distinguishing underground nuclear explosions (UNEs) from civilian applications without knowing the detonation time. If two isotopes are available this event characterization approach to distinguish nuclear explosion and nuclear reactor sources can only be applied to an early release, e.g. less than a few days. Due to the short half-life of ^{135}Xe (9.14 h), for all combinations of isotopes with ^{135}Xe in the numerator it takes less than five days before the isotopic ratios for non-fractionated release from a nuclear explosion crosses the typical value for a nuclear power plant. For other pairs of two radioxenon isotopes it can take up to 10 days or longer for $^{133}Xe/^{131m}Xe$. Beyond that delay from the fission event, the discrimination power of a single isotope ratio fades away but an additional isotope ratio provides a better discrimination power. If all four isotopes are detected, the nuclear explosion and nuclear reactor domains are clearly separated and the event can, in general, be associated with just one of these two event types (Kalinowski and Pistner 2006, Kalinowski et al. 2010 Kalinowski 2011).

2.4.1. Event Screening Flags in Sample-Specific Radionuclide Reports

Xenon flags for event screening are based on the Bayesian approach estimating the upper and

lower limits using Gaussian distribution. Lower limits of isotopic activity ratios are used as event screening flags in the IDC radionuclide products. Three pairs, $^{135}Xe/^{133}Xe$ >5, $^{133m}Xe/^{133}Xe$ >0.3 and $^{133m}Xe/^{131m}Xe$ >2, were deployed (Zaehringer and Kirchner, 2008), and the other one $^{133}Xe/^{131m}Xe$ >1000 is proposed.

2.4.2. Isotopic Ratio Analysis

The discrimination between the highly variable radioxenon background caused by nuclear facilities and CTBT-relevant events is a challenging but crucial task. The characterization of a fission event is based on isotopic activity ratio analysis of CTBT-relevant radionuclide observations at IMS stations and expected releases from nuclear explosions. The source term of the radioisotopes generated by a nuclear explosion is simulated by mathematical modelling of the activity evolution after the detonation time. Event screening of a nuclear explosion from releases of civil facilities are performed based on isotopic ratio analysis, e.g. four radioxenon plot of $^{135}Xe/^{133}Xe$ versus $^{133m}Xe/^{131m}Xe$. Estimation of the explosion time of a nuclear event is based on an assumed scenario and a function of isotopic ratios over time, such as pairs of parent-daughter decay chains of $^{95}Zr/^{95}Nb$, $^{140}Ba/^{140}La$ and $^{133m}Xe/^{133}Xe$ or pairs of independent fission products of $^{133}Xe/^{131m}Xe$, $^{103}Ru/^{106}Ru$, etc.

2.4.3. Requirements of Expert Technical Analysis

The isotopic activity ratio analysis needs to consider both the source term and sample measurements. A robust method is required that tests the isotopic activity ratios of samples against prepared information aggregated from a comprehensive set of all relevant release scenarios that could possibly explain the ratios detected at IMS radionuclide stations. Recent research results on the source mechanisms, including in-growth and decay, cavity-melt fractionation and seepage of cavity gases, are used to develop best estimate input source terms as well as minimum and maximum isotopic activity ratio boundaries as a function of time.

Libraries of scenarios for source term evolution are generated from the method coupling isotopic activity evolution of the gas phase radioactive inventory to realistic physical models of cavity evolution. The input data is aggregated to determine the envelope of isotopic activity ratios associated with UNEs. The output is scored for the consistency of the observations within the boundaries of all possible nuclear explosion signals.

In the applications related to IMS observations, this envelope can be constrained with the aid of available observational data. Using isotopic analysis of the sample and related ATM simulations, the isotopic activity ratios at the source can be reconstructed as a function of time and geographic location. With additional information from waveform technologies this can be further constrained. For screening purposes, the reconstructed source ratios are compared with the envelope of possible isotopic activity ratios to provide a probabilistic estimate that the observations are associated with a UNE.

2.5. Statistical Hypotheses from Spectrum Analysis to Event Characterization

Characterization of CTBT-relevant nuclear events may use the evolution of isotopic ratios over time, which goes from the release of an assumed UNE, through atmospheric transport, to sample collection and measurements. The statistical hypotheses behind analysis procedures are different in different stages from sample measurements to event characterization. The first hypothesis is to determine whether radioxenon is detected, H_0: the null hypothesis of detector background; H_1: the alternative of radioxenon detection. The radioxenon is assumed to be detected if the net number of counts is above the decision threshold. The second hypothesis is formulated regarding the radioxenon background at an IMS station: H_0, the null hypothesis of normal radioxenon background; H_1, the alternative of anomalous radioxenon detection. The abnormal concentration threshold is estimated based on the statistical analysis of the previous samples in a specified period, such

as 365 days, resulting in two categories of B and C, while Level A is assigned to samples with no radioxenon detection. Finally, discrimination of a nuclear explosion source against releases of nuclear facilities is based on isotopic ratio analysis, e.g. relationship plots of four or three radioxenon isotopes. Both Level C and B samples in the IDC sample categorization scheme are used. The hypothesis is formulated: H_0, the null hypothesis of releases from nuclear facilities; H_1, the alternative of a nuclear explosion source. The overlap between the discrimination line and lower and upper limits of the coverage interval of isotopic ratios is tested.

3. ISOTOPIC ACTIVITY RATIO ANALYSIS

The activity ratios of two radioxenon isotopes detected routinely at IMS stations, such as ^{133}Xe/^{131m}Xe, are typically found in a range which might originate from nuclear facilities, such as medical isotope production facilities, or from a delayed release of a nuclear test (Kalinowski and Liu 2020). For example, the activity ratios of ^{133}Xe/^{131m}Xe recorded in April 2013 are considered strong evidence for the nuclear nature of a seismic event on 12 February 2013 related to an announced nuclear test by the Democratic People's Republic of Korea. Both ^{133}Xe and ^{131m}Xe were detected in three samples at the IMS station RN38 and two samples at the IMS station RN58 more than 50 days after the announced test. The activity ratios of ^{133}Xe/^{131m}Xe are consistent with simplified simulations of delayed releases (Ringbom et al., 2014) and with more detailed simulations of radioxenon accumulated in a void/tunnel due to convection driven leakage from the explosive cavity/chimney (Carrigan et al. 2016, 2020).

The detonation time of a nuclear explosion can be estimated by using a function of the isotopic activity ratio from the time of detonation up to the time of collection stop based on assumed scenarios, e.g. pairs of ^{140}Ba and ^{140}La, ^{95}Zr and ^{95}Nb, and ^{133}Xe and ^{131m}Xe (Ringbom et al. 2014, Carrigan et al. 2016, Yamba et al. 2016). If the same decay chain is assumed before a release at the surface and during atmospheric transport, the elapsed time since the time of detonation can be estimated by solving activity evolution equations numerically and/or analytically (Bateman 1910, Kalinowski et al. 2010, Yamba et al. 2016). The associated uncertainty estimation of the elapsed time can be performed using the MCM regarding non-linear functions of exponentials and logarithms (ISO/IEC 2008, Kalinowski and Liu 2020) and numeric derivatives (ISO 2019).

Conceptually, there are three stages of isotopic activity ratios involved from the initial release up to sample measurements. The first one is the ratio of activities of two isotopes at the time of release. The second one is the ratio of activity concentrations in the radioactive air crossing a sampling location at the end of a sample collection period. The third one is the ratio of activities collected in a sample either at the time of collection stop or acquisition start. Some studies used the activity ratio of ^{131m}Xe to ^{133}Xe determined in the sample measurements for the characterization of the 2013 event by the Democratic People's Republic of Korea, including the estimation of the explosion time (Axelsson and Ringbom, 2014, Ringbom et al. 2014). This differs from investigations using the isotopic ratios of activity concentrations in the plume (Kalinowski and Pistner 2006, Kalinowski et al. 2010, Kalinowski 2011). Fundamentally the isotopic activity ratio as a function of time (i.e. the curve of activity evolution) needs to be derived for characterizing a nuclear release event. The isotopic ratio of activity concentrations in the plume of air connects the two ends of activity evolution from release to sample measurement. The activity concentration profile in a plume can be related to the released activities from a UNE by using ATM. Since an air mass containing passive tracers (plume) is transported from a nuclear explosion site to a measurement station, ATM simulations provide valuable contributions

assuming that the released activities form a linear[1] relationship with activity concentrations in the air mass (Wotawa et al. 2003, Becker et al. 2007).

For isotopic activity ratio analyses based on sample measurements, the first step is to estimate the isotopic ratio of two activity concentrations at the time of collection stop under the assumption of a constant concentration profile during the sampling. The upper and lower limits of the isotopic activity ratio can be estimated using Fieller's theorem (Axelsson and Ringbom 2014) or Bayesian statistics (Zaehringer and Kirchner 2008) for the event screening flags. Principally the uncertainty estimation of the explosion time can be based on the propagation of uncertainties (Yamba et al. 2016). However, when the Bateman equations are used for a complicated decay chain, this might turn out to be a non-trivial undertaking and even an impossible one. It is more practical to apply the MCM directly to activities measured in the samples or to associated peak counts in the spectrum analysis, especially in the case of the non-linear relationship between the elapsed time and isotopic activity ratio (Liu and Kalinowski 2021).

3.1. Activities Released from a Nuclear Explosion

The activity evolution from a nuclear explosion up to the release of gases into the atmosphere is a complicated process. It is related not only to radioactive decay chains, but also the convection and diffusion of radioxenon gases from the explosion chimney to the ground surface. The chemistry of precursors to radioxenon isotopes, geology and time of release post-detonation, amongst other factors, can influence the amount of activity released. Radioxenon gases could be accumulating in a tunnel related to the nuclear test, resulting in a delayed release (Carrigan et al. 2016, 2020).

In an ideal and well-mixed system activities can be estimated based on mass decay/ingrowth

chains using Bateman equations (Bateman 1910, Kalinowski 2011). The isotopic ratio of released activities is given by:

$$R(t_1) = A_2(t_1)/A_1(t_1). \qquad (1)$$

Here, $A_1(t_1)$ and $A_2(t_1)$ are activities of two isotopes (Bq) at time t_1. The time t_1 marks the start of the release into the atmosphere since the time of detonation.

3.2. Activity Concentrations in the Air Over an International Monitoring System Station

The radioxenon isotopes that are released from ground or water into the air at t_1 are picked up by the winds and are further subject to the dynamics of the atmosphere. ATM is required to follow the radioxenon isotopes by computing the travel paths from the release location to any other relevant location of reception across the globe. For this, the Comprehensive Nuclear-Test-Ban Treaty Organization (CTBTO) employs the versatile and efficient particle transport model Flexpart (Stohl et al. 1998, 2005, Stohl and Thomson 1999), which is a Lagrangian particle dispersion model able to perform backward (explicit inverse modelling) and forward tracer transport by computing the so-called source–receptor relationship. This relationship links the relevant start and endpoint of the transport of a unit tracer in an integrated fashion by filling a source–receptor matrix. Source attribution (e.g. for radioisotopes) can be efficiently done by matrix multiplication. The resulting SRS field is expressed as a product of a spatial–temporal source at discrete locations and time intervals through $C_{ijn} = S_{ijn} \times M_{ijn}$, where C is the attributed concentration of the tracer (Bq m^{-3}), S is the source attribution (Bq), and M is the source–receptor matrix as a dilution field (m^{-3}) (Stohl et al. 2005, Wotawa et al. 2003, Becker et al. 2007, Kusmierczyk-Michulec et al. 2021).

In the ATM pipeline of the CTBTO, SRS fields with activity concentrations (Bq m^{-3}) can

---

[1] This is a simplified source-receptor matrix concept without considering non-linear chemistry.

be simulated based on a nuclear explosion with a release strength of $1\,Bq$[2]. The time resolution is one hour, and the spatial resolution of each SRS matrix element is 0.5 by 0.5 degrees. The simulated activity concentration at a measurement site – assuming the plume traverses the site – shows one value every one hour and is constant over a large domain during each timestep compared to an IMS observation, which entails a point location collecting radioxenon isotopes for twelve hours per sample (or sometimes twenty-four hours, depending on the sampling equipment used). The space and time parameters differ when comparing or combining activity concentration simulations with observations: 0.5 by 0.5 degrees every hour for ATM vs. point location every 12 hours for IMS. It should be noted that the spatial difference is not covered in this paper as it focuses only on the temporal aspect of matching simulations with observations.

The simulated activity concentrations need to be matched to the concentration obtained from the measurement at the time of collection stop (after twelve hours of sampling). This can be done by simply computing the average concentration for the four consecutive interval values of one hour. A more accurate approach, however, would consider the short half-lives of certain isotopes for the current sampling time, which requires a more comprehensive computation.

When this final simulated activity concentration is computed, it can be divided by the 1 Bq source attribution to get the dilution matrix M in (m^{-3}) at the station. The time of collection stop is designated by t_2 for backward isotopic analysis and use both $C(t_2)$, the activity concentration measured at the station and the simulated dilution value in $M(t_2)$ to get $A(t_2)$ through:

$$A(t_2) = \frac{C(t_2)}{M(t_2)}. \qquad (2)$$

In the most simplified approach, only one source and one release time are considered. In that case, the terms in Eq. (2) are scalars. If multiple sources and many possible release time intervals are considered, this becomes a matrix operation. A mathematical solution for this complex case still needs to be developed. In this paper, the basic principles for the case of a single one-time source are explained. Using Eq. (2), the isotopic activity ratio at the time of collection stop can be estimated by

$$R(t_2) = \frac{A_2(t_2)}{A_1(t_2)} = \frac{C_2(t_2)/M(t_2)}{C_1(t_2)/M(t_2)} = \frac{C_2(t_2)}{C_1(t_2)}. \qquad (3)$$

Regarding the activity evolution, the isotopic ratio in Eq. (3) is defined by the released activities of the source term first but estimated by activity concentrations in the air mass passing the sampling location in the end.

The isotopic activity ratio at the release site using Eq. (1) needs to be related to the ratio at the IMS station in Eq. (3), through the ATM assumption in Eq. (2). Since for ATM part a universal tracer is applied (though source attributed), the activity decay during forward transport is not included in Eq. (2) but can be processed a posteriori to get a decay corrected dilution value (for each radionuclide of relevance). The impact on the isotopic ratio estimation caused by the concentration profile and decay correction during sampling are being investigated and will be presented in the future.

3.3. Activities Collected in Samples at an International Monitoring System Station

Activity concentrations are assumed to be constant during sampling. Therefore, the activities collected in a sample at the time of collection stop are estimated by Eq. (4), irrespective of an independent decay or parent-daughter decay chain.

$$A_s(t_2) = C(t_2)V_s\frac{1-e^{-\lambda\tau_c}}{\lambda\tau_c}, \qquad (4)$$

where, V_s is the air volume sampled (m^3), the

---

[2] The dilution matrix could be directly used (to get the m^{-3} quantity), see later in Eq. (2), but activity concentrations based on an initial activity (with default or any strength of choice) are standard output for CTBTO's ATM pipeline studies, see also Kuśmierczyk-Michulec et al. 2021. The default for CTBTO's pipeline is 1.3E+15 Bq; here we choose 1 Bq for convenience.

subscript s indicates the sample; λ is the decay constant (s^{-1}); τ_c is the duration of collection (s); $A_s(t_2)$ is the activity collected in the sample at the time of collection stop. The activity concentration is referenced at the time of collection stop in Eq. (4), which is consistent with Eq. (3).

Using Eq. (3) and (4), the isotopic ratio of activity concentrations in the plume of air is related to the isotopic ratio of activities collected in the sample at the collection stop time, $R_s(t_2)$, by:

$$R_s(t_2) = \frac{A_{2s}(t_2)}{A_{1s}(t_2)} = R(t_2)\frac{\lambda_1}{\lambda_2}\frac{1-e^{-\lambda_2\tau_c}}{1-e^{-\lambda_1\tau_c}}. \qquad (5)$$

The isotopic ratio of activities collected in the sample is dependent on the decay constants (λ_1, λ_2) as well as the collection time τ_c. In contrast, the isotopic ratio of activity concentration in the plume of air in Eq. (3) is only dependent on decay parameters. Therefore, the isotopic ratio of activity concentrations in the plume instead of the isotopic ratio of activities collected in the sample is used to characterize the activity evolution from the time of detonation until sample measurement, as indicated in Eqs (1) and (3).

3.4. Activities Measured at the Time of Acquisition Start

For an independent decay, the activity $A_{1s}(t_3)$ (Bq) collected in the sample at the time of acquisition start (t_3) is determined by Eq. (6).

$$A_{1s}(t_3) = \frac{x_1}{\varepsilon_1 BR_1}\frac{\lambda_1}{1-e^{-\lambda_1\tau_a}} \qquad (6)$$

where x_1 is the net number of counts for an isotope 1 (the subscript indicates an independent isotope or the parent isotope of a parent-daughter decay chain) determined in spectrum analysis; ε_1 is the efficiency; BR_1 is the branching ratio; τ_a is the real acquisition time (s) of the spectrum.

For a decay chain of parent to daughter, the activity of the daughter isotope is estimated by Eq. (7).

$$A_{2s}(t_3) = \frac{x_2}{\varepsilon_2 BR_2}\frac{\lambda_2}{1-e^{-\lambda_2\tau_a}} -$$
$$A_{1s}(t_3)\frac{\lambda_2}{\lambda_2-\lambda_1}\left(\frac{\lambda_2}{\lambda_1}\frac{1-e^{-\lambda_1\tau_a}}{1-e^{-\lambda_2\tau_a}} - 1\right). \qquad (7)$$

After the collection stop, there is a processing period (τ_p), the decay time of 24 h for particulate samples or the processing time of a few hours for noble gas samples. Considering decay corrections, the activity for the parent isotope, $A_{1s}(t_2)$, and the activity for the daughter isotope of parent-daughter decay chain, $A_{2s}(t_2)$, at the time of collection stop can be estimated by Eq. (8) and (9), respectively.

$$A_{1s}(t_2) = A_{1s}(t_3)e^{\lambda_1\tau_p} \qquad (8)$$

$$A_{2s}(t_2) = \left(A_{2s}(t_3) - A_{1s}(t_3)\frac{\lambda_2}{\lambda_2-\lambda_1}\right.$$
$$\left.\left(1 - e^{-(\lambda_2-\lambda_1)\tau_p}\right)\right)e^{\lambda_2\tau_p}. \qquad (9)$$

Sampling is completed at the collection stop time. Activities collected in the sample depend on decay chains and further processing of samples. The collected sample might be measured by using different approaches, such as re-analysis in IMS radionuclide laboratories. It would be practical to give the activities referenced at the time of collection stop, especially for the estimation of activity concentrations.

Applying Eqs (8) and (9) into Eq. (5), the isotopic ratio of activity concentrations at the time of collection stop, $R(t_2)$, based on the sample measurement, is estimated by Eq. (10).

$$R(t_2) = \frac{\lambda_2}{\lambda_1}\frac{1-e^{-\lambda_1\tau_c}}{1-e^{-\lambda_2\tau_c}}\frac{e^{-\lambda_1\tau_p}}{e^{-\lambda_2\tau_p}}\left[\frac{A_{2sT}(t_3)}{A_{1s}(t_3)} - \frac{\lambda_2}{\lambda_2-\lambda_1}\right.$$
$$\left.\left(\frac{\lambda_2}{\lambda_1}\frac{1-e^{-\lambda_1\tau_a}}{1-e^{-\lambda_2\tau_a}} - e^{-(\lambda_2-\lambda_1)\tau_p}\right)\right] \qquad (10)$$

where $A_{2sT}(t_3) = \frac{x_2}{\varepsilon_2 BR_2}\frac{\lambda_2}{1-e^{-\lambda_2\tau_a}}$ indicates the activity of the daughter isotope determined by the peak counts without the parent-daughter decay correction (subscript T), which is the same as Eq. (6).

Applying Eqs (6) and (7) into Eq. (10), the isotopic ratio of activity concentrations at the time of collection stop is estimated by Eq. (11), based on net numbers of peak counts.

$$R(t_2) = \frac{\lambda_2}{\lambda_1} \frac{1-e^{-\lambda_1\tau_c}}{1-e^{-\lambda_2\tau_c}} \frac{e^{-\lambda_1\tau_p}}{e^{-\lambda_2\tau_p}} \left[\frac{x_2}{x_1} \frac{\varepsilon_1 BR_1}{\varepsilon_2 BR_2} \frac{\lambda_2}{\lambda_1} \frac{1-e^{-\lambda_1\tau_a}}{1-e^{-\lambda_2\tau_a}} - \right.$$

$$\left. \frac{\lambda_2}{\lambda_2-\lambda_1} \left(\frac{\lambda_2}{\lambda_1} \frac{1-e^{-\lambda_1\tau_a}}{1-e^{-\lambda_2\tau_a}} - e^{-(\lambda_2-\lambda_1)\tau_p} \right) \right].$$

(11)

3.5. Analysis Procedure

Activities released from a nuclear event, activity concentrations in the plume passing over an IMS station and activities collected in a sample at the IMS station can be related based on an analysis procedure including the activity evolution from an assumed UNE, through ATM simulations, to sample measurements. The activity concentrations in the plume serve a key role between release and sample measurement. On the one hand, activities released from a nuclear explosion can be estimated based on an assumed scenario in order to have the predicted activity concentrations at a station based on the forward ATM simulations. On the other hand, activities collected in the sample are determined based on spectra analysis and the accompanying activity concentrations are estimated under the assumption of the concentration profile during sampling. As mentioned above, the isotopic ratio of activities collected in the sample differs from the one of activity concentrations in the plume as shown in Eqs (1), (3) and (5). It is a backward procedure to estimate the isotopic ratios of activity concentrations in the plume, based on activities measured in the sample, as shown in Figure 1.
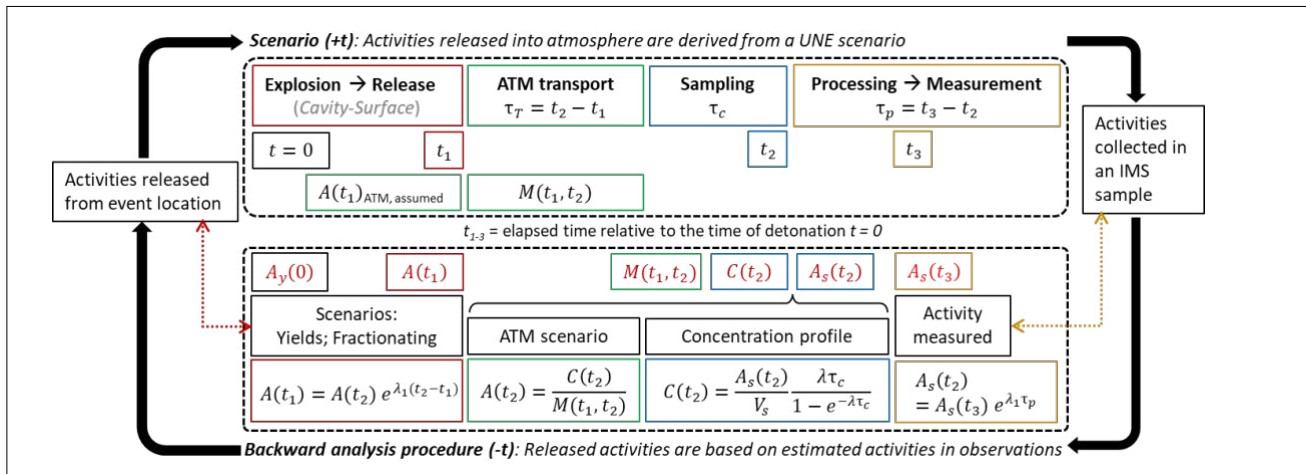
FIGURE. 1.

Schematic sequence of processes from the explosion (t = 0) to the release time (t_1), the collection stop time (t_2), and the acquisition start time (t_3). In contrast, the analysis is performed in reverse order, from the activity measured in the sample back to the activity released.

4. SOURCE TERM OF NUCLEAR EXPLOSION

4.1. Schematic Sequence of Underground Nuclear Explosion

The sequence of cavity evolution following a UNE is illustrated by (Carrigan et al. 2020). During the rapid expansion of a detonation cavity following a UNE (Figure 2(a)), high pressure and temperature result in the formation of a melt zone on the walls of the cavity and form a melt puddle at the bottom of the cavity resulting in a two-phase system with a volatile gas and vapor overlying a zone of melted rock (Figure 2(b)). During the rapid cooling of the vapor phase, the vaporized iodine precursors condense out, mixing with the melt phase in the puddle, while some small fraction of the radioxenon isotopes produced in the puddle may possibly be transported back to the gas phase in the cavity. Collapse of the cavity/chimney may enhance gas seepage and/or prompt venting of radioxenon isotopes produced from decay/ingrowth in the cavity (Figures 2(c) and 2(d)).
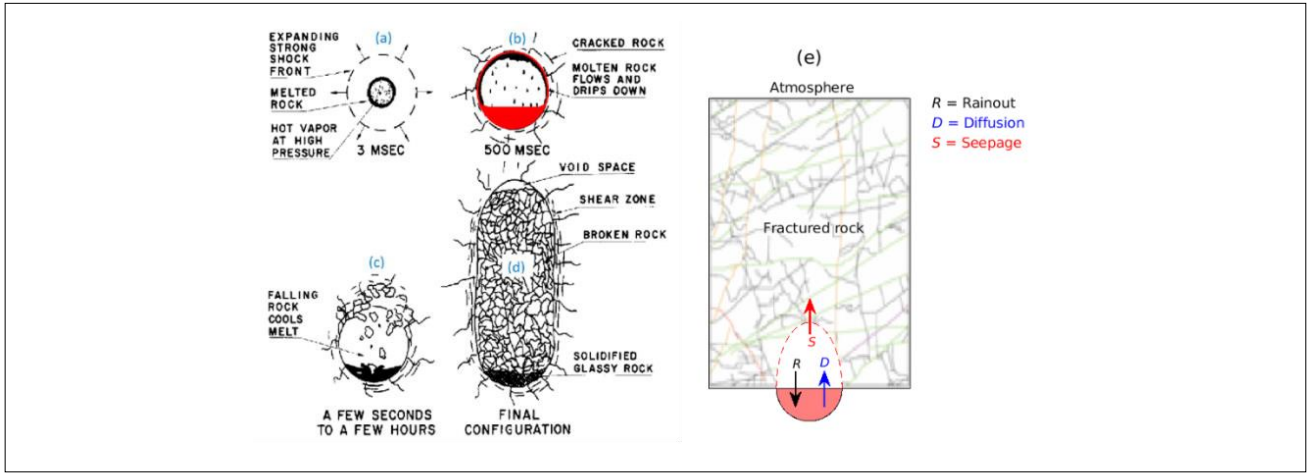
FIGURE 2.

The sequence of events giving rise to the zone of melt at the bottom of a UNE cavity and chimney is illustrated by (Schwartz et al. 1984) as periods of (a) cavity expansion, (b) rock melting, (c) cavity collapse and (d) chimney formation. The conceptual model of source-term activities is referred to Sun et al. (2021). R, D and S in the cavity represent rainout, back diffusion, and seepage, respectively, in (e).

4.2. Activity Evolution Using Bateman Equations

Released activities can be estimated based on mass decay chains using the generalized Bateman equation Eq. (12) (Bateman 1910, Kalinowski and Pistner 2006, Kalinowski 2011).

$$N_{m,n}(t) = \sum_{k=1}^{n} \left[N_{m,k}^0 \cdot \prod_{l=k}^{n-1} b_{m,l} \cdot \sum_{j=1}^{n} \left(\frac{\tau_{m,n}}{\tau_{m,j}} \cdot \prod_{\substack{i=1 \\ l><j}}^{n-1} \frac{1}{1 - \frac{\tau_{m,i}}{\tau_{m,j}}} e^{-ln2 \cdot t/\tau_{m,j}} \right) \right]$$

(12)

where, t is the elapsed time relative to the time of detonation; $N_{m,n}(t)$ is the number of the n-th nuclide in the mass chain m at the time t; $\tau_{m,n}$ is the half-life of the n-th nuclide in the mass chain m. Independent fission yields $N_{m,k}^0$ and decay branching fractions $b_{m,l}$ are taken from England and Rider (1994). The Bateman equation for a given mass chain is solved numerically for each time frame. All possible paths through the branches of the decay chain are treated individually and the results are added up.

Due to the isotope separation from their precursors, the parameters related to decay chains need to be adjusted accordingly, such as assumed modes of full- and part-in-growth. For example, radioxenon decay chains are evolving along with their iodine precursors in the chimney after a UNE. However, after release at the surface, iodine isotopes might be separated completely and only the radioxenon isotopes are transported in the plume.

4.3. Activity Evolution Using Analytical Solution Development

Yamba et al. (2018) were the first to solve Eq. (12) analytically. The resulting four analytical solutions for ^{131m}Xe, ^{133m}Xe, ^{133}Xe and ^{135}Xe describe full in-growth through the decay chain without taking any fractionation into account.

Carrigan et al. (2020) and Sun et al. (2021) described source-term activities (rainout from cavity to puddle, back diffusion from puddle to cavity, and seepage from the cavity to host rock, see Figure 2(e)) together with radioactive decay/in-growth using ordinary differential equations (ODEs)

$$\frac{d\mathbf{c}}{dt} = \mathbf{A}\,\mathbf{c} = (\mathbf{S}\,\Lambda\,\mathbf{S}^{-1})\,\mathbf{c}.$$

(13)

In Eq. (13), $\mathbf{c}$ is the vector of concentrations, t is time, $\mathbf{A}$ is the reaction matrix describing radioactive decay/ingrowth and source-term activities, $\mathbf{S}$ is the matrix whose columns are the eigenvectors of $\mathbf{A}$, $\mathbf{S}^{-1}$ is the inverse matrix of $\mathbf{S}$ and Λ is the eigenvalue matrix of $\mathbf{A}$.

Defining $\mathbf{a} = \mathbf{S}^{-1}\,\mathbf{c}$,

$$\frac{d\mathbf{a}}{dt} = \mathbf{\Lambda}\,\mathbf{a} \qquad (14)$$

is solved analytically. The solution of $\mathbf{c}$ is derived using "$\mathbf{c} = \mathbf{S}\,\mathbf{a}$" as

$$\mathbf{c}(t) = \mathbf{S} \begin{bmatrix} \exp(\lambda_n t) & \cdots & 0 \\ \vdots & \ddots & \vdots \\ 0 & \cdots & \exp(\lambda_n t) \end{bmatrix} \mathbf{S}^{-1}\mathbf{c}_0 \qquad (15)$$

where, $\mathbf{c}_0$ is the vector of initial concentrations. For details of the analytical formulation of $\mathbf{S}$ and $\mathbf{S}^{-1}$, refer to Sun et al. (2015) and Sloan et al. (2016).

4.4. Advanced Analysis Using Complicated Activity Evolution Models

In the case of detection of UNEs involving the observation of explosion produced radionuclides in atmospheric air samples, radionuclide interference can come from sources such as medical isotope production facilities and commercial nuclear reactors (Saey and De Geer 2005). Fortunately comparing in a 4-isotope plot, certain ratios of different radioxenon isotopes (^{131m}Xe, ^{133}Xe, ^{133m}Xe, ^{135}Xe) due to commercial sources against values predicted by a radioactive-decay-chain model of post-detonation isotopic evolution indicates that many, if not all, civilian sources of atmospheric background can be distinguished from UNE sources by a 'discrimination' line (Kalinowski et al. 2010) as illustrated in Figure 3. This 'discrimination line' (red dashes) lies to the left separating the England & Rider isotopic evolution model from most, if not all, atmospheric signals associated with nuclear reactor sources (Kalinowski et al. 2010). Exceptions of nuclear reactor sources that might overlap with the nuclear explosion domain could result from short term irradiation as done in medical isotope production (Kalinowski et al. 2010). Cyan coloured lines are two different isotopic evolution paths predicted by Carrigan et al. (2020) assuming different 'rainout rates' of condensing refractory precursors of radioxenon into underlying molten rock with faster condensation and rainout moving the path to the right of the plot. Magenta coloured lines

represent the evolutionary paths of radioxenon trapped in the underlying molten rock, which is a result of the rainout process and the initial partitioning of part of the radioactive inventory into the melt (Carrigan et al. 2020). Finally, the independent yield (I.Y.) (blue dashed line) represents the evolutionary path of radioxenon isotopes produced at the time of detonation and before significant decay of precursors of radioxenon as shown as well in Kalinowski and Liao. (2014). Daily timelines are shown by the cyan coloured dot dashed lines.

The decay-chain model, mathematically represented by a version of the Bateman equation (Sun et al. 2015, Sloan et al. 2016), is based on the compilation of radioactive-decay data by England and Rider (1994) of those elements in the decay chain of a UNE. However, Carrigan et al. (2020) pointed out that this decay-chain model includes two assumptions that are not likely to be rigorously satisfied. The first requires refractory precursors (e.g. Sn, In, Sb, Te) to remain well mixed with gases including iodine and its radioxenon daughters during the evolution of the radionuclide inventory in the post-detonation cavity, while the second assumption requires gases not to leak from the cavity during the period of evolution.

Recently, the potential effects on the evolution of isotopic activity ratios of deviations from both assumptions (i.e. no leakage from the cavity and a well-mixed cavity) have begun to be explored. It has been known for decades from radiochemical studies of drill cores (e.g. Johnson and Violet 1958, Borg 1975) that a substantial portion of the post-detonation radioactive inventory is partitioned into a melt zone that forms at the bottom of the detonation cavity. The possibility that partitioning of the radioactive inventory or deviation from the well-mixed state might affect observable radioxenon activity ratios was proposed by De Geer (2013) to interpret atmospheric radioxenon observations from UNEs by the Democratic People's Republic of Korea. The exact nature of the process of partitioning or separation of refractory parents from radioxenon daughters is uncertain, but basic process models have been created and evaluated with the intent
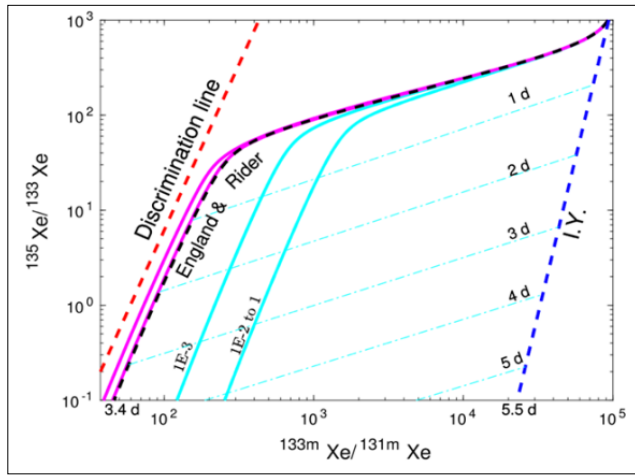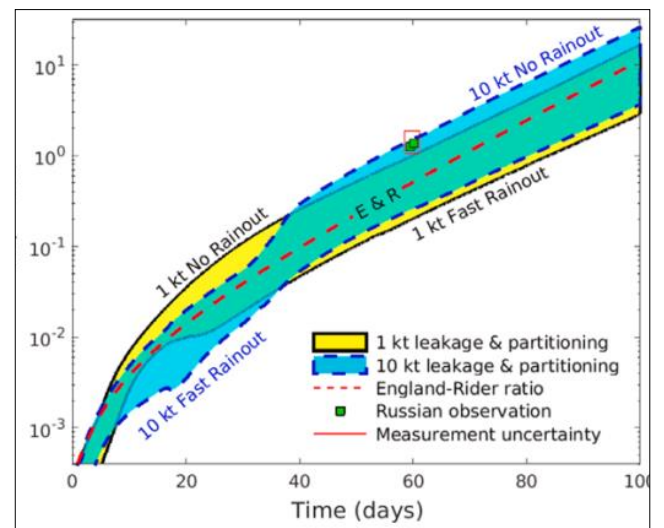
FIGURE 3.
The standard 4-isotope plot shows the England & Rider (E & R)-based model (black dashes) of radioxenon evolution assuming a well-mixed post-detonation cavity with no leakage of gases. Daily timelines are shown by the cyan coloured dot dashed lines. Replotted from Figure 5 of Carrigan et al. (2020). Details are explained in the text.Boundary Estimation Under Different Scenarios and Methods

of estimating the impact of deviations from the well-mixed state (Carrigan et al. 2020). Figure 4 shows the effects of condensation and rainout of refractory parents during cooling of the gas phase followed by their capture in the melt zone of the detonation cavity. The idealized England & Rider model (i.e. full inventory remains well mixed with no long term leakage from cavity) has been plotted (red dashed line) for comparison with the other cases. The rate of rainout or loss of refractory precursor inventory from the well-mixed state generally varies from the case of no rainout (system remains well-mixed) above the England & Rider line to rapid rainout below that line. The RN58 measurements of the isotopic ratio resulting from the 2013 event by the Democratic People's Republic of Korea, which are interpreted as samples released from the cavity, are included for reference with the red box representing the estimated range of error for those measurements. While the curves presented are appropriate for a ^{235f}U detonation, it is unknown what kind of fission event actually occurred. Cavity-gas seepage rates are only estimated for the 2013 event by the Democratic People's Republic of Korea. The main effect of partitioning by condensation and rainout of refractories is to shift the England & Rider evolutionary curve

from its position near the discrimination line further to the right toward the independent yield line. The extent of the rightward shift depends on how quickly condensation and rainout can occur following detonation. For the example considered by Carrigan et al. (2020), the cyan lines show what happens when a condensing species has rainout half-life in the gas phase of approximately 700 seconds (label: 1.E-3) and 0.7 seconds (label: 1) (Figure 3). To move any further rightward requires more rapid cooling to the starting point of precursor condensation. This result suggests that considering deviations from the assumption of a well-mixed radioactive inventory will generally increase the separation on the four radioxenon plot (Figure 3) between atmospheric isotopic 'noise' and the post-detonation radioxenon evolutionary curve.

It was found that relaxing the assumption of no leakage from the detonation cavity causes isotopic evolution to become dependent on nuclear yield through post-detonation heating and the resulting multiphase, thermally driven flow, which affects the time dependent leakage rate (Sun et al. 2016, Carrigan et al. 2016). The 2013 UNE by the Democratic People's Republic of Korea was evaluated given evidence for long

FIGURE 4.
Evolution of the isotopic activity ratio ^{131m}Xe to ^{133}Xe in a detonation cavity is plotted against time for nuclear yields of 1 and 10 kt subject to assumed conditions of rainout and continuing loss of radionuclide inventory from the gas/vapor phase with leakage into the zone of containment. Replotted from Fig. 6 of Carrigan et al. (2020).

term leakage from the cavity. Radionuclide observations of the nuclear test were unusual as radioxenon was not observed in the atmosphere until almost two months following the detonation with detections occurring first at RN38 and a few days later at RN58 (Ringbom et al. 2014). The measured ratios were somewhat different, leading to a possible interpretation by Ringbom and colleagues that the radioxenon measured first at RN38, from what was evidently a well-contained UNE, was released in opening and ventilating the tunnel complex at the test site of the Democratic People's Republic of Korea while the RN58 observation, with large measurement errors (Ringbom et al., 2014), came from a location in the tunnel complex nearer to the point of detonation in the Democratic People's Republic of Korea. Using their leaky reactor model in a variational study, Carrigan et al. (2016) reached a similar conclusion except that the RN58 measurements were found to best agree with radioxenon evolution in the actual detonation cavity or chimney itself, for a yield of 5–8 kilotons, which happens to be in approximate agreement with the seismic yield estimates for that event (Ringbom et al. 2014). This led to the hypothesis that the RN58 measurements resulted from a prompt release caused by drilling back into the detonation cavity, a common post-detonation procedure for nuclear test evaluation.

5. CHARACTERIZATION OF COMPREHENSIVE NUCLEAR-TEST-BAN TREATY-RELEVANT RADIONUCLIDE EVENTS BASED ON ISOTOPIC RATIOS

The relationships of quantities involved in the three stages of isotopic activity evolution, namely, in the subsurface prior to the release into the atmosphere, in the air mass transported by the wind fields and in the sample collected at an IMS station, are discussed in this paper, including the uncertainty estimation involved. The analysis procedures and results of the IMS observations related to the 2013 nuclear test event by the Democratic People's Republic of Korea, Fukushima Daiichi nuclear accident and daily radioxenon background are provided as examples.

After more than 50 days after the announced third Democratic People's Republic of Korea nuclear test event in 2013, three consecutive Level C samples at RN38 and two consecutive Level C samples at RN58 were considered that might have originated from this event (Ringbom et al. 2014, Carrigan et al. 2016, 2020). These five samples as well as the samples related to the Fukushima Daiichi nuclear accidentand daily radioxenon background at IMS stations are provided as examples demonstrating the described procedures of the isotopic activity ratio analysis.

5.1. Calculation Methods of Isotopic Ratio

Isotopic ratios and associated uncertainties are dependent on not only concentrations but also their uncertainties and covariances. For a non-linear model of division operation, ratios of concentrations and associated uncertainties are estimated by high-order Taylor terms and dependent on uncertainties of denominators. For low level samples, it is better to use the MCM, estimating isotopic ratios and their uncertainties based on activities measured in the sample or associated peak counts directly.

The concentration and associated uncertainty values are given in IDC analysis reports. The nominal value and the associated uncertainty of the isotopic activity ratio are estimated by Eq. (15),

$$r_0 = \frac{c_2}{c_1}; \, u^2(r_0) = r_0^2 \left(\frac{u^2(c_1)}{c_1^2} + \frac{u^2(c_2)}{c_2^2} - 2\frac{\text{Cov}(c_1, c_2)}{c_1 c_2} \right).$$

$$(15)$$

Notice that r_0 in Eq. (15) is calculated from the values of activity concentrations, c_1 and c_2, as taken from analysis reports. However, $R(t_2)$ in

Eq. (3) is defined as the ratio of two random variables, i.e. the activity concentrations $C_1(t_2)$ and $C_2(t_2)$. There is no formula for calculating the expectation and variance of a ratio of random variables without reference to any specific probability distribution. The way forward is to perform a Taylor expansion of $E[R(C_1,C_2)]$ and $Var[R(C_1,C_2)]$ at the values c_1 and c_2, the results of which in first order are then the values of Eq. (15). By extending the Taylor expansion to the second order, we obtain the ratio r and the associated uncertainty $u(r)$, as shown in Eq. (16).

$$r = r_0\left(1 + \frac{u^2(c_1)}{c_1^2} - \frac{\text{Cov}(c_1,c_2)}{c_1 c_2}\right),$$

$$u^2(r) = r_0^2\left(\frac{u^2(c_2)}{c_2^2}\left(1 + 3\frac{u^2(c_1)}{c_1^2}\right) + \right.$$

$$\left. \frac{u^2(c_1)}{c_1^2}\left(1 + 8\frac{u^2(c_1)}{c_1^2}\right) - 2\frac{\text{Cov}(c_1,c_2)}{c_1 c_2}\right). \quad (16)$$

The biases are mainly dependent on the uncertainty of the denominator, as shown in Eq. (16), especially with large relative uncertainties of the concentrations for low level samples.

Differing from the analytical approach described above, a numerical approach utilizing the MCM can accomplish the propagation of probability distributions (ISO/IEC 2008). The analysis model is dependent on the measurement process and the spectrum analysis of the sample. First, the values of input parameters, such as activity concentrations from the analysis report or original peak counts from the spectrum, are sampled based on associated probability distributions. Then the distributions of isotopic activity ratios and/or explosion times are derived. Finally, the mean values of isotopic activity ratios and/or detonation times associated uncertainties and limits of the coverage interval are estimated accordingly (Liu and Kalinowski 2021).

5.2. Sample Association

The consistency of activity ratios across multiple isotope observations with respect to a given radioactive decay curve is a plausible indication that these isotopes have originated from the same source. For three level C samples (red dot) from RN38 in Figure 5, the blue decay curve was estimated using the second sample due

to smaller relative uncertainties of concentrations, including the blue bandwidth (the upper and lower limits of the coverage interval under the probability of 95%). For two samples from RN58 (red squares), the second sample was used to derive the green decay curve and its bandwidth. The isotopic activity ratios of three Level C samples at RN38 are consistent with a blue decay curve within the blue bandwidth, and two Level C samples at RN58 with the green decay curve and its bandwidth. The blue bandwidth does not overlap with the green bandwidth. This indicates that there were two distinct releases at the test site of the Democratic People's Republic of Korea from the viewpoint of decay-consistent isotopic activity ratios.

Moreover, ATM simulations might improve confidence in sample association by identifying the air masses that link a release to multiple samples. It might be possible that the Level B samples that overlap with the blue bandwidth can be associated with these three Level C samples at RN38. For this confirmation, a so-called possible source region analysis is performed based on correlation algorithms used on SRS fields and
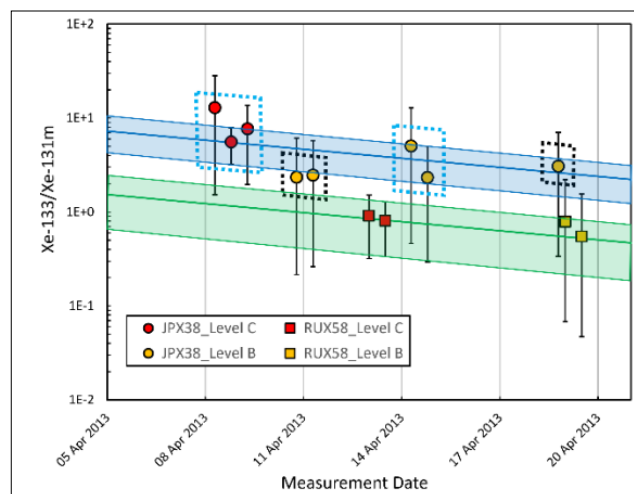
FIGURE 5.

Decay consistent analysis of isotopic activity ratios for three Level C samples at JPX38, two Level C samples at RN58 as well as the Level B samples in the period. Level B samples marked by a blue dotted box are associated with the level C samples at RN38, confirmed by the so-called possible source region analysis resulting from ATM simulations (Kijima et al. 2022). The ratio values are given with second order polynomial and the error bars are the limits of the coverage interval with 95%.

radionuclide observations. The results of possible source region analysis, see (Kijima et al. 2023), indicate that the level B samples marked by a blue dotted box in Figure 5 are associated with the three level C samples at RN38. So, it might be possible that these samples originate from the same release. On the other hand, the Level B samples marked by black dotted boxes in Figure 5 are not associated with these Level C samples indicating they did not originate from the same release.
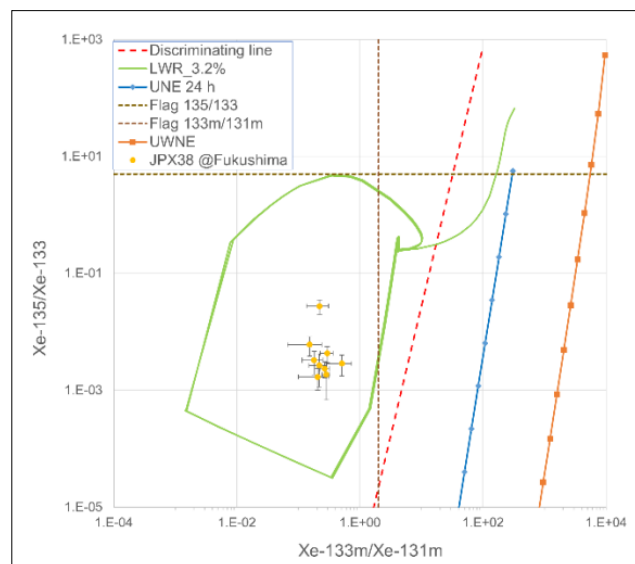
The criteria for associating relevant episode samples using consistent isotopic activity ratios as well as the analysis procedure combined with ATM simulations was investigated in another study (Kijima et al. 2023).

5.3. Relationship Plot of Four Radioxenon Isotope Detections

For both discrimination of a nuclear test and estimation of the explosion time, the isotopic ratio at the stop of collection is related to activity concentrations in the air plume instead of activities collected in the sample. One of the reasons is due to the basic assumption that activities released are linearly correlated to activity concentrations in the plume described by ATM simulations. The ratio of activities collected in the sample, however, is not only related to the decay constants but also the duration of sampling, as decay chains can be interrupted due to activity accumulation during sampling. Isotopic activity ratios of radioxenon measured in IMS noble gas samples may routinely indicate a gas release from an underground nuclear test, despite the true cause being emissions from nuclear facilities. A robust method is required to test isotopic ratios of samples against prepared information aggregated from a comprehensive set of all relevant release scenarios.

In the case of the 2013 event of the Democratic People's Republic of Korea, only radioxenon isotopes ^{133}Xe and ^{131m}Xe were detected, therefore, the four radioxenon plot was not applicable. In the case of the Fukushima Daiichi nuclear accident in 2011, all four radioxenon isotopes were detected in a few samples at RN38. Due to

the scale of this incident, anomalous radioxenon detections were frequently observed. As shown in Figure 6, the detections from the Fukushima Daiichi nuclear accident are in the domain of nuclear facility releases, inside the evolution trajectory of the isotopic activity ratios through three reactor circles of light water reactor (LWR) burnup for 3.2% ^{235f}U enrichment.

FIGURE 6.

Four radioxenon plot of ^{135}Xe/^{133}Xe versus ^{133m}Xe/^{131m}Xe. The evolution curves of the isotopic activity ratios for the two scenarios of ^{239f}Pu are included: UNE release at 24 h after detonation and underwater nuclear explosion immediate release (Burnett et al. 2019). The uppermost point indicates the release at 24 h after the detonation time for UNE and zero hour for an underwater nuclear explosion. The trajectory of LWR burnup for 3.2% ^{235}U enrichment (evolution through three reactor circles) was replotted from Figure 8 of Kalinowski et al. (2010). Four radioxenon isotopes were detected in a few samples at RN38 after the Fukushima Daiichi nuclear accident in 2011 (uncertainties of the isotopic activity ratios with two standard uncertainty).

## 5.4. Combined Analysis Between Concentrations and Isotopic Ratios

The ^{131m}Xe/^{133}Xe activity ratio of the three level C samples at RN38 related to the 2013 event of the Democratic People's Republic of Korea are shown in Figure 7. The values between 0.1-1 are within the range of the 'normal' observed values at RN38 during the selected period. Figure 8 shows the timeline of the ^{131m}Xe/^{133}Xe activity ratios at RN38 resulting from the Fukushima Daiichi nuclear

accident, which are increasing with time. The main reason for the linear shape of the entries is the decay over time as the plume travelled through the atmosphere and was remeasured (there were also several releases). The ratios related to earlier releases in Figure 8 are also in the range between 0.1 and 1 in Figure 7, i.e. similar to those recorded in April 2013 and associated with the 2013 announced test of the Democratic People's Republic of Korea. Only when including the activity concentration values into the comparison, clear differences are noted between the 'normal' daily measurements in the lower left blue cluster in Figure 9. These are clearly separated from the higher activity observations following the Fukushima Daiichi nuclear accident marked in purple colour and from the red coloured samples related to the 2013 event of Democratic People's Republic of Korea. The activity concentrations of both ^{131m}Xe and ^{133}Xe in the three level C samples associated with the 2013 Democratic People's Republic of Korea event (red triangles) lie outside of the domain of the general radioxenon background at RN38 (blue dots) as well as below the ones from the Fukushima Daiichi nuclear accident (purple diamond). Therefore, both values of isotopic activity ratios and associated activity concentrations may be instrumental to scrutinize with respect to assumed scenarios. Further information on an event under consideration can be gained from related ATM simulations.

The values of isotopic activity ratios related to the 2013 event of the Democratic People's Republic of Korea are in the range of normal background samples during the selected period (the day zero is the date of the announced 2013 event of the Democratic People's Republic of Korea). Ratio values are presented with the
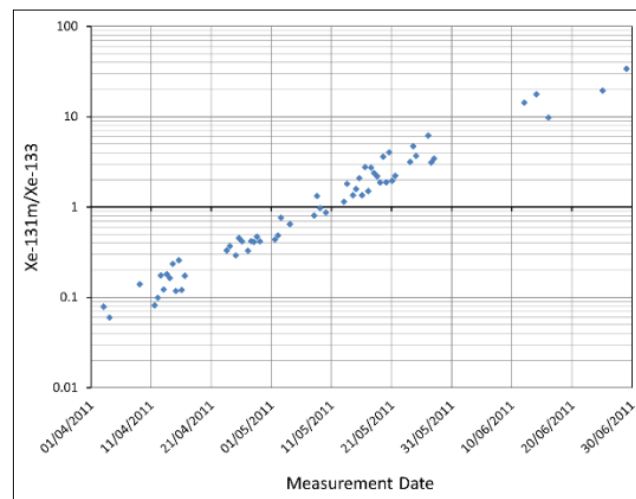
FIGURE 8.
Isotopic activity ratios of ^{131m}Xe to ^{133}Xe in samples at JPX38 from 1 April to 30 June 2011 are increasing with time due to the increasing age of the release sources from the Fukushima Daiichi nuclear accident. Ratio values are presented with the nominal values, but their associated uncertainties are not given, which are in the range of (5%, 39%) with the median of 15% in one standard uncertainty.
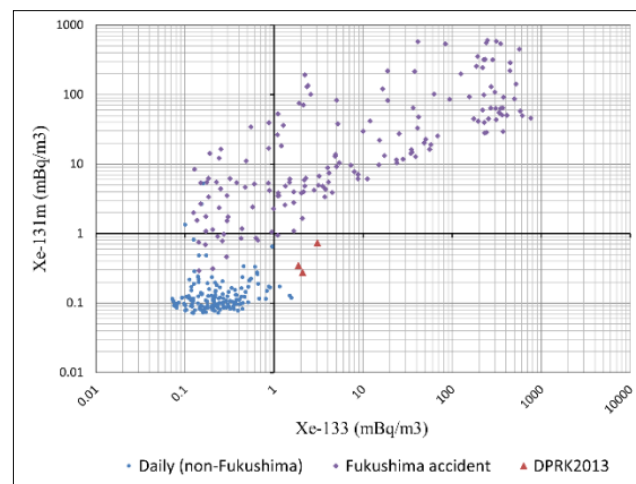
FIGURE 9.
Scatter plot for a pair of activity concentrations at RN38, ^{133}Xe versus ^{131m}Xe. The daily samples from 1 July 2011 to 30 April 2013 are clearly separated from the Fukushima Daiichi nuclear accident and the samples from the 2013 event of the Democratic People's Republic of Korea. Uncertainties of activity concentrations are not presented.
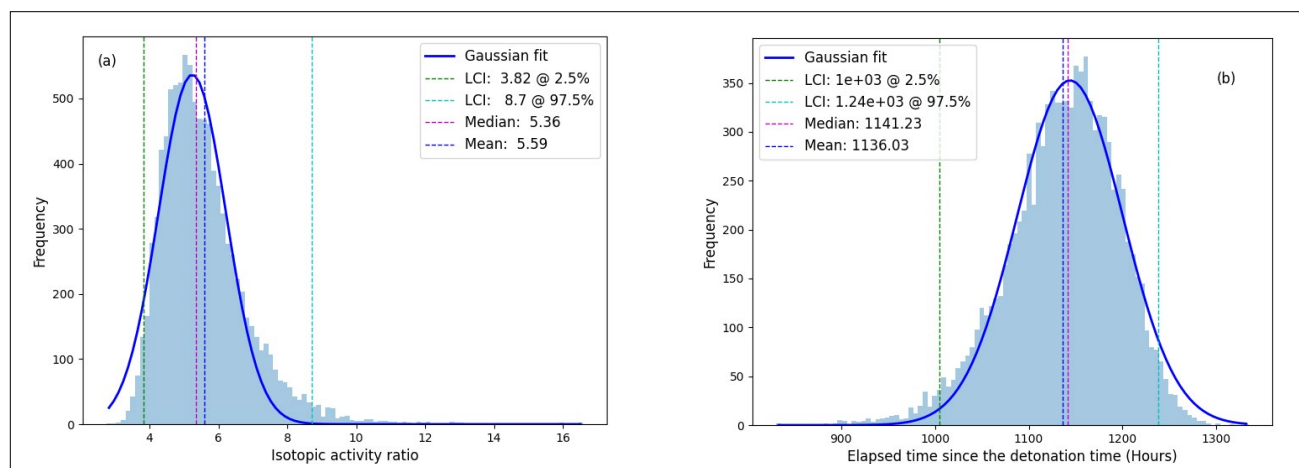

FIGURE 7.
Isotopic activity ratios of ^{131m}Xe to ^{133}Xe in samples at RN38 that had both isotopes detected.

nominal values, but their associated uncertainties are not given, which are in the range of (16%, 140%) with the median of 59% in one standard uncertainty.

5.5. Event Timing

The explosion time can be estimated by using a function of the isotopic ratio with time, assuming a zero length containment time (in some inter-comparison exercises, up to 24 h was previously used).

In one case study, the isotopic activity ratio and elapsed time for one of the samples related to the DPRK2013 nuclear test event were estimated using the MCM. For the sample at RN38 at 19:00 on 8 April 2013 (collection stop), the concentrations are ^{133}Xe 3.05±0.14 (one standard deviation unless otherwise stated)

distributions of isotopic activity ratios and elapsed times were estimated accordingly, which differs slightly from the fitted Gaussian curves in Fig. 11 (a, b). This is due to the exponentials and logarithms involved as well as the relative uncertainty of 19% for ^{131m}Xe. The ^{133}Xe/^{131m}Xe isotopic ratio of activity concentrations is 5.59±1.29, different from the nominal value of 5.35±1.06 but within one standard uncertainty. Under a simplified full-ingrowth model, the mean values of elapsed times since the time of detonation are 47.3±2.5 and 45.5±2.4 days for the fission material ^{235}U and ^{239}Pu respectively, which are close to the actual 54.5 days. The parameters and assumptions involved need to be further investigated, such as the model based on activities or net numbers of peak counts, or even directly based on the gross numbers of peak counts in the NCC method used for the beta-gamma coincidence spectrum analysis.

FIGURE 10.
Distributions derived by MCM (a) Distribution of isotopic activity ratios ^{133}Xe/^{131m}Xe; (b) Distribution of elapsed times (hours).

and ^{131m}Xe 0.57±0.11 (mBq m^{-3}). For the isotopic ratio of ^{133}Xe to ^{131m}Xe in Eq. (15) and (16), the nominal and second order polynomial values are 5.35±1.06 and 5.55±1.20, respectively. The bias is due to the relative uncertainty of 19% for ^{131m}Xe in the denominator.

The isotopic ratios in the activity concentration model in Eq. (3) were estimated by the MCM, where Gaussian distributions for two activity concentrations were used. Both

5.6. Radioxenon Background Estimation and Subtraction

One of the issues in the isotopic activity ratio analysis is whether the contribution of the radioxenon background needs to be subtracted. This was the case with ^{131m}Xe and observations of radioxenon in the days after the nuclear test announced by the Democratic People's Republic of Korea in 2006 (Ringbom et al. 2009). Simulations are performed with

ATM to determine an activity concentration and its associated uncertainty from known releases of nuclear facilities to each IMS sample measurement, resulting in a residual between the IMS observation and ATM simulated concentration. Ideally, event discrimination can be performed based on the residual. However, there might be relatively large fluctuations in ATM simulated activity concentrations in some cases, resulting in outliers in the distributions of the residuals. In light of this issue, for the Nuclear Explosion Signal Screening Open Inter-Comparison Exercise 2021, ATM simulations were performed to estimate the activity concentrations originating from hypothetical radioxenon releases of pre-defined UNEs as well as releases from known sources of nuclear facilities, resulting in a second set of synthetic activity concentrations at IMS stations. An ongoing study aims to get a better estimation of the radioxenon background to distinguish between known sources and potential (hidden or weaker) UNE signals. This will be done by exploring several methods that include statistical uncertainty for ATM simulated activity concentrations. Ultimately, the activity ratios of detected radioxenon isotopes are compared between the real IMS observations (typical radioxenon background), simulated concentrations from hypothetical nuclear explosion sources (pure signals without radioxenon background) and synthetic ones.

5.7. Data Fusion Between Radionuclide Observations and Waveform Events

The IMS network continuously monitors the globe for nuclear explosions through seismic, hydroacoustic, infrasound (SHI) and radionuclide measurements to detect signals from possible nuclear explosions. SHI monitoring stations continuously record waveform signals and the events identified using three technologies are fused into a combined event bulletin. Due to the different nature of SHI and radionuclide measurements, the results are reported in separate bulletins. In order to fully characterize a hypothetical UNE, the radionuclide detections must be matched in time and space to an event that was constructed from the waveform data of the SHI networks. The IDC offers a fusion tool that regularly performs data fusion between radionuclide detections and waveform based events using the source–receptor sensitivity fields from the ATM simulations. In the scenarios considered here, a UNE creates an immediate seismic signal, but with an a-priori unknown delay until the release of radionuclides. The data fusion pipeline at the IDC accounts for possible delayed releases of up to 60 days, but additional information is required to more precisely determine which waveform based event should be associated with given radionuclide detections. The results described here, in particular the determination of the release (containment) time and the detonation time, can provide further information to the data fusion algorithm.

6. SUMMARY

For spectral analysis, three sets methods are implemented; the single channel analyser curve for particulate, the least squares regression on gamma and X ray peaks of xenon isotopes for high resolution spectra and the net count calculation method for beta–gamma coincidence spectra for noble gas, which are based on conventional frequentist statistics. Enhancements on current methods for beta–gamma coincidence might include optimization regression analyses of standard spectra, 3-D fitting and gross counts, or machine learning. There are new requirements for noble gas analysis from lessons learned in past years. Under estimation of decision thresholds, due to negative net numbers of counts, led to a too high false alarm rate; the inclusion of uncertainty components related to interference corrections; deconvolution of X ray contributions of xenon isotopes and radon; and the estimating the covariances of net numbers of counts between ROIs for isotopic activity ratio analysis. Along with the development of 'memory free' detectors, the memory correction could be performed in a 'smart' mode, i.e. only if

a radioxenon isotope is detected in the associated gas background spectrum. Reporting the results of the sample itself, the gas background, and the sample with memory corrections separately would be a better solution for the systems with gas background measurements.

IDC data analysis and categorization is applied on each measurement, for each sample at IMS stations. No repeated measurements are available, except for re-analysis at CTBT laboratories for certain selected samples. The numbers of peak counts in the single measurement are estimated by using the likelihood function, which has the same formula with the probability density function of the a priori distribution. The associated uncertainties are systematic uncertainties. The detector background is estimated based on the a priori distribution and related measurements. Most daily IMS spectra have low counts close to background level. Decision thresholds using Currie's definition tend to be underestimated for beta–gamma coincidence spectrum analysis. This is due to a probability density function that is inappropriate for low count samples, and therefore causes an increase in false positive detections. Developments and enhancements of analysis algorithms should be consistent with estimation of measurement uncertainty and characterization limits based on Bayesian statistics.

IDC radionuclide analysis reports could be enhanced by reporting not only results and their uncertainties but also associated characterization limits as recommend in ISO 11929:2019. Traceability of analysis results for particulate samples is obtained by using standard sources with certificates from source providers. It is a pending issue for the traceability of the beta–gamma coincidence analysis. Standard sources are not available for all four xenon isotopes so far. On the other hand, beta–gamma coincidence measurements in a near 4-pi detector geometry can be characterized as an absolute measurement, where the activity values of standard sources are not needed for efficiency estimation.

Isotopic activity ratios of fission products detected at IMS radionuclide stations are used for characterization of a fission event. For both discrimination of a nuclear test and estimation of the detonation time, the isotopic ratio at the time of collection stop is related to activity concentrations in the plume of air instead of activities collected in the sample. The nominal value of the isotopic activity ratio is estimated directly by the division of two activity concentrations and associated uncertainties given in IDC analysis reports. For a non-linear model of division operation, the biased value of an isotopic activity ratio and associated uncertainty needs to be estimated by high order Taylor terms, e.g. the second order polynomial, and they are dependent mainly on uncertainties of denominators, especially with large uncertainties of concentrations for low level samples. It is better to use the MCM, estimating isotopic ratios and their uncertainties based on activities measured in the sample or associated peak counts directly. The lower limits of isotopic activity ratios based on the Bayesian approach are used as the event screening flags in IDC radionuclide products. The function of the isotopic activity ratio over the time from detonation to sample measurement is used for discrimination of a nuclear test, such as a four radioxenon plot of the activity ratio relationship of ^{135}Xe/^{133}Xe versus ^{133m}Xe/^{131m}Xe, and estimation of the time of detonation.

Characterization of radioxenon detections at IMS stations requires connecting or relating physical processes at the two ends of the radioxenon isotope (and their isotopic activity ratio) lifecycles. At one end, the radioisotopes are generated by a nuclear explosion and at the other they are directly measured in IMS samples. Mathematical modelling is used to explore the relationship between these two points, with ATM a crucial tool in this regard. The investigation of IMS samples for possible nuclear test signatures requires constant vigilance and a thorough understanding of both underground nuclear test scenarios and the dynamic anthropogenic radioxenon background.

REFERENCES

Axelsson, A., Ringbom, A. (2014). On the calculation of activity concentrations and nuclide ratios from measurements of atmospheric radioactivity. *Applied Radiation and Isotopes* **92**, 12–17.

Bateman, H. (1910). "Solution of a system of differential equations occurring in the theory of radioactive transformation". *Mathematical proceedings of the Cambridge Philosophical Society* (Proceedings of the Cambridge Philosophical Society, Cambridge) **15** (1908-10) 423–427.

Becker, A., et al. (2007). Global backtracking of anthropogenic radionuclides by means of a receptor oriented ensemble dispersion modelling system in support of Nuclear-Test-Ban Treaty verification. *Atmospheric Environment* **41** (21) 4520–4534.

Borg, I.Y. (1975). Radioactivity trapped in melt produced by a nuclear explosion. *Nucl. Technol. 26 (1),* 88–100. http://dx.doi.org/10.13182/NT75-A24406.

Burnett, J.L., Eslinger, P.W., Milbrath, B.D. (2019). The detectability of the Wigwam underwater nuclear explosion by the radionuclide stations of the International Monitoring System. *Journal of Environmental Radioactivity* **208–209**.

Cagniant, A., et al. (2018). SPALAX NG: A breakthrough in radioxenon field measurement. *Applied Radiation and Isotopes* **134** 461-465.

Carrigan, C., et al. (2016). Delayed signatures of underground nuclear explosions. *Scientific Reports* **6** 23032.

Carrigan, C.R., Sun, Y., Pili, E., Neuville, D., & Antoun, T. (2020). Cavity-melt partitioning of refractory radionuclides and implications for detecting underground nuclear explosions. *Journal of Environmental Radioactivity* **219** 106269.

Cooper, M.W., Ely, J.H., Hayes, J.C., McIntyre, J.I, Schrom, B.T. (2016). *Minimum Detectable Concentration and Concentration Calculations*. PNNL-25418, Pacific Northwest National Laboratory, U.S. Department of Energy, USA.

Cooper, M.W., et al. (2019a). *β–γ Absolute Calibration*. PNNL-27572 Rev. 1, Pacific Northwest National Laboratory, U.S. Department of Energy, USA.

Cooper, M.W., et al. (2019b). Radioxenon net count calculations revisited. *Journal of Radioanalytical and Nuclear Chemistry* **321** 369-382.

Currie, L.A. (1968). Limits for qualitative detection and quantitative determination. Application to radiochemistry *Analytical Chemistry* **40** (3) 586–593.

De Geer, L.E. (2001). Comprehensive Nuclear-Test-Ban Treaty: relevant radionuclides. *Kerntechnik*, **66** (3) 113-120.

De Geer, L.E. (2004). Currie detection limit concepts in gamma-ray spectroscopy. *Applied Radiation and Isotopes* **159** (2-3) 151–160.

De Geer, L.E. (2007). The Xenon NCC Method Revisited. FOI-R-2350-SE. Swedish Defence Research Agency.

De Geer, L.E. (2013). Reinforced evidence of a low-yield nuclear test in North Korea on 11 May 2010. *Journal of Radioanalytical and Nuclear Chemistry* **298** 2075–2083.

Deshmukh, N., Prinke, A., Miller, B., McIntyre, J. (2017). Comparison of new and existing algorithms for the analysis of 2D radioxenon beta gamma spectra. *Journal of Radioanalytical and Nuclear Chemistry* **311** (3) 1849–1857.

England, T.R., Rider, B.F. (1995). Evaluation and compilation of fission product yields: 1993. United States.

Goodwin, A.M., Davies, V.A., Britton R., et al. (2023). Radionuclide measurements of the international monitoring system. PTS report for 25-year anniversary.

International Organization for Standardization/International Electrotechnical Commission (2009). *Uncertainty Of Measurement - Part 3: Guide To The Expression Of Uncertainty In Measurement, Supplement 1: Propagation Of Distributions Using A Monte Carlo Method.* ISO/IEC Guide 98-3/Suppl1:2008/COR 1:2009, Switzerland.

International Organization for Standardization (2019). Determination of the Characteristic Limits (Decision Threshold, Detection Limit and Limits of the Coverage Interval) for Measurements of Ionizing Radiation – Fundamentals and Application. ISO 11929-1:2019, Switzerland.

Johnson, G.W., Violet, C.E. (1958). *Phenomenology of Contained Nuclear Explosions*. University of California, Lawrence Radiation Laboratory, UCRL-5124 (Rev. 1), US Atomic Energy Commission.

Kalinowski, M.B., Pistner, C. (2006). Isotopic signature of atmospheric xenon released from light water reactors. *Journal of Environmental Radioactivity* **88** (3) 215–235.

Kalinowski, M.B., et al. (2010). Discrimination of nuclear explosions against civilian sources based on atmospheric xenon isotopic activity ratios. *Pure and Applied Geophysics* **167** 517–539.

Kalinowski, M.B. (2011). Characterisation of prompt and delayed atmospheric radioactivity releases from underground nuclear tests at Nevada as a function of release time. *Journal of Environmental Radioactivity* **102** (9), 824–836.

Kalinowski, M.B., Liao, Y-Y (2014). Isotopic characterization of radioiodine and radioxenon in releases from underground nuclear explosions with various degrees of fractionation. *Pure and Applied Geophysics* **171** (3) 677–692.

Kalinowski, M.B., Liu, B. (2020). "Calculation of isotopic ratios of fission products detected at IMS radionuclide stations". (Proceedings of the 61st Annual Meeting of the Institute of Nuclear Materials Management, Baltimore, MD, 2020).

Kalinowski, M.B., Tayyebi, P., Lechermann, M., Tatlisu, H. (2021). Global radioxenon emission inventory from nuclear research reactors. *Pure and Applied Geophysics* **178** (7) 2711-2739.

Kijima Y., et al. (2022). "Investigation on sample association by using anomalous concentration episodes and decay-consistent isotopic ratios at IMS radionuclide stations". (Proceedings of the 61st Annual Meeting of the Institute of Nuclear Materials Management, Baltimore, MD, 2020).

Kijima, Y., et al. (2023). Investigation on atmospheric radioactivity sample association using consistency with isotopic ratio decay over time at IMS radionuclide stations. *Journal of Environmental Radioactivity* **270** 107301.

Kuśmierczyk-Michulec, J., et al. (2021). Advancements in Atmospheric Transport Modelling (ATM) at the CTBTO PTS during the past two decades and plans for the future. CTBT: Science and Technology Conference 2021 (SnT2021).

Liu, B., Kalinowski, M.B. (2021). "Estimation of isotopic ratios of fission products by using the Monte-Carlo method". (Proceedings of the Institute of Nuclear Materials Management and European Safeguards Research & Development Association Joint Virtual Annual Meeting, 2021).

Liu, B., Kalinowski, M., Muramoto T. (2020). Enhancements on the decision threshold algorithm of the net count calculation method. *Applied Radiation and Isotopes* **159** 109084.

Liu, B., et al. (2023). Characterization of CTBT-relevant radioxenon detections at IMS stations using isotopic activity ratio analysis. *Pure and Applied Geophysics* **180** 1521-1540.

Ringbom, A., et al. (2009). Measurements of radioxenon in ground level air in South Korea following the claimed nuclear test in North Korea on October 9, 2006. *Journal of Radioanalytical and Nuclear Chemistry* **282** (3) 773-779.

Ringbom, A., et al. (2014). Radioxenon detections in the CTBT international monitoring system likely related to the announced nuclear test in North Korea on February 12, 2013. *Journal of Environmental Radioactivity* **128** 47–63.

Ringbom, A., Axelsson, A. (2020). A new method for analysis of beta-gamma radioxenon spectra. *Applied Radiation and Isotopes* **156** 108950.

Saey, P.R.J., De Geer, L.-E. (2005). Notes on radioxenon measurements for CTBT verification purposes. *Applied Radiation and Isotopes* **63** (5-6) 765–773.

Schwartz, L., Piwinskii, A., Ryerson, F., Tewes, H., Beiriger, W. (1984). Glass produced by underground nuclear explosions. *Journal of Non-Crystalline Solids* **67** *(1–3)* 559–591.

Sloan, J., Sun, Y., Carrigan, C. (2016). Uncertainty quantification for discrimination of nuclear events as violations of the comprehensive nuclear-test-ban treaty. *Journal of Environmental Radioactivity* **155-156** 130–139.

Stohl, A., Hittenberger, M., Wotawa, G. (1998). Validation of the lagrangian particle dispersion model FLEXPART against large-scale tracer experiments. *Atmospheric Environment 32*, 4245–4264.

Stohl, A., Thomson, D.J. (1999). A density correction for Lagrangian particle dispersion models. *Boundary-Layer Meteorology* **90** 155–167.

Stohl, A., Forster, C., Frank, A., Seibert, P., Wotawa, G. (2005). Technical Note: The Lagrangian particle dispersion model FLEXPART version 6.2. *Atmospheric Chemistry and Physics*. **5** (9) 2461-2474.

Sun, Y., Carrigan, C.R., Hao, Y. (2015). Radioxenon production and transport from an underground nuclear detonation to ground surface. *Pure and Applied Geophysics* **172** 243–265.

Sun, Y., & Carrigan, C.R. (2016). Thermally driven advection for radioxenon transport from an underground nuclear explosion. *Geophysical Research Letters* **43** (9) 4418–4425.

Sun, Y., et al. (2021). A closed-form solution for source-term emission of xenon isotopes from underground nuclear explosions. *Transport in Porous Media* **139** 131–153.

Wotawa, G., De Geer, L., Denier, P., et al. (2003). Atmospheric transport modelling in support of CTBT verification-overview and basic concepts. *Atmospheric Environment* **37** (18) 2529–2537.

Yamba, K., Sanogo, O., Kalinowski, M.B., Nikkinen, M., Koulidiati, J. (2016). Fast and accurate dating of nuclear events using La-140/Ba-140 isotopic activity ratio. *Applied Radiation and Isotopes* **112** 141–146.

Yamba, K., Kalinowski, M.B., Sanogo, O. (2018). Nuclear event zero time determination using analytical solutions of radioxenon activities under in-growth condition. *Applied Radiation and Isotopes* **139** 217–223.

Zaehringer, M., Kirchner, G. (2008). Nuclide ratios and source identification from high-resolution gamma-ray spectra with Bayesian decision methods. *Nuclear Instruments and Methods in Physics Research Section A: Accelerators, Spectrometers, Detectors and Associated Equipment*. **594** (3) 400–406.

Advancements in Atmospheric Transport Modelling at the International Data Centre and Plans for the Future

J. Kuśmierczyk-Michulec, P. Bourgouin, A. Tipka, M. Kalinowski
Comprehensive Nuclear-Test-Ban Treaty Organization, Vienna, Austria

A. Becker
Deutscher Wetterdienst, Germany

G. Wotawa
Geosphere Austria, Austria

M. Krysta
Bureau of Meteorology, Australia

Abstract

The Comprehensive Nuclear-Test-Ban Treaty monitors for nuclear explosions based on the detection of waveform signals and the related event localization, and on detection of traces of Treaty-relevant radioisotopes in the atmosphere. In doing so, the co-location of a seismic event and a series of radionuclide detections is required to establish the link and the attribution to a Treaty-relevant event. This task remained a challenge until a suitable atmospheric transport modelling (ATM) system with special post-processing routines was implemented and the relevant capacity built up in-house of the Provisional Technical Secretariat to the Comprehensive Nuclear-Test-Ban Treaty Organization. The suitability and performance was demonstrated by providing ATM support during events of special interest, like the Fukushima accident and the nuclear tests announced by the Democratic People's Republic of Korea. However, some deficiencies were unveiled which has triggered enhancements. For example, a best suitable ATM support during the first Democratic People's Republic of Korea event in 2006 required the temporal extension of the backward trajectory calculations from six to 14 days. More recent enhancements included an increase of the geo-temporal resolution of the in and output fields of the ATM system from one degree to 0.5 degrees and from three hours to one hour, respectively. The Provisional Technical Secretariat aims at developing and maintaining its ATM system at state of the art level and takes all opportunities to validate it against systems from other major ATM centres, e.g. through participation in multimodel exercises called ATM Challenges. This paper also addresses a vision for the longer term.

1. INTRODUCTION

The Comprehensive Nuclear-Test-Ban Treaty Organization (CTBTO) developed the International Monitoring System (IMS), which is a global system of monitoring stations based on three waveform verification technologies — seismic, hydroacoustic and infrasound, and the complementary radionuclide technology. The latter is the only one capable to confirm whether an explosion detected and located by the others is indicative of a nuclear test. The radionuclide network comprises 80 stations, of which more than 60 are certified as of October 2022. The aim of this radionuclide network is the global monitoring of radioactive aerosols and radioactive noble gases, supported by atmospheric transport modelling (ATM) to track measurements back to their possible source regions.

The Comprehensive Nuclear-Test-Ban Treaty (CTBT) monitors for nuclear explosions based on detections of waveform signals and their related event localization, and on detection of traces of Treaty-relevant radioisotopes in the atmosphere. However, 25 years ago, it was a challenge to attribute a series of radionuclide detections to the corresponding waveform event characterizing the related explosion as nuclear in origin. This challenge remainded until a suitable ATM system, with special post-processing routines, was implemented and the relevant expertise built up. The additional challenge related to source localization is that both remote and nearby sources might contribute to an elevated level of radionuclide detected at an IMS station. In case of radioxenon, this challenge is magnified by the presence of a radioxenen background from known sources.

Radioxenon is a fission product with a high fission yield. It can be produced either during a nuclear explosion, forming an important tracer to prove the nuclear character of an explosion, or be emitted by civil industrial nuclear facilities, e.g. nuclear power plants or isotope production facilities. The regular operational releases of radioxenon from nuclear installations contribute significantly to both the global and regional background (e.g. Kalinowski and Tuma 2009,

Saey 2009, Wotawa et al. 2010, Achim et al. 2016, Gueibe et al. 2017). In the East Asia region (in the context of this paper, East Asia is a region defined as shown in Figure 1), radioxenon background at most of the IMS stations located there is dominated by the contribution of nuclear power plants, and for some stations, simulated concentrations above the detection limit may include observable contributions from up to 19 different sources per daily sample; at the same time the sample being sensitive to 80 or more possible sources of radioxenon (Kuśmierczyk-Michulec et al. 2022).

Understanding the radioxenon background at the radionuclide stations of the IMS network is vital for improving the verification capability of the CTBTO. This is especially true for the nobel gas IMS stations in the East Asia region that have been crucial for the monitoring of announced nuclear tests by the Democratic People's Republic of Korea.

In order to address the inherent uncertainties of the ATM simulations associated with the dynamics of the atmosphere, the Provisional Technical Secretariat (PTS) cooperates with the World Meteorological Organization (WMO) and its Regional Specialized Meteorological Centres (RSMCs) in the field of dispersion modelling. In the framework of the cooperation agreement that entered into force on 11 July 2003, WMO supports
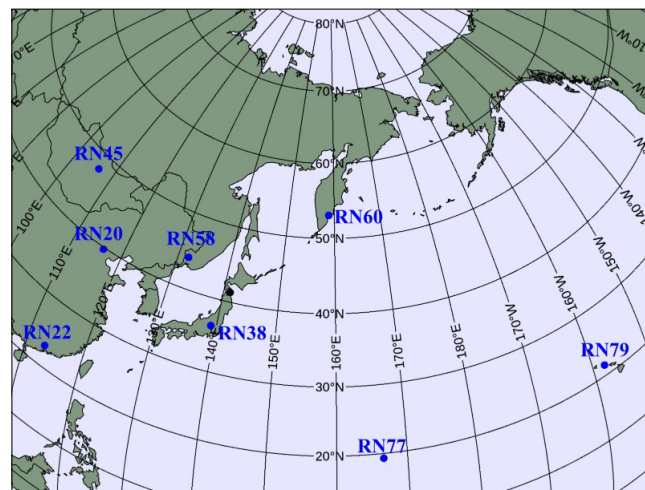
FIGURE 1.
Map showing the region of East Asia.

CTBTO by coordinating the ATM computations performed on request in the framework of the joint CTBTO-WMO Level 5 support system. Each detection identified by the IMS particulate network as Level 5 (multiple anomalous anthropogenic radionuclide measurements) gives rise to a request for support issued to the RSMCs. In response, the RSMCs produce and upload their own ATM simulations. The different models and input data used by the RSMCs address the ATM uncertainties by indicating the degree in consistency of geographic areas and times being covered in the regions of possible sources. How this can be visualized is described in Section 3.1.3 of this paper. More details on the foundation of the CTBTO-WMO response system can be found in Becker et al. (2005), Wotawa and Becker (2008) and Wotawa et al. (2009).

To meet the needs of the verification system for the CTBT, the International Data Centre (IDC) aims to develop, maintain and validate a state of the art ATM system. In doing so the unique opportunity of having access to both IMS measurements and daily stack ^{133}Xe emission data from the Australian Nuclear Science and Technology Organization (ANSTO) radiopharmaceutical facility in Sydney, Australia, the Institut des Radioéléments (IRE) radiopharmaceutical plant in Fleurus, Belgium and the Canadian Nuclear Laboratories (CNL), gave us a chance to initiate the process of validating our ATM simulations. The IDC participated in three multimodel exercises entitled the ATM

Challenges in 2015, 2016 and 2019, which allowed comparisons of IDC results with those produced by other major ATM centers (Eslinger et al. 2016, Maurer et al. 2018, 2022). The second ATM challenge highlighted the importance of high quality meteorological fields. Even from around 17 000 km away from the source or even after 8-13 days of travel time, the plume timing of the measured samples can be perfectly reproduced when the simulations are done using advanced and validated ATM driven by high quality meteorological fields (Maurer et al. 2018).

This paper is based on the invited talk presented at the Science and Technology Conference 2021, during the session dedicated to the 25th Anniversary of the Comprehensive Nuclear-Test-Ban Treaty (Kuśmierczyk-Michulec et al. 2021). Section 2 provides a historical overview of the ATM system and its major elements. Section 3 describes two main ATM postprocessing tools, WEB-GRAPE desktop and WEB-GRAPE IBS (internet based service), which are used for visualization and post-processing of the ATM outputs, called source-receptor sensitivity (SRS) fields. Section 4 addresses the ATM support during historical events like the nuclear tests in the Democratic People's Republic of Korea and the Fukushima accident. Section 5 and 6 describe the enhancements of the ATM system and the approach to its verification, respectively. Section 7 reveals plans for the future.

2. THE ATMOSPHERIC TRANSPORT MODELLING SYSTEM

2.1. Main Elements of the Current System

The ATM system deployed at CTBTO, includes four major elements which are essential for the proper functioning of the entire system; acquisition of meteorological data, modelling, post-processing and visualization. The current ATM operational system is based on a Lagrangian Particle Dispersion Model, FLEXPART (Stohl et al. 2005) driven by the global meteorological fields provided by the European Centre for Medium-

Range Weather Forecasts (ECMWF) and the National Centers for Environmental Prediction (NCEP) at a resolution of 0.5 degrees.

FLEXPART is an open source code, released under the GNU General Public License and maintained by a scientific community (http://flexpart.eu). FLEXPART can operate in forward as well as backward mode. In forward mode, the dispersion of tracers from their sources is simulated forward in time, i.e. particles are

released from one or multiple sources and concentrations are determined downwind on a grid independent from the meteorological input data grid. In backward mode, the potential source contributions for given receptors are determined based on simulations backward in time, i.e. particles are released from a receptor location (e.g. a measurement site) and a four dimensional (three dimensional in space plus time) response function (sensitivity) to emission input is calculated.

For the purposes of the CTBTO, the global and real time monitoring of radionuclide, the simplified source-receptor matrix concept has been developed (Wotawa et al. 2003, Becker et al. 2007). In that approach, it is assumed that transport is a linear process, non-linear chemistry does not need to be considered, and the vertical source receptor sensitivity (SRS) component is not needed.

Operationally, the ATM system is used in a backward mode i.e. from the location of the receptor, to compute SRS fields for each sample at all radionuclide measurement locations. The ATM results are stored as ASCII files, including the coordinates (latitude, longitude), time step and SRS values.

To enable visualization of the ATM outputs and identification of possible source areas of radionuclide detections at IMS stations, the IDC had designed and developed the Web-connected graphics engine (WEB-GRAPE) software and its online version WEB-GRAPE Internet based service (IBS).

2.2. Historical Overview

The first operational ATM system deployed and used at the IDC was delivered by the the prototype IDC in 1999. At that time, the backward simulations were generated for all radionuclide particulate systems using the Hybrid Single-Particle Lagrangian Integrated Trajectory Model (HYSPLIT) with meteorological input data from the United States National Centre for Environmental Prediction (NCEP) (Kalinowski 2001). These results were archived for six months and deleted afterwards because of insufficient storage space. A mass storage system was procured in 2000, which eventually facilitated archiving the data. The Operational Multi-scale Environmental Model with Grid-Adaptivity (OMEGA) was used as a regional atmospheric transport model with a resolution going down to 10 km. For postprocessing and visualization the commercial tool called Enhanced Digital Geodetic Exploitation (EDGE) was used (Kalinowski 2001).

Atmospheric Transport Modelling System						
Milestones	August 2002	2003	October 2004	November 2012	November 2013	December 2014	November 2017
Global ATM	FLEXPART 2.0	FLEXPART 2.0	FLEXPART 5.0	FLEXPART 5.0	FLEXPART 9.0	FLEXPART 9.0	FLEXPART 9.3 Optimized version for CTBTO
High Resolution ATM				FLEXPART-WRF	FLEXPART-WRF	FLEXPART-WRF	FLEXPART-WRF
Software for visualization &post-processing		WEB-GRAPE Desktop	WEB-GRAPE Desktop	WEB-GRAPE Desktop	WEB-GRAPE Desktop	WEB-GRAPE Desktop WEB-GRAPE Internet Based Service (IBS)	WEB-GRAPE Desktop WEB-GRAPE Internet Based Service (IBS)

FIGURE 2.

Milestones associated with enhancements of the global ATM, including the main model FLEXPART, the high resolution model FLEXPART-WRF and the visualization and post-processing software WEB-GRAPE.
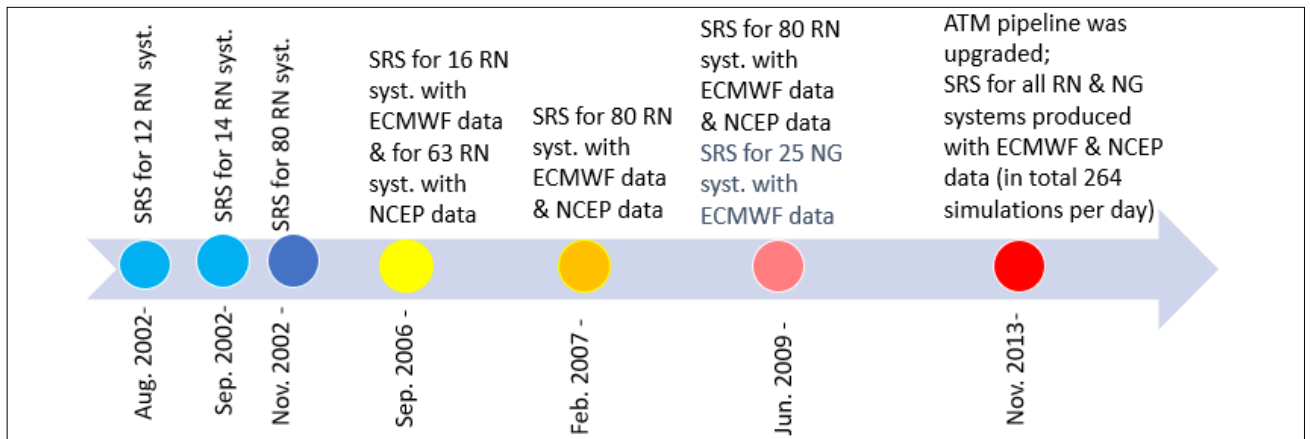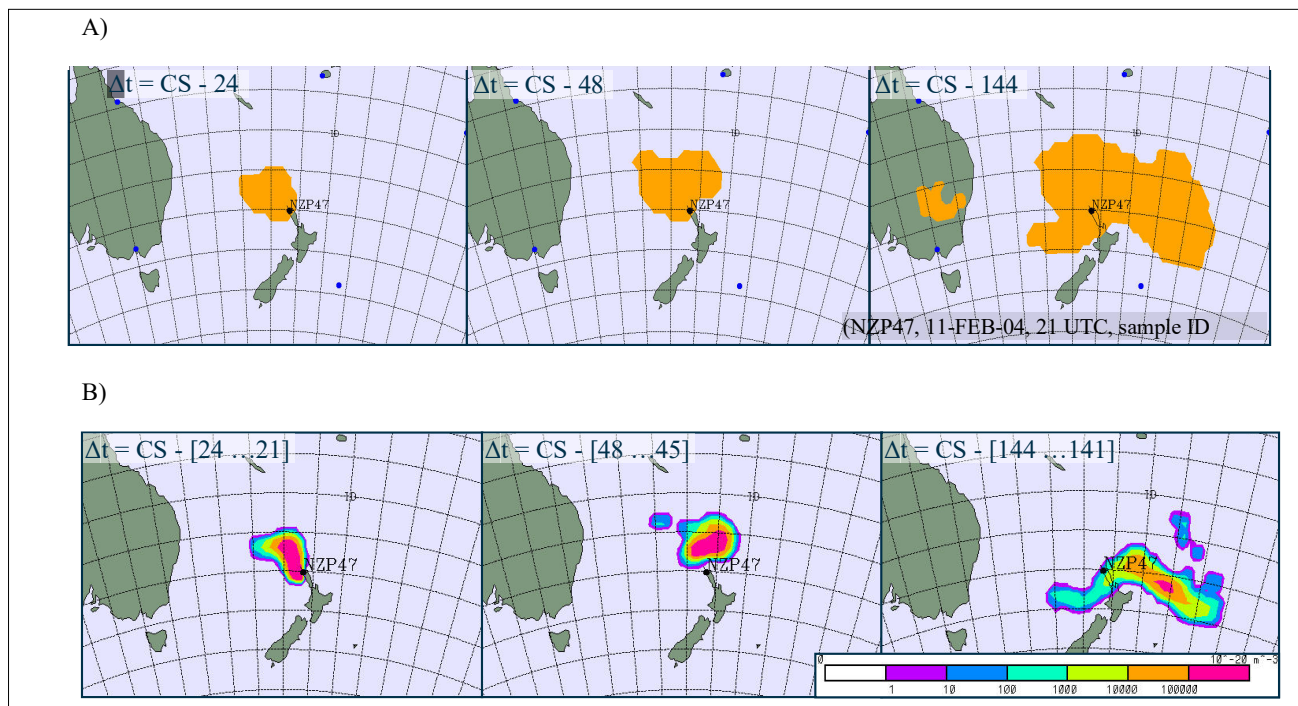
FIGURE 3.
Brief historical overview of the development of the ATM processing capabilities between 2002 and 2013.

The initial ATM system was completely replaced by in-house developments with open source software. Figure 2 gives an overview of the milestones associated with the enhancements of the global ATM system, including the two main components, the FLEXPART model and the visualization and post-processing software WEB-GRAPE. When a new updated version of FLEXPART was available, the ATM pipeline was also upgraded to include the new version.

Figure 3 illustrates the historical development of the ATM processing capabilities. In 2002, the backward simulations were initially generated for 12 radionuclide systems, but shortly their number increased to 80. In 2007 the number of daily backward simulations doubled, due to using two different meteorological inputs by adding sets of simulations with the ECMWF meteorological data in addition to the initial one driven by NCEP data. At that time the noble gas station locations had been a subset of the 80 radionuclide station locations, assuming for all systems 24-hour sampling time. In the IMS network, three different noble gas systems based on 12-hour and 24-hour sampling times are used. To account for it, additional simulations for noble gas systems were added in 2009, initially only with ECMWF data. In 2013, the ATM pipeline was upgraded with the newest version of FLEXPART, Version 9. From that moment on, the SRS files were produced for all particulate and noble gas systems with two different meteorological input data, i.e. ECMWF and NCEP.

2.3. Field of Regard

If an IMS station detects an elevated level of radionuclides in a particular sample, ATM calculations performed in a backward mode are used to identify the origin of air masses. In many cases, detections of radionuclides occur at a single station, without nearby stations measuring a signal. In this case, a simple Field of Regard (FOR) concept is used to determine the location of a release across a broad area. In this context, the FOR denotes the possible source region for material detected within one single sample, taken during the collection time (e.g. 12 h or 24 h) at one single IMS radionuclide station. It is a function of time, and three ways of presenting FORs are available. The incremental FOR, also known as the differential FOR, is generated for the time interval of one hour or three hours, depending on the time step in the ATM simulation, illustrating the dynamics of the air masses prior to the collection stop. The quantitative FOR, is a different version of the incremental FOR, with retained some of the quantitative information contained in the SRS fields and giving contour lines for a selection of sensitivities. The cumulative FOR, known also as the integral FOR, accumulates the incremental FORs per day, from the collection stop backwards up to 14 days (or up to the maximum number of days assumed in the ATM simulation). The source strength (Bq) can be calculated by dividing the nuclide activity concentration (measured at the station) in Bq/m^3 by the colour-coded value (1/m^3). Decay

A)

Δt = CS - 24 ... NZP47

Δt = CS - 48 ... NZP47

Δt = CS - 144 ... NZP47

(NZP47, 11-FEB-04, 21 UTC, sample ID

B)

Δt = CS - [24 ...21] ... NZP47

Δt = CS - [48 ...45] ... NZP47

Δt = CS - [144 ...141] ... NZP47

FIGURE 4.

Example of static Field Of Regard (FOR) images included in the Reviewed Radionuclide Report.

A) Integral binary FOR images. The orange colour marks areas where, according to the ATM computations, a near-ground source during at least one three-hour time period within one, two and six days, respectively, before sample collection stop would yield a detection at the station.

B) Differential quantitative FOR images. The coloured areas mark regions where, according to the ATM computations, a near-ground source for the single three-hour period preceding one, two and six days, respectively, before sample collection stop would yield a detection at the station.

corrections may be made using the elapsed time shown on each figure. For example, if the detection is 1 µBq/m³ and the colour-coding at the point of interest is blue, a release between 1 and 10 TBq would be needed within the three-hour period to explain the measurement. It should be noted that FOR images, as well as their animations, are attached to every IDC analysis report on a radionuclide sample, called the Reviewed Radionuclide Report (see Figure 4).

2.4. Forward Simulations

A backward simulation is the method of choice when a source is unknown. In special cases, when a source location is known (e.g. as a result of a seismic event localization) such as an announced nuclear explosion test by the Democratic People's Republic of Korea or the Fukushima nuclear accident, forward modelling is done. The ATM in a forward mode is used to predict which of the IMS radionuclide stations are likely to be affected by a potential radioactive release.

3. ATM TOOLS

3.1. WEB-GRAPE Desktop and Its Functionalities

To enable interactive visualization of the ATM outputs and identify possible source areas of radionuclide detections at IMS stations, the IDC has designed and developed the WEB-connected GRAPhics Engine (WEB-GRAPE) software. The project on WEB-GRAPE was initiated in 2003 (Becker and De Geer 2005). Since then many new
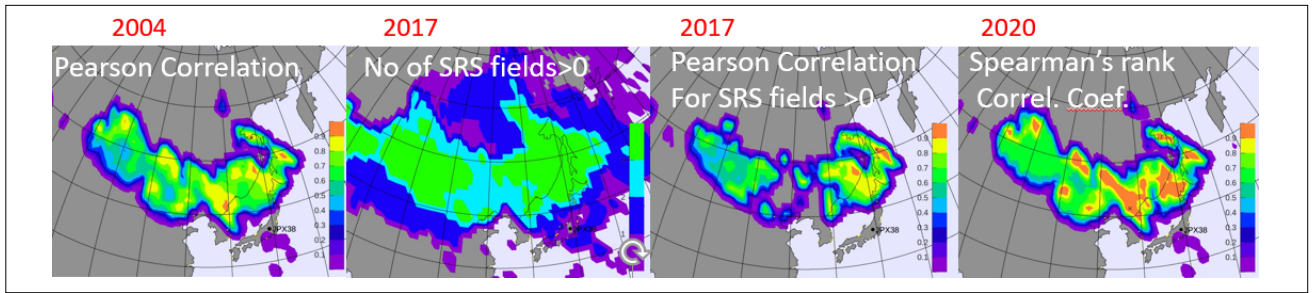
FIGURE 5.

Snapshot of PSR for 26 September 2017 for noble gas samples from RN38 and RN79, as seen by four different algorithms. The relatively high values of PSR indicate Democratic People's Republic of Korea, but also other areas as potential source regions. The year on top of each panel reveals when a given algorithm was implemented in the WEB-GRAPE desktop version.

functionalities have been added or enhanced (Kuśmierczyk-Michulec et al. 2019b, Preparatory Commission for the CTBTO 2020).

3.1.1. Possible Source Region

On some occasions, multiple detections might occur at one or more IMS stations. Depending on the nature of these detections and on prevailing meteorological conditions, it is possible that all these detections come from a unique source, and thus the possible source region (PSR) concept can be used that provides a more precise possible source location. The PSR is produced for each grid point in space and time by calculating the correlation coefficients between the measured and simulated activity concentration values based on SRS fields.

The sequence of images in Figure 5 shows the snapshot of PSR on 26 September 2017 for samples from the IMS stations RN38 (two samples with anomalously high concentrations on 2 October 2017) and RN79 (two anomalous samples on 7 and 8 October 2017) as seen by four different algorithms. At the same time, it demonstrates how the PSR functionality has evolved over the years. The first option of PSR, the Pearson Correlation, has already been implemented in the first version of WEB-GRAPE. It calculates and displays the correlation between measured and simulated activity concentrations (SRS values) for each grid point in time and space. This algorithm includes all values, even very small SRS values close to a threshold, which is not always wanted by a user. In 2017, two additional options of displaying the

Pearson correlation were added, which allow a user to have more control over the data. In 2020, the additional option to calculate PSR based on Spearman's rank correlation coefficient was added.

3.1.2. Multiple Model Field of Regard (MMFOR)

In case of anomalous detection registered by the IMS particulate network, classified as Level 5, CTBTO sends a request for support to RSMCs. In response, they produce and upload their own backward simulations. The Multiple Model FOR (MMFOR) functionality in WEB-GRAPE is then used to display and intercompare the results. An example of MMFOR is illustrated in Figure 6.
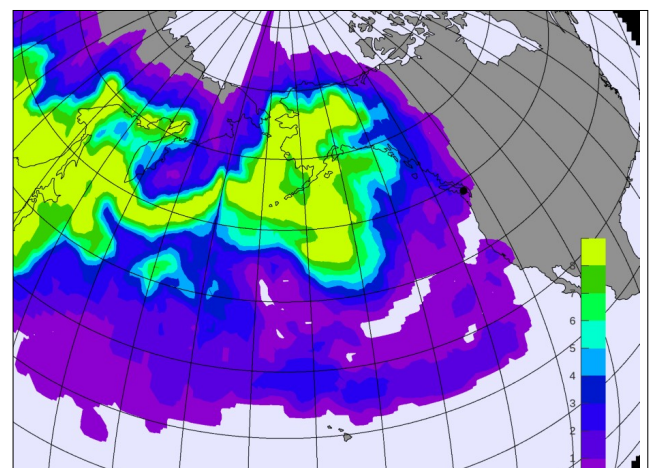
FIGURE 6.

Example of MMFOR for the IMS station RN14 in Canada related to the Fukushima accident. The overlapping result, MMFOR, is calculated for nine models: seven models from WMO RSMCs and two from CTBTO. The yellow colour represents the area in space and time where all models were in agreement.

The image shows a comparison of backward simulations (SRS files) received in response to a Level 5 radionuclide detection registered on 20 March 2011 at the IMS station RN14 in Canada, related to the Fukushima accident. Figure 6 shows the overlapping result, MMFOR, for nine models: seven models from WMO RSMCs and two from CTBTO. The yellow colour represents the area in space and time where all models were in agreement. It should be noted that CTBTO output compares well with results from those RSMCs.

3.1.3. Multiple Models Possible Source Region

A multiple models possible source region (MMPSR) is derived from the overlapping or simple averaging of an ensemble of single model PSR results (see Figure 7a). This functionality takes advantage of additional models delivered by the CTBTO-WMO response system, i.e. the same models used by the MMFOR functionality. The ensemble modelling for the backward ATM mode can be superior to any single model result.
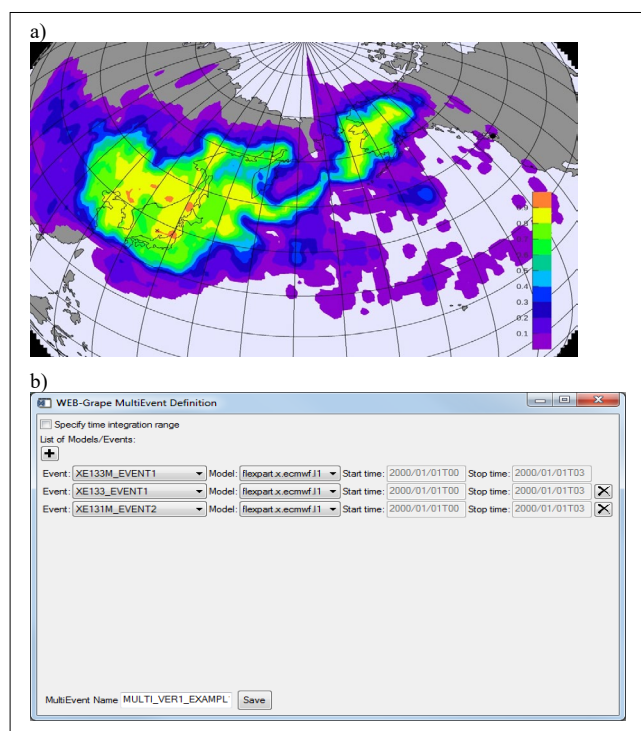
FIGURE 7.
A) Example of MMPSR for the IMS station RN14 in Canada related to the Fukushima accident.

B) Snapshot illustrating the input options to MultiPSR functionality.

In particular, if there is uncertainty on the exact time of the (nuclear) release to be located. This uncertainty requires setting a longer period in the calendar of the integral PSR calculator yielding a less confined 'plateau style' PSR result if based on a single model only. Taking the multiple model's PSR instead, returns a more structured PSR with a much better defined maximum making it possible to spatially confine the source location estimation. Obviously, the ensemble of models delivers additional constraints to confine the backtracking result. With access to ensembles like the multiple PTS in-house workflows and the SRS data delivered by the CTBTO-WMO response system, WEB-GRAPE can take advantage of ensemble modelling methods in order to increase the accuracy of atmospheric backtracking of CTBT relevant radionuclide events.

MMPSR is the functionality which allows displaying the averaged PSR generated by multiple models for the same radionuclide. In 2015, a MultiPSR functionality was added. It is the enhanced version of MMPSR, which allows for combining PSRs generated for multiple radionuclides and models (see Figure 7b).

3.1.4. Data Fusion

In August 2012, a new functionality called data fusion was added. In a data fusion process, the ATM computations link the radionuclide detections with those waveform events which fall within the regions of possible source of radionuclides. More details related to the concept of data fusion can be found in Krysta and Becker (2010), Krysta et al. (2013) and Krysta and Carter (2015).

In practice, it means that data fusion functionality investigates the overlap in space and time of seismic waveform error ellipses with ATM products like FOR, PSR, MMFOR or MMPSR, for a given time range. In addition, ellipses that overlap only in space and that occur earlier in time are also highlighted. This accounts for a possible temporal delay between the actual event and the release into the atmosphere. This concept was also implemented in the fusion tool on the secure web portal of the CTBTO (Krysta et al. 2016).

3.1.5. Continuously Emitting Sources

In October 2015, the continuously emitting sources (CES) functionality was added. It allows the user to calculate the influence of a set of continuously emitting sources, like medical facilities or nuclear power plants, on the measurements of a set of stations for a given time range based on the available SRS fields. Given a set of sources with their location and their individual daily release rates for a certain time range, the continuously emitting sources functionality predicts the measured concentrations for a set of stations and dates. The functionality was further enhanced in June 2020 and continuously emitting sources calculations for mixed temporal and/or spatial resolution SRS data were enabled.

3.1.6. Network Coverage

The network coverage (NET) is a product which displays a colour coded percentage indicating which parts of a given area are monitored by the selected station or network with sufficient sensitivity to trigger detection. The network coverage where a sufficient sensitivity is determined by reaching the minimum detectable concentration (MDC) is the NET-MDC. The colours indicate how well the considered network monitors the visualized area. The area is covered with a grid corresponding to the SRS grid i.e. $1^0 \times 1^0$ or $0.5^0 \times 0.5^0$ (spatial resolution). For a given time interval (three hours or one hour) a grid point is considered to be monitored if it results in at least one detection above the MDC in the considered network. Each colour represents the percentage of the analysed time interval during which a source strength defined by the user would have been detected in at least one of the stations of the analysed network. The colour coded percentages range from zero to 100% in 10% intervals.

The NET-MDC product has a double functionality. It shows the area which could be monitored in case of a nuclear release but also reveals the most probable region of influence at ground level for a selected time period. An example is illustrated in Figure 8. The quarterly NET-MDC products calculated for RN9, assuming a sources strength of ^{133}Xe to be 2.0E+12 Bq/day,
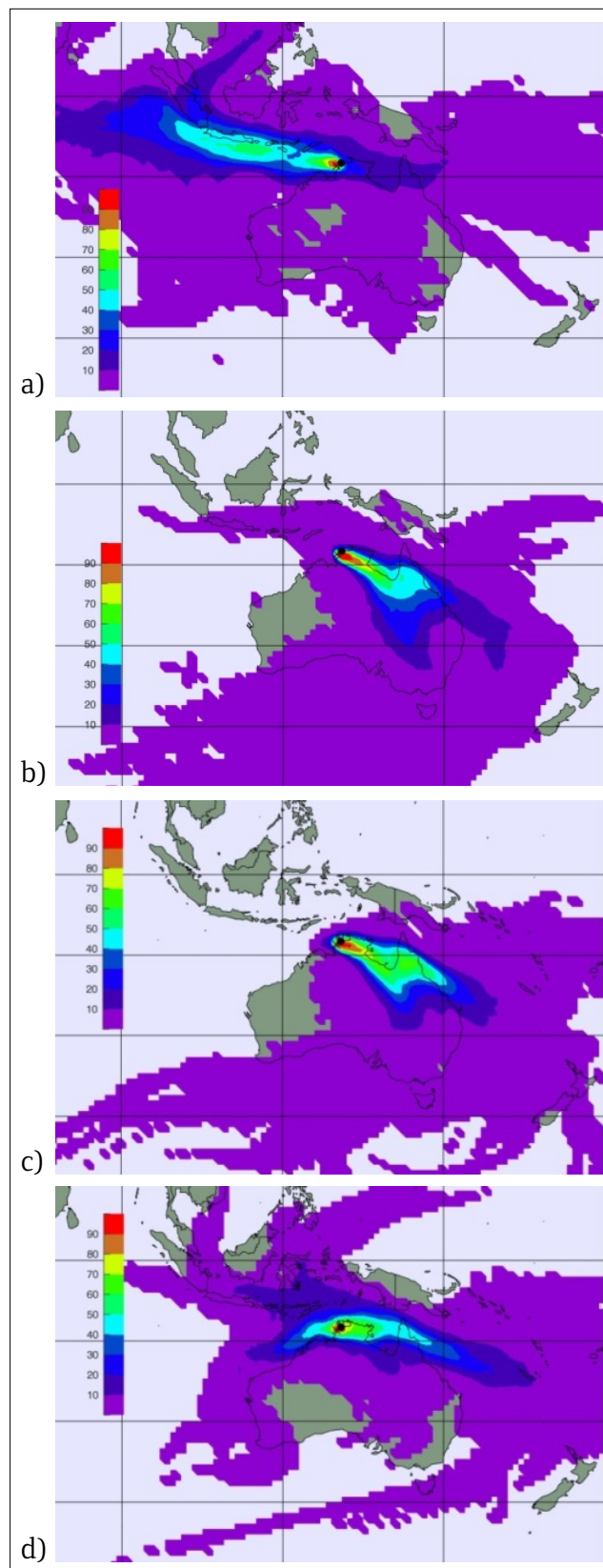
FIGURE 8.
Quarterly NET-MDC products for the IMS station RN09. A) Q111, b) Q211, c) Q311, d) Q411. Note that Q311, e.g. stands for the third quarter of 2011 (July, August and September).

358
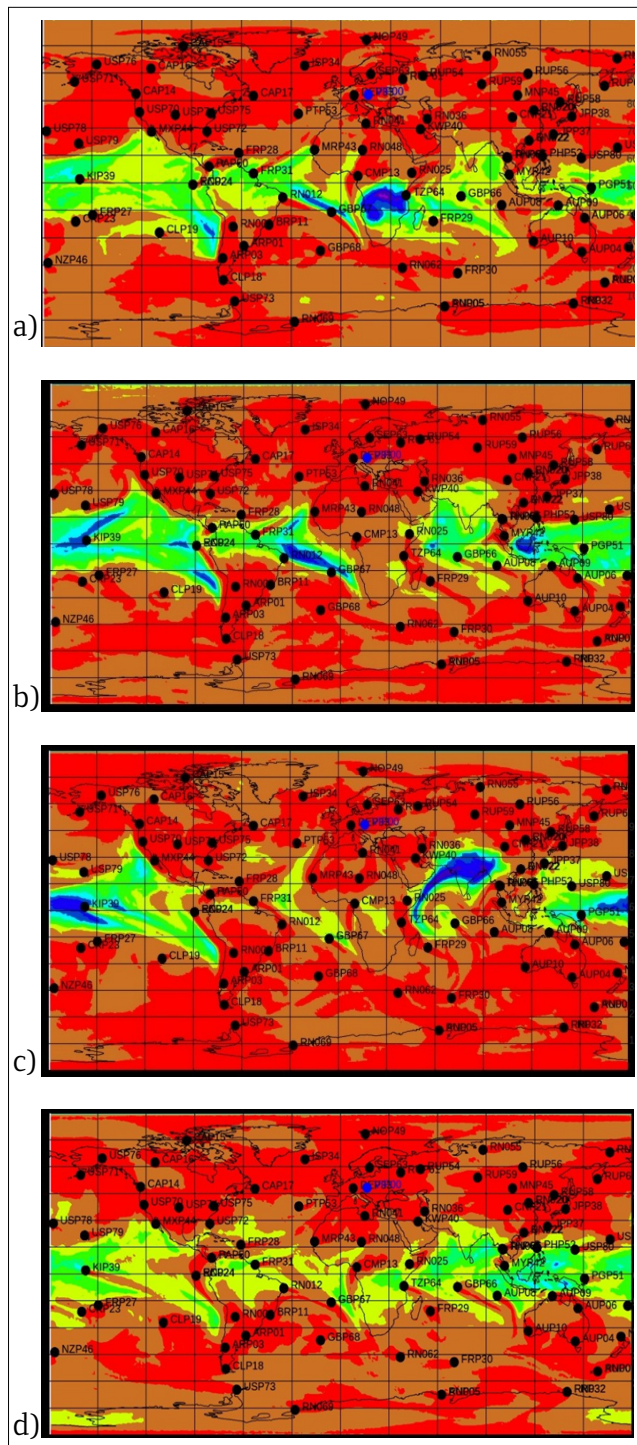
FIGURE 9.

Example of network performance for detecting ^{140}Ba by 79 particulate stations for each season of 2017.

A) Winter (1 January-15 February), B) Spring (1 April-15 May), C) Summer (1 July-15 August), D) Autumn (1 October-15 November).

that represents the average daily emission value for ANSTO (e.g. Achim et al. 2016), reveal that at the end and at the beginning of the wet season, the wind direction changes and either easterly or westerly winds dominate.

Initially, this functionally assumed the same value of MDC for all stations included in the network. In 2016, an option for calculating the network performance where each station has its own typical MDC was added, which allowed for an more realistic assessment. Figure 9 provides an example of the network performance for detecting ^{140}Ba by 79 particulate stations for each season of 2017. The total activity released was assumed to be 2×10^{15} Bq and the minimum detectable concentration was assumed to be 30 Bq/m^3.

3.2. WEB-GRAPE Internet Based Service

In December 2014, a project to develop an online version of the WEB-GRAPE Desktop software was initiated. WEB-GRAPE IBS provides authorized users the capability for post-processing, visualizing and interactively analysing the products of the ATM pipeline through a web application, without the need to install commercial software on a local computer. Following the successful execution of a security test in December 2017, the operational version of the application was deployed in February 2018. The production version of WEB-GRAPE IBS is available to all secure web portal users via their single-sign-on credentials at: https://webgrape. ctbto.org.

The first version of WEB-GRAPE IBS allowed users to calculate and visualize FOR products against the backdrop of a world map in two dimensional and three dimensional mode. In the following years, work on the technical and functional enhancements was continued. In 2021, the deployed WEB-GRAPE IBS version was upgraded twice, in April and in September. The technical enhancements allowed for improvement in stability, usability and scalability by adjusting resource availability to demand. On the list of newly implemented functionalities was the MMFOR. This functionality allows the calculation, overlap, and intercomparison of the

FOR products for an ensemble of models received from RSMCs. In addition to the interactive option, i.e. generating the MMFOR by a user; the automatic generation of MMFOR was also added. This new feature allows rendering MMFOR with all available models and generating URLs that could be integrated with all future Standard Screened Radionuclide Event Bulletin for Level 5 samples.

Other functionalities implemented in 2021 included custom SRS, allowing users to upload and visualize their own SRS files, and the PSR, based on the Pearson correlation. Further enhancements will continue, as well as a systematic approach of implementing the functionalities existing in WEB-GRAPE Desktop into WEB-GRAPE IBS.

4. HISTORICAL EVENTS

The effectiveness of the ATM system was demonstrated by providing ATM support during events of special interest like the Fukushima accident and the nuclear tests announced by the Democratic People's Republic of Korea. The sections below provide more details about each of these special events.

4.1. Announced Tests of the Democratic People's Republic of Korea

As of today the IDC provided support during six nuclear tests conducted by the Democratic People's Republic of Korea in 2006, 2009, 2013, twice in 2016 and in 2017 (Preparatory Commission for the CTBTO 2006, 2009, 2013, 2016a, 2016b, 2017).

The first one was announced on 9 October 2006. The announced test was well recorded throughout the world by the IMS. The information about time and location of the event provided by the seismic data was used to generate an ATM simulation in a forward mode to predict which of the IMS radionuclide stations were likely to be affected by a potential radioactive release.

It is worth noting that in October 2006, only 10 out of 40 planned stations with noble gas systems were operational in test mode. The smaller number of noble gas stations means that any traces of noble gases released from the Democratic People's Republic of Korea site would need to travel much longer than today to be detected. Two weeks after the event, the radionuclide noble gas station at Yellowknife,

Canada, registered an elevated concentration of ^{133}Xe. The ATM simulation in a backward mode demonstrated that this registration was indeed consistent with a hypothesized prompt release from the Democratic People's Republic of Korea event site. More details can be found in Becker et al. (2009). It is worth noting that before this event, the backward simulations generated operationally were calculated for six days. The lessons learned from ATM support in 2006 led to the extension of backward simulations from 6 to 14 days.

Similar ATM support was provided during the subsequent Democratic People's Republic of Korea tests announced on 25 May 2009, 12 February 2013, 6 January 2016, 9 September 2016 and 3 September 2017, respectively. None of these tests was confirmed by a prompt release. However, a delayed release occurred about 50
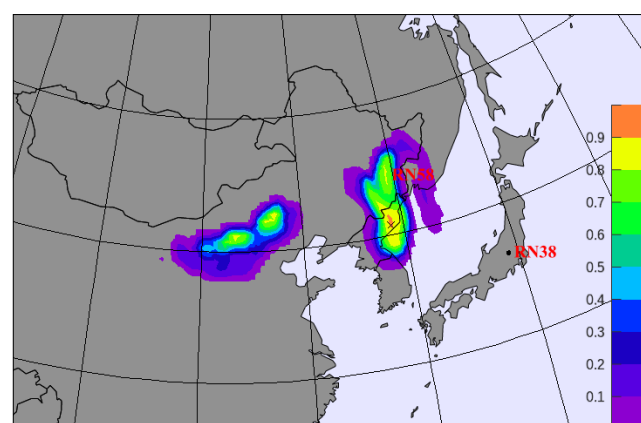
FIGURE 10.
Snapshot of PSR on 7 April, between 3 am and 6 am, calculated by the Spearman's Rank algorithm. The results are based on five ^{133}Xe samples registered at RN38.

days after the test of 2013. Isotopic activity ratios indicated the origin time of the fission gases to be consistent with the date when that test was announced. ATM was used to confirm that the observed radioxenon may most likely have been released from the Punggye-ri nuclear test site a few days prior to its observation at the IMS station at Takasaki, Japan (Ringbom et al., 2014). An example of PSR related to that event is shown in Figure 10. One important aspect of radionuclide monitoring after a nuclear test is related to the meteorological conditions, e.g. how the conditions influence the transport of the released emissions. Whether a given station is likely to be affected by a potential release strongly depends on the strength of a release, the MDC value, but also on the season, i.e. seasonal changes in the wind field. In the case of the first test (9 October 2006) and the third one (12 February 2013), radioxenon observations were immediately found to be associated with the time and location of the relevant seismic events and therefore consistent with the assumption that they were emitted from the Democratic People's Republic of Korea test site. It was not the case for other tests. More details can be found in Kalinowski et al. (2019).

It should be stressed that each event was different and thus, required a specific approach. Continuous communication between ATM and radionuclide specialists was critical. Examples of ATM techniques used for the purpose of radionuclide monitoring after the nuclear tests of the Democratic People's Republic of Korea on 6 January and 9 September 2016 are described in Kuśmierczyk-Michulec et al. (2017b); the IMS radioxenon monitoring is explained in Kalinowski et al. (2017).

4.2. Fukushima Accident in March 2011

In the aftermath of the Fukushima incident, atmospheric transport forward modelling had been used to predict which of the IMS radionuclide stations were likely to be affected by a radioactive release and to estimate the time of a first detection for each of them (Krysta et al. 2012). A source term had been hypothesized to emit continuously starting from 12 March 2011 at 05:30 UTC until the end of the calculations. It should be added that a passive tracer was simulated, so the model did not take into account the washout (removing particles by rainfall) or radioactive decay. Figure 11 is an example of such
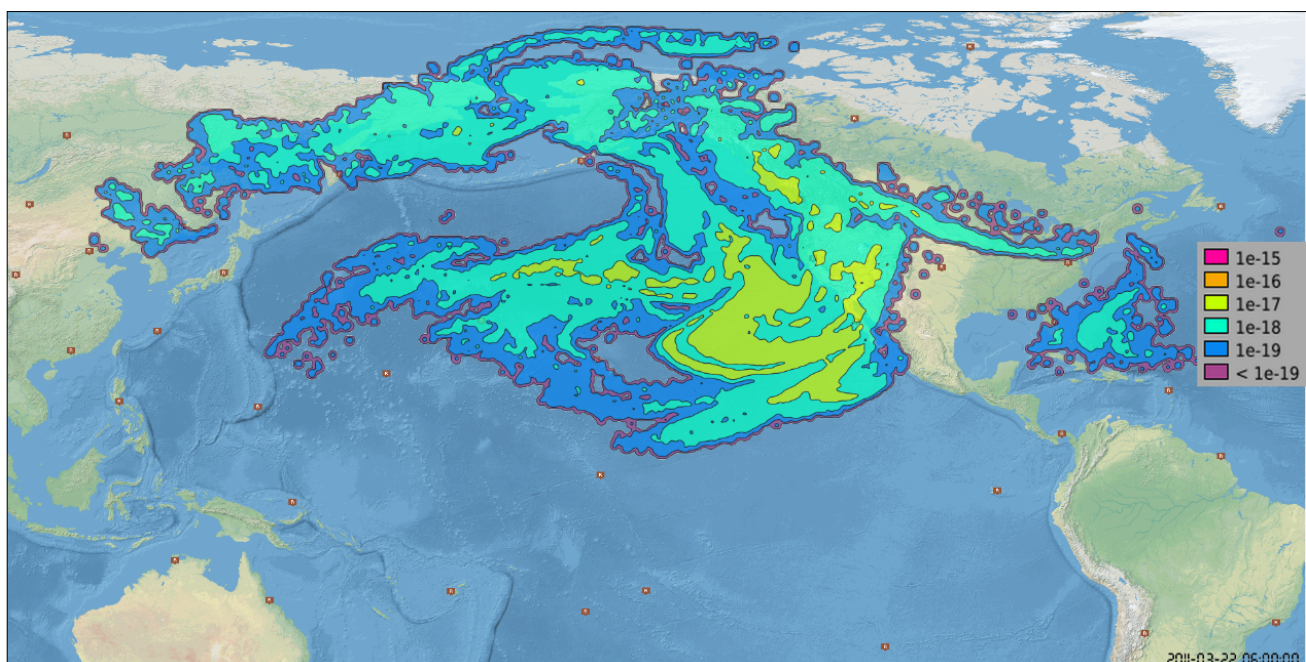
FIGURE 11.

Snapshot taken on 22 March 2011, 10 days after the Fukushima incident. The forward atmospheric simulation is only qualitative and the colours express a limited sequence of orders of magnitude relative to the release amount. The brown dots represent the radionuclide IMS stations.

361

a simulation. They were produced until the end of this event. It should be noted that the Daiichi nuclear power plant in Fukushima released radioactivity in such an amount so that the IMS system on the Northern hemisphere observed its emissions for about three months after 12 March 2011. More details related to ATM activities at CTBTO in the aftermath of the Fukushima incident are given by Krysta et al. (2012).

4.3. ATM Support Recognition

The demonstrated effectiveness of the ATM system was broadly recognized. In February 2012, the Government of Japan made a voluntary contribution to the CTBTO to enhance the ATM system (Voluntary Contribution 2012, Press Release 2012). This voluntary contribution from Japan provided hardware infrastructure, which enabled the development of the higher global (FLEXPART) and mesoscale (FLEXPART-WRF) resolution ATM system.

5. ENHANCEMENT OF THE ATMOSPHERIC TRANSPORT MODELLING SYSTEM

5.1. Global Atmospheric Transport Modelling

In 2014 the work towards increasing the resolution of the SRS fields from 3 hours to 1 hour temporal resolution and from 1.0 degree to 0.5 degree spatial resolution was initiated. The first attempt to introduce these changes resulted in a significant increase in runtime – from about 4 hours to over 30 hours. To address these issues a project on enhancements to the FLEXPART software was initiated in December 2014 with the requirement that a simulation should take less than 12 hours in order to timely deliver the SRS products. In November 2017 a tool to create pre-processed meteorological input files and a new version of FLEXPART (version 9.3) using these files were introduced. In August 2018 the first milestone was achieved by increasing the spatial resolution of SRS files from 1.0 degree to 0.5 degrees. Two years later the work towards increasing the temporal resolution of the SRS fields from 3 hours to 1 hour was completed. By optimizing the FLEXPART model code and procuring new ATM servers in 2019, the time to complete a single ATM simulation does currently not exceed 4 hours. In total 296 simulations are generated daily. Figure 12 illustrates the timeline related to these major milestones.

In December 2020 the CTBTO, under funding from the European Union Council Decision VIII,

launched a project to upgrade the ATM pipeline by including the newest release version of the Lagrangian particle dispersion model FLEXPART. The enhanced version, FLEXPART v10.4, will provide computational performance gains and more reliable and robust processing. In addition, the added value of using graphics processing units (GPU) in further acceleration of ATM simulations will be studied. These changes will allow the upgraded pipeline to operate in the most optimal way and to extend the ATM capabilities to include ensemble modelling for special expert technical analysis. Using ensemble prediction system analyses will allow estimating confidence levels in ATM guidance.

5.2. High Resolution Atmospheric Transport Modelling

On a global scale high resolution modelling is neither feasible nor required. However on a regional scale, in the case of regions of complex topography, such modelling would be beneficial for the quality of ATM support. The work on the concept and development was initiated in 2012. Funding provided by the European Union in February 2021 resulted in the CTBTO developing a basic version of the high resolution atmospheric transport modelling based on FLEXPART-WRF, driven by the mesoscale numerical weather prediction model weather research and forecasting model (WRF). The WRF model itself is driven
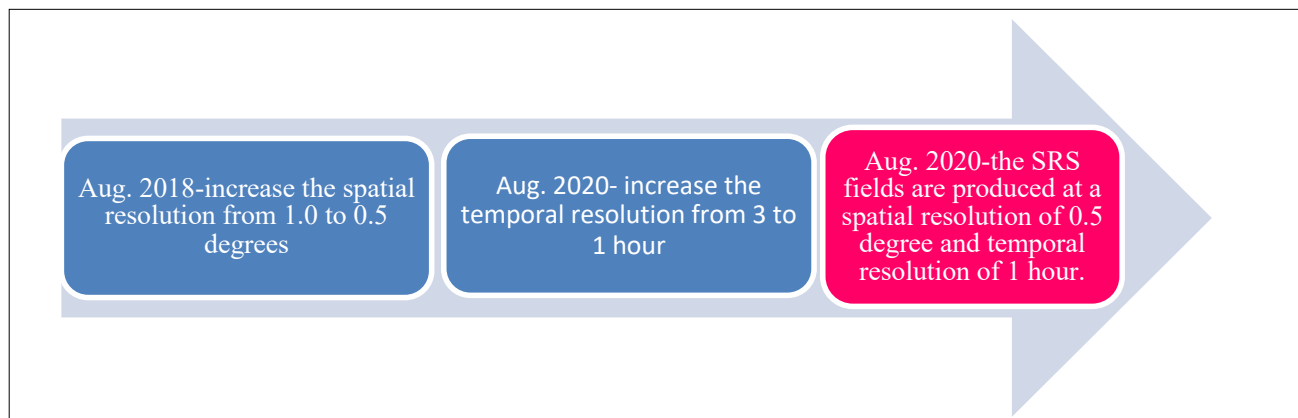
FIGURE 12.
Enhancement of the ATM system: Major milestones.

by the global meteorological fields provided by NCEP. Initial tests revealed which features had to be enhanced or implemented differently in order to have a fully reliable pipeline (e.g. Krysta et al. 2014, Krysta 2015, Schoeppner et al. 2017).

Several technical enhancements are on the list of tasks e.g. adding the option to use ECMWF input meteorological data for WRF. The enhanced high resolution atmospheric transport modelling, i.e. the semi-automated software to support high resolution ATM at a regional scale, will become one of the ATM tools used by ATM experts and National Data Centers to test and validate hypotheses related, for instance, to the estimation of the source term or of the source location.

6. ASSESSMENT OF THE ATMOSPHERIC TRANSPORT MODELLING SYSTEM

6.1. Atmospheric Transport Modelling Challenges

The first ATM Challenge (Eslinger et al. 2016) used ^{133}Xe stack emission data from the IRE radiopharmaceutical plant in Fleurus, Belgium, and activity concentration data collected at the closest noble gas IMS station, i.e. RN33 in Schauinsland, Germany (located at a distance of 380 km from IRE). The second ATM Challenge (Maurer et al. 2018) used ^{133}Xe stack emission data provided by the isotope production facilities ANSTO in Sydney, Australia, and activity concentration data from six noble gas IMS radionuclide stations located in the Southern Hemisphere. The distance between the release point in Australia (ANSTO) and the samplers was between 680 km and 17 000 km. Despite the different settings of both ATM exercises, there was common evidence that daily emission data with an uncertainty of up to 20% (in the daily stack emission) is sufficient to provide reliable results, at least for the current IMS sampling time intervals. The third ATM Challenge was launched with the ultimate goal to provide an ensemble analysis of radioxenon background levels at IMS stations frequently impacted by industrial emissions (Maurer et al. 2022). The ensemble in this context means a multi-input multi-model approach which relies on the concept that a group of diverse, but at the same time reasonably accurate models, can be optimally combined thus giving more accurate simulations. The unique opportunity of having access to the radioxenon stack emission data from two isotope production facilities, i.e. IRE in Belgium and CNL in Canada, for the calendar year of 2014, motivated the organisers to set up the multi-model ensemble modelling exercise in the Northern Hemisphere.

The results of these exercises indicate that the performance of the CTBTO simulations is very good (Eslinger et al. 2016, Maurer et al. 2018, 2022), in most cases above the average and occasionally on the top. Maurer et al. (2018) demonstrated that neither a distance nor a travel time is an issue when the simulations are done using advanced and validated ATM driven by high quality meteorological fields. Even around 17 000 km away from the source or even after between 8 and 13 days of travel time, the plume timing of the measured samples can be reproduced. The authors also noted that in the case of a few samples, an inappropriate depiction of boundary layer processes that are dependent on the quality of meteorological data caused the wrong estimation of surface concentrations, emphasising the importance of reliable meteorological input. The perfect reproduction of individual samples even around 17 000 km away from the source mentioned above highlights that the challenge needed for CTBT monitoring, with a sample-by-sample comparison between measurements and simulations, can be met with proper data and under favourable conditions.

The third ATM Challenge demonstrated that the benefit of knowing the actual high quality IRE and CNL emission profiles is in general easily offset by poorly characterized or even unknown other emitters as well as atmospheric transport errors and long IMS sampling times (Maurer et al. 2022). It highlighted the need to gain more knowledge about emissions from the relevant sources, established in the global radioxenon emission inventory of nuclear power plants and isotope production facilities (Kalinowski 2022). It was noted that the collected samples had to be predominantly (≥50%) influenced by the emitter (e.g. IRE or CNL), to demonstrate the added value of measured daily resolved stack emissions rather than annual release estimates (Maurer et al. 2022). The benefit of a time resolution of less than 24 hours was shown for individual samples.

The advantage of knowing stack data from a single emitter is easier to demonstrate for IMS stations in the Southern Hemisphere as in the Northern Hemisphere, because the number of various emitting sources is significantly lower (Kuśmierczyk-Michulec et al. 2019a).

The third ATM Challenge revealed that assembling a multitude of dispersion calculations is a necessary but insufficient condition toward obtaining an optimal ensemble. Unfortunately model results are often not independent. The study demonstrated that the full ensemble, including six Lagrangian models, one Eulerian model (LdX-C3X) and one mixed model (HYSPLIT-GEM), was highly redundant (Maurer et al. 2022). One of the reasons was that there were dominating transport models (FLEXPART and HYSPLIT) in combination with dominant meteorological drivers (ECMWF-IFS and NCEP-GFS). It seems that an ensemble prediction system-based ensemble may be a better alternative.

6.2. Validation of the Operational Configuration — Relevance of Convection

Due to the importance of computational performance and the necessity of being flexible in the post-processing steps to use different species, the operational configuration uses a passive tracer in the ATM simulations. The question arises as to whether including other atmospheric processes, such as convection, which would have a varying influence on different species, would improve the results.

To address the question of whether including the convective transport in ATM simulations will change the results significantly, the differences between the outputs of with and without convective transport in FLEXPART were computed and further investigated (Kuśmierczyk-Michulec et al. 2017a). The hypothetical release point was at the ANSTO facility in Australia. On the southern hemisphere the number of medical facilities is limited and the short term sphere of influence of other sources that rarely reach Australia, thus one of the main sources of ^{133}Xe observed at the neighbouring stations comes from the ANSTO facility. Availability of both daily emission values and measured ^{133}Xe activity concentration values was an opportunity to validate the simulations.

It was estimated that the overall uncertainty of simulations, without the convective transport, lies between 0.08 and 0.25 mBq/m^3. The uncertainty for the simulations with convective transport

included is slightly shifted to the lower part of values and is in the range between 0.06 and 0.20 mBq/m^3. This can be attributed to uncertainties in the daily emission values, uncertainties related to the meteorological input and also to the imperfect modelling of atmospheric processes in FLEXPART. It is not evident that the accuracy of simulated activity concentration would be significantly improved by including the convective transport. Therefore, it was recommended to run operational simulations without convective transport and use convection for special case studies. The practical aspect of including convective transport in the ATM simulations is related to the significant increase of the processing time, by about 50%, depending on the number of jobs.

6.3. Verification via Application to Various Events

The efficiency of the ATM system has been demonstrated through investigation of various events. It is recommended that the verification effort should be enhanced through the adaptation and implementation of new ideas and through the paced adoption of novel technologies (Preparatory Commission for the CTBTO 2015).

For example, the ATM system was applied to test the hypothesis that regular signals of radioactive ^{137}Cs observed during the summers of 2003 and 2004, far away from nuclear activities, could be explained by transport from fires burning in the boreal forests of North America and Asia (Wotawa et al. 2006). On the one hand, this study has demonstrated that ^{137}Cs deposited worldwide from past nuclear testing is reinjected into the atmosphere by combustion to a significant extent and on a large scale and is subsequently transported across long distances. On the other hand, the analysis has demonstrated that the receptor-oriented modelling concept, as developed by the PTS, can be used for a variety of applications related to data from measurement networks, including the validation and improvement of emission inventories.

ATM results were combined with ^{7}Be observations collected during 2009–2015 by three radionuclide stations from the IMS, located in Mauritania, Kuwait and Panama, to study the influence of Saharan dust on changes in ^{7}Be surface concentrations (Kuśmierczyk-Michulec and Bourgouin 2018). It has been demonstrated that an influx of dust at high levels (3-10 km) tends to locally increase surface ^{7}Be concentrations in the area under the influence of subsiding dust plumes. It has also been shown that an influx of dust at lower altitudes (up to 1 km) will have the opposite effect on surface concentrations. In case dust is present in the whole column of the atmosphere, its final impact depends on the ratio between its amount in the upper layers (3-10 km) and lower layers (0-1 km). At the same time, this study demonstrated that an advanced and validated ATM driven by high quality meteorological fields represents a powerful tool to explore the dispersion of different atmospheric constituents.

The synergy of the ATM system with other technologies also proved to be efficient. This was demonstrated, for example, with the synergy between ATM, radionuclide and infrasound observations from the volcanic activity of Bogoslof in Alaska, USA (Kuśmierczyk-Michulec et al. 2020). The study period covered three months of intense eruptive activity, from 19 December 2016 to 8 March 2017, recorded by the IMS infrasound station located in Alaska, USA. The results have demonstrated that an influx of volcanic ash up to the tropopause (1.5-12 km) tends to locally increase surface ^{7}Be concentrations in the area under the influence of subsiding ash plume. A similar mechanism was previously described in relation to dust particles. The increase in ^{7}Be surface measurements, exceeding 2.5 times the seasonal median, can be considered as an indication of a possible inflow of aerosol particles up to the tropopause taking place a few days earlier. It was revealed that, with the arrival of volcanic ash at the surface level, the enrichment in radioactive particulates like uranium, thorium, and potassium was observed.

It has been shown that the benefit of combining IMS data and IDC products from various technologies offer interesting perspectives for the monitoring of, for example, volcanic activity. Using the synergy of technologies opens the path to improved monitoring capabilities and possibly leads towards a quantitative description of the eruptive source.

7.   WAY FORWARD

The presence of a noble gas background in constant evolution in the atmosphere makes the positive identification of a sample associated with a nuclear test challenging. An estimation of the radioxenon contribution from known sources to every sample collected by noble gas systems at IMS stations should be generated by a xenon background estimator tool (XeBET). This estimation will help to decide if the detection can be explained by known sources.

In February 2021, the IDC initiated two related projects through funding from the EU Council Decision VIII to generate a validation data set and a software system to evaluate xenon background estimators and conduct an exercise called: 1st nuclear explosion signal screening open intercomparison exercise 2021. The exercise was launched on 1 December 2021 with a closure date 30 June 2022. Its purpose was to identify the most suitable scientific approach of radioxenon background estimation and to explore methods for characterizing the source of an event regarding release time, location, and source type and strength. The test data set used in the exercise was prepared with input from internationally recognized experts from the radionuclide/ATM community and consisted of real IMS observations with additional contributions from hypothetical nuclear test releases. A set of validation metrics was defined to measure the performance of background estimation to generate the best screening results with regard to the objective of identifying nuclear tests signals. The expected outcome of this exercise for CTBT purposes is to identify the approach with the best screening capability but not necessarily the one that reproduces the observations best.

On the list of planned advancements is the enhancement of the Standard Screened Radionuclide Event Bulletin by including the automatic creation of the MMFOR with RSMC's SRS fields for samples of special interest. It is also foreseen to include the automatic creation of the PSR, in case three or more samples would be associated with the same release event.

Furthermore, the new developments will include a method for identifying samples associated with the same release event. This is uselful for confining the possible source region and applying the PSR method. A more ambitious objective for future enhancements is the reconstruction of the atmsohperic radioxenon concentrations by assimilating the emission inventory and the IMS observations and producing a best fit of simulated concentrations to these input data. Ideally, the activities collected in IMS samples can be explained with known sources and residual concentrations can be highlighted as potentially coming from an unknown source. The purpose is to implement a flag called *ATM backtracking to known sources* which has to be reported by the IDC for each radioxenon sample. It is also foreseen to develop an ATM method for characterization of the key source parameters of an event (probability of the start time, duration of a release from a given location, source strength) as an input for hypothesis testing for an observation being possibly caused by a nuclear explosion. Whatever can be automated will enter the standard IDC products including the data fusion tool. The more sophisticated enhancements will be implemented in expert technical analysis.

It is anticipated to explore machine learning algorithms to identify an anomalous observation inconsistent with previous observations and known sources.

SUMMARY

This paper provided an overview of different projects and activities during the past two decades, which have contributed to the development and advancement of the ATM system deployed at the CTBTO. The ATM system that we have today is the result of the incremental enhancement and implementation that took place during the last 25 years.

REFERENCES

Achim, P., et al. (2016). Characterization of Xe-133 global atmospheric background: Implications for the international monitoring system of the Comprehensive Nuclear-Test-Ban Treaty. *Journal of Geophysical Research: Atmospheres* **121** (9) 4951– 4966.

Becker, A., De Geer,L.-E. (2005). A new tool for NDC analysis of atmospheric transport calculations. *CTBTO Spectrum* **7** 19.

Becker, A., Wotawa, G., De Geer, L.-E. (2005). On the CTBTO-WMO response system set up for ensemble calculation of standardised source-receptor relationship information for the purpose of source attribution of airborne radioactivity measurements raised within the CTBTO International Monitoring System, *Geophysical Research Abstracts* **7** 06316.

Becker, A., et al. (2007). Global backtracking of anthropogenic radionuclides by means of a receptor oriented ensemble dispersion modelling system in support of nuclear-test-ban treaty verification. *Atmospheric Environment*. **41** 4520-4534.

Becker, A., Wotawa, G., Ringbom, A., Saey, P.R.J. (2009). Backtracking of Noble Gas Measurements Taken in the Aftermath of the Announced October 2006 Event in North Korea by Means of PTS Methods in Nuclear Source Estimation and Reconstruction, *Pure and Applied Geophysics* **167** (4) 581-599.

Eslinger, P.W. et al. (2016). International challenge to predict the impact of radioxenon releases from medical isotope production on a comprehensive nuclear test ban treaty sampling station *Journal of Environmental Radioactivity* **157** 41-51.

Gueibe, C., et al. (2017). Setting the baseline for estimated background observations at IMS systems of four radioxenon isotopes in 2017. *Journal of Environmental Radioactivity* **178** 297-314.

Kalinowski, M.B. (2001). Atmospheric transport modelling related to radionuclide monitoring in support of Comprehensive Nuclear-Test-Ban Treaty verification. *Kerntechnik* **66** (3)129-133.

Kalinowski, M.B., Tuma, M.P. (2009). Global radioxenon emission inventory based on nuclear power reactor reports. *Journal of Environmental Radioactivity* **100** (1) 58-70.

Kalinowski, M., et al. (2017). "IMS radioxenon monitoring after the announced nuclear tests of the DPRK on 6 January and 9 September 2016". (Presentation at the CTBT: Science and Technology Conference, Vienna, Austria 2017).

Kalinowski, M. et al. (2019). "Search for radioxenon signals at IMS stations possibly associated with announced Democratic People's Republic of Korea nuclear tests". (Presentation at the CTBT: Science and Technology Conference, Vienna, Austria 2019).

Kalinowski, M.B. (2022). Global emission inventory of ^{131m}Xe, ^{133}Xe, ^{133m}Xe, and ^{135}Xe from all kinds of nuclear facilities for the reference year 2014. *Journal of Environmental Radioactivity* (in preparation).

Krysta, M., Becker, A. (2010). Data fusion as an example of a powerful constraint on the reconstruction of atmospheric sources of radionuclides for the verification of the Comprehensive Nuclear-Test-Ban Treaty (CTBT). *Geophysical Research Abstracts* **12**.

Krysta, M., Coyne, J., Nikkinen, M., Gheddou, A., Stöhlker, U. (2012). Atmospheric Transport Modelling Activities at CTBTO in the Aftermath of the Fukushima Release. *Geophysical Research Abstracts* **14**.

Krysta, M., Kuśmierczyk-Michulec, J., Kushida, N. (2013). Fusion of radionuclide and waveform information at CTBTO in support of the NPE12. *Geophysical Research Abstracts* **15**.

Krysta, M., Szintai, B., Kuśmierczyk-Michulec, J., Carter, J. , Given, J.W. (2014). "High resolution atmospheric transport modelling in support of radionuclide detections at CTBTO network". (American Geophysical Union Fall Meeting, San Francisco, 2014).

Krysta, M. (2015). "Impact of Higher Resolution Meteorological Fields on the Results of Atmospheric Transport Modelling". (Presentation at the CTBT: Science and Technology Conference, Vienna, Austria 2015).

Krysta, M., Carter, J. (2015). "On refinements which could be integrated into the data fusion process (Presentation at the CTBT: Science and Technology Conference, Vienna, Austria 2015).

Krysta, M., Kushida, N., Kotselko, Y., Carter, J. (2016). Fusion of waveform events and radionuclide detections with the help of atmospheric transport modelling. *Geophysical Research Abstracts* **18**.

Kuśmierczyk-Michulec, J., Krysta, M., Kalinowski, M., Hoffmann, E., Baré, J. (2017a). Long-range transport of Xe-133 emissions under convective and non-convective conditions. *Journal of Environmental Radioactivity* **175-176**, 135-148.

Kuśmierczyk-Michulec, J., Kalinowski, M., Krysta, M., Gheddou, H. (2017b). "Atmospheric Transport Modelling for radionuclide monitoring after the nuclear tests of the Democratic People's Republic of Korea on 6 January and 9 September 2016". (Presentation at the CTBT: Science and Technology Conference, Vienna, Austria 2017).

Kuśmierczyk-Michulec, J., Bourgouin, P. (2018). Influence of mineral dust on changes of [7]Be concentrations in air as measured by CTBTO global monitoring system. *Journal of Environmental Radioactivity* **192** 454–466.

Kuśmierczyk-Michulec, J., Deconninck, B., Kalinowski, M., Hoffmann, E. (2019a). "Quantifying uncertainties in the atmospheric modelling (ATM) simulations resulting from different emission time resolution". (Presentation at the CTBT: Science and Technology Conference, Vienna, Austria 2019).

Kuśmierczyk-Michulec, J., Kalinowski, M., Sommerer, W., Bourgouin, P. (2019b). "CTBTO experience in visualisation of ensembles and derived products." (Presentation at the Using ECMWF's Forecasts workshop, UK, Reading, 2019).

Kuśmierczyk-Michulec, J., Bittner, P., Mialle, P., Kalinowski, M. (2020). Synergy Between Radionuclide and Infrasound Observations and Atmospheric Transport Modelling Simulations: Case of Bogoslof. *Pure and Applied Geophysics* **178** 2627-2649.

Kuśmierczyk-Michulec, J., et al. (2021). "Advancements in atmospheric transport modelling (ATM) at the CTBTO PTS during the past two decades and plans for the future". (Presentation at the CTBT: Science and Technology Conference, Vienna, Austria 2021).

Kuśmierczyk-Michulec, J., Baré, J., Kalinowski, M., Tipka, A. (2022). Characterisation of Xe-133 background at the IMS stations in the East Asian region: insights based on known sources and Atmospheric Transport Modelling. *Journal of Environmental Radioactivity* **255**.

Maurer, Ch., et al. (2018). International challenge to model the long-range transport of radioxenon released from medical isotope production to six Comprehensive Nuclear-Test-Ban Treaty monitoring stations. *Journal of Environmental Radioactivity* **192** 667-686.

Maurer, Ch., et al (2022). Third international challenge to model the medium-to long-range transport of radioxenon to four Comprehensive Nuclear-Test-Ban Treaty monitoring stations, *Journal of Environmental Radioactivity* **255**.

Ministry of Foreign Affairs of Japan (2012). Press Release. Japan's Voluntary Contribution for the Enhancement of the Atmospheric Transport Modeling System of the Comprehensive Nuclear-Test-Ban Treaty Organization.

Preparatory Commission for the Comprehensive Nuclear-Test-Ban Treaty Organization (2006). *The CTBT verification regime put to the test – the event in the Democratic People's Republic of Korea on 9 October 2006*. Preparatory Commission for the CTBTO, Vienna.

Preparatory Commission for the Comprehensive Nuclear-Test-Ban Treaty Organization (2009). *Next phase in the analysis of the announced Democratic People's Republic of Korea nuclear test*. Preparatory Commission for the CTBTO, Vienna.

Preparatory Commission for the Comprehensive Nuclear-Test-Ban Treaty Organization (2013). *Update on CTBTO findings related to the announced nuclear test by North Korea*. Preparatory Commission for the CTBTO, Vienna.

Preparatory Commission for the Comprehensive Nuclear-Test-Ban Treaty Organization (2015). *Disaster warning and promoting human welfare – the civil and scientific uses of CTBTO data*. Preparatory Commission for the CTBTO, Vienna.

Preparatory Commission for the Comprehensive Nuclear-Test-Ban Treaty Organization (2016a, 2016). *Democratic People's Republic of Korea announced nuclear test*. Preparatory Commission for the CTBTO, Vienna.

Preparatory Commission for the Comprehensive Nuclear-Test-Ban Treaty Organization (2016b). *CTBTO Executive Secretary Lassina Zerbo on the unusual seismic event detected in the Democratic People's Republic of Korea*. Preparatory Commission for the CTBTO, Vienna.

Preparatory Commission for the Comprehensive Nuclear-Test-Ban Treaty Organization (2017). *CTBTO Executive Secretary Lassina Zerbo on the unusual seismic event detected in the Democratic People's Republic of Korea*. Preparatory Commission for the CTBTO, Vienna.

Preparatory Commission for the Comprehensive Nuclear-Test-Ban Treaty Organization (2020). *WEB-GRAPE 1.8.6 Technical Report*. Preparatory Commission for the CTBTO, Vienna.

Ringbom, A., et al. (2014). Radioxenon detections in the CTBT international monitoring system likely related to the announced nuclear test in North Korea on February 12, 2013. *Journal of Environmental Radioactivity* **128** 47-63.

Saey, P.R.J. (2009). The influence of radiopharmaceutical isotope production on the global radioxenon background. *Journal of Environmental radioactivity* **100** (5) 396-406.

Schoeppner, M., Kalinowski, M., Kuśmierczyk-Michulec, J., Klinkl, G. (2017). "Performance assessment of the high-resolution atmospheric transport model at the IDC of the CTBTO". (Presentation at the CTBT: Science and Technology Conference, Vienna, Austria 2017).

Wotawa, G., et al. (2003). Atmospheric transport modelling in support of CTBT verification – Overview and basic concepts. *Atmospheric Environment* **37** (18) 2529-2537.

Wotawa, G., et al. (2006). Inter- and intra-continental transport of radioactive cesium released by boreal forest fires. *Geophysical Research Letters* **33** (12).

Wotawa, G. (2010). Computation and analysis of the global distribution of the radioxenon isotope ^{133}Xe based on emissions from nuclear power plants and radioisotope production facilities and its relevance for the verification of the nuclear-test-ban treaty. *Pure and Applied Geophysics*, **167** (4) 541-557.

Wotawa, G., Becker, A. (2008). The CTBTO/WMO Atmospheric backtracking response system and the Data Fusion exercise 2007, (Proceedings of the 30th Monitoring Research Review: Ground-Based Nuclear Explosion Monitoring Technologies, 23-25 Sep 2008, Portsmouth).

Wotawa, G., the CTBTO-WMO Response System Team (2009). The operational CTBTO-WMO Atmospheric Backtracking Response system for Nuclear Test-Ban Treaty Monitoring. *Geophysical Research Abstracts* **11**.

Development of the First Comprehensive Draft List of Equipment for Use During On-Site Inspections

G. Malich

INSPECC, Germany

P. Labak

Comprehensive Nuclear-Test-Ban Treaty Organization, Vienna, Austria

Abstract

The Preparatory Commission for the Comprehensive Nuclear-Test-Ban Treaty Organization (Commission) is required to develop a list of equipment for use during on-site inspections (OSIs). The list is needed to ensure that only approved equipment is used by the inspection team within the inspection area. The Commission started work on this verification task as early as the first OSI workshop in 1997 and has since considered both the structure of the list and the specifications of the equipment to be listed.

A proposal for the first comprehensive draft list of equipment for use during OSIs was presented by the Provisional Technical Secretariat Preparatory Commission for the Comprehensive Nuclear-Test-Ban Treaty Organization (Commission) of the Commission in 2021. Considering relevant Comprehensive Nuclear-Test-Ban Treaty (CTBT) provisions and guidance from the Commission the draft list covers all permitted inspection activities and techniques except for drilling.

This paper provides a summary of the development of the first comprehensive draft list of equipment for use during OSIs from the outset. It shows how advances in science and technology have influenced the proposed specifications of OSI equipment since the CTBT opened for signature and explains why the draft list marks an important milestone in the development of OSI capabilities.

1. LIST OF EQUIPMENT FOR USE DURING ON-SITE INSPECTIONS

This section is aimed at providing a common understanding of the list, the equipment and the first comprehensive draft list of equipment for use during during an on-site inspection (OSI).

1.1. The List

The CTBT in Article II, paragraph 26, identifies as one of the functions of the Conference of the States Parties at its initial session upon entry into force of the Treaty the approval of any draft agreements, arrangements, provisions, procedures, operational manuals, guidelines, and any other documents that will have been developed and recommended by the Commission. According to the Protocol to the Treaty (Part II, paragraph 36), one of those documents to be approved is the list of equipment for use during OSIs and paragraphs 38 and 51 of Part II make it clear that for an inspection, all types of approved equipment shall be available and that equipment that has not been approved may be excluded by the inspected State Party.

In line with these provisions, the Resolution establishing the Commission explicitly tasks the Commission to develop and prepare for the approval at the initial session of the Conference of the States Parties a list of equipment for use during OSIs. It also expresses an expectation that this list contains detailed specifications for this equipment, however, there is no indication as to the parameters and details of these specifications to be included.

1.2. The Equipment

Equipment for use during OSIs consists of core and auxiliary equipment. The former is equipment related to the application of the permitted inspection activities and techniques and the latter is equipment required for the effective and timely conduct of an inspection (Protocol to the Treaty, Part II, paragraph 37). While there is no clear definition in the Treaty or its Protocol as to what auxiliary equipment entails, this is different regarding

During all Inspection Periods

- Position finding
- Visual observation, video and still photography, and multi-spectral imaging including infrared measurements
- Measurement of levels of radioactivity using gamma radiation monitoring and energy resolution analysis
- Environmental sampling and analysis
- Passive seismological monitoring

During the Continuation Period only

- Resonance seismometry
- Active seismic surveys
- Magnetic field mapping
- Gravitational field mapping
- Ground penetrating radar
- Electrical conductivity measurements

Any time after EC-Approval

- Drilling

FIGURE 1.
Inspection activities and techniques (Protocol to the CTBT, Part II, paragraph 69).

core equipment. In fact, paragraph 37 of Part II refers to paragraph 69 in which the inspection activities and techniques are described. For ease of reference and for a better understanding of the complexity of developing the list of equipment, Figure 1 summarizes those distinct activities and techniques that the inspection team is allowed to undertake and apply during an OSI. As can be seen from Figure 1, not all inspection activities and techniques are permitted at any time of an OSI. Particularly those that are useful mostly for narrow area searches may be used only after the Executive Council received the progress inspection report from the inspection team and allowed the OSI to continue. Another constraint relates to the equipment for drilling. Such equipment can be used only after the Executive Council approved a proposal from the inspection team to conduct drilling. This proposal may be submitted at any time during an OSI.

1.3.   The First Comprehensive Draft List

The first comprehensive draft list of equipment for use during OSIs was issued by the PTS early in 2021 (CTBT/PTS/INF.1573). It is presented in tabular format following a short introductory text on background, scope, and structure of the draft list (Figure 2). This format followed a proposal by the OSI Task Leaders in a paper on the further development of the OSI equipment list in 2018 (CTBT/WGB/TL-4/47) taking into account all previous relevant guidance by the Commission and the comments received during a technical discussion on the subject matter in 2017 and 2018. This paper also proposed the inclusion of the following parameters in the list for its ultimate approval at the initial session of the Conference of the States Parties: function, technical specifications, specific operational requirements and specific certification requirements.

The draft list contains proposed specifications relating to the core equipment for an OSI including items providing the capability to review, classify, store, process, and visualize the derived data. Auxiliary equipment necessary for the effective and timely conduct of OSIs has also not been included because equipment for the inspection activities and techniques was given priority when preparing the first comprehensive draft list for its paramount significance during an inspection and related sensitivities.

FIGURE 2.
Cover and tabular format of the first comprehensive draft list (CTBT/PTS/INF.1573).

2. PROGRESSION OF IDENTIFYING AND PROPOSING SPECIFICATIONS

This section recalls the process of how the list and its content evolved since the beginning of the Organization to date.

Early in 1997, about six months after the CTBT opened for signature, the PTS started its work to assist the Commission in the establishment of a global verification regime to monitor compliance with the comprehensive ban on explosive nuclear testing. Because its capacities built up only gradually, States Signatories not only needed to provide guidance to the PTS but also offer substantial involvement and contributions to facilitate the fulfilment of its functions. Over time, this dependence became more balanced as the PTS grew increasingly competent and capable to initiate, implement and monitor technical and operational activities and programmes to serve its support role to the Commission.

Regarding the development of a capability to conduct OSIs, there were – and still are – several mechanisms for input by States Signatories to the work of the PTS. Amongst those are submissions of national papers, in which States present their expert opinions on certain aspects such as on OSI equipment items or their technical specifications. There are also workshops organized by the PTS that are dedicated to OSI topics. They allow in-depth discussions with nominated experts from States, who share their expertise, offer their views, and make proposals. Further, there are the OSI Task Leaders appointed by the Commission upon nominations from States Signatories. They also summarize the status and outlook of OSI developments in specific papers to consolidate or instigate further developments, as appropriate. And lastly, there are many programmatic activities of the PTS that rely on participation of national experts. They are conducted in line with the OSI programme approved by the Commission. All these mechanisms have been used from the beginning in the context of identifying and proposing equipment specifications for inclusion in the draft list of equipment for use during OSIs.

2.1. National Papers

In the early days of the Organization, national papers have been a key resource for the initial discussions on OSI equipment and their technical specifications. Table 1 shows equipment specifications for video cameras (video and still photography) and seismometers (passive seismological monitoring) that were proposed in two national papers.

Table 1. Comparison of Equipment Specifications from 1998 and 2021

Extracts from National Papers, 1998[1]	Extract from First Comprehensive Draft, 2021
Video Cameras	

a) General requirements: Visual spectrum, hand-held, standard non-digital VHS/NTSC or VHS/PAL format.
 	
b) Technical details:
  1. Multiple focal lengths (zoom & zoom-enhancement capabilities and focal length – TBD);
  2. Auto exposure;
  3. Title overlay capable;
  4. Non-stabilized or capable of turning off and locking image stabilization;
  5. Battery life >3 hours (Numbers of batteries on-board TBD);
  6. Weight <3 kg;
  7. Image recording on removable media;
  8. UV/Skylight filter; no special filters.
 	
c) Recommended recording media: High strength (TBD) video tape, VHS format.
	Item: Handheld digital video camera
	
	Function: Acquire and store colour video.
	
	Technical Specifications:
	• Resolution: full HD 1080p or better
	• Frame rate: 120 per second or better
	• Screen: >5 cm
	• Active image stabilization: can be enabled
	• Optical zoom: >8×
	• No internal data storage
	• Data storage: standard data storage device, e.g. SD card
	• Storage device capable of storing at least two hours of video at HD resolution
	• Tripod mount and tripod

---

[1] CTBT/PC/V/WGB/US/10 and CTBT/WGB-6/IL/1.

Table 1. Comparison of equipment specifications from 1998 and 2021 (cont.)

Seismometers	
1. Three-component (vertical, North horizontal, East horizontal), single package, rugged and compact for transportation and installation 2. Minimum frequency band from 1 Hz to 50 Hz with good coherence (>0.9 between 1 and 25 Hz) 3. Velocity sensor. A corner frequency of 1 or 2 Hz is acceptable 4. Minimum sensitivity to ground motion: 110 volts/meter/sec at damping 0.64	Item: Seismometers: three component (3-C) with installation kits Function: Measure seismic ground motion; provide data to digitizer in appropriate frequency band. Technical Specifications: • 3-C, short period, single package • Minimum frequency bandwidth: approximately 1 Hz to 40 or 50 Hz • Velocity sensor: 0.5-2 Hz corner frequency • Clip recovery: 10 s or better • Flat response at least in the bandwidth 1-35 Hz • Total harmonic distortion: ⩽−70 dB in on-axis sinusoidal excitation • Cross-axis coupling: ⩽−70 dB for inherent cross-axis; ⩽−40 dB for cross-axis due to misalignment of active axis relative to case reference • Relatively insensitive to levelling errors • Minimum sensitivity to ground motion: 400 V × s/m at critical damping • Root mean square noise at 1 Hz less than 3 nm/s • Dynamic range >135 dB • Radio frequency interference susceptibility: to be defined

Table 1 compares these specifications against those as contained in the first comprehensive draft list of equipment for use during OSI. They evidently changed since 1998 but the significance of those changes is different for the two selected items. For seismometers, the new specifications reflect an ongoing evolution of technology and provide, inter alia, a higher minimum sensitivity as deemed necessary for the detection of possible aftershocks after an underground nuclear explosion. In contrast, for video cameras, the new specifications reflect a major shift from analogue to digital equipment because advances of science and technology over time made equipment that comply with the previously proposed specifications obsolete. Those advances have been reflected, as deemed appropriate, in national papers but also have been considered following OSI workshop discussions or development work from OSI programmatic activities of the PTS.

2.2. Workshops

The purpose of OSI workshops is to give experts from States Signatories and the PTS the opportunity to discuss current OSI issues in detail. The focus of the 24 OSI workshops conducted to date varied but most of them also covered to some extent the specifications, development, or use of inspection equipment.

The workshops shown in Figure 3 specifically addressed issues surrounding the list of equipment for use during OSIs.

At the second OSI workshop in 1998, lists of equipment with some initial specifications were drafted for inspection activities and techniques that are permitted during all inspection periods ('initial period techniques'). They were mostly based on national papers and expert presentations at OSI workshops. The next relevant workshop was OSI workshop six which took place in 2000[2]. One focus of the presentations and discussions

---

[2] The first six OSI workshops were conducted within a period of only three years while the average frequency of OSI workshops after the year 2000 dropped to less than one per year. This underlines that technical OSI developments during the early stages after the CTBT opened for signature were dependent primarily on direct expert involvement and input from States Signatories due to the nascent technical capacities of the PTS.
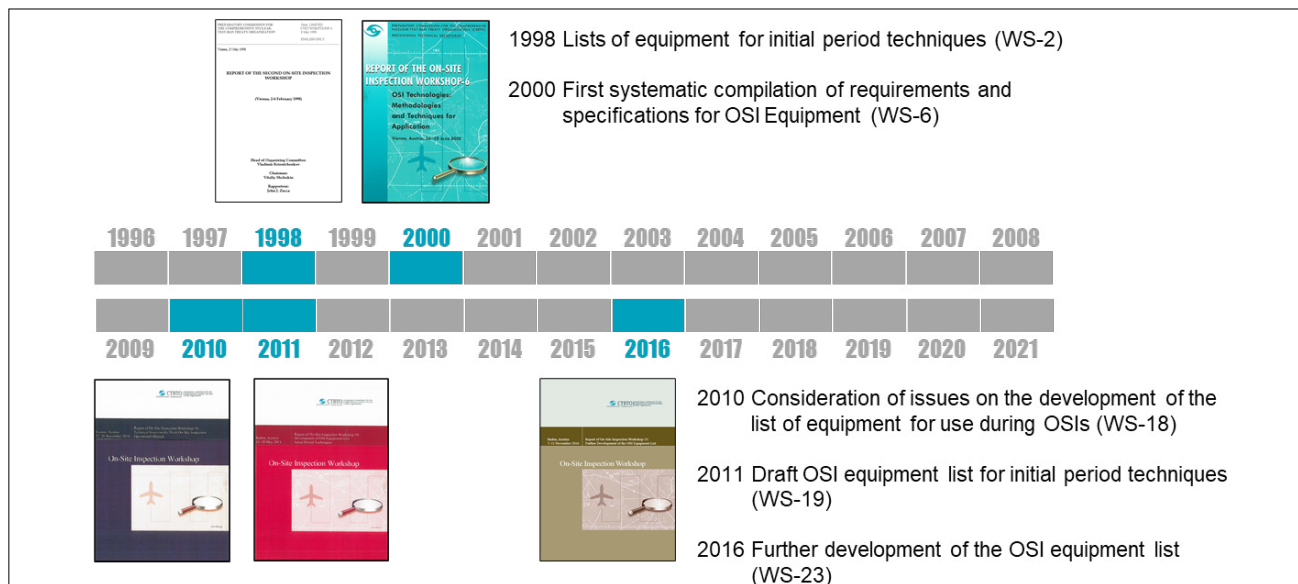
FIGURE 3.
OSI workshops of relevance for the list of equipment for use during OSIs.

at this workshop was on the specifications and functional and operational requirements for equipment relating to overflights and those techniques that are permitted only during the continuation period of an OSI. As such, this workshop complemented the earlier lists of equipment for initial period techniques even though the specifications and requirements were kept qualitative to a large extent.

A significant step towards the actual list of equipment for use during OSIs was OSI workshop 18, ten years later in 2010. Unlike the previous lists, which mainly served to identify equipment for testing and training purposes, this time the list of equipment as per the Protocol to the Treaty (Part II, paragraph 36) was considered. However, the output of the workshop was not a list of items and specifications. Instead, recommendations were made on how the list, an important deliverable of the work of the Commission as emphasized in the Resolution establishing the Preparatory Commission, should be developed. For this, issues discussed during the workshop included: how to deal with software; what is the level of detail needed in the list; is there relevant experience from other treaties; and how should be proceeded to a final version of the list. These discussions led in fact to an important OSI Task Leader paper in 2011, which for the first time provided a proposal for a template of the list (CTBT/WGB/TL-4/40). It was modelled on the

format of the list of inspection equipment of the Organization for the Prohibition of Chemical Weapons and was subsequently trialed during the next OSI workshop later that year. OSI workshop 19 resulted in a draft equipment list for initial period techniques and provided feedback on the template proposed in the above OSI Task Leader paper.

Five years and a lot of field experience later, the further development of the OSI equipment list was discussed again in 2016 during OSI workshop 23. It was the first workshop addressing equipment specifications for almost all OSI activities and techniques in detail (except for drilling) and there were substantial discussions also on the structure and content of the list. This workshop and subsequent discussions led the OSI Task Leaders to drafting a new paper on the further development of the OSI equipment list (CTBT/WGB/TL-4/47) which guided the PTS in preparing the first comprehensive draft list of equipment for use during OSIs.

2.3. Task Leader Papers

The two OSI Task Leader papers referenced in the previous section were critical but not the only ones of relevance for the development of the list of equipment for use during OSIs. Figure 4 provides an overview of these Task Leader papers.
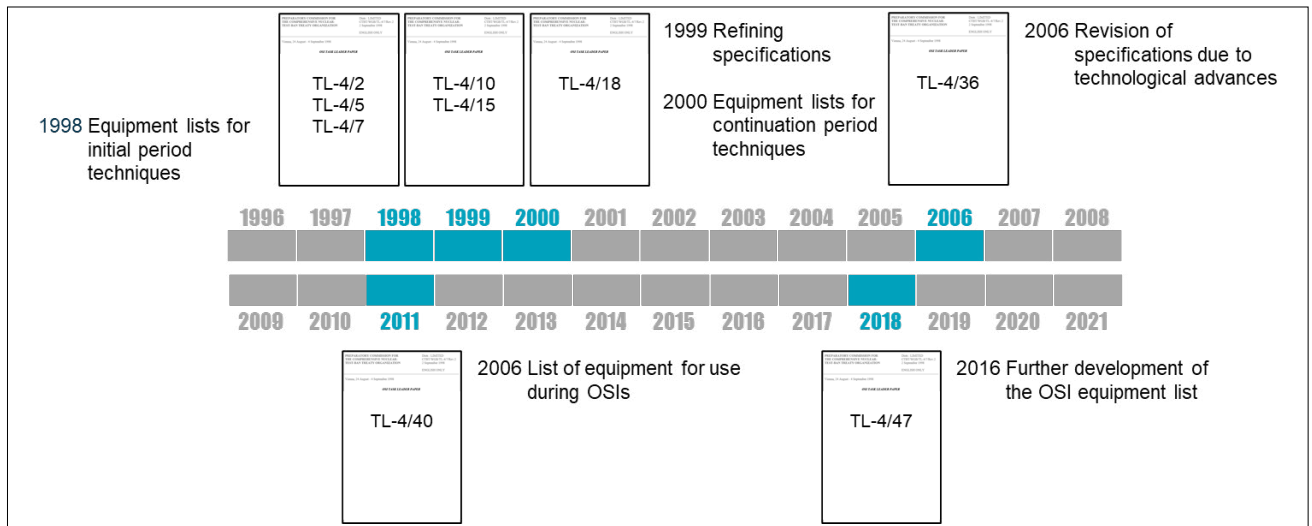
FIGURE 4.
Relevant OSI Task Leader papers for the list of equipment for use during OSIs.

Table 2. Structure and Definitions for the List of Equipment for Use During OSIs (TL-4/47)

Equipment Category: <designation>					
Identification Code	Item	Function	Technical Specifitions	Speccifications Operational Requirements	Specific Certification Requirements
<identifier>	<designation>	<description>	<specifications>	<requirements>	<requirements>
...	...	...	...	...	...

Term	Definition
OSI Equipment List	List of equipment for use during on-site inspections, to be considered and approved by the Conference of the State Parties at its initial session (Protocol to the CTBT, Part II, paragraph 36).
Equipment Category	Equipment grouping to correlate with the inspection activities and techniques specified in paragraph 69 or with the requirement for the effective and timely conduct of on-site inspections (Protocol to the CTBT, Part II, paragraph 37).
Identification Code	A unique identifier that allows the item to be identified and cross-referenced to the list. This code would be affixed to the actual piece of equipment and used in any relevant database or document.
Item	Hardware and/or software on its own or a combination of hardwarenad/or software as a system or sub-system capable of performing a required function in relation to the inspection activities and techniques or to the effective and timely conduct of on-site inspections. *Examples of items: handheld digital camera, environmental sampling kit, radioxenon processing and measurement system, UHF/VHF repeater station, etc.*
Function	Description of the use and functionality of the item and /or its data products.
Technical Specifications	Defined parameters for those technical specifications that need to be met to ensure that the item is functional and delivers its expected outputs. *Examples of parameters: accuracy, precision, sensitivity, resolution, range (distance, frequency, energy,...), data collection rate, output format, failure rate, reliability, stability, etc.*
Specific Operational Requirements	Defined parameters for those operational requirements that need to be met to ensure that the item can be handled and operates as expected during an inspection. *Examples of parameters: dimensions, weight, environmental ruggedness, convenience, consumables, power supply, maintenability infield logistics and infrastructure support, etc.*
Specific Certification Requirements	Defined type, scope and frequency of certification that is needed, if any, to confirm the (continued) suitability of the item for its described use and functionality of the item and the data it produces *Examples of certification: airworthiness, health and safety, etc.*

The OSI Task Leader papers in 1998 and 1999 were mostly a compilation of proposed equipment items with few or only basic specifications. They were issued and revised in due course as more national papers were submitted and OSI workshop discussions held. As mentioned before, these lists focused at first on initial period techniques only. However, following OSI workshop 6 in 2000, equipment lists were also compiled for continuation period techniques.

The importance of technology refreshment and foresight in the context of OSI equipment became apparent for the first time in the context of digital photography. Following discussions on this issue the OSI Task Leader drafted a paper in 2006 that proposed updates to the earlier equipment lists in relation to still photography and the introduction of handheld digital cameras (TL-4/36) due to technological advances and obsolescence of earlier equipment specifications.

The significance of the two remaining OSI Task Leader papers shown in Figure 4, TL-4/40 and TL-4/47, was mentioned in Section 2.2 as they ultimately led the way to the development of the first comprehensive draft list of equipment for use during OSI. In particular, TL-4/47 not only summarized previous efforts on the proposal of equipment specifications and the drafting of the list, it also presented a revised structure and template for the list along with the definition of key terms (Table 2). This ensured that the parameters, scope and level of detail of information contained in the list – as deemed necessary for approval of the list at the initial session of the Conference of the States Parties during discussions at OSI workshop 23 – would be adequate and consistent for all equipment items.

2.4. PTS Activities

PTS activities of relevance for the list of equipment for use during OSIs are field experiments and exercises because they are aimed, amongst others, at validating OSI capabilities and related parameters such as technical specifications. Figure 1 provides an overview of the OSI field experiments and exercises which were conducted to date.

Marked in blue in Figure 5 are the three largest exercises so far. They were conducted in 2002, 2008 and 2014 (FE02, IFE08 and IFE14 respectively). Even though the many smaller scale activities such as laboratory or field tests are not included in Figure 5, the approach taken by the PTS for the development of OSI capabilities has been centred on the preparation and conduct of large scale, integrated exercises through a series of focused activities such as the four directed exercises during the period 2004 to 2007, prior to the first Integrated Field Exercise (IFE) in 2008. Figure 5 also shows that this approach became more structured after this exercise through the introduction of multi-year actions plans such as during the period 2010 to 2013 prior to the latest IFE14. In fact, the compilation of the first comprehensive draft list of equipment for use during OSIs followed the implementation of the many projects on OSI technology development that were part of the OSI action plan 2016-2019.

3. OBSERVATIONS FOR FUTURE CONSIDERATION

This section shares a few observations that show the way for further developments of the list and the need for its regular review in future.

3.1. Main Phases of Development

Considering the progression of identifying and proposing specifications until today as described in Section 2, four distinct phases of development of the inspection activities and techniques can be distinguished (Figure 2). They ultimately led to the compilation of the first comprehensive draft list of equipment for use during OSIs.

The first of these phases ran until 2002, when the first large scale exercise was conducted.
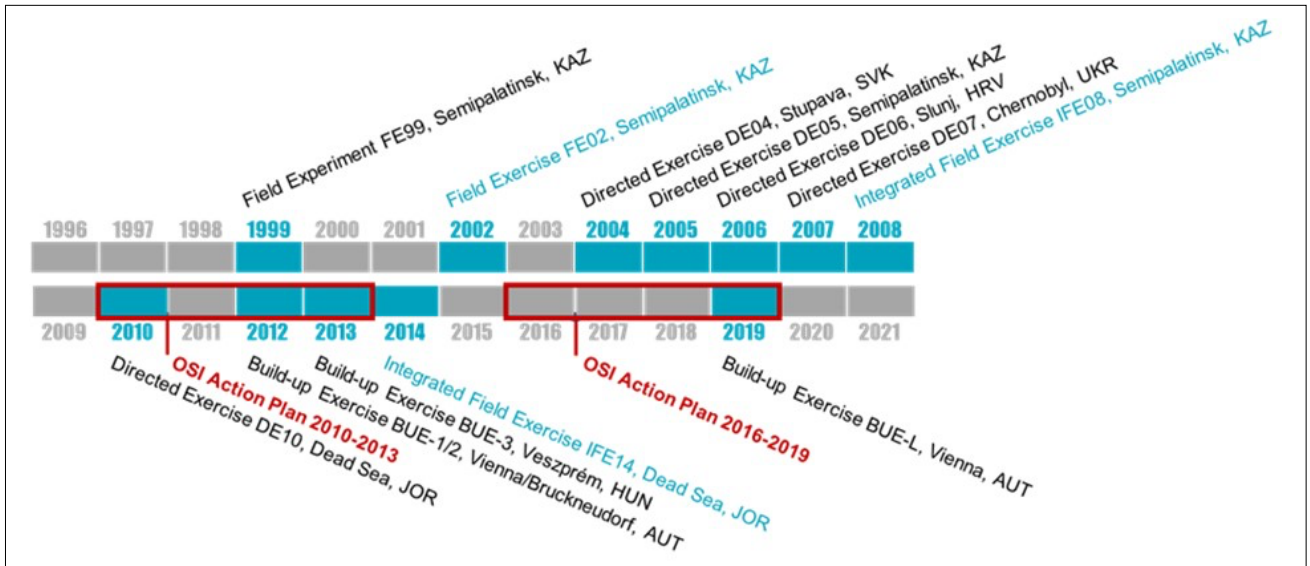
FIGURE 5.
OSI field experiments and exercises 1999 to 2019.

This phase saw the proposal, discussion, and compilation of initial lists of OSI equipment and were based on early national papers, workshops, and a series of OSI Task Leader papers. The lists contained already some requirements and specifications which allowed the acquisition of equipment for testing and training. However, operational activities were conducted only to a limited degree during this phase due to the gradual buildup of the technical capacities of the PTS at that time.

The second phase (2003-2008) then saw a much more focused development of the inspection techniques. To a large extent, this was due to the considerably increased capacities of the PTS to run technical development programmes, including specific projects for unique equipment such as the deployable noble gas systems. During this phase, more consideration was also given to scientific and technological developments, and the field testing and exercising considered more and more the integration of the developing OSI capabilities using realistic scenarios. This phase concluded with the first IFE in Kazakhstan in 2008 (IFE08).

The systematic analysis of lessons from this exercise marked the beginning of the third phase of development (2009-2014). It led to the decision to approach further developments in a more coordinated manner through a designated OSI action plan (2010-2013) which included

the implementation of specific projects on the inspection activities and techniques. In parallel, the purpose of discussions on equipment specifications and related lists shifted from testing and training to the mandated preparation of the list of equipment for use during OSIs. A milestone in this regard was the proposal of the first template of this list in 2011 (TL-4/40) which was subsequently trialled and tested. This phase concluded in 2014 following completion of the OSI action plan and conduct of the largest OSI field exercise to date in Jordan (IFE14).

The latest development phase (2015-2021) began like the previous with a systematic review of lessons from a large scale field exercise, this time IFE14. Also like before, another designated OSI action plan (2016-2019) was prepared which was complemented by a specific OSI exercise plan (2016-2020) that was aimed at testing progress in the implementation of the action plan and at validating its overall achievements. With the conduct of OSI workshop 23 and the subsequent drafting of OSI Task Leader paper TL-4/47, specific attention was given during this phase to the list of equipment for use during OSIs. Its first draft was issued by the PTS in 2021 after implementation of all relevant technical projects of the OSI action plan with a recommendation that in-depth technical discussions with and reviews by national and PTS experts be organized.

• Compilation and discussion of initial lists of OSI equipment items • Inclusion of some requirements and specifications • Limited testing and exercising							• Focused development of techniques • Specific projects for unique equipment • Consideration of technological advances • Testing and exercising with some integration					
1996	1997	1998	1999	2000	2001	2002	2003	2004	2005	2006	2007	2008
2009	2010	2011	2012	2013	2014	2015	2016	2017	2018	2019	2020	2021
• Coordinated development through OSI Action Plan 2010-2013 • Initial draft structure and content of the OSI equipment list and its compilation • Integrated testing and exercising at near full scale						• Systematic approach to technique development and OSI equipment list • Revised structure and content of the OSI equipment list • First comprehensive draft list after implementation of OSI Action Plan 2016-2019						

FIGURE 6.
Four distinct phases of OSI development.

3.2. Scientific and Technological Advances

Scientific and technological advances have influenced the development of OSI capabilities since the beginning of the Organization. The technical specifications in the first comprehensive draft list of equipment for use during OSIs clearly reflect this if compared to the earlier equipment lists.

Looking back over the last 25 years, the most obvious area where such advances have affected the development of inspection activities and techniques was the digital transformation of techniques, data, and processes. They progressed and accelerated dramatically during that time. To name a few, non-degraded signals from global navigation satellite systems became available for position finding, tracking, and recording of inspection activities such as inspector movements and data collection; data recording and transfer capacities including of wireless methods increased substantially and benefit inspection activities and techniques where large data sets are generated such as for imaging; computing power multiplied which helps in data processing and may support inspection planning such as for the selection of measurement and sampling points through modelling or for the interpretation of collected data through the use of advanced algorithms. All these enhancements rendered numerous earlier proposals for OSI equipment specifications obsolete.

And the evolution of science and technology continues. Further advances of information technology such as blockchain and other distributed ledger technologies might offer better solutions for robust, secure, and credible access, validation, and data updating which is essential for the credibility of the work of the inspection team. Data fusion also is expected to benefit from future developments to standardize data structures, formats, and sharing protocols. This might facilitate the conduct of OSIs both during the launch phase when gathering information from within the PTS or other sources to develop the initial inspection plan, and during the inspection phase in the field when data from all inspection activities and techniques are synthesized to simplify and expedite the flow and interpretation of the available information. The PTS already examines the potential of innovative materials and automatization such as in the context of noble gas sampling and separation to improve sample collection.

It is likely that there will be further scientific and technological developments of relevance for OSIs. Their consideration and review is required as per Article II of the CTBT, paragraph 26 (f), and assigned to the Conference of the States Parties following the CTBT's entry into force.

3.3.   Looking Ahead

The list of equipment for use during OSIs is to be developed and prepared by the Commission for its approval at the initial session of the Conference of the States Parties. The first comprehensive draft of this list was compiled and issued by the PTS following four major phases of development during which a systematic approach to developing the capability to apply the permitted inspection activities and techniques has been established. As the draft signifies a proposed baseline regarding these activities and techniques, its presentation marks an important milestone. It serves as single point of reference regarding the specifications of OSI equipment and shifts the focus from initial developments to further improvements.

It is clear that advances of science and technology are likely to be relevant for these improvements. The PTS therefore must stay abreast of these advances mainly to:

- Fill gaps on the first comprehensive draft list such as in relation to drilling and the OSI auxiliary equipment;
- Improve detection capabilities of the inspection techniques as required for the purposes of an OSI;
- Manage obsolescence;
- Gain efficiencies and reduce workload of the inspection team given the time and human resources restrictions.

But there is more to be done. The details of the draft list need to be discussed and reviewed in-depth with national experts. Also, consideration must be given to inspection equipment that is suitable for detecting observables that are associated with nuclear explosions conducted in environments other than underground. Further, a process is to be established by which the draft list is reviewed and updated prior to its finalization for the initial session of the Conference of the States Parties. Considering the experience since 2010 when the work on the list commenced during OSI workshop 18, this should involve cycles of testing, refining, exercising and validating of improvements in continuation of the previous development phases. And finally, the review and update of the list following its approval will also need to be agreed.

A process to address all of this has already been embarked on. OSI workshop 25, titled "First Comprehensive Draft List of Equipment for Use during OSIs" was held late in 2022. During this workshop, over 80 participants from 41 countries and PTS staff undertook a technical review of CTBT/PTS/INF.1573. In addition, discussions addressed a number of the above issues to be tackled including the ongoing management and review of the draft list of equipment for use during OSIs towards its completion and finalization for consideration and approval at the initial session of the Conference of the States Parties

To continue this process, guidance from States Signatories and active involvement of national experts and institutions remains indispensable. This is because the progression of identifying and proposing equipment specifications for OSI to date has largely been driven by multinational collaboration and advances of science and technology.

REFERENCES

Preparatory Commission for the Comprehensive Nuclear-Test-Ban Treaty Organization (1996). *Comprehensive Nuclear-Test-Ban Treaty (CTBT).* Preparatory Commission for the CTBTO, Vienna.

Resolution Establishing the Preparatory Commission for the Comprehensive Nuclear-Test-Ban Treaty Organization (1996). Preparatory Commission for the CTBTO, Vienna.

First comprehensive draft list of equipment for use during OSIs (2021). Doc. No. CTBT/PTS/INF.1573. Preparatory Commission for the CTBTO, Vienna.

BIBLIOGRAPHY

Report of the Second On-Site Inspection Workshop (1998). Doc. No. CTBT/WGB-6/PTS/INF.4. Preparatory Commission for the CTBTO, Vienna.*Draft initial equipment list for training and testing purpose and indicative specifications (1998)*. Doc. No. CTBT/WGB-6/TL-4/2. Preparatory Commission for the CTBTO, Vienna.

Draft initial equipment list for training and testing purpose and indicative specifications (1998). Doc. No. CTBT/WGB-6/TL-4/5. Preparatory Commission for the CTBTO, Vienna.

Initial equipment list for training and testing purpose and indicative specifications (1998). Doc. No. CTBT/WGB/TL-4/7/Rev.2. Preparatory Commission for the CTBTO, Vienna.

Refining specifications for radionuclide survey and analysis equipment (1999). Doc. No. CTBT/WGB/TL-4/10. Preparatory Commission for the CTBTO, Vienna.

Equipment for Xenon sampling, separation and measurement (1999). Doc. No. CTBT/WGB/TL-4/15/Rev.1. Preparatory Commission for the CTBTO, Vienna.

Equipment for the continuation period of an on-site inspection (2000). Doc. No. CTBT/WGB-11/TL-4/18. Preparatory Commission for the CTBTO, Vienna.

Technical specifications of OSI equipment for still photography: possible update (2006). Doc. No. CTBT/WGB/TL-4/36/Rev.1. Preparatory Commission for the CTBTO, Vienna.

List of equipment for use during OSIs (2011). Doc. No. CTBT/WGB/TL-4/40. Preparatory Commission for the CTBTO, Vienna.

Further development of the OSI Equipment List (2018). Doc. No. CTBT/WGB/TL-4/47. Preparatory Commission for the CTBTO, Vienna.

Report of the On-Site Inspection Workshop-6 (2000). Doc. No. CTBT/WS/OSI-6/1. Preparatory Commission for the CTBTO, Vienna.

Report of On-Site Inspection Workshop-19 (2011). Doc. No. CTBT/WS/OSI-19/1. Preparatory Commission for the CTBTO, Vienna.

Report of On-Site Inspection Workshop-23 (2017). Doc. No. CTBT/WS/OSI-23/1. Preparatory Commission for the CTBTO, Vienna.

Report of On-Site Inspection Workshop-18 (2011). Doc. No. CTBT/WS/OSI-18/1. Preparatory Commission for the CTBTO, Vienna.

Status of Preparations for the Support of On-Site Inspections

P. Labak, A. Rowlands

Comprehensive Nuclear-Test-Ban Treaty Organization, Vienna, Austria

Abstract

On-site inspections (OSIs) are a central pillar of the verification regime of the Comprehensive Nuclear-Test-Ban Treaty. Until entry into force, the Comprehensive Nuclear-Test-Ban Treaty Organization is charged with developing OSI capability – by testing equipment and procedures, developing a training programme for inspectors, preparing a draft Operational Manual and exercising these in a holistic manner to ensure that OSI capability will be ready when the Treaty does enter into force. This paper reflects on developments across the spectrum of OSI activities over the past 25 years and highlights the collective efforts of the Provisional Technical Secretariat and States Signatories.

1. INTRODUCTION

This paper provides a retrospective over the last 25 years on key developments in the on-site inspection (OSI) pillar of the Comprehensive Nuclear-Test-Ban Treaty (CTBT) verification regime. While the Treaty text has remained a constant, the ability of the Comprehensive Nuclear-Test-Ban Treaty Organization (CTBTO) to meet the requirements of an OSI has evolved and matured. Underground nuclear explosion (UNE) observables that were partially understood are now better understood (e.g. vegetation stress), techniques that were in their infancy have now matured (e.g. active seismic measurements) and technology that was considered high tech is now mainstream (e.g. analogue replaced by digital cameras). These developments have not occurred in a vacuum. Staff at the Provisional Technical Secretariat (PTS) together with experts from States Signatories have hypothesized, tested, exercised and evaluated in various fora over this period, leading to step changes in support and inspection technique capabilities.

At the outset it must be highlighted that the sole purpose of an OSI according to the CTBT, as specified in Article IV of the Treaty, is "to clarify whether a nuclear weapon test explosion or any other nuclear explosion has been carried out" and "to gather any facts which might assist in identifying any possible violator." OSIs are to provide this clarity through the collection of information and the detection within the inspection of relevant observables. In this context the Treaty and the Protocol set exact limits on the maximum size of the inspection area (1000 km^2) and the maximum number of inspectors (40 at the same time in the Inspected State Party) as well as the duration of an inspection (up to 130 days). Critically, for this paper, inspectors must use approved inspection equipment drawn from the list of inspection techniques listed in paragraph 69 of the Protocol, Part II. However, inspection techniques in isolation without an understanding of UNE observables would be futile, therefore this paper aims to highlight how, over the last 25 years, progress has been made in the understanding and detection of UNE observables.

1.1. The Preparatory Commission

The opening of the CTBT for signatures was followed by the Resolution establishing the Preparatory Commission (Commission) for the Comprehensive Nuclear-Test-Ban Treaty Organization (adopted on 19 November 1996). The text on the establishment of the Commission includes the following paragraph with respect to on-site inspections:

"15. The Commission shall make all necessary preparations, in fulfilling the requirements of the Treaty and its Protocol, for the support of on-site inspections from the entry into force of the Treaty. It shall, inter alia:

(a) Develop and prepare for the approval of the initial session of the Conference of the States Parties:

(i) An operational manual containing all appropriate legal, technical and administrative procedures; and

(ii) A list of equipment for use during on-site inspections;

(b) Develop a programme for the training of inspectors; and

(c) Acquire or otherwise make provision for the availability of relevant inspection equipment, including communications equipment, and conduct technical tests of such equipment as necessary."

Over the last 25 years points *a* to *c* listed in this paragraph have been the focus of significant attention. Working Group B has elaborated the draft On-Site Inspection Operational Manual and the PTS, together with the support of experts from States Signatories, has developed a draft list of equipment for use during OSIs based on experience gained during extensive field testing and exercises. Findings of field tests and exercises have been elaborated and discussed at expert meetings and workshops (see Figure 1), which in turn have fed into key documents that will be discussed in this paper.

FIGURE 1.
Participants of OSI Workshop 24 in the United Kingdom that focussed on inspections in different environments and events other than underground.

2. OBSERVABLES AND CONCEPT OF OPERATIONS FOR ON-SITE INSPECTION TECHNIQUES

The choice of techniques listed in paragraph 69 of the Protocol reflect the relationship between UNE related observables and methods to detect those observables. A nuclear explosion, its preparation or post-shot activities, are likely to leave signatures on the landscape no matter if attempts are made to disguise them. Some signatures can also arise naturally and some are time dependent and decay over time. Anomalies or unusual features of the landscape alone are not nuclear explosion indicators but should be sought as a basis for further investigation and not regarded as a 'smoking gun'.

An understanding of relevant observables, such as surface observables (Figure 2) has been a necessary condition for the development of OSI techniques. This entails quantitative knowledge of the capability of a particular technique or instrument to detect the relevant observable and an understanding of the time scale over which the observable may become undetectable. While some observables and their detection means are well understood, it is not the case for others. Over the last 25 years, through field tests supported by experts from States Signatories, knowledge of those observables has improved leading to a better understanding of the means and conditions by which they can or cannot be detected.

For each it is critical to understand the scale that the observable is detectable, the resolution of the observables above background and its longevity. OSI workshops from 1997 to 2000 paid significant attention to this topic relying heavily on experts from States Signatories and built on the work of experts at the Conference on Disarmament (CD 1994).

This knowledge is critical for the systematic progress of an inspection, which now revolves around a search logic concept called inspection team functionality (ITF), developed as a lesson learned from the Integrated Field Exercise (IFE) in 2008 (IFE08) in Kazakhstan. The application of ITF is now enshrined in all training and exercises and is based upon missions to search zones within the inspection area that are raised in response to technique agnostic questions. The general principle being that over the course of an inspection the search area decreases to focus on significantly smaller areas where more intrusive techniques are applied.
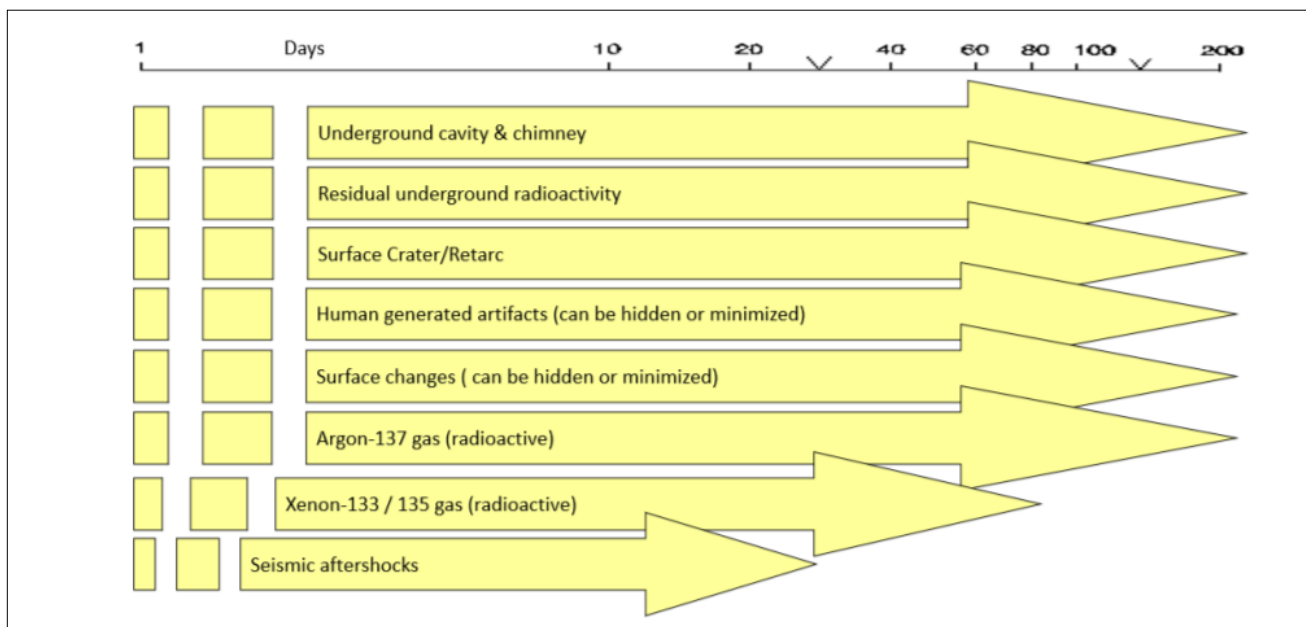
The development of some elements of concepts of operation and also inspection techniques has relied heavily on trying to mimic observables (see Figure 3) in order to assess

FIGURE 2.
Visual observables as detected form the air and the ground during IFE08 in Kazakhstan.

FIGURE 3.
Engineered observables generated for testing events. Left: a hole prepared for a chemical explosive to mimic the impact of ground fluffing; Right: Preparatory work to assess the impact of changes to the water table on multispectral signatures.

FIGURE 4.
Typical lifetime of UNE observables in days after the event.

the effectiveness of the technique at detecting the observable (Figure 4). These have ranged from detonating small quantities of chemical explosives to generate shock waves for field tests on vegetation stress potentially detectable using multispectral imaging to quarrying rock faces to reveal unweathered surfaces. In other cases, field tests have been located in areas with features that resemble UNE observables, for example, cave and tunnel complexes. Each of these field tests

contributes to knowledge and understanding on the application of a technique and their ability to detect UNEs. In this respect, the method of application of a given technique is key. Over the past 25 years, based on field tests and exercises, methods of application have been reworked and refined in order to tailor the technique to the detection of relevant observables.

Field tests have been performed in a broad cross-section of environments – a fact that is often overlooked, but it is critical to ensure that the relative merits of the application of different techniques in different environments are understood. Field tests and exercises have been conducted in a spectrum of environments ranging from desert-like conditions in Jordan during the Integrated Field Exercise in 2014 (IFE14) to thick snowpack conditions in Canada during a test of airborne gamma spectrometry in 2017 (Figure 5). Likewise, field tests have tested the application of techniques in areas of dense vegetation and in areas of high relief. These events have allowed the PTS to understand the challenges of deploying and inspecting in such environments. It is however true that not all techniques have been tested in all environments. However, progress has been made in understanding the broader issues of deploying in more challenging environments.

Tests and exercises have been key in the development of both inspection techniques and the evolution of support activities such as the rapid deployment capability. These support capabilities are key enablers for inspection activities. Developments in this respect include the introduction of intermodal rapid deployment containers, the inception and evolution of base of operations infrastructure to meet power, working and accommodation requirements and tools to support the deployment and return of equipment (Figure 6). These capabilities were tested extensively during the integrated field exercises and continue to be used and tested during smaller scale activities.

3. OVERVIEW OF DEVELOPMENT OF ON-SITE INSPECTION CAPABILITIES

3.1. Equipment Development

Knowledge of observables has enabled the development of OSI capabilities to detect those observables. Capabilities are typically discussed in terms of the equipment and procedures to perform the inspection activities covered in paragraphs 69 and 80 of the Protocol but these are only enabled with appropriately trained surrogate inspectors and the infrastructure to maintain and deploy an inspection team together with support infrastructure at headquarters (Figure 7). Development of capabilities has not been uniform over the last 25 years, with techniques such as passive seismic monitoring achieving a level of maturity sooner than other techniques, such as multispectral imaging. As demonstrated in field tests and exercises and measured by key performance indicators, the majority of OSI technique based capabilities have now attained a level of maturity that renders them fit for purpose.

Table 1 is illustrative of the development path of a selected number of OSI techniques. Multispectral imaging from the air was not evaluated by the PTS until a field test in Hungary in 2011. Tests over subsequent years with engineered UNE-type observables enabled the PTS to set about a path to procure a custom OSI array of sensor that would become the multispectral imaging from the air capability. This only becomes a capability once procedures are enshrined in relevant documents and inspectors are trained in the installation and operation of equipment and are competent in the processing of data. For techniques such as active seismic survey and the measurement of argon noble gas, the use of contribution in kind has been invaluable in developing capability. This has led

Table 1. Illustrative Development Path for Some of the On-Site Inspection Techniques

Technique	Event		
	IFE08	IFE14	IFE25
Passive seismic monitoring	Fully deployed --->		
Multispectral imaging from the air	Not available	Available as a mix of contributions in kind and PTS owned equipment	PTS owned configuration
Active seismic measurements	Not available	Contributions in kind configuration	PTS owned configuration
Argon noble gas measurement and analysis	Not available	Contributions in kind configuration	TBD

FIGURE 7.
Principle elements of OSI capability.

to projects to develop custom OSI solutions for these techniques.

As an illustration of the current state of development, a major landmark was achieved with the publication of the first comprehensive draft list of equipment specifications for use during OSI (CTBT/PTS/INF.1573). Issued in 2021 and its revision in 2023, the Information Paper covers all OSI techniques but drilling and is a single point of reference for further equipment development. The specifications listed in this Information Paper represent the collective findings of equipment tests and exercises performed by the PTS with the support of experts form States Signatories over the last 25 years. These specifications are, by default, bound to the Treaty and the Protocol and carefully chosen to enable relevant observables to be resolved.

3.2. Procedures

Information Paper 1573 (Rev.1) aims to address synergies between equipment specifications, e.g. attribution of location to inspection data. This is symptomatic of a broader shift away from an information conduit that traverses vertical levels efficiently but does not

disperse widely, i.e. focussing on the results from a given technique in isolation rather than treating data holistically. This is best illustrated by the introduction of ITF, which was used for the first time in the build-up and the conduct of IFE14. This approach to search logic is now engrained in every aspect of the training programme and is central to decision making during an inspection.

Over the last 25 years, the means by which data are recorded has changed significantly, facilitated of course by developments in technology. IFE08 was essentially a paper-based exercise with printed forms and stand-alone laptops to process and analyse data. IFE14 saw the introduction of an electronic system to record metadata associated with certain techniques and a central application to support the implementation of ITF. The Integrated Information Management System (IIMS) as it was known, provided a tool to delineate areas of interest (search zones), pose questions for those areas, plan missions to answer questions and resource field teams. Inspection data classified as protected were then displayed on a separate geographical information system called the field information management system (FIMS).

Lessons learned during IFE14 paved the way for an integrated system building on IIMS and FIMS. The result is a platform called the Geospatial Information Management for OSI system (GIMO). GIMO is a software platform that that facilitates inspection search logic, equipment and human resourcing and data flow. It encompasses different stand-alone applications tailored to meet the requirements of inspection data gathering, environmental sampling handover, environmental sample measurement and analysis, search logic and data dissemination within the inspection team. The platform is therefore integral to the acquisition of inspection data, their review and classification, and their visualization. GIMO, and its associated hardware, is designed to respect data security while facilitating data flow with requisite airgaps between different areas and data classification statuses. GIMO also supports the fusion of data from different techniques by displaying these on a map interface and supports the generation of inspection reports. In this respect GIMO embodies the spirit of ITF by enabling a more holistic approach to data analysis and avoids narrow stove-piped mentality.

Key to an effective and transparent inspection are well defined procedures that inspectors are trained in and follow. Over the last 25 years, standard operating procedures, work instructions, field guides and manuals have been developed in line with the Quality Management System of the OSI Division. These have been developed in parallel with the elaboration of the draft OSI Operational Manual and the development of OSI techniques and methodologies. These documents have evolved over time to reflect knowledge and understanding of the relationship between techniques and observables. These have been critical in the development of the training programme for surrogate inspectors and the execution of field activities including build-up exercises and integrated field exercises. The expanded use of field guides, also available electronically on inspection tablets, will enhance workflow transparency and consistency of application.

3.3. Infrastructure

To facilitate the testing and development of equipment, the development of the training programme and the conduct of exercises, the OSI Division has operated facilities outside the Vienna International Centre with appropriate space to store and maintain equipment and to host training events and to conduct exercises. The Equipment Storage and Maintenance Facility (ESMF), located in Guntramsdorf near Vienna, operated from 2011 to 2016 and served the period bracketing IFE14. The rented facility was used extensively for the preparation of equipment leading up to IFE14 and then served as the location of the Operations Support Centre during the event. Following a period on the temporary premises on the campus of the Austrian Institute of Technology in Seibersdorf, the PTS commissioned a purpose-built facility on the same campus in 2019 (Figure 8). While the Comprehensive Nuclear-Test-Ban Treaty Organization (CTBTO) Technology Support and Training Centre serves the entire PTS, the

FIGURE 8.
Left: The operational support centre during the build-up exercise in November 2019; Right: View of the loading bays at the CTBTO Technology Support and Training Centre in Seibersdorf.

facility also has a dedicated storage area for OSI deployable equipment, equipment maintenance areas and training facilities.

The move to the Seibersdorf facility represented a step change in the ability of the PTS to maintain, calibrate and protect OSI deployable equipment in line with the requirements of paragraph 38 of the Protocol. The introduction of a clearly demarcated area for OSI deployable equipment, two-factor authentication for access keys and video surveillance, assures the protection of the equipment. The site also includes an outdoor area with buried subsurface objects to test the application of shallow geophysical techniques and the fuselage of a helicopter for the testing of equipment related to airborne techniques.

OSI maintained a basic component prototyping capability from the outset. Over the course of the last 25 years this capability has evolved to include the use of computer aided design, scanning technology to reverse engineer and equipment such as 3-D printers, milling machines and laser cutters to fabricate items, including custom components to facilitate the work of inspectors.

With respect to meeting the requirements of paragraph 38 of the Protocol, to support and record information pertaining to the lifecycle of equipment, the PTS developed the Equipment and Instrumentation Management system for OSI, a one-stop repository providing immediate and complete information on OSI equipment including their maintenance, storage and calibration. It is used operationally at the CTBTO and on deployment to facilitate the work of PTS staff and surrogate inspectors. The custom application is designed to be as user-friendly as possible with photographs to facilitate item identification and integration with printing and RFID hardware. On deployment, the Equipment and Instrumentation Management system for OSI is designed to work alongside GIMO to facilitate the selection of equipment configurations for field missions and to manage equipment and their maintenance at the base of operations.

3.4. Personnel

Unlike the International Atomic Energy Agency and the Organisation for the Prohibition of Chemical Weapon, the CTBTO will not have a standing inspectorate, a fact that has an impact on the training and availability of surrogate inspectors (Figure 9). The role of inspectors has been mentioned on several occasions in this paper, but it is worth emphasizing that paragraph 15 of the text on the establishment of the Commission mentions the need to "Develop a programme for the training of inspectors" rather than creating an inspectorate per se. In response to this, task three inspector training cycles have been held with a new round taking place in the form of a linear training programme with multiple entry points. The training of surrogate inspectors through introductory and advanced blocks comprising general as well as technique

FIGURE 9.
Left: OSI Regional Introductory Course in 2016 in South Africa; Right: Introductory Course for the Third OSI Training Cycle in Slovakia in 2016.

specific courses has been effective. The inclusion of soft skills and negotiating training has proven to be valuable as evidenced in the integrated field exercises. While challenging for the inspector training programme, the Covid-19 pandemic incentivized and accelerated the use of a variety of distance learning methods. This served as a vital tool during the pandemic, keeping surrogate inspectors engaged in the programme and enhancing their learning opportunities.

4. CONCLUSIONS

Several aspects of an OSI would make it unique and challenging but after 25 years OSI deployment, inspection technique capabilities, data flow and data security have evolved and matured. Through the active engagement of experts from States Signatories and PTS staff, the OSI pillar of the verification regime is stronger and more robust than ever. Within the pillar there is synchroneity between technique development, procedure development and training, which bodes well for future development.

Not all capabilities have fully matured so there is room for development. For those more mature techniques there is a need for technology refreshment. There is therefore potential for technical developments and innovations and opportunities for further improvement of OSI capabilities within the framework of the Treaty and Protocol.

These capabilities – as they currently stand – will be put to the test as part of the exercise programme over the coming years culminating in an IFE in 2025 in Sri Lanka. This event, like previous IFEs, will serve as an important benchmark of OSI capabilities.

REFERENCE

Conference on Disarmament (1994). On-site Inspection for the Comprehensive Test Ban Treaty: Phenomena, Technology, OSI Examples, Costs. CD/NTB/WP.198, United Nations, Geneva.

Civil and Scientific Applications of International Monitoring System Data

Z. Mindaoudou Souley, J. Kuśmierczyk-Michulec, M. Kalinowski, P. Mialle, J. Ylo, R. Le Bras
Comprehensive Nuclear-Test-Ban Treaty Organization, Vienna, Austria

P. Nielsen
Esbjerg, Denmark

Abstract

Although the main purpose of the International Monitoring System (IMS) is nuclear explosion monitoring, this unique asset of available global data may also be used for scientific and civil purposes. Scientific applications follow the decision of the Comprehensive Nuclear-Test-Ban Treaty Organization (CTBTO) Preparatory Commission from November 2000, in which it was stated that the Provisional Technical Secretariat may provide IMS data and International Data Centre (IDC) products to organizations for the purpose of conducting research associated with the development of the IMS and IDC. Since 2011, the virtual Data Exploitation Centre (vDEC) has allowed scientists and researchers access to the vast amount of CTBTO data archived over more than two decades. The vDEC contract is a zero-cost contract which contains legal requirements. vDEC provides scientists and researchers from many different disciplines from around the globe with access to IMS data to conduct research and publish new findings. These applications benefit detecting nuclear explosions by improving monitoring algorithms and discriminating between explosion signals and what is considered noise from the Comprehensive Nuclear-Test-Ban Treaty (CTBT) perspective. Having many scientists collect and evaluate data also enhances data quality. Following the Sumatra earthquake on 26 December 2004, it was decided that national and regional tsunami warning centres recognized by the Intergovernmental Oceanographic Commission of the United Nations Educational, Scientific and Cultural Organization can sign an arrangement with the CTBTO to receive IMS data for tsunami early warning. After the Fukushima Daiichi nuclear power plant accident, CTBTO became a member of the Inter-Agency Committee on Radiological and Nuclear Emergencies. Further civil applications for disaster risk reduction have been proposed. This paper reviews the progress on civil and scientific applications made in the 25 years since the opening of the CTBT for signature.

1. INTRODUCTION

The International Monitoring System (IMS), installed operated and maintained by the Comprehensive Nuclear-Test-Ban Treaty Organization (CTBTO), is a global system of monitoring stations, composed of four complementary technologies: seismic, hydroacoustic, infrasound and radionuclide. Data from all IMS stations are collected and transmitted through the Global Communications Infrastructure (GCI) to the International Data Centre (IDC). The primary purpose of the Comprehensive Nuclear-Test-Ban Treaty (CTBT) verification regime is to verify compliance with the CTBT effectively. The verification technologies of the IMS and the data, technologies and products of the IDC have the potential to offer many civil and scientific applications which could contribute to sustainable development and human welfare. Civil and scientific applications are a possible added benefit that States Signatories could gain from participation in the CTBT verification regime.

The CTBT explicitly states that the States Parties may benefit from the application of monitoring technologies for peaceful purposes (Art. IV, Para. 12 in the CTBTO Treaty): "The States Parties undertake to promote cooperation among themselves to facilitate and participate in the fullest possible exchange relating to technologies used in the verification of this Treaty in order to enable all States Parties to strengthen their national implementation of verification measures and to benefit from the application of such technologies for peaceful purposes."

Another paragraph opens the opportunity for utilizing IMS data for scientific purposes (Art. IV, Para. 10 in the CTBTO Treaty): "The provisions of this Treaty shall not be interpreted as restricting the international exchange of data for scientific purposes."

The Preparatory Commission for the CTBTO (Commission) has defined the rules and procedures for data sharing. The main category are authorized users who are designated by the States Signatories to use IMS data and IDC products for nuclear explosion monitoring. Many authorized users with access to data also use them for civil and scientific applications of national or regional interest. The Commission has decided that the Provisional Technical Secretariat may provide data to other users for two specific civil applications: tsunami warnings for all national and regional tsunami warning centres that are acknowledged by the Intergovernmental Oceanographic Commission of the United Nations
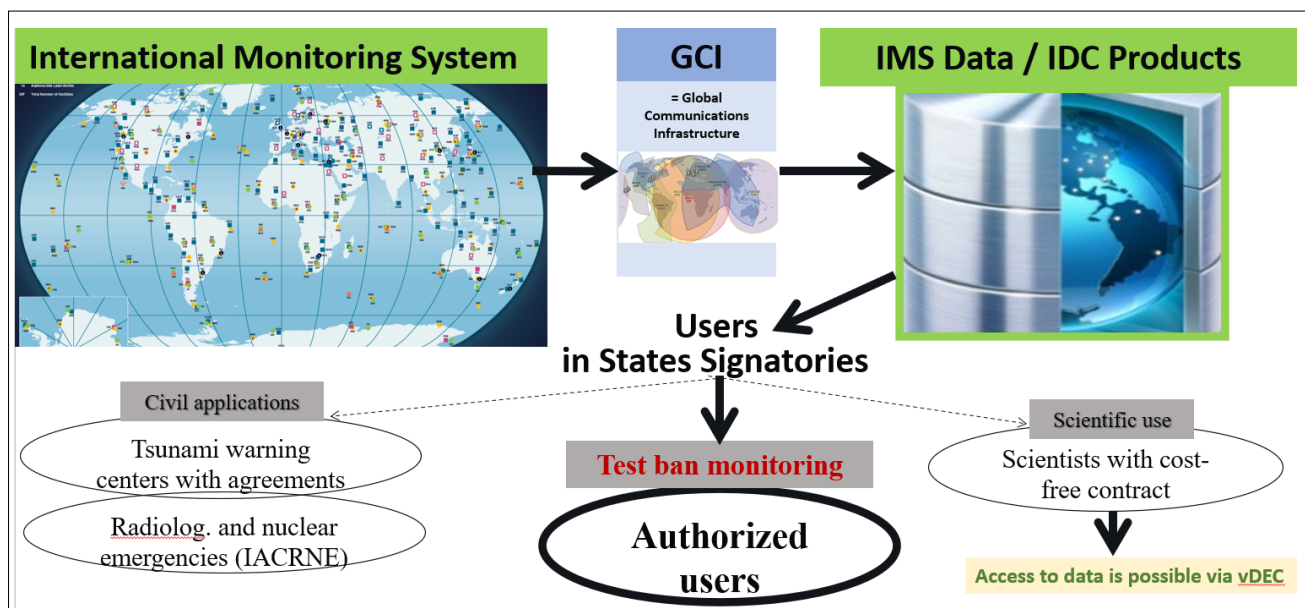
FIGURE 1.
Dissemination channels to different users of IMS data and IDC products.

Educational, Scientific and Cultural Organization, and to the International Atomic Energy Agency and the World Meteorological Organization for radiological and nuclear emergencies in the case of the Fukushima Daiichi nuclear power plant accident. Further, the Commission has given permission to the Provisional Technical Secretariat to share IMS data for scientific applications.

2. CIVIL APPLICATIONS OF INTERNATIONAL MONITORING SYSTEM DATA

Civil applications of IMS data refer to natural and man-made disasters which require data to be available in near real time.

Seismic and hydroacoustic data form the basis for providing tsunami early warning announcements. There are frequent underwater earthquakes and many of them have tsunamigenic potential. Following the Sumatra earthquake on 26 December 2004, the Commission decided that national and regional tsunami warning centres can sign an arrangement with the CTBTO to receive IMS data for tsunami early warning, if they are recognized by the Intergovernmental Oceanographic Commission of the United Nations Educational, Scientific and Cultural Organization. So far, 20 national or regional tsunami warning centres in 19 States have signed a tsunami warning agreement with the CTBTO and receive data from 98 IMS stations. These are Australia, Chile, France, Greece, Honduras, Indonesia, Italy, Japan, Madagascar, Malaysia, Myanmar, Philippines, Portugal, the Republic of Korea, the Russian Federation, Spain, Thailand, Türkiye and the United States of America.

In March 2011, the Fukushima Daiichi nuclear power plant accident released radioactivity into the atmosphere that an IMS system observed on the Northern hemisphere for about three months after 14 March 2011. These IMS radionuclide observations were shared with the International Atomic Energy Agency and the World Meteorological Organization. They were also given to the United Nations Scientific Committee on the Effects of Atomic Radiation (UNSCEAR) for inclusion in the scientific annex of their 2013 report (UNSCEAR 2013) as being unique in terms of the global coverage and the broader range of radionuclides then reported elsewhere, including four radioxenon isotopes. In 2012, the CTBTO joined the Inter-Agency Committee on Radiological and Nuclear Emergencies. In June 2016, the International Atomic Energy Agency and the CTBTO signed the practical arrangements on cooperation in the area of response to radiation incidents and emergencies. For the CTBTO, the critical response task during an emergency phase would be to provide real time particulate and noble gas monitoring data including confirmation of no detection. The CTBTO may also provide related expertise and may give advice on atmospheric transport and dispersion predictions.

In addition to the two already specified agreed uses of IMS data, there is the potential for IMS data to be a component of disaster risk mitigation. Approximately half of all National Data Centres are hosted by national seismological centres and their primary purpose is earthquake monitoring for evaluation of seismic hazard.

Hydroacoustic data have several potential civil applications in addition to tsunami warning. These data reveal submarine volcanic activity and can be used for iceberg tracking. Hydroacoustic data were also used to investigate signals possibly caused by missing airplanes. Another application was the search for the missing Argentine submarine ARA San Juan in which IMS hydroacoustic data was instrumental in confining the search region.

Infrasound observations offer a range of possible civil applications, including detecting and locating meteorite impacts, tracking storms and characterizing disastrous chemical explosions. The most mature application of infrasound is the capability of identifying explosive volcanic eruptions that promptly release large amounts of

ash into the atmosphere and pose a severe threat to airplanes. Years ago the International Civil Aviation Organization requested the CTBTO to look into assessing the usefulness of infrasound data for monitoring volcanic activity. Under the patronage of International Civil Aviation Organization and the World Meteorological Organization, the Volcanic Ash Advisory Centre of Toulouse was tasked to report on the progress and development of this activity. Together with the scientific community, the Volcanic Ash Advisory Centre Toulouse explored the technical challenges with access to IMS data as a scientific application. This led to the development of the Volcanic Information System that demonstrates the maturity and technical potential of the application.

Radionuclide monitoring data can be used for other civil applications in addition to nuclear and radiological emergencies. A novel application of radioisotope ^{7}Be data achieves monsoon onset prediction a month ahead of time as compared to one week with current modelling methods.

3. SCIENTIFIC APPLICATIONS OF INTERNATIONAL MONITORING SYSTEM DATA

IMS data are also made available for scientific applications except for the most recent data that remain initially reserved for Treaty monitoring purposes and are made available after a delay of three months. For this purpose, a separate access method has been implemented by establishing the virtual Data Exploitation Centre (vDEC).

3.1. What is the Virtual Data Exploitation Centre?

The virtual Data Exploitation Centre provides scientists and researchers from many different disciplines and from around the globe access to IMS data and all IDC products to conduct research to publish new findings. Data access through vDEC is based on a zero-cost contract. It is an agreement (also referred to as vDEC contract in this paper) which does not contain any monetary remuneration between the parties for services or property but contains legal requirements.

The vDEC agreement is concluded between the CTBTO and a legal entity involved in engineering or scientific research. It is valid for two years and allows for up to three specified users affiliated with the legal entity to have access to vDEC data after each user signs a separate confidentiality agreement. Applications for a vDEC agreement can be initiated by filling out and submitting an online application form which can be found on the vDEC page of the CTBTO web portal.

3.2. Examples of the Virtual Data Exploitation Centre Scientific Application Projects

Since 2011 vDEC contracts have been concluded with institutions representing 29 countries (see Figure 2a) Argentina, Australia, Austria, Belgium, Brazil, Canada, China, Cyprus, Denmark, Egypt, Finland, France, Germany, India, Iran (Islamic Republic of), Ireland, Israel, Italy, Japan, Korea (Republic of), Nigeria, Portugal, the Russian Federation, Spain, Sweden, Switzerland, the United Kingdom of Great Britain and Northern Ireland, Ukraine and the United States of America. Scientific projects being done by scientists under these agreements utilize data representing different technologies (see Figure 2b).

There are many examples of the use of IMS data with vDEC projects for scientific purposes. For instance, IMS radionuclide data were used to determine the quantities of key radionuclides released by the Fukushima accident.

The effects of climate change can be monitored using all four technologies. More than two decades of global IMS data allow for studying seasonal and yearly variations of some atmospheric properties. Infrasound is useful to assess changes in the tropopause height, seismic and hydroacoustic technologies to measure ice
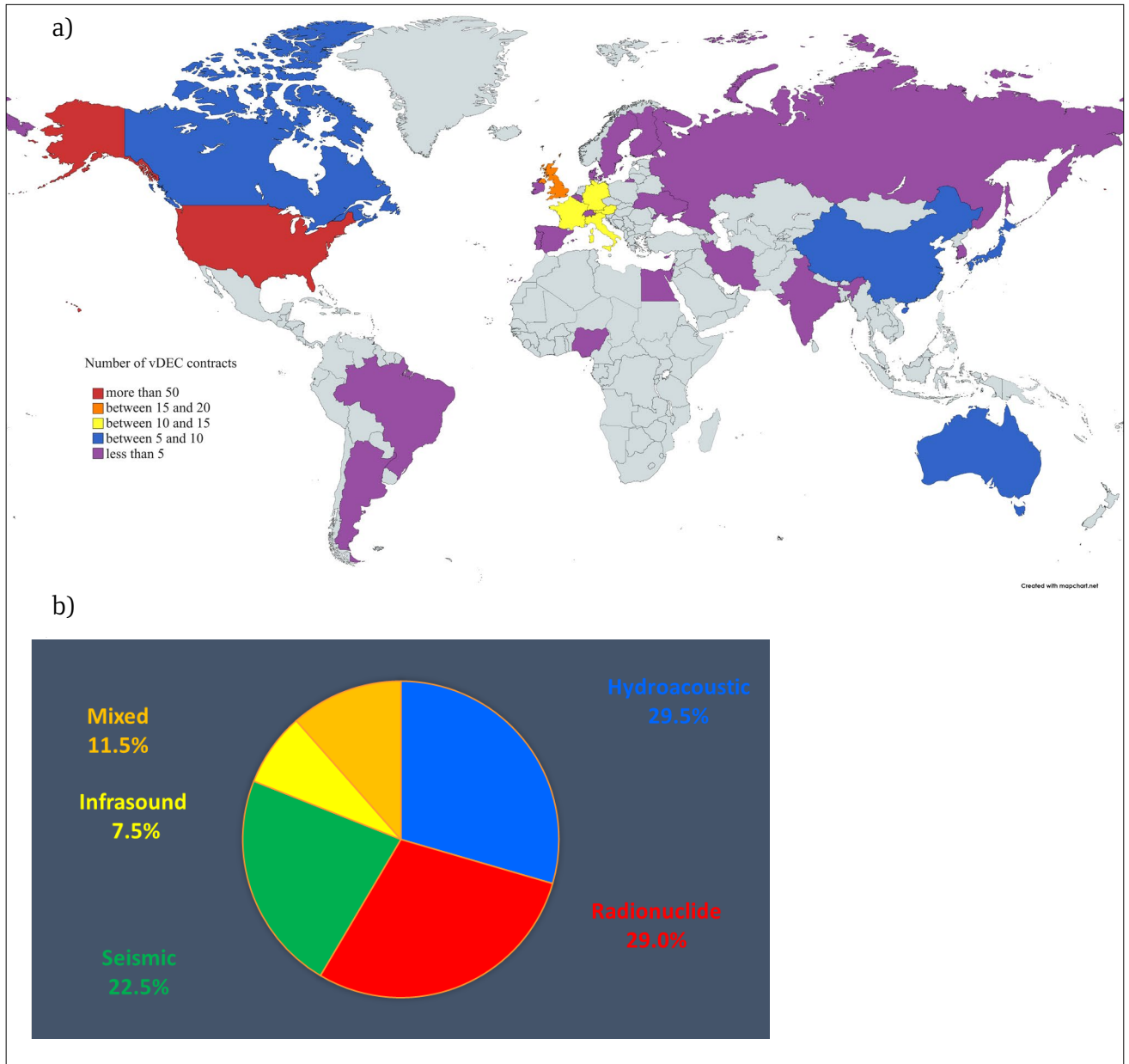
FIGURE 2.

(a) Distribution of vDEC contracts per country. (b) Number of vDEC contracts per technology in [%]. Mixed technologies refer to the following combination of technologies: seismic and infrasound, hydroacoustic and seismic, seismic and radionuclide, hydroacoustic, seismic and infrasound.

shelf cracking and iceberg calving, warming of the oceans even very deep under the sea surface via thermoacoustic. Radionuclides, e.g. ^{7}Be can be used as tracers to validate global climate models and to monitor changes of the stratosphere-troposphere exchange. The altitude dependency of ^{7}Be concentrations combined with its propensity to attach easily to mineral dust makes this radionuclide a well-founded tracer of Saharan dust (Kuśmierczyk-Michulec and Bourgouin 2018). Furthermore, ^{7}Be can be used as a tracer of global atmospheric circulation patterns that may possibly be caused by global warming. Terzi et al. (2021) applied ^{7}Be measurements at IMS radionuclide stations to confirm that major changes in the atmospheric circulation are currently ongoing, including modifications of tropopause heights over the past decade which can, at least to some extent, be attributable to global warming.

IMS radionuclide observations following the Fukushima Daiichi nuclear power plant accident were used and quoted in dozens of peer-

reviewed scientific papers for various scientific applications, including source term reconstruction for ^{137}Cs, ^{131}I, or ^{133}Xe and for enhancements of atmospheric transport modelling methods.

Atmospheric radionuclide tracers are often used to quantify uncertainties of global atmospheric transport modelling. The CTBTO itself is involved in the multi-model atmospheric transport modelling (ATM) exercises entitled *ATM Challenges* which use IMS radionuclide observations to investigate enhancements for identifying possible nuclear explosion signals against normal radioxenon background variations. These exercises allow assessment of the performance of ATM simulations by the IDC and other groups (Eslinger et al. 2016. Maurer et al. 2018, 2022). The IDC participated in three ATM Challenges in 2015, 2016 and 2019. One of the goals of the third exercise was to investigate to what extent actual daily emission data provides an added value compared to average emission values known from literature. The goal of the latest intercomparison exercise goes beyond the previous by exploring the screening power for identifying simulated signals of hypothetical nuclear tests added to the real IMS radioxenon background observations. It should be noted that the goal of all these ATM exercises is to provide an ensemble analysis of radioxenon background levels at IMS stations frequently affected by industrial emissions. Currently, the IDC is supervising the first nuclear explosion signal screening open intercomparison exercise 2022, which was launched in December 2021. These exercises have shown encouraging results using known sources of emissions to the atmosphere, and high fidelity measurements from the IMS.

Hydroacoustic data can be used in various scientific projects. For example, they were used to understand the inter-annual and seasonal occurrence of blue and fin whales at mid- and low latitudes in the Southern Hemisphere and to study the impact of shipping noise on baleen whales. Recently, because of access to IMS hydroacoustic data through a vDEC contract, scientists have discovered a completely new colony of pygmy blue whales in the Indian Ocean (Jordan 2021). Whale populations are identified by their specific vocalization, and some of the observed whale calls recorded at IMS hydrophone stations remain unidentified.

A novel methodology has been developed to estimate global temperature changes in the ocean by long term monitoring of travel time changes of hydroacoustic T phases (Tertiary phases) generated by repeating natural earthquakes and recorded at IMS hydrophone stations. This method utilizes template matching to obtain high temporal sampling of repeating earthquakes. The template matching combined with high quality IMS hydrophone data provides estimates of global scale ocean temperature changes at higher temporal resolution compared to current techniques used to generate similar observations.

The most striking examples of scientific applications with IMS seismometer data are related to the nuclear tests announced by the Democratic People's Republic of Korea. Scientists are studying the characteristics of the depths of the source to improve treaty monitoring methods based on moment tensor analysis or cross-correlation. The sixth announced nuclear explosion by the Democratic People's Republic of Korea was also detected by six IMS hydrophone triplets, and the localization of the event using these hydrophone data compares well with the localization using 125 IMS seismic stations.

Various atmospheric phenomena generate infrasound signals that are noise for Treaty monitoring, but of interest for scientific research. These sources of noise effects bear potential for a wide range of investigations. For example, they have the potential to help identify and characterize volcanic eruptions and study thunderstorm activity or large wildfires in remote regions, as these occurrences increase with global warming and development of human activity. IMS data were instrumental for scientific studies on the Hunga volcano eruption in Tonga on 15 January 2022. Matoza et al. (2022) use IMS data to study the atmospheric waves and global seismoacoustic observations of this unusually energetic explosive event. Beyond natural phenomena observation and application, vDEC also offers scientists the possibility to test their

algorithms, for instance to investigate kernel based machine learning techniques for infrasound classification, which could have direct application at the IDC. Infrasound data can be used to study the atmospheric dynamics over large periods of time and at high altitude where other observation methods are limited. Infrasound data allow for the characterization of processes like sudden stratospheric warming episodes, which could enable longer term weather predictions.

Another scientific application that benefitted from vDEC is the monitoring of near-Earth objects impacting the atmosphere, which generate infrasound waves that can travel over regional to global distances and reach IMS infrasound sensors which are picked up automatically by the IDC automatic system. A scientific project initiated in 2016, considered this activity able to contribute to a near real time monitoring system of interest to the planetary defence community including United Nations Office for Outer Space Affairs (UNOOSA) (Ott et al., 2020).

The results of the vDEC projects help the CTBTO expert community in turn refine methods for discriminating explosion signals from the noise.

4. CONCLUSIONS

The core mission of the comprehensive verification regime of the CTBT is nuclear test monitoring, however, the IMS provides a treasure trove of data that can be used for a variety of applications, such as climate change research as well as disaster warning and mitigation.

There are two specific civil applications of IMS data implemented by the CTBTO: Tsunami early warning by regional and national tsunami warning centres and international cooperation in case of nuclear and radiological emergencies.

There is potential for more applications. The most mature one is volcano ash plume warning.

The vDEC offers the opportunity for IMS data to be used for scientific purposes. The strong relationship between the scientific and technological community and the CTBTO helps ensure that the IMS remains at the forefront of technological innovation, the sensor network performs at an impressive high level, including the associated data processing, and that no nuclear explosion goes undetected.

REFERENCES

Eslinger, P.W., et al. (2016). International challenge to predict the impact of radioxenon releases from medical isotope production on a comprehensive nuclear test ban treaty sampling station. *Journal of Environmental Radioactivity* **157** 41–51.

Jordan R. (2021). "Nuclear Bomb Detectors Accidentally Discovered Secret Blue Whale Colony!" *Nature World News* 14 June 2021.

Kuśmierczyk-Michulec, J., Bourgouin, P. (2018). Influence of mineral dust on changes of ^{7}Be concentrations in air as measured by CTBTO global monitoring system. *Journal of Environmental Radioactivity* **192** 454–466.

Matoza, R.S., et al. (2022). Atmospheric waves and global seismoacoustic observations of the January 2022 Hunga eruption, Tonga. *Science* 377 (6601).

Maurer, Ch., et al. (2018). International challenge to model the long-range transport of radioxenon released from medical isotope production to six Comprehensive Nuclear-Test-Ban Treaty monitoring stations. *Journal of Environmental Radioactivity* **192** 667-686.

Maurer, Ch., et al. (2022). Third International challenge to model the medium-to long-range transport of radioxenon to four Comprehensive Nuclear-Test-Ban Treaty monitoring stations. *Journal of Environmental Radioactivity* **255**.

Ott, T., et al. (2020). NEMO - The NEar real-time MOnitoring system – Harvesting information online for a fireball monitoring and alert system. *Acta Astronautica*, **177** 172-181.

Preparatory Commission for the Comprehensive Nuclear-Test-Ban-Treaty Organization (1996). *Comprehensive Nuclear-Test-Ban-Treaty (CTBT).* Preparatory Commission for the CTBTO, Vienna.

Terzi, L., et al. (2020). Radioisotopes demonstrate changes in global atmospheric circulation possibly caused by global warming. *Scientific Reports* **10** (1).

United Nations Scientific Committee on the Effects of Atomic Radiation (UNSCEAR) (2013). *Levels and Effects of Radiation Exposure due to the Nuclear Accident After the 2011 Great East-Japan Earthquake and Tsunami*. United Nations Scientific Committee on the Effects of Atomic Radiation, UNSCEAR Report 1 (Annex A), United Nations, New York.

PRESENTATIONS AT SNT2021 ON THE 25TH ANNIVERSARY

I01-722 – Challenges and Achievements of Monitoring for Nuclear Test Explosions in the Context of the CTBT

Is1-353 – New Applications at the IDC for SHI Expert Technical Analysis

I02-718 – The CTBT Hydroacoustic Network at 25 Years

Is2-283 – Advancements in Hydroacoustic Signal Processing at the IDC During the Past Two Decades and Plans for the Future

I03-714 – 25 Years of Infrasound Monitoring: Achievements and New Challenges

Is3-381 – Infrasound Processing System at the IDC, from Rudimentary to Maturity

Is6-454 – Machine Learning Prospects for Automatic SHI Processing

I04-717 – The IMS Radionuclide Network: A Unique Machine Not Yet Fully Exploited

Is7-604 – Review and Outlook of Radionuclide Screening Methods for Discriminating Nuclear Explosion Signals from Normal Radioactivity Background in the Atmosphere

P3.5-507 – Is There Potential for Further Enhancing IDC Spectrum Analysis Methods of CTBT Radionuclide Measurements After 25 Years of Progressive Development?

Is4-332 – Advancements in Atmospheric Transport Modelling at the CTBTO PTS During the Past Two Decades and Plans for the Future

Is5-239 – Development of the First Comprehensive Draft List of Equipment for Use During On-Site Inspections

I05-727 – Status of Preparations for the Support of On-Site Inspections

One more presentation made at SnT2021 is included in this collection of papers. This is the introductory talk that preceded the Civil and Scientific Applications technical panel:

I06-721 - Civil and Scientific Applications of IMS Data

BIBLIOGRAPHY

Becker, A., Schurr, B., Kalinowski, M.B., Koch, K., Brown, D. (2010). Recent Advances in Nuclear Explosion Monitoring. *Pure and Applied Geophysics (PAGEOPH)* **167** (4-5).

Dahlman, O., Mackby, J., Mykkeltveit, S., Haak, H. (2011). Detect and deter: can countries verify the nuclear test ban? Springer Science & Business Media.

De Groot-Hedlin, C., Orcutt, J. A. (2001). Monitoring the Comprehensive Nuclear-Test-Ban Treaty: Hydroacoustics. *Pure and Applied Geophysics (PAGEOPH)* **158** (3).

Der, Z.A., Shumway, R.H., Herrin, E.T. (2002). Monitoring the Comprehensive Nuclear-Test-Ban Treaty: Data Processing and Infrasound. *Pure and Applied Geophysics (PAGEOPH)* **159** (5).

Ekström, G., Denny, M., Murphy, J.R. (2001). Monitoring the Comprehensive Nuclear-Test-Ban Treaty: Source Processes and Explosion Yield Estimation. *Pure and Applied Geophysics (PAGEOPH)* **158** (11).

Kalinowski, M.B., Becker, A. (2014). Recent Advances in Nuclear Explosion Monitoring. *Pure and Applied Geophysics (PAGEOPH)* **171** (3).

Kalinowski, M.B., Mialle, P. (2021). Nuclear Explosion Monitoring and Verification: Scientific and Technological Advances. *Pure and Applied Geophysics (PAGEOPH)* **178** (7).

Kalinowski, M.B., Mialle, P. (2024). Nuclear Explosion Monitoring and Verification: Science and technology to tackle global challenges. Under preparation by *Pure and Applied Geophysics (PAGEOPH)*.

Kalinowski, M.B., Sarid, E., Mialle, P., Zampolli, M., Haralabus, G. (2023). Nuclear Explosion Monitoring and Verification: Innovation in Technology and Scientific Methods for Nuclear Explosion Monitoring and Verification. *Pure and Applied Geophysics (PAGEOPH)* **180** (4).

Levshin, A. L., Ritzwoller, M. H. (2001). Monitoring the Comprehensive Nuclear-Test-Ban Treaty: Surface Waves. *Pure and Applied Geophysics (PAGEOPH)* **158** (8).

Maceira, M., et al. (2017). Trends in Nuclear Explosion Monitoring Research & Development – A Physics Perspective. United States.

Patton, H. J., Mitchell, B. J. (2001). Monitoring the Comprehensive Nuclear-Test-Ban Treaty: Regional Wave Propagation and Crustal Structure. *Pure and Applied Geophysics (PAGEOPH)* **158** (7).

Peter Marshall, Daniela Rozgonova, Wolfgang Weiss. (2001).Testing times: The road to a Comprehensive Nuclear-Test-Ban Treaty. Kerntechnik **66**, (3), 73-151.

Pilger, C., Ceranna, L., Bönnemann, C. (2017). Monitoring Compliance with the Comprehensive Nuclear-Test-Ban Treaty (CTBT). Schweizerbart Science Publishers, Stuttgart, Germany.

Ringdal, F., Kennett, B. L. N. (2001). Monitoring the Comprehensive Nuclear-Test-Ban Treaty: Source Location. *Pure and Applied Geophysics (PAGEOPH)* **158** (1/2).

SnT (2011 – 2023), CTBT: Science and Technology conference series, CTBTO https://www.ctbto.org/news-and-events/science-and-technology-conference.

Walter, W.R., Hartse, H.E. (2002). Monitoring the Comprehensive Nuclear-Test-Ban Treaty: Seismic Event Discrimination and Identification. *Pure and Applied Geophysics (PAGEOPH)* **159** (4).

CTBTO PREPARATORY COMMISSION

COMPREHENSIVE NUCLEAR-TEST-BAN TREATY ORGANIZATION